IMPERIAL

Monitoring breast tumour response to radiotherapy using super-resolution ultrasound and quantitative magnetic resonance imaging

Megan Celyn Morris

Department of Bioengineering

Imperial College London

This thesis is presented for the degree of

Doctor of Philosophy

27th June 2025

Abstract

Super-resolution ultrasound (SRUS), diffusion-weighted (DW), and dynamic contrast-enhanced (DCE) MRI can detect microenvironmental changes in tumours following treatment, with advantages over size-based methods for evaluating response. Assessing repeatability, prognostic value, and sensitivity of imaging biomarkers is critical for clinical translation.

Clinical data were collected from locally advanced breast cancer patients undergoing radiotherapy. Test-retest and longitudinal imaging assessments were conducted pre-radiotherapy, and at 2-weeks, 6-, 12-, and 24-months post-radiotherapy. Ultrafast contrast-enhanced ultrasound was used to generate 2D SRUS maps of microvascular structure and dynamics. DW-MRI analyses used mono-exponential and stretched exponential models, and DCE-MRI utilised Tofts modelling and non-parametric analysis. Quantitative parameters were extracted and evaluated. Radiological response was determined by expert breast radiologists. Biopsies from a subset of participants at baseline and 2-weeks post-radiotherapy were stained for CD31 and scored by a consultant breast histopathologist.

Repeatable and sensitive MRI response biomarkers included ADC from DW-MRI, reflecting changes in cellular density, and DCE-MRI parameters including K_{trans}, initial wash-in rate ($iWIR$), final wash-out rate ($fWOR$), and final wash-out AUC (AUC_{fWO}), which captured microvascular properties. ADC demonstrated the greatest sensitivity to early changes. DCE-MRI parameters were more informative for long-term monitoring, successfully detecting relapse nodules not evident on ADC maps. Trends showed non-responders at 12-months had higher pre-treatment ADC values and smaller post-treatment changes, and higher pre-treatment $iWIR$; though these trends did not reach statistical significance. SRUS-derived vessel density, vessel diameter, and blood velocity were repeatable and sensitive to early treatment changes. SRUS

vessel density did not correlate significantly with CD31 count.

This is the first study to utilise SRUS, DW-MRI, and DCE-MRI to monitor long-term response (> 6-months) of breast cancer post-radiotherapy. Imaging biomarkers demonstrated repeatability and sensitivity to early and late treatment changes. Variability in treatment regimens and a small cohort classified for radiological response introduced challenges in evaluating prognostic potential.

Statement of Originality

The work presented in this thesis is my own, and all else is appropriately referenced. In brief, patient recruitment and consent were carried out by the KORTUC trial team. MRI acquisition, SRUS acquisition, contrast injections, and biopsies were performed by the Royal Marsden radiology team and clinicians. The MRI protocol was developed by Matthew Blackledge. Some SRUS acquisition and processing scripts were developed by other members of the Ultrasound Laboratory for Imaging and Sensing (ULIS) team and are credited appropriately throughout the manuscript. Regions of interest (ROIs) for SRUS and MRI were created alongside Emily Durie and checked and modified by Victoria Sinnett and Nina Tunariu, respectively. The response assessment criteria were developed by Navita Somaiah and Emily Durie, and assessments were conducted by Seema Salehi-Bird, Nuala Healy, Archana Seth, and Steven Allen. Biopsies were processed by Selvakumar Anbalagan and Emily Durie and analysed by Ioannis Roxanis.

Copyright Declaration

The copyright of this thesis rests with the author. Unless otherwise indicated, its contents are licensed under a Creative Commons Attribution-Non Commercial 4.0 International Licence (CC BY-NC). Under this licence, you may copy and redistribute the material in any medium or format. You may also create and distribute modified versions of the work. This is on the condition that: you credit the author and do not use it, or any derivative works, for a commercial purpose. When reusing or sharing this work, ensure you make the licence terms clear to others by naming the licence and linking to the licence text. Where a work has been adapted,

you should indicate that the work has been changed and describe those changes. Please seek permission from the copyright holder for uses of this work that are not included in this licence or permitted under UK Copyright Law.

Acknowledgments

First and foremost, I would like to say a huge thank you to my supervisors, Mengxing Tang, Navita Somaiah, and Matthew Blackledge. Your guidance, support, and encouragement throughout this PhD have been exceptional. I feel incredibly fortunate to have been part of such an enriching project under your mentorship. I have learned so much from each of you, and your kindness and expertise have made this experience both rewarding and enjoyable.

I would also like to give a heartfelt thanks to the research groups that I had the privilege to be a part of: the Ultrasound Lab for Imaging and Sensing (ULIS) at Imperial College London, the Translational Breast Radiobiology group, and the Computational Imaging group at the Institute of Cancer Research. Special thanks go to Emily Durie, whose clinical insights were key in shaping this work. I really valued our time collaborating and the perspective you brought to this project. To Selvakumar Anbalagan, your advice, encouragement and timely snacks were always appreciated. Matthieu Toulemonde, thank you for getting my project off to such a smooth start. Our discussions were a big part of my learning and progress. Justine Hughes, Claire Lucy and Lone Gothard, working with you both was always a pleasure, and I always looked forward to our chats.

To the amazing clinical staff who offered their time and expertise, especially Victoria Sinnett, Nina Tunariu, Samantha Nimalasena, Julie Scudder, Tanja Gagliardi, Archana Seth, Nuala Healy, and Seema Salehi-Bird, thank you for your time, expertise, and for accommodating me despite your busy schedules. I learned so much from working alongside you. Thank you to the XNAT team, in particular Simon Doran, Thesha Thavaraja, and James D'Arcy for their support on the project and for getting the data together so quickly for analysis.

I owe so much to my family and friends for their support. Diolch yn fawr, Mam a Dad,

for making the final stretch so much easier with your care, understanding, and home-cooked meals. Your encouragement means so much to me. To my wonderful friends, thank you for cheering me on, even if you weren't quite sure what I was working on ("something important" is close enough!). Finally, to Shahzeb - thank you for being a source of calm during the stress and challenges. Your patience and belief in me is so appreciated.

This research project and MM is supported by the CRUK Convergence Science Centre at The Institute of Cancer Research, London, and Imperial College London (A26234). We acknowledge funding from Kortuc Inc., Japan, NHS funding to the NIHR Biomedical Research Centre at The Royal Marsden NHS Foundation Trust and the Institute of Cancer Research, the National Institute for Health Research (grant No. NIHR200972) and the ICiC and IAA funding from Imperial College. Thank you to the healthcare staff at the Rapid Diagnostic Centres at the Royal Marsden, and the patients who kindly agreed to participate in this study.

To everyone who has been part of this journey — thank you from the bottom of my heart.

Contents

1 Introduction **12**

1.1 Breast Cancer and Radiotherapy 12

1.1.1 Clinical Problem 12

1.1.2 Tumour Microvasculature 13

1.1.3 Radiotherapy and Hypoxia 14

1.2 Tumour Response Assessment 17

1.2.1 RECIST 1.1 17

1.2.2 Medical Imaging Biomarkers 18

1.2.3 Developments in Tissue Imaging 19

1.2.4 Developments in Microvasculature Imaging 21

1.3 Super-Resolution Ultrasound 24

1.3.1 Ultrasound Localisation Microscopy 25

1.3.2 Application 27

1.4 Diffusion Weighted MRI 29

1.4.1 Apparent Diffusion Coefficient 31

1.4.2 Intravoxel Incoherent Motion 32

1.4.3 Stretched Exponential Model 34

1.4.4 Repeatability and Reproducibility 34

1.4.5 Applications 35

1.5 Dynamic Contrast-Enhanced MRI 38

1.5.1 Accelerated Scanning Techniques 39

1.5.2 Quantitative Analysis 40

1.5.3 Non-Parametric Analysis 41
1.5.4 Parametric Modelling 42
1.5.5 Applications 44
1.6 Research Aims 46

2 Materials and Methods **49**
2.1 Clinical Trial 49
2.1.1 Study Design 49
2.1.2 Study Cohort 51
2.2 Super-Resolution Ultrasound 51
2.2.1 Participant Population 51
2.2.2 Ultrasound Equipment 53
2.2.3 Acquisition Settings 54
2.2.4 Patient Set-Up 55
2.2.5 Contrast-Enhanced Data Processing 58
2.2.6 SRUS Data Processing 63
2.2.7 Region of Interest 65
2.2.8 Quantitative Parameters 65
2.3 Diffusion-Weighted MRI 68
2.3.1 Participant Population 68
2.3.2 Patient Set-Up 69
2.3.3 Imaging Parameters 70
2.3.4 Image Pre-Processing 74
2.3.5 Region of Interest 75
2.3.6 Mono-exponential Model 75
2.3.7 Stretched Exponential Model 77
2.3.8 Repeatability 78
2.4 Dynamic Contrast-Enhanced MRI 78
2.4.1 Participant Population 78
2.4.2 Patient Set-Up 79

2.4.3 Imaging Parameters . . . 80
2.4.4 Region of Interest . . . 85
2.4.5 Image Processing . . . 85
2.4.6 Non-Parametric Analysis . . . 88
2.4.7 Parametric Analysis . . . 90
2.4.8 Repeatability . . . 92
2.5 Radiological Response Assessment . . . 92
2.6 Biopsies and Immunohistochemical Staining . . . 94
2.7 Statistical Analysis . . . 94
2.7.1 Repeatability . . . 95
2.7.2 Statistics . . . 97

3 Results Chapter 1: Super-Resolution Ultrasound 99
3.1 Repeatability . . . 99
3.2 Breast Tumour and Healthy Breast Tissue . . . 108
3.3 Response Assessment . . . 111
3.3.1 SRUS Quantitative Parameter Changes . . . 111
3.3.2 SRUS Quantitative Parameters and Radiological Response . . . 122
3.4 CD31 Vessel Count and SRUS Vessel Density . . . 129

4 Results Chapter 2: Diffusion-Weighted MRI 131
4.1 Repeatability . . . 131
4.2 Response Assessment . . . 135
4.2.1 Parameter Maps . . . 135
4.2.2 Changes in Signal Decay Curves . . . 137
4.2.3 Sensitivity to Post-Treatment Changes . . . 138
4.2.4 Pre-Treatment Values . . . 143
4.2.5 Whole Tumour Response Assessment . . . 143
4.2.6 Estimating Response . . . 147

4.2.7 Predictive Value of Baseline Measurements and Early Changes for Treatment Response . . . 148
4.3 Sub-Types . . . 151

5 Results Chapter 3: Dynamic Contrast-Enhanced MRI 153

5.1 Repeatability . . . 153
5.1.1 Tofts Model Parameters . . . 153
5.1.2 Piecewise Linear Model Parameters . . . 158
5.1.3 Semi-Quantitative Parameters . . . 162
5.2 Response Assessment . . . 166
5.2.1 Changes in Contrast Concentration Curves . . . 166
5.2.2 Sensitivity to Post-Treatment Changes . . . 167
5.2.3 Pre-Treatment Values . . . 179
5.2.4 Parameter Maps . . . 179
5.2.5 Whole Tumour Response Assessment . . . 184
5.2.6 Estimating Response . . . 197
5.2.7 Predictive Value of Baseline Measurements and Early Changes for Treatment Response . . . 205
5.3 SRUS and MRI Comparative Analysis . . . 210

6 Discussion 212

6.1 Super Resolution Ultrasound . . . 213
6.2 Diffusion-Weighted MRI . . . 220
6.2.1 Repeatability and Sensitivity . . . 220
6.2.2 Predictive and Longitudinal Trends . . . 221
6.2.3 Breast Cancer Subtype Analysis . . . 224
6.2.4 Technical Considerations and Limitations . . . 225
6.2.5 Other DW-MRI Techniques . . . 226
6.3 Dynamic Contrast-Enhanced MRI . . . 227
6.3.1 Repeatability and Sensitivity . . . 228

6.3.2 Predictive and Longitudinal Trends . . . 231
6.3.3 Technical Considerations and Limitations . . . 235

7 Conclusion **238**

A Results Chapter 2: Diffusion-Weighted MRI **277**

A.1 Repeatability . . . 277
A.2 Response Assessment . . . 281
A.2.1 Sensitivity to Post-Treatment Changes . . . 281
A.2.2 Whole Tumour Response Assessment . . . 284
A.2.3 Estimating Response . . . 287
A.3 Sub-Types . . . 288

B Results Chapter 3: Dynamic Contrast-Enhanced MRI **289**

B.1 Repeatability . . . 289
B.1.1 Tofts Model Parameters . . . 289
B.1.2 Piecewise Linear Model Parameters . . . 293
B.1.3 Semi-Quantitative Parameters . . . 299
B.2 Response Assessment . . . 305
B.2.1 Sensitivity to Post-Treatment Changes . . . 305
B.2.2 Whole Tumour Response Assessment . . . 320
B.2.3 Estimating Response . . . 340
B.3 Sub-Types . . . 346
B.3.1 Tofts Model Parameters . . . 346
B.3.2 Semi-Quantitative Parameters . . . 348

Chapter 1

Introduction

1.1 Breast Cancer and Radiotherapy

1.1.1 Clinical Problem

Breast cancer is the most commonly diagnosed malignancy in women worldwide. Almost every second, a patient is diagnosed with breast cancer, globally escalating to 2.3 million new cases each year [1], which accounts for over 10% of all newly diagnosed cancers.

In countries with sufficient public awareness, healthcare access, and national breast cancer screening programmes, most patients are fortunately diagnosed at an early stage (stages I and II). However, approximately 20% of breast cancer patients are diagnosed at late clinical stages (stages III and IV) in high-income countries [2–4]. This percentage rises to around 50% in low to middle-income countries and can reach up to 80% in some regions. A late-stage diagnosis presents significant challenges in patient management.

Locally advanced breast cancer (LABC) [5] is a type of late-stage breast cancer. LABC is a cancer that cannot be surgically removed without prior treatment, such as chemotherapy, hormone therapy, immunotherapy, or radiotherapy. A tumour is surgically unresectable if it has invaded nearby structures, such as the chest wall or ribs, making it impossible to completely remove during surgery, leading to an increased risk of postoperative recurrence. Patients may present with fungating breast tumours, where the cancer grows through the skin. These tumours often require frequent dressing changes due to discharge or bleeding, are prone to infection, can

cause pain, and significantly impact the patient's quality of life due to considerable morbidity [6].

Traditionally, breast cancer treatment involves surgical tumour removal followed by adjuvant[1] radiotherapy or chemotherapy, or in some cases, neoadjuvant chemotherapy. However, more trials are investigating and highlighting the benefits of neoadjuvant[2] radiotherapy [7]. This approach is an effective treatment for patients with LABC. Its primary objectives are to shrink the local disease, achieve long-term locoregional control, and alleviate or prevent patient suffering. In cases where a complete response is achieved, neoadjuvant radiotherapy may even eliminate the need for surgery.

1.1.2 Tumour Microvasculature

Normal breast tissue consists of mammary glands embedded within a fibrous and fatty connective tissue stroma. Its organised blood supply - comprising a hierarchical network of arteries, arterioles, capillaries, venules and veins - ensures the efficient delivery of oxygen, nutrients, and metabolites.

In contrast, breast tumours are highly cellular and characterised by abnormal microvasculature. Solid tumour formation begins with the transformation of undifferentiated cells into cancer cells, acquiring several characteristics known as the hallmarks of cancer [8, 9]. These cells sustain uncontrolled proliferation, forming a tumour that soon outgrows its blood supply. Angiogenic factors, HIF1-α, are released by cancer cells in response to increasing tissue hypoxia [10], triggering pathological angiogenesis [11–13]. Angiogenesis, the process by which new blood vessels form from pre-existing ones, is an early hallmark of cancer [9]. It ensures the tumour receives sufficient oxygen and nutrients to sustain its rapid growth.

Initially, tumour blood vessels form as 'mother vessels' [14], which develop from venules and capillaries through angiogenesis. These vessels are enlarged, tortuous, hyperpermeable, and prone to collapse. Over time, they evolve into more stable 'daughter vessels', including normal-like capillaries, glomeruloid microvascular proliferations (a tangle of tiny, hyperpermeable, poorly perfused vessels), and large vascular malformations. Additionally, larger tortuous blood

[1] Adjuvant therapy is an additional cancer treatment following the primary treatment, which is usually surgery, to reduce the risk of relapse.

[2] Neoadjuvant therapy is a cancer treatment given to shrink the tumour size prior to the primary treatment, which is usually surgery.

vessels develop through arteriogenesis and venogenesis, forming feeder arteries and draining veins to supply and drain the tumour. The larger, organised vessels are more stable than the smaller, disordered ones.

These tumour vessels display irregular diameters, tortuous paths, and chaotic branching patterns. Blood flow through these vessels is significantly reduced compared to healthy tissue, with perfusion being both spatially and temporally heterogeneous [15]. Blood velocity and flow paths are highly variable, with some vessels showing intermittent use or alternating flow directions [16, 17]. Additionally, tumour vasculature frequently forms arterio-venous shunts, further exacerbating inefficient blood delivery.

As a result, the tumour microvasculature is structurally and functionally disorganised and inefficient. Blood vessels branch chaotically, leading to heterogeneous tumour perfusion. Peripheral tumour regions typically exhibit a higher density of larger vessels, while central regions have a lower density of smaller vessels, resulting in chronic hypoxia. This lack of oxygen and nutrients causes cell death and the formation of necrotic cores. Paradoxically, the disorganised microvasculature supports the tumour's survival and progression [17, 18].

1.1.3 Radiotherapy and Hypoxia

During radiotherapy, a high dose of ionising radiation is deposited in the tumour, causing DNA damage and triggering cell death. For low-LET[3] radiotherapy, such as with X-rays, sufficient oxygenation within a solid tumour is crucial for an effective response [19]. However, due to the tumour's chaotic neovasculature, some regions may be viable but oxygen-deficient, i.e. hypoxic.

Chronic hypoxia arises from the large distances between the blood supply - which carries essential oxygen, nutrients and metabolites - and the tumour cells. In addition, some tumour regions may experience acute hypoxic due to intermittent blood flow, where blood vessels periodically open and close, for example, due to shunting or vessel collapse. The diffusion distance of oxygen in tissue typically ranges from 100-150 μm, as observed in experiments measuring the distance from necrotic areas to the nearest blood vessel [20].

Both chronic and acute hypoxia contribute to spatial and temporal heterogeneity of oxygen

[3]Linear energy transfer (LET) refers to the energy an ionising particle transfers to the matter it travels through, per unit distance.

levels within tumours. In normal tissues, oxygen concentrations, in terms of percentage oxygen ($\%O_2$), typically range between 5-8% O_2, whereas in tumours, this decreases to 1-4% O_2. Radiobiological hypoxia, the level of hypoxia associated with radioresistance, is defined as oxygen concentrations below 0.13% O_2 [21]. Hypoxic tumours are typically more aggressive and radioresistant, leading to poorer treatment outcomes, while well-oxygenated tumours tend to be more radiosensitive. It requires three times the dose of X-ray radiation to kill the same number of tumour cells in hypoxic conditions compared to normal oxygen levels [22].

The Oxygen Fixation Hypothesis explains the correlation between oxygen levels and a positive radiotherapy response [23]. During radiotherapy, ionising radiation can directly damage DNA. However, the most common form of DNA damage is indirect. The incident radiation interacts with molecules within the cell, producing reactive oxygen species (ROS), which are highly reactive free radicals. Free radicals have unpaired electrons and seek to neutralise their electronic charge by reacting with cellular components, including DNA [24], causing chemical bond breaks and biological damage. The hydroxyl radical, which forms from water molecules, is the most common ROS.

The damaging effect of ROS is mitigated by scavenging reactions involving antioxidant enzymes peroxidase and catalase, which inactivate the ROS, and the recruitment of repair enzymes when the cell detects damage. However, in well-oxygenated cells, the site of DNA damage becomes oxidised, preventing repair and leading to permanent oxidative DNA damage and subsequent cell death. In hypoxic environments, with insufficient oxygen availability, tumour cells become radioresistant, as oxidative DNA damage does not occur even with high-dose irradiation. Thus, oxygenation of a hypoxic tumour can increase its radiosensitivity [25].

Cancer cells may not be the only target of radiotherapy; research suggests that endothelial cells in the tumour vasculature may also be damaged [26,27]. Damaging the vasculature reduces blood perfusion and could enhance radiation-induced cell death by limiting the oxygen supply.

However, hypoxia can also increase, driving vasculogenesis, the formation of blood vessels from circulating endothelial progenitor cells [26, 27]. This process can restore blood flow in the radiation-damaged tumour to meet oxygen demands, allowing any remaining viable cancer cells to regrow into a recurrent tumour.

Radiosensitisers

The link between hypoxic tumours and radioresistance has driven significant research into developing effective radiosensitisation strategies, such as using radiosensitisers. Radiosensitisers are compounds or molecules designed to enhance tumour sensitivity to radiation while minimising damage to healthy tissue [28, 29]. There is an urgent need for a safe, effective, and affordable radiosensitising method for clinical use [30, 31], particularly for breast cancer.

Intra-tumoural hydrogen peroxide H_2O_2 is a promising radiosensitiser. Initial *in vitro* experiments involving H_2O_2 and radiation on radioresistant human cell lines demonstrated a significant increase in cell death compared to radiation alone [32–34].

Irradiation with H_2O_2 has been shown to increase reactive oxygen species (ROS) [35]. Antioxidant enzymes, peroxidase and catalase, tightly regulate intracellular ROS scavenging. However, the increased concentration of H_2O_2 can inactivate these enzymes through enzyme-substrate reactions, reducing the cell's ability to scavenge ROS.

Peroxidase and catalase degrade H_2O_2 into oxygen and water, which re-oxygenates the tumour. Increased ROS and oxygen levels result in oxidative DNA damage and enhanced cell death. Furthermore, an excess of H_2O_2 induces lysosomal membrane dysfunction due to its corrosive and toxic nature. This releases powerful oxidants, which damage mitochondria, ultimately leading to cell death [36, 37].

A clinically feasible, low-cost H_2O_2 radiosensitising treatment, known as KORTUC (Kochi Oxydol-Radiation Therapy for Unresectable Carcinomas) was developed [38, 39]. In this approach, a H_2O_2 solution is intratumourally injected under ultrasonographic guidance [39,40]. Sodium hyaluronate is added to the solution to extend the duration of oxygenation by increasing its viscosity and slowing the degradation of hydrogen peroxide [41]. This not only prolongs the radiosensitivity of the tumour but also reduces hydrogen peroxide-induced tissue inflammation and toxicity.

KORTUC has been demonstrated to be safe when used alongside low-LET radiotherapy for treating various tumours, including breast cancer, with only mild side-effects including discomfort at the injection site [40, 42–44]. Due to its low cost and ease of manufacture and storage, it holds particular promise for use in developing countries. The first randomised Phase II

trial comparing radiotherapy alone versus radiotherapy combined with intratumoural KORTUC treatment is currently underway in the UK (clinicaltrials.gov NCT 03946202).

1.2 Tumour Response Assessment

The non-surgical treatment of breast cancer with radiotherapy presents a unique challenge in effectively monitoring the patient's response. Given that these patients may have life expectancies of several years, it is crucial to track how the breast tumour changes over time after treatment. Early detection of treatment response, resistance or relapse would enable timely adjustments to the treatment plan, helping to prevent disease progression.

1.2.1 RECIST 1.1

The current radiological gold standard for monitoring the response of solid tumours to treatment is the measurement of tumour size, using criteria such as RECIST[4] 1.1. [45]. RECIST measurements typically use CT or MRI scans with intravascular contrast agents to highlight the tumour. In follow-up scans, the longest diameter of the tumour is measured and compared to the baseline and/or the nadir measurement of the longest diameter. In brief, a complete response is when the tumour completely disappears; a partial response is a reduction greater than 30%; stable disease means no significant change and progressive disease is defined by an increase of more than 20% or the appearance of new lesions. Tumour shrinkage is used as an indicator of the effectiveness of cytotoxic therapies, as it typically reflects a reduction in the number of cancer cells.

While RECIST provides a standardised method for tumour measurement, it has faced significant criticism [46, 47]. Key concerns include high inter- and intra-observer variability, both within the same scan and across repeat scans. Such variability makes it difficult to reliably distinguish actual changes over time.

One-dimensional size measurements fail to capture the full complexity of tumour morphology and biological heterogeneity. These measurements can underestimate treatment response

[4]RECIST: Response Evaluation Criteria In Solid Tumours.

or fail to detect recurrence, as they do not account for tumour viability or microenvironmental changes, which often precede size alterations. This limitation is particularly problematic in solid tumours, such as breast cancer, treated with radiotherapy, where stromal fibrotic reactions, such as tissue thickening and scarring, can mimic residual enhancing lesions on standard imaging [48–51]. Moreover, unidimensional measurements are less reliable for irregular or asymmetric tumours and tumours curving along anatomical structures like the chest wall.

Solid in-situ tumours treated with radiotherapy may undergo structural and metabolic changes, such as tumour necrosis and microvascular disruption, without significant tumour shrinkage. Challenges like pseudo-progression [52], where a tumour initially grows or stabilises before eventually shrinking due to inflammation caused by an immune response, further complicate morphological evaluation. These limitations of size-based criteria have prompted adaptations that include alternative biomarkers of viable tumour regions, such as intratumoural enhancement, to assess treatment response more accurately. These shortcomings highlight the need for more sensitive clinical imaging tools that investigate the tumour microenvironment. Such tools could enable the early detection of treatment responses, resistance, or relapse before measurable changes in tumour size occur, ultimately leading to improved patient outcomes.

1.2.2 Medical Imaging Biomarkers

Medical imaging biomarkers have become indispensable tools for quantitatively evaluating tumour response to treatment in clinical trials and routine cancer care [47]. By enabling the detection of early pathological changes, often preceding clinical detection, these biomarkers serve as valuable predictors of treatment efficacy. They can assist clinicians in monitoring tumour regression or progression over time. Beyond response assessment, imaging biomarkers can act as predictive classifiers, allowing for personalised treatment strategies and thereby optimising therapeutic outcomes.

Measuring the entire tumour volume is one approach, requiring imaging modalities and sequences with high 3D spatial resolution to capture subtle morphological changes [53, 54]. Functional and metabolic imaging techniques further enhance tumour evaluation by detecting microscopic changes in the microenvironment, addressing critical aspects of tumour biology.

Voxel-wise[5] parametric maps derived from functional and metabolic imaging provide detailed visualisation of tumour heterogeneity, overcoming the limitations of averaged parameter values that may obscure significant variations within the tumour. This approach is particularly valuable for assessing tumour aggressiveness and understanding the microenvironment's role in treatment response.

To facilitate the integration of imaging biomarkers into routine practice, standardisation of imaging protocols and techniques is essential. Additionally, establishing correlations between imaging findings, pathological complete response, and survival outcomes will be critical for their clinical adoption.

1.2.3 Developments in Tissue Imaging

A range of imaging techniques have been developed for both research and clinical settings, to extract quantitative parameters that characterise cancer biology and response to treatment.

Positron emission tomography (PET) uses intravenously injected radiolabelled tracers to quantitatively assess tumour metabolic activity, including glucose metabolism, proliferation [55], hypoxia [56], and apoptosis [57]. These tracers are biologically active molecules labelled with positron-emitting radioisotopes such as fluorine-18, oxygen-15, carbon-11, or nitrogen-13, which bind to specific targets depending on the imaging application. PET imaging detects the radioactivity emitted by the tracers, and the degree of their uptake provides a quantitative measure of the biological process under investigation. By mapping metabolic activity, PET imaging can identify spatially localised treatment response or tumour recurrence [58, 59].

MRI techniques provide important information about tissue composition and structure. In simple terms, MRI uses a strong magnetic field to align hydrogen protons within tissue. A radiofrequency (RF) pulse is then applied, which excites the protons and causes them to move out of alignment with the magnetic field and into phase with each other. As the protons relax back to their original alignment, they release RF energy, which is detected by receiver coils. Different tissues release RF energy at different rates, i.e. they have varying relaxation times, which creates contrast in MRI images.

[5] A voxel is a 3D equivalent of a pixel, representing a value on a regular grid in 3D space.

During relaxation, two key parameters are considered. The longitudinal relaxation time (T1) measures how quickly longitudinal magnetisation recovers as protons realign with the magnetic field. T1 relaxation occurs through energy transfer between protons and their surroundings. The transverse relaxation time (T2 and T2*) measures how quickly transverse magnetisation decays as protons fall out of phase with each other. T2 relaxation occurs through energy transfer between neighbouring protons, and T2* relaxation includes T2 relaxation and additional dephasing caused by magnetic field inhomogeneities, which is potentially reversible. T1 relaxation times are generally longer than T2 relaxation times.

T1- and T2-weighted images are generated by adjusting imaging parameters such as repetition time (TR), the time between successive RF excitation pulses, and echo time (TE), the time between the RF excitation pulse and the peak of the collected echo signal. Image contrast is also influenced by manipulating pulse sequences, such as the application of refocusing pulses.

In T1-weighted imaging, contrast is primarily determined by differences in T1 relaxation times, which requires a short TR and short TE. Tissues with short T1 times, such as fat, appear bright, while fluid has long T1 times and appears dark. In T2-weighted imaging, contrast is primarily determined by differences in T2 relaxation times, which requires a long TR, a long TE, and refocusing pulses to minimise dephasing from the additional T2* relaxation effects. Tissues with long T2 times, such as fluid and inflammation, appear bright.

MRI techniques can image hypoxia or tissue oxygenation levels by exploiting the paramagnetic properties[6] of dissolved oxygen and deoxyhaemoglobin, which reduces T1 and T2* relaxation times [60]. Oxygen-enhanced (OE) MRI primarily focus on changes in T1 relaxation caused by dissolved oxygen after 100% oxygen inhalation, while blood oxygenation level-dependent (BOLD) MRI examines T2* relaxation, which is sensitive to the concentration of deoxyhaemoglobin.

Diffusion-weighted (DW) MRI is widely used to gain valuable insights into tissue microstructure that are not given by conventional MRI techniques. It is highly sensitive to the diffusion of water molecules in tissues; in highly cellular environments, such as tumours, diffusion is often restricted due to densely packed cells. Quantitative diffusion-weighted biomarkers, such

[6]Paramagnetism is the weak attraction of a material to a magnetic field, due to an unpaired electron aligning with the field.

as the Apparent Diffusion Coefficient (ADC), are used to assess the degree of water diffusion. Low ADC values typically indicate restricted diffusion, which is characteristic of tissues with high cellularity. ADC measurements can also provide an indication of treatment response by detecting changes in water diffusion associated with cell death. DW-MRI and the role of ADC will be discussed further in Section 1.4.

1.2.4 Developments in Microvasculature Imaging

A promising microenvironmental target for cancer therapy is the tumour microvasculature. Chronic and acute hypoxia, resulting from disorganised microvasculature, is linked to poor patient outcomes [61], as it correlates with resistance to cytotoxic therapies such as chemotherapy [62], radiotherapy [63], and immunotherapy [64].

The microvasculature provides critical insights into tumour aggressiveness [65], demonstrates both diagnostic [66] and prognostic potential [67], and plays a pivotal role in monitoring tumour response to therapy [68, 69].

Tumour-associated microvascular abnormalities have already developed in millimetre-scale tumours [70], suggesting that imaging the microvasculature of suspicious lesions can detect and characterise disease in its earliest stages. The tumour microvasculature can guide therapeutic stratification, enabling personalised treatment approaches [71]. Early detection of pathological responses to treatment can predict outcomes, identify non-responders [72], and minimise unnecessary toxicity while allowing timely therapeutic adjustments. Therefore, visualising the structure and dynamics of the tumour's blood supply is critical.

To achieve this, clinical microvasculature imaging technologies are necessary, along with accurate cancer biomarkers. Functional perfusion imaging modalities, such as dynamic contrast-enhanced (DCE-) magnetic resonance imaging (MRI) and computed tomography (CT), fluorodeoxyglucose (FDG-) positron emission tomography (PET), and Doppler ultrasound, have been developed and are widely used in clinical practice and tumour management [73,74], helping bridge the gap between tumour size and biology [75].

However, these imaging methods provide only surrogate measures of microvascular structure

and perfusion due to limitations in spatial and temporal resolution[7] The image voxels typically exceed 100 μm, while the microvasculature is often smaller than 100 μm [76, 77], and blood flow is slower than the imaging frame rate. High background noise further complicates the quantification and assessment of structural and functional metrics at the single-voxel level, rendering them difficult and unreliable.

Alternative imaging techniques with higher spatial resolution, capable of resolving the microvasculature, either require biopsies (e.g., *ex vivo* histopathology and micro-CT), sacrificing dynamic information, or offer limited imaging penetration depth (e.g., optical imaging modalities such as intravital microscopy, optical coherence tomography, photoacoustic imaging, and laser Doppler) but can assess blood flow [78–80]. These methods have small fields of view, with coherent light penetration limited to approximately 1 mm in tissues, providing only a snapshot of the larger tumour. To clinically examine microvasculature, an *in vivo* vascular imaging tool with improved resolution, a larger field of view, and ideally non-invasive, non-ionising, and non-toxic, is required [81].

Doppler ultrasound imaging is a contrast-free technique sensitive to blood perfusion. Using high-frequency ultrasound transducers, it detects the motion of red blood cells, which act as acoustic scatterers. Advanced Doppler ultrasound systems, such as ultrafast plane-wave Doppler imaging, have enhanced sensitivity to smaller, slower-flow vessels. However, they still encounter challenges detecting blood vessels smaller than 100 μm in diameter [82]. These limitations arise from the slow velocities of blood flow in microvessels, reduced amount of red blood cells traversing them, and weak ultrasound scattering. These factors make it challenging to distinguish microvessels from surrounding tissue motion. Additionally, increasing the frequency improves the resolution for detecting small structures; however, it reduces penetration depth, making it suitable primarily for superficial organs. The probe's alignment relative to the direction of blood flow influences Doppler velocity methods.

[7] Spatial resolution is the smallest physical area a system can differentiate; higher spatial resolution means finer detail and smaller features can be observed. Temporal resolution is the frequency at which data is collected over the same area; higher temporal resolution means data is collected more frequently.

Contrast-Enhanced Ultrasound

Contrast-enhanced ultrasound (CEUS) is a clinically established technique that enhances conventional ultrasound imaging by improving blood contrast [83, 84]. CEUS uses ultrasound contrast agents composed of gas-filled microbubbles encapsulated in a lipid shell, similar in size to red blood cells, with mean diameters of less than 5 μm. These microbubbles are administered intravenously and circulate throughout the vascular system, enhancing the visualisation of blood flow within the ultrasound field. Their small size allows them to traverse even the smallest microscopic blood vessels ($\sim 5\mu$m with slow flow velocities that are otherwise undetectable using conventional non-contrast ultrasound techniques, such as Doppler imaging. However, their size is sufficient to prevent them from permeating out of the vasculature.

Microbubbles scatter ultrasound energy strongly, partly due to the large reflection coefficient between air and water. More importantly, they resonate at frequencies within the clinical ultrasound range (MHz). When exposed to these frequencies, microbubbles undergo strong oscillations, causing them to scatter ultrasound nonlinearly and generate high harmonics. This non-linear scattering behaviour distinguishes microbubbles from tissue, which linearly scatters ultrasound.

Microbubble signals can be captured using B-mode imaging[8] and further refined through advanced processing techniques, such as spatiotemporal filtering (e.g., singular value decomposition, SVD), to separate static or slowly moving tissue from flowing microbubbles. Additionally, significant advancements have been made in contrast-enhanced imaging by leveraging the non-linear scattering properties of microbubbles [85–90]. Techniques like multi-pulse sequences, including pulse inversion and amplitude modulation, suppress linear tissue signals while enhancing non-linear microbubble signals, thereby improving imaging sensitivity and specificity.

CEUS provides both morphological and functional perfusion information about the microvasculature [91–96]. Tumour vascularity is assessed by analysing the area of the microbubble signal in the maximum intensity projection. However, due to the point spread function (PSF)[9]

[8]Brightness (B-) mode ultrasound imaging provides a greyscale tissue image. It works by emitting sound waves and capturing their echoes, with the brightness of each pixel representing the intensity of the echo.

[9]The Point Spread Function (PSF) in ultrasound describes how a point source is spread out in the resulting

of the ultrasound system, the apparent size of the microbubbles is significantly larger than their actual micron-scale size. This prevents CEUS from fully resolving the microvascular network, leading to an overestimation of tumour vascularity [97–100].

The spatial resolution of conventional ultrasound imaging is diffraction-limited, preventing the separation of sources closer than half the wavelength of the transmitted pulse due to interference from scattered ultrasound. Even with high-frequency probes, resolution is typically constrained to around 100 μm at the expense of penetration depth. However, the microvasculature includes vessels smaller than 100 μm. Factors such as transducer aperture and imaging depth further affect resolution.

Functional vascular information is derived by analysing replenishment kinetics from time-intensity curves [101, 102], which can detect decreases in tumour vascularisation and perfusion following treatment. However, this approach is often limited to global interpretations of vascular perfusion rather than voxel-wise analysis due to high background noise [98, 103, 104].

Ultrasound offers a large penetration depth, reaching several centimetres, which allows CEUS to visualise the microvasculature of deep-seated organs effectively. It is FDA-approved for cardiac and liver imaging in the United States and is widely approved in Europe and Asia for various clinical applications. CEUS is a low-cost, safe, and portable imaging technology, making it highly accessible and versatile in clinical practice.

1.3 Super-Resolution Ultrasound

Super-Resolution Ultrasound (SRUS) is a cutting-edge imaging technology that revolutionises ultrasound by achieving microvascular resolution down to tens of micrometres while maintaining a large field of view. By utilising advanced post-processing algorithms, SRUS overcomes the spatial resolution limitations of contrast-enhanced ultrasound, enabling detailed visualisation of microvascular structures at sub-wavelength scales [100, 105–107].

image, reflecting the system's resolution and image quality. A narrower PSF indicates better resolution, while a wider PSF leads to blurring.

1.3.1 Ultrasound Localisation Microscopy

A sub-division of SRUS, Ultrasound Localisation Microscopy (ULM), is inspired by super-resolution fluorescence microscopy techniques [108–110]. ULM uses algorithms to localise and track microbubble contrast agents across multiple imaging frames, reconstructing microvascular structures with microscopic precision. This allows for quantifying vascular features like structure, organisation, and blood velocities.

SRUS-ULM achieves a tenfold improvement in spatial resolution, reaching approximately 10 μm [111], while maintaining a clinically useful large field of view for imaging entire organs. By detecting and tracking isolated microbubbles, SRUS-ULM enables non-invasive, high-resolution visualisation of microscopic blood vessels ($< 10\mu$m).

Isolation

To generate SRUS-ULM images, isolated microbubble signals are crucial for accurate and precise localisation. When two microbubbles are closer than the diffraction limit, their signals overlap, making them difficult to distinguish. Achieving isolated signals requires careful control of microbubble concentration during injection. Although higher concentrations can reduce acquisition time for vessel saturation, they increase the likelihood of signal overlap.

In ultrasound images, diffraction-limited microbubble signals appear as circular blurs. These isolated signals can be identified based on distinct features, such as size, shape, and intensity [112]. Interfering microbubble signals, tissue clutter, and noise can be rejected by comparing the detected signals to the predefined microbubble characteristics.

Advanced detection strategies, including deep learning algorithms trained to recognise interference patterns of closely spaced microbubbles, have been developed. These methods allow for accurate and precise localisation of individual microbubble sources, even within the diffraction limit [113].

Localisation

After detecting isolated microbubble signals, the centre of each microbubble is estimated to correspond to the centre of the blur, assuming the image results from the convolution of

the original scatterer signal with the system's point spread function (PSF). By determining the system's diffraction-limited PSF and employing localisation methods such as centroid-based localisation or 2D Gaussian fitting [114], the position of each microbubble can be pinpointed with micrometric and sub-wavelength precision. Accumulating these accurately localised positions across multiple imaging frames enables the creation of a super-resolved map of the microvasculature.

However, localisation presents several challenges. Microbubbles may respond inconsistently to ultrasound, leading to signal variability - the onset localisation method [115] accounts for this variation, reducing localisation errors. Additionally, acquisition parameters can influence localisation precision [111], introducing errors and limiting achievable resolution.

Signal-to-noise ratio (SNR) also plays a crucial role in localisation accuracy. A higher SNR improves microbubble isolation and localisation precision by reducing noise, which can otherwise obscure or mimic microbubble spatial features. Advanced denoising methods, such as the non-local means (NLM) filter [116], leverage spatial and temporal information to effectively distinguish microbubble signals from noise, further enhancing localisation outcomes.

Tracking

To generate SRUS-ULM images, hundreds or even thousands of frames are acquired at conventional (<100 Hz) or high-frame rates. High temporal resolution is essential for capturing dynamic processes. Microbubbles are tracked across frames as they flow through the microvasculature, creating super-resolved maps of blood flow direction and velocity [112]. Using high-frame rate plane-wave imaging [117–119], even very slow blood velocities in a single vessel can be tracked.

Tracking algorithms often begin by defining a search window based on the maximum distance a microbubble could travel, determined by its maximum speed. Maximum intensity cross-correlation can match the microbubble in the next frame based on similar features to resolve the trajectory. More advanced algorithms have been developed to enhance tracking precision [107], such as a Kalman motion model [120].

The directional maps generated from this tracking provide valuable insights into the mi-

crovascular structure, enabling the distinction of closely spaced blood vessels, revealing branching patterns, and detecting opposing blood flow directions within the same vessel. These tracking algorithms also resolve the velocity of individual microbubbles, allowing for accurate measurements of a wide range of blood flow speeds.

Other Considerations

Long acquisition times are crucial for adequately sampling the microvasculature, especially for visualising the smallest vessels where blood velocities are slow. Moreover, since blood flow in tumours fluctuates continuously, longer acquisition times can capture these dynamic changes.

The accuracy of the final super-resolution image depends significantly on the motion correction technique. Even minor motion artefacts can degrade the precision of microvessel mapping, leading to errors in the order of tens of microns by losing overlap with vessels, which may cause an increase in vessel size or split vessels, or by imaging a different plane. Therefore, ensuring precise motion compensation is essential to maintain the spatial resolution of microvascular structures in the final super-resolved image.

Due to the promising clinical potential, the SRUS technique has quickly gained interest and has been demonstrated and validated in phantom experiments [121–123]. The SRUS technology, from acquisition to post-processing, is continuously being developed and optimised for complex cases, aiming to improve image quality and computational speed [112] [124–144].

1.3.2 Application

Since the initial demonstrations of super-localisation [100, 105, 122, 123] and super-resolved flow velocity mapping [112, 124], SRUS has gained significant interest as a powerful tool for investigating diseases such as cancer. It has evolved beyond proof-of-principle and is now used to study cancer in pre-clinical [145–147] and clinical settings [119, 131, 137, 148, 149]. This technique has promise in oncology, providing valuable insights into tumour microvasculature and response to therapy. SRUS can generate high-resolution 3D reconstructions of the microvasculature and track blood velocities, making it a potential imaging tool for cancer diagnosis, prognosis, and monitoring therapy responses.

Quantitative Parameters

SRUS imaging enables the extraction of quantitative parameters from microvascular reconstructions, providing valuable structural and functional data that serve as diagnostic, prognostic, and response biomarkers, such as vascular density, tortuosity, distance to the closest vessel, local flow direction entropy and blood velocity.

Vascular density is a critical parameter, assessed by calculating the percentage of pixels in the tumour region through which microbubbles pass [93, 131]. Tumour tissue typically exhibits higher vascular density compared to healthy tissue [93]. Furthermore, vessel density measurements indicate the oxygenation status of tumours, as hypoxia is strongly dependent on vascular supply.

Tortuosity, a key morphological feature of tumour vasculature, can be quantified using distance metrics (DMs) and sum of angles metrics (SOAMs) [150]. The microvessel centreline is extracted using a segmentation algorithm [151]. DMs are calculated by dividing the vessel length by the straight-line distance between endpoints; values near 1 indicate a straight vessel, while higher values suggest greater tortuosity. The SOAM is calculated by integrating the angles between successive points along the vessel's centreline, then normalising by vessel length. DMs are more effective for arching curves, while SOAMs are sensitive to high-frequency variations in curvature. Studies have shown that microvascular tortuosity is significantly higher in tumour tissue, with greater vascular heterogeneity, compared to healthy tissue [91, 93]. Tortuosity decreases with distance from the tumour but remains higher in surrounding tissue than in healthy tissue [94], indicating that tumours impact the surrounding tissue vasculature.

Other useful metrics include distance-to-closest-vessel maps, which reveal microvascular organisation [131]. Short distances and high vessel densities are characteristic of tumours with a homogeneously distributed network of microvessels, indicative of immature neovasculature. In contrast, large distances and lower densities suggest less vascularised tumours with large non-perfused areas, indicative of a more mature neovasculature. A mixture of small and large distances reflects a heterogeneous vascular network with highly and poorly vascularised regions.

Local flow direction entropy quantifies the degree of order or disorder within the microvascular network [131]. In healthy tissue, where blood flow follows more organised, predominant

directions, entropy values tend to be low. In contrast, tumours, characterised by more chaotic blood flow, display higher entropy values.

Blood velocity can also be studied, with velocities in the capillaries typically on the order of mm/s. Blood velocities can be divided into high and low groups, with the mean velocity value as the threshold, separating inflow (arteries) from outflow (veins) [131].

Biomarkers should be capable of differentiating tumour microvessel patterns from surrounding tissue. SRUS imaging has shown promise in classifying lesions based on their vascular phenotypes [145, 149, 152], and providing quantitative measures of haemodynamics and surrogate biomarkers for intra-tumoural oxygenation to assess hypoxia status [147]. Robust and precise parameters are necessary when measuring response to therapy. Therefore, validating predictive biomarkers is crucial for developing a reliable clinical assessment tool. These response biomarkers should indicate increases or decreases in abnormal vascularity and shed light on the effects of therapy on the microvasculature.

For example, SRUS imaging identified changes in perfusion and blood flow direction prior to any changes in tumour size following neoadjuvant chemotherapy for breast cancer [131].

1.4 Diffusion Weighted MRI

Diffusion-weighted MRI (DW-MRI) is a powerful technique for both qualitative and quantitative cancer imaging, commonly used for diagnostics and monitoring treatment response [153]. Its utility is recognised in clinical trials for assessing tumour response to therapies across numerous cancer types and treatments.

Diffusion refers to the random thermal motion of molecules in a system. In a simple medium like pure water, molecules diffuse randomly and isotropically. However, in biological tissues, there are obstacles. The mobility of water molecules provides valuable insights into tissue architecture at the microscopic level [154].

Broadly, tissue microstructure consists of three main components: the extracellular-extravascular space, the intracellular space, and the intravascular space. Water molecules diffuse relatively freely through the extracellular-extravascular space in environments with sparse cel-

lular density. However, diffusion is more restricted in highly cellular environments due to the abundance of cell membranes, which obstruct water movement [155]. Water molecules in the intravascular space of microvessels experience a different form of motion, termed *pseudo-diffusion* or perfusion. This movement is driven by blood flow, with longer diffusion distances dependent on blood velocity and the vascular architecture [156].

DW-MRI captures the displacement of water molecules over distances of approximately 1 to 20 μm (for reference, the average size of human cells is around 10 μm), before they encounter structural barriers such as cell membranes, fibres, or macromolecules. As a result, DW-MRI is sensitive to tissue microstructural properties at the cellular spatial scale, such as cell density, membrane integrity and vascularity. Image contrast arises from variations in water diffusion. By analysing the different diffusion characteristics, advanced imaging and modelling techniques can distinguish information from the tissue and intravascular space [156].

To capture diffusion information, diffusion-sensitising gradients are added to standard MRI sequences, typically along three orthogonal directions, to investigate water diffusion along each gradient axis. The geometric average of the diffusion signals is calculated to generate *trace* weighted images.

For example, in a T2-weighted spin-echo sequence – where a 90° radiofrequency pulse is followed by 180° radiofrequency refocusing pulses – equal amplitude de-phasing and re-phasing gradient pulses are symmetrically applied on either side of the 180° pulse. This is known as the Stejskal-Tanner pulsed gradient spin echo sequence. The de-phasing gradient introduces position-dependent phase shift in protons, while the re-phasing gradient attempts to reverse these shifts. If water molecules move in the time between the two gradient pulses, the re-phasing gradient will not completely reverse the changes, as the water protons are subjected to different field strengths. Water molecules in restricted environments return closer to their initial state, while water molecules with greater freedom of movement will experience more significant phase shifts. In a diffusion-weighted image, restricted, cell-dense areas will appear bright, while less restricted, cell-sparse areas will appear darker due to greater signal attenuation. However, image contrast may also arise from T1 or T2 relaxation effects from the MR sequence.

The degree of diffusion weighting applied by the diffusion-sensitising gradient pulses is

quantified by the *b-value*. The b-value (s/mm^2) depends on several parameters, including the strength (G) and duration (δ) of the de-phasing and re-phasing diffusion gradients, as well as the time between them (Δ), as defined by the following equation:

$$b = \gamma^2 G^2 \delta^2 (\Delta - \frac{\delta}{3}), \tag{1.1}$$

where γ is the gyromagnetic ratio of hydrogen protons (42.58 MHz/T). Higher b-values increase sensitivity to diffusion, resulting in greater signal attenuation in cell-sparse areas, and enhances tissue contrast based on differences in water mobility. Therefore, DW images with high b-values highlight cell-dense tissues more prominently.

One of the key advantages of DW-MRI is that it provides high image contrast without the need for externally administered contrast agents, making it a non-invasive technique. It also offers short scan times, typically lasting just a few minutes depending on the number of b-values, and is relatively easy to implement in routine clinical practice [157].

1.4.1 Apparent Diffusion Coefficient

Water diffusion in tissue is quantified in DW-MRI using the Apparent Diffusion Coefficient (ADC) [155]. ADC reflects the net diffusion pattern of water molecules within each voxel. This diffusion pattern directly influences the degree of signal attenuation, and the ADC is calculated using the mono-exponential Stejskal-Tanner equation:

$$\frac{S(b)}{S_0} = e^{-b \cdot ADC} \tag{1.2}$$

where:

- b (s/mm^2) is the b-value, the degree of diffusion weighting applied by the diffusion-sensitising gradient pulses,
- $S(b)$ represents the signal intensity after applying diffusion weighting,
- S_0 is the signal intensity without diffusion weighting (b = 0 s/mm^2), and

- ADC (mm^2/s) is the Apparent Diffusion Coefficient, a quantitative measure of water diffusion in tissue.

ADC maps are generated by acquiring diffusion-weighted volumes with at least two different b-values, achieved by varying the strength of the diffusion-weighting gradients. The ADC valued for each voxel is then inferred by plotting the logarithm of the relative signal intensity $\ln(\frac{S(b)}{S_0})$ against the corresponding b-values. The slope of this plot provides the ADC, and the more b-values used, the more accurate the estimation of ADC becomes. A steep slope of signal loss would represent a high ADC value and vice versa.

For clinical DW-MRI, b-values typically range between 0 and 1000 s/mm^2. ADC maps provide image contrast that reflects differences in diffusion properties, eliminating the influence of T1 or T2 relaxation effects from the underlying MR sequence and the dependence on magnetic field strength.

ADC is defined as the average area a water molecule occupies per unit time, providing insights into tissue microstructure. ADC values are inversely correlated to cellularity [158] and the concentration of extracellular matrix proteins. In regions with restricted diffusion, such as areas with dense cellular structures - corresponding to a shallow slope of signal attenuation with increasing b-value - ADC values are lower. Conversely, regions with higher ADC values suggest increased water diffusion and appear brighter on ADC maps.

Since different choices of b-values investigate different underlying biological properties, multiple models have been proposed to capture this information, such as the bi-exponential and stretched exponential models.

1.4.2 Intravoxel Incoherent Motion

The relationship between signal attenuation and diffusion weighting is complex, particularly in highly-perfused tissues. Tumours with increased vascularity may have significant perfusion contributions to the diffusion measurements [159]. At low b-values (e.g., $0 - 100$ s/mm^2), rapid signal attenuation may primarily be caused by blood perfusion in the microcapillaries due to large molecular water movement [155, 160–162]. At higher b-values (> 100 s/mm^2), contribution to signal decay from smaller diffusion distances in tissue becomes more significant,

with perfusion effects vanishing. Consequently, diffusion coefficients may vary depending on the b-values used, with low b-values capturing perfusion-sensitive diffusion and higher ones reflecting perfusion-insensitive diffusion.

While ADC is conventionally calculated using a mono-exponential model across all b-values, this approach can overestimate tissue diffusion due to the confounding effects of perfusion. For example, in breast cancers, the high cellularity may result in low diffusion. At the same time, the increased vascularity may lead to higher pseudo-diffusion, both of which can influence the ADC values. Intravoxel incoherent motion (IVIM) analysis uses a bi-exponential function to separate tissue diffusion, given as:

$$\frac{S(b)}{S_0} = fe^{-bD^*} + (1-f)e^{-bD} \tag{1.3}$$

where:

- b is the diffusion sensitisation factor measured in s/mm^2,
- $S(b)$ represents the signal intensity after applying diffusion weighting,
- S_0 is the signal intensity without diffusion weighting ($b = 0$ s/mm^2),
- D^* (mm^2/s) is the pseudo-diffusion coefficient, a quantitative measure of water perfusion in the intravascular space,
- D (mm^2/s) is the diffusion coefficient, a quantitative measure of water diffusion in the tissue space, and
- f is the tissue perfusion fraction, a quantitative measure of the fraction of water perfusion, with values between 0 and 1.

For reliable estimation of perfusion parameters, many acquisitions at low b-values are necessary, as these are more sensitive to noise due to the rapid signal decay [163, 164]. In contrast, acquisitions at higher b-values require fewer acquisitions, as the signal decay is slower for the diffusion component at these values [165]. The IVIM model may be sensitive to other fluid flows, such as glandular secretions in breast tissue [166], which can also impact low b-value measurements.

1.4.3 Stretched Exponential Model

Describing the DW signal-decay curve using one or two diffusion coefficients may oversimplify the complex relationship between signal attenuation and diffusion weighting. The stretched exponential model, however, accounts for the continuous distribution of diffusion coefficients within each voxel, offering a more accurate representation of the underlying tissue heterogeneity [167]. This model is defined as:

$$\frac{S(b)}{S_0} = e^{-(b \cdot DDC)^{\alpha}} \tag{1.4}$$

where:

- b is the diffusion sensitisation factor measured in s/mm^2,
- $S(b)$ represents the signal intensity after applying diffusion weighting,
- S_0 is the signal intensity without diffusion weighting (b = 0 s/mm^2),
- DDC (mm^2/s) is the distributed diffusion coefficient, a quantitative measure of the mean water diffusion in tissue, and
- α is the intra-voxel diffusion heterogeneity index, with values between 0 and 1.

The heterogeneity index, α, does not have a direct biological interpretation related to tissue structure, but it may be sensitive to microstructural changes by quantifying tissue complexity. It is negatively correlated with diffusion heterogeneity, which refers to the degree of dispersion of diffusion coefficients in the distribution and represents how much the signal attenuation deviates from mono-exponential behaviour. A value of α close to 1 indicates a highly mono-exponential behaviour. This model is particularly advantageous because it does not require the predefined selection of the number of exponential components.

1.4.4 Repeatability and Reproducibility

Repeatability measures the consistency of results when the same experiment is performed under the same conditions, by the same person, and with the same equipment. Reproducibility

measures the consistency of results when the same experiment is performed under different conditions, by different people, or with different equipment.

In the clinic, ADC and its statistics have exhibited excellent repeatability unaffected by field strength and strong intra- and inter-operator reproducibility, with within-subject Coefficients of Variation (wCV) mostly under 10% across studies and Intraclass Correlation Coefficients (ICCs) greater than 0.9 [168–171]. As expected, the inter-observer variability was larger than the intra-observer variability [171–173]. Despite variability in intra- and inter-reader Regions of Interest (ROIs), the whole-tumour mean ADC remained robust and reproducible, emphasising the reliability of whole-tumour ADC measurements [169].

Repeatability within benign breast lesions was also investigated, revealing the highest repeatability and lowest wCVs within tissue diffusion parameters – specifically D from the bi-exponential model and ADC [174]. Both Distributed Diffusion Coefficient (DDC) and α were also repeatable. However, the pseudo-diffusion parameters derived from the bi-exponential model had the worst repeatability with high wCVs. Standardised protocols are required to ensure repeatability and reproducibility of DW measurements.

1.4.5 Applications

Diagnostics

DW-MRI is highly valuable in cancer detection and diagnosis. Solid malignant tumours have high cellularity and a small extracellular-extravascular space compared to benign lesions; therefore, water molecules are more restricted. As a result tumours typically exhibit lower ADC values [175–177], so ADC maps can differentiate between malignant and benign lesions, across 1.5 and 3 T scanners and different choices of b-values. Across 123 studies, the mean ADC value of malignant lesions was 1.03×10^{-3} mm^2/s, and the mean value of benign lesions was 1.50×10^{-3} mm^2/s [177].

Diagnostic performance of IVIM parameters to discriminate malignant and benign breast lesions is varied, with inconsistent results across studies. However, meta-analyses showed significantly lower D values and higher f values for malignant tumours than benign lesions, indicating greater cellularity and tissue perfusion, respectively [178]. Acquisitions at low b-values

can be used to identify malignancy and determine the therapy effect on the tumour vasculature. For example, in prostate, pancreatic and colorectal liver cancer, IVIM analysis revealed that the parameters associated with perfusion (or pseudo-diffusion) were lower compared to the healthy tissue [179–181].

DW-MRI and ADC maps can be employed within a multiparametric MRI protocol, alongside T1 and T2 weighted imaging to differentiate malignant and benign lesions, where the high-quality anatomical images are complemented by diffusion information to make an accurate clinical diagnosis [182].

Prognostics

Assessing ADC values to predict therapy response is crucial for individualising therapy regimes. Tumours with a high density of cancer cells exhibit low ADC values. Therefore, ADC can potentially serve as a prognostic surrogate marker, offering insights into cancer aggressiveness [183] and proliferation state [184].

Several studies have explored whether pretreatment ADC values can predict the pathological complete response (pCR) of breast cancer to treatment, though results have been inconsistent [185]. In neoadjuvant chemotherapy, a meta-analysis revealed that the pooled pretreatment mean ADC value of responders (0.98: 95% CI = [0.94, 1.03]) was lower than that of non-responders (1.05: 95% CI = [1.00, 1.10] $\times 10^{-3}$ mm^2/s) [185]. However, the groups had significant overlap, suggesting that ADC alone is insufficient for predicting pCR. Some studies within the meta-analysis reporting significant differences found that solid tumours with low pretreatment ADC values responded well to chemotherapy. Conversely, higher ADC values often indicated necrotic tumours, typically hypoxic, acidic and hypo-perfused – characteristics associated with resistance to chemotherapy [186]. However, for a study investigating breast cancer after neoadjuvant radiation, pathological responders exhibited higher median ADC values (0.87 [0.82-1.07]) compared to non-responders (0.77 [0.61-1.15]) [187].

Additionally, in breast cancer, there is no consistent evidence linking ADC values with tumour grade or stage [188], nor correlates been established between ADC and hormone receptor status [189].

Response Assessment

ADC values can detect early pathological changes induced by cytotoxic therapies before visible tumour size reductions. An increase in ADC shortly after treatment initiation (e.g., within 1 week) predicted a long-term positive response [190–192]. This makes ADC a promising early biomarker for differentiating responders from non-responders. DW-MRI has been widely used to monitor tumour response to chemotherapy [155, 193], where a significant increase in average ADC values typically correlates with effective treatment outcomes [194, 195]. Treatment-induced tumour cell death creates necrotic regions, increasing water diffusion due to the loss of cell membrane integrity and cell death, leading to higher extracellular extravascular space (EES) [196, 197]. While changes in ADC have been extensively studied in various solid tumours after radiotherapy, such as head and neck cancer [198], fewer studies exist for in-situ breast cancer.

In a murine breast cancer model, ADC values significantly and positively correlated with the percentage of apoptotic cells, and increases in ADC corresponded to decreases in cell nuclei [199]. For patients with early-stage, low-risk breast cancer, ADC changes after a single-dose preoperative radiotherapy regime have been explored. One study observed a decrease in ADC 1-week post-treatment, likely due to suboptimal dosing regimens [200]. Another study reported a median ADC increase of 32% at 1-week post-RT, rising to 53% by 6-months [187]. Pathological responders exhibited higher median ADC values compared to non-responders, with a 33% ADC increase at 1-week in responders compared to 23% in non-responders. By 6-months, responders had a 48% increase in ADC, whereas non-responders showed no significant change.

In a study of early-stage breast cancer patients receiving fractionated whole-breast irradiation, a 36% increase in ADC was observed 5 days post-radiotherapy, accompanied by a 47% decrease in the Ki-67 proliferation index [201]. A previous study has shown that ADC changes can be a surrogate marker for Ki-67 index alterations [202].

DW-MRI provides a non-invasive, quantitative approach to assessing tumour cellular density across the entire tumour, avoiding the sampling errors associated with biopsies, particularly in heterogeneous breast tumours with necrotic regions. Despite the promise of ADC as a

biomarker, there is a shortage of studies examining DW-MRI for response monitoring in in-situ breast tumours post-radiotherapy. A 2024 review identified only three relevant studies utilising ADC values to assess treatment response after neoadjuvant radiotherapy [203], which were explored above [187, 200, 201].

1.5 Dynamic Contrast-Enhanced MRI

Dynamic contrast-enhanced (DCE) MRI is a perfusion imaging technique essential in oncology to assess tumour vascularity, function, and potential damage after cancer treatment. The tumour microvasculature is affected by pathological neovascularisation, a factor often associated with tumour aggressiveness.

DCE-MRI involves continuously acquiring T1-weighted images before, during, and after intravenous injection of a paramagnetic gadolinium-based contrast agent. Gadolinium shortens T1, the longitudinal relaxation time, enhancing the MR signal within blood vessels. The resulting changes in signal intensity over time reflect the concentration of the contrast agent in the tissue. Analysing the contrast enhancement kinetics of each tissue voxel enables a detailed characterisation of tissue vasculature. These kinetics depend on tissue perfusion, capillary permeability, blood volume, and interstitial space.

In tumours, blood vessels tend to be hyperpermeable, facilitating the adequate delivery of nutrients and oxygen for tumour growth [204]. The parameters derived from the time-intensity curves of DCE-MRI reflect these physiological properties and are valuable for characterising tumours and monitoring their response to therapy.

To accurately assess the early post-contrast phase of the time-intensity curve in DCE-MRI, high temporal resolution is needed to capture the precise shape of the uptake curve. Furthermore, the initial arterial phase of contrast uptake can help distinguish enhancing breast lesions from background parenchymal enhancement. During this phase, contrast enhancement is most prominent within the tumour, while surrounding breast tissue shows minimal enhancement. This early distinction highlights tumour-associated vasculature and perfusion characteristics, while the slower, more diffuse perfusion of surrounding parenchymal tissue becomes apparent

in later phases of contrast uptake.

1.5.1 Accelerated Scanning Techniques

Given the need for both high temporal and spatial resolution and image quality (e.g., signal-to-noise ratio, SNR), MRI sequence parameters in DCE imaging must be optimised for accurate tumour characterisation. Temporal resolution is influenced by Repetition Time (TR) (the time between successive RF excitation pulses), with shorter TRs improving temporal resolution but potentially lowering SNR due to reduced signal intensity. The flip angle[10] also impacts temporal resolution, with smaller angles improving it but reducing SNR. Larger matrix sizes (the number of pixels along the rows and columns in a 2D MRI image) improve spatial resolution but may reduce temporal resolution, while a smaller Field of View (FOV) (the spatial extent of a 2D MRI image, which depends on the pixel and matrix size and is measured in millimetres) increases spatial resolution for a given matrix size but limits coverage. Slice thickness affects spatial resolution, with thinner slices improving detail but lowering SNR; a greater number of slices reduces temporal resolution but increases the 3D FOV. When kept short, Echo Time (TE) (the time between the RF excitation pulse and the peak of the collected echo signal) helps maintain temporal resolution and reduces motion artefacts, though it may compromise tissue contrast.

Advanced acceleration techniques have been developed to improve temporal resolution further. Ultrafast DCE-MRI scans can now achieve temporal resolutions of only a few seconds while maintaining sufficient spatial resolution for clinical use [205]. One such technique is *View-sharing*, which accelerates image acquisition by sampling and reusing portions of k-space data across different phases. k-space is a data space where raw MRI data (spatial frequency data) is collected before it is transformed into an image via the Fourier transform. The centre of the k-space contains low-frequency data, which captures the image's general brightness and overall structure. The periphery contains high-frequency data, which provides fine details and edges. Time-sensitive changes, such as contrast uptake, are updated more frequently, focusing on the

[10]The flip angle is the angle by which the net magnetisation of the hydrogen protons is rotated away from its equilibrium position, aligned with the main magnetic field, due to the application of a radiofrequency (RF) pulse. The flip angle is determined by the amplitude and duration of the RF pulse. For example, a 90° flip angle rotates the net magnetisation from the longitudinal axis into the transverse plane, while a 180° flip angle inverts the net magnetisation along the longitudinal axis.

central portion of k-space where most signal energy is concentrated [206]. Techniques include differential subsampling with Cartesian ordering (DISCO) and time-resolved angiography with interleaved stochastic trajectories (TWIST). Acceleration techniques are increasingly common in clinical practice as more MRI scanners support these advanced capabilities.

A standard error in quantitative analysis with the view-sharing technique is temporal blurring. Temporal blurring is an averaging effect when the k-space data is reused or interpolated across several phases. This averaging can obscure sharp, time-sensitive changes in contrast uptake, such as the initial enhancement or patient motion, causing a smearing effect and reducing the accuracy of dynamic measurements [206].

1.5.2 Quantitative Analysis

The signal intensities of DCE-MRI T1-weighted images can vary across scanners and acquisition settings. The signal intensity-time curve is converted into contrast agent concentration within the tissue to ensure accurate quantitative analysis that allows comparison across MRI parameters. The effect of the contrast agent on the longitudinal proton relaxation time, T1, depends on its concentration. In T1-weighted DCE-MRI, the signal is described by the following equation for a spoiled gradient echo sequence [207]:

$$S(t) = S_0 \frac{(1 - e^{-(TR/T1(t))}) \sin(\alpha)}{1 - \cos(\alpha) e^{-(TR/T1(t))}}, \tag{1.5}$$

where S_0 is the scaling factor, α is the flip angle, TR is the repetition time (msec), and $T1(t)$ is the longitudinal relaxation time at time t.

The native pre-contrast relaxation times $T1_0$ are most commonly calculated using the variable flip angle method. Two flip angles are used to determine $T1_0$ analytically. However, the dual-flip angle approach is sensitive to B1 inhomogeneities because variations in the B1 field can cause deviations from the intended flip angles, leading to inaccuracies in $T1_0$ quantification [208].

For a more accurate estimation of $T1_0$, multiple-inversion recovery sequences are acquired, though these have longer acquisition times. If multiple flip angles are acquired, non-linear regression can be applied to fit the data and estimate the $T1_0$ value, or Equation 1.5.2 can be

rearranged to produce a linear relationship, allowing for linear regression to determine $T1_0$.

$T1(t)$ is computed at all post-contrast phases. The contrast agent concentration as a function of time $C(t)$ can be derived from the change in $T1$ over time, as described by the following equation [209]:

$$C(t) = \frac{1}{r}(\frac{1}{T1(t)} - \frac{1}{T1_0}), \tag{1.6}$$

where r is the relaxivity of the contrast agent. $T1$ and concentration values are independent of the scanner and acquisition settings.

1.5.3 Non-Parametric Analysis

Contrast enhancement curves can be qualitatively and quantitatively assessed to evaluate contrast agent (CA) kinetics and infer perfusion properties. Measurements derived directly from the enhancement curve include:

- time-to-peak (TTP): time from contrast injection to the peak concentration
- peak enhancement (PE): the maximum concentration value over time
- final enhancement (fE): the concentration value at the last time-point
- wash-in rate (WIR): early phase contrast uptake - the gradient between the pre-contrast concentration to the peak enhancement (PE)
- wash-out rate (WOR): contrast clearance from the tumour - the gradient between the peak enhancement (pE) and the final enhancement (fE)
- area under the wash-in curve (AUC_{WI}): the area under the curve between the pre-contrast concentration to the peak enhancement (PE)
- area under the wash-out curve (AUC_{WO}): the area under the curve between the peak enhancement (pE) and the final enhancement (fE).

These curve classification measurements allow for non-parametric DCE-MRI analysis through straightforward calculations without complex modelling. While these parameters do

not directly measure the underlying physiology, they correlate with perfusion processes and require no prior assumptions [207].

Tumours can be classified based on their DCE time-signal or time-concentration curves. Malignant tumours typically exhibit a sharp initial rise in contrast uptake, peaking early, followed by a gradual decline (wash-out type). In contrast, benign tumours and healthy tissue show a steady and gradual increase in enhancement over time (persistent type). An intermediate pattern, characterised by an initial uptake followed by a stable phase (plateau type), may also be observed.

1.5.4 Parametric Modelling

Parametric or pharmacokinetic modelling provides a sophisticated method to analyse contrast concentration curves, aiming to extract biologically meaningful parameters that reflect the underlying tissue physiology. These parameters, such as capillary permeability, blood volume, and interstitial volume, offer insights beyond simple correlations. The choice of model depends on the application, such as the type of tissue or tumour under investigation, and is based on specific biological assumptions.

Arterial Input Function

A key requirement for pharmacokinetic modelling is the arterial input function (AIF), which represents the time-dependent contrast agent concentration in the blood plasma of a vessel supplying the tissue. Accurate determination of the AIF is essential for model reliability and can be achieved through various methods [207].

The AIF can be determined by direct measurement, analysing blood samples taken at frequent intervals to determine contrast concentration [210]. While highly accurate, this method is invasive and impractical in clinical settings. Population averages have been proposed from this method [211], but it may suffer from variability in injection rates, doses, and individual patient responses.

Other methods include analysing the time-intensity curve of a large artery feeding into the tissue of interest [212]. However, this large artery may not be present in the imaging

field of view, and the technique requires high temporal resolution. Parameters describing the AIF can be estimated alongside the pharmacokinetic parameters during the model fitting of the concentration curve [213], which decreases the bias and uncertainty in pharmacokinetic parameters but at a higher computational cost. Another approach is to use single or multiple reference tissues with known kinetic parameters [214,215] to derive the AIF; however, this does not consider the inter-patient variability of the reference tissue. The AIF is assumed to be the same throughout the patient.

Compartmental Models

Compartmental models describe the diffusive contrast exchange between the microvasculature and the tissue space [207]. The two-compartment model is the most used model due to its simplicity and its small number of parameters to be estimated. The model consists of an intravascular (plasma) and an extravascular-extracellular compartment. It depends on and quantifies vascular properties such as blood vessel perfusion and permeability and the volume of the extravascular-extracellular space (EES).

The AIF describes the influx of contrast agent into the intravascular compartment. Volume transfer constants describe the contrast exchange rates between the plasma and EES, and their values are related to vascular permeability. An excretion rate describes the loss of contrast from the intravascular compartment. The compartments are assumed to be homogeneous, where the contrast concentration is spatially uniform. Various compartmental models exist based on different assumptions of the underlying biology and give different quantitative parameters.

The most well-known and used model is the Tofts two-compartment model [216], which evaluates the leakage of the contrast agent into the interstitial space to assess microvessel permeability, fractional volumes of plasma and fractional volumes of the EES. The pharmacokinetic parameters are K_{trans} (min^{-1}), the volume transfer constant, v_e, the volume of EES per unit volume of tissue, and v_p, the volume of plasma per unit volume of tissue.

The Tofts model describes the contrast agent concentration using the following equation [216,217]:

$$C(t) = v_p C_p(t) + K_{trans} \int_0^t C_p(\tau) e^{-\frac{K_{trans}}{v_e}(t-\tau)} d\tau\}, \tag{1.7}$$

which is the convolution of the AIF ($C_p(t)$) with the impulse response function $K_{trans}e^{-\frac{K_{trans}}{v_e}t}$. Convolution is an integral that expresses the overlap of one function as it is shifted over another.

K_{trans} represents the transfer rate of the contrast agent from the intravascular plasma space to the extracellular-extravascular space. It measures plasma blood flow and vascular permeability and primarily determines the wash-in rate of the time-concentration curve. v_e denotes the volume available for contrast distribution. It measures cell membrane viability and cell density, influencing the peak height and time-to-peak of the time-concentration curve. v_p measures vascular density and affects several aspects of the time-concentration curve, including the wash-in rate, time-to-peak, and wash-out rate. Its behaviour is closely linked to the AIF.

Pharmacokinetic modelling has difficulties in clinical practice, with variability among the results due to inaccurate pre-contrast T1 values and AIF estimates. Furthermore, the models may not accurately describe the underlying biology.

1.5.5 Applications

Diagnostics

Curve classification measurements from DCE-MRI are valuable in differentiating between benign and malignant lesions. Malignant breast tumours are usually hypervascular and hyperpermeable compared to breast parenchyma or benign lesions; therefore, contrast leaks quickly into the tissue. Benign lesions show a slow concentration increase over time, whilst hyper-vascular malignant lesions demonstrate a fast initial wash-in rate with a short time-to-peak and large peak enhancement, followed by a slow wash-out rate in the delayed phase. For studies assessing these semi-quantitative values in differentiating benign and malignant lesions, the mean wash-in rate was significantly higher in the malignant group than in the benign group [218–220], while the mean values of wash-out rate [218] and time-to-peak [218, 220] were significantly lower in the malignant group.

Using pharmacokinetic parameters, K_{trans} was found to be significantly higher in atypical/malignant breast lesions compared to visible benign lesions, with a boundary value of 0.04 min^{-1} distinguishing the two [221]. Similarly, another study demonstrated that K_{trans} and v_p are both significantly higher in malignant breast lesions [222]. Notably, both studies reported

no significant difference in v_e.

Prognostics

More extensive studies have been performed in determining the prognostic value of semi-quantitative DCE-MRI parameters for neoadjuvant chemotherapy. One study showed that tumours with greater wash-out kinetics were more likely to obtain pCR after neoadjuvant chemotherapy than those with plateau-type tumours [223]. Another report determined no significant correlation between pretreatment measurements and eventual pCR after neoadjuvant chemotherapy (NAC) [224]. Large changes in the kinetics curve from wash-out type to persistently enhancing after one or two cycles of NAC were indicative of eventual pCR [223, 224], without a significant decrease in or correlation with tumour size. Predicting response early during treatment is important to improve patient care and forecast clinical outcomes.

Response Assessment

DCE-MRI is a valuable tool for assessing functional changes in breast cancer after treatment. Semi-quantitative and pharmacokinetic parameters can be useful in monitoring response over visual assessment. Following successful treatment, decreases in the rate and amount of enhancement are typically observed, whereas minimal changes indicate poor outcomes [187, 225].

However, immediately after radiotherapy, an initial increase in rate and amount of enhancement is often seen [187, 200, 226]. This is likely due to increased blood flow, microvascular permeability and acute inflammatory effects caused by treatment-induced injury such as endothelial cell death. For example, one study reported a significant increase in the area under the contrast concentration curve (AUC) and v_e one week after radiotherapy, [200], and another observed tumours enhancing more rapidly and extensively with greater wash-out type kinetics [187].

Tumour responses were investigated at one week and 2-3 weeks post-radiotherapy [226]. At one week, there was a significant increase in enhancement, mean K_{trans} and standard deviation of K_{trans} (σK_{trans}), whilst at 2-3 weeks there was a mixed response, with some patients showing increased enhancement (but less so than at one week). Others show decreases, alongside a

decrease in mean K_{trans}, and an increase in mean v_e and (σv_e). This transient enhancement may reflect improved tumour regression and local control due to reduced hypoxia [200]. However, it has also been suggested to delay imaging (>2.5 weeks post-treatment) to minimise these acute inflammatory effects [226].

By 6-months post-treatment, enhancement slowed and decreased significantly [187], especially in radiologic and pathologic complete responders, compared to non-complete responders. This suggests that faster reductions in enhancement correlate with better outcomes.

Similarly, for patients receiving carbon-ion radiotherapy, continuous decreases in wash-in AUC from pretreatment to 1 and 3 months post-treatment was reported [225]. Lower AUC values at these time points were significantly associated with complete response at 12 months, whereas tumour volume at those intervals showed no such correlation.

1.6 Research Aims

The randomised clinical trial KORTUC, led by the Institute of Cancer Research, is testing the effectiveness of an intra-tumoural injection of hydrogen peroxide, H_2O_2, as a radiosensitiser for recurrent or locally advanced primary breast cancer. These tumours are typically associated with regions of hypoxia and, therefore, are radioresistant and poorly controlled long-term with radiotherapy alone.

To improve patient stratification, the development and validation of accurate, repeatable and minimally invasive response and prognostic imaging biomarkers is essential. By obtaining biomarkers that spatially map the heterogeneous biology of the tumour (e.g., hypoxia levels, vasculature properties, and cellularity) and quantify response, treatment plans can be adapted appropriately, such as boosting the radiotherapy dose to more aggressive regions.

The tumour and healthy breast parenchyma will be imaged using contrast-enhanced ultrasound for super-resolution ultrasound (SRUS) and bilateral diffusion-weighted (DW) and dynamic-contrast enhanced (DCE) breast MRI pre-radiotherapy, and 2-weeks, 6-, 12- and 24-months post-radiotherapy, to evaluate early- and long-term treatment response.

For clinical use, quantitative imaging parameters must be robust and accurately characterise

the tumour microvasculature. To the best of our knowledge, the repeatability of SRUS has not been well established in the literature. However, evaluation of the test-retest repeatability is vital for clinical translation [227]. This study aimed to evaluate the SRUS, DW-, and DCE-MRI test-retest repeatability in breast cancer patients. Reproducibility was not assessed, as this would have required an additional imaging session using different MRI or ultrasound equipment or varying the imaging protocols. Additionally, it aimed to identify the quantitative imaging parameters that are sensitive in detecting significant post-treatment changes, and which have prognostic potential. This study contributes especially towards establishing SRUS as a reliable clinical assessment tool, offering a low-cost solution for monitoring patients undergoing cancer treatment.

Despite the promise of DW- and DCE-MR imaging and their quantitative biomarkers, there is a shortage of studies examining DW- and DCE-MRI for response monitoring in in-situ breast tumours post-radiotherapy. A 2024 review [203] identified limited relevant studies utilising ADC values from DW-MRI and DCE-MRI parameters to assess treatment response after neoadjuvant radiotherapy [187, 200, 201, 226].

In contrast, more extensive analysis using multi-parametric MRI has been conducted for response monitoring and the identification of early indicators of therapeutic response efficacy in breast tumours undergoing neoadjuvant chemotherapy (NAC). Notably, the multi-centre I-SPY 2 TRIAL (Investigation of Serial studies to Predict Your Therapeutic Response with Imaging And moLecular analysis 2) has aimed to advance personalised medicine by integrating imaging and molecular data. The I-SPY I TRIAL demonstrated that multivariate models incorporating semi-quantitative DCE-MRI, histopathology, and breast cancer subtype were the most predictive of therapeutic response [228]. The I-SPY 2 TRIAL led to several sub-studies, including the ACRIN 6698 trial, which evaluated the repeatability and reproducibility of DW-MRI [169, 170] and its potential as an early biomarker of breast cancer response to NAC [229], with imaging conducted at pre-treatment, early, and mid-treatment time-points. Another example is BMMR2 (Breast Multiparametric MRI for prediction of NAC Response), a challenge that investigated image-based biomarkers derived from DW-MRI and DCE-MRI, along with clinical and molecular data such as HER2 status and Ki-67, to predict pathological complete response (pCR) [230].

Numerous meta-analyses have also evaluated the role of MRI, primarily DCE-MRI and DW-MRI, in detecting pathological response to NAC in breast cancer [231–234]. Both modalities have demonstrated high sensitivity and specificity for predicting treatment response early in the therapeutic course. Multi-parametric methods that combine DCE-MRI and DW-MRI, along with receptor subtype, significantly outperform individual metrics. However, a high degree of heterogeneity exists across studies, with magnetic field strength and the timing of imaging during treatment emerging as key factors influencing prognostic performance.

The overall goal of this project is to develop a state-of-the-art protocol that combines SRUS with clinical DCE-MRI and DW-MRI to non-invasively monitor long-term radiotherapy response of breast cancer at multi-spatial (microns to centimetres) and temporal (sub-millisecond to minutes) scales. Biopsies were obtained from a subset of participants at baseline and 2-weeks post-RT, then stained and scored for the endothelial cell marker CD31 as a ground truth measure of vessel density.

Treatment response will be monitored by quantifying tumour microvessel structure and dynamics and tumour cellularity to provide a deeper understanding of vascular and cellular change following radiotherapy. Imaging biomarkers that serve as prognostic and response monitoring tools will be identified. Hopefully, this protocol will also be a sensitive tool to pick up early radioresistance and relapse. Breast tumour response to chemotherapy has been measured using SRUS [148]. However, it has not been applied to monitor tumour response to radiotherapy, with a high imaging frame rate (>100Hz) for better microbubble tracking and spatial resolution. The administration of KORTUC was blinded, as the trial was ongoing and not scheduled to finish until 2027.

Chapter 2

Materials and Methods

2.1 Clinical Trial

2.1.1 Study Design

The data for this study were derived from the randomised controlled KORTUC Phase 2 clinical trial (ClinicalTrials.gov: NCT03946202), a multi-centre, interventional, and prospective study. A total of 64 participants from the KORTUC trial were included in this thesis. The trial commenced in June 2020, with recruitment set to complete in 2025 and the trial ending in 2027. The estimated enrolment is 184 participants. The trial is being conducted across the following sites:

- The Royal Marsden NHS Foundation Trust, London, United Kingdom
- NHS Greater Glasgow and Clyde, Glasgow, United Kingdom
- The Christie NHS Foundation Trust, Manchester, United Kingdom
- University Hospitals of North Midlands NHS Trust, Stoke-on-Trent, United Kingdom
- Royal Cornwall Hospitals NHS Trust, Truro, United Kingdom
- Cambridge University Hospitals NHS Foundation Trust, Cambridge, United Kingdom
- Tata Medical Center, Kolkata, India

- Regional Cancer Centre, Trivandrum, India
- Stavanger University Hospital, Stavanger, Norway

The KORTUC trial recruits patients with inoperable, primary or recurrent locally advanced breast cancer, with or without metastases. These patients require high-dose palliative radiotherapy for lifetime control of their breast tumours. It aims to evaluate the efficacy of intra-tumoural KORTUC injections (KORTUC Inc., Palo Alto, CA, USA), a highly dilute (0.5%) hydrogen peroxide-based radiosensitiser, combined with radiotherapy to enhance the sensitivity of large cancerous breast tumours to radiation. KORTUC is cost-effective, readily available, and was demonstrated to be well tolerated in the KORTUC Phase 1 clinical trial [40].

Participants in the study receive a standard course of radiotherapy to the whole breast, with or without KORTUC. The radiotherapy regimens either consisted of 36 Gy delivered in six twice-weekly fractions of 6 Gy over three weeks, or, 49.5 Gy in 18-daily fractions of 2.75 Gy +/- a sequential boost in 3-5 daily fractions of 2-2.75 Gy. Out of the 64 participants included in this thesis, only 7 participants had the 49.5+ Gy regimen.

The intratumoural KORTUC injection started in the second calendar week of radiotherapy and was administered within 2 hours before each fraction for a total of 4 injections. The procedure involves numbing the skin with a local anaesthetic, followed by ultrasound-guided intratumoural injection performed by a radiologist or radiographer. Upon injection, oxygen bubbles were released, aiding accurate delivery. Hydrogen peroxide is suspended in a 1% sodium hyaluronate gel for slow release over 48 hours. The administration of KORTUC was blinded, as the trial was ongoing and not scheduled to finish until 2027.

Following radiotherapy, participants had various systemic oncological treatment based on their breast cancer subtypes.

A total of 64 participants from the KORTUC trial were included in this thesis; however, the number varied across imaging modalities (super-resolution ultrasound (SRUS), diffusion-weighted (DW) MRI, and dynamic contrast-enhanced (DCE) MRI) as well as across time-points (pre-radiotherapy (RT), and at 2-weeks, 6-months, 12-months, 18-months, and 24-months post-RT). Additionally, the healthy breast was analysed in a subset of participants for both SRUS

and DCE-MRI. Information on participant numbers at each stage of analysis, along with age distributions, molecular subtypes, and total RT dose received, is provided in Table 2.1

All participants provided written informed consent for the trial and its associated imaging sub-studies (discussed in detail later). Participants were given the option to decline participation in any component of the study. Ethical approval for the trial was granted by the West of Scotland Research Ethics Committee (REC reference 20/WS/0019). Analysis was conducted blind to treatment allocation involving KORTUC.

2.1.2 Study Cohort

To be included in the study, participants must be over 18 years of age, physically and mentally fit for treatment, and have a predicted life expectancy of at least 12 months. They must also be suitable for magnetic resonance imaging (MRI).

Eligibility criteria further require that any present metastases are stable or oligo-metastatic. Additionally, the target tumour must be accessible for safe intra-tumoural injection (i.e. without contiguous major blood vessels or brachial plexus), with at least one tumour having a measurable diameter between 30 and 150 mm. Participants must not have had prior radiotherapy to the target area or have concomitant chemotherapy or biological therapy except Herceptin, Pertuzumab and Denosumab, endocrine therapies and bisphosphonates.

2.2 Super-Resolution Ultrasound

2.2.1 Participant Population

In this multi-centre study, the super-resolution ultrasound (SRUS) imaging sub-study was conducted at The Royal Marsden NHS Foundation Trust (RMH). For the final analysis, 16 participants underwent research SRUS, yielding 62 scans. At the various imaging time-points, 15 scans were conducted at baseline, 15 at 2-weeks post-radiotherapy (RT), 1 at 3-months, 12 at 6-months, 11 at 12-months, 4 at 18-months, and 4 at 24-months post-RT. The scan at the 3-months post-RT time-point was only part of the repeatability study.

Imaging Modality	Time-Point	No. of Participants	Age years	Molecular Subtype	Total Dose Gy
SRUS	Pre-RT	15	80 [37-91]	LA (9) LB (3) HER2+ (1) TN (2)	
	2W Post-RT	15	80 [37-91]	LA (9) LB (3) HER2+ (1) TN (2)	36 (14) 49.5+ (1)
	6M Post-RT	13	81 [53-91]	LA (9) LB (3) HER2+ (0) TN (1)	36 (13)
	12M Post-RT	10	80.5 [64-91]	LA (7) LB (2) HER2+ (0) TN (1)	36 (10)
	18M Post-RT	3	81 [75-87]	LA (1) LB (1) HER2+ (0) TN (1)	36 (3)
	24M Post-RT	2	77.5 [68-87]	LA (1) LB (0) HER2+ (0) TN (1)	36 (2)
	Healthy Breast	9	80 [64-89]		
DCE-MRI	Pre-RT	61	67.5 [37-91]	LA (36) LB (12) HER2+ (4) TN (8)	
	2W Post-RT	33	72.5 [37-91]	LA (18) LB (7) HER2+ (2) TN (5)	36 (27) 49.5+ (5)
	6M Post-RT	40	73 [37-91]	LA (25) LB (9) HER2+ (1) TN (4)	36 (34) 49.5+ (5)
	12M Post-RT	22	76.5 [43-91]	LA (14) LB (7) HER2+ (0) TN (1)	36 (21) 49.5+ (1)
	24M Post-RT	10	71.5 [43-87]	LA (6) LB (2) HER2+ (0) TN (2)	36 (8) 49.5+ (2)
	Healthy Breast	41	68 [37-91]		
DW-MRI	Pre-RT	59	68 [37-94]	LA (33) LB (13) HER2+ (4) TN (8)	
	2W Post-RT	36	72 [37-91]	LA (21) LB (7) HER2+ (2) TN (5)	36 (30) 49.5+ (5)
	6M Post-RT	40	75 [37-91]	LA (24) LB (10) HER2+ (1) TN (4)	36 (35) 49.5+ (4)
	12M Post-RT	23	77 [43-91]	LA (14) LB (7) HER2+ (0) TN (2)	36 (22) 49.5+ (1)
	24M Post-RT	10	71.5 [43-87]	LA (6) LB (2) HER2+ (0) TN (2)	36 (8) 49.5+ (2)
Total		64	68 [37-94]	LA (38) LB (13) HER2+ (4) TN (8)	36 (56) 49.5+ (7)

Table 2.1: Summary of the participant demographics and breast tumour characteristics across imaging modalities and time-points. This table details the number of participants assessed using each imaging modality (super-resolution ultrasound (SRUS), diffusion-weighted MRI (DW-MRI), and dynamic contrast-enhanced MRI (DCE-MRI)) at each imaging time-point: pre-radiotherapy (Pre-RT), 2-weeks (2W), 6-months (6M), 12-months (12M), 18-months (18M), and 24-months (24M) post-RT. Data are also given for healthy breast imaging where applicable. Age is reported as median [range]. Molecular subtypes include luminal A (LA), luminal B (LB), HER2-positive (HER2+), and triple-negative (TN). The RT regimens either consisted of 36 Gy delivered in six twice-weekly fractions of 6 Gy over three weeks, or, 49.5 Gy in 18-daily fractions of 2.75 Gy +/- a sequential boost in 3-5 daily fractions of 2-2.75 Gy. Age, molecular subtype, and dose was not obtained for one participant.

Several scans were excluded from the final analysis for various reasons, which have already been excluded from the number of participants and scans above. Specifically, the initial scans of the first trial participants were acquired before the SRUS protocol was finalised. Missing time-points for participants were due to early study termination or the participants not yet having reached those time-points.

Repeatability Study

For the SRUS repeatability study, 13 participants from the KORTUC trial were recruited, resulting in 27 repeatability scans. Eight participants underwent separate repeatability scans at multiple time-points. While pre-treatment repeatability studies are standard practice [227], this study also aimed to include post-treatment repeatability. Repeatability scans were performed at the following time-points: five participants at baseline, nine at 2-weeks post-radiotherapy (RT), one at 3-months, four at 6-months, three at 12-months, two at 18-months, and three at 24-months post-RT.

Scans conducted at different time-points for the same participant were treated as independent during statistical analysis due to the post-treatment changes that occurred over that time. Repeatability was assumed to be consistent across all imaging time-points. Each repeatability scan was completed within a single 20-minute imaging session.

Response Assessment Study

15 participants from the KORTUC trial were included in the response assessment study. Imaging was conducted at multiple time-points, with 15 scans performed at baseline, 15 at 2-weeks post-RT, 12 at 6-months, 10 at 12-months, 3 at 18-months, and 2 at 24-months post-RT.

2.2.2 Ultrasound Equipment

Ultrasound acquisitions initially employed a Verasonics L12-3v linear array probe (Verasonics Inc., Kirkland, WA, USA) for the first eight scans, which included baseline and 2-weeks post-RT scans from four participants. Early in the study, the probe was upgraded to a GE L3-12-D linear array transducer (GE HealthCare Technologies Inc., Chicago, IL, USA), featuring an increased

number of elements (256 compared to 192) and an expanded field of view from approximately 2.5 to 5 cm. This larger field of view was particularly advantageous for imaging large locally advanced breast tumours, as it allowed visualisation of both the tumour centre and periphery. Participants initially imaged with the Verasonics L12-3v probe were subsequently imaged with the GE L3-12-D probe for their remaining post-RT time-points. The probes were used with a Verasonics Vantage 256 research scanner (Verasonics Inc., Kirkland, WA, USA).

A Verasonics Matrix 1024 8MHz matrix array probe (Verasonics Inc., Kirkland, WA, USA) was trialled on two participants at baseline and 2-weeks post-RT, with one participant also imaged at 6-months post-RT. However, no useful microbubble signal was obtained after processing. For the participant who continued to further time-points (12- and 24-months post-RT), imaging was performed using the GE L3-12-D probe.

3D ultrasound imaging was also explored using a 128 + 128 element Row-Column Array supplied by Vermon SA (Tours, France). However, analysis of this data was beyond the scope of this study and will be addressed in future research, specifically in comparison to the linear array probe.

Throughout the remainder of the thesis, the analysis will focus on scans performed with the GE L3-12-D probe. The participants imaged with the Verasonics linear array, Verasonics matrix array and Row-Column array were not included in the final analysis.

2.2.3 Acquisition Settings

Amplitude-modulated[1] plane-waves were transmitted at 5 MHz with steering angles ranging from -10° to 10°, using a mechanical index of 0.1 (transmit voltage of 5V) and 1-cycle sinusoids. A mechanical index of 0.1 was sufficient to oscillate microbubbles and produce non-linear responses without bursting them, even under high pulse repetition rates. The ultrasound frequency of 5 MHz lies within the resonant frequency of the microbubbles.

[1] Amplitude modulation imaging is a contrast-enhanced ultrasound mode. In this technique, a series of plane waves with half, full and half pulse amplitudes were transmitted sequentially for a single frame. Microbubbles exhibit a non-linear response to these pulses due to the ultrasound imaging frequency (5 MHz) being within their resonant frequencies. By combining the received echoes from the two half-amplitude pulses and subtracting them from the full-amplitude pulse, signals from non-linear microbubble scatterers were preserved. In contrast, signals from linear tissue scatterers were effectively cancelled. This selective enhancement highlights microbubble signals within blood vessels, improving the visualisation of vascular structures.

Data were acquired at compounded frame-rates of 100 frames per second (fps) over 5 seconds of acquisition. Raw radiofrequency data were saved for offline post-processing. The number of compounded angles varied between participants (but remained consistent within each participant), ranging from 4 to 10 over an angle range of -10° to 10°. In most cases, 10 compounded angles were used to create high-quality B-mode images for tumour segmentation (23 of 27 repeatability scans in the repeatability study; 11 of 15 participants in the response assessment study).

The Verasonics L12-3v linear array probe used 11 compounded angles, a frame-rate of 200 fps over 4.25 seconds of acquisition. Transmit voltages ranged from 4 to 8V across acquisitions to determine the optimal mechanical index, with a final voltage of 5V (mechanical index 0.1) selected for the linear array probes based on real-time feedback. The Verasonics Matrix 1024 8 MHz matrix array probe used 5 compounded angles, with a frame-rate of 250 fps over 5 seconds of acquisition. Transmit voltages ranged from 10 to 20V across acquisitions to determine the optimal mechanical index. The acquisition scripts for the Verasonics L12-3v, GE L3-12-D, and Verasonics Matrix 1024 8MHz probes were developed by Matthieu Toulemonde, while the script for the 128 + 128 element Row-Column Array probe was developed by Joseph Hansen-Shearer.

Hardware constraints necessitated trade-offs between the compounded frame-rate, acquisition duration, and the number of compounded angles, as data collection per acquisition was limited. As a result, four participants in the response assessment study and four scans in the repeatability study had fewer compounded angles (4-8) to achieve higher compounded frame-rates (200-400 fps). These frame-rates were subsequently reduced to 100 fps during post-processing to maintain consistency in repeatability statistics and response assessment. The effect of increasing the frame-rate on SRUS image quality and SRUS-derived quantitative parameters will be investigated in future studies.

2.2.4 Patient Set-Up

Designing the Imaging Protocol

For the initial participants, the imaging protocol was initially optimised using a Verasonics L12-3v linear array probe (Verasonics Inc., Kirkland, WA, USA), which was subsequently upgraded

to a GE L3-12-D linear array probe (GE HealthCare Technologies Inc., Chicago, IL, USA). This optimisation process involved 6 participants across 15 scans, with 8 scans performed using the Verasonics probe and 7 using the GE probe, conducted at the following time-points: 5 scans at baseline, 4 at 2-weeks post-radiotherapy (RT), 2 at 6-months, and 4 at 12-months post-RT.

The parameters to determine included the optimal volume of the contrast bolus (SonoVue®; Bracco S.p.A., Milan, Italy) and the timing of the contrast concentration peak post-injection to commence imaging. Based on visual inspection of the real-time feedback, an injection of 2.5 mL of SonoVue provided sufficient but isolated microbubbles for localisation, tracking and microvasculature reconstruction. Smaller volumes (1 and 2 mL) were also trialled but were insufficient. Given that one vial of SonoVue contains 5 mL, imaging could be performed over two injections. For a 2.5 mL injection, the microbubble bolus consistently reached peak concentration approximately 35 seconds post-injection, which was standardised as the acquisition start time for the remainder of the trial.

A Verasonics Matrix 1024 8 MHz matrix array probe was trialled on 2 participants (5 scans). However, minimal microbubble signal was observed in real-time feedback and subsequent post-processing, making the probe unsuitable for further use.

Initially, only one or two imaging planes of the tumour were captured. It was important to recognise the heterogeneity of tumours and their microvasculature by capturing multiple planes of the tumour volume. Since 3D imaging with a matrix array was not pursued, it was decided to sample multiple planes of the tumour. In clinical practice, breast sonographers are highly trained in locating the tumour centre, making it practical to sample this region from standardised and reproducible angles, chosen as horizontal 0°, 90°, 45° clockwise, and 45° anticlockwise. While tumour shape and size changes make returning to the same imaging planes impossible, standardising the acquisition angles reduces sampling bias (e.g., avoiding selective imaging of the most vascularised regions).

Although microbubble concentration decreased between the first and last imaging plane, the order of the imaging planes remained consistent. Each plane could thus be reliably compared to the same plane in repeat scans or scans acquired at different time-points.

Finalised Imaging Protocol

The finalised imaging protocol is illustrated in Figure 2.1. A 2.5 mL bolus of SonoVue was injected intravenously over 15 seconds, followed by a saline flush. Ultrasound acquisitions began 35 seconds post-injection. The probe was hand-held horizontally by a consultant breast radiographer at the tumour's centre, then rotated sequentially to imaging planes at 90°, 45° clockwise and 45° anticlockwise. At each plane, the tumour centre was relocated. The anatomical location of the probe was recorded on a diagram to ensure reproducibility at later time-points.

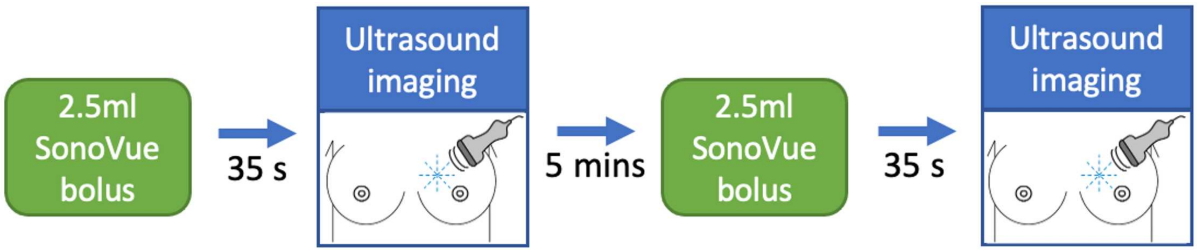


Figure 2.1: The SRUS imaging protocol. A 2.5 mL bolus of SonoVue contrast was administered intravenously. Ultrasound acquisitions commenced 35 seconds post-injection, starting in the horizontal plane, followed by 90°, 45° clockwise and 45° anticlockwise, imaging at the tumour centre. The protocol was repeated 5 minutes after the initial bolus injection, either to assess SRUS repeatability of the tumour, to image a different part of the tumour, or to evaluate the contralateral healthy breast.

For repeatability scans, the imaging protocol was repeated 5 minutes after the initial bolus injection. If the tumour was particularly large or split into two masses, a different part was sampled during the second injection. In some cases, the contralateral healthy breast was imaged during the second injection at the anatomical location mirroring the tumour site; this was done for 9 participants.

During the scans, participants breathed normally. The short acquisition time of 5 seconds enabled the radiographer to maintain a stable probe position with minimal out-of-plane motion. The inherent stiffness of tumours and post-therapy fibrotic tissue further reduced the impact of breathing motion. However, any datasets affected by significant motion artefacts, such as those caused by probe or participant movement, were excluded. This affected only two repeatability scans. Imaging the healthy breast sometimes required patient breath-holding to minimise motion artefacts, as it was more susceptible to breathing-related movement.

Before administering the second bolus, clearance of the first bolus was visually confirmed using real-time feedback. A 5-minute interval between bolus injections ensured clearance of microbubbles from the microvasculature.

Each SRUS imaging session lasted approximately 20 minutes. The setup process, including cannulation, a preliminary clinical ultrasound, and SonoVue preparation, took about 10 minutes. The clinical ultrasound was necessary to locate the tumour, as it provided superior real-time B-mode image quality and a broader field of view. Afterwards, the clinical probe was replaced with the research probe, and the tumour centre was relocated. The SRUS imaging, from the start of microbubble injection to the completion of multi-plane imaging, took less than 2 minutes, aligning with the duration of usable contrast.

The second bolus injection was administered after a 5-minute interval, with total imaging time taking under 10 minutes. Transitioning between imaging planes required approximately 5 seconds for the radiographer to locate the tumour's central slice using B-mode feedback. Acquisition saving time was around 5 seconds, resulting in a 10-second interval between imaging planes.

Overall, participants tolerated the imaging procedure well. Some participants with ulcerating tumours reported mild discomfort; however, they could complete the scans.

2.2.5 Contrast-Enhanced Data Processing

Data processing was conducted offline using custom MATLAB® software (vR2019a; The MathWorks Inc., Natick, MA, USA).

Ultrasound Beamforming

The raw radiofrequency ultrasound data was coherently compounded using a MATLAB script written by Dr. Chee Hau Leow and Dr. Matthieu Toulemonde. The data was reconstructed with a pixel size of 100 μm laterally and 30.8 μm axially. Figure 2.2 illustrates an example of a B-mode image of a tumour alongside a single contrast-enhanced frame prior to data processing.

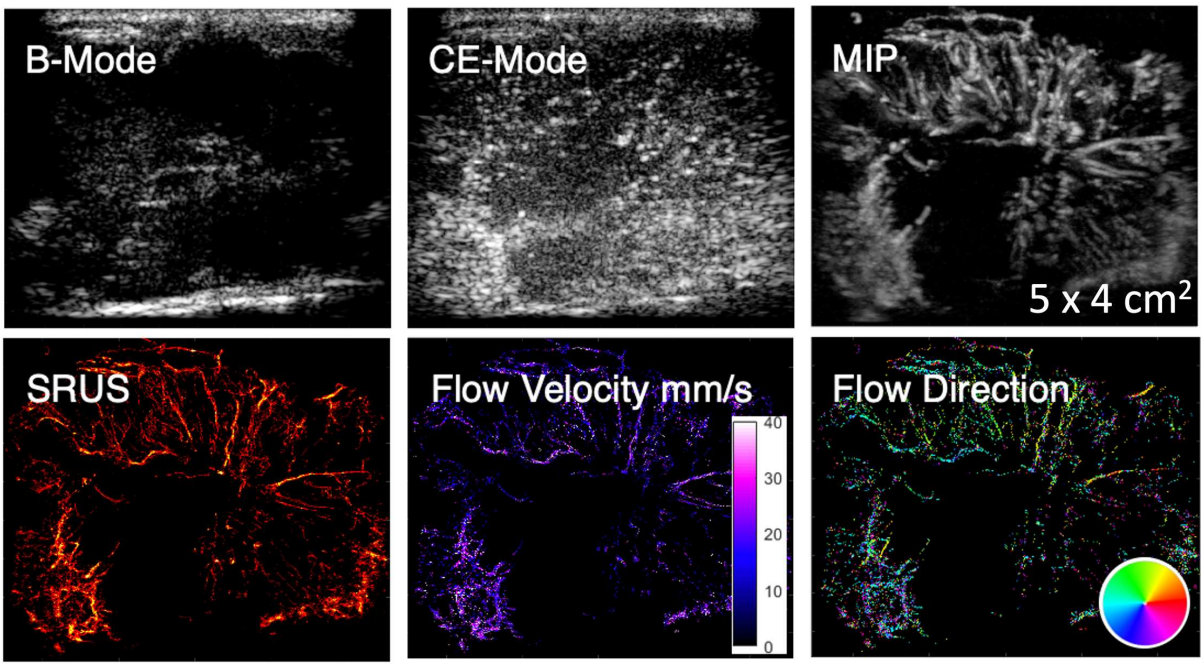


Figure 2.2: The current clinical capabilities of ultrasound with intravenous contrast for breast tumour imaging, including a B-mode tissue image, the corresponding contrast-enhanced image (single frame), and the maximum intensity projection (MIP) of the processed contrast-enhanced data. Below are the corresponding super-resolution ultrasound (SRUS) maps, reconstructed from the contrast-enhanced ultrasound scan. Contrast tracking was used to generate blood velocity and direction maps.

Motion Correction

An in-plane motion correction algorithm was applied to minimise the effects of the hand-held probe and breathing motion. A non-rigid registration algorithm was used to estimate and apply motion correction from B-mode images to contrast-enhanced (CE-) mode data [235,236], implemented in MATLAB by Dr. Xinhuan Zhou. In brief, a B-spline free-form deformation was applied to align the moving frame with the reference frame. This process involved placing a grid of B-spline control points over the moving frame and estimating the deformation field, which defines how each control point influences the surrounding image pixels. The equal spacing between the control points in the depth and lateral directions were specified prior to motion estimation. The computed deformation field was then applied to the CE-mode data for motion correction.

Before motion correction, the beamformed B-mode data was processed by taking the absolute value of the data to extract the amplitude of the ultrasound signals. Each data frame was then spatially smoothed using a 2D Gaussian filter (`imgaussfilt`, MATLAB, Image Pro-

cessing Toolbox) with a standard deviation of 300μm in the depth and lateral directions. This smoothing improves tissue visualisation and reduces noise. A logarithmic compression (base 10) was applied afterwards, enhancing image contrast, especially at greater depths. Fewer ultrasound waves reach greater depths due to reflection, resulting in a weaker signal. A scaling factor of 20 was applied to increase the intensity of the final output. The intensity window was set from 40 to 10 units below the maximum pixel value across frames (i.e., from -40 dB to -10 dB), enhancing relevant structures for motion correction.

The reference B-mode frame for motion correction was determined by averaging all frames to create a target reference frame. The sum of squared differences (SSD) between each frame and the target reference frame was calculated to assess how much each frame deviates from the target. The frame with the lowest SSD, indicating the greater similarity to the target, was selected as the final reference frame.

The motion correction algorithm required spacing of the B-spline control points in both the depth and lateral directions, as well as a curvature penalty term. The curvature penalty term was to avoid large and unphysical deformations caused by out-of-plane motion. The default penalty value of 50 was used, as initial investigations showed that values above 0 did not result in any significant differences. A large spacing of the B-spline control points was used to correct for larger-scale translation motion, specifying 64 pixels in the depth and lateral directions. This spacing was chosen during initial parameter investigations, which revealed that a spacing of 64 significantly improved effectiveness compared to smaller values, and later values did not result in any significant differences.

The deformation field estimated from each frame was used as the initial estimate for the subsequent frame. In the first 10-20 frames, the deformation field did not fully align the moving frame with the reference frame, but it gradually stabilised as the initial estimate improved. The deformation field was initially estimated over the first 10 frames and then refined by working backwards to the first frame, providing a better initial estimate for further calculations.

The motion correction algorithm required the beamformed CE-mode data to be in a non-complex form. However, subsequent processing (e.g., moving average subtraction, discussed next) benefited from preserving the complex nature of the data. The CE-mode data was split into

real and imaginary components, with the estimated deformation field applied to each component separately. The real and imaginary components were recombined for further processing. Motion correction was performed first, as the moving average subtraction was more effective when the CE-mode data was adequately aligned, ensuring that any remaining tissue clutter overlapped between frames to remove fully.

Moving Average

A moving average was subtracted from each frame to remove residual signals from static or slow-moving tissue. The optimal window size (~0.11s; 11 frames at 100 fps) was determined based on the minimum blood velocity and residual tissue motion.

Visual inspection of the maximum intensity map of the processed data revealed that smaller window sizes removed slow-moving microbubbles. In comparison, larger window sizes failed to remove all residual tissue and did not reveal additional blood vessels, as shown in Figure 2.3.

Based on the frequency response of the moving average filter, the half-power (-3 dB) cut-off frequency was 6.9 Hz. Using the Doppler frequency formula, with a frame-rate of 100 fps and a transmission frequency of 5 MHz, the axial cut-off velocity for this window size was 1 mm/s, corresponding to the mean blood velocity in capillaries. This window size was applied across all datasets.

Smoothing and Image Formation

After subtracting the moving average, the absolute value was taken, and the data was smoothed spatially (300 μm width) and temporally (3 frames) using a 3D Gaussian filter (`imgaussfilt3`, MATLAB, Image Processing Toolbox) to enhance microbubble visualisation and reduce noise, followed by logarithmic compression.

Subtraction of Noise Background

The noise background was estimated from an air acquisition using the same acquisition settings and processing steps as the contrast-enhanced data, except without motion correction. The maximum intensity projection of the processed air acquisition provided the upper noise

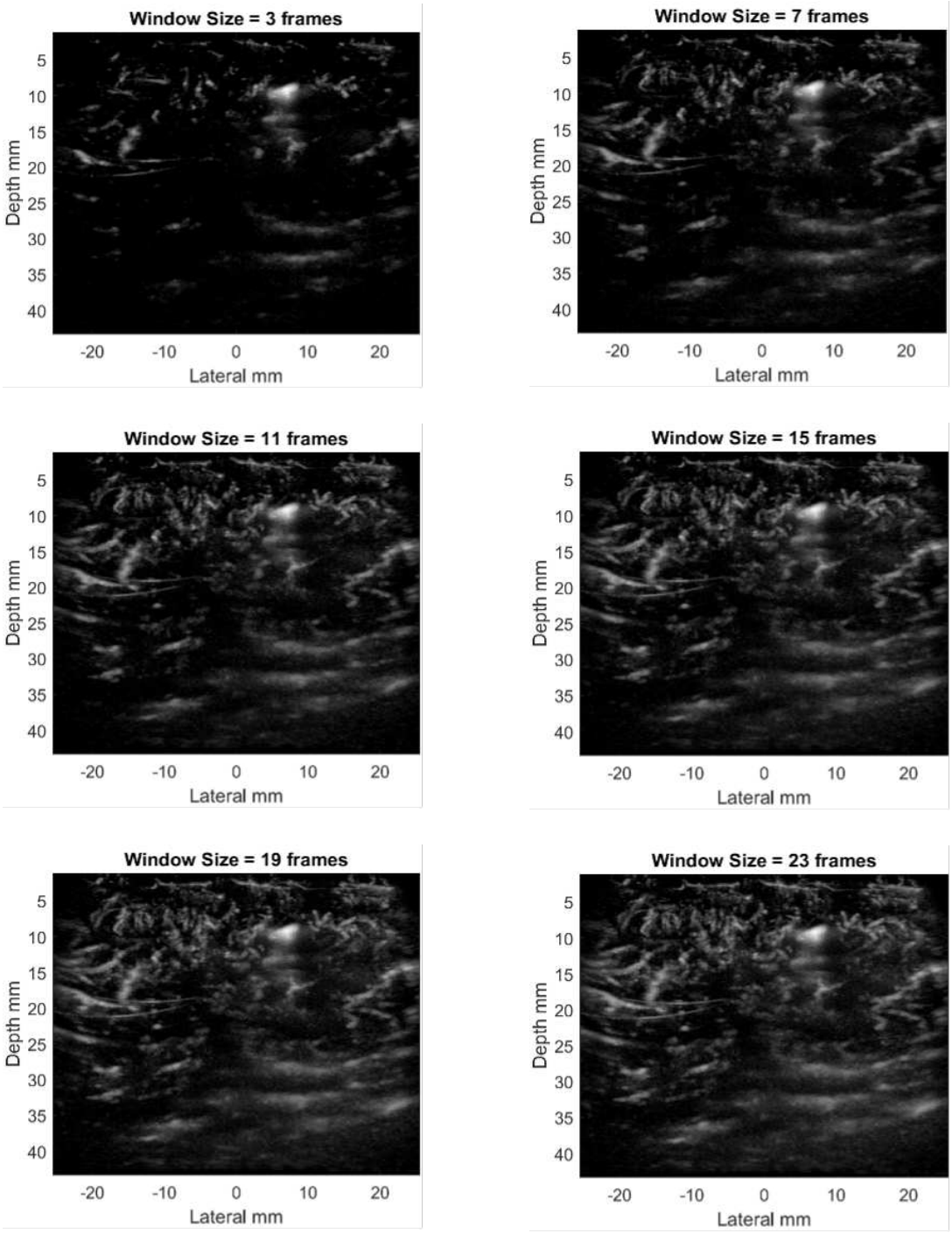


Figure 2.3: Maximum intensity projection, with time as the third dimension, of the processed contrast-enhanced data. The acquisition consisted of 500 frames (5 seconds) at a frame-rate of 100 fps, and a moving average window was subtracted across the frames. Results are presented for varying window sizes, ranging from 3 to 23 frames, to evaluate the effect of window size on the outcome.

threshold.

A copy of the upper noise threshold was created for each frame. During motion correction, the same estimated deformation field applied to the CE-mode data was also applied to the corresponding frame of the upper noise threshold. This noise threshold matrix was then subtracted from the processed clinical data, with values below zero considered noise.

An example of a maximum intensity projection of processed contrast-enhanced data is shown in Figure 2.2.

2.2.6 SRUS Data Processing

Localisation Uncertainty

The localisation uncertainty refers to the error in the localisation position and represents the resolution limit of the technique. A stationary wire was imaged in a water tank over 100 frames to determine this uncertainty, using the same ultrasound equipment and acquisition settings described above. The stationary wire, which simulates a microbubble scatterer, was localised across the frames.

The wire was imaged at various positions within the imaging field, including depths of 5, 15, 25, and 35 mm, and laterally at 0, 10, and 20 mm. The standard deviation of the x and z localisation coordinates was calculated for each position, as shown in Figure 2.4. The average standard deviation across all positions was then computed, with the most significant deviation occurring for the x localisation coordinate, which had an average value of 20μm (to one significant figure). This value was taken as the localisation uncertainty.

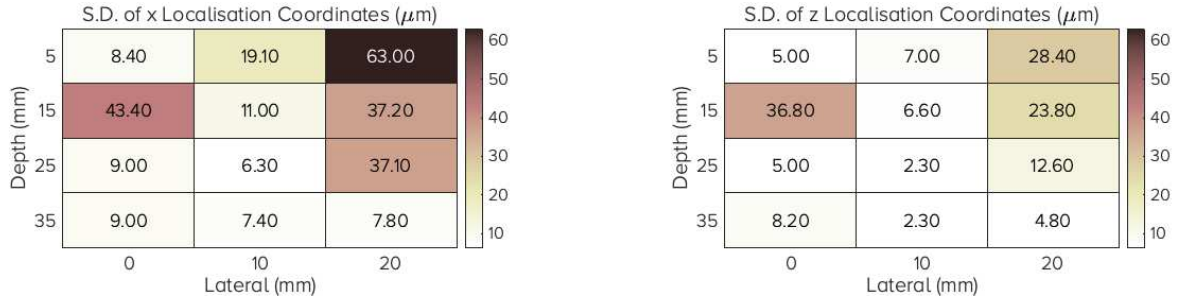


Figure 2.4: The standard deviation of the SRUS localisation coordinates in the x and z direction, at 12 different imaging positions, determined by repeatedly localising a wire in a water tank.

The localisation uncertainty experiment was performed alongside Dr. Matthieu Toulemonde.

Localisation, Tracking and SRUS Maps

SRUS maps were reconstructed on a grid with a lateral and axial resolution of 3.1 μm. This pixel size was determined by reducing the smallest pixel dimension (30.8 μm in the axial direction) of the beamformed data by a factor of ten. However, the 20 μm localisation uncertainty sets the resolution limit.

The SRUS algorithms were implemented in-house using MATLAB. Microbubble properties (area, power, eccentricity, unimodality and solidity) were defined to differentiate microbubbles from remaining clutter. These property limits were manually selected by identifying microbubbles across participants and scans to establish the value ranges. While noise was largely eliminated during CE-data processing, some residual noise remained. The MATLAB function `graythresh` (MATLAB, Image Processing Toolbox) was used to estimate a noise threshold and further distinguish low-intensity microbubbles from noise. `graythresh` computes a global threshold for a grayscale image using Otsu's method [237]. Otsu's method selects the threshold that minimises the intraclass variance of the pixel intensities, effectively separating the image into two classes — foreground and background — by maximising the between-class variance.

The SRUS algorithm localised isolated microbubble centres and tracked them between frames using a Kalman motion model-based tracking algorithm [120, 238], implemented in MATLAB by Dr. Jipeng Yan and Biao Huang. Using a constant velocity motion model, this algorithm predicts the next position of the microbubble based on its previous position and velocity. The predicted position was then updated using the actual measurement, with the correction weighted by the relative confidence in both the prediction and the measurement. This iterative process improves tracking accuracy over time by continuously combining predictions with observations.

Accumulating localisations and tracks over time generated super-resolved maps of microvascular structure, blood velocity and direction, with examples shown in Figure 2.2.

All acquisition frames were used for SRUS reconstruction, as the dataset had minimal out-

of-plane motion. Removing frames would negatively impact repeatability and post-radiotherapy response assessment, as a different number of frames would be used to create the final SRUS image and quantitative parameters. Missing frames would also affect the tracking algorithm. Any data with significant motion artefacts were excluded. Significant motion artefacts were identified by tissue signal breakthrough after the moving average subtraction and were caused by probe movement rather than breathing-induced motion.

A 2D Gaussian filter (`imgaussfilt`, MATLAB, Image Processing Toolbox) was applied to the created maps with a standard deviation related to the localisation uncertainty, calculated at 20 μm.

The entire dataset was processed because some quantitative parameters also required the vessels outside the tumour, such as the distance to the nearest vessel.

2.2.7 Region of Interest

Tumour regions of interest (ROIs) were manually delineated on B-mode tissue images, with additional guidance from the maximum intensity projection of the processed CE-data and the clinical ultrasound image at the corresponding time-point. The ROIs were reviewed and modified by a consultant breast radiographer (Victoria Sinnett). Tumour ROIs were redefined at each time-point, using the tumour's ROI from the previous scans as a reference.

2.2.8 Quantitative Parameters

SRUS quantitative parameters were extracted from the super-resolved maps of microbubble localisation, blood velocity, and blood flow direction within the tumour. These parameters are described below. All calculations were performed using MATLAB. Structural quantitative parameters, including vessel density, distance to vessel, vessel diameter, and fractal dimension, were calculated from the SRUS maps of microbubble localisations and tracks, incorporating additional blur due to localisation uncertainty as discussed. Pixels through which a microbubble passed had values >1, whereas pixels not traversed by a microbubble had values of 0.

Vessel Density

Vessel density was defined as the percentage of pixels within the delineated tumour that a microbubble passed through, based on microbubble localisations and tracks. Tumours typically exhibit denser vascular areas than healthy tissue due to neo-angiogenesis.

Distance to Vessel

The distance from each pixel within the tumour, excluding those containing blood vessels, to the nearest blood vessel edge, either inside or outside the tumour, was calculated using `bwdist` (MATLAB, Image Processing Toolbox). This computation provided a distance to vessel value for each pixel location within the tumour. Tumour microvasculature is typically chaotic, with regions of dense blood vessel distribution and hypoxic areas with sparse or absent vasculature.

Vessel Diameter

Vessel diameter was computed by first skeletonising the binary image of the microvasculature using `bwmorph` (MATLAB, Image Processing Toolbox) to obtain the blood vessel centrelines. The distance from each pixel on the centreline to the nearest edge of the blood vessel was calculated using `bwdist` (MATLAB, Image Processing Toolbox). The edges of the blood vessels were defined as the nearest pixels to the centrelines that had not been traversed by a microbubble. The vessel radius at each point was determined, and the vessel diameter was calculated as twice the radius. A vessel diameter value was calculated for every location along the centreline. Tumours generally exhibit larger microvessel diameters compared to healthy tissue [14, 239].

Blood Velocity

Blood velocity values were extracted from the super-resolved blood velocity maps obtained from microbubble tracking. Blood velocity was calculated as the distance between linked microbubbles divided by the frame-rate. The blood velocity was averaged at each vessel pixel, accounting for the multiple microbubbles passing through that pixel.

Blood Flow Direction Entropy

Blood flow direction entropy quantifies the organisation of the microvasculature [131]. This was calculated using the super-resolved blood flow direction maps from microbubble tracking. Blood flow direction is the angle (ranging from 0 to 360°) between linked microbubbles. The directions were binned into 180 bins covering 0 to 360°, and entropy was calculated using the formula:

$$Entropy = \sum \left(\frac{N}{\sum N} \times log \left(\frac{N}{\sum N} \right) \right), \tag{2.1}$$

where N is the count in each bin. Tumour blood vessels tend to be tortuous and exhibit chaotic branching (higher entropy), while healthy tissue vessels are typically more linear and ordered (lower entropy).

Fractal Dimension

Fractal dimension was calculated using a box-counting method, available online (`https://www.mathworks.com/matlabcentral/fileexchange/13063-boxcount`). This method determines the number of boxes of varying sizes required to cover the entire microvascular structure. The fractal dimension was then obtained as the slope of the log-log plot of box size versus the number of boxes needed to cover the structure at each box size. Fractal dimension quantifies structural complexity by measuring how completely a structure fills space across different scales. A simple, linear structure (like a straight vessel) has a fractal dimension close to 1, as it resembles a one-dimensional line. As the structure becomes more branched, tortuous, and dense, the fractal dimension approaches 2, meaning it occupies more two-dimensional space. Tumour microvasculature is generally more chaotic with higher fractal dimension compared to the more ordered vessels in healthy tissue.

For vessel density, blood flow direction entropy, and fractal dimension, the tumour was subdivided into biopsy-sized boxes (1.6 mm × 1.6 mm) to mimic biopsy sampling at the scale of micro-metastases. These parameters were calculated within each box to compute in-plane statistics. Values were obtained across many pixels for distance to vessel, blood velocity, and vessel diameter, so in-plane statistics were available without subdivision. The in-plane statistics

were used to evaluate the limitations of biopsies within heterogeneous tumours.

The measurements of SRUS quantitative parameters can be influenced by various ultrasound acquisition settings (such as imaging frequency, mechanical index, frame-rate, and acquisition duration), the imaging protocol (including microbubble concentration, volume and injection rate, and the timing of acquisitions following bolus injection), as well as each step of the SRUS data processing pipeline. These factors primarily affect the number of microbubbles that are successfully localised and tracked. For instance, in the case of vessel density, if fewer microbubbles pass through the tumour microvasculature during imaging, the measured vessel density will decrease. This highlights the necessity of a standardised protocol.

2.3 Diffusion-Weighted MRI

2.3.1 Participant Population

In this multi-centre, prospective study, 62 participants underwent research DW-MRI, resulting in 178 scans for the final analysis. The distribution of participants and scans across different centres is as follows:

- The Royal Marsden NHS Foundation Trust (RMH): 27 participants contributed 92 scans,
- NHS Greater Glasgow and Clyde (GGC): 4 participants contributed 16 scans,
- University Hospitals of North Midlands NHS Trust (UHNM): 3 participants contributed 7 scans,
- Cambridge University Hospitals NHS Foundation Trust (CUH): 4 participants contributed 13 scans,
- Tata Medical Center (TMC): 18 participants contributed 33 scans,
- Regional Cancer Centre (RCC): 5 participants contributed 12 scans, and
- Stavanger University Hospital (SUH): 1 participant contributed 5 scans.

Several scans were excluded from the final analysis for various reasons. These included DW-MRI sequences that did not adhere to the research protocol[2], scans terminated either before or during the DW sequence, and scans that entirely lacked the DW sequence. Additional exclusions occurred due to data acquisition issues, such as incomplete or missing b-values. These scans also had data acquisition issues with the dynamic contrast-enhanced MRI sequence. Furthermore, some scans were excluded due to poor signal quality in the DW images where the tumour was present. Lastly, scans acquired after the data analysis period were also excluded. Some participants with excluded scans had DW data available at other time-points and will be included in the analysis. Additional reasons for missing time-points include missed scans due to illness, early study termination, or participants not yet reaching those time-points.

Across the imaging time-points, 59 scans were conducted at baseline, 8 at a second baseline, 36 at 2-weeks post-radiotherapy (RT), 2 at 3-months, 39 at 6-months, 1 at 9-months, 23 at 12-months, and 10 at 24-months post-RT. Only a limited number of participants consented to the 3- and 9-month time-points, as these were later additions to the trial protocol for a radiomics sub-study, which was beyond the scope of this work.

2.3.2 Patient Set-Up

Most participants were imaged in the prone position, which minimises breast movement during free-breathing acquisitions and ensures optimal data quality. However, 10 participants were imaged in the supine position at one or more time-points due to discomfort in the prone position (e.g. due to fungating tumours). Of these, six participants who were imaged in the supine position at baseline continued in this position for subsequent imaging sessions.

Although imaging in the supine position introduced the potential for more motion and flattens the breast, which could affect image quality and visualisation, this protocol was not designed to screen for potential small lesions, so participant comfort could be prioritised if prone positioning was intolerable.

[2]For context, our protocol involves a DW acquisition with 14 b-values. However, some participants underwent a standard protocol with 2-4 b-values.

2.3.3 Imaging Parameters

The research DW protocol is an axial 2D echo-planar imaging series with SPAIR fat suppression, designed by Dr Matthew Blackledge (The Institute of Cancer Research) for the KORTUC clinical trial. Across all scanner sites, the imaging parameters were standardised as closely as possible and were required to remain consistent throughout the trial at each centre. Image quality was assessed centrally prior to participant acquisitions. The DW protocol was acquired before contrast injection for the dynamic contrast-enhanced MRI sequence.

Full coverage of both breasts was acquired using bilateral breast coils, which improved the signal-to-noise ratio and enabled parallel imaging techniques. Bilateral breast coverage was also acquired to evaluate the healthy breast and monitor for new disease.

2D slices were acquired in the axial plane. For intravoxel incoherent motion, 14 b-values were acquired, specifically 0, 10, 20, 30, 50, 70, 100, 150, 200, 400, 600, 800, 1000 and 1200 s/mm^2. The b_0 volume was obtained without the diffusion-sensitising gradients. For the rest of the acquired b-values, three perpendicular diffusion gradients were applied, acquired and stored independently for each b-value. The diffusion gradients were along the phase-encoding axis (along the columns), the frequency-encoding axis (readout direction, i.e., the direction along which the MR signal is sampled - along the rows), and the slice direction. The three source volumes are sensitive to diffusion along the direction of the diffusion gradient. A parallel imaging factor of 2 was applied in the phase-encoding direction.

The mean total scan time was 4.73 minutes, where the acquisition of one source volume (for one b-value at one diffusion direction) was equal to the repetition time, with a mean value of 7.09 seconds.

RMH, GGC and SUH used a Siemens 1.5T scanner, CUH a GE 1.5T scanner, and UHNM, TMC and RCC a Siemens 3T scanner, with the addition of lateral breast coils. Repetition time (TR) and echo time (TE) varied within and across sites, ranging from TR 6500-10500 ms and TE 71-91 ms. The number of signal averages was 1 across all sites and a flip angle of 90° was used.

For the research DW protocol, RMH, GGC, UHNM, RCC and SUH, the default image size was 96×160, for CUH 256×256, and for TMC 160×160. From RMH, GGC, UHNM, TMC,

Hospital	Scanner	TR ms	TE ms	No. of Averages	FA	Rows	Columns	Pixel Spacing mm
RMH n = 92	Siemens Aera/Sola 1.5T	6500 [6500-8500]	81 [78-91]	1	90	96 [96-128]	160 [160-174]	2.375 [2.375-2.586]
GGC n = 16	Siemens Aera 1.5T	6500 [6500-6600]	81	1	90	96	160	2.375
UHNM n = 7	Siemens Vida 3T	6500	72 [71-72]	1	90	96	160	2.375
CUH n = 13	GE SIGNA Artist 1.5T	10500	74	1	90	256	256	1.328
TMC n = 33	Siemens Vida 3T	6900 [6900-8800]	79	1	90	160	160	2.375
RCC n = 12	Siemens Vida 3T	7900 [6500-8100]	72 [71-72]	1	90	96	160	2.375 [2.375-2.400]
SUH n = 5	Siemens Sola 1.5T	6800	83	1	90	96	160	2.375

Table 2.2: A summary of the diffusion-weighted MRI imaging parameters across the clinical trial centres. n: no. of scans; TR: repetition time; TE: echo time; and FA: flip angle.

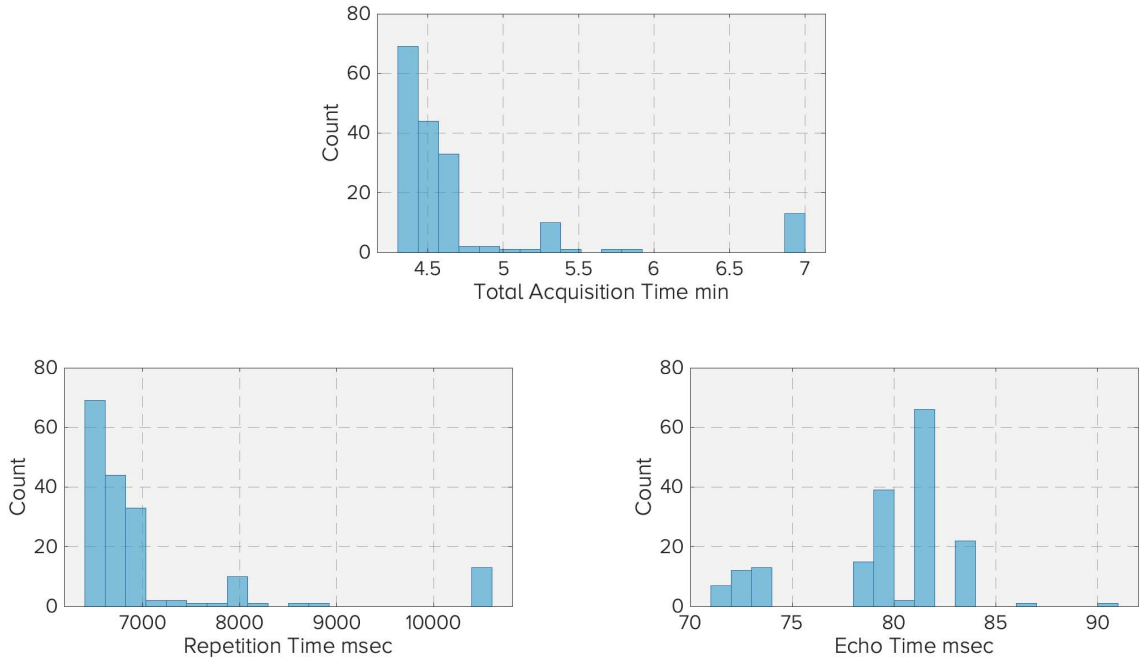


Figure 2.5: The distribution of the total acquisition time, repetition time (TR) and echo time (TE) across the cohort for the diffusion-weighted MRI sequence.

RCC and SUH, the default pixel spacing was 2.375 × 2.375 mm, and for CUH, 1.328 × 1.328 mm. Pixel spacing and/or image size were increased when a larger in-plane field of view (FOV) was required.

The in-plane FOV ranged from 228 to 380 mm along the y-axis and 340 to 450 mm along the x-axis. In all cases, the entire breast, on both sides, was encompassed. A coronal saturation band was used to reduce artefacts from the chest wall, placed as close to the base of the breast as possible without losing any signal from the breast tissue itself.

For RMH, GGC, UHNM, CUH, TMC and SUH, the default number of slices and slice thickness was 35 and 5 mm, respectively, and for RCC, 45 and 4 mm. The number of slices could be increased to capture the entire tumour. The default slice gap used at all sites was 0 mm, apart from RCC, which had a slice gap of 0.4 mm. As a result, the standard depth (no. of slices × (slice thickness + slice gap)) was 175 mm across all sites apart from RCC, which was 198 mm, and the depth ranged from 155 to 250 mm.

Hospital	FOV mm^2	No. of Slices	Slice Thickness mm	Slice Gap mm	Depth mm
RMH n = 92	228×380 [(228-309)×(380-450)]	35 [35-45]	5 [4-5]	0 [0-0.4]	175 [175-210]
GGC n = 16	228×380	35	5	0	175
UHNM n = 7	228×380	35	5	0	175
CUH n = 13	340×340	35 [31-40]	5	0	175 [155-200]
TMC n = 33	380×380	35 [35-45]	5 [4-5]	0	175 [175-200]
RCC n = 12	228×380 [(228-230)×(380-384)]	45 [35-45]	4 [4-5]	0.4 [0-0.4]	198 [175-198]
SUH n = 5	228×380	35	5	0	175

Table 2.3: A summary of the diffusion-weighted MRI imaging parameters across the clinical trial centres. n: no. of scans; and FOV: field of view.

2.3.4 Image Pre-Processing

The independent diffusion directions were combined to calculate the trace diffusion-weighted images by taking the geometric mean of the signal intensities:

$$S_{trace} = \sqrt[3]{S_p S_r S_s}, \tag{2.2}$$

where S_{trace} is the trace signal, and S_p, S_r and S_s are the source volumes for the phase-encoding axis (p), readout direction (r) and slice direction (s).

The DW images were viewed, interacted with and analysed using Horos v3.3.6, an open source DICOM medical image viewer based on OsiriX^{TM} and using the python plugin, PyOsiriX [240].

A value for a single pixel may be impacted by noise. Therefore, results should be averaged over several pixels for more reliable quantitative measurements. The trace signals were smoothed in-plane using `gaussian_filter`, from the SciPy multidimensional imaging processing package (`scipy.ndimage`) [241], by convolution with a Gaussian kernel with a standard deviation equal to 1 in both axes. The filter was truncated at 4 standard deviations. When the filter overlaps a border, the input array was extended by reflecting about the edge of the last pixel. This did not impact the tumour region of interest, as they were never on the border.

For the scans acquired using a 3T scanner, there could be a shift in the y-direction as the b-values increase. The extent of the pixel shift was manually determined by finding an anatomical landmark and determining how many pixels it has shifted from b_0 at each b-value. The diffusion volume was corrected, with rows taken off the top or bottom so the ROI aligns at each b-value. The ROI was segmented on b_0, and the extracted mask was manipulated similarly to the b_0 volume. The shift can occur either up or down across scans but will continuously go up/down in the same scan.

The trace signals at each b-value were divided by the trace signal at b_0 = 0 s/mm^2.

2.3.5 Region of Interest

Tumour regions of interest (ROIs) were initially outlined by two researchers (Megan Morris and Dr Emily Durie) on the DCE-MRI sequence, with guidance from all available MR sequences, including post-contrast DCE subtraction images. The tumours were manually segmented on all slices they were visible.

For DW-MRI, tumour ROIs were copied from the corresponding DCE-MRI slices and manually adjusted to account for any geometric distortions and differing acquisition parameters (e.g., spatial resolution, slice location). The scanner software provided an automated pixel-wise calculation of ADC maps. Hyper-intensity on high b-value DW trace volumes (b = 800-1200 s/mm^2) and relatively low ADC values in the pre-processed maps were used to refine the tumour boundaries. All distinct tumour regions were outlined for extensive, multi-centric disease to ensure full tumour coverage, excluding any intervening stroma. The analysis was performed using all voxels included within the multiple ROIs. Delineations were performed on the DICOM viewer Horos using the pencil and repulse function. A consultant radiologist (Dr Nina Tunariu) checked and modified the ROIs.

Tumour ROIs were redefined at each time-point, using the location of the lesion from previous scans as a guide. For tumours without residual enhancement on DCE and hyper-intensity on high b-value DW trace volumes, ROIs were placed in the same tissue region as the prior time-point, with additional guidance from the other MR sequence to identify the tumour bed.

2.3.6 Mono-exponential Model

During the combination of the independent diffusion directions, the individual direction-sensitive diffusion coefficients, D_p, D_r and D_s (p: phase-encoding axis; r: readout direction; s: slice direction), were averaged to create an apparent diffusion coefficient (ADC). Biological tissue is anisotropic, so the diffusion coefficients vary depending on the direction.

$$S_p = S_0 e^{-bD_p} \quad S_r = S_0 e^{-bD_r} \quad S_s = S_0 e^{-bD_s}, \tag{2.3}$$

$$S_{trace}(b) = \sqrt[3]{S_p S_r S_s} = S_0 e^{-b(D_p+D_r+D_s)/3} = S_0 e^{-bADC}, \tag{2.4}$$

where,

- S_p, S_r and S_s are the source volumes for the phase-encoding axis (p), readout direction (r) and slice direction(s),
- S_0 is the signal intensity without diffusion weighting (b = 0 s/mm^2), and
- b is the diffusion sensitisation factor measured in s/mm^2,
- $S_{trace}(b)$ represents the trace signal intensity after applying diffusion weighting,
- ADC (mm^2/s) is the Apparent Diffusion Coefficient, a quantitative measure of water diffusion in tissue.

The trace DW images possessed both diffusion weighting and T2-weighting, where very long/short T2 values can create bright/dark regions independent of diffusion. The T2 effects were removed by creating apparent diffusion coefficient (ADC) maps, which are purely parametric.

The logarithm was taken to linearise the equation:

$$\ln\left(\frac{S(b)}{S_0}\right) = -(b \times ADC) + c. \tag{2.5}$$

After this step, infinite values were set to NaN.

ADC was estimated pixel-wise using the `curve_fit` function from the SciPy optimization and root finding package (`scipy.optimize`) [241], with '+c' to account for noise. The `curve_fit` function uses non-linear least squares for fitting. All b-values were used to create the ADC maps.

No initial parameter guesses were specified, so the default value of 1 was used, and no parameter boundaries were specified. The optimisation method employed was the Levenberg-Marquardt algorithm, appropriate for this unconstrained problem. Introducing parameter limits could cause the fitted values to reach those boundaries, potentially mistaken for convergence,

leading to biased results and artificially reduced variability. By avoiding limits, noise was captured to extract complete information from the data.

2.3.7 Stretched Exponential Model

To account for multiple continuous diffusion coefficients contributing to the signal decay, we investigated the DW images with the stretched exponential model:

$$S(b) = S_0 e^{-(bDDC)^{\alpha}} \tag{2.6}$$

where:

- b is the diffusion sensitisation factor measured in s/mm^2,
- $S(b)$ represents the signal intensity after applying diffusion weighting,
- S_0 is the signal intensity without diffusion weighting (b = 0 s/mm^2),
- DDC (mm^2/s) is the distributed diffusion coefficient, a quantitative measure of the mean water diffusion in tissue, and
- α is the intra-voxel diffusion heterogeneity index, with values between 0 and 1.

The logarithm is taken to linearise the equation:

$$\ln\left(\frac{S(b)}{S_0}\right) = -(b \times DDC)^{\alpha} + c. \tag{2.7}$$

After this step, infinite values were set to NaN.

DDC and α were estimated pixel-wise using the `curve_fit` function from the SciPy optimization and root finding package (`scipy.optimize`) [241], with '+c' to account for noise. The `curve_fit` function uses non-linear least squares for fitting. All b-values were used to create the parameter maps.

No initial parameter guesses were specified, so the default value of 1 was used, and no parameter boundaries were specified. The optimisation method employed was the Levenberg-Marquardt algorithm, appropriate for this unconstrained problem. Introducing parameter limits

could cause the fitted values to reach those boundaries, potentially mistaken for convergence, leading to biased results and artificially reduced variability. By avoiding limits, noise was captured to extract complete information from the data.

2.3.8 Repeatability

For 8 participants, double baseline DW-MRI scans were acquired. Three participants were at RMH, one at CUH, three from RCC and one from SUH. The time between the two baseline scans ranged from 5 to 18 days, with an average of 9.3 days.

Of these 8 participants, 5 had identical imaging parameters at both baselines. However, repeatability Participant 1 had a variation in TR (6900/7100 ms) and TE (78/79 ms), Participant 6 had a variation in TR (8000/8100 ms), and Participant 7 had a variation in slice thickness (5/4 mm), TR (6500/8000 ms) and pixel spacing (2.375/2.4 mm).

2.4 Dynamic Contrast-Enhanced MRI

2.4.1 Participant Population

In this multi-centre, prospective study, 61 participants underwent complete dynamic contrast-enhanced (DCE) MRI, resulting in 172 scans for the final analysis. The distribution of participants and scans across different centres is as follows:

- The Royal Marsden NHS Foundation Trust (RMH): 26 participants contributed 88 scans,
- NHS Greater Glasgow and Clyde (GGC): 4 participants contributed 15 scans,
- University Hospitals of North Midlands NHS Trust (UHNM): 4 participants contributed 9 scans,
- Cambridge University Hospitals NHS Foundation Trust (CUH): 4 participants contributed 13 scans,
- Tata Medical Center (TMC): 18 participants contributed 33 scans,

- Regional Cancer Centre (RCC): 4 participants contributed 10 scans,
- Stavanger University Hospital (SUH): 1 participant contributed 4 scans.

Several scans were excluded from the final analysis for various reasons. These included DCE-MRI sequences that did not adhere to the research protocol[3], and some scans terminated before or during the DCE sequence. For reference, in the research protocol, a complete DCE acquisition extended beyond 470 seconds post-contrast. Additional exclusions occurred due to data acquisition issues, such as incomplete or missing dynamic data. These scans also had data acquisition issues with the diffusion-weighted MRI sequence.

Furthermore, one scan was excluded due to an early contrast injection, which resulted in the absence of pre-contrast dynamic volumes, and one scan had no contrast injected at all. Lastly, scans acquired after the data analysis period were also excluded. Some participants with excluded scans had DCE data available at other time-points and will be included in the analysis. Additional reasons for missing time-points include missed scans due to illness, early study termination, or participants not yet reaching those time-points.

Across the imaging time-points, 59 scans were conducted at baseline, 7 at a second baseline, 32 at 2-weeks post-radiotherapy (RT), 2 at 3-months, 39 at 6-months, 1 at 9-months, 22 at 12-months, and 10 at 24-months post-RT. Only a limited number of participants consented to the 3- and 9-month time-points, as these were later additions to the trial protocol for a radiomics sub-study, which was beyond the scope of this work.

2.4.2 Patient Set-Up

A gadolinium-based MRI contrast agent, specifically gadoteric acid contrast agent (also known as DOTA-Gd or gadoterate meglumine), marketed under the brands Dotarem® (Guerbet, Villepinte, France) or Clariscan® (GE Healthcare, Chicago, IL, USA), was administered intravenously using an automatic power injector. The contrast agent was dosed at 0.1 mmol/kg and injected at a rate of 3 mL/s, followed by a 20 mL saline flush at 2 mL/s.

[3]For context, our protocol involves a DCE acquisition with 45 phases at fast temporal resolutions of ~12s. However, some participants underwent a standard contrast-enhanced protocol with ~6 phases at slow temporal resolutions of ~60-70s.

Most participants were imaged in the prone position; however, 11 participants were imaged in the supine position at one or more time-points due to discomfort in the prone position (e.g. due to fungating tumours). Of these, 7 participants who were imaged supine at baseline remained in this position for subsequent imaging sessions. The prone position minimises breast movement to obtain the best quality data. For participants in a supine position, there was a possibility for more motion. The participants were free breathing throughout the examination.

2.4.3 Imaging Parameters

The research DCE-protocol is a high temporal resolution 3D isotropic, spoiled gradient recalled echo T1-weighted imaging sequence designed by Dr Matthew Blackledge (The Institute of Cancer Research) for the KORTUC clinical trial. Across all scanner sites, the parameters were standardised as closely as possible and were required to remain consistent throughout the trial at each centre.

Full coverage of both breasts was acquired using bilateral breast coils, which improved the signal-to-noise ratio and enabled parallel imaging techniques. Bilateral breast coverage was also acquired to evaluate the healthy breast and monitor for new disease.

RMH, GGC and SUH used a Siemens 1.5T scanner, CUH a GE 1.5T scanner, and UHNM, TMC and RCC a Siemens 3T scanner. For all sites, repetition time (TR) was 6 ms, apart from TMC, which used 4.5 ms. Echo time (TE) varied across sites, with the Siemens 1.5T scanners having TE of 4.77 ms, the GE 1.5T scanner TE of 4.46 ms, and the Siemens 3T scanners having TE of 2.46 ms. The number of signal averages was 1 across all sites except for CUH, which was 0.7.

A pre-contrast proton density map was obtained using a (low) flip angle of 3°, while the pre- and post-contrast dynamic images were acquired using a (high) flip angle of 16°, except at CUH, where a 15° flip angle was used. All other parameters remained the same for the low and high flip angle scans.

Initially, the protocol acquired a single low flip angle map, which was later amended to four. All scans involved acquiring 45 high flip angle phases, except for RCC, where participants had 30 phases due to a longer temporal resolution per phase. The mean total dynamic scan time,

Hospital	Scanner	TR ms	TE ms	No. of Averages	LFA	HFA	Rows	Columns	Pixel Spacing mm
RMH n = 88	Siemens Aera/Sola 1.5T	6	4.77	1	3	16	160 [160-192]	160 [156-160]	2.1875 [2.0625-2.5]
GGC n = 15	Siemens Aera 1.5T	6	4.77	1	3	16	160	160	2.1875
UHNM n = 9	Siemens Vida 3T	6	2.46	1	3	16	160	160	2.1875 [2.1875-2.3125]
CUH n = 13	GE SIGNA Artist 1.5T	6	4.46	0.7	3	15	256	256	1.3672 [1.3281-1.3672]
TMC n = 33	Siemens Vida 3T	4.5	2.46	1	3	16	192	192	1.8229
RCC n = 10	Siemens Vida 3T	6	2.46	1	3	16	160 [160-192]	160 [156-160]	2.1875 [2.1875 - 3]
SUH n = 4	Siemens Sola 1.5T	6	4.77	1	3	16	160	160	2.1875

Table 2.4: A summary of the dynamic contrast-enhanced MRI imaging parameters across the clinical trial centres. n: no. of scans; TR: repetition time; TE: echo time; LFA: low flip angle; and HFA: high flip angle.

Hospital	No. of Pre-Contrast LFA Phases	No. of HFA Phases	No. of Pre-Contrast HFA Phases	Temporal Resolution s	Total Time min	DCE Time min
RMH n = 88	4 [1-4]	45	5 [2-6]	12.23 [12.05-14.72]	9.88 [9.88-12.63]	8.76 [7.83-9.81]
GGC n = 15	1	45	5 [2-6]	12.23 [12.23-14.72]	10.70 [9.88-12.63]	7.95 [7.95-9.81]
UHNM n = 9	1	45	6 [2-6]	12.23 [12.23-19.46]	10.70 [9.88-16.70]	7.95 [7.95-12.97]
CUH n = 13	1	45	4 [4-5]	13.65 [13.46-13.65]	11.15 [11.00-11.38]	9.33 [8.98-9.33]
TMC n = 33	1	45	3 [2-7]	12.61 [12.61-18.58]	10.40 [10.19-16.26]	8.83 [7.99-12.08]
RCC n = 10	4	30 [24-30]	5	19.02 [19.02-26.52]	11.10 [11.10-15.47]	7.93 [7.91-11.05]
SUH n = 4	4	45	5	12.23	10.50	8.15

Table 2.5: A summary of the dynamic contrast-enhanced MRI imaging parameters across the clinical trial centres. n: no. of scans; LFA: low flip angle; and HFA: high flip angle.

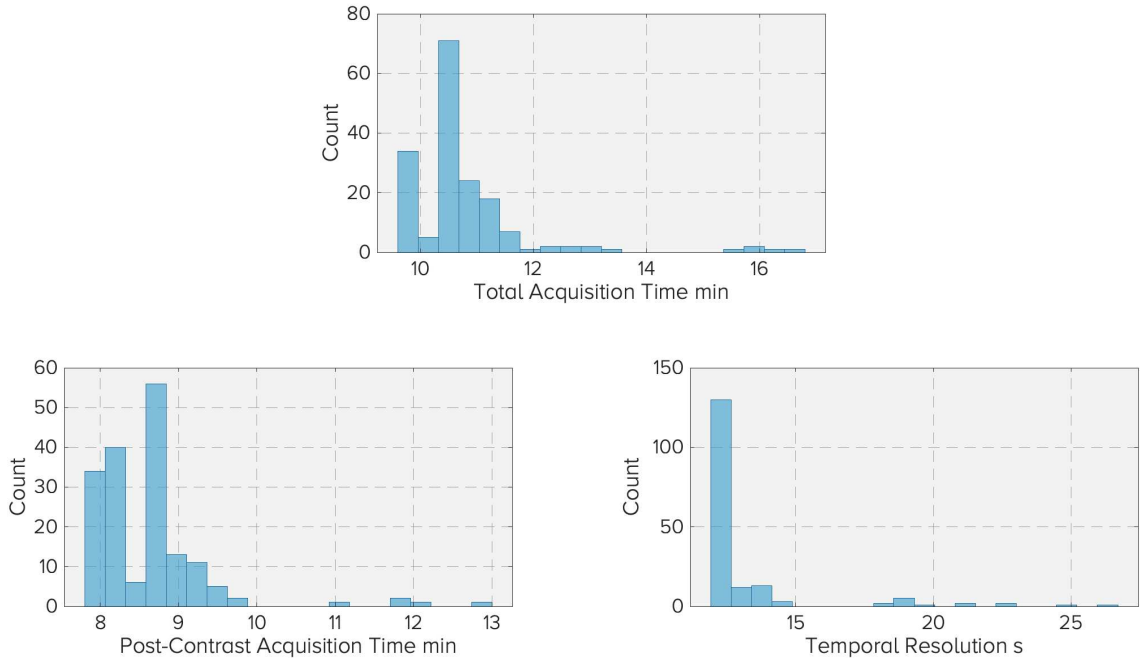


Figure 2.6: The distribution of the total acquisition time, post-contrast acquisition time, and temporal resolution across the entire cohort for the dynamic contrast-enhanced MRI sequence.

including the pre-contrast low and high flip angle acquisitions, was 10.78 minutes. The initial protocol specified acquiring two high flip angle phases before contrast administration, which was later amended to five. However, the number of pre-contrast dynamic images was not always consistent, as the process required manually pressing a button on the screen, which appeared after the 2nd or 5th phase as specified. The mean post-contrast dynamic scan time was 8.63 minutes. The number of pre-contrast low and high flip angle maps were increased to improve the accuracy of the T1 map estimation.

A mean temporal resolution of 13.19s was achieved across the DCE-MRI dataset using TWIST (time-resolved angiography with interleaved stochastic trajectories) view sharing (central region 33%, sampling density 33%), or DISCO (differential subsampling with Cartesian ordering) view-sharing at CUH, enabling the quantification of contrast dynamics while maintaining sufficient spatial resolution to capture intra-tumoural heterogeneity.

For RMH, GGC, UHNM, RCC and SUH, the default image size and pixel spacing was 160×160 and 2.1875×2.1875 mm, 256×256 and 1.3672×1.3672 mm for CUH and 192×192 and 1.8229×1.8229 mm for TMC. Pixel spacing was increased when a larger in-plane field of view (FOV) was required.

Hospital	FOV mm^2	No. of Slices	Slice Thickness mm	Slice Gap mm	Depth mm
RMH n = 88	350×350 [(330-450)×(330-400)]	72 [72-88]	2.2 [2.2-2.9]	0 0	158 [158-209]
GGC n = 15	350×350	72 [72-84]	2.2	0	158 [158-185]
UHNM n = 9	350×350 [(350-370)×(350-370)]	72 [72-118]	2.2 [1.8-2.2]	0	158 [158-212]
CUH n = 13	350×350 [(340-350)×(340-350)]	88 [88-90]	1.8	0	158 [158-161]
TMC n = 33	350×350	88	1.8 [4-5]	0	158
RCC n = 10	350×350 [(350-500)×(350-480)]	72 [72-96]	2.2 [4-5]	0 [0-0.4]	158 [158-211]
SUH n = 4	350×350	72	2.2	0	158

Table 2.6: A summary of the dynamic contrast-enhanced MRI imaging parameters across the clinical trial centres. n: no. of scans; and FOV: field of view.

The in-plane FOV ranged from 330 to 500 mm along the y-axis and 330 to 480 mm along the x-axis. In all cases, the entire breast, on both sides, was encompassed.

For RMH, GGC, UHNM, RCC and SUH, the default number of slices and slice thickness was 72 and 2.2 mm, respectively, and for CUH and TMC, 88 and 1.8 mm. The number of slices was increased when needed to capture the entire tumour, though this resulted in a longer temporal resolution. All sites used a slice gap of 0 mm. As a result, the default depth (no. of slices $\times$ slice thickness) was 158 mm across all sites, and the depth ranged from 158 to 212 mm.

Fat- and water-suppressed volumes were also acquired at each time-phase, using half the in-phase echo time and a DIXON sequence.

2.4.4 Region of Interest

Tumour regions of interest (ROIs) were outlined by two researchers (Megan Morris and Dr Emily Durie) on the DCE-MRI sequence, with guidance from all available MR sequences, including post-contrast DCE subtraction images. The tumours were manually segmented on all slices they were visible.

For extensive, multi-centric disease, all distinct tumour regions were outlined to ensure complete coverage, excluding any intervening stroma. The analysis was performed using all voxels included within the multiple ROIs. Delineations were performed on the DICOM viewer Horos using the pencil and repulse function. A consultant radiologist (Dr Nina Tunariu) checked and modified the ROIs.

Tumour ROIs were redefined at each time-point, using the location of the lesion from previous scans as a guide. For tumours without residual enhancement on DCE, ROIs were placed in the same tissue region as the prior time-point, with additional guidance from the other MR sequence to identify the tumour bed.

2.4.5 Image Processing

The DCE images were viewed, interacted with and analysed using Horos v3.3.6, an open-source DICOM medical image viewer based on OsiriX^{TM} and using the python plugin, PyOsiriX [240].

T1-weighted images with a low and high flip angle were acquired for calculating the T1 map.

Across the dataset, the low flip angle (LFA) and high flip angle (HFA) volumes generally cover the same field of view (FOV), and their pixel maps align, except for 8 scans where different FOVs were covered in the axial direction. Slices not covering the same FOV were discarded. The best matching slices had axial location differences ranging from 0.04-0.80 mm, with a mean value of 0.39 mm. For 11 scans where the number of slices in the LFA and HFA volumes did not match, the extra slices were discarded.

For one scan, although the LFA and HFA volumes covered the same FOV, the slice thickness differed (1.00 mm for LFA and 1.79 mm for HFA). The best matching slices from the LFA volume were aligned to the HFA volume, with location differences ranging from 0 to 0.4 mm between the slices.

For two scans, the LFA and HFA volumes were not aligned due to different in-plane FOVs. To resolve this, rows and columns not covering the same FOV were discarded to align the pixel maps.

For another scan, the LFA volume was rotated relative to the HFA volume, necessitating realignment using the `rotate` function from the SciPy multidimensional image processing package (`scipy.ndimage`) [241].

Concentration Maps

The signal intensity-time curves were converted into contrast agent concentration within the tissue. The signal intensities from the pre-contrast low flip angle (LFA) and high flip angle (HFA) T1-weighted volumes were used to calculate the T1 map. When more than one pre-contrast LFA and HFA were acquired, the last acquired one was used unless there was significant motion, and then a previous one was used. The last pre-contrast HFA volume was determined by manually checking for the onset of contrast, which could be seen as the wash-in of contrast in the heart chambers. For a spoiled gradient echo T1-weighted DCE-MRI sequence, the following equation describes the signal [207]:

$$S(t) = S_0 \frac{(1 - e^{-(TR/T1(t))}) \sin(\alpha)}{1 - \cos(\alpha) e^{-(TR/T1(t))}}, \tag{2.8}$$

where S_0 is the scaling factor, α is the flip angle, TR is the repetition time (msec), and $T1(t)$ is the longitudinal relaxation time at time t.

The native pre-contrast $T1(0) = T1_0$ relaxation time was analytically calculated using the two-flip angle method. By using the pre-contrast signal intensities for these two flip angles (S_{α_1} and S_{α_2}), and taking the ratio of the two measurements, the equation was rearranged to solve for $T1_0$:

$$T1_0 = TR \cdot \left[\ln \left(\frac{S_{\alpha_1} \cdot \cos(\alpha_1) \cdot \sin(\alpha_2) - S_{\alpha_2} \cdot \sin(\alpha_1) \cdot \cos(a_2)}{S_{\alpha_1} \cdot \sin(\alpha_2) - S_{\alpha_2} \cdot \sin(\alpha_1)} \right) \right]^{-1} \tag{2.9}$$

To calculate the scaling factor S_0, Equation 2.4.5 was rearranged for one of the flip angles at time = 0, using the calculated $T1_0$. The post-contrast $T1(t)$ relaxation times were computed using this scaling factor and the corresponding signal intensities at each time-point.

The contrast agent concentration as a function of time $C(t)$ was derived from the change in $T1$ over time, as described by the following equation [209]:

$$C(t) = \frac{1}{r}(\frac{1}{T1(t)} - \frac{1}{T1_0}), \tag{2.10}$$

where r is the relaxivity of the gadolinium-based contrast agent and $T1_0$ is the pre-contrast T_1 value, and $R_1 = \frac{1}{T_1}$ is the relaxation rate. $T1$ and concentration values are independent of the scanner and acquisition settings. The effect of the contrast agent on the longitudinal proton relaxation time, T1, depends on its concentration.

Across the participants, the contrast used was either Dotarem or Clarisican, which have the same relaxivity. At 1.5 T, this is 3.9 $s^{-1}mM^{-1}$, and at 3 T, this is 3.4 $s^{-1}mM^{-1}$ [242]. The calculated T1 values are reported in milliseconds (ms). Therefore, relaxivity values were divided by 1000 to express in millimolar (mM) concentrations.

A value for a single pixel may be impacted by noise. Therefore, results were averaged over several pixels for more reliable quantitative measurements. The concentration maps were smoothed in-plane using `gaussian_filter`, from the SciPy multidimensional imaging processing package (`scipy.ndimage`) [241], by convolution with a Gaussian kernel with a standard deviation equal to 1 in both axes. The filter was truncated at 4 standard deviations.

When the filter overlaps a border, the input array was extended by reflecting about the edge of the last pixel. This did not impact the tumour region of interest, as they were never on the border.

Since the post-contrast acquisition times of the DCE sequences varied, it was determined that 470 seconds was the minimum time reached by all scans. To ensure consistency in calculating quantitative parameters, only the post-contrast HFA scans up to and including the subsequent acquisition after 470 seconds were used.

2.4.6 Non-Parametric Analysis

For non-parametric analysis, quantitative parameters can be directly derived from the time-concentration curves without complex modelling.

To determine the wash-in and wash-out gradient that occurs before and after the peak of the concentration curve, a piecewise linear fit was, using the `piecewise` function from NumPy (`numpy`) [243]. The piecewise linear model segments the concentration curve (x) into two regions, $R1$ and $R2$, based on a turning point (x_0), with each region described by a separate linear equation.

$$R1 = k_1 x + y_0 - k_1 x_0 \quad R2 = k_2 x + y_0 - k_2 x_0. \tag{2.11}$$

Below x_0, the function has a slope k_1, and is adjusted to pass through a specified point (x_0, y_0), while above x_0, it transitions to a slope k_2, maintaining continuity at (x_0, y_0).

The parameters were estimated pixel-wise using the `curve_fit` function from the SciPy optimization and root finding package (`scipy.optimize`) [241]. The `curve_fit` function uses non-linear least squares for fitting.

No initial parameter guesses were specified, so the default value of 1 was used, and no parameter boundaries were specified. The optimisation method employed was the Levenberg-Marquardt algorithm, appropriate for this unconstrained problem. Introducing parameter limits could cause the fitted values to reach those boundaries, potentially mistaken for convergence, leading to biased results and artificially reduced variability. By avoiding limits, noise was

captured to extract complete information from the data.

The parameters extracted from the fit include the wash-in rate ($k_1 = WIR$), wash-out rate ($k_2 = WOR$), time-to-peak ($x_0 = TTP$), and peak enhancement ($y_0 = PE$). By extension, the wash-in area under the curve (AUC_{WI}) and wash-out area under the curve (AUC_{WO}) were calculated, using the `trapz` function from NumPy (`numpy`) [243].

As well as the piecewise linear fit model, quantitative parameters were directly derived from the time-concentration curve. The concentration at three time-points, 60 s, 180 s and 470 s were estimated by interpolation to maintain consistency across scans. By determining the two measured time-points that these specified time-points fall between, e.g., $t_{<60s}$ and $t_{>60s}$, the proportion that the specified time-point t_{60s} was from $t_{<60s}$ relative to the time between $t_{<60s}$ and $t_{>60s}$, i.e., $P_{60s} = \frac{t_{60s} - t_{<60s}}{t_{>60s} - t_{<60s}}$, was calculated. This proportion, multiplied by the difference between the concentration at $t_{>60s}$ ($C_{>60s}$) and $t_{<60s}$ ($C_{<60s}$) was then added to $C_{<60s}$, i.e., $C_{60s} = C_{<60s} + P_{60s}(C_{>60s} - C_{<60s})$.

Using these time-points on the concentration curve, the following parameters were calculated:

- $iWIR$: initial wash-in rate for the first 60 seconds,
- $fWOR$: final wash-out rate from 180 to 470 seconds,
- AUC_{iWI}: initial wash-in area under the curve for the first 60 seconds,
- AUC_{fWO}: final wash-out area under the curve from 180 to 470 seconds,
- AUC_T: total area under the curve from 0 to 470 seconds,
- fE: final enhancement at 470 seconds.

The area under the curves were calculated using the `trapz` function from NumPy (`numpy`) [243].

The 60-second and 180-second time-points were determined through visual analysis of the averaged concentration curves across the participant cohort. Early contrast enhancement typically occurred within the first minute, while late contrast enhancement, characterised by wash-out, generally began around 180 seconds. The interval between these time-points encompassed the turning point, representing the peak concentration. Although wash-in could

extend beyond 60 seconds and wash-out could commence before 180 seconds, selecting these time-points ensured adequate separation to avoid the concentration peak. 470 seconds was chosen as the end-point because it was the minimum time reached by all scans.

2.4.7 Parametric Analysis

For parametric analysis, physiologically meaningful quantitative parameters can be derived from the time-concentration curves using the pharmacokinetic Tofts model.

Arterial Input Function

For 18 participants who had DCE-MRI using the same temporal resolution, the descending aorta was delineated on the phase with peak contrast. The aorta was segmented across multiple slices that it is visible on, avoiding the first and last 10 slices where the signal was affected by edge effects. These participants were scanned on a 1.5 T scanner with Dotarem or Clariscan.

The blood plasma concentration from the AIF is higher than the contrast concentration calculated from Equation 2.4.5 by a factor related to the haematocrit ($Hct = 0.42$) [244], the volume percentage of red blood cells in the blood:

$$C_p(t) = \frac{C(t)}{1 - Hct}. \tag{2.12}$$

The haematocrit was assumed to be constant across patients and imaging time-points, both pre- and post-treatment. The median concentration curve was averaged across the 18 participants. To calculate the parameters characterising the population average, the AIF concentration curve was modelled using the Orton model [245, 246]:

$$C_p(t) = D(a_1 t e^{-m_1 t} + a_2(e^{-m_2 t} - e^{-m_1 t})), \tag{2.13}$$

where D is the dose of the contrast agent (D = 0.1 mmol/kg), and a_1 and a_2 are the amplitude of the exponential components with decay m_1 and m_2. The Orton model assumes that the bolus disperses within the blood supply before reaching the tissue, which is realistic for physiological conditions with blood flow patterns and vascular branching. This causes the shape of the

AIF to broaden. Models with no dispersion, e.g. the bi-exponential model, assume a sharp bolus arriving at the target tissue, which can overestimate the peak concentration and skew the pharmacokinetic parameters. Furthermore, the Orton model fitted the population average AIF well.

For the population average AIF, a_1 = 59.37 kg/L, a_2 = 12.20 kg/L, m_1 = 2.466 min^{-1} and m_2 = 0.09034 min^{-1}.

Tofts Model

The Tofts model is described as [216]:

$$C(t) = v_p C_p(t) + C_p(t) \otimes \{K_{trans} e^{-\frac{K_{trans}}{v_e} t}\} \tag{2.14}$$

where K_{trans} (min^{-1}) is the volume transfer constant, v_e is the volume of EES per unit volume of tissue, and v_p is the volume of plasma per unit volume of tissue. The symbol $\otimes$ represents the convolution operator, where convolution is an integral that expresses the overlap of one function as it is shifted over another.

Using the Orton model in Equation 2.4.7, the concentration curve is given as [245]:

$$\begin{aligned} C(t) = D[v_p(a_1 t e^{-m_1 t} + a_2(e^{-m_2 t} - e^{-m_1 t})) \\ + \frac{K_{trans} a_1}{k_{ep} - m_1}\left(t e^{-m_1 t} - \frac{e^{-m_1 t} - e^{-k_{ep} t}}{k_{ep} - m_1}\right) \\ + K_{trans} a_2 \left(\frac{e^{-m_2 t} - e^{-k_{ep} t}}{k_{ep} - m_2} - \frac{e^{-m_1 t} - e^{-k_{ep} t}}{k_{ep} - m_1}\right)] \end{aligned} \tag{2.15}$$

where k_{ep} is substituted for K_{trans}/v_e.

The Tofts model parameters were estimated pixel-wise using the `curve_fit` function from the SciPy optimization and root finding package (`scipy.optimize`) [241]. The `curve_fit` function uses non-linear least squares for fitting.

No initial parameter guesses were specified, so the default value of 1 was used. Not specifying boundaries gave unphysical parameter values; therefore, upper and lower bounds were specified. These boundaries were 0 to 2 min^{-1} for K_{trans}, 0.001 to 1 for v_e, and 0 to 1 for

v_p.

The optimisation method employed was the Trust Region Reflective algorithm, which was appropriate for this constrained problem. Introducing parameter limits could cause the fitted values to reach those boundaries, potentially mistaken for convergence, leading to biased results and artificially reduced variability.

2.4.8 Repeatability

For 7 participants, a double baseline DCE-MRI scan was acquired. Three participants were at RMH, one at CUH, and three from RCC. The time between the two baseline scans ranged from 5 to 12 days, with an average of 9.3 days.

Of these 7 participants, 5 had identical imaging parameters at both baselines. However, DCE repeatability Participant 2, Participant 5, and Participant 6 had variations in temporal resolution (13.18/12.05 s, 21.005/19.02 s, and 24.97/22.56 s, respectively), and Participant 6 also had variation in the image size (160×160/192×156) and pixel spacing (3/2.5 mm).

2.5 Radiological Response Assessment

For the KORTUC clinical trial, treatment efficacy was determined using the MR images. Three expert breast radiologists (Dr Seema Salehi-Bird, Dr Nuala Healy, and Dr Archana Seth) qualitatively assessed radiologic response at 6-, 12- and 24-months post-radiotherapy. The response was assessed individually, followed by moderation meetings to reach a consensus. A modified version of the RECIST criteria was developed by Dr Navita Somaiah and Dr Emily Durie to assess the radiotherapy response of in situ breast tumours using MRI. These tumours may undergo fibrosis, so the mass may not disappear despite responding very well or completely. As a result, standard clinical radiology reports based on RECIST may not be suitable for these cases.

The diffusion-weighted MR images were often visually noisy; therefore, they were only used for response evaluation when the quality was adequate. However, they were extremely useful quantitatively, as shown later.

Response		Definition
1	CR	No tumour mass on MRI.
2A	CR	No evidence of enhancement above background in residual mass.
2B	CR	Evidence of minimal enhancement but diffusion images in keeping with fibrosis.
3	PR	Reduced tumour size by >30% with enhancement above background that is not in keeping with the tumour being entirely fibrotic.
4	SD	Stable tumour size with some enhancement.
5A	PD	Increased tumour size >20%; OR new foci of tumour within target lesion.
5B	PD	Loco-regional tumour spread; OR new foci of tumour outside target lesion.

Table 2.7: Radiological response assessment criteria created for the KORTUC clinical trial, for radiotherapy response of in situ breast tumours, as assessed by MRI, including contrast-enhanced MRI and diffusion-weighted MRI.

Subsequent time-points were compared to the nadir of tumour size., i.e. the smallest tumour size recorded across time-points. Furthermore, the following criteria was specified to distinguish complex cases of partial response, stable disease and progressive disease.

- PD: CR on the previous scan, but a new disease is visible at the tumour site.
- PD: PR on the previous scan, but >20% tumour growth since the previous scan.
- PR: PR on the previous scan with <20% tumour growth since the previous scan and still >30% tumour shrinkage since baseline.
- SD: PR on the previous scan but <20% tumour growth since the previous scan and now <30% tumour shrinkage since baseline.

Patients were grouped as either responders (rCR, rPR) or non-responders (rSD, rPD) when assessing the quantitative parameters. Pathologic response could not be evaluated since the tumours were not excised.

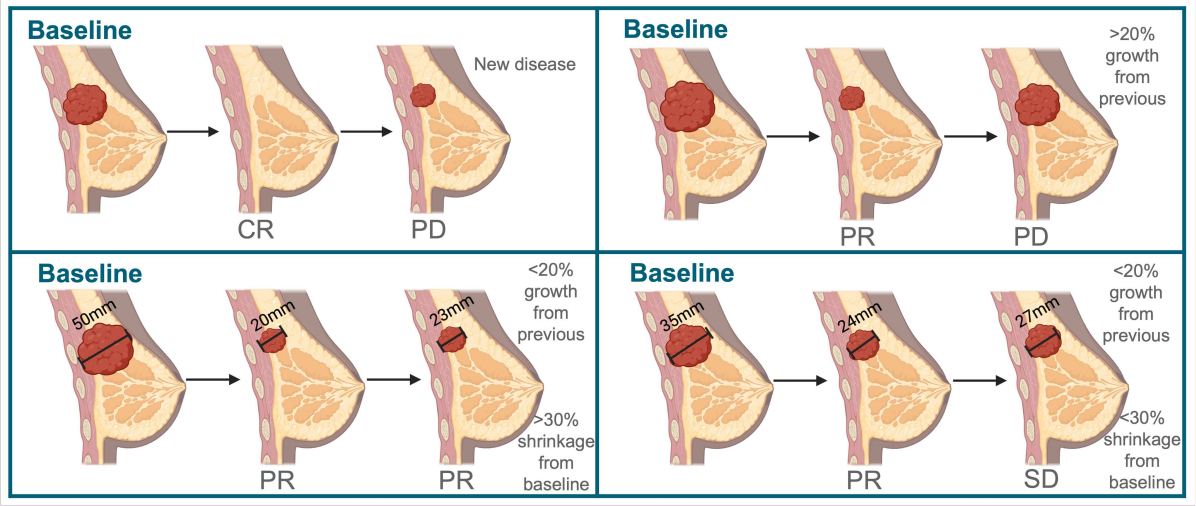


Figure 2.7: Radiology response assessment criteria to distinguish difficult cases of partial response (PR), stable disease (SD) and progressive disease (PD) when assessed, where CR is complete response. Provided by Emily Durie.

2.6 Biopsies and Immunohistochemical Staining

Duplicate core biopsies were obtained from 10 participants at baseline and 2-weeks post-RT from two non-necrotic areas of the tumour to capture heterogeneity, guided by clinical ultrasound.

Biopsies were processed into formalin fixed paraffin embedded blocks (FFPE). Immunohistochemical staining for endothelial cell marker CD31 (clone JC70A) was performed on 3μm sections using a Leica Bond III platform and Bond Refine Detection Kit (HSL Laboratories) for vessel density and diameter analysis. Slides were digitised at 40X magnification using a Nanozoomer© (Hamamatsu) digital slide scanner. Processing was performed by Dr Selvakumar Anbalagan and Dr Emily Durie.

A consultant breast histopathologist (Dr Ioannis Roxanis) scored CD31 staining, with 1=0-5; 2=5-10; 3=10-15; 4=15-20; 5=20-25; 6=25-30; 7=30-35 vessels per 0.5mm^2. Mean scores were calculated from duplicate biopsies.

2.7 Statistical Analysis

For the SRUS parameters, repeatability was assessed for the within-plane mean and within-plane standard deviation, averaged across the four imaging planes. For the DW-MRI and DCE-MRI

parameters, the median, 25th percentile, 75th percentile, and interquartile range (IQR) were assessed.

2.7.1 Repeatability

For repeatability, statistics were calculated for each quantitative parameter, X_{ij}, where $i = 1, \ldots, N$ represents the repeatability scan, N is the number of repeatability scans, and $j = 1, 2$ is the test-retest measurement, i.e., the quantitative parameter after the first and second bolus. The following statistics were calculated:

Within-subject standard deviation:

$$SD_{ws} = \sqrt{\frac{1}{2N}\sum_{i=1}^{N}(X_{i1} - X_{i2})^2}, \tag{2.16}$$

within-subject mean squares:

$$MS_{ws} = \frac{1}{N}\sum_{i=1}^{N}[(X_{i1} - \bar{X}_i)^2 + (X_{i2} - \bar{X}_i)^2], \tag{2.17}$$

between-subject mean squares:

$$MS_{bs} = \frac{2}{N}\sum_{i=1}^{N}(\bar{X}_i - \bar{\bar{X}})^2, \tag{2.18}$$

and between-subject standard deviation:

$$SD_{bs} = \sqrt{\frac{MS_{bs} - MS_{ws}}{2}}, \tag{2.19}$$

where:

$$\bar{X}_i = \frac{X_{i1} + X_{i2}}{2} \tag{2.20}$$

is the average value of the repeat measurements, and

$$\bar{\bar{X}} = \frac{1}{N}\sum_{i=1}^{N}\bar{X}_i. \tag{2.21}$$

is the average value of $\bar{X}_i$ across participants.

Repeatability was assessed for each parameter by calculating the within-subject Coefficient of Variation (wCV), the Intraclass Correlation Coefficient (ICC) and Repeatability Coefficient (RC), calculated as:

$$wCV = \frac{SD_{ws}}{\bar{\bar{X}}} \times 100\% \tag{2.22}$$

$$ICC = \frac{SD_{bs}^2}{SD_{bs}^2 + SD_{ws}^2}, \tag{2.23}$$

$$RC = 1.96 \times \sqrt{\frac{1}{N}\sum_{i=1}^{N}(x_{i2} - x_{i1})^2} = 2.77 \times SD_{ws} \tag{2.24}$$

Following the guidance from [247], the criteria to assess repeatability was defined as:

(i) ICC < 0.5: poor repeatability,

(ii) ICC 0.5 – 0.75: moderate repeatability,

(iii) ICC 0.75 – 0.9: good repeatability,

(iv) ICC > 0.9: excellent repeatability.

A high Intraclass Correlation Coefficient (ICC) requires the between-subject standard deviation to be significantly greater than the within-subject standard deviation. Values below 0.5 indicate that the within-subject standard deviation exceeds the between-subject standard deviation.

For the SRUS quantitative parameters, the tumours provided four measurements of within-plane mean and standard deviation due to multiple imaging planes acquired during the scan. The repeatability statistics were calculated for all the imaging plane combinations to investigate the impact of averaging across the imaging planes. In other words, quantitative parameter

repeatability was investigated for a single imaging plane and then for a combination of two, three and four imaging planes.

For the response assessment studies, the changes in the quantitative parameters at post-RT time-points were analysed to assess their potential as sensitive response biomarkers. The repeatability coefficient was used to evaluate significant change. The analysis was conducted blind concerning the treatment group (with or without KORTUC) and clinical outcome.

2.7.2 Statistics

The two-sided Wilcoxon rank sum test was used to assess differences between healthy tissue and tumours groups for both SRUS and MRI quantitative parameters, as well as for differences between radiological response groups (i.e., complete response (CR), partial response (PR), stable disease (SD) and progressive disease (PD) for MRI quantitative parameters. Additionally, it was used to analyse the pre-treatment differences between responders and non-responders to determine if these groups exhibited statistically significant variations.

Paired t-tests were conducted to evaluate differences between baseline and post-radiotherapy (RT) time-points for SRUS and MRI parameters. Statistical significance levels were denoted as follows: $*p < 0.05$, $**p < 0.01$, and $***p < 0.001$.

The Spearman correlation coefficient was used to examine correlations between SRUS vessel density and CD31 count. The Pearson correlation coefficient was used to examine correlations between baseline values and post-RT responses in quantitative parameters, and also for the relationship between quantitative parameters from SRUS, DW-MRI and DCE-MRI. The strength of the correlation was categorised as follows: $0-0.2$ (very weak), $0.2-0.4$ (weak), $0.4-0.6$ (moderate), $0.6-0.8$ (strong), and $0.8-1.0$ (very strong).

The analysis evaluated the predictive power of pre-treatment and early post-treatment changes of parameters in distinguishing between responders (CR/PR) and non-responders (PD) at 12-months post-RT using a receiver operating characteristic (ROC) curve and the area under the curve (AUC).

For a combination of parameters, logistic regression modelling was performed using a generalised linear model with a binomial distribution and Jeffrey's prior for likelihood penalty;

predicted probabilities were generated, and model performance was evaluated using a ROC curve and the AUC. The Wald test is used to test whether the corresponding predictor variable has a significant effect on the response variable.

The AUC was interpreted as follows: AUC = 0.5 (no predictive power); AUC > 0.7 (acceptable predictive power), and AUC > 0.9 (excellent predictive power). All statistical analyses were performed using MATLAB.

Chapter 3

Results Chapter 1: Super-Resolution Ultrasound

3.1 Repeatability

From the super-resolution ultrasound (SRUS) repeatability study, the super-resolved maps obtained after the first and second boluses revealed similar reconstructed microvascular structures, as shown in Figure 3.1 for an example participant. This consistency was observed across multiple imaging planes of the tumour, including the horizontal position (0°), 90°, 45° clockwise and 45° anticlockwise. The white dashed boxes in the super-resolved maps highlight these similar microvessel structures following both boluses, demonstrating the capability of an experienced breast radiographer to return to similar regions across multiple imaging planes at the tumour centre. Exact relocation of the identical ultrasound slice is not possible due to the micrometre to millimetre precision required by the hand-held probe and visual determination of the central slice.

The repeatability study investigated how the repeatability coefficients (RCs) of SRUS quantitative parameters were influenced by the number of imaging planes used for averaging within the tumour. For each SRUS-derived parameter, the metrics analysed included the in-plane mean and the standard deviation, representing heterogeneity.

Figure 3.2 demonstrates the impact of increasing the number of imaging planes on the RCs.

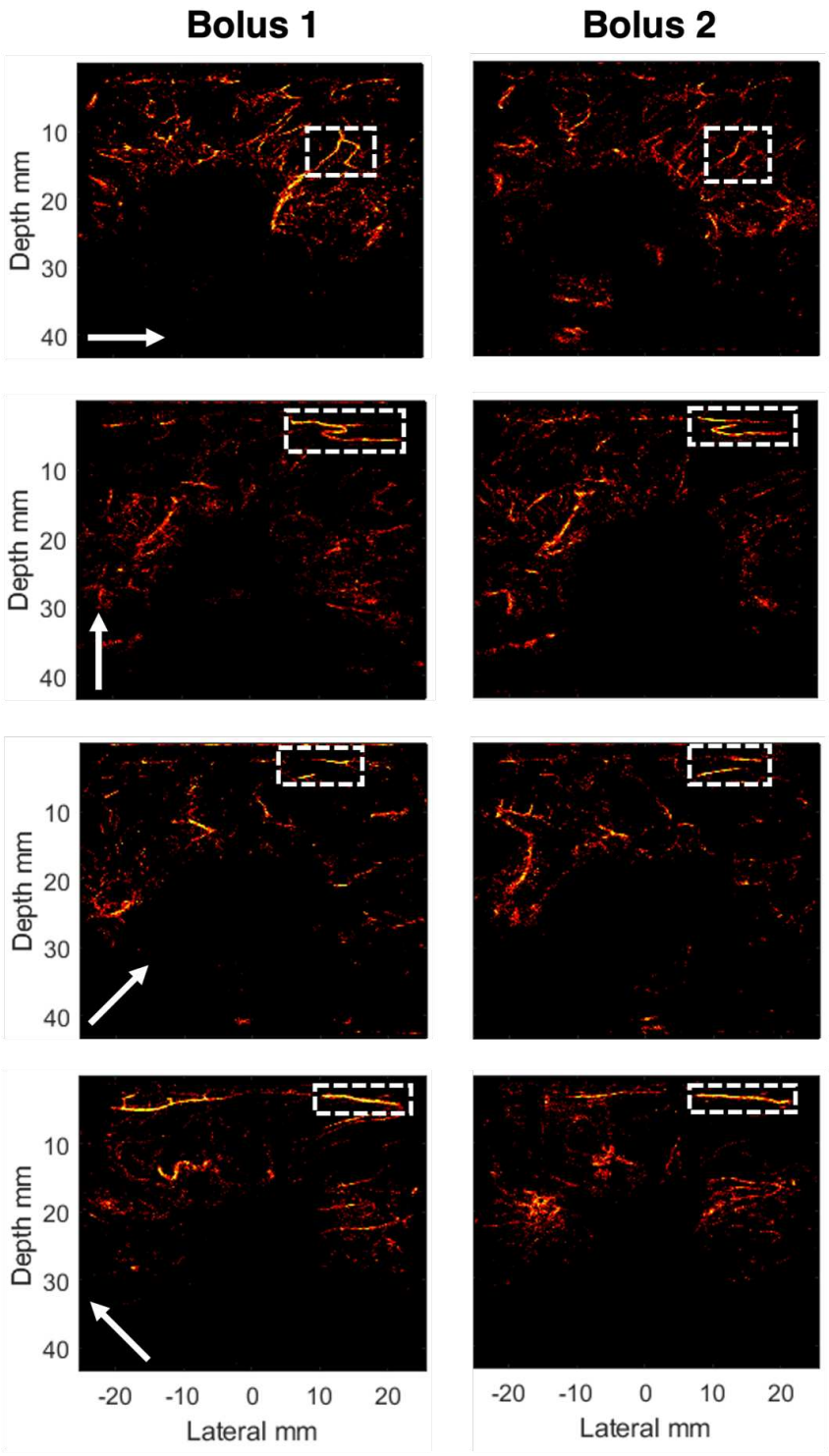


Figure 3.1: Example of a super-resolution ultrasound repeatability scan. Super-resolved maps of the breast tumour microvasculature were acquired at four imaging planes at the tumour centre (horizontal 0°, 90°, 45° clockwise and 45° anticlockwise). These scans were repeated twice, following the first and second contrast boluses. Brightness in the images represents the number of microbubble localisations per pixel. The white arrows indicate the orientation of the ultrasound probe, while white boxes highlight similar microvascular structures observed after both boluses.

Across all quantitative parameters, a clear trend was observed: RCs consistently decreased as more imaging planes were included in the averaging process. This reduction in RCs was attributed to a decrease in within-subject variability, indicating that averaging across multiple imaging planes yields more repeatable and robust quantitative parameters.

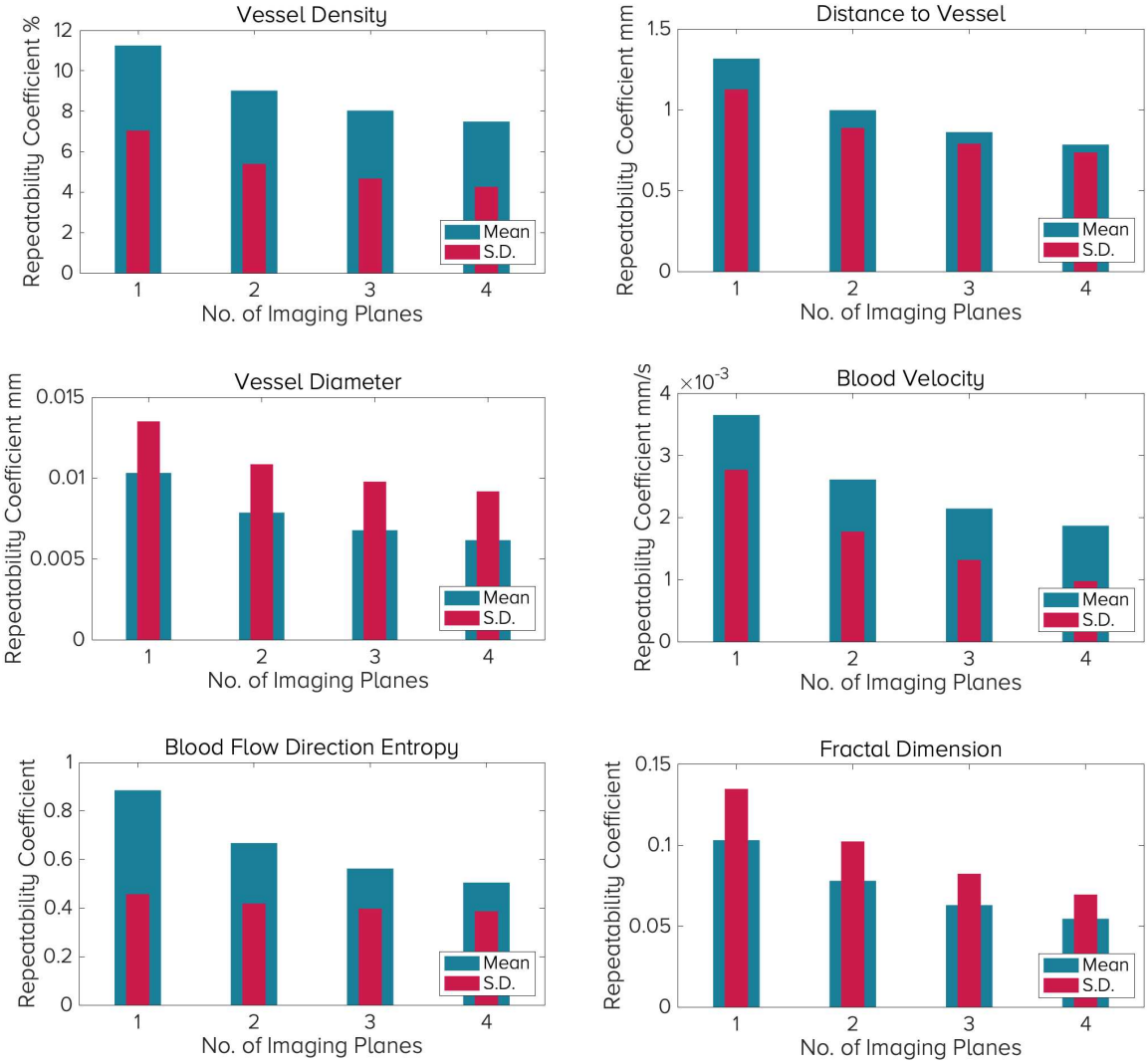


Figure 3.2: Repeatability coefficients (RCs) of super-resolution ultrasound (SRUS) quantitative parameters as a function of the number of imaging planes used for averaging. The metrics shown include the in-plane mean (blue) and standard deviation S.D. (red).

In comparison to single-plane measurements, averaging across two imaging planes reduced the RCs for the in-plane mean of the SRUS quantitative parameters by 20-28%. Further reductions were observed with three and four imaging planes, with RCs decreasing by 29–41% and 33–49%, respectively. Among the parameters, mean vessel density showed the smallest decrease in RCs with additional imaging planes, while blood velocity exhibited the largest re-

duction. Similarly, the RCs for the in-plane standard deviation of SRUS quantitative parameters decreased by 8–36%, 13–52%, and 15–65% when averaged over two, three, and four imaging planes, respectively. For these parameters, the standard deviation of blood flow direction entropy showed the least improvement with additional imaging planes, while blood velocity again demonstrated the largest reduction.

Although incorporating additional imaging planes continued to improve RCs, the reduction rate decreased with more planes. This could indicate convergence on a representative value for the entire tumour and/or reflect the diminishing microbubble concentration over time. Despite this plateauing effect, the results strongly highlight the benefits of a multi-plane imaging approach for achieving more reliable and consistent SRUS quantitative parameters.

Detailed results for the Intraclass Correlation Coefficient (ICC) and Within-Subject Coefficient of Variation (wCV) are provided in Table 3.1 for the SRUS parameters.

		ICC	**wCV %**	**RC**
Vessel Density %	Mean	0.81	41.34	7.49
	S.D.	0.87	20.09	4.26
Distance to Vessel mm	Mean	0.92	21.97	0.78
	S.D.	0.90	24.31	0.74
Vessel Diameter mm	Mean	0.74	3.95	0.0062
	S.D.	0.63	9.86	0.0092
Blood Velocity mm/s	Mean	0.89	4.80	1.87
	S.D.	0.77	4.16	0.97
Blood Flow Direction Entropy	Mean	0.88	5.88	0.50
	S.D.	-0.14	14.36	0.39
Fractal Dimension	Mean	0.80	1.19	0.055
	S.D.	0.27	20.16	0.070

Table 3.1: Intraclass Correlation Coefficients (ICC), Within-Subject Coefficients of Variation (wCV), and Repeatability Coefficients (RC) for the mean and standard deviation (S.D.) metrics of super-resolution ultrasound (SRUS) parameters: Vessel Density, Distance to Vessel, Vessel Diameter, Blood Velocity, Blood Flow Direction Entropy and Fractal Dimension. These parameters were extracted from in-plane ultrasound acquisitions of breast tumours and averaged across four imaging planes (horizontal, 90°, 45° clockwise and 45° anticlockwise). The repeatability metrics were calculated using 27 test-retest contrast-enhanced ultrasound scans.

The vessel density and distance to vessel metrics show good and excellent ICC values, respectively (0.81-0.87 and 0.90-0.92), but moderately high wCV values (20.09-41.34% and

21.97-24.31). This suggests relatively high variability within subjects and substantial variability between subjects for these measurements.

Vessel diameter and blood velocity show moderate and good ICC values, respectively (0.63-0.74 and 0.77-0.89), along with low wCV values (3.95-9.86% and 4.16-4.80%). This suggests low variability within and between subjects for these parameters.

The mean values for blood flow direction entropy and fractal dimension demonstrate good ICC values (0.88 and 0.80, respectively). However, their standard deviations show poor ICC values (-0.14 to 0.27). Correspondingly, the mean values have low wCV (5.88 and 1.19%, respectively), while their standard deviations show comparatively higher wCV values (14.36 and 20.16%, respectively). These findings indicate good reliability and low variability within subjects for the mean values, suggesting good precision. In contrast, the standard deviation measurements are less reliable in capturing between-subject differences due to small between-subject variability and inconsistent within-subject measurements. For blood flow direction entropy and fractal dimension, there are differing repeatability patterns across their metrics.

The low ICC (< 0.5) for blood flow direction entropy and fractal dimension standard deviation indicates that within-subject variability exceeds between-subject variability. A negative ICC occurs when within-subject mean squares exceed between-subject mean squares. This can result in complex values for between-subject standard deviation. Mathematically, squaring this complex number during the calculation would lead to a negative ICC.

The repeatability results for the SRUS quantitative parameters are graphically presented as Bland-Altman plots in Figures 3.3 for the in-plane mean and 3.4 for the in-plane standard deviation.

The SRUS quantitative parameters (X) were averaged over four imaging planes for 27 repeatability scans. Perfect repeatability would result in equal test-retest measurements, yielding a difference ($X_2 - X_1$) of 0. For the in-plane mean and standard deviation of vessel density, distance to vessel, vessel diameter, blood velocity, and fractal dimension, and the standard deviation of blood flow direction entropy, no apparent bias was observed, as the zero difference line (represented by the black dotted line at 0 on the y-axis) falls within the 95% confidence interval of the mean of the differences (indicated by the blue shaded area). However, for

mean blood flow direction entropy, 0 lies just below the 95% confidence interval, suggesting a potential bias.

Repeatability was assumed to be consistent for all imaging time-points, ranging from pre-treatment to 24-months post-treatment. In the Bland-Altman plots, different markers were used to represent different treatment phases. No clear evidence was found to suggest that repeatability varied across time-points. However, further statistical analysis was not feasible due to the small sample size at each time-point. The markers were visually well mixed across the different imaging time-points for all the quantitative parameters. The markers appeared well mixed across the different imaging time-points for all quantitative parameters, which was expected given the substantial inter-patient heterogeneity of baseline tumours.

For the SRUS metrics, repeatability appears to be homoscedastic for blood velocity, blood flow direction entropy, and fractal dimension measurements in this study, meaning the difference between the repeat measurements did not depend on the average value of those measurements. However, for vessel density, distance to vessel, and vessel diameter measurements, repeatability appears to be heteroscedastic, i.e., the variability was related to the mean. In these cases, as the average value of the repeat measurements increased, the difference between the repeat measurements also increased, so more vascular tumours exhibited relatively poorer absolute repeatability. With a larger dataset, more advanced modelling could be applied to better describe this relationship.

Figure 3.5 shows SRUS maps across the four imaging planes for the participant with the largest within-subject difference in vessel density between the first and second bolus. This large, heterogeneous tumour made returning to the same imaging plane difficult, likely capturing different regions after each bolus injection. This variability increased the repeatability coefficient for vessel density and distance to vessel by increasing the within-subject standard deviation. A noticeable difference in microvasculature is observed between the two bolus injections.

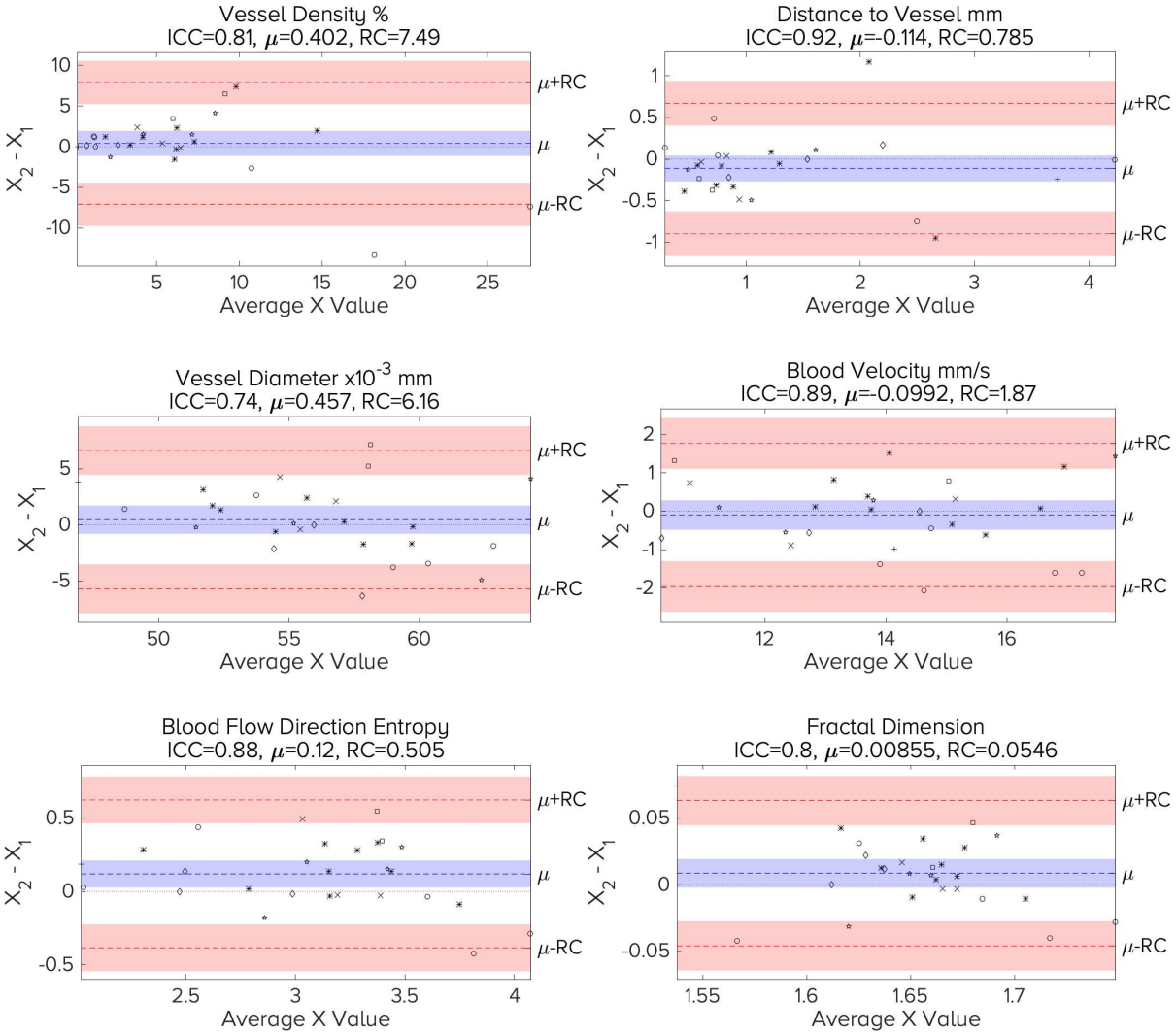


Figure 3.3: Bland-Altman plots for 27 repeatability scans, using the in-plane mean of the super-resolution ultrasound (SRUS) quantitative parameters for statistical analysis. The y-axis is the difference between the quantitative parameter X, averaged across all four imaging planes, from the two repeat measurements (after the first bolus X_1 and the second bolus X_2). The x-axis is the average value of the two repeat measurements of the quantitative parameter. The blue dashed line indicates the mean of the differences (μ), with its 95% confidence interval represented by the shaded blue area. The black dotted line corresponds to zero difference between the test-retest measurements. The mean of the differences ± the repeatability coefficient (μ±RC) is shown as the red dashed line, with the 95% confidence interval of the repeatability coefficient represented by the shaded red area. Markers represent individual repeatability scans (N=27), with: ∘ representing five baseline scans; ∗ nine 2-weeks post-radiotherapy (RT); + one 3-months post-RT; ☆four 6-months post-RT; × three 12-months post-RT; □ two 18-months post-RT; and ⋄ three 24-months post-RT.

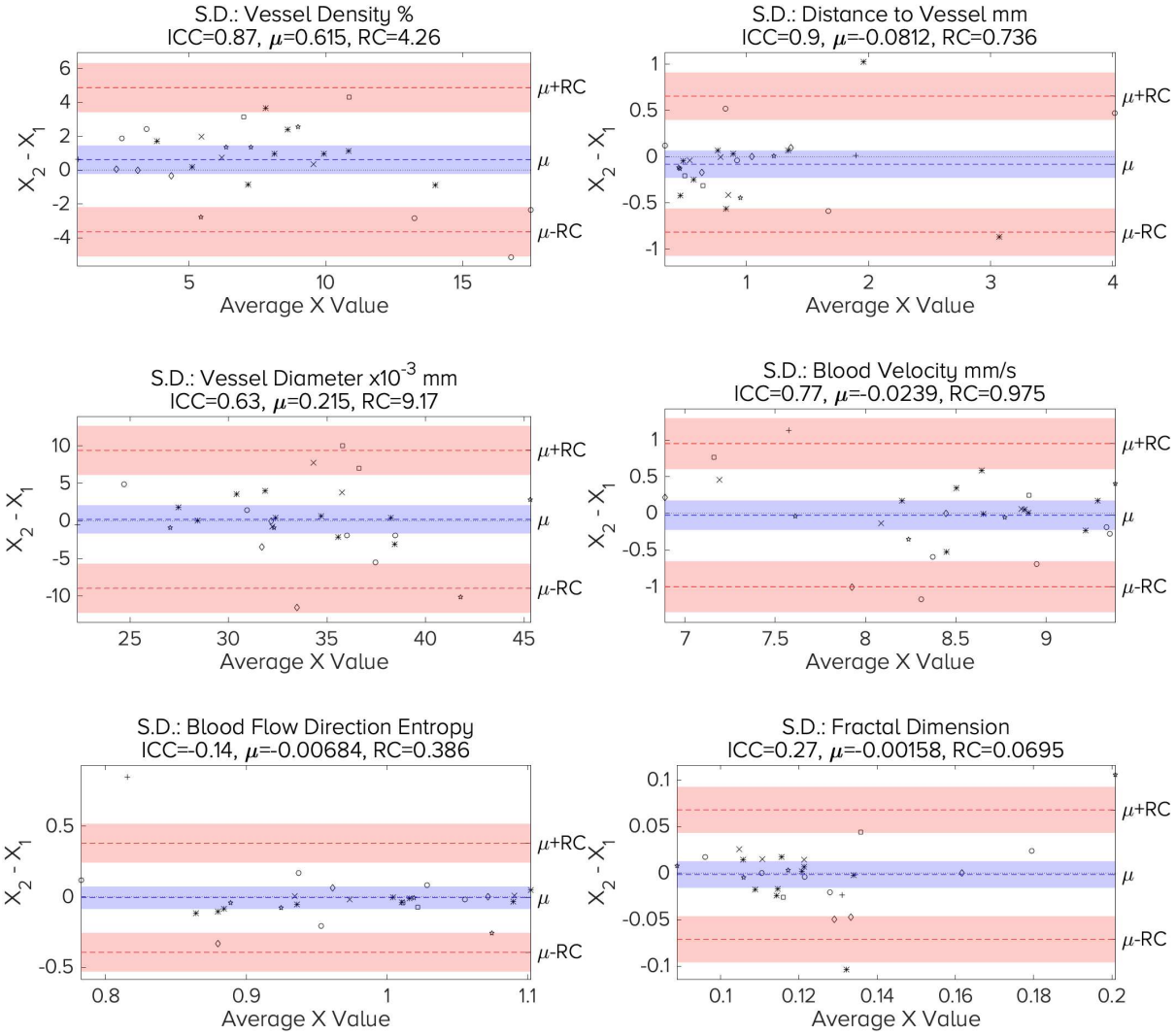


Figure 3.4: Bland-Altman plots for 27 repeatability scans, using the in-plane standard deviation of the super-resolution ultrasound (SRUS) quantitative parameters for statistical analysis. The y-axis is the difference between the quantitative parameter X, averaged across all four imaging planes, from the two repeat measurements (after the first bolus X_1 and the second bolus X_2). The x-axis is the average value of the two repeat measurements of the quantitative parameter. The blue dashed line indicates the mean of the differences (μ), with its 95% confidence interval represented by the shaded blue area. The black dotted line corresponds to zero difference between the test-retest measurements. The mean of the differences ± the repeatability coefficient (μ±RC) is shown as the red dashed line, with the 95% confidence interval of the repeatability coefficient represented by the shaded red area. Markers represent individual repeatability scans (N=27), with: ∘ representing five baseline scans; ∗ nine 2-weeks post-radiotherapy (RT); + one 3-months post-RT; ☆four 6-months post-RT; × three 12-months post-RT; □ two 18-months post-RT; and ⋄ three 24-months post-RT.

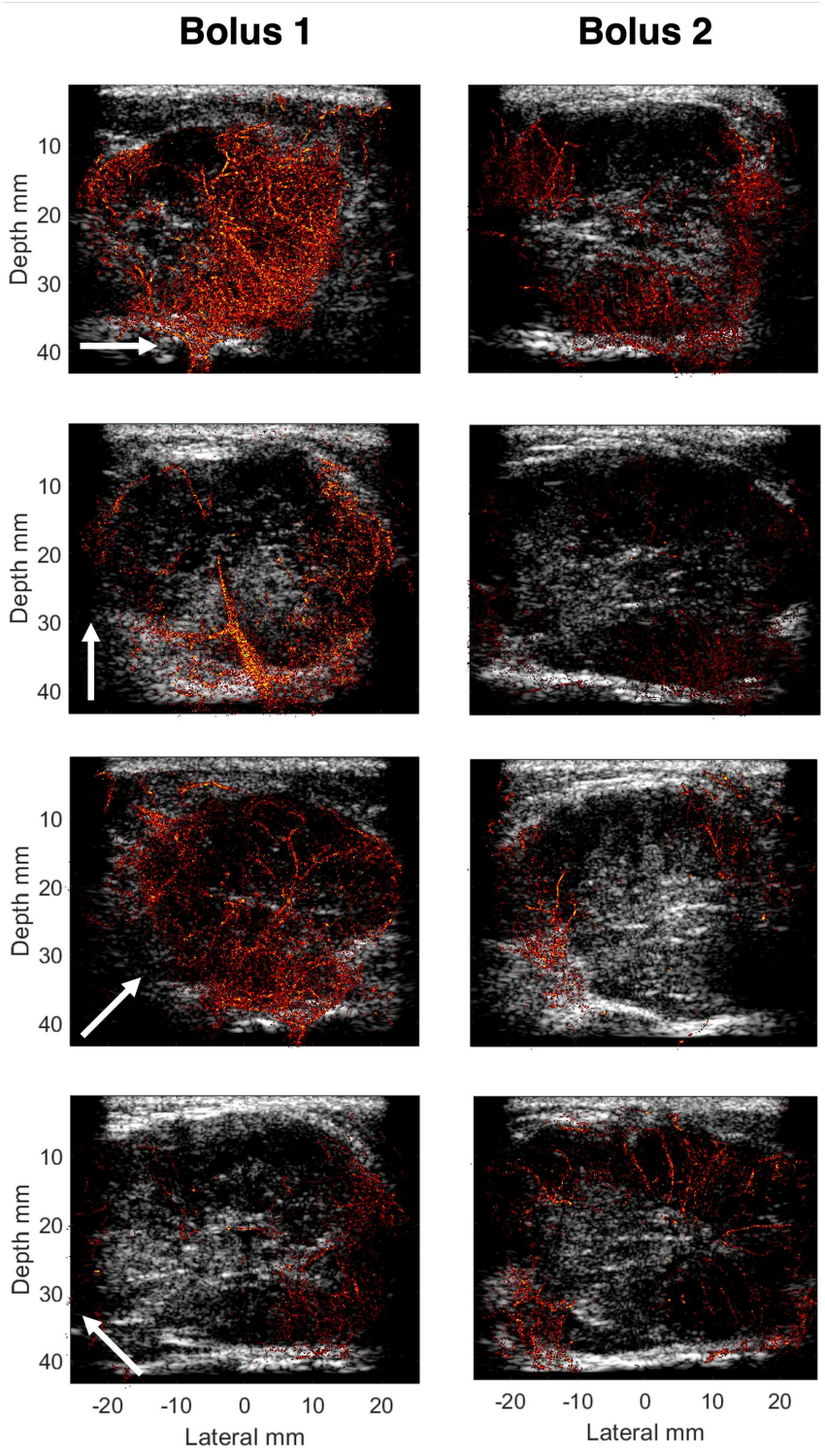


Figure 3.5: Example of a super-resolution ultrasound repeatability scan for a large heterogeneous tumour. Super-resolved maps of the breast tumour microvasculature were acquired at four imaging planes at the tumour centre (horizontal 0°, 90°, 45° clockwise and 45° anticlockwise). These scans were repeated twice, following the first and second contrast boluses. Brightness in the images represents the number of microbubble localisations per pixel. The white arrows indicate the orientation of the ultrasound probe.

3.2 Breast Tumour and Healthy Breast Tissue

Figure 3.6 presents super-resolved microvascular maps of the healthy breast tissue and breast tumour at baseline for three participants. In the healthy breast, the microvasculature is evenly distributed. For one participant (top), the microvascular patterns in the healthy breast and tumour appear visually similar; however, the tumour region shows larger areas devoid of microvasculature. In a second participant (middle), dense microvasculature is present around the periphery of the tumour, but the core is devoid of microvasculature. The third participant shows a notably denser microvasculature throughout the tumour area compared to the more sparse distribution in the healthy breast.

The SRUS quantitative parameters were extracted from both healthy breast tissue and pre-treatment breast tumours, as presented in Table 3.2 and Figures 3.7 and 3.8, which display the distribution of these parameters across both cohorts.

		Healthy N=9	Tumour N=15	p-value
Vessel Density %	Mean	4.72±2.71	12.50±12.26	0.31
	S.D.	7.95±3.24	11.25±7.69	0.37
Distance to Vessel mm	Mean	0.98±0.33	1.28±1.13	1.00
	S.D.	0.82±0.23	1.16±0.90	0.59
Vessel Diameter mm	Mean	0.060±0.0030	0.058±0.007	0.44
	S.D.	0.040±0.005	0.035±0.009	0.049*
Blood Velocity mm/s	Mean	17.04±2.03	16.99±1.96	0.21
	S.D.	9.30±0.39	8.94±0.65	0.14
Blood Flow Direction Entropy	Mean	2.90±0.21	3.22±0.81	0.15
	S.D.	1.13±0.04	1.00±0.15	0.015*
Fractal Dimension	Mean	1.65±0.02	1.68±0.06	0.34
	S.D.	0.14±0.01	0.11±0.02	0.0035**

Table 3.2: The average ± standard deviation of the SRUS quantitative parameter metrics (in-plane mean and standard deviation, averaged across four imaging planes) for healthy breast (N=9) and pre-treatment breast tumour (N=15), where N is the number of participants. Significance levels are given as $^{*} = p < 0.05$, $^{**} = p < 0.01$, $^{***} = p < 0.001$.

For vessel density, distance to vessel, and blood velocity, there were no significant differences in the in-plane mean and standard deviation between healthy breast tissue and breast tumours. Similarly, there were no significant differences in the in-plane mean values of vessel diameter,

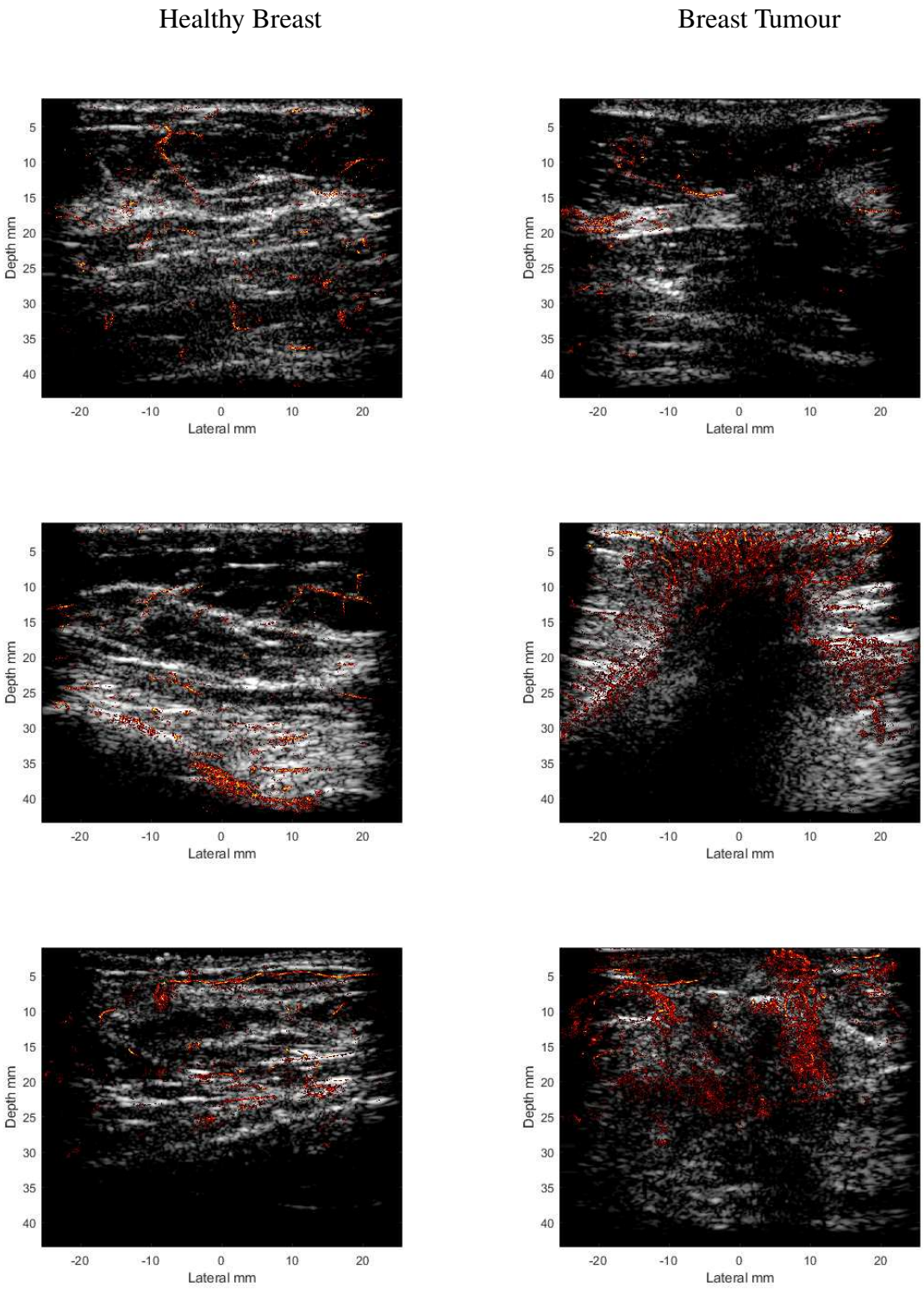


Figure 3.6: Example of super-resolution ultrasound scans from three participants of their healthy breast (left) and breast tumour (right) microvasculature. Brightness in the images represents the number of microbubble localisations per pixel.

blood flow direction entropy, and fractal dimension. However, the in-plane standard deviations for these parameters were significantly higher in healthy breast tissue compared to tumours ($p = 0.049^{*}$; 0.015^{*}; 0.0035^{**}, respectively).

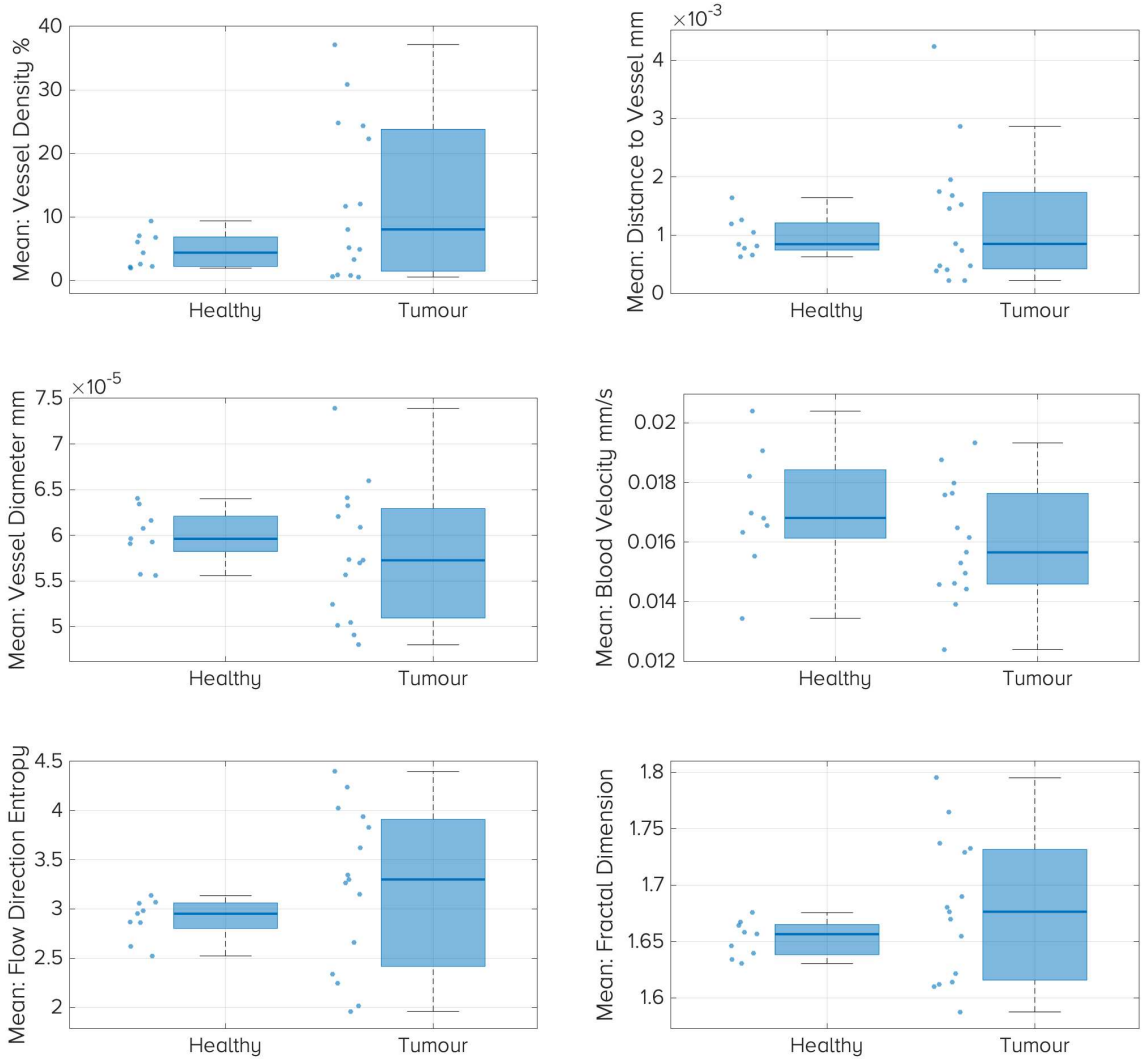


Figure 3.7: Box-plots depicting the distribution of the in-plane mean SRUS quantitative parameters (averaged across four imaging planes) for healthy breast tissue (N=9) and pre-treatment breast tumours (N=15), where N is the number of participants. The central line represents the median, while the upper and lower box edges correspond to the 75th and 25th percentiles, respectively. The dashed lines indicate the whiskers; the whisker length is capped at 1.5 times the interquartile range, providing 99.3% coverage for normally distributed data, and the whiskers extend to the most extreme data point within the maximum whisker length. The circular markers are individual participants.

Although no statistically significant differences were observed between the healthy breast tissue and breast tumour groups, a comparison of the cohort mean/median values from Table 3.2 and Figures 3.7 and 3.8 shows that the in-plane mean values for vessel density, distance to

vessel, blood flow direction entropy, and fractal dimension were higher in the breast tumours compared to healthy tissue. Similarly, the in-plane standard deviations for vessel density and distance to vessel were also higher in tumours. In contrast, the in-plane mean and standard deviation of vessel diameter and blood velocity were lower in breast tumours.

In Figures 3.7 and 3.8, the between-participant variability in the in-plane mean and standard deviation of vessel density, distance to vessel, blood flow direction entropy, and fractal dimension was notably smaller in healthy breast tissue compared to breast tumours. The variability for blood velocity was comparable between the two groups.

For vessel density, distance to vessel, vessel diameter, blood flow direction entropy and fractal dimension, some breast tumours exhibit values that overlap with the range observed in healthy breast tissue. However, there are also tumour cases with values that fall distinctly below or above the healthy range. This indicates that values outside the healthy range are more likely to signify a tumour. In contrast, values within the healthy range make it difficult to distinguish tumours from healthy tissue reliably.

3.3 Response Assessment

3.3.1 SRUS Quantitative Parameter Changes

Figure 3.9 presents four examples of super-resolution ultrasound (SRUS) microvascular maps of tumours and surrounding tissue, taken at baseline, 2-weeks and 6-months post-radiotherapy (RT). Baseline microvascular structures showed significant heterogeneity across tumours, with post-treatment responses varying among participants. Tumours with high vessel density at baseline showed noticeable decreases following treatment. However, visual assessment of changes was challenging in cases with low baseline vessel density.

Figure 3.10, 3.11, 3.12, 3.13, 3.14 and 3.15 illustrate changes in the in-plane mean and standard deviation of SRUS quantitative parameters at 2-weeks, 6-, 12-, 18- and 24-months post-RT for 15 participants, with significant changes defined as those exceeding the repeatability coefficient. Of the 15 participants, 11 were imaged at 6-months, 10 at 12-months, 4 at 18-months and 2 at 24-months.

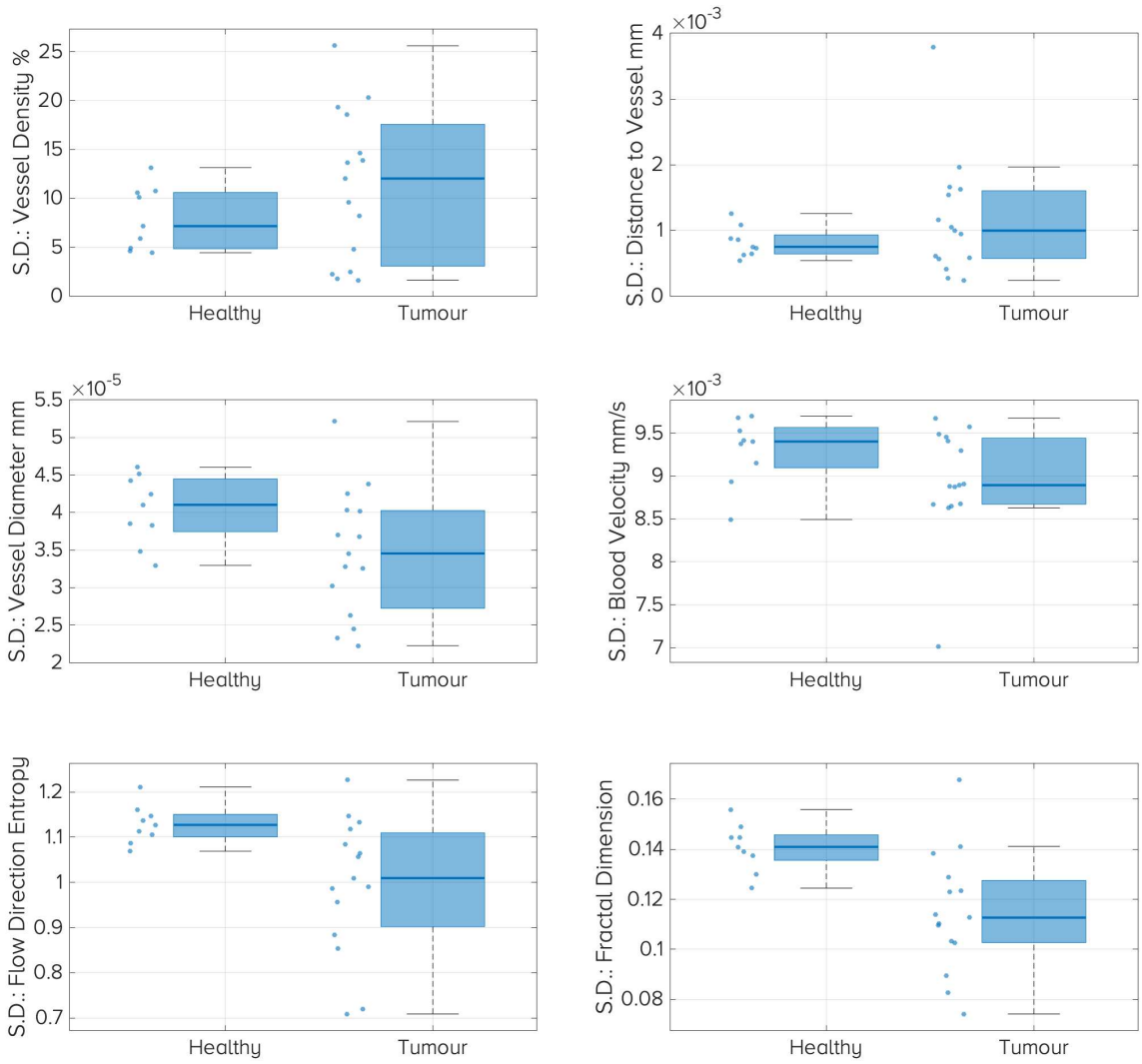


Figure 3.8: Box-plots depicting the distribution of the in-plane standard deviation (S.D.) SRUS quantitative parameters (averaged across four imaging planes) for healthy breast tissue (N=9) and pre-treatment breast tumours (N=15).

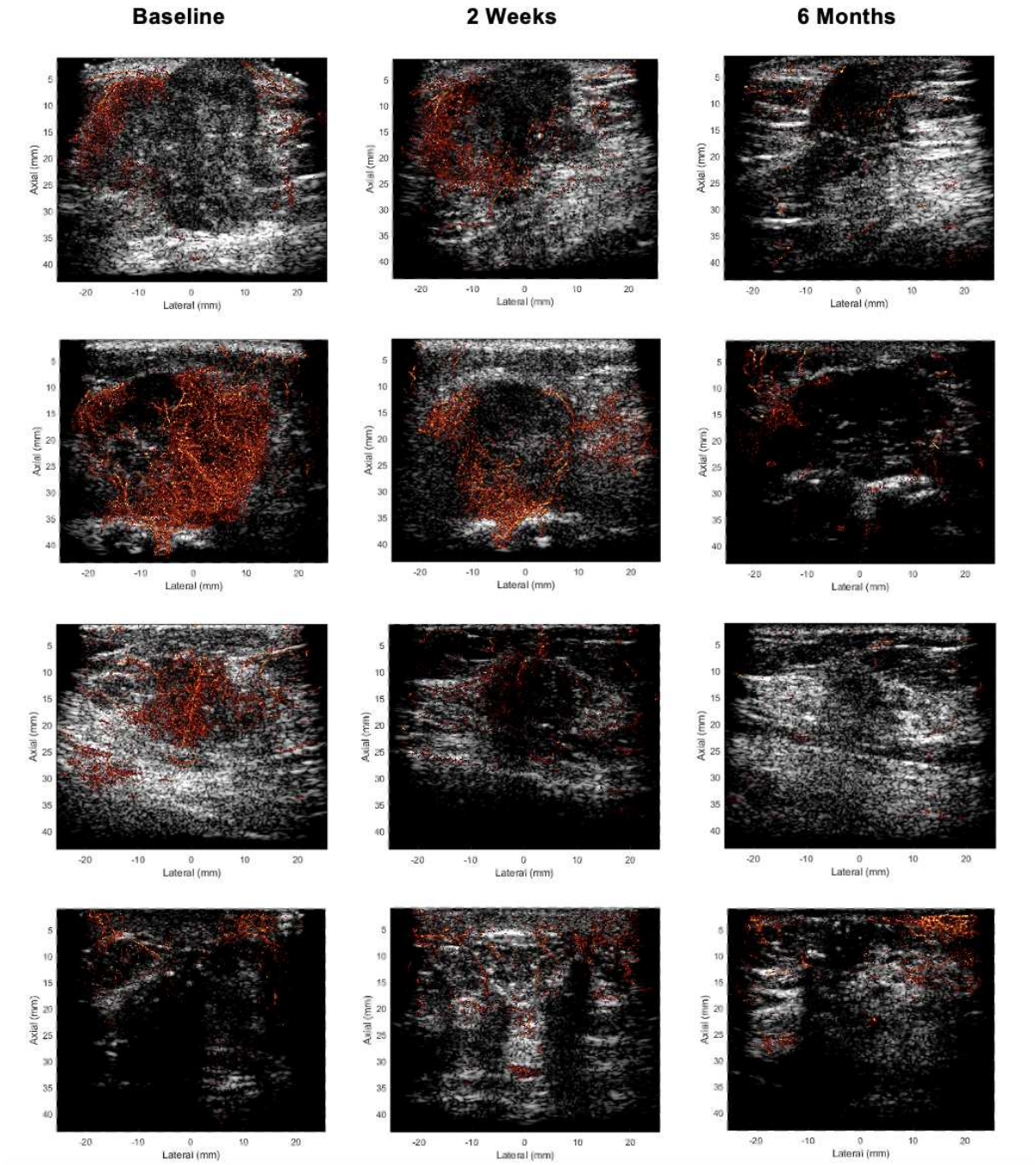


Figure 3.9: Four examples of super-resolution ultrasound microvascular maps of tumours and surrounding tissue overlaid on the B-mode tissue images, captured at baseline, 2-weeks, and 6-months post-radiotherapy (RT). Brightness represents the number of localisations per pixel. Baseline tumour microvascular structures demonstrate significant heterogeneity, with post-treatment responses varying widely across participants. (i) The baseline tumour shows microvessels concentrated around the periphery but not within the core. There was a visible decrease in vascular density by 6-months post-RT. (ii) and (iii) The tumours have dense baseline microvasculature, with a visible reduction in intra-tumoural blood vessels as early as 2-weeks post-RT. (iv) The tumour exhibits low baseline vascularity, with a small increase in microvessels post-treatment.

Among the 15 participants, 4 had baseline vessel density values below the healthy range. For these 4 participants, dashed lines will be used in the plots as their trends differed from the others.

For mean vessel density in Figure 3.10, 5 out of 15 participants showed a significant decrease at 2-weeks post-RT ($p = 0.024$). Of these, 2 participants who were imaged at later time-points showed a further decrease at 6-months ($p = 0.059$), followed by stabilisation at 12- and 24-months. Four additional participants showed decreases by 6-months post-RT, stabilising across the later time-points, although these changes were not significant. Participants with consistent vessel densities tended to have the lowest values at baseline, either within or below the healthy range.

For the standard deviation of vessel density, 6 out of 15 participants showed a significant decrease at 2-weeks post-RT ($p = 0.034$), with a continued decrease at 6-months post-RT ($p = 0.033$) followed by stabilisation. An additional 2 participants showed a significant decrease by 6-months and a third participant by 12-months post-RT. Those with the lowest baseline values showed no changes or increases in vessel density heterogeneity.

Participants with mean and standard deviation vessel densities above the healthy range at baseline gradually approached, and in some cases exceeded, the healthy range. Many participants with baseline values within the healthy range remained stable. Two participants with initial vessel density measurements below the healthy range increased to fall within the healthy range.

For both mean and standard deviation of the distance to vessel in Figure 3.11, there was no clear trend post-treatment (mean - 2-weeks/6-months post-RT: $p = 0.601/0.189$; standard deviation - $p = 0.997/0.613$), with values showing an equal distribution in both directions at the post-treatment time-points. Some negative correlation was observed between distance to vessel and vessel density: as vessel density decreased, distance to vessel increased, and vice versa.

Excluding participants with very low vessel density values at baseline (dashed lines), those with distance to vessel values above the healthy range decreased into the healthy range at 2-weeks post-RT; however, one participant subsequently showed an increase at 6-months, moving back

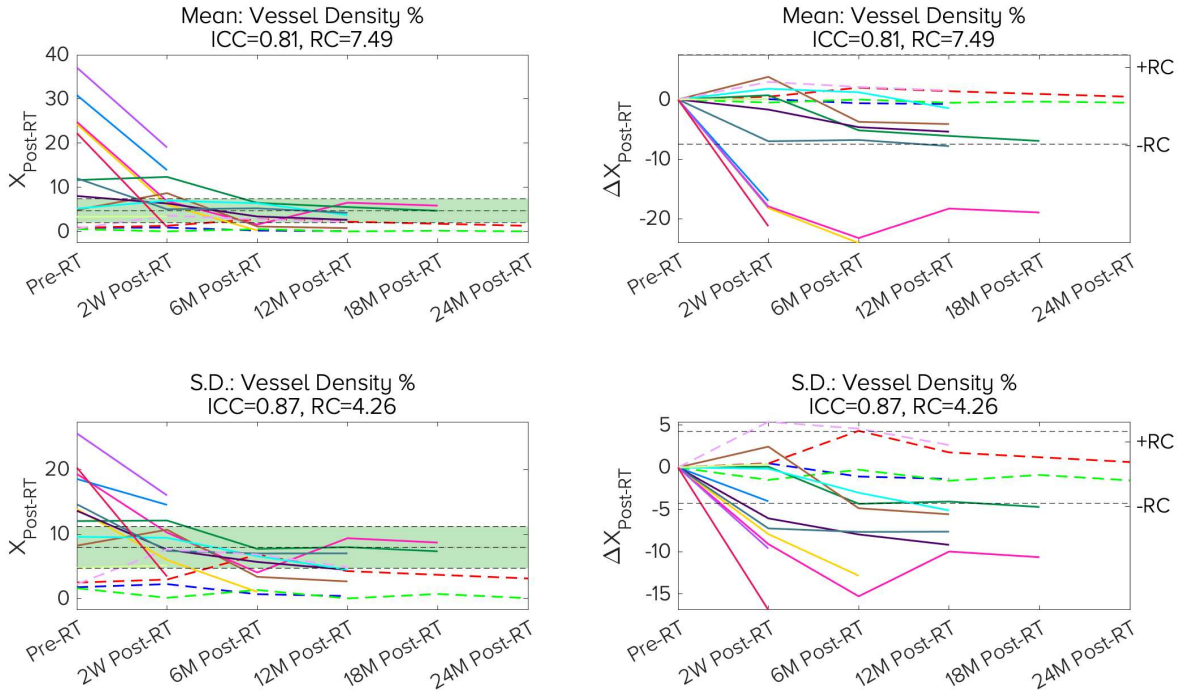


Figure 3.10: The changes in the mean (top) and standard deviation (bottom) of the super-resolution ultrasound (SRUS) vessel density at 2-weeks, 6-, 12-, 18- and 24-months post-radiotherapy (RT) from 15 participants. The 4 participants with baseline vessel density values below the healthy range are plotted with dashed lines, as their trends differed from the others. (Left) The y-axis shows the absolute value of the quantitative parameter (averaged across 4 imaging planes) at baseline and post-RT time-points. The green shaded area is the healthy range of values measured across 9 participants, covering the mean ± the standard deviation. (Right) The y-axis shows the change in the mean of the quantitative parameter (averaged across 4 imaging planes) from baseline at post-RT time-points. The dashed black lines represent the repeatability coefficient as an indicator of significant change, i.e., if the difference post-treatment is larger than the repeatability coefficient, then the change is significant.

out of the healthy range. Participants who started below the healthy range increased towards or beyond the healthy range.

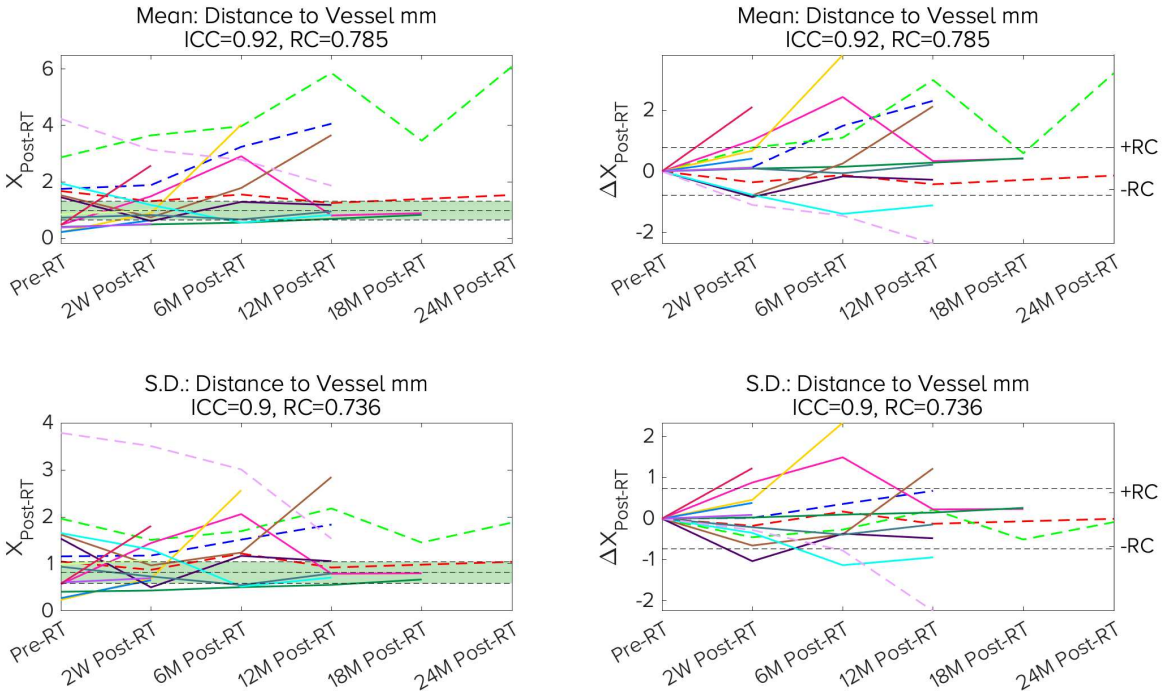


Figure 3.11: The changes in the mean (top) and standard deviation (bottom) of the super-resolution ultrasound (SRUS) distance to nearest vessel at 2-weeks, 6-, 12-, 18- and 24-months post-radiotherapy (RT) from 15 participants. The 4 participants with baseline vessel density values below the healthy range are plotted with dashed lines, as their trends differed from the others. (Left) The y-axis shows the absolute value of the quantitative parameter (averaged across 4 imaging planes) at baseline and post-RT time-points. The green shaded area is the healthy range of values measured across 9 participants, covering the mean ± the standard deviation. (Right) The y-axis shows the change in the mean of the quantitative parameter (averaged across 4 imaging planes) from baseline at post-RT time-points. The dashed black lines represent the repeatability coefficient as an indicator of significant change, i.e., if the difference post-treatment is larger than the repeatability coefficient, then the change is significant.

For mean vessel diameter in Figure 3.12, 6 out of 15 participants showed a significant decrease by 2-weeks post-RT ($p = 0.112$). Of these, 3 continued to show a decrease or stabilisation at 6-months post-RT ($p = 0.388$) and subsequent time-points. Five other participants exhibited trends towards a decrease over 2-weeks and 6-months, but two showed an increase again at 12-months. By 6-months post-RT, 3 out of 11 participants showed significant increases, stabilising at subsequent time-points. Two of these participants were those with low vessel densities at baseline. The standard deviation showed similar trends, though fewer changes were significant (2-weeks/6-months post-RT: $p = 0.278/0.591$)

Excluding participants with very low vessel density values, a trend of decreasing vessel diameter towards or beyond the healthy range was observed at 2-weeks post-RT, with further decreases and stabilisation at later time-points. However, two participants showed an increase back into the healthy range by 12-months post-RT. One participant, who started below the healthy range, exhibited the opposite trend, increasing into the healthy range at post-RT time-points.

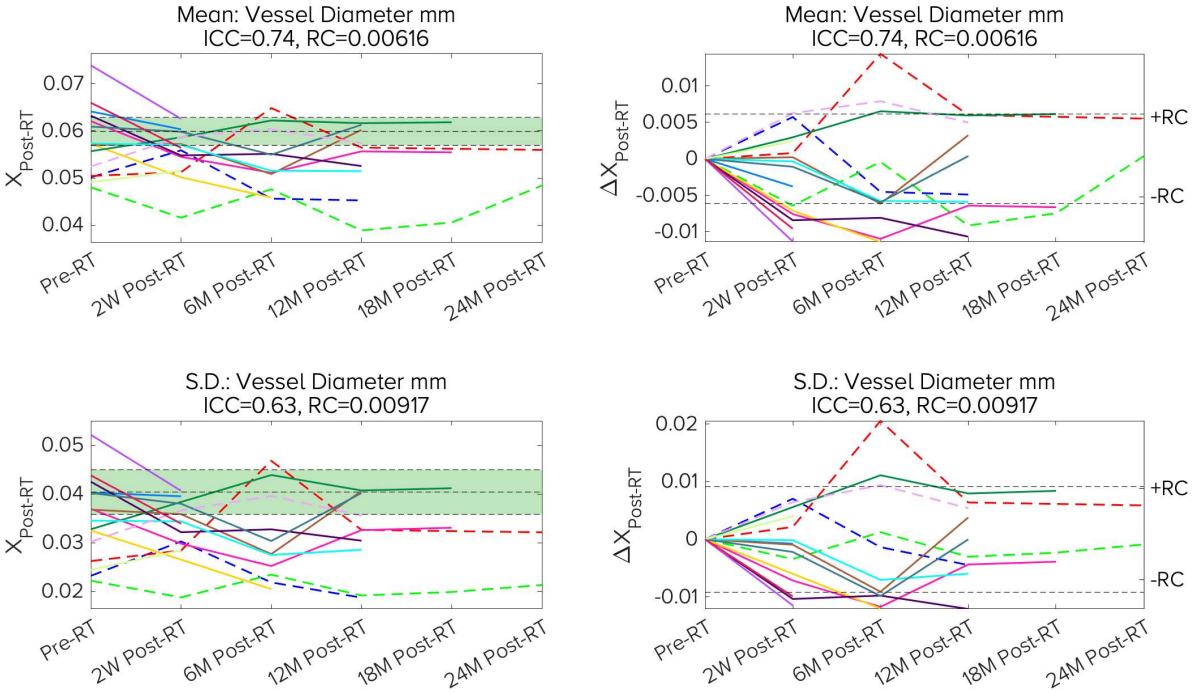


Figure 3.12: The changes in the mean (top) and standard deviation (bottom) of the super-resolution ultrasound (SRUS) vessel diameter at 2-weeks, 6-, 12-, 18- and 24-months post-radiotherapy (RT) from 15 participants. The 4 participants with baseline vessel density values below the healthy range are plotted with dashed lines, as their trends differed from the others. (Left) The y-axis shows the absolute value of the quantitative parameter (averaged across 4 imaging planes) at baseline and post-RT time-points. The green shaded area is the healthy range of values measured across 9 participants, covering the mean ± the standard deviation. (Right) The y-axis shows the change in the mean of the quantitative parameter (averaged across 4 imaging planes) from baseline at post-RT time-points. The dashed black lines represent the repeatability coefficient as an indicator of significant change, i.e., if the difference post-treatment is larger than the repeatability coefficient, then the change is significant.

For mean blood velocity in Figure 3.13, 9 out of 15 participants showed a significant decrease by 2-weeks ($p = 0.045$) or 6-months post-RT ($p = 0.022$), with stabilisation at subsequent time-points. The 4 participants showing more complicated trends were those with very low vessel densities at baseline, resulting in fewer microbubble tracks available for velocity calculations, which may have made these measurements more susceptible to noise. However, 2

of these participants showed a significant decrease at 12-months post-RT. The standard deviation similarly showed a trend towards decreasing and stabilisation, but few participants demonstrated significant change (2-weeks/6-months post-RT: $p = 0.233/0.012$).

Excluding those with low vessel density values, most participants had blood velocity within the healthy range at baseline. A trend towards a decrease beyond the healthy range was observed at later time-points, followed by stabilisation.

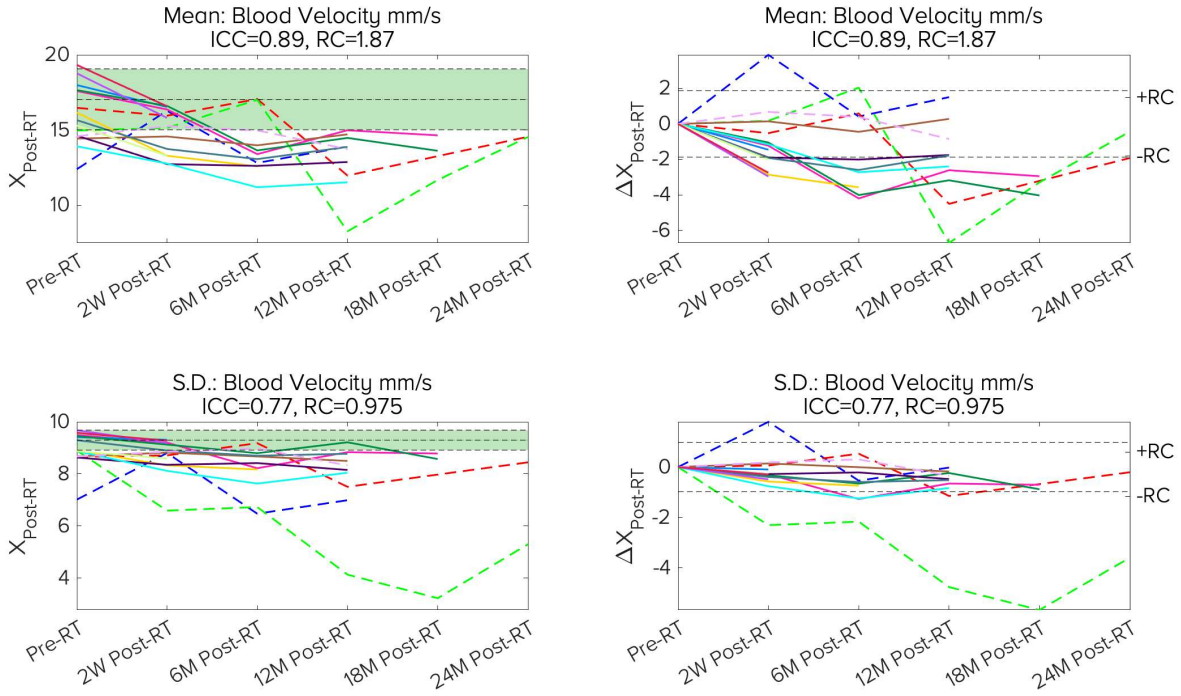


Figure 3.13: The changes in the mean (top) and standard deviation (bottom) of the super-resolution ultrasound (SRUS) blood velocity at 2-weeks, 6-, 12-, 18- and 24-months post-radiotherapy (RT) from 15 participants. The 4 participants with baseline vessel density values below the healthy range are plotted with dashed lines, as their trends differed from the others. (Left) The y-axis shows the absolute value of the quantitative parameter (averaged across 4 imaging planes) at baseline and post-RT time-points. The green shaded area is the healthy range of values measured across 9 participants, covering the mean ± the standard deviation. (Right) The y-axis shows the change in the mean of the quantitative parameter (averaged across 4 imaging planes) from baseline at post-RT time-points. The dashed black lines represent the repeatability coefficient as an indicator of significant change, i.e., if the difference post-treatment is larger than the repeatability coefficient, then the change is significant.

For mean blood flow direction entropy in Figure 3.14, 3 out of 15 participants showed a significant decrease by 2-weeks post-RT ($p = 0.088$), excluding one participant with low vessel density at baseline who displayed an inconsistent trend over time. Two of these showed further decreases followed by stabilisation at later time-points. Five other participants demonstrated a

trend towards decreasing by 6-months post-RT ($p = 0.239$) followed by stabilisation, with three showing significant changes by 12-months post-RT. Two participants with low vessel density exhibited significant increases by 2-weeks or 6-months post-RT.

For the standard deviation, no clear trend emerged, with some participants increasing and others decreasing post-treatment, though none of these changes were significant (2-weeks/6-months post-RT: $p = 0.698/0.270$).

Excluding those with low vessel density values, a trend of decreasing entropy towards or beyond the healthy range was observed. Regarding the standard deviation, participants appeared to converge around a value of 1, with those below this value increasing and those above it decreasing at subsequent time-points. However, this value is below the healthy range.

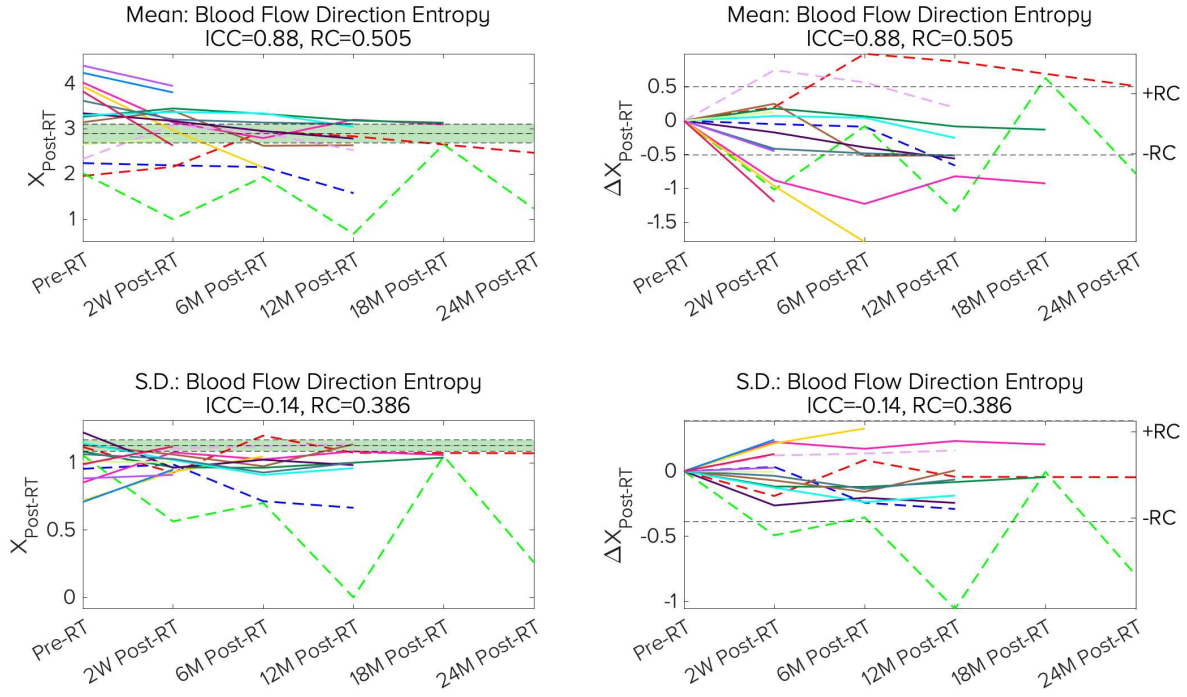


Figure 3.14: The changes in the mean (top) and standard deviation (bottom) of the super-resolution ultrasound (SRUS) blood flow direction entropy at 2-weeks, 6-, 12-, 18- and 24-months post-radiotherapy (RT) from 15 participants. The 4 participants with baseline vessel density values below the healthy range are plotted with dashed lines, as their trends differed from the others. (Left) The y-axis shows the absolute value of the quantitative parameter (averaged across 4 imaging planes) at baseline and post-RT time-points. The green shaded area is the healthy range of values measured across 9 participants, covering the mean ± the standard deviation. (Right) The y-axis shows the change in the mean of the quantitative parameter (averaged across 4 imaging planes) from baseline at post-RT time-points. The dashed black lines represent the repeatability coefficient as an indicator of significant change, i.e., if the difference post-treatment is larger than the repeatability coefficient, then the change is significant.

Mean fractal dimension in Figure 3.15 showed similar individual trends to those observed for blood flow direction entropy. Four out of 15 participants showed a significant decrease by 2-weeks post-RT ($p = 0.023$), excluding one participant with low vessel density at baseline who displayed an inconsistent trend over time. Two of these participants, imaged at later time-points, demonstrated further decrease followed by stabilisation. Five additional participants showed a trend towards decreasing by 6-months post-RT ($p = 0.062$), although this change was not significant.

For the standard deviation, no clear trend emerged, with some participants showing increases and others showing decreases post-treatment; however, none of these changes were significant (2-weeks/6-months post-RT: $p = 0.206/0.784$).

Excluding those with low vessel density values, a trend of decreasing fractal dimension towards or beyond the healthy range was observed. Regarding the standard deviation, most participants remained consistent and below the healthy range at post-RT time-points.

In summary, the general trend for vessel density and its heterogeneity post-RT is a decrease for participants with higher baseline vessel densities ($> 5\%$), moving towards or beyond the healthy range. Tumours with a baseline mean vessel density $> 20\%$ exhibited significant decreases as soon as 2-weeks post-RT.

For distance to vessel and its heterogeneity, values above the healthy range decreased post-RT. In contrast, values below the healthy range increased towards or beyond it, excluding those with very low vessel densities ($< 5\%$).

For vessel diameter and its heterogeneity, there is a decrease post-RT towards or beyond the healthy range, with some participants showing an increase by 12-months post-RT. However, this increase brings the values back towards the healthy range.

For blood velocity and its heterogeneity, tumours initially fell within the healthy range but decreased at post-RT time-points, eventually stabilising after 6-months.

For blood flow direction entropy and fractal dimension, participants with the highest baseline vessel densities had the highest values, indicating greater chaoticness. Conversely, those with vessel densities below the healthy range also had entropy and fractal dimension values below the healthy range. Both mean parameters decreased post-RT, moving towards the healthy range.

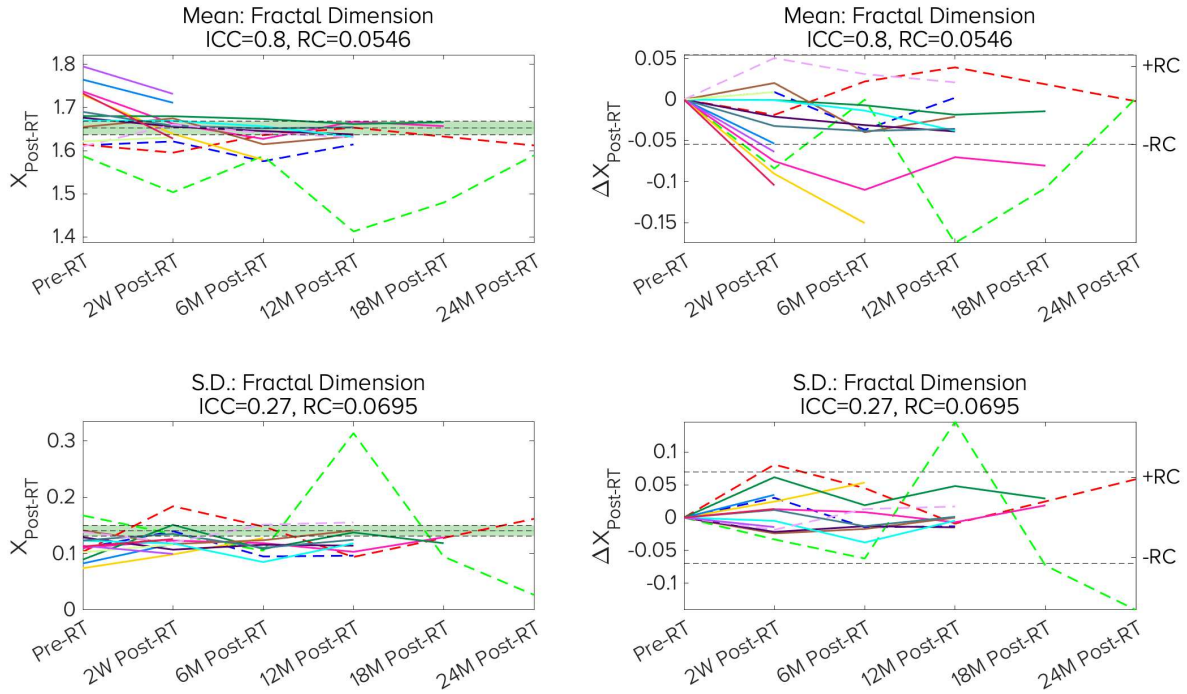


Figure 3.15: The changes in the mean (top) and standard deviation (bottom) of the super-resolution ultrasound (SRUS) fractal dimension at 2-weeks, 6-, 12-, 18- and 24-months post-radiotherapy (RT) from 15 participants. The 4 participants with baseline vessel density values below the healthy range are plotted with dashed lines, as their trends differed from the others. (Left) The y-axis shows the absolute value of the quantitative parameter (averaged across 4 imaging planes) at baseline and post-RT time-points. The green shaded area is the healthy range of values measured across 9 participants, covering the mean ± the standard deviation. (Right) The y-axis shows the change in the mean of the quantitative parameter (averaged across 4 imaging planes) from baseline at post-RT time-points. The dashed black lines represent the repeatability coefficient as an indicator of significant change, i.e., if the difference post-treatment is larger than the repeatability coefficient, then the change is significant.

The heterogeneity of these parameters stabilised below the healthy range post-RT.

3.3.2 SRUS Quantitative Parameters and Radiological Response

Response was assessed on MRI at 12-months and 24-months post-RT (for those that reached that time-point) for 8 participants that had SRUS at the same time-point, with 2 having complete response (CR), 3 having partial response (PR) and 3 having progressive disease (PD). In Figures 3.16, 3.17, 3.18, 3.19, 3.20, and 3.21, the green line signifies participants with CR at 12-months (and 24-months if available) post-RT, the yellow line PR, and the red line PD. Among the 8 participants, 3 had baseline vessel density values below the healthy range. For these 3 participants, dashed lines will be used in the plots as their trends differed from the others. Interestingly, these participants were split between CR, PR and PD.

For mean vessel density, excluding the participants with very low vessel densities, the CR participant and one PR participant had a significant decrease by 2-weeks post-RT, while the other PR participant showed a non-significant decrease over time. The two PD participants had either a non-significant increase or no change in vessel density at 2-weeks post-RT, followed by non-significant decreases at 6- and 12-months post-RT.

For the heterogeneity (standard deviation) of vessel density, again excluding the participants with very low vessel densities, the CR and PR participants demonstrated significant decreases by 2-weeks post-RT. In contrast, the PD participants had significant decreases only by 6-months post-RT, though these decreases were less pronounced than those observed in the PR and CR participants. The PD participants were those within or closest to the healthy range of heterogeneity values.

Progressive disease was assessed using MRI, so the returning nodule of disease may not have been captured within the SRUS imaging plane.

For mean distance to vessel, there is no apparent difference between the trends of the mean and standard deviation of distance to vessel for the responders and non-responders.

For mean vessel diameter, excluding the participants with very low vessel densities, the CR and PR participants had significant decreases by 2-weeks post-RT. The two PD participants had either a non-significant increase or no change in vessel diameter at 2-weeks post-RT, followed

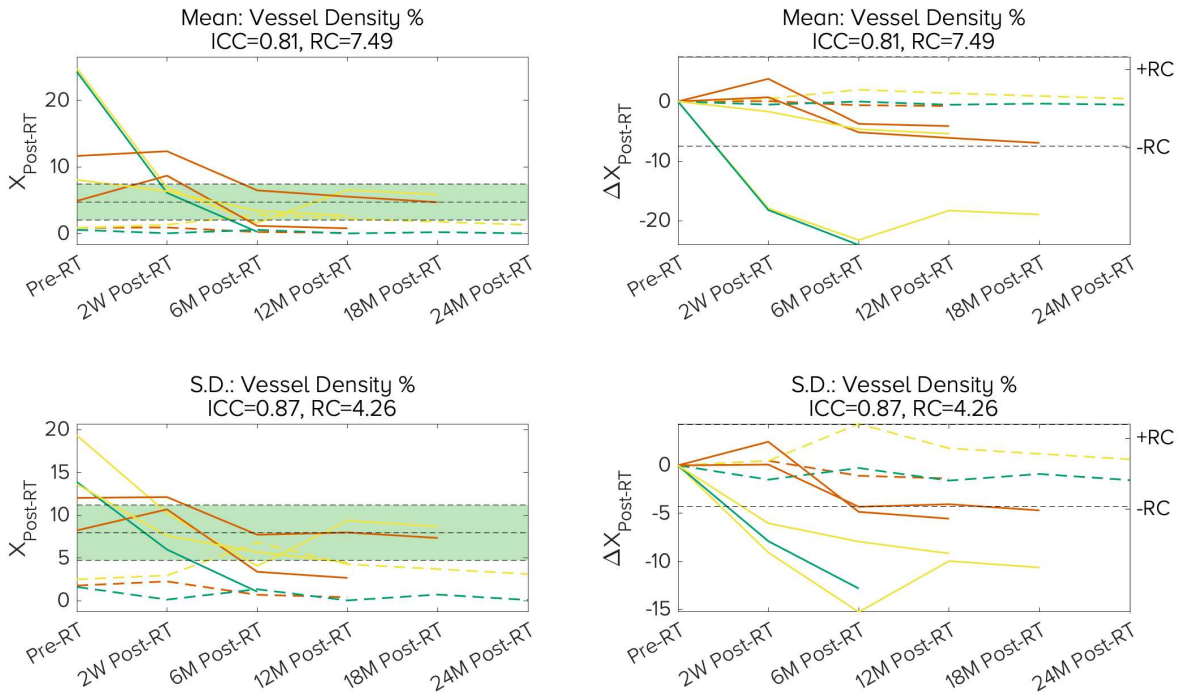


Figure 3.16: The changes in the mean (top) and standard deviation (bottom) of the super-resolution ultrasound (SRUS) vessel density at 2-weeks, 6-, 12-, 18- and 24-months post-radiotherapy (RT) from 8 participants assessed for radiological response using MRI. The green line signifies participants with CR at 12-months (and 24-months if available) post-RT, the yellow line PR, and the red line PD. The 3 participants with baseline vessel density values below the healthy range are plotted with dashed lines, as their trends differed from the others. (Left) The y-axis shows the absolute value of the quantitative parameter (averaged across 4 imaging planes) at baseline and post-RT time-points. The green shaded area is the healthy range of values measured across 9 participants, covering the mean ± the standard deviation. (Right) The y-axis shows the change in the mean of the quantitative parameter (averaged across 4 imaging planes) from baseline at post-RT time-points. The dashed black lines represent the repeatability coefficient as an indicator of significant change, i.e., if the difference post-treatment is larger than the repeatability coefficient, then the change is significant.

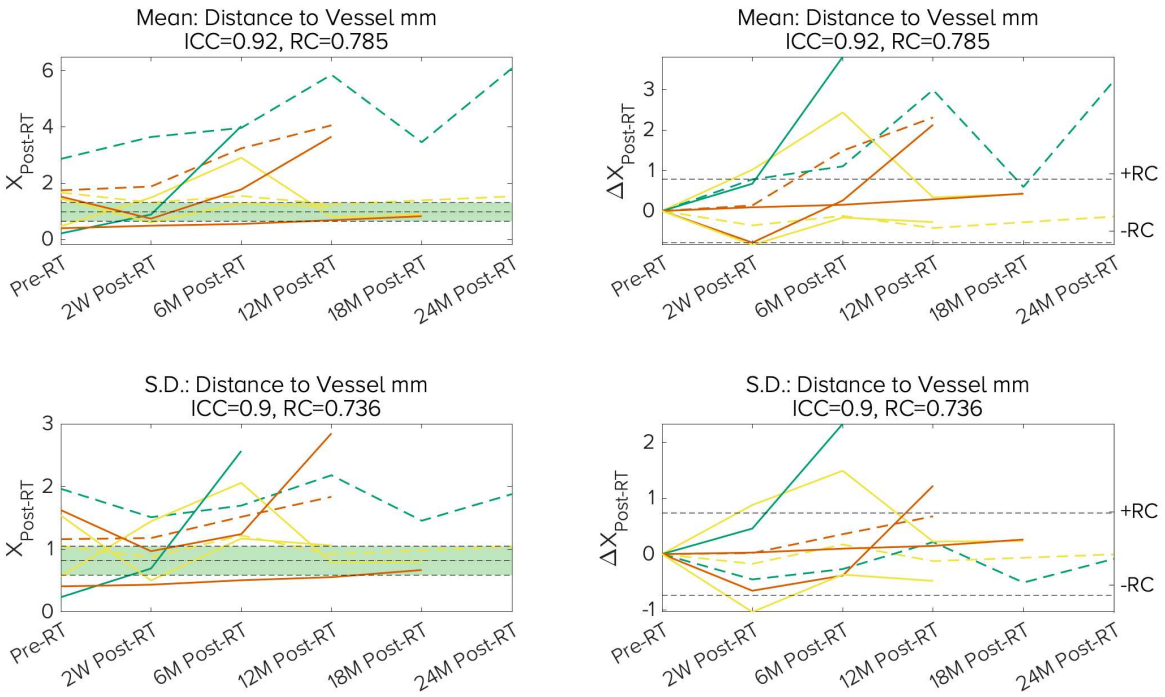


Figure 3.17: The changes in the mean (top) and standard deviation (bottom) of the super-resolution ultrasound (SRUS) distance to vessel at 2-weeks, 6-, 12-, 18- and 24-months post-radiotherapy (RT) from 8 participants assessed for radiological response using MRI. The green line signifies participants with CR at 12-months (and 24-months if available) post-RT, the yellow line PR, and the red line PD. The 3 participants with baseline vessel density values below the healthy range are plotted with dashed lines, as their trends differed from the others. (Left) The y-axis shows the absolute value of the quantitative parameter (averaged across 4 imaging planes) at baseline and post-RT time-points. The green shaded area is the healthy range of values measured across 9 participants, covering the mean ± the standard deviation. (Right) The y-axis shows the change in the mean of the quantitative parameter (averaged across 4 imaging planes) from baseline at post-RT time-points. The dashed black lines represent the repeatability coefficient as an indicator of significant change, i.e., if the difference post-treatment is larger than the repeatability coefficient, then the change is significant.

by one participant significantly increasing by 6-months post-RT, and the other decreasing but increasing again at 12-months post-RT.

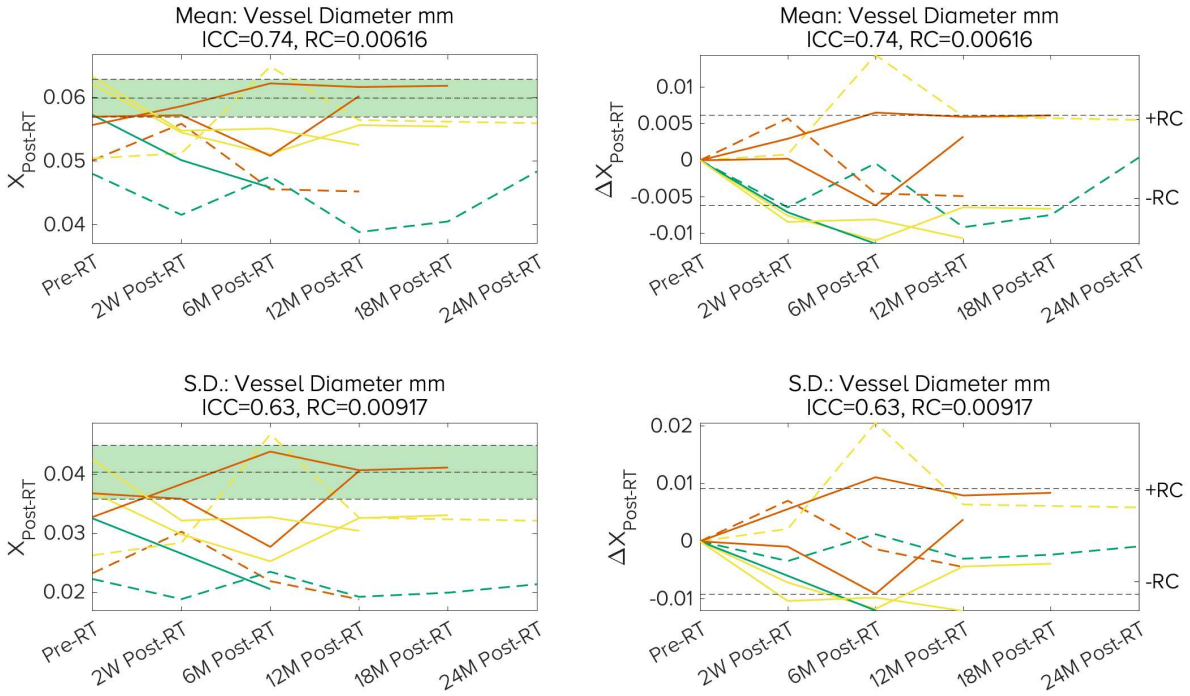


Figure 3.18: The changes in the mean (top) and standard deviation (bottom) of the super-resolution ultrasound (SRUS) vessel diameter at 2-weeks, 6-, 12-, 18- and 24-months post-radiotherapy (RT) from 8 participants assessed for radiological response using MRI. The green line signifies participants with CR at 12-months (and 24-months if available) post-RT, the yellow line PR, and the red line PD. The 3 participants with baseline vessel density values below the healthy range are plotted with dashed lines, as their trends differed from the others. (Left) The y-axis shows the absolute value of the quantitative parameter (averaged across 4 imaging planes) at baseline and post-RT time-points. The green shaded area is the healthy range of values measured across 9 participants, covering the mean ± the standard deviation. (Right) The y-axis shows the change in the mean of the quantitative parameter (averaged across 4 imaging planes) from baseline at post-RT time-points. The dashed black lines represent the repeatability coefficient as an indicator of significant change, i.e., if the difference post-treatment is larger than the repeatability coefficient, then the change is significant.

For blood velocity, no clear trend distinguishes responders from non-responders, except that non-responders exhibited less change in velocity at 2-weeks post-RT, excluding those with low baseline vessel densities. One participant with PD showed no change in blood velocity over time.

For mean blood flow direction entropy, excluding participants with very low vessel densities, the PD participants had baseline values closest to the healthy range, with non-significant increases at 2-weeks post-RT. In contrast, responders had higher baseline values and non-

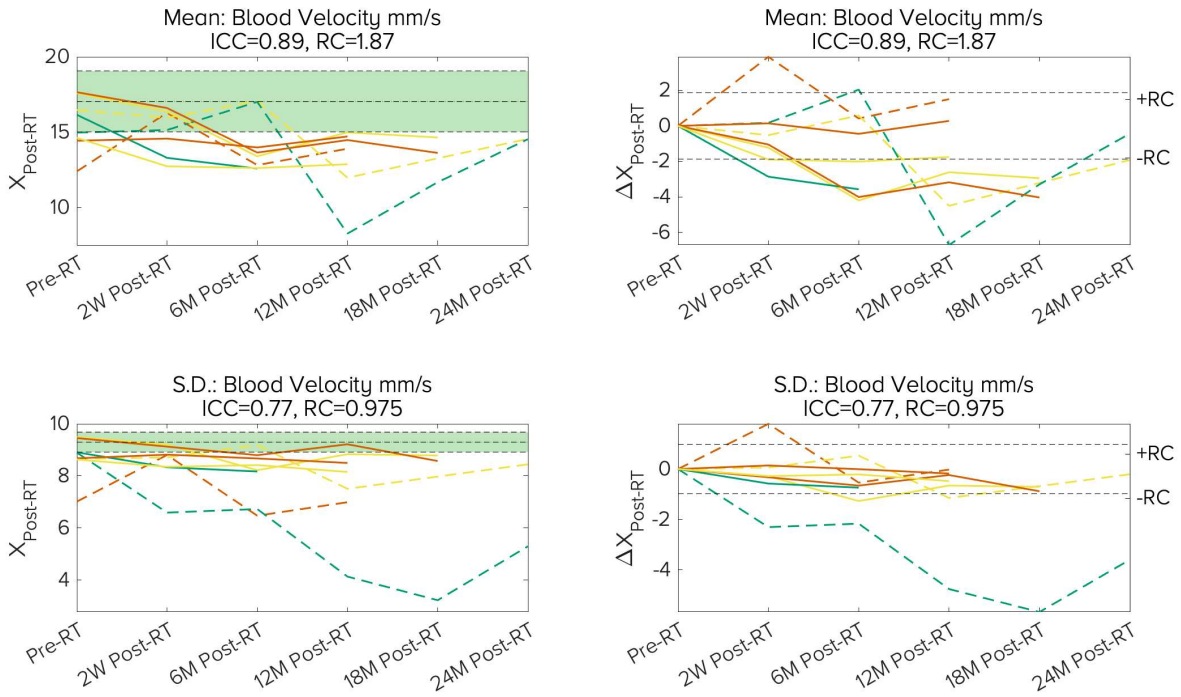


Figure 3.19: The changes in the mean (top) and standard deviation (bottom) of the super-resolution ultrasound (SRUS) blood velocity at 2-weeks, 6-, 12-, 18- and 24-months post-radiotherapy (RT) from 8 participants assessed for radiological response using MRI. The green line signifies participants with CR at 12-months (and 24-months if available) post-RT, the yellow line PR, and the red line PD. The 3 participants with baseline vessel density values below the healthy range are plotted with dashed lines, as their trends differed from the others. (Left) The y-axis shows the absolute value of the quantitative parameter (averaged across 4 imaging planes) at baseline and post-RT time-points. The green shaded area is the healthy range of values measured across 9 participants, covering the mean ± the standard deviation. (Right) The y-axis shows the change in the mean of the quantitative parameter (averaged across 4 imaging planes) from baseline at post-RT time-points. The dashed black lines represent the repeatability coefficient as an indicator of significant change, i.e., if the difference post-treatment is larger than the repeatability coefficient, then the change is significant.

significant or significant decreases at 2-weeks post-RT. One PD participant showed no change over time and remained above the healthy range.

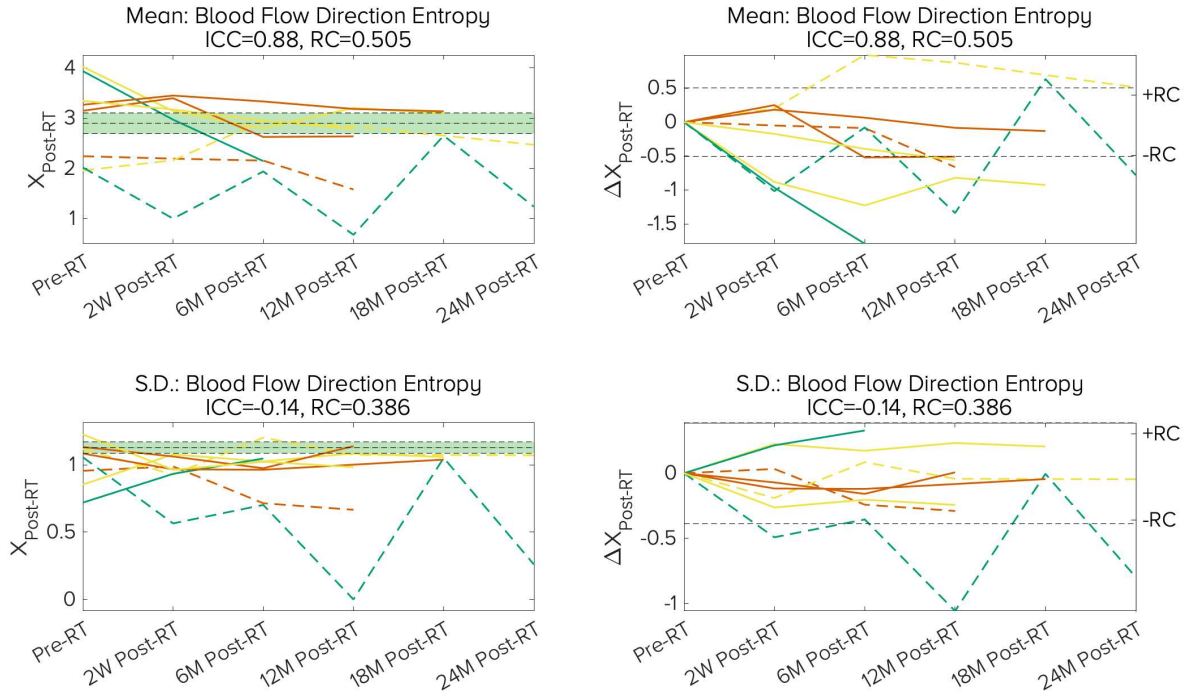


Figure 3.20: The changes in the mean (top) and standard deviation (bottom) of the super-resolution ultrasound (SRUS) blood flow direction entropy at 2-weeks, 6-, 12-, 18- and 24-months post-radiotherapy (RT) from 8 participants assessed for radiological response using MRI. The green line signifies participants with CR at 12-months (and 24-months if available) post-RT, the yellow line PR, and the red line PD. The 3 participants with baseline vessel density values below the healthy range are plotted with dashed lines, as their trends differed from the others. (Left) The y-axis shows the absolute value of the quantitative parameter (averaged across 4 imaging planes) at baseline and post-RT time-points. The green shaded area is the healthy range of values measured across 9 participants, covering the mean ± the standard deviation. (Right) The y-axis shows the change in the mean of the quantitative parameter (averaged across 4 imaging planes) from baseline at post-RT time-points. The dashed black lines represent the repeatability coefficient as an indicator of significant change, i.e., if the difference post-treatment is larger than the repeatability coefficient, then the change is significant.

For mean fractal dimension, excluding participants with very low vessel densities, the PD participants had baseline values within or near the healthy range, showing minimal change at 2-weeks post-RT and no significant changes over time. In contrast, responders had higher baseline values and non-significant or significant decreases at 2-weeks post-RT. One PD participant showed no change over time, remaining above or at the upper end of the healthy range.

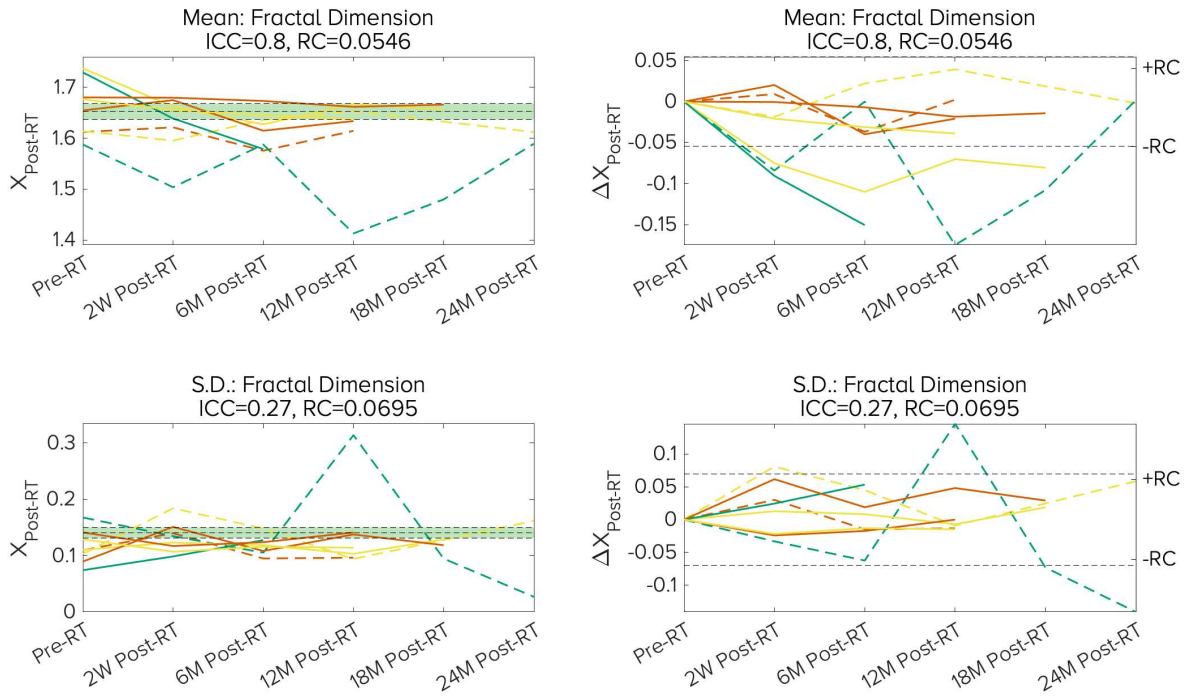


Figure 3.21: The changes in the mean (top) and standard deviation (bottom) of the super-resolution ultrasound (SRUS) fractal dimension at 2-weeks, 6-, 12-, 18- and 24-months post-radiotherapy (RT) from 8 participants assessed for radiological response using MRI. The green line signifies participants with CR at 12-months (and 24-months if available) post-RT, the yellow line PR, and the red line PD. The 3 participants with baseline vessel density values below the healthy range are plotted with dashed lines, as their trends differed from the others. (Left) The y-axis shows the absolute value of the quantitative parameter (averaged across 4 imaging planes) at baseline and post-RT time-points. The green shaded area is the healthy range of values measured across 9 participants, covering the mean ± the standard deviation. (Right) The y-axis shows the change in the mean of the quantitative parameter (averaged across 4 imaging planes) from baseline at post-RT time-points. The dashed black lines represent the repeatability coefficient as an indicator of significant change, i.e., if the difference post-treatment is larger than the repeatability coefficient, then the change is significant.

3.4 CD31 Vessel Count and SRUS Vessel Density

Figure 3.22 presents an example from a participant demonstrating a reduction in blood vessels at 2-weeks post-radiotherapy (RT), as shown by histopathological staining and the corresponding SRUS microvascular map. The histopathological staining also reveals less conspicuous lumens, agreeing with the reduction in the SRUS vessel diameter.

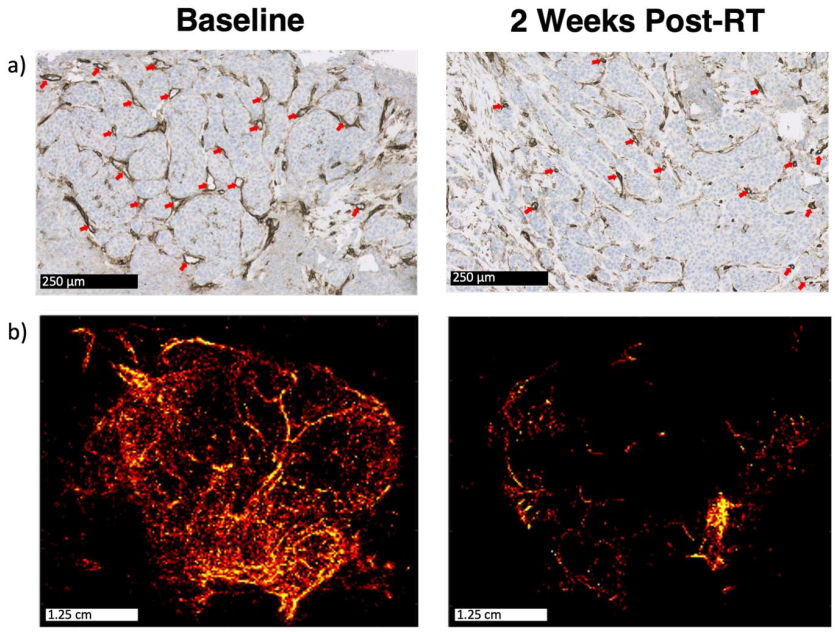


Figure 3.22: Breast tumour core $3\mu m$ biopsy sections from a participant sample, stained for CD31 (an endothelial cell marker), at baseline (left) and 2-weeks post-radiotherapy (RT) (right), taken from non-necrotic tumour regions guided by clinical ultrasound. Slides were digitised at 40× magnification. Examples of blood vessels are highlighted with red arrows, showing that the stained vessel lumens generally appear smaller post-radiotherapy, indicating reduced vessel diameters. A noticeable reduction in blood vessels is observed. Below are SRUS images from the same participant at baseline (left) and 2-weeks post-RT (right), illustrating a corresponding decrease in vascular density. However, differences exist between the two techniques. Immunohistochemical staining is limited to millimetre-scale tissue sections, while SRUS provides a wider centimetre-scale field of view. Additionally, some tumour blood vessels may form without endothelial cells and therefore lack CD31 expression, making them undetectable by this staining method. CD31 staining does not differentiate between functional and non-functional blood vessels, whereas SRUS visualises only perfused vessels.

Quantifying the immunohistochemical staining revealed a decrease in CD31 vessel count at 2-weeks post-RT for 8 out of 10 participants with core biopsies. The plot of SRUS vessel density against CD31 count in Figure 3.23 includes data from two time-points (baseline and 2-weeks post-RT) for the same participants, differentiated by distinct markers for time-points

(baseline (●) and 2-weeks post-RT (*)) and colours for participants (matches previous colours). Baseline SRUS vessel density and CD31 vessel count showed a moderate, positive association (Spearman's rank correlation coefficient $\rho = 0.494$; $p = 0.147$) in Figure 3.23, though the association is non-significant. SRUS vessel density and CD31 vessel count values at 2-weeks post-RT had a weak, non-significant association ($\rho = 0.253$; $p = 0.480$); one participant (red *) with a high CD31 count demonstrated very low vessel density.

Changes in SRUS vessel density and changes in CD31 count 2-weeks post-RT had a weak, non-significant positive association ($\rho = 0.318$, $p = 0.371$). Additionally, some participants with decreases in CD31 count showed increases or minimal changes in SRUS vessel density; however, these changes were within the repeatability coefficient range of SRUS vessel density (7.5%). Here we were testing whether SRUS vessel density and CD31 vessel count correlate, as they both reflect tumour vascularity. For the changes observed at 2-weeks post-RT, we would expect most data-points to fall within the bottom left quadrant (indicating a decrease in both vessel density and CD31 count) or the top right quadrant (indicating an increase in both measures). However, this expected pattern was not consistently observed across participants, suggesting potential differences in what each method captures.

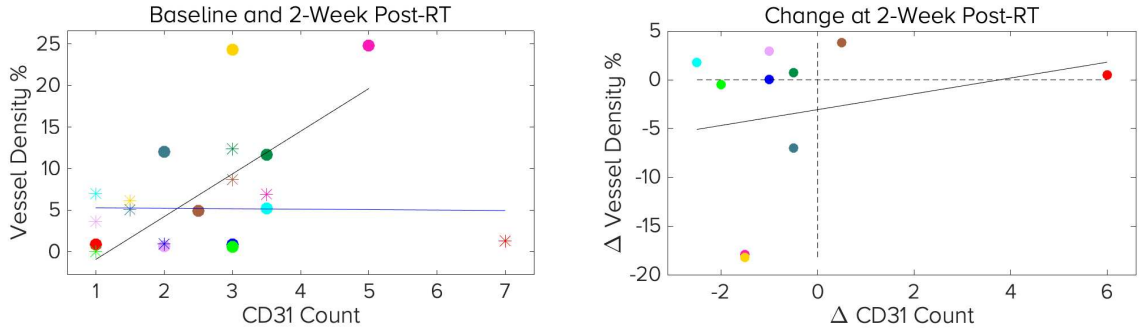


Figure 3.23: (Left) Plot of SRUS vessel density against CD31 count, for 10 participants pre-radiotherapy (RT) (●) and 2-weeks post-RT (*), with the black and blue line being a line of best fit for pre- and post-RT, respectively. A Spearman correlation showed a moderate, non-significant positive association pre-RT ($\rho = 0.494$; $p = 0.147$), and a weaker, non-significant association post-RT ($\rho = 0.253$; $p = 0.480$). (Right) Plot of the change in SRUS vessel density against change in CD31 count at 2-weeks post-RT for 10 participants. The black line is the line of best fit, and the horizontal and vertical dashed black lines represent no change in SRUS vessel density and CD31 count, respectively. A Spearman correlation indicated a weak, non-significant positive association ($\rho = 0.318$, $p = 0.371$). Colours represent individual participants. CD31 staining was scored by a consultant breast histopathologist: 1=0-5; 2=5-10; 3=10-15; 4=15-20; 5=20-25; 6=25-30; 7=30-35 vessels per $0.5mm^2$. Mean scores were calculated from duplicate biopsies.

Chapter 4

Results Chapter 2: Diffusion-Weighted MRI

4.1 Repeatability

Detailed results for the Intraclass Correlation Coefficient (ICC) and Within-Subject Coefficient of Variation (wCV) are presented in Table 4.1 for the DW parameters Apparent Diffusion Coefficient (ADC) from the mono-exponential model, Distributed Diffusion Coefficient (DDC) and the intra-voxel diffusion Heterogeneity Index (α) from the stretched exponential model. The repeatability results are graphically presented as Bland-Altman (BA) plots in Figures 4.1 for the median values of ADC, DDC and α, and in Figures A.1, A.2 and A.3 for the 25th percentile, 75th percentile and interquartile range (IQR) of ADC, DDC and α.

For ADC measurements, the median, 25th percentile, and 75th percentile show excellent ICC values (0.94-0.96) and low wCV values (4.8-5.5%). This suggests high reliability and low variability within subjects for these measurements and, therefore, high precision. Across the ADC-metrics, the Repeatability Coefficients (RCs) are very similar, indicating consistent repeatability patterns (RC = [0.16-0.18] $\times 10^{-3}$ mm^2/s). In Figure A.1, across the ADC-metrics, the median value has a mean of the differences μ (represented by the dashed blue line) that is closest to the zero difference line (indicated by the solid black line). This suggests that it is the metric with the least bias, while the IQR exhibits the greatest difference and, therefore, the most

		ICC	wCV %	RC
ADC $\times 10^{-3}$ mm^2/s	Median	0.96	4.8	0.16
	25th Percentile	0.96	5.5	0.16
	75th Percentile	0.94	4.9	0.18
	IQR	0.17	18.9	0.16
DDC $\times 10^{-3}$ mm^2/s	Median	0.91	10.1	0.39
	25th Percentile	0.94	8.2	0.26
	75th Percentile	0.90	10.1	0.47
	IQR	0.63	20.8	0.29
α	Median	0.13	8.1	0.17
	25th Percentile	-0.12	8.9	0.17
	75th Percentile	0.20	10.3	0.24
	IQR	-0.01	53.1	0.25

Table 4.1: Intraclass Correlation Coefficients (ICC), Within-Subject Coefficients of Variation (wCV), and Repeatability Coefficients (RC) for the median, 25th percentile, 75th percentile, and interquartile range (IQR) metrics of Apparent Diffusion Coefficient (ADC), Distributed Diffusion Coefficient (DDC), and intra-voxel diffusion Heterogeneity Index (α) extracted from entire breast cancer tumours. The repeatability statistics were calculated using 8 double baseline diffusion-weighted MRI scans.

bias. However, no biases were significant.

For DDC, the metrics similarly demonstrate excellent ICC values (0.90-0.94) and relatively low wCV values (8.2-10.1%). Although these values indicate high reliability, the wCV is slightly higher than that for ADC measurements, reflecting marginally greater within-subject variability. In contrast to the ADC-metrics, the RCs for the DDC-metrics show greater variation (RC = [0.26-0.47] $\times 10^{-3}$ mm^2/s), suggesting differing repeatability patterns. Since both ADC and DDC are expressed in the same units, a larger change in the DDC is required to be considered significant (i.e., to surpass the RC) compared to the ADC. In Figure A.2, across the DDC-metrics, the 25th percentile has the least bias, while the IQR exhibits the most.

In contrast, α shows poor ICC values (-0.12-0.20), suggesting low reliability in capturing between-subject differences due to a small between-subject variability. However, it has low wCV values (8.1-10.3%), indicating consistent within-subject measurements. The Heterogeneity Index, α, is a unitless parameter that ranges from 0 to 1. Its metrics exhibit relatively large RCs compared to this range, with values between 0.17 and 0.25. Therefore, only large changes in α can be considered reliable. In Figures A.3, across the α-metrics, the 25th percentile has the

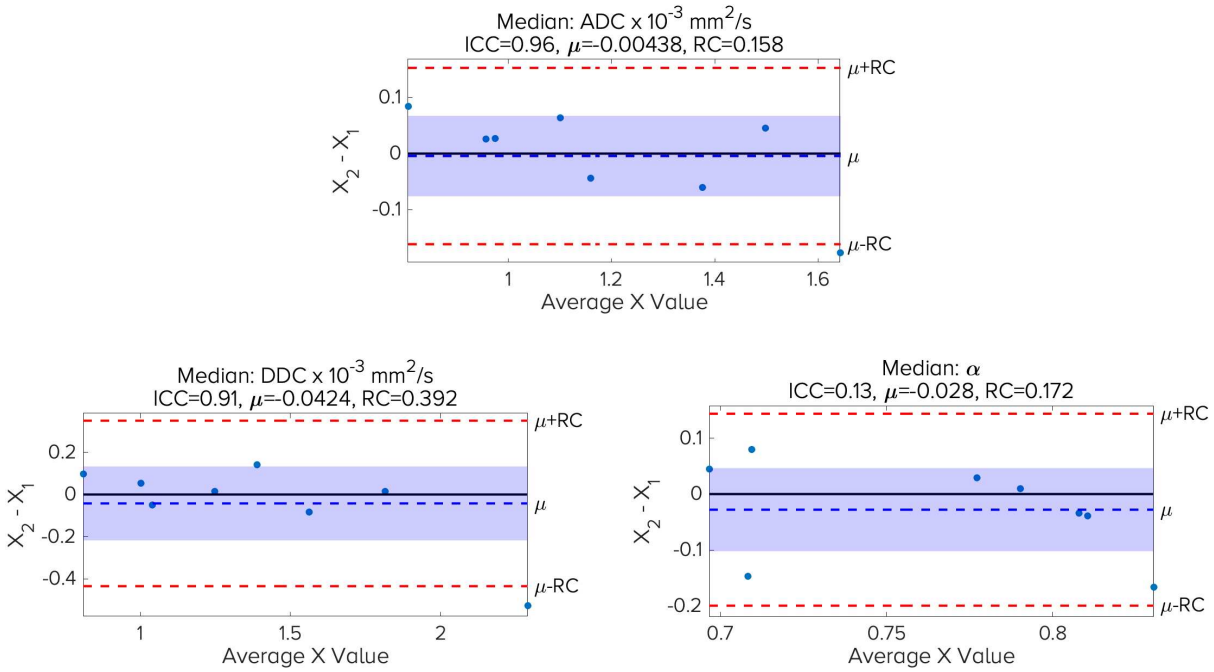


Figure 4.1: Bland-Altman plots for 8 repeatability diffusion-weighted MRI, with the Apparent Diffusion Coefficient (ADC), Distributed Diffusion Coefficient (DDC) and the intra-voxel diffusion Heterogeneity Index (α) extracted from each pixel across the entire tumour. The median, 25th percentile, 75th percentile and interquartile range (IQR) were assessed for repeatability. The y-axis is the difference between the quantitative parameter X from the 2 repeat measurements (after the first baseline scan X_1 and the second baseline scan X_2). The x-axis shows the average value of the 2 repeat measurements of the quantitative parameter. The mean of the differences (μ) is indicated by the blue dashed line, with its 95% confidence interval represented as the shaded blue area. The dotted line represents 0 difference between the test-retest measurement. The mean of the differences ± the repeatability coefficient ($\mu\pm$ RC) is shown as the red dashed line. The 95% confidence interval of the repeatability coefficient is not displayed due to overlap with the shaded blue area. The Intraclass Correlation Coefficient (ICC) is also provided.

least bias, while the 75th percentile value exhibits the most.

The IQR values for ADC, DDC, and α reveal low ICCs (ADC: 0.17, DDC: 0.63, α: -0.01) and high wCVs (ADC: 18.9%, DDC: 20.8%, α: 53.1%). These results suggest IQR values are less reliable for between-subject differentiation across all metrics and reflects greater within-subject measurement variability.

A negative ICC, observed for α, occurs when the within-subject mean squares exceed the between-subject mean squares. This situation can yield complex values for between-subject standard deviation, according to Equation 2.7.1. Mathematically, squaring this complex number during the ICC calculation in Equation 2.7.1 would lead to a negative ICC.

In Figures 4.1, A.1, A.2 and A.3, the zero difference line (indicated by the solid black line) falls within the standard error of the mean of the differences for all metrics, indicating no discernible bias. The large standard error is attributable to the small sample size, resulting in lower degrees of freedom and a higher t-value. Consequently, the BA plots demonstrate no systematic differences between ADC-, DDC- and α-metrics. However, there are substantial wCVs for the IQR of ADC, DDC and α.

For all DW parameters and their metrics, the repeatability appears to be homoscedastic across the range of values in this study. However, a larger data-set is required to confirm homoscedasticity.

Figure 4.2 illustrates the signal decay curves for 8 participants undergoing repeatability assessment of DW-MRI quantitative parameters. Examining the parameters used to model these decay curves in Table 4.2, it is evident that Participants 3, 7 and 8 exhibit the largest within-subject differences for α between the first and second baselines. This contributes to a larger repeatability coefficient for α by increasing the within-subject standard deviation. The low ICC (ICC < 0.5) indicates that the within-subject standard deviation exceeds the between-subject standard deviation. For Participants 3 and 7, there are notable differences in signal decay at low b-values between baseline 1 and baseline 2. Additionally, Participant 8, with the third largest difference in α, shows a deviation at a b-value of 400 s/mm^2. Due to the small sample size, these deviations significantly impact the repeatability statistics. Whether the deviations are biological or technical is unclear. Furthermore, the median curve was investigated here,

whereas pixel-wise modelling will be subjected to more noise.

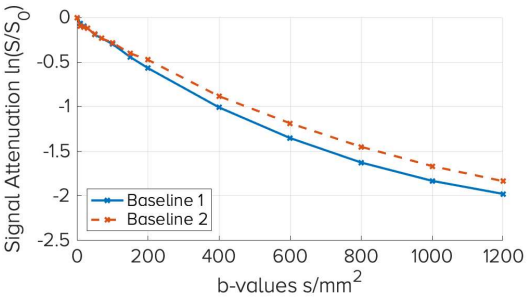
Participant		ADC $\times 10^{-3}$ mm^2/s	DDC $\times 10^{-3}$ mm^2/s	α
1	B1	1.72	2.49	0.68
	B2	1.56	2.03	0.72
2	B1	1.48	1.80	0.75
	B2	1.53	1.82	0.78
3	B1	1.19	1.32	0.77
	B2	1.16	1.47	0.63
4	B1	0.77	0.76	0.82
	B2	0.85	0.85	0.79
5	B1	1.40	1.59	0.81
	B2	1.35	1.52	0.80
6	B1	0.98	1.05	0.75
	B2	0.97	1.02	0.78
7	B1	0.96	0.98	0.88
	B2	0.97	1.04	0.73
8	B1	1.07	1.24	0.68
	B2	1.13	1.25	0.76

Table 4.2: Apparent Diffusion Coefficient (ADC) values extracted from the mono-exponential model, along with Distributed Diffusion Coefficient (DDC) and intra-voxel diffusion Heterogeneity Index (α) values derived from the stretched exponential model, fitted to the median diffusion-weighted (DW) signal decay curves across the entire breast tumours of 8 participants. The participants underwent double baseline (B1: baseline 1; B2: baseline 2) DW-MRI scans for repeatability analysis, which assesses the consistency of diffusion measurements across multiple scans.

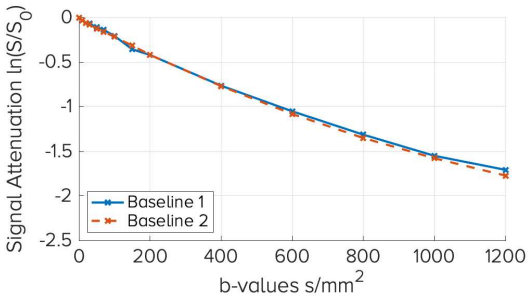
4.2 Response Assessment

4.2.1 Parameter Maps

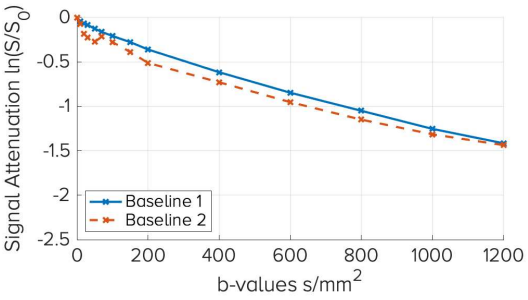
Figure 4.3 presents DW-MRI parameter maps, including the Apparent Diffusion Coefficient (ADC), Distributed Diffusion Coefficient (DDC), and intra-voxel diffusion Heterogeneity Index (α), derived from the entire breast tumour of one participant pre-radiotherapy. The ADC and DDC maps show similar spatial distributions, with regions of higher diffusion in the tumour centre, likely indicative of a necrotic core, and lower diffusion regions at the periphery, potentially reflecting more densely packed tumour cells.



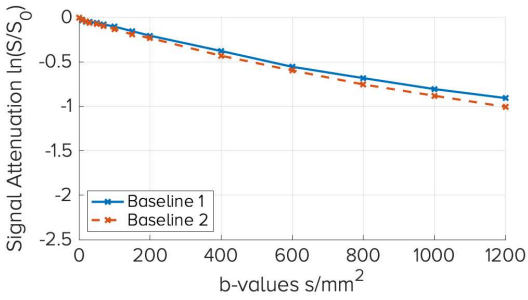
Participant 1



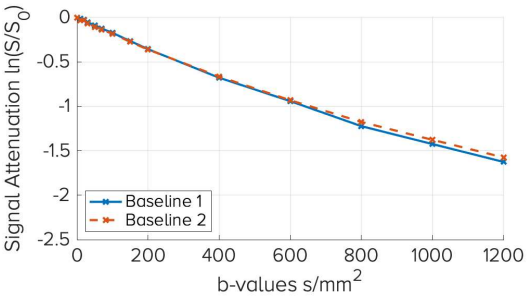
Participant 2



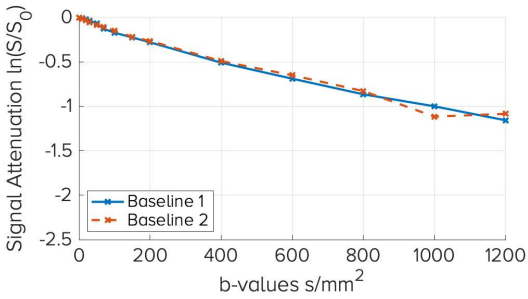
Participant 3



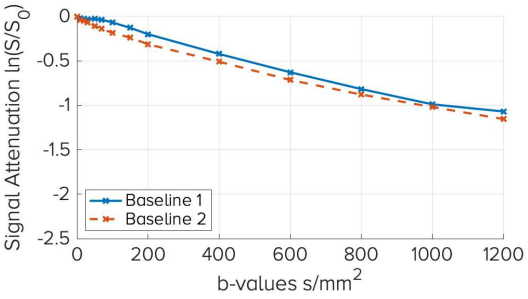
Participant 4



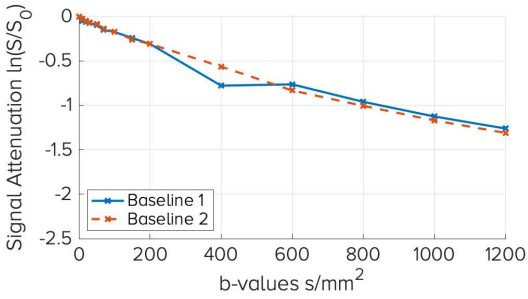
Participant 5



Participant 6



Participant 7



Participant 8

Figure 4.2: Diffusion-weighted signal decay curves from breast tumours of 8 participants, who underwent double baseline MRI scans for repeatability analysis. The median signal across the entire tumour was used. Signal attenuation, calculated as $\ln(\frac{S}{S_0})$, where S is the signal intensity after applying diffusion weighting, and S_0 is the signal intensity without diffusion weighting ($b = 0$ s/mm^2), is plotted against 14 b-values up to 1200 s/mm^2, marked by crosses ($\times$). The blue solid curve represents the signal decay for the first baseline scan, and the orange dashed curve represents the second baseline.

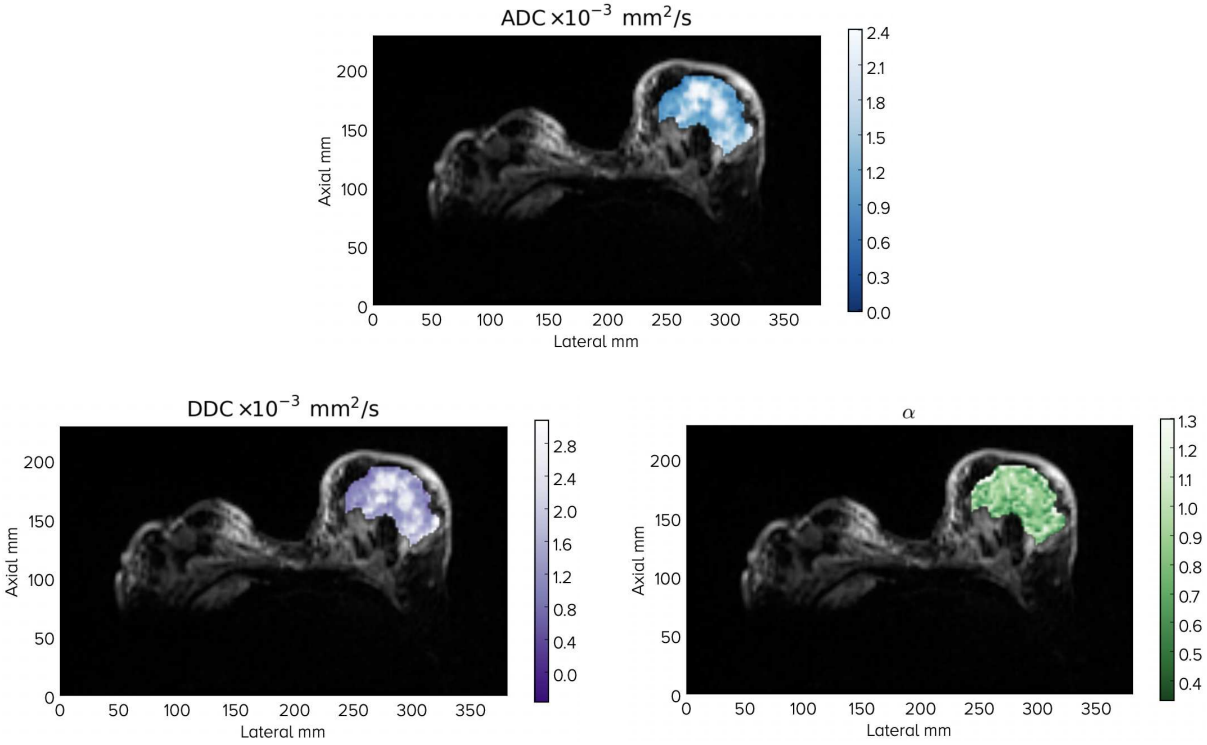


Figure 4.3: Example of diffusion-weighted MRI parameter maps including the Apparent Diffusion Coefficient (ADC), Distributed Diffusion Coefficient (DDC), and intra-voxel diffusion Heterogeneity Index (α) derived from the entire breast tumour of one participant pre-radiotherapy.

4.2.2 Changes in Signal Decay Curves

Examining the signal decay curves for all participants in Figure 4.4 and Figure 4.5, there is an increase in the gradient of the curve from baseline to 2-weeks post-radiotherapy (RT), followed by a continued increase at 6-months post-RT. This trend stabilises at 12- and 24-months post-RT. Additionally, the variability among participants (the solid blue line represents the median curve across participants, while the shaded blue area covers the 25th to 75th percentile range in Figure 4.4) increases after RT, with the largest spread at 6-months post-RT.

Comparing the baseline signal decay curves for responders and non-responders in Figure 4.4 and 4.5, non-responders show a steeper decay, indicating a larger gradient. There is minimal overlap between the responders' and non-responders' 25th to 75th percentile range at baseline. Both groups' decay curves at 2-weeks, 6-months and 12-months post-RT are similar, with the 25th to 75th percentile range of the responders and non-responders overlapping. The gradients of the decay curves increase progressively from baseline to 2-weeks and then to 6-months post-RT, followed by a decrease at 12-months post-RT. By 24-months post-RT, the gradient

for responders stabilises and aligns with the 12-month post-RT curve. In contrast, for non-responders, it decreases further to align with the baseline curve, with minimal overlap between the 25th to 75th percentile range.

4.2.3 Sensitivity to Post-Treatment Changes

Following radiotherapy, changes in the ADC, DDC and α-metrics were evaluated at 2-weeks, 6-, 12- and 24-months in Figure 4.6 for the median values, and Figures A.4, A.5 and A.6 for the 25th percentile, 75th percentile and interquartile range (IQR). This information is summarised in Table 4.3, giving the percentage of participants showing changes in the DW parameters at the post-RT time-points. Each metric is analysed in terms of median, 25th and 75th percentile, and IQR, with changes categorised as increases (↑), decreases (↓), or no change (within the repeatability coefficient, RC).

At 2-weeks post-treatment, most participants showed a significant increase from baseline (exceeding the RC) in the median, 25th percentile and 75th percentile of the ADC values (73.5-79.4%). Across these metrics, a larger percentage had increased at 6-months post-RT (84.2-89.5%), somewhat stabilising at 12-months post-RT (81-85.7%), then decreasing at 24-months post-RT (66.7-77.8%).

In comparison, across the same metrics of the DDC values, there were fewer participants with significant increases at 2-weeks post-RT (47.1-70.6%), suggesting that ADC may be more sensitive to early post-treatment biological changes. At 6-, 12- and 24-months post-RT, more participants showed significant changes in the aforementioned ADC-metrics compared to the DDC-metrics. The IQR of both ADC and DDC values showed low sensitivity to change, with many participants exhibiting no significant change at post-treatment time-points.

For α, most participants had no significant change across all metrics (94.1-100%) at 2-weeks post-RT. This percentage decreased somewhat at 6-months (81.6-92.1%) and 12-months (81.0-95.2%) post-RT. However, there was a shift from a higher percentage of participants showing significant increases at 6-months to a higher percentage showing significant decreases at 12-months. Furthermore, no clear trend emerges over time as seen in Figures 4.6 and A.6.

Among the three parameters, ADC is the most sensitive to changes post-treatment. In

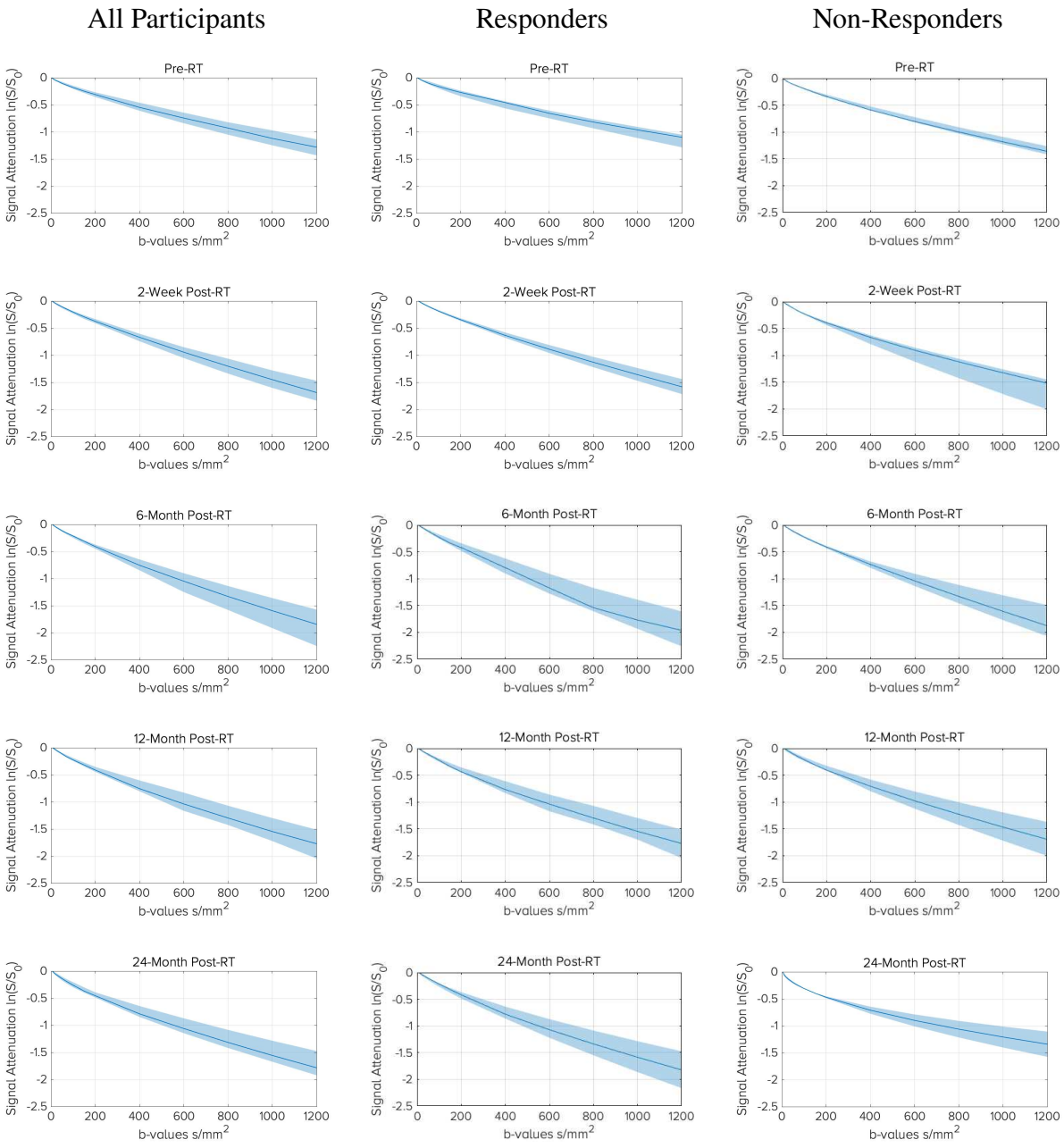


Figure 4.4: Diffusion-weighted MRI signal decay curves from breast tumours of all participants (left; pre-radiotherapy (RT) N=59, 2-weeks post-RT N=36, 6-months post-RT N=40, 12-months post-RT N=23, 24-months post-RT N=10), the responding patients (middle; pre-RT N=13, 2-weeks post-RT N=8, 6-months post-RT N=14, 12-months post-RT N=14, 24-months post-RT N=5) and non-responding participants (right; pre-RT N=5, 2-weeks post-RT N=4, 6-months post-RT N=5, 12-months post-RT N=5, 24-months post-RT N=2). Responding participants had a partial response or complete response at 12- or 24-months post-RT, and non-responding participants had a stable disease or progressive disease at 12- or 24-months post-RT. The median signal across the entire tumour was used. Signal attenuation, calculated as $\ln\left(\frac{S}{S_0}\right)$ where S is the signal intensity after applying diffusion weighting, and S_0 is the signal intensity without diffusion weighting (b = 0 s/mm^2), is plotted against 14 b-values up to 1200 s/mm^2. The blue solid curve represents the median signal decay curve across participants, and the blue shaded area represents the 25th and 75th percentile.

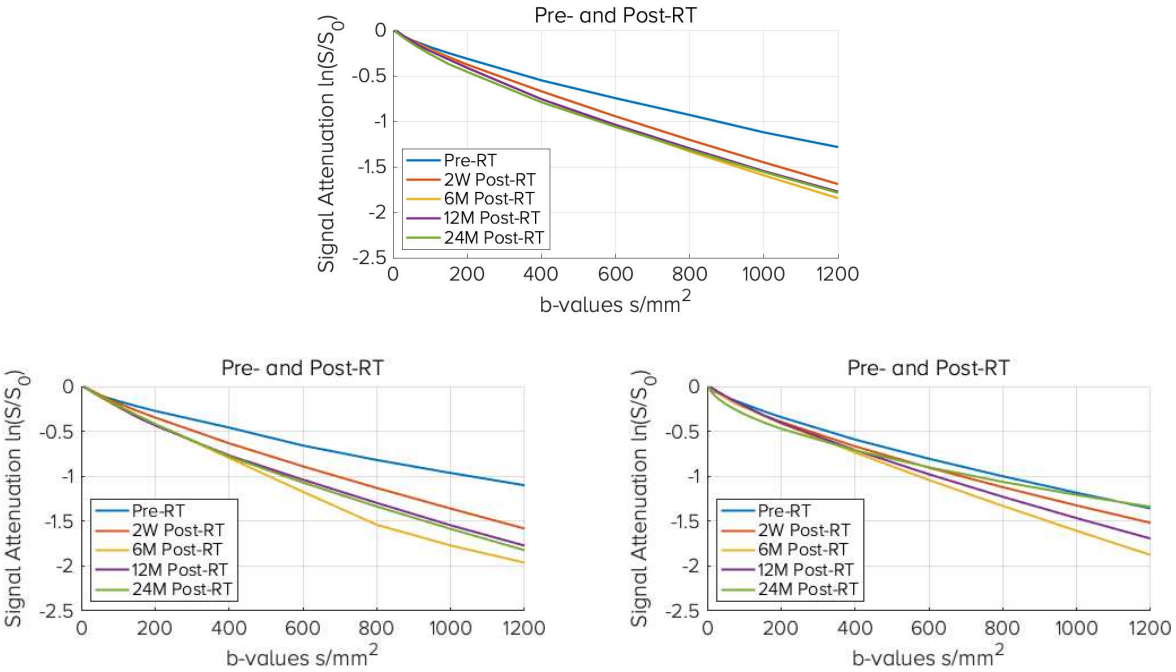


Figure 4.5: Diffusion-weighted MRI signal decay curves from breast tumours of all participants (top; pre-radiotherapy (RT) N=59, 2-weeks post-RT N=36, 6-months post-RT N=40, 12-months post-RT N=23, 24-months post-RT N=10), the responding patients (bottom left; pre-RT N=13, 2-weeks post-RT N=8, 6-months post-RT N=14, 12-months post-RT N=14, 24-months post-RT N=5) and non-responding participants (bottom right; pre-RT N=5, 2-weeks post-RT N=4, 6-months post-RT N=5, 12-months post-RT N=5, 24-months post-RT N=2). Responding participants had a partial response or complete response at 12- or 24-months post-RT, and non-responding participants had a stable disease or progressive disease at 12- or 24-months post-RT. The median signal across the entire tumour was calculated for each participant. The solid curves represent the median signal decay curve across participants, pre-RT, 2-weeks, 6-month, 12-month, and 24-months post-RT.

		2W Post-RT % N=34			6M Post-RT % N=38			12M Post-RT % N=21			24M Post-RT % N=9		
		↑	↓	-	↑	↓	-	↑	↓	-	↑	↓	-
ADC	Median	79.4	5.9	14.7	89.5	2.6	7.9	85.7	0.0	14.3	66.7	11.1	22.2
	25th Percentile	76.5	5.9	17.6	84.2	2.6	13.2	81.0	0.0	19.0	66.7	11.1	22.2
	75th Percentile	73.5	0.0	26.5	89.5	5.3	5.3	85.7	0.0	14.3	77.8	11.1	11.1
	IQR	11.8	2.9	85.3	13.2	7.9	78.9	28.6	14.3	57.1	22.2	0.0	77.8
DDC	Median	58.8	0.0	41.2	76.3	0.0	23.7	71.4	4.8	23.8	77.8	0.0	22.2
	25th Percentile	70.6	2.9	26.5	81.6	0.0	18.4	66.7	4.8	28.6	66.7	0.0	33.3
	75th Percentile	47.1	0.0	52.9	73.7	2.6	23.7	61.9	4.8	33.3	66.7	0.0	33.3
	IQR	8.8	2.9	88.2	18.4	7.9	73.7	33.3	9.5	57.1	44.4	0.0	55.6
α	Median	2.9	2.9	94.1	10.5	2.6	86.8	4.8	14.3	81.0	0.0	11.1	88.9
	25th Percentile	2.9	2.9	94.1	13.2	5.3	81.6	4.8	9.5	85.7	0.0	11.1	88.9
	75th Percentile	0.0	2.9	97.1	5.3	2.6	92.1	4.8	4.8	90.5	0.0	11.1	88.9
	IQR	0.0	0.0	100	2.6	5.3	92.1	4.8	0.0	95.2	0.0	0.0	100

Table 4.3: The percentage of participants showing changes in the Apparent Diffusion Coefficient (ADC), Distributed Diffusion Coefficient (DDC), and intra-voxel diffusion Heterogeneity Index (α) metrics – specifically the median, 25th percentile, 75th percentile and interquartile range (IQR) – relative to the repeatability coefficient (RC). For each metric, participants with changes exceeding the RC (↑; indicating a significant increase), changes below -RC (↓; indicating a significant decrease), and changes within ±RC (indicating no significant change) are reported at 2-weeks, 6-month, 12-months and 24-months post-radiotherapy for breast tumours.

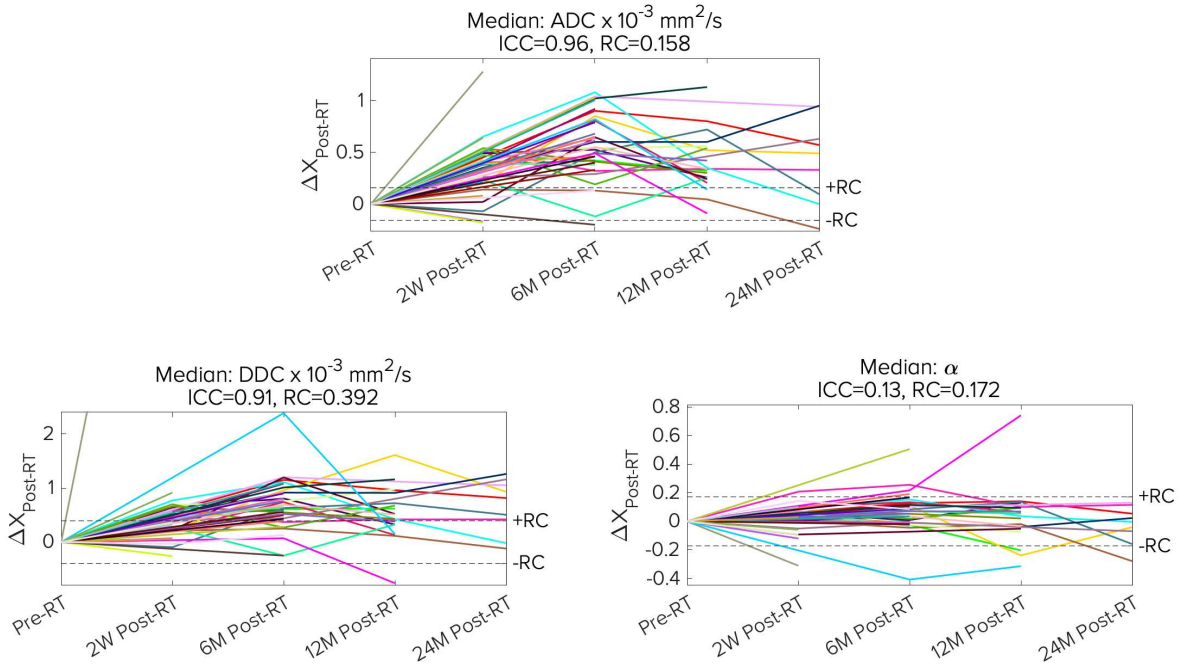


Figure 4.6: The change in the median Apparent Diffusion Coefficient (ADC), Distributed Diffusion Coefficient (DDC), and intra-voxel diffusion Heterogeneity Index (α) derived from the diffusion-weighted MRI data of the entire breast tumour, at 2-weeks (N=34), 6-months (N=38), 12-months (N=21) and 24-months (N=9) post-radiotherapy (RT) from 51 participants. The dashed black lines represent the repeatability coefficient as an indicator of significant change, i.e., if the difference post-treatment is larger than the repeatability coefficient, then the change is significant.

contrast, since only large changes in α can be considered reliable, and regardless, no clear trend emerges across the participant population, it is not useful for assessing treatment response. As the stretched exponential model does not provide additional insights beyond the mono-exponential model, ADC alone will be analysed moving forward for simplicity. Additionally, the IQR of ADC will be excluded due to its low repeatability and limited sensitivity to treatment response.

4.2.4 Pre-Treatment Values

Table 4.4 presents the average ± standard deviation of the median, 25th percentile and 75th percentile of ADC values across all participants, responders and non-responders. Although the median, 25th percentile and 75th percentile ADC values are lower in the responder group than the non-responder group, these differences are not statistically significant (p = 0.17, 0.27, and 0.11, respectively). The standard deviation in ADC values within the responder group overlaps with that of the non-responder group.

		All Participants N=59	Responders N=13	Non-Responders N=6	p-value
ADC $\times 10^{-3}$ mm^2/s	Median	1.08 ± 0.24	1.01 ± 0.26	1.12 ± 0.23	0.17
	25th Percentile	0.94 ± 0.22	0.89 ± 0.24	0.97 ± 0.22	0.27
	75th Percentile	1.24 ± 0.27	1.16 ± 0.29	1.29 ± 0.25	0.11

Table 4.4: The average ± standard deviation of the ADC-metrics at baseline for all participants, responders, and non-responders. The statistical significance of the difference between the baseline values of the responders and non-responders is given as a p-value.

4.2.5 Whole Tumour Response Assessment

Figure 4.7 illustrates the average ADC histograms for all participants, responders and non-responders. Among all participants, there is an observable shift from lower ADC values from baseline to 2-weeks post-RT, followed by a shift to higher values at 6-months post-RT. At 12- and 24-months post-RT, ADC values return to levels like those at 2-weeks, but with a lower peak due to reduced tumour size.

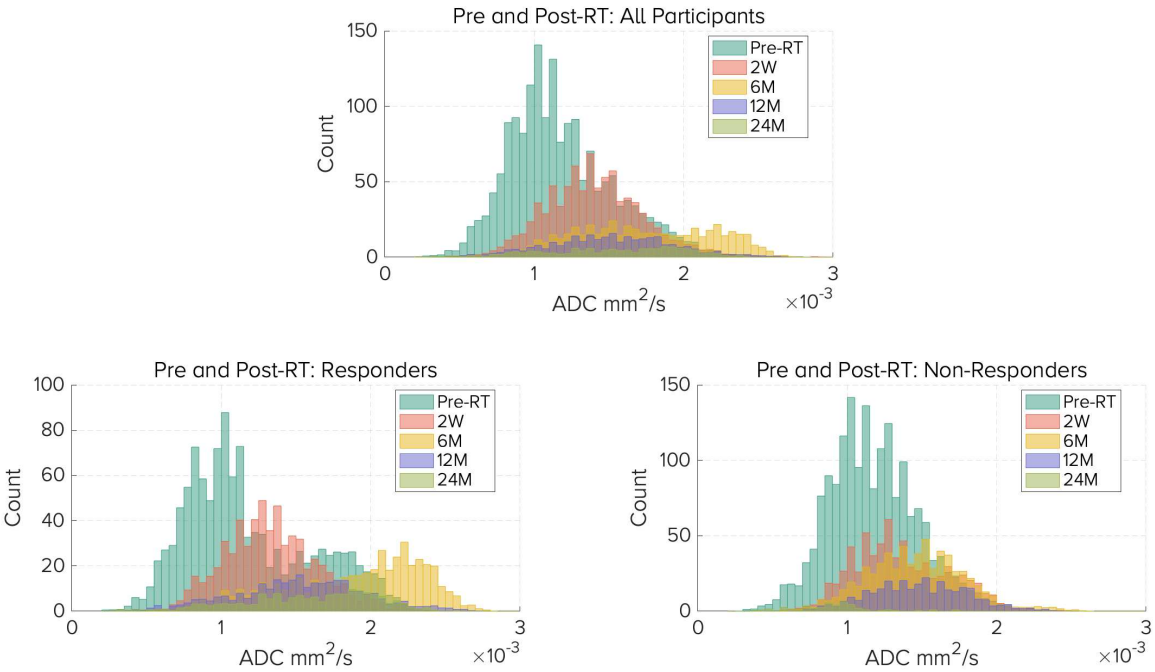


Figure 4.7: The average ADC histogram across all participants for the entire tumour, pre-RT and 2-weeks, 6-, 12- and 24-months post-radiotherapy (RT).

This trend is reflected in Figure 4.8, A.7 and 4.5. Table 4.5 summarises the ADC-metrics for all participants, responders and non-responders at pre-RT and the post-RT time-points. Figure 4.8 illustrates the median ADC values across imaging time-points for the participant cohort, and the changes in median ADC values at post-RT time-points. Significant changes are indicated by values exceeding the repeatability coefficient (dashed black lines). The 25th percentile, 75th percentile and IQR metrics are shown in Figure A.7.

At baseline, the heterogeneity of ADC values is evident. Following treatment, there is a heterogeneous response. There is a shift in the 25th percentile, median, and 75th percentile to higher values at 2-weeks and 6-months post-RT, with most participants having a change beyond the RC across these metrics. At 12-months, there is a shift back towards 2-week ADC values across the metrics and stabilisation at 24-months.

In the responder group, the trend mirrors that of the overall participant cohort, as seen in Figure 4.7, 4.8, A.8 and 4.5, suggesting that most participants are responding to treatment. At baseline, a secondary peak at higher ADC values is noted; further analysis reveals this peak is attributable to a single participant, which can be seen as an outlier in Figures 4.8 and A.8 at baseline.

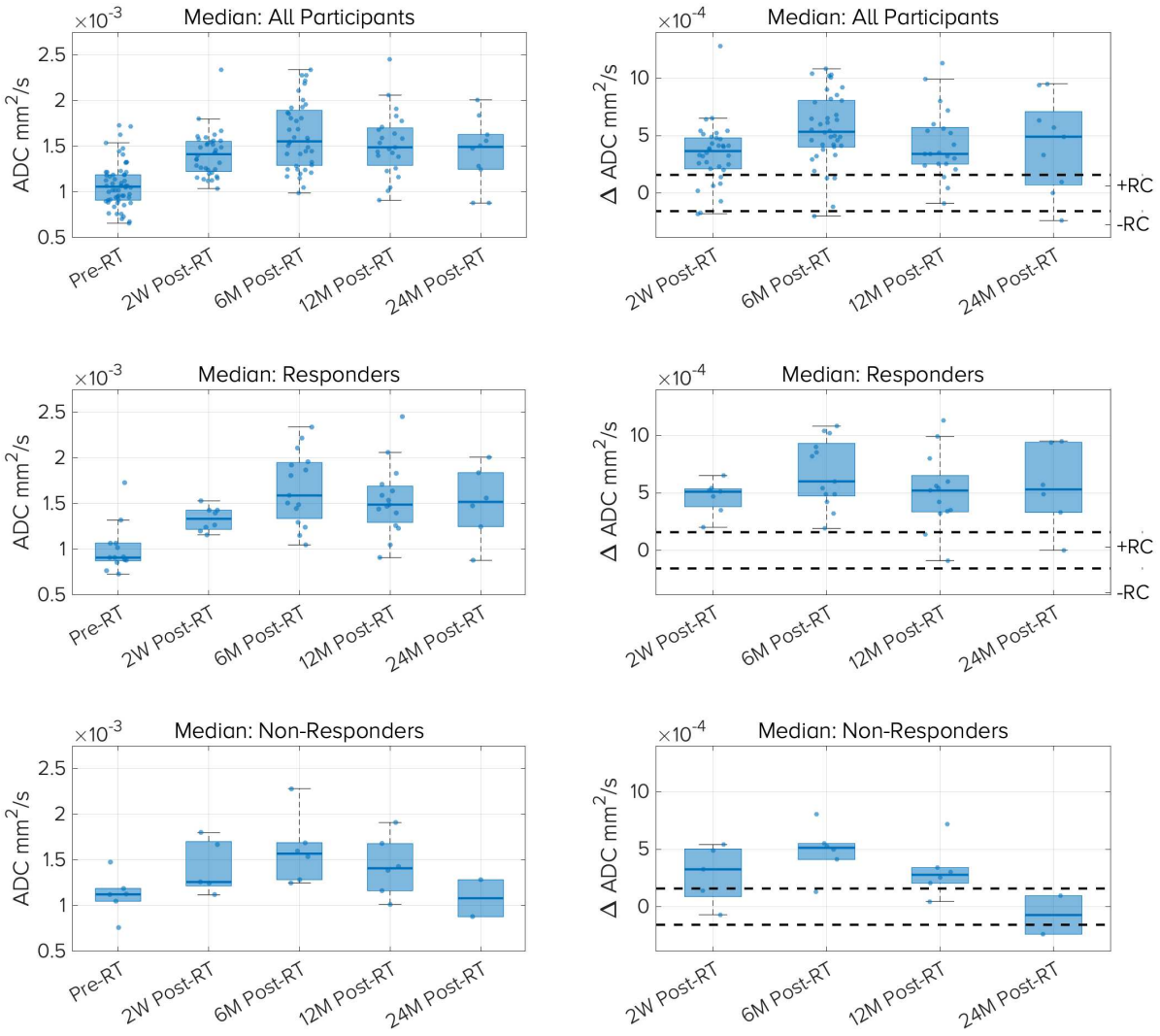


Figure 4.8: (Left) The median ADC derived from the diffusion-weighted MRI data of the entire breast tumour, pre-RT and at 2-weeks, 6-months, 12-months and 24-months post-radiotherapy (RT) for all participants, responders, and non-responders. (Right) The change in the ADC-metrics from baseline (pre-RT) at 2-weeks, 6-months, 12-months and 24-months post-radiotherapy (RT) for all participants, responders, and non-responders. The dots are individual participants.

		ADC×10^{-3} mm^2/s (Average ± SD)				
		Pre-RT	2W Post-RT	6M Post-RT	12M Post-RT	24M Post-RT
		N=59	N=36	N=40	N=23	N=10
All Participants	Median	1.08 ± 0.24	1.41 ± 0.25***	1.62 ± 0.37***	1.52 ± 0.35***	1.43 ± 0.37*
	25th Percentile	0.94 ± 0.22	1.25 ± 0.23***	1.44 ± 0.40***	1.33 ± 0.39***	1.28 ± 0.36*
	75th Percentile	1.24 ± 0.27	1.58 ± 0.26***	1.78 ± 0.35***	1.71 ± 0.33***	1.60 ± 0.41*
		N=13	N=8	N=14	N=14	N=5
Responders	Median	1.01 ± 0.26	1.33 ± 0.13***	1.67 ± 0.40***	1.54 ± 0.39***	1.50 ± 0.41*
	25th Percentile	0.89 ± 0.24	1.17 ± 0.11***	1.51 ± 0.43***	1.32 ± 0.44**	1.33 ± 0.37*
	75th Percentile	1.16 ± 0.29	1.51 ± 0.16***	1.83 ± 0.36***	1.74 ± 0.34***	1.70 ± 0.46*
		N=5	N=4	N=5	N=5	N=2
Non-Responders	Median	1.12 ± 0.23	1.42 ± 0.30$^{p=0.065}$	1.61 ± 0.37**	1.43 ± 0.33*	1.08 ± 0.29$^{p=0.740}$
	25th Percentile	0.97 ± 0.22	1.29 ± 0.28*	1.46 ± 0.38**	1.28 ± 0.31*	0.92 ± 0.27$^{p=0.761}$
	75th Percentile	1.29 ± 0.25	1.55 ± 0.30$^{p=0.096}$	1.77 ± 0.35**	1.59 ± 0.36*	1.27 ± 0.42$^{p=0.855}$

Table 4.5: The average ± standard deviation of the ADC-metric values for all participants, responders, and non-responders at the pre-RT, 2-weeks, 6-month, 12-month, and 24-months post-RT time-points. Significance levels are given as $^{*} = p < 0.05$, $^{**} = p < 0.01$, $^{***} = p < 0.001$, otherwise the p-values are given.

In the non-responder group, a distinct trend emerges in Figure 4.7. At 6-months post-RT, there is a minimal shift from the 2-week post-RT values, and the 12-month data largely overlaps with the 6-month time-point. By 24-months, there is a shift towards lower baseline ADC values. In Figures 4.8 and A.9 and Table 4.5, the ADC-metrics return to baseline values at 24-months post-RT.

From Table 4.5, significant changes in the median, 25th, and 75th percentile ADC values were observed between baseline and all time-points post-RT for all participants and responders, with significance level dropping at 24-months post-RT. For non-responders, significant changes are evident between baseline and 6- and 12-months for all ADC-metrics - at a lower significance level to the responders - but not at 2-weeks or 24-months post-RT.

4.2.6 Estimating Response

To evaluate the correlation between ADC-metrics and radiological response assessed using MRI, the ADC-metrics are categorised according to the response types: complete response (CR), partial response (PR), stable disease (SD), and progressive disease (PD), assessed at 6, 12, and 24 months post-radiotherapy. Figure 4.9 illustrates the median ADC values, while Figure A.10 presents the 25th and 75th percentiles.

For the ADC-metrics, the response groups overlap, meaning that absolute ADC values do not correspond to distinct radiological assessments. The only significant difference is between the median ADC of the CR and PD group ($p = 0.0381$), with some separation between groups. However, the ADC values cannot reliably distinguish between CR and PR ($p = 0.1975$) and PR and PD ($p = 0.2886$).

Regarding changes in ADC values, there is a noticeable separation between CR and PD across the metrics. A significant difference is observed between the median change in ADC for the CR and PD groups ($p = 0.0023$), but no significant differences are found between CR and PR ($p = 0.1313$) or between PR and PD ($p = 0.0644$). For the 75th percentile, significant differences are observed across all groups: CR and PD ($p = 0.0007$), CR and PR ($p = 0.0178$), and PR and PD ($p = 0.0477$).

Additionally, analysis was conducted to assess whether ADC values measured at 12-months

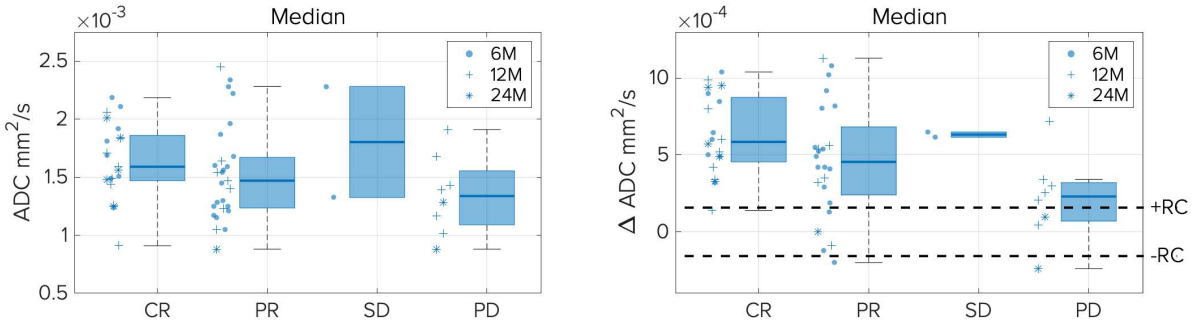


Figure 4.9: Boxplots of the median ADC grouped by radiological response assessment at 6-months (blue dot ●), 12-months (blue plus +) and 24-months (blue asterisk *). The radiological response assessment groups are complete response (CR), partial response (PR), stable disease (SD) and progressive disease (PD). On the left are the absolute values, and on the right is the change from baseline; the dashed lines are the repeatability coefficients and changes beyond this are significant.

post-RT could distinguish between responders and non-responders at the same time-point, using a receiver operating characteristic (ROC) curve. Among the 21 participants included (15 responders and 6 non-responders), the area under the curve (AUC) for the median ADC value was 0.60 (p = 0.557), indicating poor agreement with the radiological assessment. These findings suggest that ADC values at 12-months post-RT were not effective in differentiating between treatment response and relapse.

4.2.7 Predictive Value of Baseline Measurements and Early Changes for Treatment Response

The analysis evaluated the predictive power of baseline ADC values in distinguishing between responders and non-responders at 12-months post-RT using a receiver operating characteristic (ROC) curve. Among the 19 participants included (13 responders and 6 non-responders), the area under the curve (AUC) was calculated at 0.71 for the median ADC value (25th percentile/75th percentile: 0.67/0.74), indicating the moderate discriminative ability of baseline ADC values in predicting treatment response. However, this was non-significant with a p-value of 0.361 (0.458/0.324).

The analysis also assessed the predictive power of ADC changes at 2-weeks post-RT. Among the 12 patients included (7 responders and 5 non-responders), the ROC analysis yielded an AUC of 0.71 for the median ADC change, indicating moderate predictive ability, although this was

not statistically significant (p = 0.127). The 75th percentile of ADC changes demonstrated the highest discriminative ability, with an AUC of 0.83, supported by a p-value of 0.0525, approaching significance, indicating that larger ADC changes in the upper quartile may better differentiate responders from non-responders. The 25th percentile of ADC changes demonstrated the worst discriminative ability, with an AUC of 0.60 and a p-value of 0.348.

The analysis further evaluated the predictive power of combining baseline ADC values with ADC changes at 2-weeks post-RT to predict patient response at 12-months. Among the 12 patients included (7 responders and 5 non-responders), the combination of baseline and 2-weeks change ADC values showed improved discriminative ability. The ROC analysis yielded an AUC of 0.80 for the median values, surpassing the performance of baseline and 2-weeks change values when considered independently, suggesting that combining baseline and early post-treatment ADC changes may enhance predictive accuracy. This was supported by a p-value of 0.104, suggesting a trend toward better performance compared to a constant model, though not statistically significant. The 75th percentile combination also yielded an AUC of 0.80, with a p-value of 0.0909, but performed slightly worse than the 2-weeks change values alone. The 25th percentile combination, with an AUC of 0.77, showed moderate improvement over baseline and 2-weeks change values individually, but with a p-value of 0.166, it indicated only a non-significant enhancement over the baseline model.

To investigate the relationship between pre-radiotherapy ADC measurements, early treatment response and long-term response, the correlations between the pre-RT ADC-metrics and their changes at 2-weeks post-radiotherapy were evaluated, colour coded by radiological response. These correlations are shown in Figure 4.11 for the median, 25th percentile, and 75th percentile values.

The baseline ADC-metrics of tumours and the changes observed 2-weeks post-RT were moderately negatively correlated (R = -0.49 to -0.52), indicating that lower initial ADC values are associated with a greater early increase immediately following RT. On observation, the non-responders tend to cluster around higher pre-RT ADC-metrics and lower changes 2-weeks post-RT, apart from one, whereas the responding group tend to cluster around lower pre-RT ADC and larger changes 2-weeks post-RT.

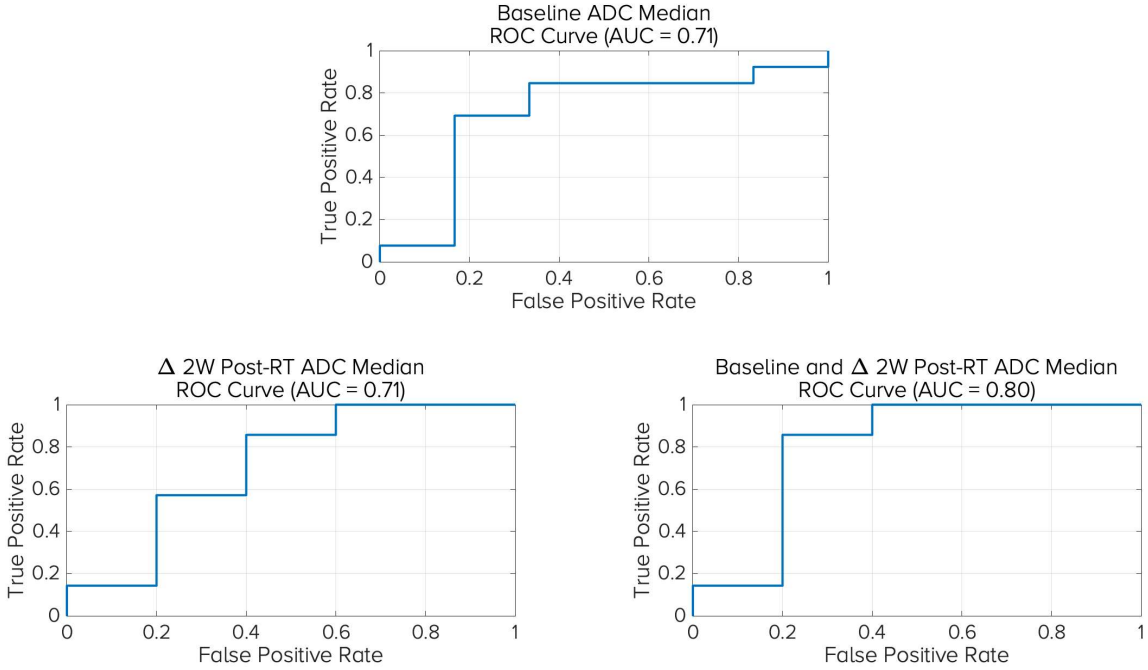


Figure 4.10: Receiver Operating Characteristic (ROC) curve depicting the true positive rate (sensitivity) against the false positive rate (1-specificity) in predicting responders versus non-responders at 12-months post-radiotherapy. For (top) the median baseline Apparent Diffusion Coefficient (ADC) values from diffusion-weighted MRI, the area under the curve (AUC) is 0.71 with a p-value of 0.361. For (bottom left) the median ADC changes at 2-weeks post-radiotherapy; the AUC is also 0.71 with a p-value of 0.127. For (bottom right) the combination of the two, the AUC is 0.80 with a p-value of 0.104.

The ADC values of the responder group significantly increased 2-weeks after radiotherapy, suggesting that changes in ADC values are associated with radiotherapy response (Table 4.5). In the non-responder group, the ADC did not significantly increase 2-weeks post radiotherapy. This suggests that early changes are predictive of overall response. The median change at 2-weeks post-radiotherapy for the responder group was greater than that in the non-responder group; however, this was non-significant (p = 0.268).

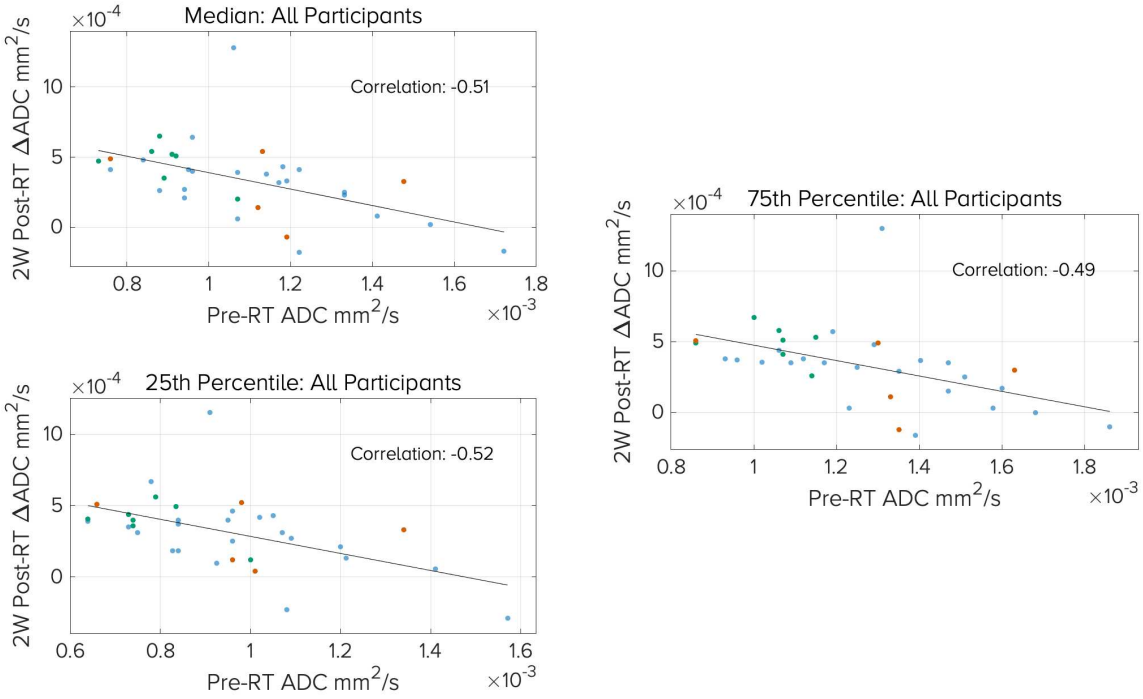


Figure 4.11: Correlation between the pre-radiotherapy (RT) and 2-weeks post-RT for median, 25th percentile and 75th percentile ADC. The correlation coefficient is specified in the plot. The green dots are the responders and the red dots are the non-responders, assessed at 12-months and 24-months post-RT. The blue dots are those that had not had radiological response assessment at 12- and 24-months post-RT.

4.3 Sub-Types

In Figures 4.12 and A.11, ADC-metrics are stratified by molecular breast cancer subtypes for the median values and 25th/75th percentile values, respectively. The median ADC value of HER2+ (N=4) and TN (N=8) were higher compared to the median ADC values for luminal A (N=30) and luminal B (N=13). However, there was not a significant difference between them (median/25th percentile/75th percentile: p = 0.3199/0.2852/0.4856). There is a large overlap in

values amongst the subtypes, with the luminal A subtype having a large spread. Furthermore, a relationship is difficult to discern from this data due to the small number of participants across the subtypes.

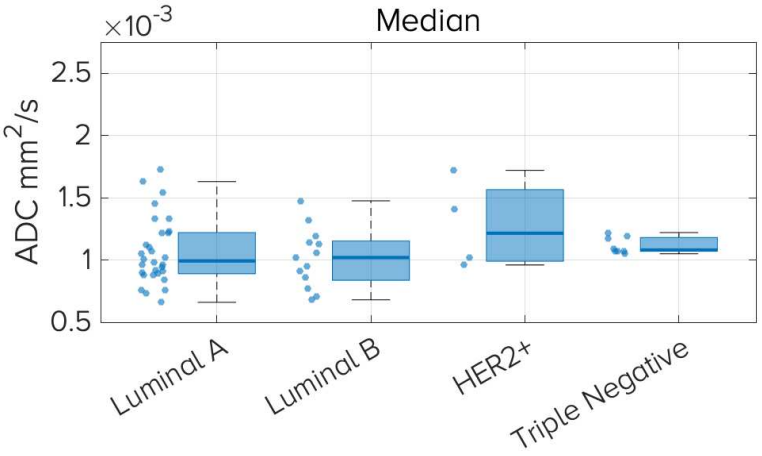


Figure 4.12: Boxplots of the median ADC and their subtypes. The subtype groups are Luminal A, Luminal B, HER2+ and Triple Negative.

.

Chapter 5

Results Chapter 3: Dynamic Contrast-Enhanced MRI

5.1 Repeatability

5.1.1 Tofts Model Parameters

Detailed results for the Intraclass Correlation Coefficient (ICC) and Within-Subject Coefficient of Variation (wCV) are presented in Table 5.1 for the Tofts model parameters. The repeatability results for the Tofts model parameters are graphically presented as Bland-Altman (BA) plots in Figure 5.1 for the median values of K_{trans}, v_e and v_e, and in Figures B.1, B.2 and B.3 for the 25th percentile, 75th percentile and interquartile range (IQR).

For K_{trans} measurements, the median, 25th percentile, and 75th percentile show excellent ICC values (0.96–0.99) and low wCV values (5.4–10.5%). This suggests high reliability and low variability within subjects for these measurements and, therefore, high precision. Across these K_{trans}-metrics, the Repeatability Coefficients (RCs) are very similar, indicating consistent repeatability patterns (RC = 0.0222–0.0239 min^{-1}). The IQR of K_{trans} demonstrates slightly lower ICC and higher wCV and RC, but is good, nonetheless. In Figure B.1, across the K_{trans}-metrics, the 75th percentile K_{trans} value has a mean of the differences μ (represented by the dashed blue line) that is closest to the zero difference line (indicated by the solid black line). This suggests that it is the metric with the least bias, while the 25th percentile exhibits the

		ICC	wCV %	RC
K_{trans} min^{-1}	Median	0.98	6.9	0.0222
	25th Percentile	0.96	10.5	0.0239
	75th Percentile	0.99	5.4	0.0230
	IQR	0.88	15.9	0.0319
v_e	Median	-0.31	44.7	0.61
	25th Percentile	0.70	16.6	0.17
	75th Percentile	0.92	8.9	0.16
	IQR	0.91	25.0	0.19
v_p	Median	0.83	41.1	0.06
	25th Percentile	0.72	57.5	0.06
	75th Percentile	0.85	37.1	0.08
	IQR	0.89	30.8	0.03

Table 5.1: Intraclass Correlation Coefficients (ICC), Within-Subject Coefficients of Variation (wCV), and Repeatability Coefficients (RC) for the median, 25th percentile, 75th percentile, and interquartile range (IQR) statistics of K_{trans}, v_e, and v_p extracted from entire breast tumours. The repeatability metrics were calculated using 7 double baseline dynamic contrast-enhanced MRI scans.

greatest difference and, therefore, the most bias. However, no biases were significant.

For v_e measurements, the statistics demonstrate a variety of ICC (-0.31–0.92), wCV (8.9–44.7%) and RC values (0.16–0.61), suggesting differing repeatability patterns. In particular, the median value shows poor reliability and the most within-subject variability. v_e is a unitless parameter ranging from 0 to 1, and since its median exhibits a relatively large RC compared to this range, only large changes in median v_e can be considered reliable. The poor results for the median v_e were caused by one outlier, which can be seen in the Bland-Altman plots 5.1. In Figures B.2, across the v_e-metrics, the 25th percentile has the least bias, while the median value exhibits the most.

v_p shows moderate to good ICC values (0.72–0.89), suggesting good reliability in capturing between-subject differences. However, it has high wCV values (30.8–57.5%), indicating inconsistent within-subject measurements. The RCs are small compared to the range of values v_p can take (between 0 and 1). In Figure B.3, across the v_p-metrics, the IQR has the least bias, while the 75th percentile value exhibits the most.

For all Tofts-metrics, the repeatability appears to be homoscedastic across the range of values in this study. However, a larger data-set is required to truly appreciate this relationship.

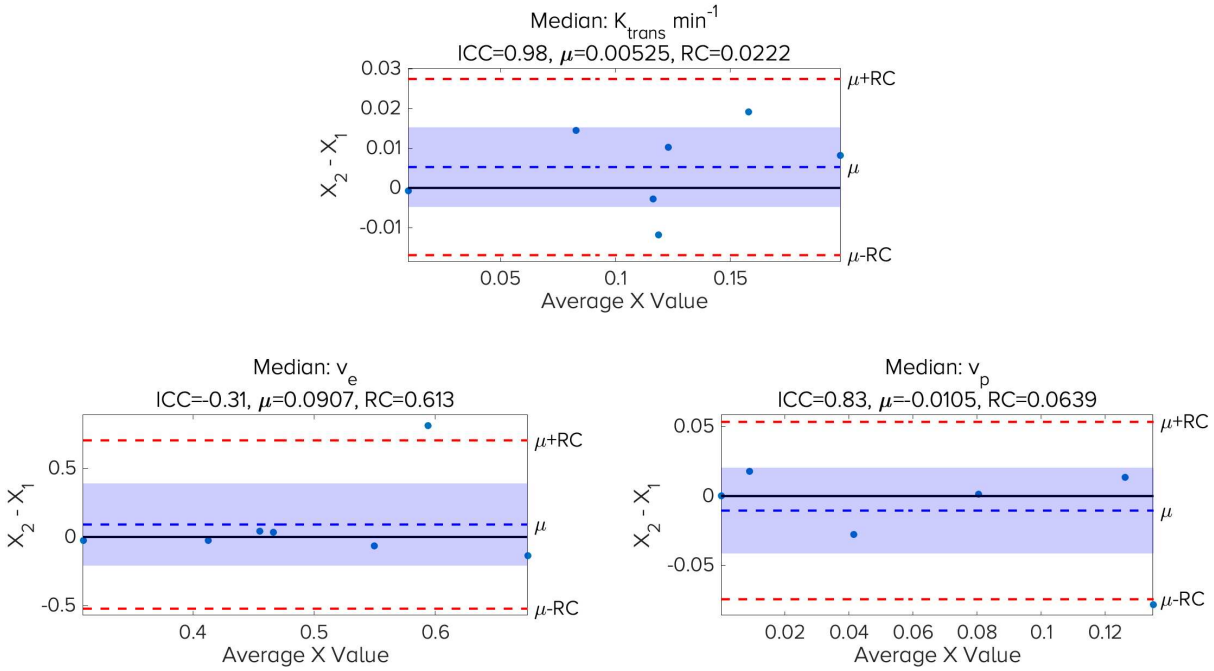
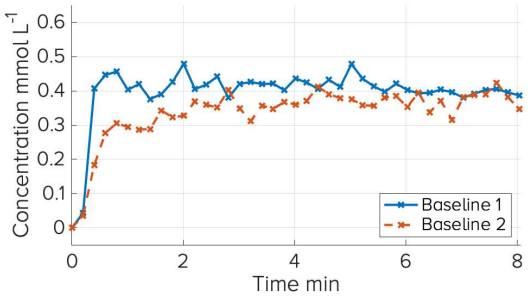


Figure 5.1: Bland-Altman plots for 7 repeatability dynamic contrast-enhanced MRI participants, with the K_{trans}, v_e and v_p values extracted from each pixel across the entire tumour. The median values were assessed for repeatability. The y-axis is the difference between the quantitative parameter X from the 2 repeat measurements (after the first baseline scan X1 and the second baseline scan X2). The x-axis shows the average value of the 2 repeat measurements of the quantitative parameter. The mean of the differences (μ) is indicated by the blue dashed line, with its 95% confidence interval represented as the shaded blue area. The dotted line represents 0 difference between the test-retest measurement. The mean of the differences ± the repeatability coefficient ($\mu\pm$ RC) is shown as the red dashed line. The 95% confidence interval of the repeatability coefficient is not displayed due to overlap with the shaded blue area. The Intraclass Correlation Coefficient (ICC) is also provided.

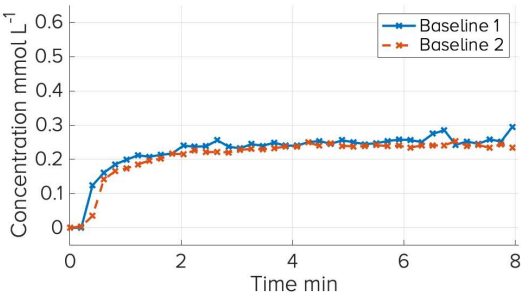
In Figures 5.1, B.1, B.2 and B.3, the zero difference line (indicated by the solid black line) falls within the standard error of the mean of the differences for all metrics, indicating no discernible bias. The large standard error is attributable to the small sample size, resulting in a lower degree of freedom and higher t-value. Consequently, the BA plots demonstrate no systematic differences between repeat K_{trans}-, v_e- and v_p-metrics. However, there are substantial wCVs for the median v_e value and v_p-metrics.

A negative ICC, observed for the median v_e, occurs when the within-subject mean squares exceed the between-subject mean squares. This situation can yield complex values for between-subject standard deviation, according to Equation 2.7.1. Mathematically, squaring this complex number during the ICC calculation in Equation 2.7.1 would lead to a negative ICC.

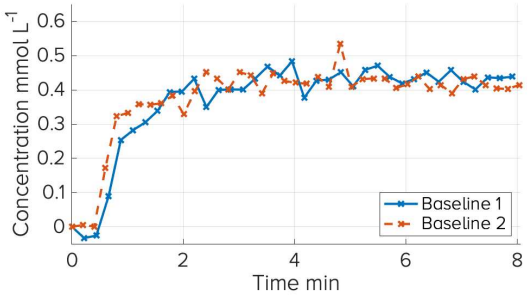
Figure 5.2 illustrates the contrast concentration curves for 7 participants undergoing repeatability assessment of DCE-MRI quantitative parameters. Examining the Tofts parameters used to model these concentration curves in Table 5.2, it is evident that Participant 6 exhibits the largest within-subject difference for v_e between the first and second baseline. This contributes to a larger repeatability coefficient for the median v_e value by increasing the within-subject standard deviation. The low ICC (ICC < 0.5) indicates that the within-subject standard deviation exceeds the between-subject standard deviation. For this participant, there are no notable differences in the first and second baseline concentration curves. However, contrast uptake is small compared to the other participants, which may impact the model's ability to fit v_e. Due to the small sample size, these deviations significantly impact the repeatability metrics. The deviations are likely technical, as v_e is at the upper limit of its range. Participant 1 has the largest within-subject difference for v_p between the first and second baseline. For this participant, there is a difference in the contrast uptake between 0 and 2 minutes, with a larger concentration peak at baseline 1. This mimics the arterial input function curve more closely, increasing the v_p estimate. Whether this deviation was biological or technical is unclear. Furthermore, the median curve was investigated, whereas pixel-wise modelling will be subjected to more noise.



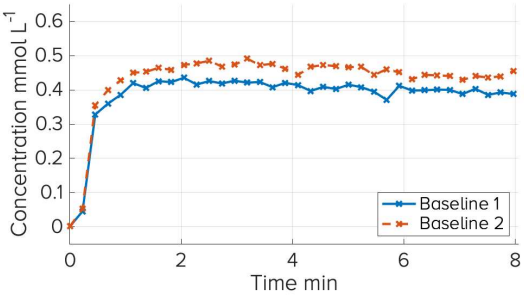
Participant 1



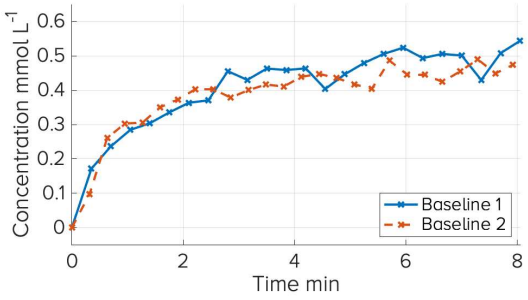
Participant 2



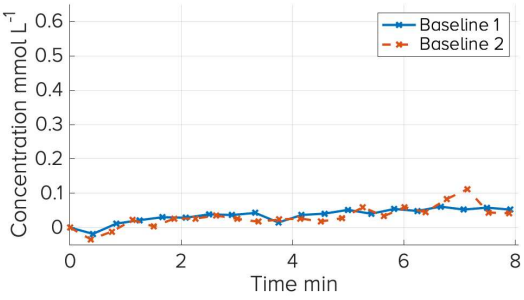
Participant 3



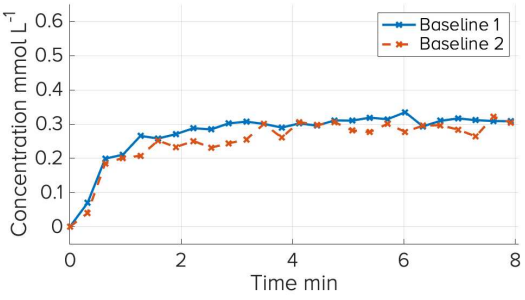
Participant 4



Participant 5



Participant 6



Participant 7

Figure 5.2: Dynamic contrast-enhanced concentration curves from breast tumours of 7 participants, who underwent double baseline MRI scans for repeatability analysis. The median signal across the entire tumour was used. The blue solid curve represents the first baseline scan, and the orange dashed curve represents the second baseline.

Participant		K_{trans} min^{-1}	v_e	v_p
1	B1	0.100	0.383	0.193
	B2	0.106	0.431	0.098
2	B1	0.074	0.307	0.058
	B2	0.089	0.290	0.029
3	B1	0.191	0.565	0.000
	B2	0.201	0.516	0.021
4	B1	0.145	0.388	0.131
	B2	0.166	0.446	0.140
5	B1	0.116	0.744	0.084
	B2	0.121	0.588	0.085
6	B1	0.010	0.146	0.000
	B2	0.008	1.000	0.000
7	B1	0.125	0.396	0.000
	B2	0.112	0.385	0.000

Table 5.2: K_{trans}, v_e and v_p values extracted from the Tofts model, fitted to the median dynamic contrast concentration curves across the entire breast tumours of 7 participants. The participants underwent double baseline (B1: baseline 1; B2: baseline 2) dynamic contrast-enhanced MRI scans for repeatability analysis, which assesses the consistency of measurements across multiple scans.

5.1.2 Piecewise Linear Model Parameters

Detailed results for the Intraclass Correlation Coefficient (ICC) and Within-Subject Coefficient of Variation (wCV) are presented in Table 5.3 for the piecewise linear model parameters. The repeatability results for the piecewise linear model parameters are graphically presented as Bland-Altman (BA) plots in Figure 5.3 for the median values, and in Figures B.4, B.5, B.6, B.7, B.8 and B.9 for the 25th percentile, 75th percentile and interquartile range (IQR).

For the piecewise linear model parameters, the median, 25th and 75th percentile PE- and AUC_{WO}-metrics show excellent ICC values (0.94–0.97 and 0.91–0.98, respectively) and low wCV values (7.4–11.8% and 6.5–14.3%, respectively). This suggests high reliability and low variability within subjects for these measurements and, therefore, high precision. Across these PE-metrics, the Repeatability Coefficients (RCs) are very similar, indicating consistent repeatability patterns (RC = 0.0788–0.0850 mmol). The IQR of PE- and AUC_{WO} demonstrates lower ICC and higher wCV. In Figure B.5, across the PE-metrics, the 25th percentile PE value

		ICC	wCV %	RC
TTP	Median	0.86	24.6	1.20
	25th Percentile	0.57	37.0	1.29
	75th Percentile	0.78	25.9	1.67
	IQR	0.24	68.6	2.05
PE	Median	0.95	9.7	0.0850
	25th Percentile	0.94	11.8	0.0810
	75th Percentile	0.97	7.4	0.0788
	IQR	0.66	21.5	0.0807
WIR	Median	0.53	52.2	0.431
	25th Percentile	0.85	25.4	0.112
	75th Percentile	0.66	42.9	0.498
	IQR	0.55	62.8	0.452
WOR	Median	0.70	90.9	0.0093
	25th Percentile	0.83	-63.8	0.0087
	75th Percentile	0.32	38.0	0.0118
	IQR	0.59	23.9	0.0107
AUC_{WI}	Median	0.42	45.5	0.253
	25th Percentile	0.76	29.4	0.106
	75th Percentile	0.66	31.8	0.281
	IQR	0.68	39.5	0.206
AUC_{WO}	Median	0.96	9.4	0.535
	25th Percentile	0.91	14.3	0.638
	75th Percentile	0.98	6.5	0.443
	IQR	0.76	20.3	0.483

Table 5.3: Intraclass Correlation Coefficients (ICC), Within-Subject Coefficients of Variation (wCV), and Repeatability Coefficients (RC) for the median, 25th percentile, 75th percentile, and interquartile range (IQR) statistics of the Time to Peak (TTP), Peak Enhancement (PE), Wash-In Rate (WIR), Wash-Out Rate (WOR), Wash-In Area Under the Curve (AUC_{WI}) and Wash-Out Area Under the Curve (AUC_{WO}) extracted from entire breast tumours using a piecewise linear model. The repeatability metrics were calculated using 7 double baseline dynamic contrast-enhanced MRI scans.

has a mean of the differences μ (represented by the dashed blue line) that is closest to the zero difference line (indicated by the solid black line). This suggests that it is the metric with the least bias, while the 75th percentile exhibits the greatest difference and, therefore, the most bias. In Figure B.9, across the AUC_{WO}-metrics, the 25th percentile AUC_{WO} value has the least bias, while the 75th percentile exhibits the most.

The remaining parameters have variable repeatability, with lower ICC values across their metrics and higher wCVs compared to the PE- and AUC_{WO}-metrics. The median and 25th percentile TTP, 25th percentile WIR, and 25th percentile AUC_{WI} had good ICC values (> 0.75), showing good reliability in capturing between-subject differences, and wCVs below 30%, indicating relatively consistent within-subject measurements. Otherwise, the metrics show poor reliability and high within-subject variability.

For all piecewise linear metrics, the repeatability appears to be homoscedastic across the range of values in this study. However, a larger data-set is required to truly appreciate this relationship.

In Figures 5.3, B.4, B.5, B.6, B.7, B.8, and B.9 the zero difference line (indicated by the solid black line) falls within the standard error of the mean of the differences for all metrics, indicating no discernible bias. The large standard error is attributable to the small sample size, resulting in a lower degree of freedom and higher t-value. Consequently, the BA plots demonstrate no systematic differences between repeat metrics. However, there are substantial wCVs for most of the metrics.

Figure 5.2 illustrates the contrast concentration curves for 7 participants undergoing repeatability assessment of DCE-MRI quantitative parameters. Examining the piecewise linear parameters used to model these concentration curves in Table 5.4, it is evident that Participant 6 exhibits the largest within-subject difference for TTP between the first and second baseline. For this participant, there are no notable differences in the first and second baseline concentration curves. However, compared to the other participants, contrast uptake is small, which may impact the model's ability to fit the change in gradient. Participant 1 has the largest within-subject difference for PE, WIR, WOR and AUC_{WO} between the first and second baseline. For this participant, there is a difference in the contrast uptake between 0 and 2 minutes, with a larger

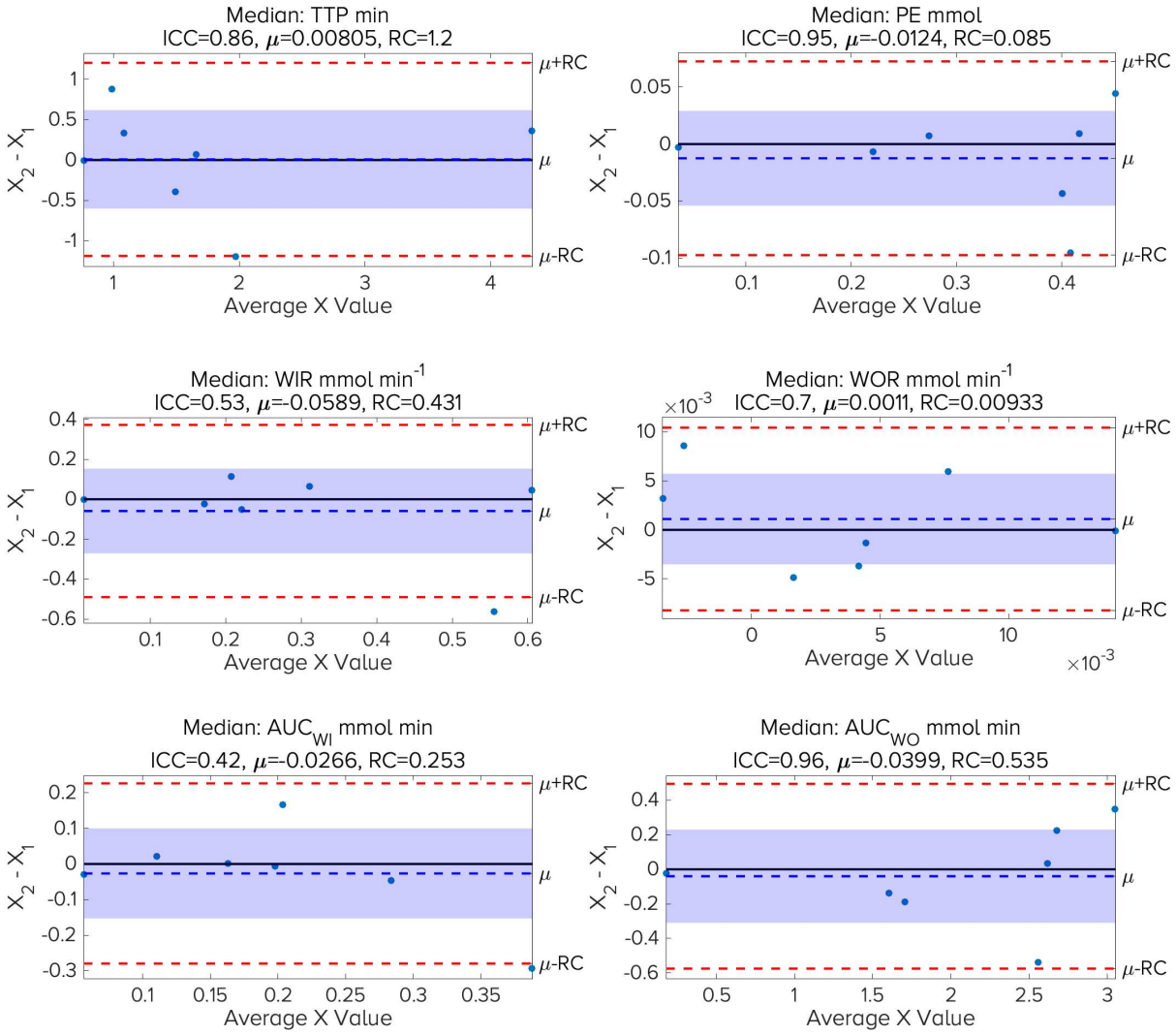


Figure 5.3: Bland-Altman plots for 7 repeatability dynamic contrast-enhanced MRI participants, with the Time to Peak (TTP), Peak Enhancement (PE), Wash-In Rate (WIR), Wash-Out Rate (WOR), Wash-In Area Under the Curve AUC_{WI}, and Wash-Out Area Under the Curve AUC_{WO} values extracted from each pixel across the entire tumour. The median values were assessed for repeatability. The y-axis represents the difference between the quantitative parameter X from the 2 repeat measurements (after the first baseline scan X_1 and the second baseline scan X_2). The x-axis shows the average value of the 2 repeat measurements of the quantitative parameter. The mean of the differences (μ) is indicated by the blue dashed line, with its 95% confidence interval represented as the shaded blue area. The dotted line represents 0 difference between the test-retest measurement. The mean of the differences ± the repeatability coefficient ($\mu\pm$ RC) is shown as the red dashed line. The 95% confidence interval of the repeatability coefficient is not displayed due to overlap with the shaded blue area. The Intraclass Correlation Coefficient (ICC) is also provided.

concentration peak at baseline 1 and a steeper wash-in curve. At baseline 1, there is a negative wash-out curve, whereas it is positive for baseline 2. Whether this deviation was biological or technical is unclear. Participant 5 has the largest within-subject difference for AUC_{WI}, caused by the difference in TTP. Furthermore, here we investigate the median curve, whereas pixel-wise modelling will be subjected to more noise.

Participant	TTP min	PE mmol	WIR mmol min^{-1}	WOR mmol min^{-1}	AUC_{WI} mmol min	AUC_{WO} mmol min
1 B1	0.474	0.436	1.036	-0.004	0.062	3.121
B2	0.707	0.322	0.487	0.010	0.134	2.515
2 B1	0.890	0.220	0.261	0.007	0.077	1.704
B2	1.253	0.216	0.180	0.005	0.123	1.535
3 B1	1.691	0.409	0.279	0.006	0.318	2.593
B2	1.240	0.403	0.365	0.004	0.205	2.755
4 B1	0.743	0.423	0.597	-0.004	0.125	2.914
B2	0.752	0.472	0.657	-0.004	0.138	3.268
5 B1	2.593	0.438	0.132	0.013	0.633	2.533
B2	1.337	0.374	0.258	0.015	0.245	2.774
6 B1	1.665	0.028	0.023	0.005	0.014	0.263
B2	4.511	0.035	0.009	0.011	0.064	0.175
7 B1	1.626	0.267	0.180	0.007	0.185	1.813
B2	1.663	0.247	0.161	0.008	0.170	1.700

Table 5.4: Semi-quantitative values extracted from the piecewise linear model, fitted to the median dynamic contrast concentration curves across the entire breast tumours of 7 participants. These include the Time to Peak (TTP), Peak Enhancement (PE), Wash-In Rate (WIR), Wash-Out Rate (WOR), Wash-In Area Under the Curve (AUC_{WI}) and Wash-Out Area Under the Curve (AUC_{WO}). The participants underwent double baseline (B1: baseline 1; B2: baseline 2) dynamic contrast-enhanced MRI scans for repeatability analysis, which assesses the consistency of measurements across multiple scans.

5.1.3 Semi-Quantitative Parameters

Detailed results for the Intraclass Correlation Coefficient (ICC) and Within-Subject Coefficient of Variation (wCV) are presented in Table 5.5 for the semi-quantitative parameters. The repeatability results for the semi-quantitative parameters are graphically presented as Bland-Altman (BA) plots in Figure 5.4 for the median values, and in Figures B.10, B.11, B.12, B.13, B.14 and B.15 for the 25th percentile, 75th percentile and interquartile range (IQR).

		ICC	wCV %	RC
$iWIR$	Median	0.90	16.1	0.125
	25th Percentile	0.82	24.2	0.140
	75th Percentile	0.96	8.9	0.087
	IQR	0.88	15.1	0.061
$fWOR$	Median	0.65	167.6	0.0110
	25th Percentile	0.87	-51.3	0.0083
	75th Percentile	0.27	51.8	0.0149
	IQR	0.69	23.9	0.0107
AUC_{iWI}	Median	0.84	26.7	0.0981
	25th Percentile	0.79	34.4	0.0904
	75th Percentile	0.89	20.5	0.0975
	IQR	0.91	15.0	0.0318
AUC_{fWO}	Median	0.97	6.8	0.298
	25th Percentile	0.96	8.7	0.312
	75th Percentile	0.97	7.3	0.374
	IQR	0.63	26.4	0.405
AUC_T	Median	0.97	8.1	0.513
	25th Percentile	0.94	11.6	0.598
	75th Percentile	0.97	6.7	0.507
	IQR	0.62	25.8	0.610
fE	Median	0.98	6.2	0.0575
	25th Percentile	0.97	7.4	0.0565
	75th Percentile	0.97	7.2	0.0773
	IQR	0.69	27.1	0.0858

Table 5.5: Intraclass Correlation Coefficients (ICC), Within-Subject Coefficients of Variation (wCV), and Repeatability Coefficients (RC) for the median, 25th percentile, 75th percentile, and interquartile range (IQR) statistics of the initial Wash-In Rate, for the first 60 seconds, (iWI), final Wash-Out Rate, from 180 to 470 seconds ($fWOR$), initial Wash-In Area Under the Curve (AUC_{iWI}), final Wash-Out Area Under the Curve (AUC_{fWO}), Total Area Under the Curve (AUC_T) and the Final Enhancement (fE) extracted from entire breast tumours. The repeatability metrics were calculated using 7 double baseline dynamic contrast-enhanced MRI scans.

For the semi-quantitative parameters, the median, 25th and 75th percentile AUC_{fWO}-, AUC_T- and fE-metrics show excellent ICC values (0.96–0.97, 0.94–0.97, and 0.97–0.98 respectively) and low wCV values (6.8–8.7%, 6.7–11.6%, 6.2–7.4%, respectively). This suggests high reliability and low variability within subjects for these measurements and, therefore, high precision. The IQR of these metrics demonstrates moderate ICC and higher wCV and RC. In Figure B.13, across the AUC_{fWO}-metrics, the 25th percentile AUC_{fWO} value has a mean of the differences μ (represented by the dashed blue line) that is closest to the zero difference line (indicated by the solid black line). This suggests that it is the metric with the least bias, while the 75th percentile exhibits the greatest difference and, therefore, the most bias. This is the same across the AUC_T- and fE-metrics in Figures B.14 and B.15.

The $iWIR$- and AUC_{iWI}-metrics show good to excellent ICC values (0.82–0.96, 0.79–0.91, respectively), with a range of wCVs (8.9–24.2%, 15.0–34.4%, respectively). The $fWOR$ shows the worst repeatability of all the metrics, with moderate to good ICC values across the median, 25th percentile and IQR (0.65–0.87) and a poor ICC value for the 75th percentile (0.27). The wCVs are much higher across the metrics compared to the other parameters (23.9–167.6%).

For all semi-quantitative metrics, the repeatability appears to be homoscedastic across the range of values in this study. However, a larger data-set is required to truly appreciate this relationship.

In Figures 5.4, B.10, B.11, B.12, B.13, B.14, and B.15 the zero difference line (indicated by the solid black line) falls within the standard error of the mean of the differences for all metrics, indicating no discernible bias. The large standard error is attributable to the small sample size, resulting in a lower degree of freedom and higher t-value. Consequently, the BA plots demonstrate no systematic differences between repeat metrics.

Figure 5.2 illustrates the contrast concentration curves for 7 participants undergoing repeatability assessment of DCE-MRI quantitative parameters. Examining the semi-quantitative parameters extracted from these concentration curves in Table 5.6, it is evident that Participant 1 exhibits the largest within-subject difference for $iWOR$, $fWOR$, AUC_{iWI} and AUC_T between the first and second baseline. For this participant, there is a difference in the contrast uptake between 0 and 2 minutes, with a larger concentration peak at baseline 1 and a steeper wash-in

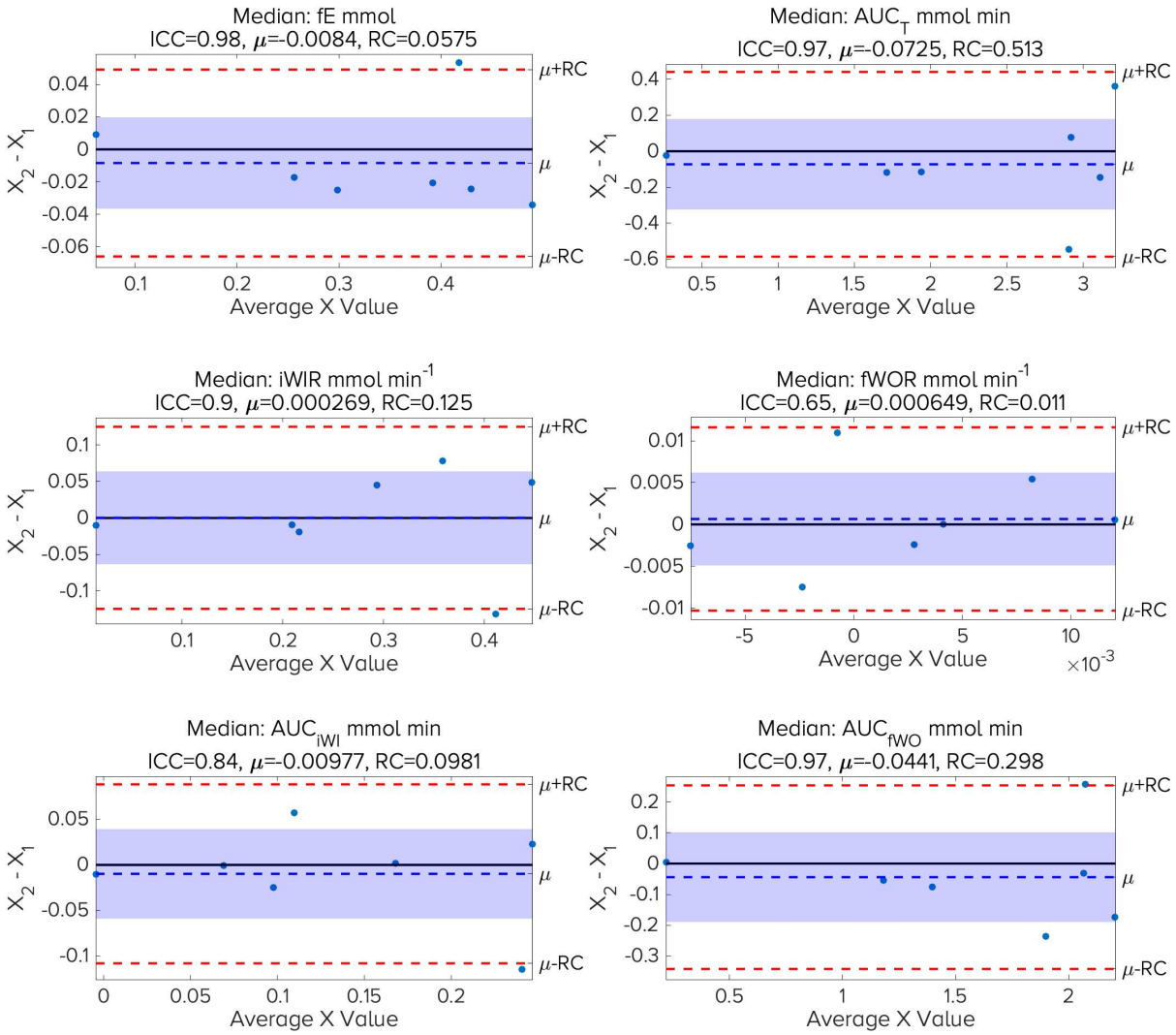


Figure 5.4: Bland-Altman plots for 7 repeatability dynamic contrast-enhanced MRI participants, with the Final Enhancement (fE), Total Area Under the Curve (AUC_T), Wash-In Rate for the initial 60 seconds ($iWIR$), Wash-Out Rate from 180 to 470 seconds ($fWOR$), Wash-In Area Under the Curve for the initial 60 seconds AUC_{iWI}, and Wash-Out Area Under the Curve from 180 to 470 seconds AUC_{fWO} values extracted from each pixel across the entire tumour. The median values were assessed for repeatability. The y-axis represents the difference between the quantitative parameter X from the 2 repeat measurements (after the first baseline scan X_1 and the second baseline scan X_2). The x-axis shows the average value of the 2 repeat measurements of the quantitative parameter. The mean of the differences (μ) is indicated by the blue dashed line, with its 95% confidence interval represented as the shaded blue area. The dotted line represents 0 difference between the test-retest measurement. The mean of the differences ± the repeatability coefficient ($\mu\pm$ RC) is shown as the red dashed line. The 95% confidence interval of the repeatability coefficient is not displayed due to overlap with the shaded blue area. The Intraclass Correlation Coefficient (ICC) is also provided.

curve. At baseline 1, there is a negative wash-out curve, whereas it is positive for baseline 2. Participant 4 has the largest within-subject difference for fE and AUC_{fWO}, which is caused by a lower plateau at baseline 1. Whether these deviations were biological or technical is unclear. Furthermore, here we investigate the median curve, whereas pixel-wise modelling will be subjected to more noise.

Participant	$iWIR$ mmol min^{-1}	$fWOR$ mmol min^{-1}	AUC_{iWI} mmol min	AUC_{fWO} mmol min	AUC_T mmol min	fE mmol
1 B1	0.478	-0.007	0.297	2.018	3.183	0.405
B2	0.340	0.006	0.182	1.785	2.649	0.393
2 B1	0.225	0.005	0.110	1.213	1.781	0.267
B2	0.207	0.002	0.085	1.153	1.658	0.249
3 B1	0.319	0.001	0.082	2.097	2.911	0.445
B2	0.398	-0.006	0.138	2.059	2.960	0.428
4 B1	0.426	-0.006	0.233	1.951	3.040	0.393
B2	0.469	-0.009	0.257	2.202	3.406	0.444
5 B1	0.270	0.014	0.168	2.289	3.166	0.506
B2	0.316	0.013	0.167	2.113	3.019	0.472
6 B1	0.021	0.006	0.001	0.219	0.277	0.058
B2	0.013	0.011	-0.009	0.212	0.239	0.070
7 B1	0.213	0.004	0.071	1.439	1.998	0.314
B2	0.207	0.006	0.068	1.353	1.871	0.298

Table 5.6: Semi-quantitative values extracted from the median dynamic contrast concentration curves across the entire breast tumours of 7 participants. These include the initial Wash-In Rate, for the first 60 seconds, ($iWIR$), final Wash-Out Rate, from 180 to 470 seconds ($fWOR$), initial Wash-In Area Under the Curve (AUC_{iWI}), final Wash-Out Area Under the Curve (AUC_{fWO}), Total Area Under the Curve (AUC_T) and the Final Enhancement (fE). The participants underwent double baseline (B1: baseline 1; B2: baseline 2) dynamic contrast-enhanced MRI scans for repeatability analysis, which assesses the consistency of measurements across multiple scans.

5.2 Response Assessment

5.2.1 Changes in Contrast Concentration Curves

Examining the contrast concentration curves for all participants in Figure 5.5 and 5.6, there is a decrease in the gradient of the wash-in curve and a flattening of the wash-out curve from baseline

to 2-week post-radiotherapy (RT), followed by a continued decrease in the wash-in gradient and an increase in the wash-out gradient at 6-, 12-months and 24-months. Over time, the curve is more similar to the healthy breast uptake curve. Additionally, the variability among participants (the solid blue line represents the median curve across participants, while the shaded blue area covers the 25th to 75th percentile range in Figure 5.5) increases 2-weeks post-RT, then decreases again at 6-month and 12-month post-RT, and increases at 24-month post-RT.

Comparing the baseline concentration curves for responders and non-responders in Figure 5.5 and 5.6, non-responders show a steeper wash-in curve and a greater area under the curve. However, there is overlap between the responders' and non-responders' 25th to 75th percentile range at baseline. Both groups have an increased area under the curve at 2-weeks post-RT. For responders, at 6-, 12- and 24-months post-RT, there is a continued decrease in the wash-in gradient, increase in the wash-out gradient, and decrease in the area under the curve. At 24-months, the concentration curve overlaps with the healthy breast contrast uptake curve. Both groups have similar curves at 2-weeks and 6-months post-RT; however, looking at the non-responding groups at 6-months in Figure 5.5, the 75th percentile shows a much steeper wash-in curve and larger area under the curve. At 12- and 24-months post-RT, non-responders have a continued increase in similarity of the curves to the pre-RT curve, with no overlap between the two groups' 25th to 75th percentile range.

5.2.2 Sensitivity to Post-Treatment Changes

Tofts Model Parameters

Following radiotherapy, changes in the K_{trans}, v_e and v_p metrics were evaluated at 2-weeks, 6-, 12- and 24-months in Figure 5.7 for the median values, and Figures B.16, B.17 and B.18 for the 25th percentile, 75th percentile, and interquartile range (IQR). This information is summarised in Table 5.7, giving the percentage of participants showing changes in the Tofts model parameters at the post-RT time-points. Each metric is analysed in terms of median, 25th and 75th percentile, and IQR, with changes categorised as increases (↑), decreases (↓), or no change (within the repeatability coefficient, RC).

At 2-week post-treatment, the majority of participants (58.0-74.2-%) showed a significant

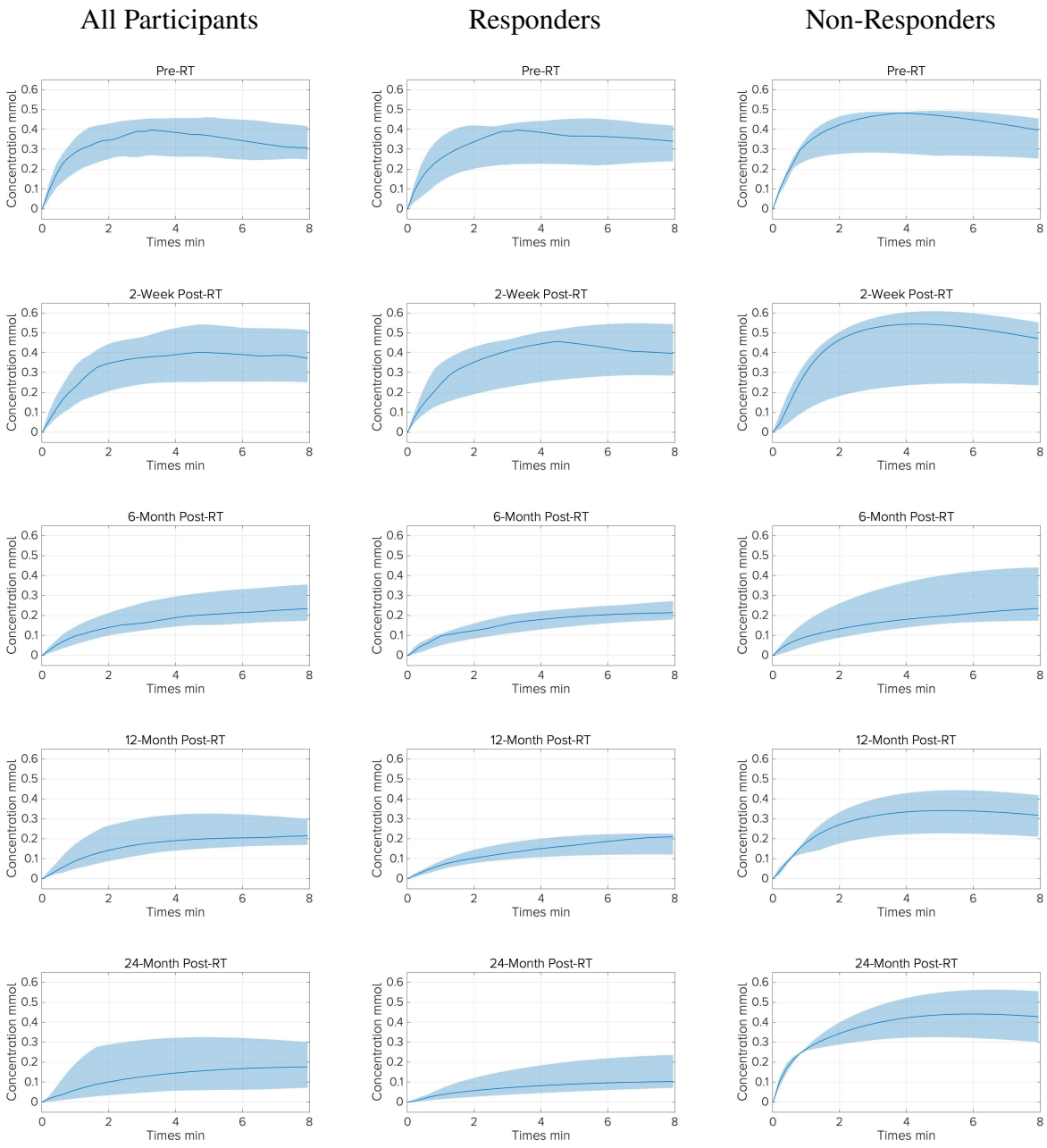


Figure 5.5: Dynamic contrast-enhanced MRI contrast concentration curves from breast tumours for all participants (left; pre-radiotherapy (RT) N=59, 2-week post-RT N=32, 6-month post-RT N=40, 12-month post-RT N=22, 24-month post-RT N=10), the responding patients (middle; pre-RT N=13, 2-week post-RT N=7, 6-month post-RT N=15, 12-month post-RT N=14, 24-month post-RT N=6) and non-responding participants (right; pre-RT N=6, 2-week post-RT N=5, 6-month post-RT N=5, 12-month post-RT N=6, 24-month post-RT N=2). The responding participants are those who had a partial response or complete response at 12- or 24-months post-RT, and non-responding participants are those who had progressive disease at 12- or 24-months post-RT. The median signal across the entire tumour was calculated for each participant. The blue solid curve represents the median concentration across participants, and the blue shaded area represents the 25th and 75th percentile.

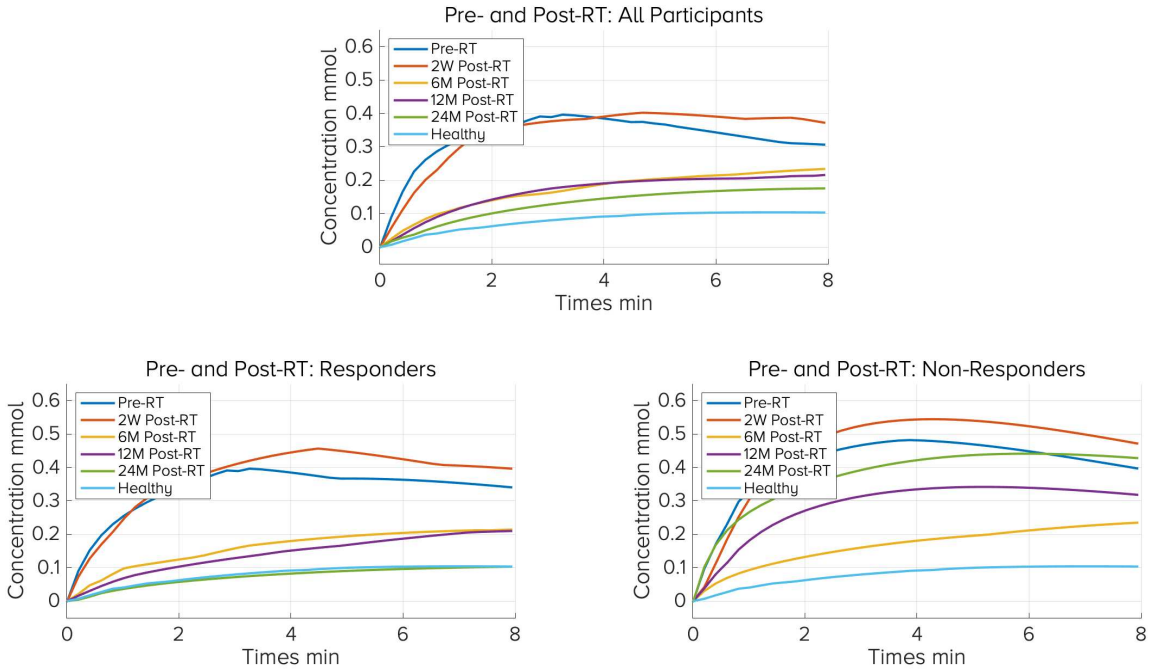


Figure 5.6: Dynamic contrast-enhanced MRI contrast concentration curves from breast tumours for all participants (top; pre-radiotherapy (RT) N=59, 2-week post-RT N=32, 6-month post-RT N=40, 12-month post-RT N=22, 24-month post-RT N=10), the responding patients (bottom left; pre-RT N=13, 2-week post-RT N=7, 6-month post-RT N=15, 12-month post-RT N=14, 24-month post-RT N=6) and non-responding participants (bottom right; pre-RT N=6, 2-week post-RT N=5, 6-month post-RT N=5, 12-month post-RT N=6, 24-month post-RT N=2). The responding participants are those who had a partial response or complete response at 12- or 24-months post-RT, and non-responding participants are those who had progressive disease at 12- or 24-months post-RT. The median signal across the entire tumour was calculated for each participant. The solid curves represent the median concentration curve across participants, pre-RT, 2-weeks, 6-months, 12-months, and 24-months post-RT.

		2W Post-RT % N=34			6M Post-RT % N=38			12M Post-RT % N=21			24M Post-RT % N=9		
		↑	↓	-	↑	↓	-	↑	↓	-	↑	↓	-
K_{trans}	Median	29.0	32.3	38.7	7.9	81.6	10.5	5.0	60.0	35.0	22.2	66.7	11.1
	25th Percentile	29.0	29.0	41.9	7.9	73.7	18.4	0.0	60.0	40.0	11.1	66.7	22.2
	75th Percentile	29.0	45.2	25.8	10.5	84.2	5.3	10.0	65.0	25.0	22.2	66.7	11.1
	IQR	6.5	35.5	58.1	7.9	71.1	21.1	5.0	55.0	40.0	0.0	44.4	55.6
v_e	Median	0.0	0.0	100	2.6	0.0	97.4	0.0	0.0	100	11.1	0.0	88.9
	25th Percentile	32.3	0.0	67.7	7.9	21.1	71.1	15.0	30.0	55.0	11.1	44.4	44.4
	75th Percentile	38.7	16.1	45.2	50.0	15.8	34.2	25.0	35.0	40.0	33.3	11.1	55.6
	IQR	9.7	22.6	67.7	47.4	7.9	44.7	25.0	10.0	65.0	44.4	11.1	44.4
v_p	Median	6.5	12.9	80.6	2.6	18.4	78.9	0.0	10.0	90.0	0.0	22.2	77.8
	25th Percentile	0.0	3.2	96.8	0.0	10.5	89.5	0.0	5.0	95.0	11.1	11.1	77.8
	75th Percentile	3.2	9.7	87.1	2.6	23.7	73.7	0.0	15.0	85.0	0.0	33.3	66.7
	IQR	6.5	16.1	77.4	2.6	44.7	52.6	0.0	30.0	70.0	0.0	66.7	33.3

Table 5.7: The percentage of participants showing changes in K_{trans}, v_e, and v_e metrics – specifically the median, 25th percentile, 75th percentile and interquartile range (IQR) – relative to the repeatability coefficient (RC). For each metric, participants with changes exceeding the RC (↑; indicating a significant increase), changes below -RC (↓; indicating a significant decrease), and changes within ± RC (indicating no significant change) are reported at 2-week, 6-month, 12-month and 24-month post-radiotherapy for breast tumours.

change from baseline (exceeding the RC) in the median, 25th and 75th percentile of the K_{trans} values, with a balanced increase and decrease, except for the 75th percentile where a greater percentage showed a decrease. A similar percentage of participants showed a decrease in the IQR, compared to the other metrics. Over time, substantially more participants significantly decreased across metrics, peaking at 6-months post-RT (71.1.7-84.2%) before decreasing slightly at later time-points.

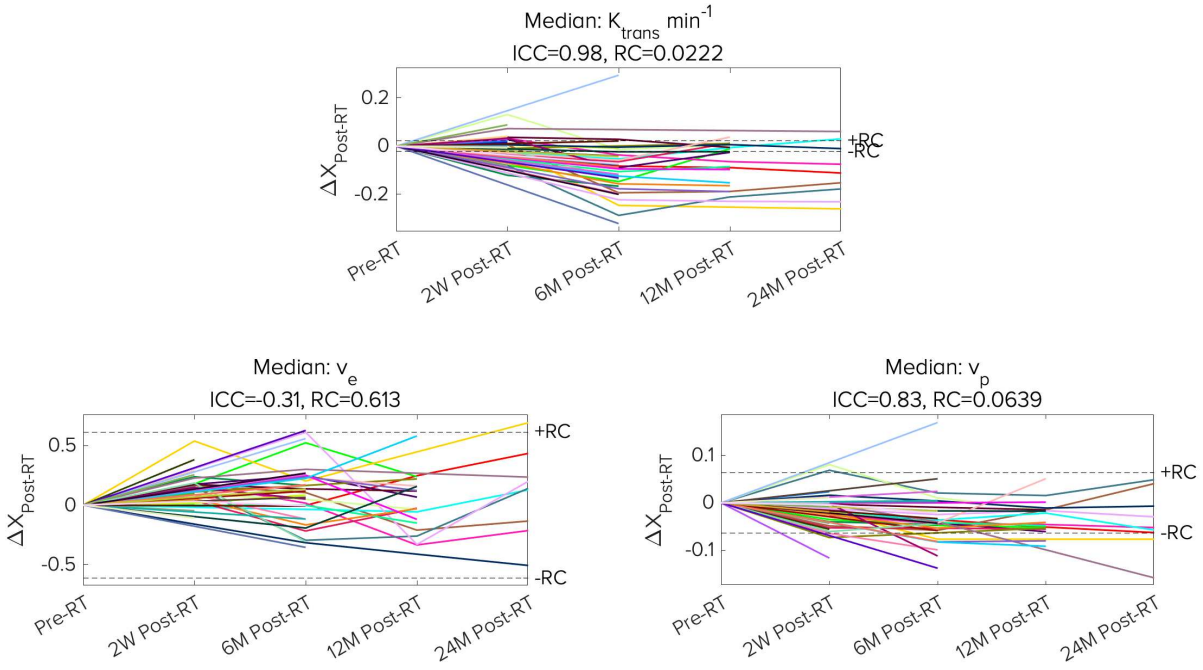


Figure 5.7: The change in the median K_{trans}, v_e, and v_p derived from the dynamic contrast-enhanced MRI data of the entire breast tumour, at 2-week (N=34), 6-month (N=38), 12-month (N=21) and 24-month (N=9) post-radiotherapy (RT) from 51 participants. The dashed black lines represent the repeatability coefficient as an indicator of significant change, i.e., if the difference post-treatment is larger than the repeatability coefficient, then the change is significant.

At all time-points, most participants exhibited no significant changes in the median v_e at post-therapy time-points (88.9–100% across time-points). No clear trend emerged for the 25th percentile either, except a decrease at later-time points for some participants. There were significant increases in the 75th percentile and IQR post-RT, peaking at 6-months (50.0% and 47.4%, respectively).

For all v_p-metrics, the proportion of participants with no change remained high across all time-points. Some participants showed decreases in the median, 25th percentile, 75th percentile and IQR at post-treatment time-points, peaking at 24-months post-RT (22.2%, 11.1%, 33.3%

and 66.7%, respectively).

Piecewise Linear Model and Semi-Quantitative Parameters

Following radiotherapy, changes in the piecewise linear and semi-quantitative metrics were evaluated at 2-weeks, 6-, 12- and 24-months in Figures 5.8 and 5.9 for the median values, and Figures B.19, B.20, B.21, B.22, B.23, B.24, B.25, B.26, B.27, B.28, B.29, B.30 for the 25th percentile, 75th percentile and interquartile range (IQR). This information is summarised in Table 5.8, giving the percentage of participants showing parameter changes at the post-RT time-points. Due to the number of piecewise linear model and semi-quantitative parameters, the median metric is first evaluated to assess for sensitivity to post-RT changes in 5.8, with changes categorised as increases (↑), decreases (↓), or no change (within the repeatability coefficient, RC). However, each metric (median, 25th and 75th percentile, and interquartile range (IQR)) is shown in the figures specified above.

	2W Post-RT % N=34			6M Post-RT % N=38			12M Post-RT % N=21			24M Post-RT % N=9		
	↑	↓	-	↑	↓	-	↑	↓	-	↑	↓	-
TTP	12.9	3.2	83.9	44.7	0.0	55.3	45.0	0.0	55.0	66.7	0.0	33.3
PE	22.6	19.4	58.1	7.9	71.1	21.1	5.0	55.0	40.0	0.0	66.7	33.3
WIR	0.0	6.5	93.5	0.0	23.7	76.3	5.0	5.0	90.0	0.0	33.3	66.7
WOR	45.2	3.2	51.6	60.5	2.6	36.8	25.0	10.0	65.0	55.6	22.2	22.2
AUC_{WI}	12.9	0.0	87.1	7.9	5.3	86.8	5.0	0.0	95.0	0.0	11.1	88.9
AUC_{WO}	22.6	9.7	67.7	5.3	71.1	23.7	5.0	50.0	45.0	0.0	66.7	33.3
$iWIR$	9.7	35.5	54.8	5.3	68.4	26.3	0.0	50.0	50.0	0.0	55.6	44.4
$fWOR$	38.7	3.2	58.1	52.6	2.6	44.7	45.0	0.0	55.0	55.6	22.2	22.2
AUC_{iWI}	3.2	19.4	77.4	2.6	55.3	42.1	0.0	35.0	65.0	0.0	55.6	44.4
AUC_{fWO}	45.2	9.7	45.2	10.5	68.4	21.1	15.0	55.0	30.0	0.0	66.7	33.3
AUC_{T}	38.7	9.7	51.6	7.9	71.1	21.1	5.0	55.0	40.0	0.0	66.7	33.3
fE	54.8	6.5	38.7	15.8	57.9	26.3	15.0	60.0	25.0	22.2	66.7	11.1

Table 5.8: The percentage of participants showing changes in the piecewise linear model and semi-quantitative metrics – specifically the median, 25th percentile, 75th percentile and interquartile range (IQR) – relative to the repeatability coefficient (RC). For each metric, participants with changes exceeding the RC (↑; indicating a significant increase), changes below -RC (↓; indicating a significant decrease), and changes within ± RC (indicating no significant change) are reported at 2-week, 6-month, 12-month and 24-month post-radiotherapy for breast tumours.

For TPP, there is a steady increase in the percentage of participants with significant increases

across the post-RT time-points, from 12.9% at 2-weeks to 66.7% at 24-months post-RT. This trend can be seen for the 25th and 75th percentile in Figure B.19.

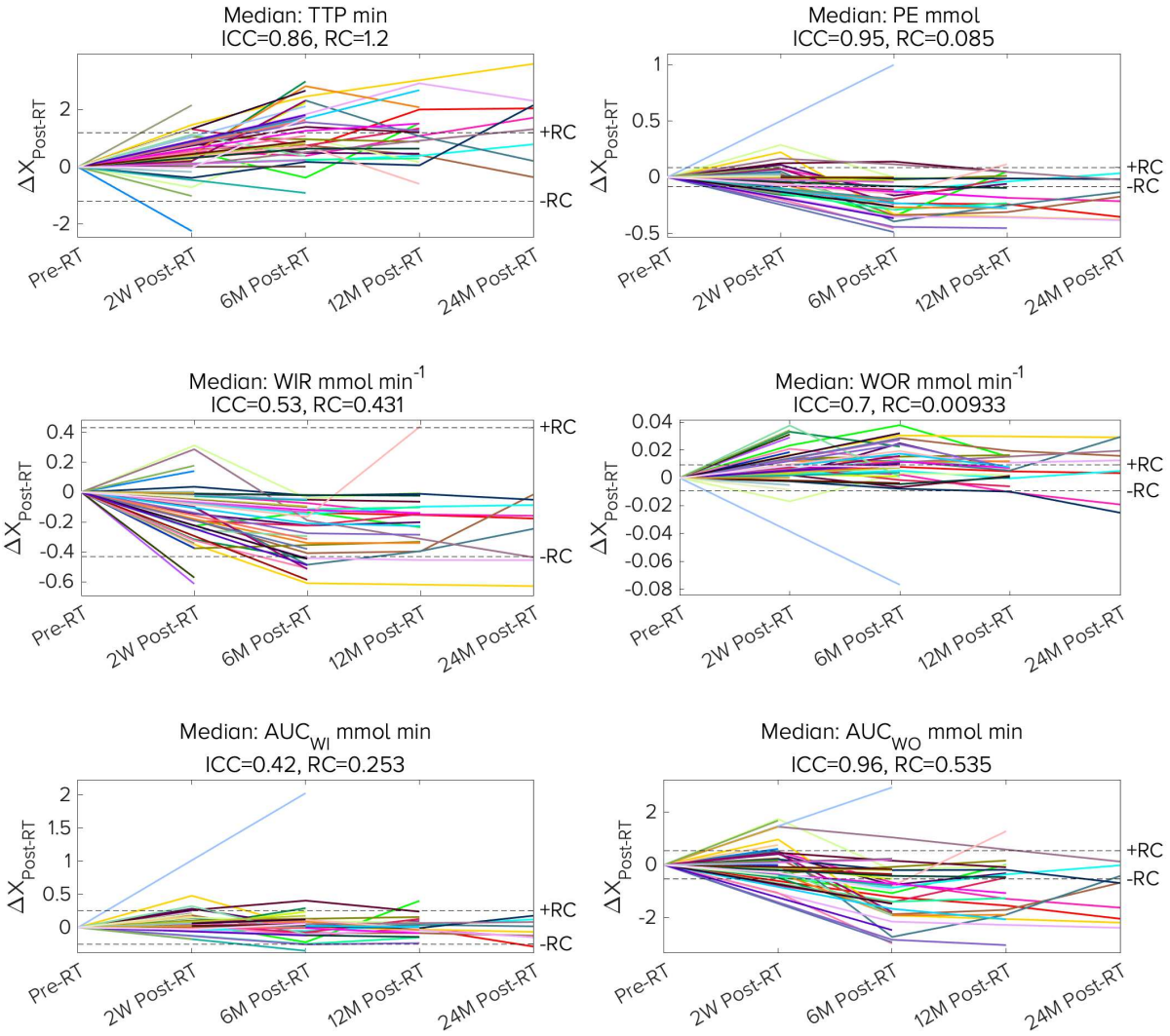


Figure 5.8: The change in the median Time to Peak (TTP), Peak Enhancement (PE), Wash-In Rate (WIR), Wash-Out Rate (WOR), Wash-In Area Under the Curve AUC_{WI}, and Wash-Out Area Under the Curve AUC_{WO} derived from the dynamic contrast-enhanced MRI data of the entire breast tumour, at 2-week (N=34), 6-month (N=38), 12-month (N=21) and 24-month (N=9) post-radiotherapy (RT) from 51 participants. The dashed black lines represent the repeatability coefficient as an indicator of significant change, i.e., if the difference post-treatment is larger than the repeatability coefficient, then the change is significant.

For PE, AUC_{WO}, $iWIR$, AUC_{iWI}, AUC_{fWO}, AUC_T, fE there is an increase in the number of participants with significant decreases across the post-RT time-points from baseline, which can also be seen for the 25th and 75th percentile. For WIR and AUC_{WI}, there is a trend towards decreases across the time-points; however, for the median metric, not many participants reach a significant decrease. For WIR, the 25th and 75th percentile are more sensitive to detecting

post-RT changes.

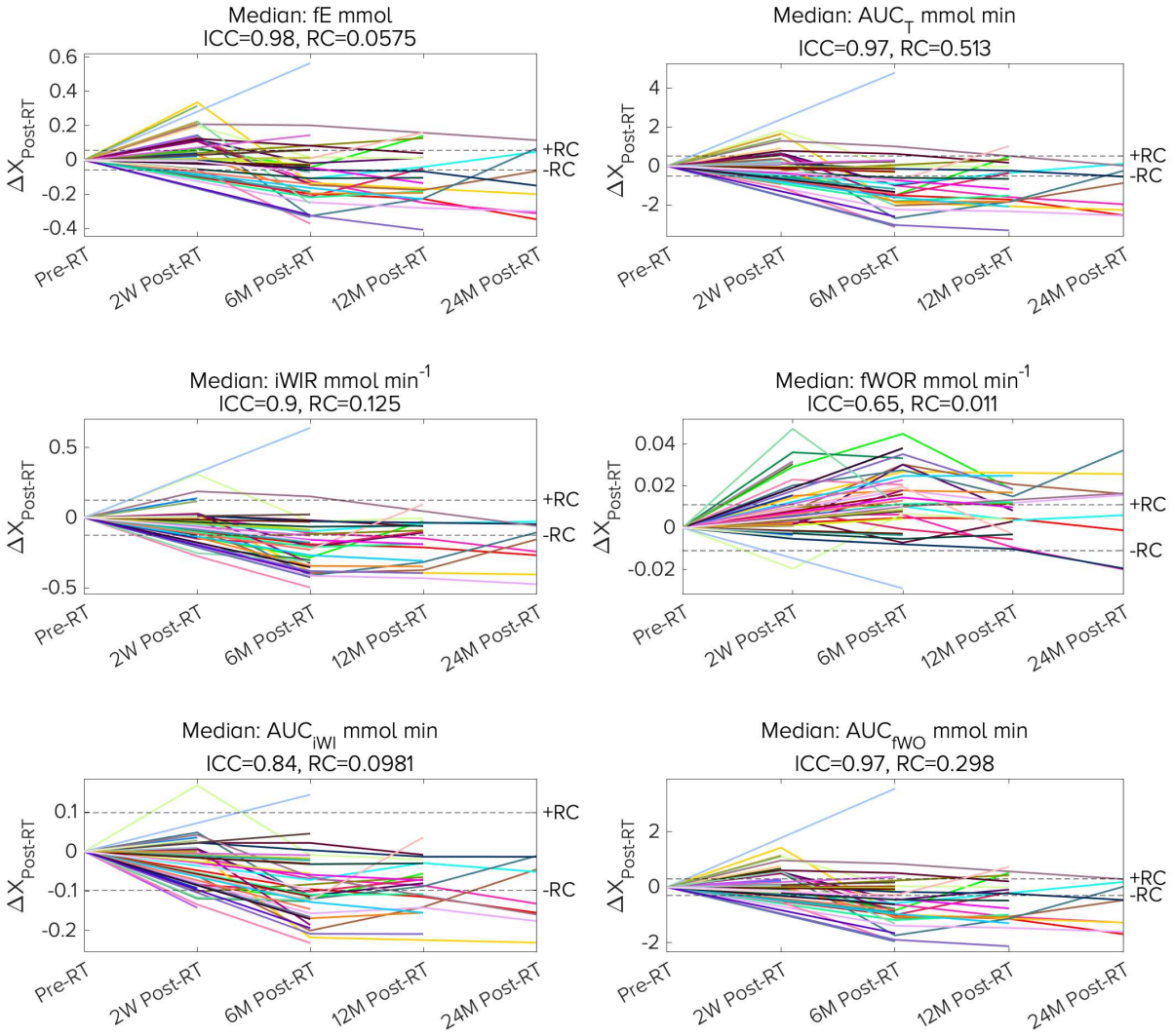


Figure 5.9: The change in the median Final Enhancement (fE), Total Area Under the Curve (AUC_T), Wash-In Rate for the initial 60 seconds ($iWIR$), Wash-Out Rate from 180 to 470 seconds ($fWOR$), Wash-In Area Under the Curve for the initial 60 seconds AUC_{iWI}, and Wash-Out Area Under the Curve from 180 to 470 seconds AUC_{fWO} derived from the dynamic contrast-enhanced MRI data of the entire breast tumour, at 2-week (N=34), 6-month (N=38), 12-month (N=21) and 24-month (N=9) post-radiotherapy (RT) from 51 participants. The dashed black lines represent the repeatability coefficient as an indicator of significant change, i.e., if the difference post-treatment is larger than the repeatability coefficient, then the change is significant.

For WOR and $fWOR$, a large percentage of participants have a significant increase at 2-weeks post-RT, which increases at 6-months post-RT, which can also be seen for the 25th and 75th percentile.

Many of the piecewise linear model and semi-quantitative parameters show the same trend and, therefore, may be highly correlated. Figure 5.10 shows the relationship between the

parameters.

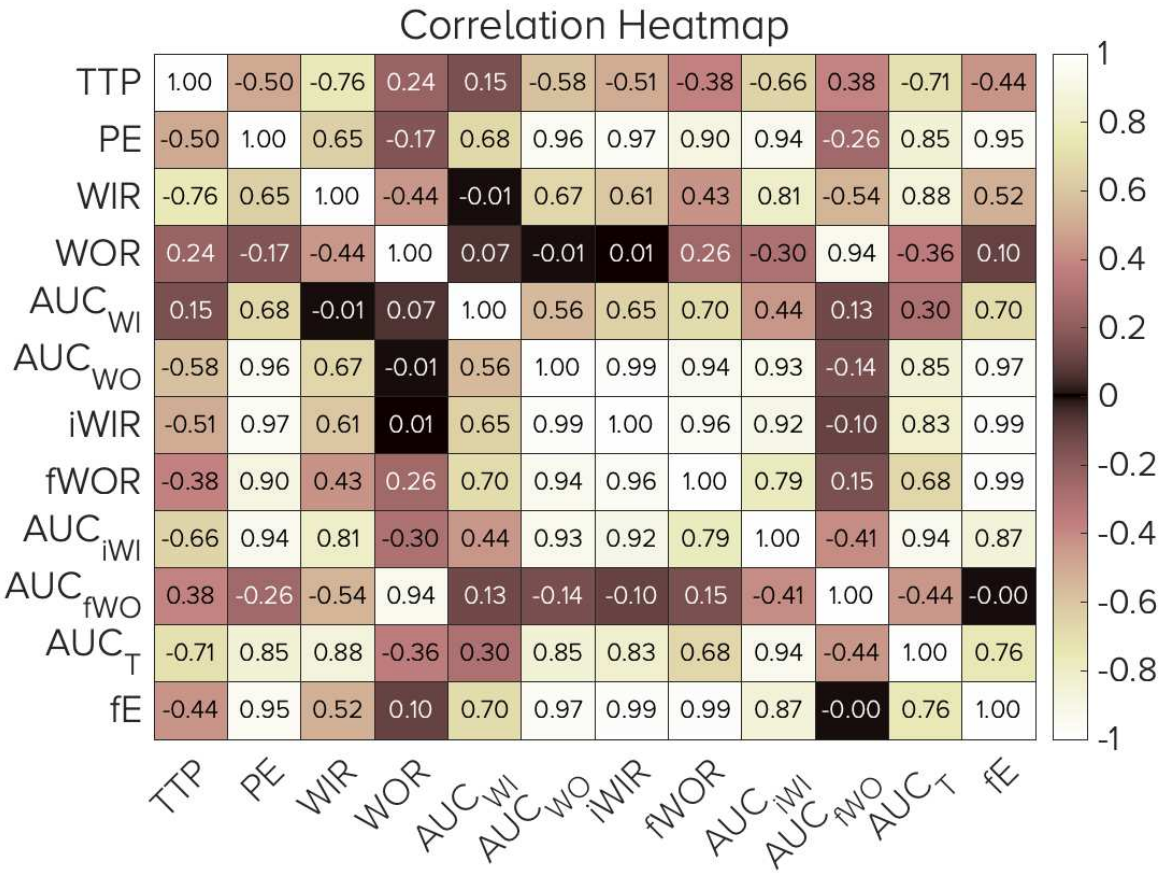


Figure 5.10: A heat map showing the correlation coefficients R between all of the piecewise linear model and semi-quantitative parameters, where R=1 is perfect positive linear correlation, R=-1 is perfect negative linear correlation, and R=0 is no linear correlation.

PE, AUC_{WO}, AUC_{fWO}, AUC_T and fE are all highly correlated (R>0.9). This can be further visualised by looking at the averaged histograms of the entire tumour across all participants in Figure 5.11, which show similar changes post-RT. Examining their repeatability, all parameters for the median, 25th percentile and 75th percentile had excellent ICC values (ICC>0.9) and low wCV values (wCV<15%). The parameters detecting the most significant changes across the post-RT time-points were AUC_{fWO} and fE. As fE is taken from a single value, AUC_{fWO} will capture more interesting information. Therefore, only AUC_{fWO} will be investigated. Furthermore, PE and AUC_{WO} are impacted by the model's ability to detect the point of change between wash-in and wash-out and, therefore, may be more noisy and difficult to compare at post-treatment time-points.

$iWIR$ and AUC_{iWI} are also highly correlated (R>0.9). This can be further visualised by

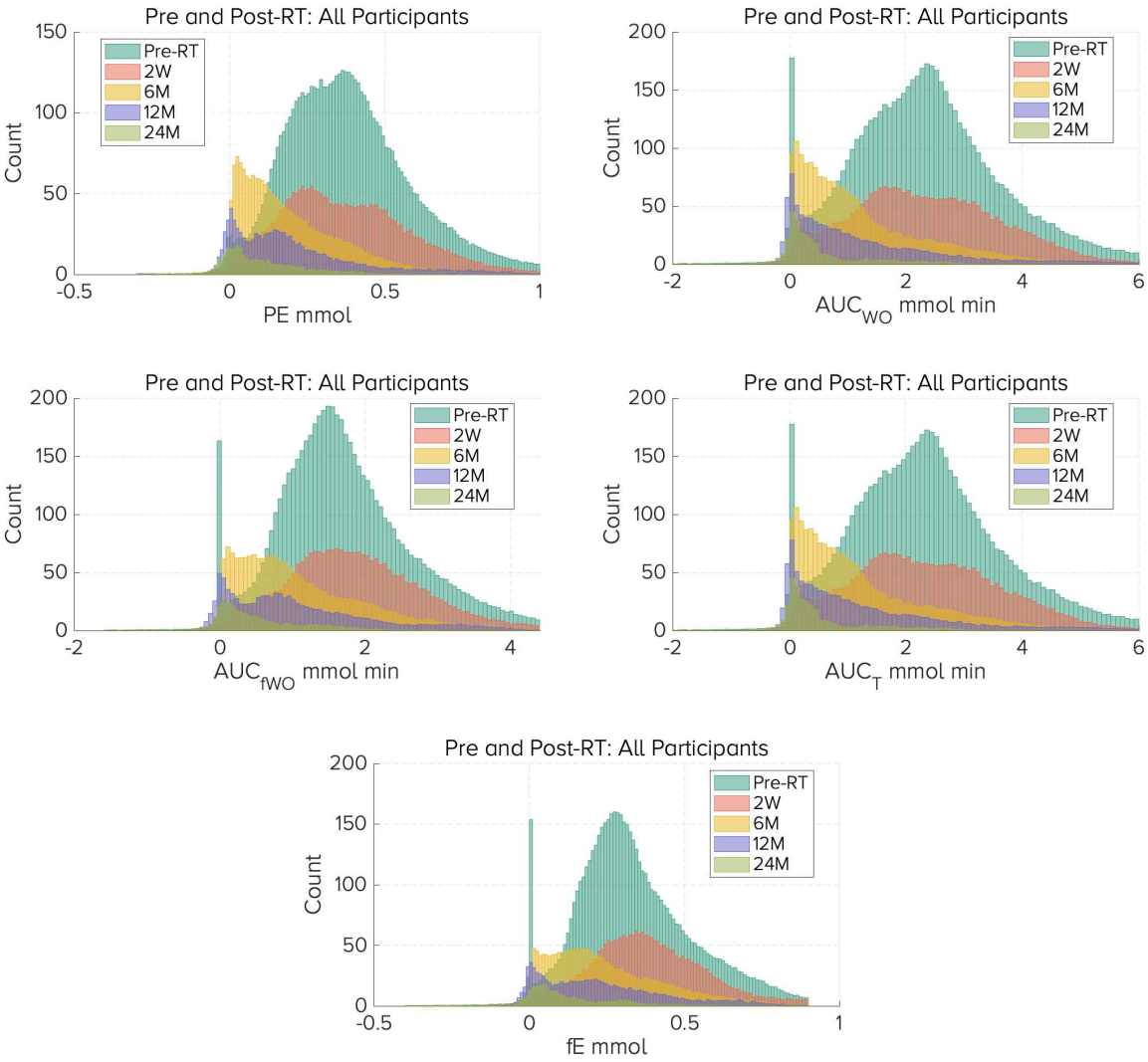


Figure 5.11: The averaged histogram for the entire tumour across all participants for PE, AUC_{WO}, AUC_{fWO} and AUC_T, pre-RT and 2-weeks, 6-, 12- and 24-months post-radiotherapy (RT).

.

looking at the averaged histograms for the entire tumour across all participants in Figure 5.12, which show similar changes post-RT. Both have good to excellent ICC values; however, $iWIR$ has higher ICC values across the median, 25th and 75th percentile metrics and lower wCVs by about 10%. Across the post-RT time-points, $iWIR$ detects more significant changes than AUC_{iWI}. The $iWIR$ is also highly correlated (R>0.9) with PE, AUC_{WO} and AUC_{T}. $iWIR$ and AUC_{iWI} should also be related to WIR, and the correlation is high (R=0.81 and 0.88, respectively). Across the post-RT time-points, $iWIR$ detects more significant changes than WIR, which is less sensitive to post-RT changes. AUC_{WI} is also less sensitive to post-RT changes. This can also be visualised in Figure 5.12, with WIR and AUC_{WI} showing more subtle changes post-RT. Therefore, $iWIR$ will be examined moving forwards, and AUC_{iWI}, WIR and AUC_{WI} will not.

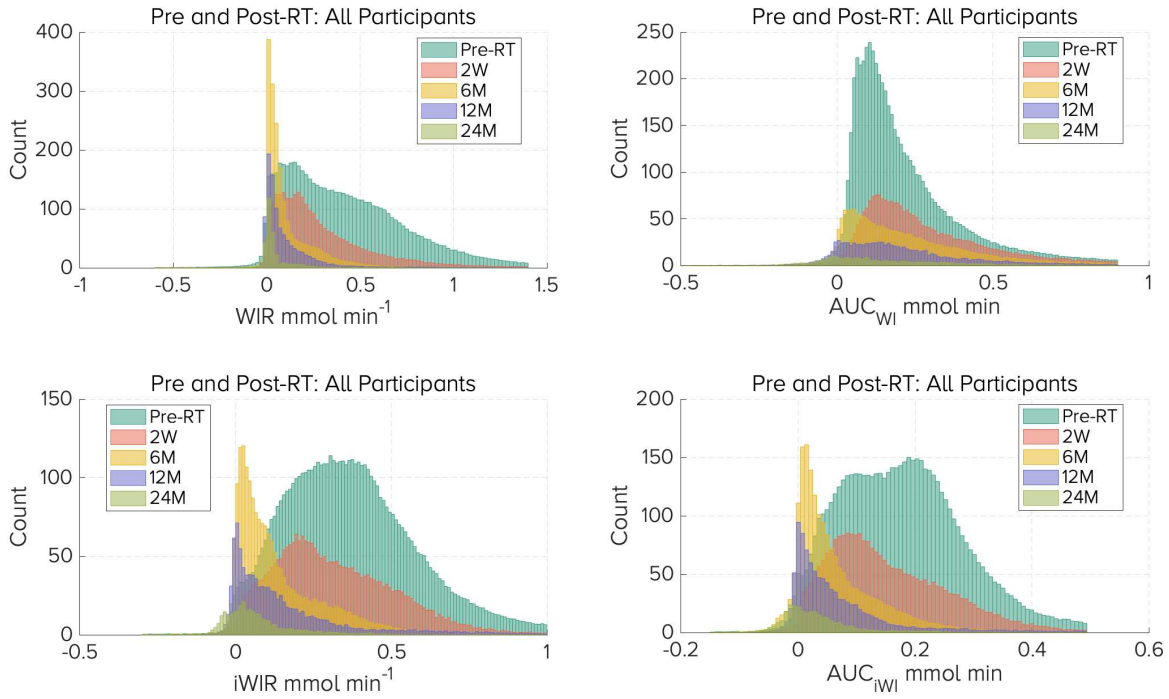


Figure 5.12: The averaged histogram for the entire tumour across all participants for WIR, AUC_{WI}, $iWIR$ and AUC_{iWI}, pre-RT and 2-weeks, 6-, 12- and 24-months post-radiotherapy (RT).

WOR and $fWOR$ are highly correlated (R>0.9). This can be further visualised by looking at the averaged histograms for the entire tumour across all participants in Figure 5.13, which show similar changes post-RT. Both have poor to good ICC values (0.32–0.83, 0.27–0.87, respectively) and relatively high wCV (23.9–90.9 %, 23.9–167.6 %). Despite this, many

participants show a significant increase in these parameters post-RT. At 2-weeks and 6-months post-RT, WOR detects a larger percentage to have had a significant increase in comparison to $fWOR$ (45.2% compared to 38.7% at 2-weeks; 60.5% compared to 52.6% at 6-months). However, at 12-months post-RT, $fWOR$ detects the larger percentage to have had a significant increase (45.0% compared to 25.0%). Both detect the same amount at 24-months (55.6%). Although the WOR has greater sensitivity at 2-weeks and 6-months, since the semi-quantitative parameters AUC_{fWO} and $iWIR$ are the ones taken forward so far, $fWOR$ will be taken forward instead of WOR.

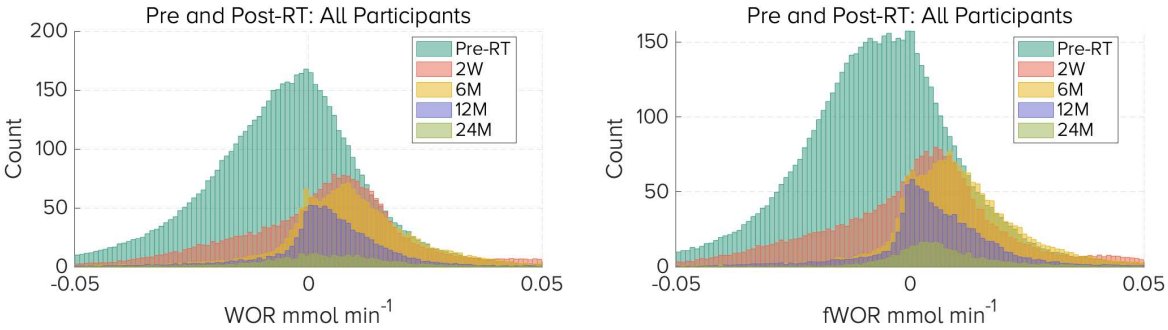


Figure 5.13: The averaged histogram for the entire tumour across all participants for WOR and $fWOR$, pre-RT and 2-weeks, 6-, 12- and 24-months post-radiotherapy (RT).

Looking at the averaged histogram for the entire tumour across all participants for TTP 5.14, it is clear that it is a noisy parameter. It is negatively correlated to the WIR (R=-0.71), therefore it is likely that as the WIR decreases and becomes increasingly more similar to the WOR, it is more difficult to determine the turning point between the wash-in and wash-out slope. As it is not as sensitive to post-RT changes as the other parameters, TPP will not be investigated.

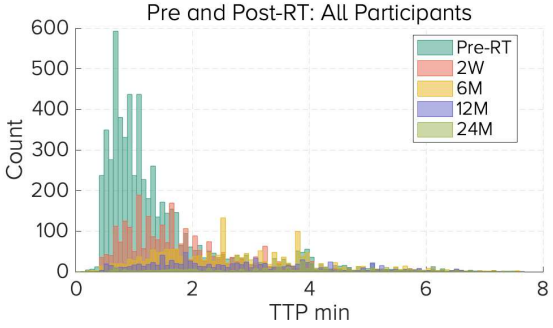


Figure 5.14: The averaged histogram for the entire tumour across all participants for TPP, pre-RT and 2-weeks, 6-, 12- and 24-months post-radiotherapy (RT).

Looking at the changes in the chosen parameter metrics in Table 5.9, there is also an increase

in the percentage of participants having a decrease in the 25th and 75th percentile and IQR of $iWIR$, with the 75th percentile being most sensitive to change. For fWO, the 25th percentile is also sensitive to significant increases, whereas the 75th percentile and IQR are less sensitive.

There is an initial increase in the AUC_{fWO} at 2-weeks post-RT, followed by a decrease at 6-, 12- and 24-month post-RT in the median, 25th and 75th percentile.

5.2.3 Pre-Treatment Values

Table 5.10 presents the average ± standard deviation of the median, 25th percentile, 75th percentile and IQR of Tofts model parameter metrics for all participants, responders and non-responders. Although the median, 25th percentile, 75th percentile and IQR values for K_{trans} are lower in the responder group compared to the non-responder group, these differences are not statistically significant (p = 0.47, 0.90, 0.28 and 0.24, respectively). The standard deviation in K_{trans}values within the responder group overlaps with that of the non-responder group. For v_e and v_p, there is also no difference between the two groups.

Table 5.11 presents the average ± standard deviation of the median, 25th percentile, 75th percentile and IQR of the semi-quantitative parameter metrics for all participants, responders and non-responders. Although the median, 25th percentile, 75th percentile and IQR values for $iWIR$ are lower in the responder group compared to the non-responder group, these differences are not statistically significant (p = 0.07, 0.24, 0.11 and 0.37, respectively). For AUC_{fWO}, the median, 25th percentile, 75th percentile, and IQR are lower for the responder group; however, this is not statistically significant.

5.2.4 Parameter Maps

Tofts Model Parameters

Figure 5.15 presents DCE-MRI parameter maps from the Tofts model, including K_{trans}, v_e, and v_p, derived from the entire breast tumour of one participant pre-radiotherapy. The K_{trans} and v_p maps show similar spatial distributions, with regions of lower permeability and plasma volume in the tumour centre, likely indicative of a necrotic core, and higher permeability and plasma

		2W Post-RT % N=34			6M Post-RT % N=38			12M Post-RT % N=21			24M Post-RT % N=9		
		↑	↓	-	↑	↓	-	↑	↓	-	↑	↓	-
$iWIR$	Median	9.7	35.5	54.8	5.3	68.4	26.3	0.0	50.0	50.0	0.0	55.6	44.4
	25th Percentile	6.5	22.6	71.0	2.6	52.6	44.7	0.0	50.0	50.0	0.0	44.4	55.6
	75th Percentile	12.9	35.5	51.6	5.3	81.6	13.2	0.0	70.0	30.0	0.0	66.7	33.3
	IQR	19.4	16.1	64.5	5.3	52.6	42.1	10.0	50.0	40.0	11.1	33.3	55.6
$fWOR$	Median	38.7	3.2	58.1	52.6	2.6	44.7	45.0	0.0	55.0	55.6	22.2	22.2
	25th Percentile	38.7	6.5	54.8	63.2	5.3	31.6	55.0	10.0	35.0	55.6	22.2	22.2
	75th Percentile	32.3	0.0	67.7	42.1	0.0	57.9	5.0	0.0	95.0	22.2	22.2	55.6
	IQR	12.9	9.7	77.4	5.3	26.3	68.4	0.0	30.0	70.0	0.0	22.2	77.8
AUC_{fWO}	Median	45.2	9.7	45.2	10.5	68.4	21.1	15.0	55.0	30.0	0.0	66.7	33.3
	25th Percentile	48.4	9.7	41.9	7.9	63.2	28.9	5.0	50.0	45.0	11.1	55.6	33.3
	75th Percentile	51.6	9.7	38.7	10.5	63.2	26.3	15.0	55.0	30.0	0.0	66.7	33.3
	IQR	6.5	3.2	90.3	2.6	10.5	86.8	5.0	20.0	75.0	0.0	11.1	88.9

Table 5.9: The percentage of participants showing changes in $iWIR$, $fWOR$, and AUC_{fWO} metrics – specifically the median, 25th percentile, 75th percentile and interquartile range (IQR) – relative to the repeatability coefficient (RC). For each metric, participants with changes exceeding the RC (↑; indicating a significant increase), changes below -RC (↓; indicating a significant decrease), and changes within ± RC (indicating no significant change) are reported at 2-week, 6-month, 12-month and 24-month post-radiotherapy for breast tumours.

		All Participants N=59	Responders N=13	Non-Responders N=6	p-value
K_{trans} min^{-1}	Median	0.16 ± 0.08	0.14 ± 0.08	0.18 ± 0.09	0.47
	25th Percentile	0.11 ± 0.06	0.10 ± 0.05	0.13 ± 0.08	0.90
	75th Percentile	0.24 ± 0.14	0.20 ± 0.11	0.28 ± 0.12	0.28
	IQR	0.13 ± 0.10	0.10 ± 0.06	0.15 ± 0.10	0.24
v_e	Median	0.42 ± 0.17	0.47 ± 0.17	0.47 ± 0.16	0.97
	25th Percentile	0.34 ± 0.15	0.38 ± 0.15	0.39 ± 0.13	0.83
	75th Percentile	0.56 ± 0.24	0.62 ± 0.25	0.58 ± 0.22	0.64
	IQR	0.22 ± 0.17	0.25 ± 0.19	0.19 ± 0.14	0.64
v_p	Median	0.06 ± 0.05	0.05 ± 0.03	0.06 ± 0.03	0.98
	25th Percentile	0.03 ± 0.04	0.03 ± 0.03	0.02 ± 0.02	0.70
	75th Percentile	0.09 ± 0.06	0.08 ± 0.04	0.09 ± 0.06	0.97
	IQR	0.05 ± 0.04	0.05 ± 0.02	0.07 ± 0.06	0.58

Table 5.10: The average ± standard deviation of the metrics of the Tofts model parameters (K_{trans}, v_e and v_p) at baseline, for all participants, responders, and non-responders. The statistical significance of the difference between the baseline values of the responders and non-responders is given as a p-value.

		All Participants N=59	Responders N=13	Non-Responders N=6	p-value
$iWIR$ mmol min^{-1}	Median	0.34 ± 0.15	0.30 ± 0.13	0.41 ± 0.11	0.07
	25th Percentile	0.25 ± 0.12	0.22 ± 0.12	0.30 ± 0.09	0.24
	75th Percentile	0.43 ± 0.19	0.38 ± 0.15	0.53 ± 0.17	0.11
	IQR	0.19 ± 0.10	0.16 ± 0.07	0.23 ± 0.15	0.37
$fWOR$ mmol min^{-1} $\times 10^{-2}$	Median	-0.39 ± 0.97	-0.04 ± 1.16	-0.50 ± 0.84	0.52
	25th Percentile	-1.29 ± 1.16	-0.91 ± 1.36	-1.52 ± 0.87	0.47
	75th Percentile	0.55 ± 0.95	0.94 ± 1.24	0.53 ± 1.04	0.47
	IQR	1.84 ± 0.94	1.86 ± 1.18	2.05 ± 1.26	0.90
AUC_{fWO} mmol min	Median	1.66 ± 0.72	1.66 ± 0.65	1.90 ± 0.59	0.37
	25th Percentile	1.32 ± 0.61	1.33 ± 0.61	1.56 ± 0.50	0.58
	75th Percentile	1.99 ± 0.84	1.95 ± 0.67	2.25 ± 0.70	0.28
	IQR	0.67 ± 0.36	0.62 ± 0.28	0.69 ± 0.32	0.64

Table 5.11: The average ± standard deviation of the metrics of the semi-quantitative parameters ($iWIR$, $fWOR$ and AUC_{fWO}) at baseline, for all participants, responders, and non-responders. The statistical significance of the difference between the baseline values of the responders and non-responders is given as a p-value.

volume regions at the periphery, potentially reflecting more vascular tumour areas.

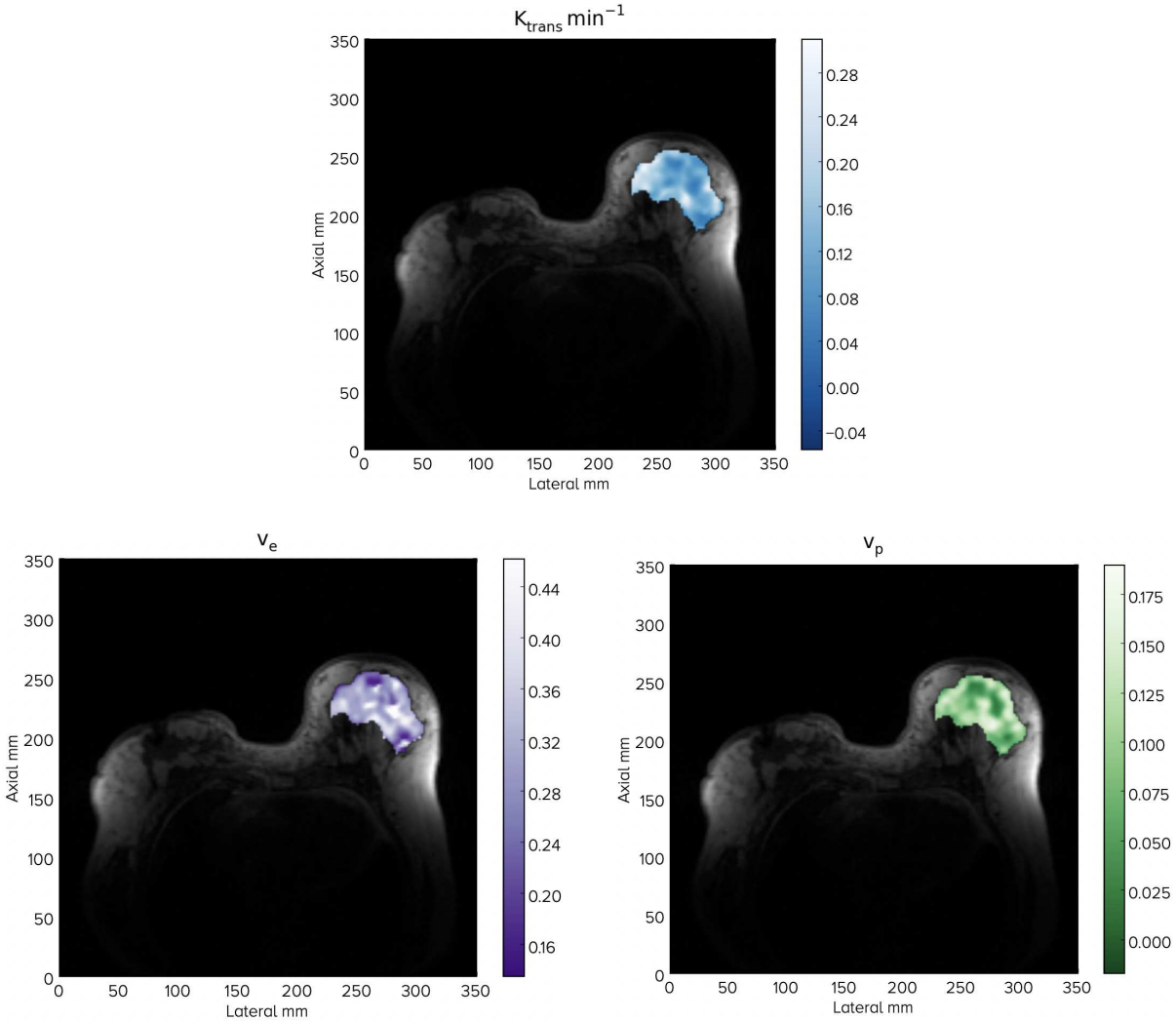


Figure 5.15: Example of dynamic contrast-enhanced MRI parameter maps from the Tofts model including K_{trans}, v_e, and v_p, derived from the entire breast tumour of one participant pre-radiotherapy.

Semi-Quantitative Parameters

Figure 5.16 presents DCE-MRI parameter maps from semi-quantitative methods, including $iWIR$, $fWOR$, and AUC_{fWO}, derived from the entire breast tumour of one participant pre-radiotherapy. The $iWIR$ and AUC_{fWO} maps show similar spatial distributions, with regions of lower contrast uptake in the tumour centre, likely indicative of a necrotic core, and higher uptake regions at the periphery, potentially reflecting more vascular tumour areas.

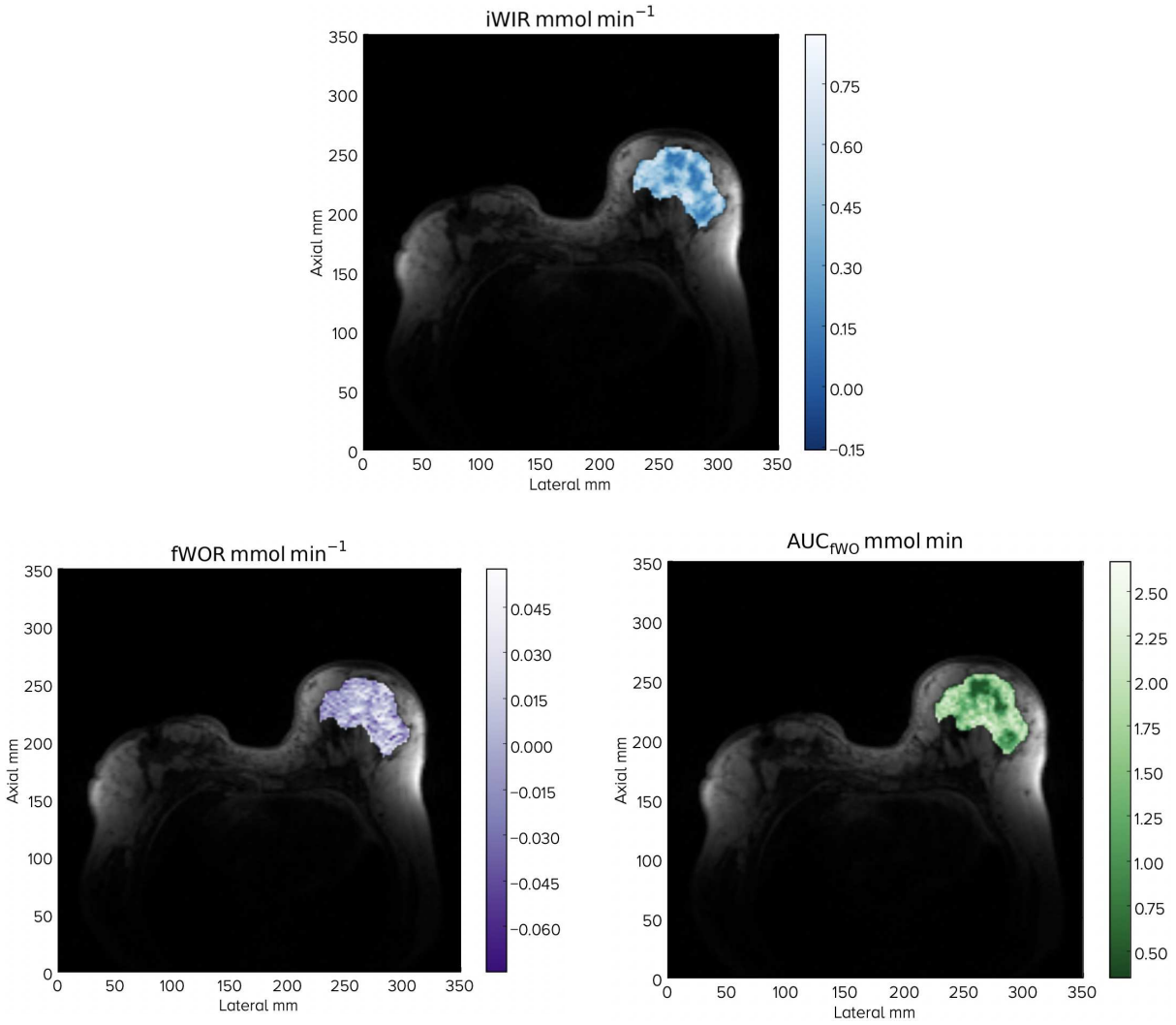


Figure 5.16: Example of dynamic contrast-enhanced MRI parameter maps from the semi-quantitative methods including $iWIR$, $fWOR$, and AUC_{fWO}, derived from the entire breast tumour of one participant pre-radiotherapy.

5.2.5 Whole Tumour Response Assessment

Tofts Model Parameters

Table 5.12 summarises the K_{trans}-metrics for all participants, responders and non-responders at pre-RT and the post-RT time-points.

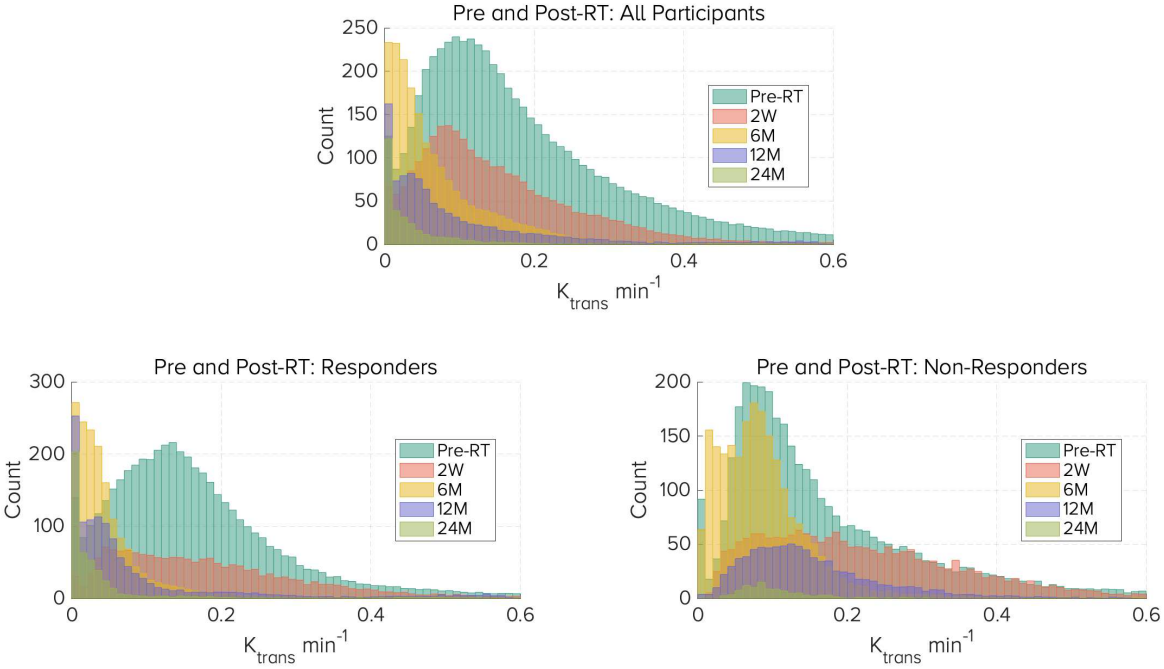


Figure 5.17: The averaged histogram for the entire tumour across all participants, responders and non-responders for K_{trans} pre-RT and 2-weeks, 6-, 12- and 24-months post-radiotherapy (RT).

Figure 5.17 illustrates the averaged histograms for all participants, responders and non-responders. Among all participants, there is an observable shift from higher K_{trans} values from baseline to 2-weeks post-RT, followed by a larger shift at 6-, 12- and 24-months post-RT, but with lower peaks due to reduced tumour size. This trend is reflected in Figure B.31, where there is a shift in the 25th percentile, median, 75th percentile and IQR to lower values at 2-weeks and 6-months and then stabilising at 6-, 12- and 24-months, with many participants reaching the range of healthy values, and having a change below the RC across these metrics.

In the responder group, the trend mirrors that of the overall participant cohort, as seen in Figure 5.17 and B.32, suggesting that most participants are responding to treatment, reaching healthy values at 6-, 12- and 24-months post-RT across the metrics and having changes below the RC.

		K_{trans} min^{-1} (Average ± SD)				
		Pre-RT	2W Post-RT	6M Post-RT	12M Post-RT	24M Post-RT
		N=59	N=32	N=40	N=22	N=10
All Participants	Median	0.162 ± 0.084	0.133 ± 0.069$^{p=0.525}$	0.072 ± 0.074***	0.074 ± 0.057**	0.059 ± 0.057*
	25th Percentile	0.107 ± 0.059	0.095 ± 0.052$^{p=0.788}$	0.050 ± 0.059***	0.050 ± 0.037**	0.043 ± 0.047*
	75th Percentile	0.242 ± 0.136	0.179 ± 0.092$^{p=0.123}$	0.104 ± 0.104***	0.106 ± 0.081***	0.081 ± 0.071*
	IQR	0.135 ± 0.101	0.084 ± 0.053**	0.054 ± 0.048***	0.056 ± 0.052**	0.038 ± 0.029$^{p=0.050}$
		N=13	N=7	N=15	N=14	N=6
Responders	Median	0.145 ± 0.076	0.137 ± 0.074$^{p=0.657}$	0.043 ± 0.021***	0.053 ± 0.048**	0.042 ± 0.053$^{p=0.070}$
	25th Percentile	0.100 ± 0.054	0.092 ± 0.041$^{p=0.763}$	0.029 ± 0.016***	0.036 ± 0.030**	0.027 ± 0.044$^{p=0.055}$
	75th Percentile	0.204 ± 0.111	0.192 ± 0.114$^{p=0.778}$	0.065 ± 0.032***	0.075 ± 0.060**	0.061 ± 0.061$^{p=0.086}$
	IQR	0.104 ± 0.063	0.100 ± 0.078$^{p=0.829}$	0.035 ± 0.021**	0.040 ± 0.038**	0.034 ± 0.024$^{p=0.140}$
		N=6	N=5	N=5	N=6	N=2
Non-Responders	Median	0.183 ± 0.093	0.171 ± 0.094$^{p=0.386}$	0.059 ± 0.037*	0.123 ± 0.050$^{p=0.235}$	0.121 ± 0.050*
	25th Percentile	0.127 ± 0.078	0.131 ± 0.077$^{p=0.860}$	0.041 ± 0.027$^{p=0.066}$	0.083 ± 0.031$^{p=0.194}$	0.095 ± 0.040$^{p=0.206}$
	75th Percentile	0.281 ± 0.123	0.223 ± 0.123$^{p=0.190}$	0.090 ± 0.054*	0.174 ± 0.086$^{p=0.135}$	0.164 ± 0.077$^{p=0.159}$
	IQR	0.154 ± 0.098	0.092 ± 0.066*	0.049 ± 0.031*	0.092 ± 0.070$^{p=0.208}$	0.069 ± 0.037$^{p=0.459}$

Table 5.12: The average ± standard deviation of the K_{trans}-metrics for all participants, responders and non-responders at 2-weeks, 6-, 12- and 24-months post-RT.

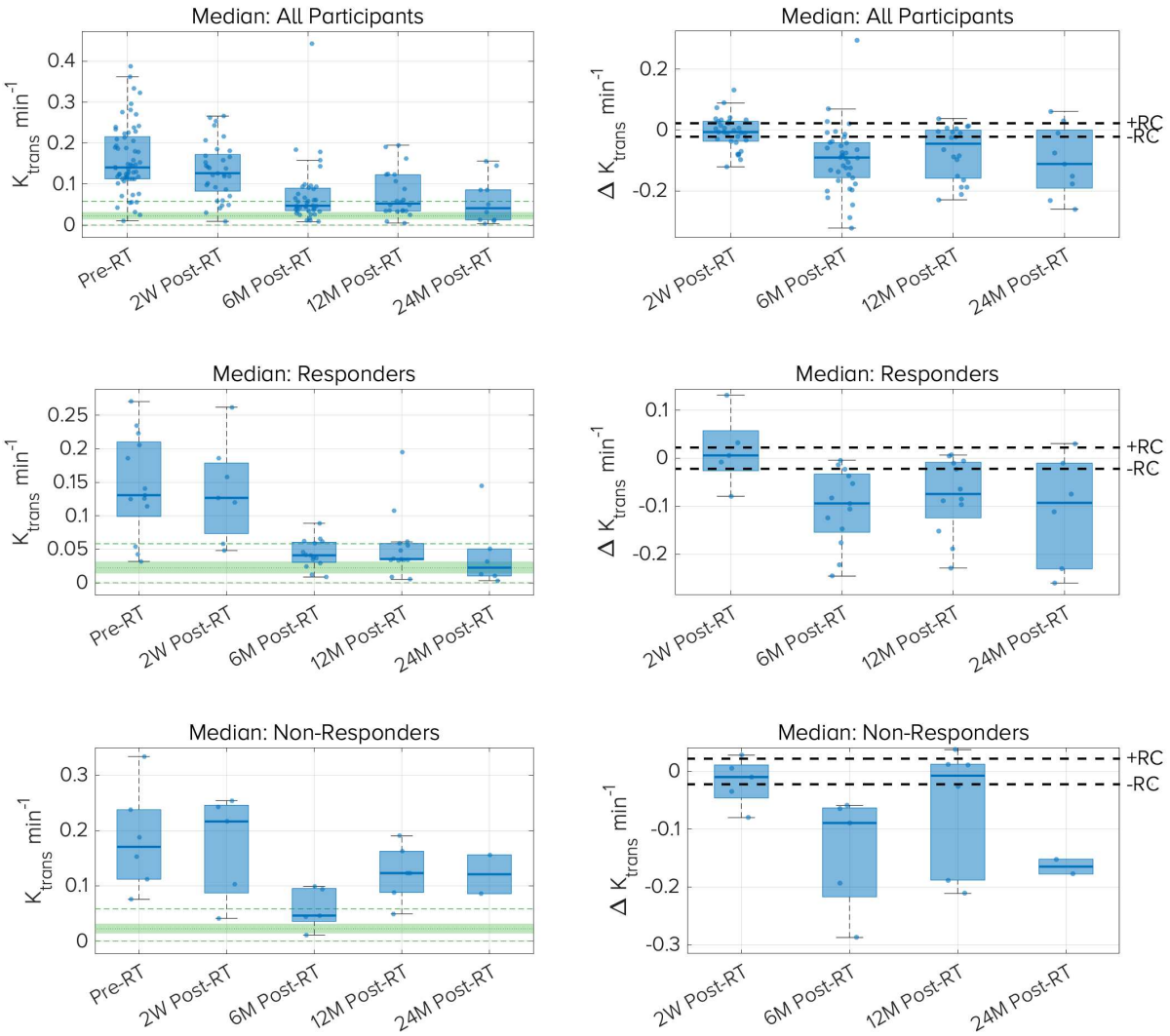


Figure 5.18: (Left) The median K_{trans} derived from the dynamic contrast-enhanced MRI data of the entire breast tumour, pre-RT and at 2-week, 6-month, 12-month and 24-month post-radiotherapy (RT) for all participants, responders and non-responders. (Right) The change in the K_{trans} statistics from baseline (pre-RT) at 2-week, 6-month, 12-month and 24-month post-radiotherapy (RT) for all participants, responders and non-responders. The dots are individual participants. The green shaded area is the healthy breast's 25th and 75th percentile range, and the dashed green lines are the whiskers.

However, non-responders in Figure 5.17 have less of a shift towards lower values at 2-weeks, and values remain high at 6-, 12- and 24-months post-RT; however, at 6-months there is some shift towards lower values. In Figure B.33, K_{trans}-metrics approach the healthy range by 6-month post-RT but increase again at 12-month and 24-month, where progressive disease was defined.

Table 5.13 summarises the v_e-metrics for all participants, responders and non-responders at pre-RT and the post-RT time-points.

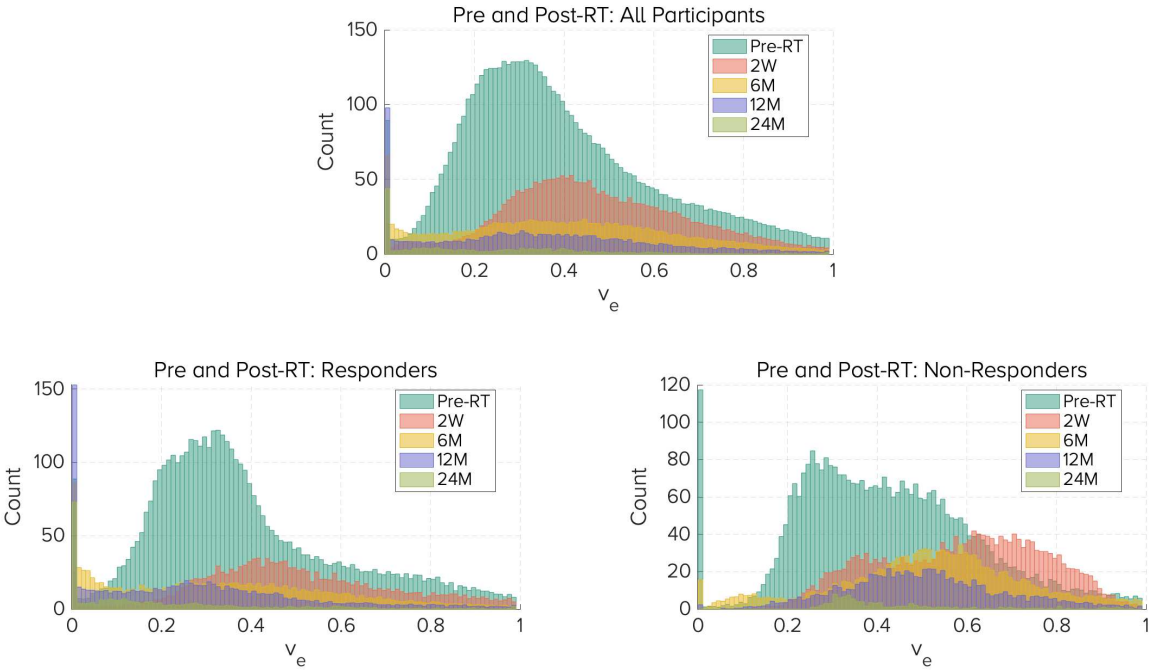


Figure 5.19: The averaged histogram for the entire tumour across all participants for v_e, pre-RT and 2-weeks, 6-, 12- and 24-months post-radiotherapy (RT).

In Figure 5.19, there is a shift towards higher values at 2-weeks post-RT, but by 6-, 12- and 24-month values spread across a range of possible values. In Figure B.34, in the 25th percentile, there is an increase in v_e 2-weeks post-RT, then a continued decrease towards healthy values at 6-, 12- and 24-months post-RT. There is not a clear trend for the median value. For the 75th percentile and IQR, the healthy range of v_e contains them at all time-points. The same is true for the responders.

Table 5.14 summarises the v_p-metrics for all participants, responders and non-responders at pre-RT and the post-RT time-points.

In Figure 5.21, many pixels take a very low value for v_p, therefore it is difficult to make out

		v_e (Average ± SD)				
		Pre-RT	2W Post-RT	6M Post-RT	12M Post-RT	24M Post-RT
		N=59	N=32	N=40	N=22	N=10
All Participants	Median	0.424 ± 0.172	0.541 ± 0.229***	0.531 ± 0.247*	0.453 ± 0.248$^{p=0.961}$	0.543 ± 0.315$^{p=0.388}$
	25th Percentile	0.337 ± 0.148	0.457 ± 0.222***	0.344 ± 0.184$^{p=0.694}$	0.304 ± 0.171$^{p=0.080}$	0.266 ± 0.221$^{p=0.225}$
	75th Percentile	0.558 ± 0.236	0.646 ± 0.248$^{p=0.143}$	0.741 ± 0.283***	0.602 ± 0.289$^{p=0.807}$	0.696 ± 0.277$^{p=0.536}$
	IQR	0.220 ± 0.167	0.189 ± 0.110$^{p=0.260}$	0.396 ± 0.251***	0.298 ± 0.254$^{p=0.177}$	0.430 ± 0.349$^{p=0.168}$
		N=13	N=7	N=15	N=14	N=6
Responders	Median	0.469 ± 0.170	0.595 ± 0.210$^{p=0.216}$	0.569 ± 0.274$^{p=0.120}$	0.442 ± 0.292$^{p=0.928}$	0.632 ± 0.321$^{p=0.520}$
	25th Percentile	0.376 ± 0.154	0.483 ± 0.172$^{p=0.106}$	0.338 ± 0.179$^{p=0.343}$	0.252 ± 0.168*	0.206 ± 0.182$^{p=0.072}$
	75th Percentile	0.624 ± 0.250	0.739 ± 0.262$^{p=0.597}$	0.784 ± 0.302$^{p=0.116}$	0.583 ± 0.316$^{p=0.898}$	0.763 ± 0.300$^{p=0.643}$
	IQR	0.248 ± 0.192	0.257 ± 0.133$^{p=0.839}$	0.446 ± 0.250$^{p=0.058}$	0.330 ± 0.277$^{p=0.269}$	0.557 ± 0.376$^{p=0.139}$
		N=6	N=5	N=5	N=6	N=2
Non-Responders	Median	0.469 ± 0.159	0.577 ± 0.211**	0.528 ± 0.291$^{p=0.908}$	0.461 ± 0.175$^{p=0.922}$	0.580 ± 0.324$^{p=0.984}$
	25th Percentile	0.385 ± 0.133	0.505 ± 0.195*	0.392 ± 0.214$^{p=0.773}$	0.390 ± 0.148$^{p=0.947}$	0.517 ± 0.282$^{p=0.813}$
	75th Percentile	0.578 ± 0.223	0.650 ± 0.227**	0.724 ± 0.394$^{p=0.589}$	0.559 ± 0.231$^{p=0.829}$	0.678 ± 0.357$^{p=0.931}$
	IQR	0.193 ± 0.140	0.145 ± 0.039$^{p=0.666}$	0.332 ± 0.198$^{p=0.209}$	0.169 ± 0.100$^{p=0.495}$	0.161 ± 0.075$^{p=0.906}$

Table 5.13: The average ± standard deviation of the v_e-metrics for all participants, responders and non-responders at 2-weeks, 6-, 12- and 24-months post-RT.

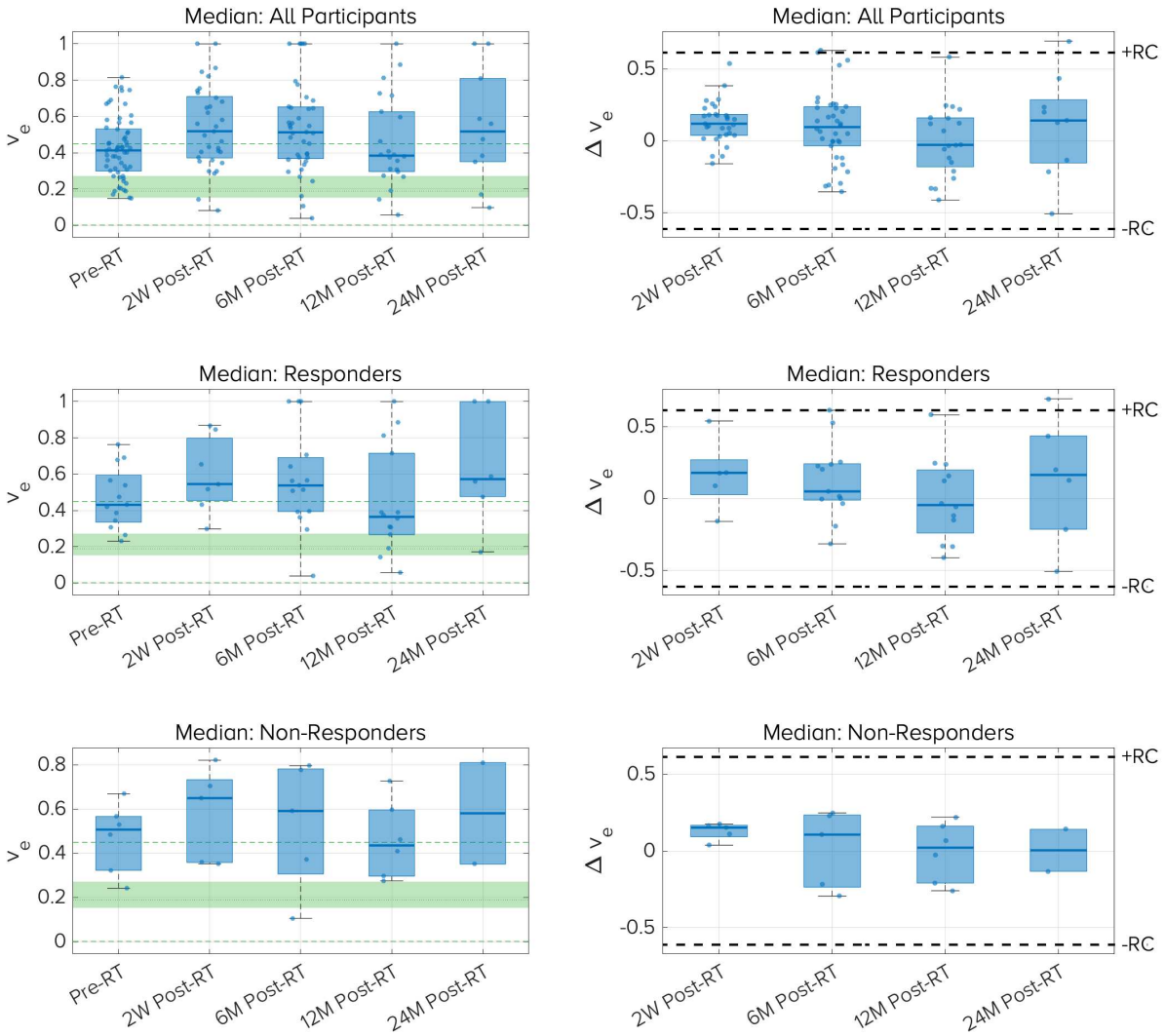


Figure 5.20: (Left) The median v_e derived from the dynamic contrast-enhanced MRI data of the entire breast tumour, pre-RT and at 2-week, 6-month, 12-month and 24-month post-radiotherapy (RT) for all participants, responders and non-responders. (Right) The change in the v_e statistics from baseline (pre-RT) at 2-week, 6-month, 12-month and 24-month post-radiotherapy (RT) for all participants, responders and non-responders. The dots are individual participants. The green shaded area is the healthy breast's 25th and 75th percentile range, and the dashed green lines are the whiskers.

		v_p (Average ± SD)				
		Pre-RT	2W Post-RT	6M Post-RT	12M Post-RT	24M Post-RT
		N=59	N=32	N=40	N=22	N=10
All Participants	Median	0.061 ± 0.046	0.044 ± 0.039**	0.029 ± 0.052***	0.020 ± 0.033***	0.019 ± 0.032$^{p=0.098}$
	25th Percentile	0.035 ± 0.035	0.025 ± 0.026*	0.013 ± 0.022***	0.008 ± 0.014**	0.014 ± 0.024$^{p=0.287}$
	75th Percentile	0.087 ± 0.060	0.068 ± 0.052**	0.058 ± 0.145$^{p=0.158}$	0.034 ± 0.052***	0.026 ± 0.039$^{p=0.057}$
	IQR	0.052 ± 0.035	0.043 ± 0.033$^{p=0.217}$	0.045 ± 0.137$^{p=0.647}$	0.026 ± 0.041**	0.012 ± 0.015*
		N=13	N=7	N=15	N=14	N=6
Responders	Median	0.053 ± 0.033	0.050 ± 0.030$^{p=0.892}$	0.016 ± 0.016**	0.013 ± 0.016***	0.003 ± 0.004**
	25th Percentile	0.032 ± 0.026	0.023 ± 0.017$^{p=0.676}$	0.008 ± 0.009**	0.006 ± 0.011**	0.001 ± 0.002*
	75th Percentile	0.078 ± 0.041	0.082 ± 0.051$^{p=0.553}$	0.026 ± 0.024***	0.026 ± 0.024**	0.006 ± 0.006**
	IQR	0.047 ± 0.025	0.059 ± 0.046$^{p=0.258}$	0.018 ± 0.016**	0.020 ± 0.020**	0.005 ± 0.005*
		N=6	N=5	N=5	N=6	N=2
Non-Responders	Median	0.058 ± 0.032	0.026 ± 0.030$^{p=0.392}$	0.019 ± 0.022$^{p=0.070}$	0.038 ± 0.056$^{p=0.340}$	0.074 ± 0.035$^{p=0.059}$
	25th Percentile	0.025 ± 0.022	0.019 ± 0.026$^{p=0.760}$	0.009 ± 0.010$^{p=0.387}$	0.016 ± 0.020$^{p=0.544}$	0.055 ± 0.024$^{p=0.163}$
	75th Percentile	0.092 ± 0.058	0.034 ± 0.033$^{p=0.254}$	0.035 ± 0.038$^{p=0.053}$	0.061 ± 0.093$^{p=0.240}$	0.095 ± 0.035$^{p=0.327}$
	IQR	0.067 ± 0.057	0.015 ± 0.008$^{p=0.111}$	0.026 ± 0.029$^{p=0.061}$	0.045 ± 0.075$^{p=0.202}$	0.039 ± 0.011$^{p=0.833}$

Table 5.14: The average ± standard deviation of the v_p-metrics for all participants, responders and non-responders at the 2-week, 6-, 12- and 24-months post-RT time-points.

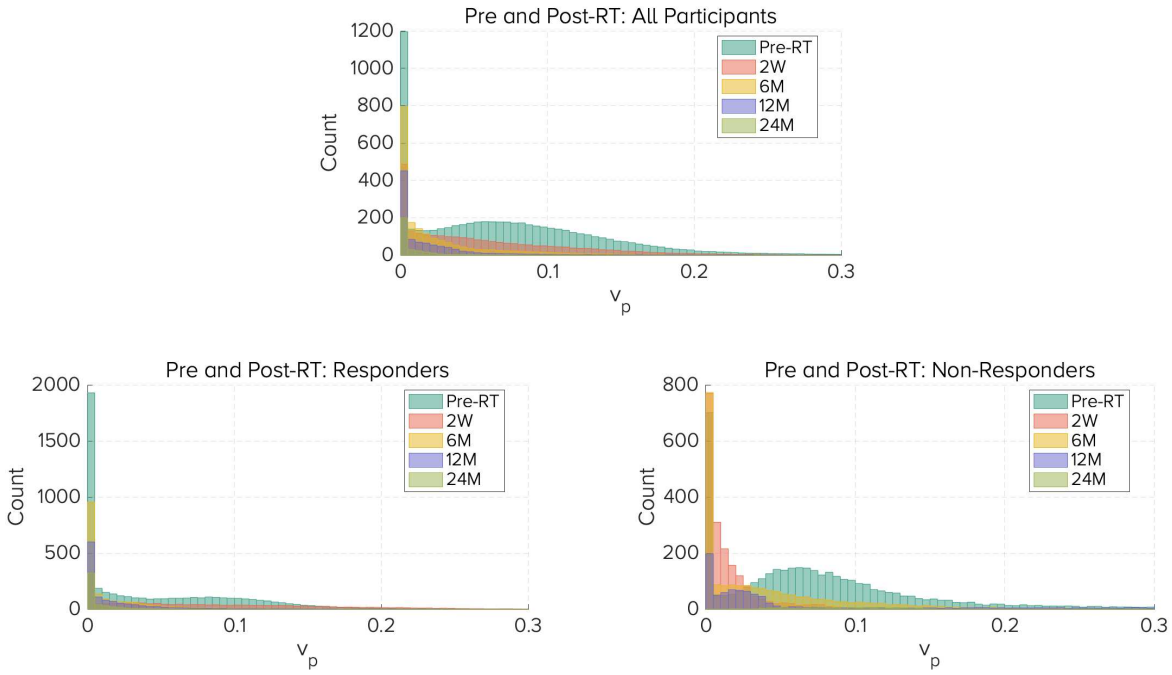


Figure 5.21: The averaged histogram for the entire tumour across all participants for v_p, pre-RT and 2-weeks, 6-, 12- and 24-months post-radiotherapy (RT).

the trend. For all participants, responders and non-responders, it appears that v_p reduces with time. This is clearer in Figure B.37, where the metrics approach the healthy range. However, across the metrics, not many participants have experienced significant changes. This is clear for the responders. For the non-responders, the metrics approach the healthy range by 6-months post-RT, and increase again at 12- and 24-months.

Semi-Quantitative Parameters

Figure 5.23 illustrates the averaged histograms for all participants, responders and non-responders. Among all participants, there is an observable shift from higher to lower $iWIR$ values from baseline to 2-weeks post-RT, followed by a shift to lower values at 6-, 12- and 24-months post-RT. This trend is reflected in Figure B.40, where there is a shift in the 25th percentile, median, and 75th percentile to lower values at 2-weeks and and a greater shift at 6-months post-RT to the healthy range, with most participants having a change beyond the RC across these metrics at 6-months. At 12-month and 24-month, there is a stabilisation in the values. There is the same trend for responders, but there it not much of a change at 2-weeks but a big change at 6-months to healthy values and beyond the RC. For non-responders, at 12-months and 24-months there is

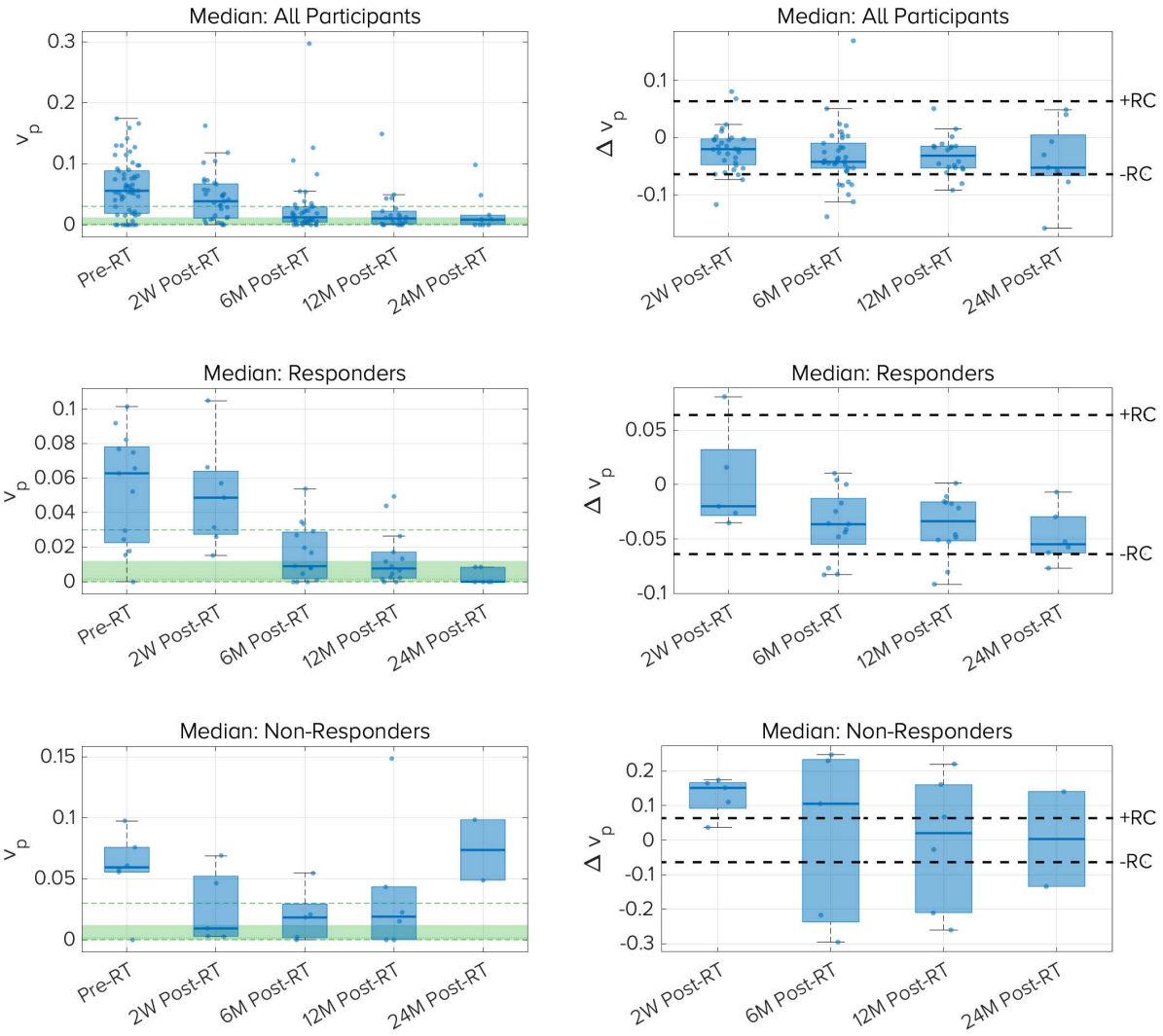


Figure 5.22: (Left) The median v_p derived from the dynamic contrast-enhanced MRI data of the entire breast tumour, pre-RT and at 2-week, 6-month, 12-month and 24-month post-radiotherapy (RT) for all participants, responders and non-responders. (Right) The change in the v_p statistics from baseline (pre-RT) at 2-week, 6-month, 12-month and 24-month post-radiotherapy (RT) for all participants, responders and non-responders. The dots are individual participants. The green shaded area is the healthy breast's 25th and 75th percentile range, and the dashed green lines are the whiskers.

an increase back to baseline values and away from the healthy range. Although the median is similar for responders and non-responders at 6-months, in Figure 5.23, a bulk of the pixels still have high $iWIR$ values.

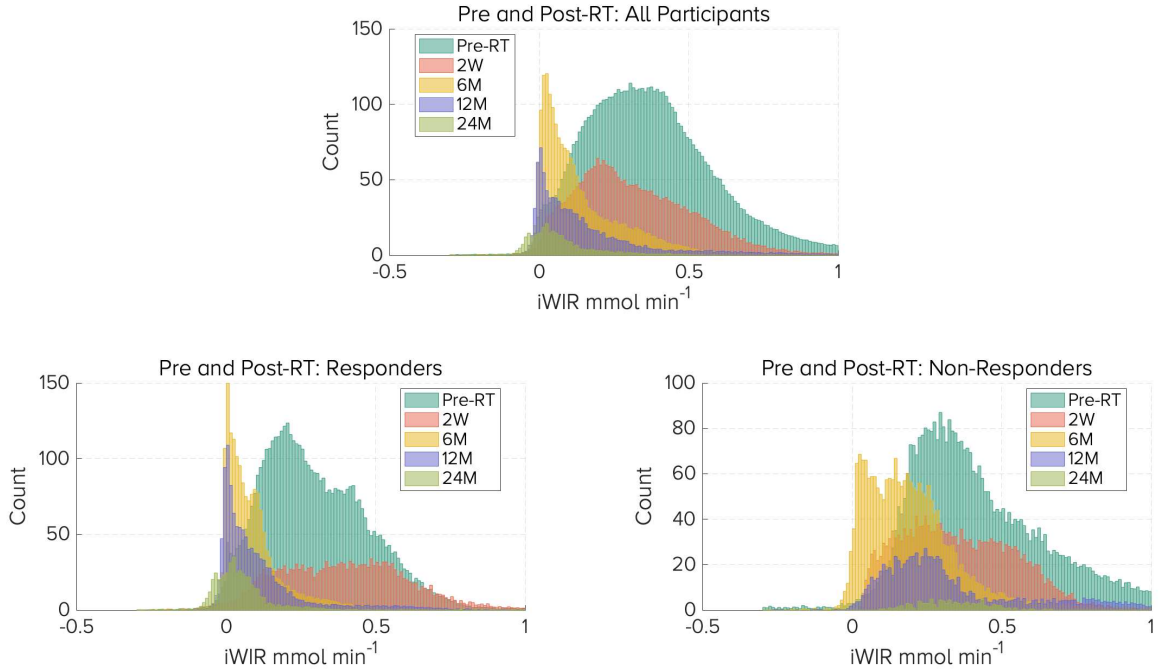


Figure 5.23: The averaged histogram for the entire tumour across all participants for $iWIR$, pre-RT and 2-weeks, 6-, 12- and 24-months post-radiotherapy (RT).

Figure 5.25 illustrates the averaged histograms for all participants, responders and non-responders. Among all participants, there is an observable shift from lower to higher $fWOR$ values from baseline to 2-weeks post-RT, followed by a decrease in lower values at 6-, 12- and 24-months post-RT. This trend is reflected in Figure B.40, where there is a shift in the 25th percentile, median, and 75th percentile to higher values at 2-weeks and 6-months and stabilisation at 12- and 24-months post-RT in the healthy range of values. About half of the participants have a change beyond the RC across these metrics at 2-weeks and 6-months post-RT. There is the same trend for responders. For non-responders, at 6-months there is a greater change to higher values beyond the healthy range, then a reduction again at 12- and 24-months post-RT.

Figure 5.27 illustrates the averaged histograms for all participants, responders and non-responders. Among all participants, there is no observable change from baseline to 2-weeks post-RT apart from a decrease in the number of pixels; however ,at 6-, 12- and 24-months

		$iWIR$ mmol min^{-1} (Average ± SD)				
		Pre-RT	2W Post-RT	6M Post-RT	12M Post-RT	24M Post-RT
		N=59	N=32	N=40	N=22	N=10
All Participants	Median	0.3377 ± 0.1494	0.2783 ± 0.1317$^{p=0.097}$	0.1535 ± 0.1693***	0.1542 ± 0.1386***	0.1326 ± 0.1493**
	25th Per	0.2457 ± 0.1193	0.2022 ± 0.1020$^{p=0.094}$	0.1043 ± 0.1228***	0.0988 ± 0.0828***	0.0958 ± 0.1221**
	75th Per	0.4313 ± 0.1880	0.3691 ± 0.1675$^{p=0.245}$	0.2168 ± 0.2463***	0.2124 ± 0.1891***	0.1752 ± 0.1752**
	IQR	0.1856 ± 0.1025	0.1668 ± 0.0860$^{p=0.724}$	0.1125 ± 0.1316**	0.1136 ± 0.1168**	0.0794 ± 0.0585*
		N=13	N=7	N=15	N=14	N=6
Responders	Median	0.2966 ± 0.1312	0.2931 ± 0.1318$^{p=0.583}$	0.0971 ± 0.0546***	0.1113 ± 0.1106**	0.0626 ± 0.0950*
	25th Per	0.2221 ± 0.1177	0.2078 ± 0.0870$^{p=0.955}$	0.0614 ± 0.0399***	0.0738 ± 0.0678**	0.0373 ± 0.0871*
	75th Per	0.3770 ± 0.1485	0.3920 ± 0.1746$^{p=0.312}$	0.1378 ± 0.0750***	0.1500 ± 0.1405**	0.0968 ± 0.1052*
	IQR	0.1550 ± 0.0746	0.1842 ± 0.1019$^{p=0.272}$	0.0764 ± 0.0468***	0.0762 ± 0.0834*	0.0595 ± 0.0248*
		N=6	N=5	N=5	N=6	N=2
Non-Responders	Median	0.4069 ± 0.1108	0.3244 ± 0.1876$^{0.121}$	0.1352 ± 0.0901**	0.2580 ± 0.1670$^{p=0.086}$	0.3689 ± 0.0677$^{p=0.119}$
	25th Per	0.3000 ± 0.0871	0.2510 ± 0.1549$^{p=0.174}$	0.0868 ± 0.0606**	0.1610 ± 0.0909*	0.2804 ± 0.0476$^{p=0.157}$
	75th Per	0.5250 ± 0.1708	0.4033 ± 0.2173$^{p=0.157}$	0.1929 ± 0.1138**	0.3578 ± 0.2408$^{p=0.090}$	0.4594 ± 0.0780$^{p=0.299}$
	IQR	0.2251 ± 0.1453	0.1523 ± 0.0865$^{p=0.192}$	0.1061 ± 0.0642*	0.1968 ± 0.1625$^{p=0.488}$	0.1790 ± 0.0303$^{p=0.784}$

Table 5.15: The average ± standard deviation of the $iWIR$-metrics for all participants, responders and non-responders at the 2-week, 6-, 12- and 24-months post-RT time-points.

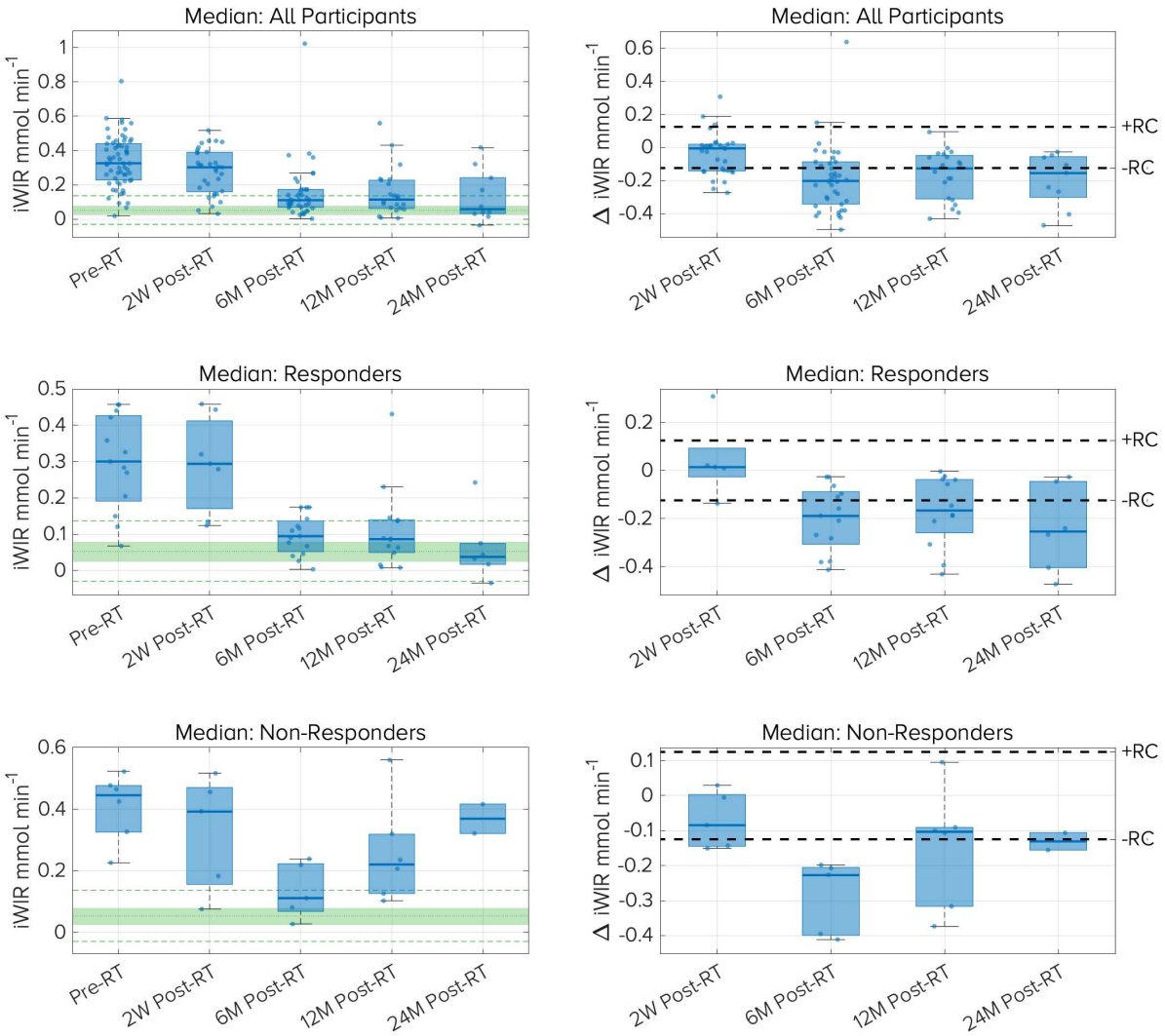


Figure 5.24: (Left) The median *iWIR* derived from the dynamic contrast-enhanced MRI data of the entire breast tumour, pre-RT and at 2-week, 6-month, 12-month and 24-month post-radiotherapy (RT) for all participants, responders and non-responders. (Right) The change in the *iWIR* statistics from baseline (pre-RT) at 2-week, 6-month, 12-month and 24-month post-radiotherapy (RT) for all participants, responders and non-responders. The dots are individual participants. The green shaded area is the healthy breast's 25th and 75th percentile range, and the dashed green lines are the whiskers.

		$fWOR \times 10^{-2}$ mmol min^{-1} (Average ± SD)				
		Pre-RT	2W Post-RT	6M Post-RT	12M Post-RT	24M Post-RT
		N=59	N=32	N=40	N=22	N=10
All Participants	Median	-0.39 ± 0.97	0.73 ± 1.29***	1.04 ± 1.10***	0.68 ± 0.56**	0.60 ± 0.69$^{p=0.223}$
	25th Per	-1.29 ± 1.16	-0.20 ± 1.56**	0.00 ± 3.10*	0.01 ± 0.85**	0.11 ± 0.59$^{p=0.150}$
	75th Per	0.55 ± 0.95	1.53 ± 1.24***	1.89 ± 1.12***	1.27 ± 0.76$^{p=0.054}$	1.21 ± 0.98$^{p=0.388}$
	IQR	1.84 ± 0.94	1.73 ± 1.10$^{p=0.526}$	1.90 ± 3.46$^{p=0.858}$	1.26 ± 1.16*	1.11 ± 0.65$^{p=0.207}$
		N=13	N=7	N=15	N=14	N=6
Responders	Median	-0.04 ± 1.16	0.66 ± 1.29$^{p=0.584}$	1.38 ± 0.90**	0.80 ± 0.59*	0.40 ± 0.49$^{p=0.887}$
	25th Per	-0.91 ± 1.36	-0.53 ± 1.94$^{p=0.769}$	0.81 ± 0.65**	0.26 ± 0.68*	-0.09 ± 0.43$^{p=0.737}$
	75th Per	0.94 ± 1.24	1.73 ± 1.03$^{p=0.387}$	1.97 ± 1.24**	1.29 ± 0.69$^{p=0.402}$	0.98 ± 0.67$^{p=0.899}$
	IQR	1.86 ± 1.18	2.27 ± 1.93$^{p=0.297}$	1.16 ± 0.85$^{p=0.064}$	1.03 ± 0.64*	1.07 ± 0.61$^{p=0.185}$
		N=6	N=5	N=5	N=6	N=2
Non-Responders	Median	-0.50 ± 0.84	0.26 ± 0.68*	1.66 ± 0.94*	0.28 ± 0.34$^{p=0.122}$	1.22 ± 1.37$^{p=0.237}$
	25th Per	-1.52 ± 0.87	-0.52 ± 1.15*	0.85 ± 0.45*	-0.62 ± 1.02$^{p=0.184}$	0.49 ± 1.20$^{p=0.127}$
	75th Per	0.53 ± 1.04	0.97 ± 0.32*	2.40 ± 1.51*	1.13 ± 1.04$^{p=0.084}$	2.24 ± 1.88$^{p=0.396}$
	IQR	2.05 ± 1.26	1.49 ± 0.92$^{p=0.542}$	1.56 ± 1.33$^{p=0.098}$	1.75 ± 1.93$^{p=0.588}$	1.75 ± 0.68$^{p=0.830}$

Table 5.16: The average ± standard deviation of the $fWOR$-metrics for all participants, responders and non-responders at the 2-week, 6-, 12- and 24-months post-RT time-points.

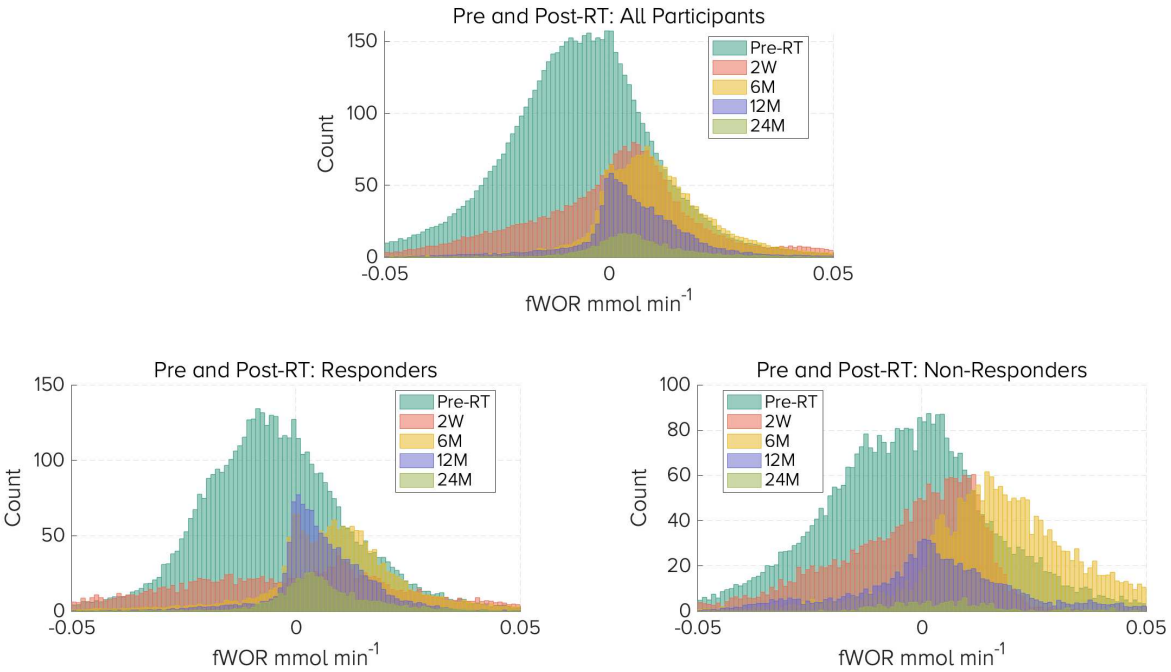


Figure 5.25: The averaged histogram for the entire tumour across all participants for $fWOR$, pre-RT and 2-weeks, 6-, 12- and 24-months post-radiotherapy (RT).

post-RT, there is an observable shift to lower values. This trend is reflected in Figure B.46, where there is a shift in the 25th percentile, median, and 75th percentile to lower values at 6-, 12- and 24-months post-RT towards the healthy range of values. About half of the participants have a change greater than the RC at 2-weeks post-RT, then a decrease beyond the RC across these metrics at 6-, 12- and 24-months post-RT. There is the same trend for responders; however, at 24-months post-RT, the metrics lie within the healthy range of values. For non-responders, at 12-months and 24-months there is an increase to higher values beyond the healthy range to baseline values. At 2-weeks and 6-months, higher values remain in comparison to responders.

5.2.6 Estimating Response

To evaluate the correlation between DCE parameters and radiological response assessed using MRI, the DCE parameters are categorised according to the response types: complete response (CR), partial response (PR), stable disease (SD), and progressive disease (PD), assessed at 6, 12, and 24 months post-radiotherapy. The SD group will not be included in statistical analysis due to a low number of data-points (N=2).

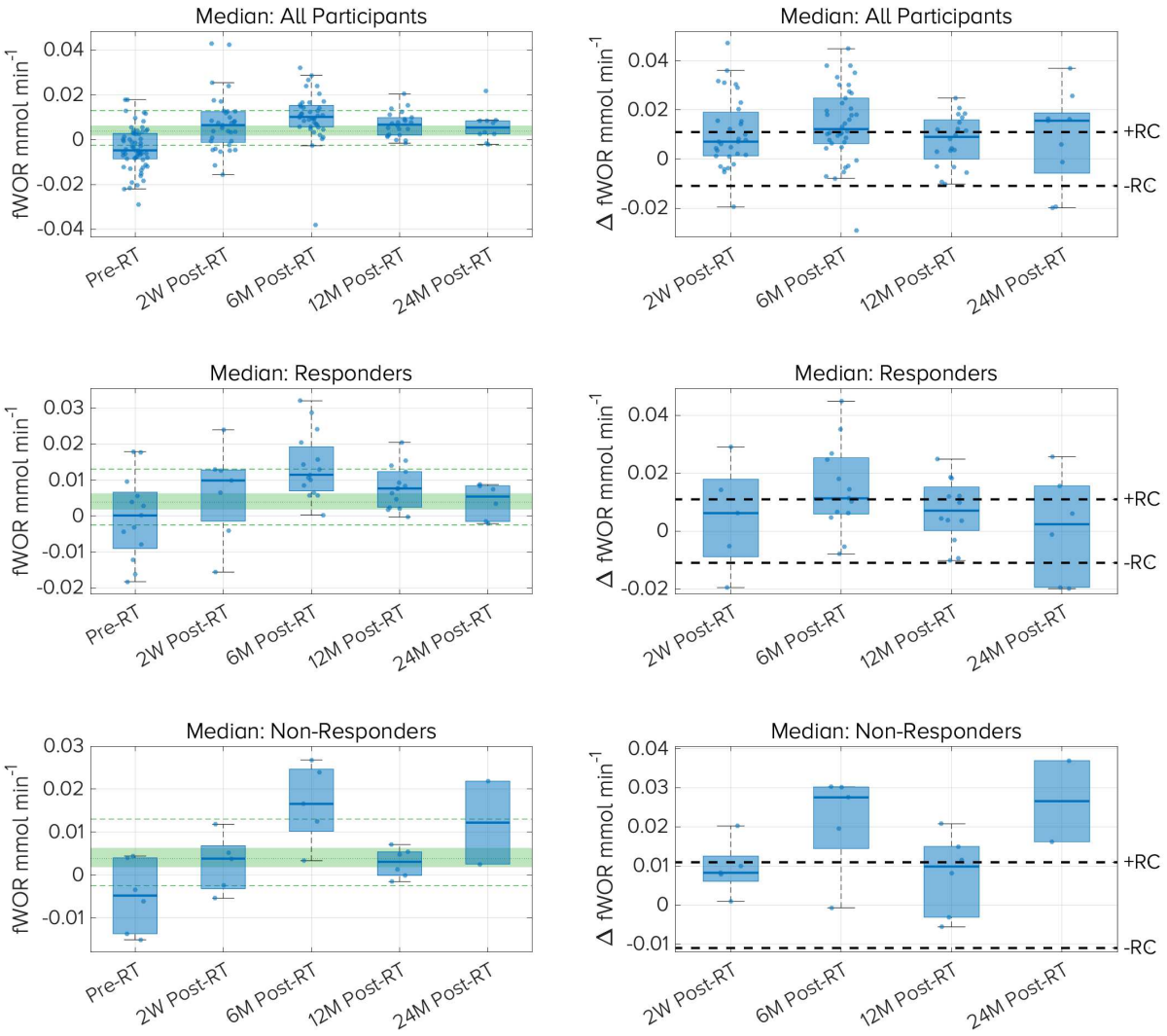


Figure 5.26: (Left) The median $fWOR$ derived from the dynamic contrast-enhanced MRI data of the entire breast tumour, pre-RT and at 2-week, 6-month, 12-month and 24-month post-radiotherapy (RT) for all participants, responders and non-responders. (Right) The change in the $fWOR$ statistics from baseline (pre-RT) at 2-week, 6-month, 12-month and 24-month post-radiotherapy (RT) for all participants, responders and non-responders. The dots are individual participants. The green shaded area is the healthy breast's 25th and 75th percentile range, and the dashed green lines are the whiskers.

		AUC_{fWO} mmol min (Average ± SD)				
		Pre-RT	2W Post-RT	6M Post-RT	12M Post-RT	24M Post-RT
		N=59	N=32	N=40	N=22	N=10
All Participants	Median	1.6630 ± 0.7162	1.8683 ± 0.8395***	1.1709 ± 0.9262***	1.1218 ± 0.7524**	0.9413 ± 0.8632*
	25th Per	1.3203 ± 0.6073	1.5167 ± 0.7371**	0.8600 ± 0.6562***	0.8482 ± 0.5876**	0.7180 ± 0.7853*
	75th Per	1.9942 ± 0.8375	2.2127 ± 0.9419***	1.5777 ± 1.5240*	1.3929 ± 0.8463**	1.1779 ± 0.9014*
	IQR	0.6739 ± 0.3598	0.6959 ± 0.2981$^{p=0.103}$	0.7177 ± 0.9913$^{p=0.704}$	0.5447 ± 0.3427$^{p=0.275}$	0.4599 ± 0.3142$^{p=0.804}$
		N=13	N=7	N=15	N=14	N=6
Responders	Median	1.6551 ± 0.6518	1.9127 ± 0.7433$^{p=0.105}$	0.8538 ± 0.3671***	0.8624 ± 0.6453**	0.6231 ± 0.6666*
	25th Per	1.3312 ± 0.6117	1.5022 ± 0.5392$^{p=0.148}$	0.6353 ± 0.3204***	0.6235 ± 0.4891**	0.3800 ± 0.5986*
	75th Per	1.9466 ± 0.6660	2.3040 ± 0.8824$^{p=0.090}$	1.1067 ± 0.4498***	1.1177 ± 0.7370**	0.9039 ± 0.7179*
	IQR	0.6154 ± 0.2817	0.8017 ± 0.3981$^{p=0.403}$	0.4714 ± 0.2272$^{p=0.061}$	0.4943 ± 0.3512$^{p=0.335}$	0.5239 ± 0.3464$^{p=0.429}$
		N=6	N=5	N=5	N=6	N=2
Non-Responders	Median	1.9034 ± 0.5863	2.0862 ± 1.0166$^{p=0.266}$	1.1286 ± 0.6906*	1.6871 ± 0.7442$^{p=0.518}$	2.0938 ± 0.8150$^{p=0.524}$
	25th Per	1.5610 ± 0.4955	1.7867 ± 0.9304$^{p=0.267}$	0.8821 ± 0.5838*	1.3266 ± 0.5492$^{p=0.363}$	1.7925 ± 0.6366$^{p=0.112}$
	75th Per	2.2471 ± 0.6972	2.3836 ± 1.0803$^{p=0.258}$	1.4944 ± 0.8317*	1.9997 ± 0.8487$^{p=0.520}$	2.3327 ± 0.9223$^{p=0.533}$
	IQR	0.6861 ± 0.3194	0.5969 ± 0.2373$^{p=0.812}$	0.6123 ± 0.3398$^{p=0.056}$	0.6731 ± 0.3521$^{p=0.935}$	0.5402 ± 0.2857$^{p=0.669}$

Table 5.17: The average ± standard deviation of the AUC_{fWO}-metrics for all participants, responders and non-responders at the 2-week, 6-, 12- and 24-months post-RT time-points.

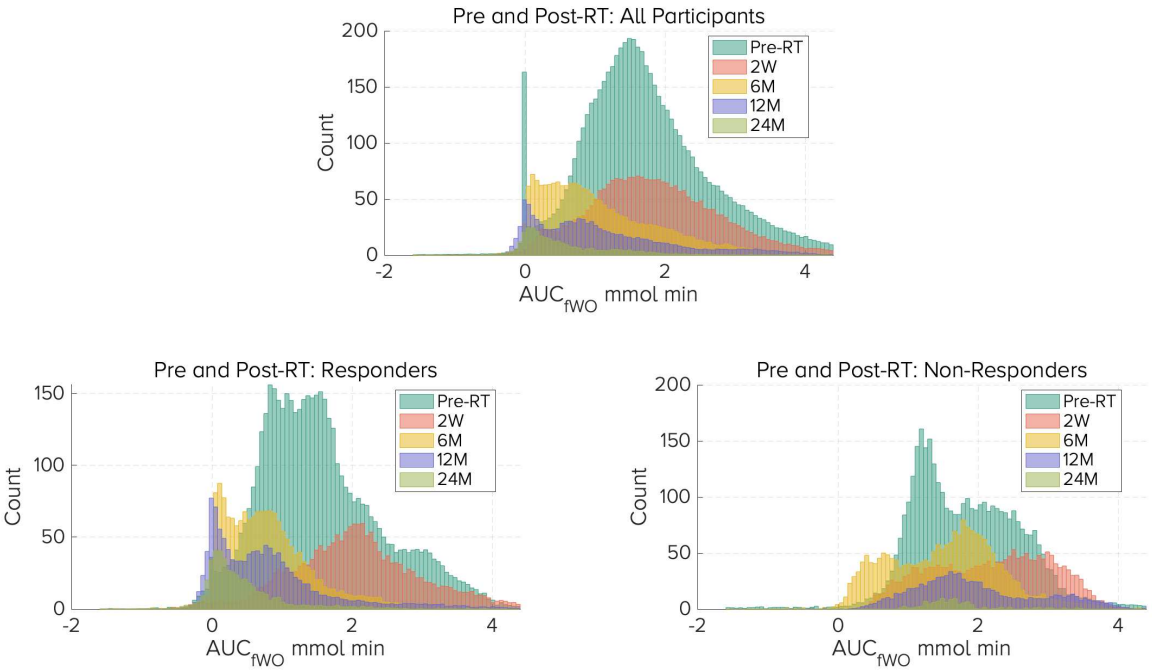


Figure 5.27: The averaged histogram for the entire tumour across all participants for AUC_{fWO}, pre-RT and 2-weeks, 6-, 12- and 24-months post-radiotherapy (RT).

Tofts Model Parameters

Figure 5.29 illustrates the median K_{trans} parameter, while Figure B.49 additionally presents the 25th percentile, 75th percentile and IQR metrics.

For the K_{trans}-metrics, the response groups show overlapping values, indicating that absolute K_{trans} measurements do not correspond to distinct radiological assessments. Specifically, the lower-end of the PR group overlaps with the CR group, while the upper-end overlaps with the PD group. A partial overlap of PR with these two groups is expected, as PR is an intermediate state.

However, the CR and PD groups exhibit a clear separation, with PD values significantly larger than those of CR for the median, 25th percentile, 75th percentile and IQR (p = 0.0002/0.0002/0.0002/0.0021). The entire CR group overlaps with the healthy range across all metrics.

Significant differences exist among the sub-groups. PR values are significantly larger than CR values (p = 0.0031/0.0196/0.0003/0.0003), and PD values are significantly larger than CR and PR values, except for the IQR (p = 0.0324/0.0239/0.0392/0.2800).

Regarding changes in K_{trans}-metrics over time, there is overlap across all groups, with no

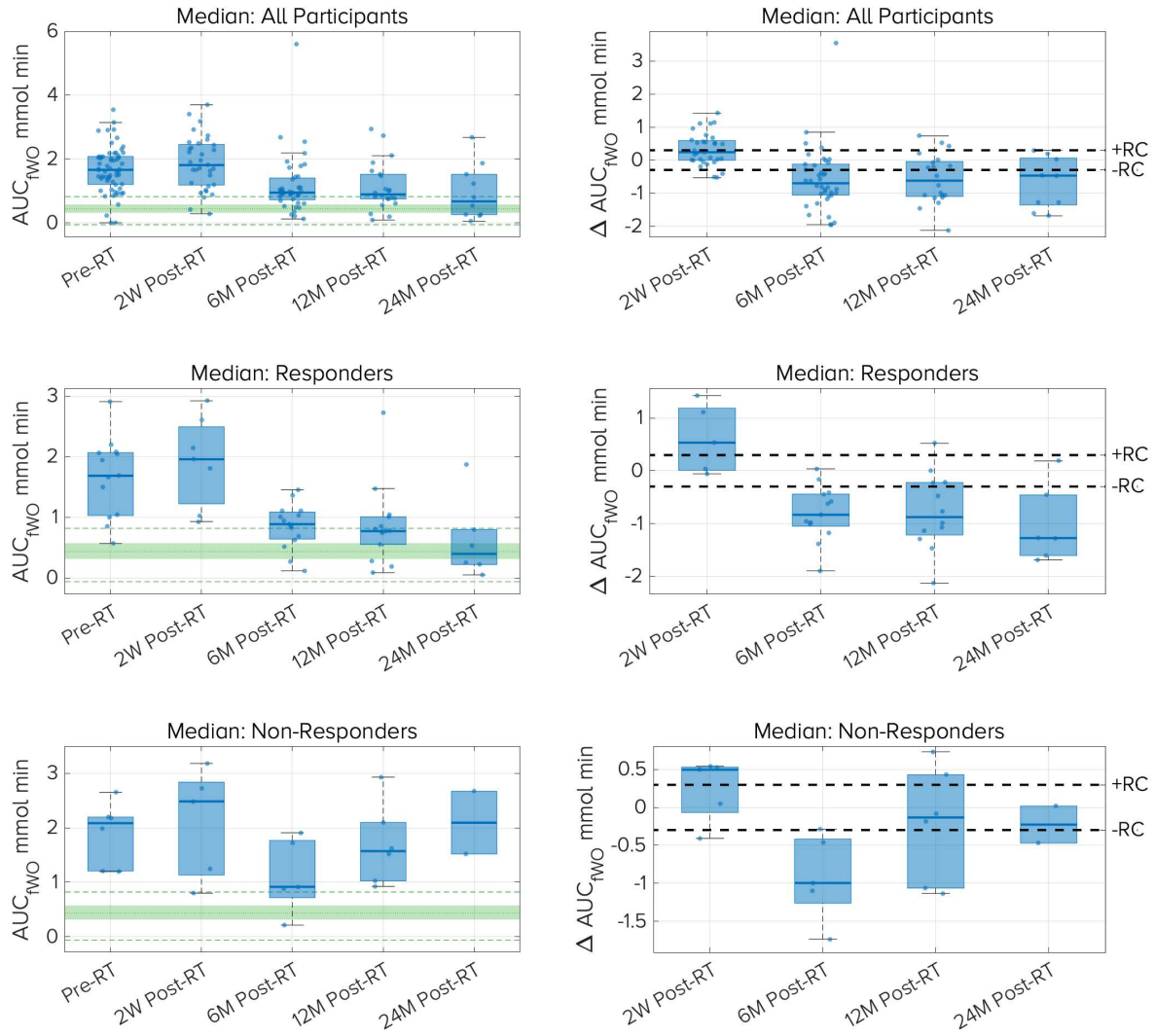


Figure 5.28: (Left) The median AUC_{fWO} derived from the dynamic contrast-enhanced MRI data of the entire breast tumour, pre-RT and at 2-week, 6-month, 12-month and 24-month post-radiotherapy (RT) for all participants, responders and non-responders. (Right) The change in the AUC_{fWO} statistics from baseline (pre-RT) at 2-week, 6-month, 12-month and 24-month post-radiotherapy (RT) for all participants, responders and non-responders. The dots are individual participants. The green shaded area is the healthy breast's 25th and 75th percentile range, and the dashed green lines are the whiskers.

clear separation between CR and PD or significant difference. However, CR demonstrates a significantly greater decrease from baseline than PR (p = 0.0092/0.0035/0.0122/0.0411). In contrast, no statistically significant differences are observed between PR and PD.

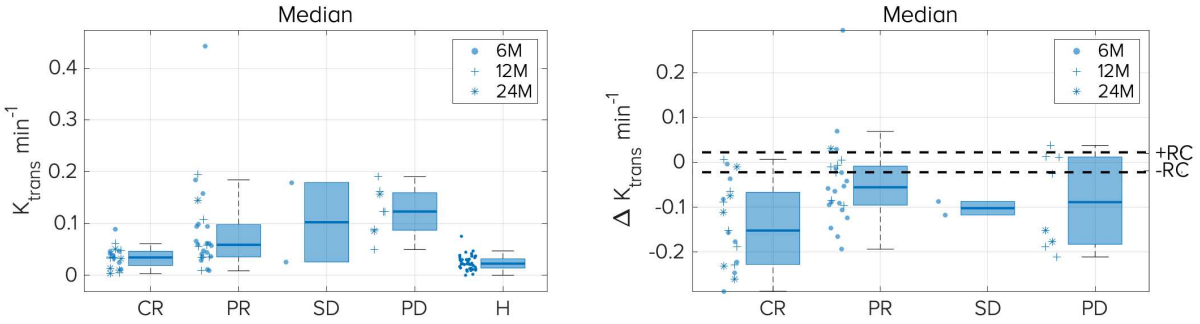


Figure 5.29: Boxplots of median K_{trans} and its radiological response assessment at 6-months (blue dot), 12-months (blue plus) and 24-months (blue asterisk). The radiological response assessment groups are complete response (CR), partial response (PR), stable disease (SD) and progressive disease (PD). On the left are the absolute values, and on the right are the changes from baseline; the dashed lines are the repeatability coefficients, and changes beyond this are significant.

Additionally, analysis evaluated the discriminative power of K_{trans} values 12-months post-RT in distinguishing between responders and non-responders using a receiver operating characteristic (ROC) curve. Among the 20 participants included (14 responders and 6 non-responders), the area under the curve (AUC) was calculated at 0.88 for the median K_{trans} value with p-value 0.0026, indicating good agreement with the radiological assessment.

Semi-Quantitative Parameters

Figure 5.30 illustrates the median $iWIR$, $fWOR$ and AUC_{fWO} parameters, while Figures B.50, B.51 and B.52 additionally present the 25th percentile, 75th percentile and IQR metrics.

For the $iWIR$-metrics, the response groups exhibit overlapping values, indicating that absolute $iWIR$ measurements do not correspond to distinct radiological assessments. Specifically, the lower-end of the PR group overlaps with the CR group, while the upper-end overlaps with the PD group. A partial overlap of PR with these two groups is expected, as PR is an intermediate state.

However, the CR and PD groups exhibit a clear separation, with PD values significantly larger than those of CR for the median, 25th percentile, 75th percentile and IQR (p

= 0.0002/0.0010/0.0002/0.0002). The entire CR group overlaps with the healthy range across all metrics.

Significant differences exist among the sub-groups. PR values are significantly larger than CR values (p = 0.0020/0.0053/0.0010/0.0008), and PD values are significantly larger than CR and PR values, except for the IQR (p = 0.0518/0.0620/0.0620/0.1207).

Regarding changes in $iWIR$-metrics over time, all groups overlap, and there is no clear separation between CR and PD. However, CR shows a significantly or near-significantly larger decrease from baseline compared to PD (p = 0.0465/0.0844/0.0465/0.0594). Furthermore, CR demonstrates a significantly greater decrease from baseline compared to PR, except for the IQR (p = 0.0025/0.0021/0.0044/0.3591). In contrast, no statistically significant differences are observed between PR and PD.

For the $fWOR$-metrics, the response groups also show overlapping values. No significant difference is observed between the CR and PR groups. For the median and 25th percentile, the PD group shows near-significantly lower values than the CR group (p = 0.0710/0.0565) and the PR group (p = 0.0804/0.0950).

Regarding changes in $fWOR$-metrics over time, no significant differences are observed across any group combinations.

Similarly, for the AUC_{fWO}-metrics, the response groups show overlapping values; the lower-end of the PR group overlaps with the CR group, while the upper-end overlaps with the PD group. However, the CR and PD groups exhibit a clear separation, with PD values significantly larger than CR's for the median, 25th percentile, 75th percentile and IQR (p = 0.0002/0.0002/0.0004/0.0394). The CR group mostly overlaps with the healthy range across all metrics.

Significant differences exist among the sub-groups. PR values are significantly larger than CR values (p = 0.0033/0.0164/0.0017/0.0069), and PD values are significantly larger than CR values, but not PR values; however, there is near-significance except for the IQR (p = 0.0804/0.0518/0.1030/0.9530).

Regarding changes in AUC_{fWO}-metrics over time, except for IQR, there is a significantly larger decrease from baseline between CR and PR (p = 0.0001/0.0001/0.0001/0.2874), and CR

and PD (p = 0.0027/0.0016/0.0073/0.3005). In contrast, no statistically significant differences are observed between PR and PD.

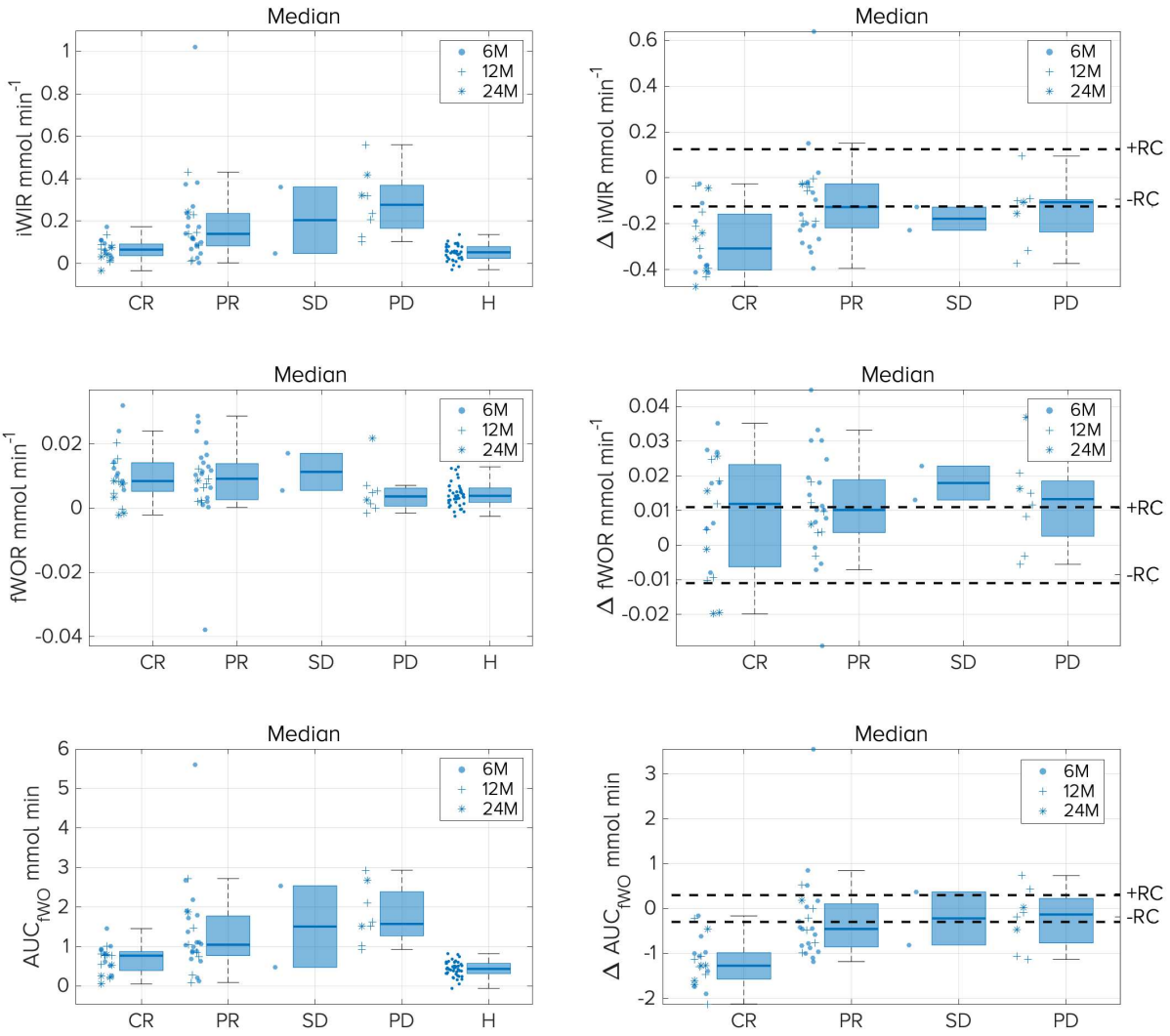


Figure 5.30: Boxplots of the median $iWIR$, $fWOR$ and AUC_{fWO} and their radiological response assessment at 6-months (blue dot), 12-months (blue plus) and 24-months (blue asterisk). The radiological response assessment groups are complete response (CR), partial response (PR), stable disease (SD) and progressive disease (PD). On the left is the absolute values, and on the right is the change from baseline; the dashed lines are the repeatability coefficients and changes beyond this are significant.

Additionally, analysis evaluated the discriminative power of $iWIR$, $fWOR$ and AUC_{fWO} values 12-months post-RT in distinguishing between responders and non-responders using a receiver operating characteristic (ROC) curve. Among the 20 participants included (14 responders and 6 non-responders), the area under the curve (AUC) was calculated at 0.83, 0.79, and 0.88, respectively, for the median values with p-value = 0.0349, 0.0371, and 0.0241, indicating good agreement with the radiological assessment.

5.2.7 Predictive Value of Baseline Measurements and Early Changes for Treatment Response

The analysis evaluated the predictive power of baseline K_{trans} values in distinguishing between responders and non-responders at 12-months post-RT using a receiver operating characteristic (ROC) curve 5.31. Among the 19 participants (13 responders and 6 non-responders), the analysis showed no discriminative ability of baseline K_{trans} values in predicting treatment response (AUC < 0.7).

The analysis also assessed the predictive power of K_{trans} changes at 2-weeks post-RT. Among the 12 patients included (7 responders and 5 non-responders), the ROC analysis yielded an AUC of 0.72 for the median K_{trans} change, indicating acceptable predictive ability. However, a p-value of 0.358 was not statistically significant.

The analysis further evaluated the predictive power of combining baseline K_{trans} values with K_{trans} changes at 2-weeks post-RT to predict patient response at 12-months. Among the 12 patients included (7 responders and 5 non-responders), the combination of baseline and 2-weeks K_{trans} values did not show improved discriminative ability.

Semi-Quantitative Parameters

The analysis evaluated the predictive power of baseline $iWIR$ values in distinguishing between responders and non-responders at 12-months post-RT using a receiver operating characteristic (ROC) curve. Among the 19 participants included (13 responders and 6 non-responders), the area under the curve (AUC) was calculated at 0.77 for the median ADC value (25th percentile/75th percentile: 0.68/0.74), indicating moderate discriminative ability of baseline $iWIR$ values in predicting treatment response. This was near significant for the median and 75th percentile values with p-values 0.071 and 0.057. For $fWOR$- and AUC_{fWO}-metrics, the baseline values did not show discriminative ability.

The analysis also assessed the predictive power of $iWIR$ changes at 2-weeks post-RT. Among the 12 patients included (7 responders and 5 non-responders), the ROC analysis yielded an AUC of 0.76 for the median $iWIR$ change, indicating moderate predictive ability; however, this was not statistically significant with a p-value of 0.154. The 75th percentile of $iWIR$ changes

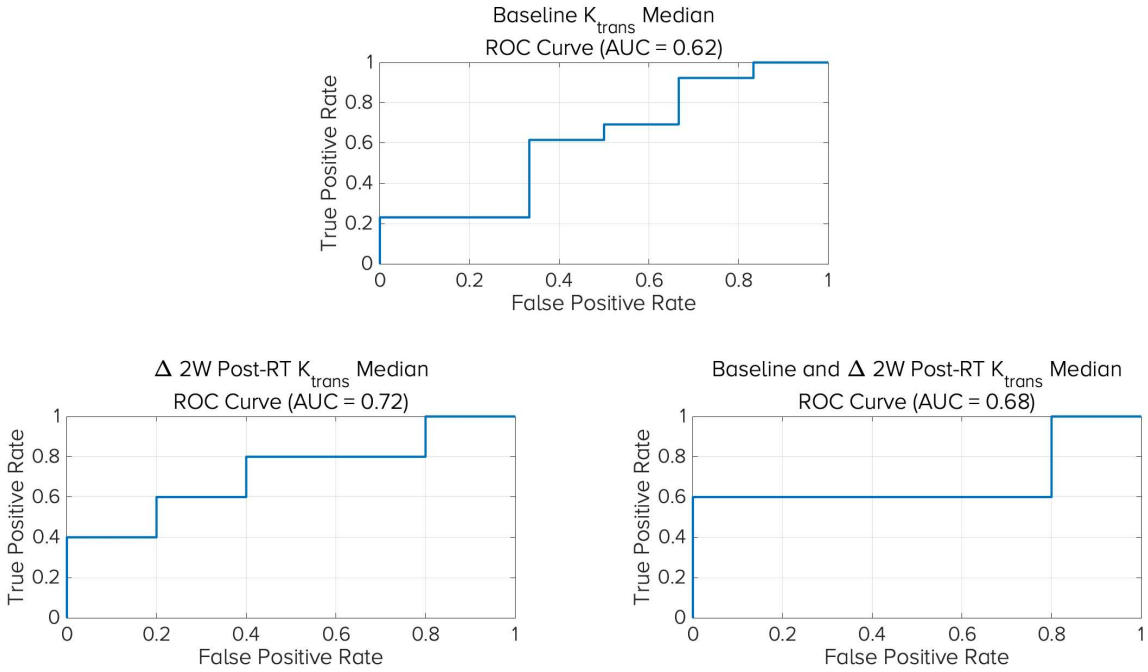


Figure 5.31: Receiver Operating Characteristic (ROC) curve depicting the true positive rate (sensitivity) against the false positive rate (1-specificity) in predicting responders versus non-responders at 12-months post-radiotherapy. For (top) the median baseline K_{trans} values from the Tofts model of dynamic contrast-enhanced MRI, the area under the curve (AUC) is 0.62 with a p-value of 0.331. For (bottom left) the median K_{trans} changes at 2-weeks post-radiotherapy, the AUC is also 0.72 with a p-value of 0.358. For (bottom right) the combination of the two, the AUC is 0.68 with a p-value of 0.613.

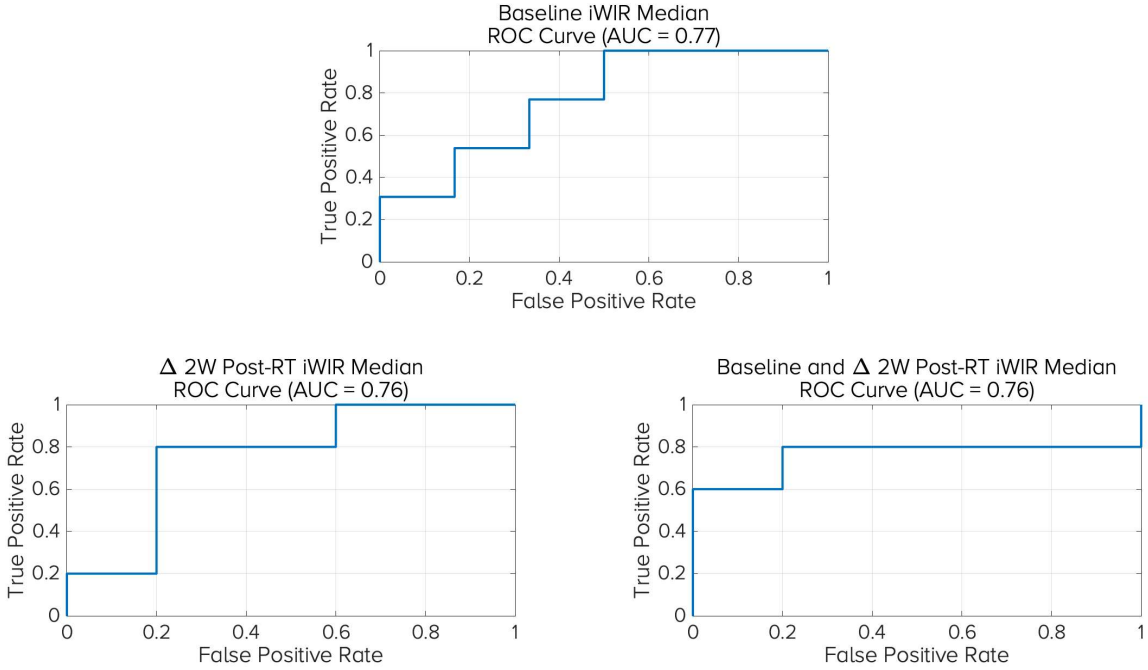


Figure 5.32: Receiver Operating Characteristic (ROC) curve depicting the true positive rate (sensitivity) against the false positive rate (1-specificity) in predicting responders versus non-responders at 12-months post-radiotherapy. For (top) the median baseline $iWIR$ values from the Tofts model of dynamic contrast-enhanced MRI, the area under the curve (AUC) is 0.77 with a p-value of 0.071. For (bottom left) the median $iWIR$ changes at 2-weeks post-radiotherapy, the AUC is 0.76 with a p-value of 0.154. For (bottom right) the combination of the two, the AUC is 0.76 with a p-value of 0.258.

demonstrated the highest discriminative ability, with an AUC of 0.80 and a near-significant p-value of 0.063, indicating that changes in the upper quartile may better differentiate responders from non-responders. The change at 2-weeks post-RT for the 25th percentile of $fWOR$ and the 75th percentile of AUC_{fWO} showed moderate predictive power (AUC = 0.76/0.72), however this was non-significant (p-value = 0.190/0.183).

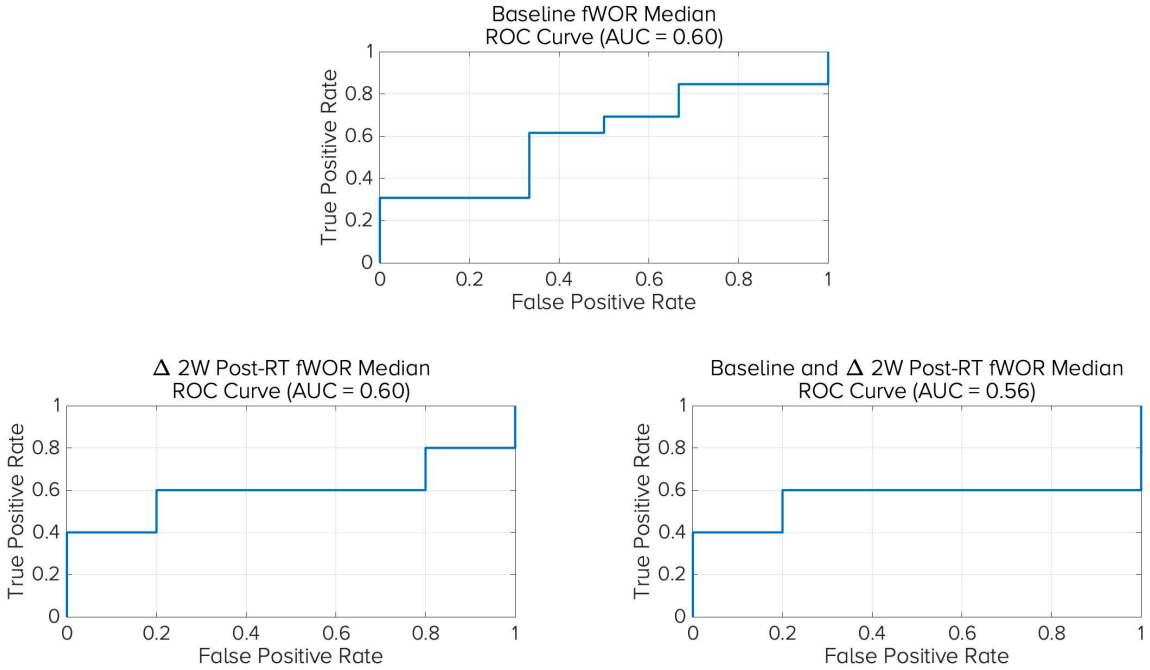


Figure 5.33: Receiver Operating Characteristic (ROC) curve depicting the true positive rate (sensitivity) against the false positive rate (1-specificity) in predicting responders versus non-responders at 12-months post-radiotherapy. For (top) the median baseline $fWOR$ values from the Tofts model of dynamic contrast-enhanced MRI, the area under the curve (AUC) is 0.60 with a p-value of 0.372. For (bottom left) the median $fWOR$ changes at 2-weeks post-radiotherapy, the AUC is 0.60 with a p-value of 0.587. For (bottom right) the combination of the two, the AUC is 0.56 with a p-value of 0.634.

The analysis further evaluated the predictive power of combining baseline $iWIR$ values with $iWIR$ changes at 2-weeks post-RT to predict patient response at 12-months. Among the 12 patients included (7 responders and 5 non-responders), the area under the curve (AUC) was calculated at 0.76 for the median ADC value 0.80 for the 75th percentile, indicating moderate discriminative ability, although these were not significant (p-value = 0.258/0.123). There was moderate predictive ability for the combination of baseline and 2-week post-RT changes for the 25th percentile and 75th percentile $fWOR$ (AUC = 0.80/0.80; p = 0.369/0.125) and median and 75th percentile AUC_{fWO} (AUC = 0.72/0.76; p = 0.364/0.251), however this was non-significant.

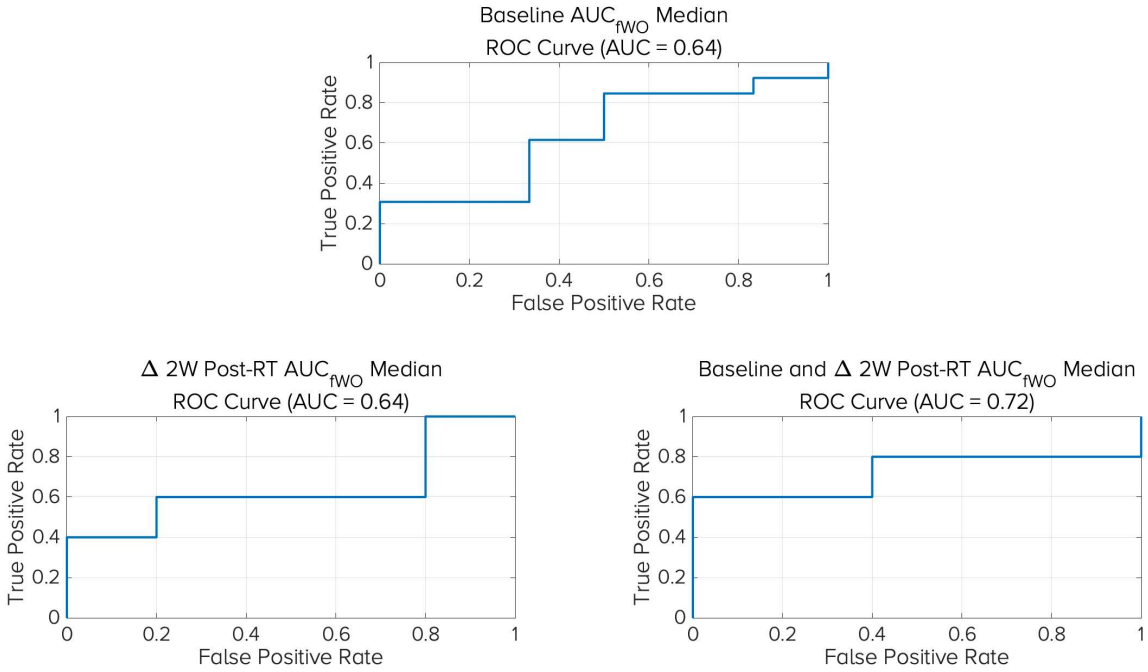


Figure 5.34: Receiver Operating Characteristic (ROC) curve depicting the true positive rate (sensitivity) against the false positive rate (1-specificity) in predicting responders versus non-responders at 12-months post-radiotherapy. For (top) the median baseline AUC_{fWO} values from the Tofts model of dynamic contrast-enhanced MRI, the area under the curve (AUC) is 0.64 with a p-value of 0.418. For (bottom left) the median AUC_{fWO} changes at 2-weeks post-radiotherapy, the AUC is 0.64 with a p-value of 0.272. For (bottom right) the combination of the two, the AUC is 0.72 with a p-value of 0.364.

5.3 SRUS and MRI Comparative Analysis

The correlation heatmap in Figure 5.35 explores the relationships among all the assessed parameters from super-resolution ultrasound imaging, diffusion-weighted (DW) MRI and DCE-MRI. Data from each time point are included, capturing absolute relationships and changes due to therapeutic intervention.

Notably, there is a moderate negative correlation between ADC and K_{trans}, $iWIR$, and AUC_{fWO}. This reflects the observed trend over time following RT, where both an increase in ADC, and a decrease in enhancement parameters occur, suggesting reduced cellularity and vascular disruption. However, there is no apparent correlation between ADC and v_e despite their association with similar physiological factors. This discrepancy is likely due to the unreliability of v_e, which requires substantial contrast leakage for accurate estimation.

Strong correlations are observed among the DCE-MRI parameters, especially between K_{trans}, $iWIR$, and AUC_{fWO}, and v_p and $iWIR$. This is expected, given their role in capturing related physiological effects.

Interestingly, a moderate positive correlation is noted between SRUS vessel density and K_{trans} and v_p, indicating that these metrics may reflect similar vascular characteristics. Additionally, SRUS distance to the nearest vessel shows a moderate negative correlation with $iWIR$ and AUC_{fWO}, and fractal dimension has a moderate positive correlation with K_{trans} and $iWIR$, further supporting their association with vascular disruption.

.

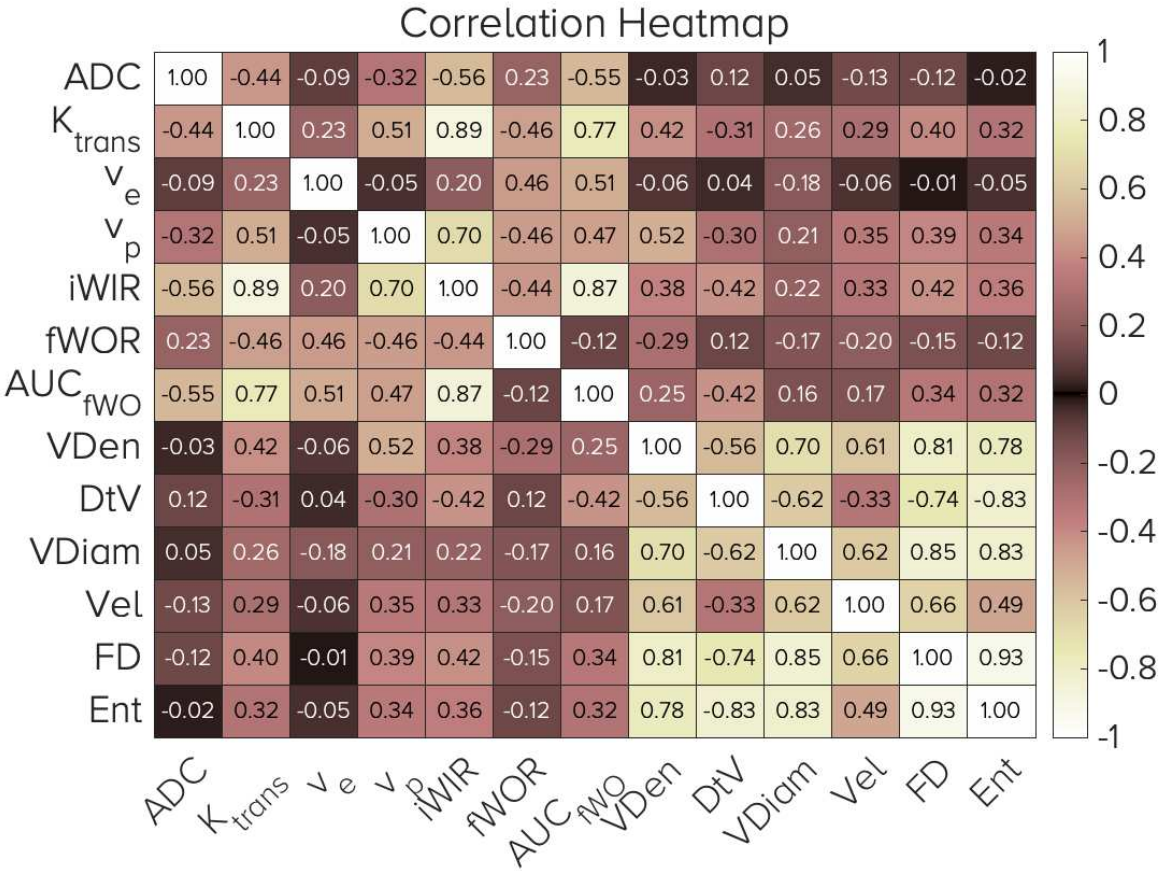


Figure 5.35: A heat map showing the correlation coefficients R between all of the investigated super-resolution ultrasound (VDen: Vessel Density; DtV: Distance to Vessel; VDiam: Vessel Diameter; Vel: Blood Velocity; FD: Fractal Dimension; Ent: Blood Flow Direction Entropy), diffusion-weighted MRI (Mono-exponential Model: ADC), and dynamic contrast-enhanced MRI (Tofts Model: K_{trans}, v_e, v_p; Semi-Quantitative: $iWIR$, $fWOR$, AUC_{fWO}) parameters, where R=1 is perfect positive linear correlation, R=-1 is perfect negative linear correlation, and R=0 is no linear correlation.

Chapter 6

Discussion

This study is the first to utilise quantitative diffusion-weighted (DW) MRI, dynamic contrast-enhanced (DCE) MRI, and super-resolution ultrasound (SRUS) to evaluate the long-term response of breast tumours to radiotherapy. Most radiotherapy research of primary breast tumours has focused on early-stage, low-risk breast cancer, often employing stereotactic ablative radiotherapy (SABR) to shrink tumours before surgery [187, 200, 225, 226], which has restricted imaging follow-up to a maximum of six months. Consequently, there has been limited investigation into the long-term effects of radiotherapy on in situ breast cancer, particularly its physiological impacts.

These limitations were addressed by quantifying post-radiotherapy changes in locally advanced and recurrent breast cancer up to 24 months post-treatment. This extended follow-up provides a unique opportunity to assess long-term physiological responses whilst also identifying the quantitative parameters that are most sensitive to detecting early post-treatment changes.

This study also aimed to identify early prognostic biomarkers, to enable timely adaptation of treatment strategies for improved clinical outcomes. To achieve this, pre-treatment values and changes 2-weeks post-radiotherapy were investigated.

Participants were categorised into responders and non-responders, with partial and complete responders combined to account for small sample sizes, albeit at the cost of reduced granularity in the analysis. A limitation of this study was the inability to assess pathological response, as no tumour resection was performed.

The data for this study were obtained from the randomised KORTUC Phase 2 clinical trial, in which participants underwent a standard course of radiotherapy to the whole breast, with or without the addition of the hydrogen peroxide-based radiosensitiser KORTUC. The radiotherapy regimen included either a total dose of 36 Gy, or 49.5 Gy with a maximum boost of 13.75 Gy. Of the 64 participants included in this thesis, only 7 received the 49.5+ Gy regimen. The administration of KORTUC was blinded, as the trial was ongoing and not scheduled to finish until 2027.

Evaluating the test-retest repeatability of quantitative parameters is crucial for clinical translation [227]. This study investigated the repeatability of SRUS, DW-MRI, and DCE-MRI in the clinical assessment of breast cancer. To our knowledge, the repeatability of SRUS has not been previously established in the literature, and it remains under-explored for DCE-MRI. Thus, this study contributes significantly to the validation of these modalities as reliable tools for clinical evaluation.

Finally, the quantitative parameters obtained from the three imaging techniques were analysed to evaluate their inter-relationships.

6.1 Super Resolution Ultrasound

The exceptional resolution and detail of microvasculature provided by super-resolution ultrasound (SRUS) offer potential for non-invasive detection of therapy-induced changes. For clinical translation, establishing SRUS's repeatability and sensitivity to post-treatment changes is crucial. Our study identified repeatable biomarkers of tumour microvasculature that are potentially sensitive to early biological changes following radiotherapy (RT).

A robust multi-plane imaging protocol was investigated to capture tumour heterogeneity, as single imaging planes are not representative of the entire tumour. Our study demonstrated that the repeatability of SRUS-derived quantitative parameters improved with the incorporation of more imaging planes, as this reduced within-subject variability. These findings suggest that averaging across multiple imaging planes yields more repeatable and representative quantitative parameters. Adequately sampling the tumour is also crucial for response monitoring, as tumour

morphology changes post-therapy, making it challenging to return to the same imaging plane.

To the best of our knowledge, no previous studies have examined SRUS repeatability in breast cancer. Related research on dynamic contrast-enhanced ultrasound imaging [248, 249] has shown that perfusion parameters from a single plane lacked repeatability, and incorporating more planes improved it. The resolution of such images are diffraction-limited, so bulk tissue is assessed rather than individual micro-vessels.

Changes in quantitative parameters were observed following radiotherapy. For vessel density, 5 out of 15 participants exhibited a decrease beyond the repeatability coefficient (RC) by 2-weeks post-RT. Participants with baseline values above the healthy range approached the healthy range following radiotherapy, with the highest baseline vessel densities showing the largest decreases. The progressive disease (PD) participants had no vessel density change beyond the RC across post-treatment time-points. Furthermore, the PD participants were those within or closest to the healthy range of vessel density heterogeneity values and decreased less following radiotherapy in comparison to responders.

For vessel diameter, 6 out of 15 participants showed a decrease beyond the RC by 2-weeks post-RT. Participants with baseline values at or above the upper limit of the healthy range tended to show reductions in vessel diameter, approaching or falling within the healthy range. In contrast, PD participants either showed no significant changes over time or a significant increase by 6-months post-RT. By 12-months post-RT, PD participants had higher vessel diameters compared to responders.

For blood velocity, 9 out of 15 participants demonstrated a decrease beyond the RC by 2-weeks or 6-months post-RT, followed by stabilisation at later time-points. Initial blood velocities were within the healthy range but decreased beyond it over time.

Additionally, blood flow direction entropy (3 out of 15 participants) and fractal dimension (4 out of 15 participants) showed reductions beyond the RC by 2-weeks post-RT, trending toward and falling within the healthy range. PD participants had baseline values close to the healthy range and no change beyond the RC at 2-weeks post-RT, in contrast to responders who had higher baseline values and decreases at 2-weeks post-RT.

A limitation of SRUS was identified for patients with very low vessel density values. Over the

post-radiotherapy time-points, changes in the microvasculature could not be reliably observed due to the already low baseline values. Interestingly, the three participants with the least vasculature exhibited a mixture of outcomes, including complete response, partial response, and progressive disease, indicating that vessel density did not hold prognostic value in these cases. These participants displayed more complex trends in SRUS quantitative parameters, such as blood velocity and blood flow direction entropy. This complexity may be attributed to the reduced number of microbubbles available for averaging, making the measurements more susceptible to noise.

To our knowledge, this is the first evaluation of SRUS-derived biomarkers in response to radiotherapy. Acoustic angiography, a contrast-enhanced, high-resolution ultrasound microvascular imaging modality, detected vascular changes earlier than changes in tumour size during the onset of recurrence in pre-clinical models [250]. Similarly, other imaging techniques, such as optoacoustic imaging [251] and optical coherence tomography [252], have observed reductions in microvessel density following tumour irradiation and subsequent revascularisation during recurrence, prior to any changes in tumour size. The destruction of the disordered microvasculature aligns with a decrease in local flow direction entropy and fractal dimension.

A microvasculature model revealed radiation-induced contraction of microvessels [253]. Additionally, in vivo micro-endoscopy [254] detected significant decreases in blood flow speed following radiotherapy. Although these techniques validate our clinical findings, they are limited by shallow penetration depth and are predominately used in pre-clinical studies. Distance to the nearest vessel was also investigated as a potential indicator of radiotherapy response. However, this parameter showed minimal significant changes at 6-months among the participants, indicating that it was not an effective parameter for response monitoring.

Although no significant statistical differences were observed between the SRUS-derived quantitative parameters of healthy breast tissue and breast tumours, this result is likely due to the substantial inter-patient variability in breast tumour characteristics. Tumour values span a wide range, often overlapping with, falling below, or exceeding the healthy range. In contrast, the parameters for healthy tissue exhibit much less variability. Values outside the healthy range may be indicative of tumours, while values within the healthy range present challenges in

reliably distinguishing between tumours and healthy tissue. Acoustic angiography also revealed higher vascular densities and larger inter-patient variabilities in tumours compared to healthy tissue and overlap between the tumour and control groups [255].

SRUS bridges the gap between histopathological analysis and *in vivo* imaging, providing a clinically relevant field of view. Baseline SRUS-derived vessel density and CD31 vessel count from immunohistochemical staining showed a moderate, positive correlation ($\rho = 0.494$), though the association was non-significant ($p = 0.147$). For absolute values and changes at 2-weeks post-RT, the correlation was weak. Therefore, although SRUS vessel density and CD31 vessel count both reflect tumour vascularity, they did not significantly correlate.

Discrepancies may arise due to differences in sampling area: immunohistochemical staining sections cover millimetre-scale dimensions, while SRUS provides a wider field of view with centimetre-scale dimensions. By imaging multiple planes, SRUS captures the heterogeneity of large breast tumours.

In breast tumours, it is possible for blood vessels to form without endothelial cells, and therefore lack expression of endothelial markers such as CD31. Instead, these vessels are lined by tumour cells with cancer stem cell features, a phenomenon known as vasculogenic mimicry [256]. Despite the absence of endothelial cells, these structures are functional and capable of perfusion, resembling tumour vasculature formed through angiogenesis.

Additionally, CD31 staining does not distinguish between viable and non-functional blood vessels, whereas SRUS visualises only functional vessels. However, some viable blood vessels might be undetected by SRUS. Solid tumours can experience acute or cyclic hypoxia due to intermittent blood flow, which can occur over minutes, a time-scale relevant to our repeatability study. Although not assessed in this study, SRUS could potentially investigate such time-varying hypoxia. SRUS might also miss the smallest blood vessels during imaging because microbubbles are less likely to pass through them within the short acquisition time. Other biological variations, such as heart-rate, could affect microbubble concentration and blood flow speed, but these variations should be minimal in a resting position.

Technical factors also impact the SRUS quantitative parameters. Hardware constraints led to a trade-off between compounded frame-rate, acquisition length, and the number of

compounded angles due to data collection limits per acquisition. While longer acquisitions can improve parameter robustness, such as vessel diameter, by increasing vascular saturation, they also pose challenges, such as greater motion artefacts, necessitating customised setups to fix the probe. A fixed probe, though, limits the flexibility needed to quickly locate the tumour's central slice when moving between imaging planes and does not mitigate patient motion. Moreover, extended acquisition times mean that later imaging planes are captured further from the concentration peak. Higher frame-rates improve tracking capabilities for estimating blood flow speed and direction, and future work will investigate the impact of frame-rate on SRUS quantitative parameters. Nevertheless, our study's acquisition time and frame-rate were sufficient for detecting post-therapy changes in SRUS quantitative parameters.

The motion correction algorithm rectified global tissue motion; however, further evaluation of its accuracy is necessary to ensure motion is corrected at the micron scale. This precision is essential to maintain proper alignment of blood vessels across acquisition frames. Inadequate motion correction could result in motion blur, artificially enlarging the blood vessels, or could even cause the blood vessel to split.

Microbubble tracking accuracy could influence blood flow speed and flow direction parameters, where accuracy may be reduced in denser microvasculature or larger, fast-flowing blood vessels. Further development and benchmarking in SRUS localisation and tracking algorithms, which was the aim of a recent international challenge [257], and standardisation of imaging protocols, such as dose and time of contrast injection for optimal and consistent distribution of microbubbles [258, 259], will increase quantitative parameter robustness.

Statistical limitations include the use of the same participants at multiple time-points. The repeatability scans from the same participants were treated as independent data-points in the statistical analysis due to the length of time between separate repeatability scans and the post-treatment changes that occurred over that time. Additionally, repeatability studies are typically conducted on pre-treatment tumours; however, we also wanted to assess repeatability post-treatment. Based on the Bland-Altman plots, there was no significant evidence suggesting that repeatability varied across different imaging time points.

Typically, repeatability studies for medical imaging technologies involve conducting repeat

scans on different days. However, this study was limited to a single imaging session. Before administering the second bolus, microbubble concentration must diminish to negligible levels. Any residual circulating microbubbles could increase the concentration of the second bolus and impact concentration-sensitive parameters. Before injecting the second bolus, the clearance of the first bolus was visually confirmed on the real-time feedback. A 5-minute interval between bolus injections allowed for the microvasculature to clear. For future work assessing the repeatability of SRUS, if possible, we would advise having repeatability scans on separate days. However, a test-retest repeatability study of Apparent Diffusion Coefficient (ADC) from diffusion-weighted MRI in breast cancer [170] employed a similar 'coffee break' approach, with scans conducted on the same day and included both baseline and mid-treatment scans.

The tumours in this study were imaged in four central planes (horizontal, 90°, 45° clockwise, and 45° anticlockwise). However, this approach oversamples the tumour centre while under-sampling the edges, where poor core perfusion and high peripheral perfusion are more clinically significant. Progressive disease was often marked by new nodes, possibly outside the ultrasound field of view, highlighting the limitations of 2D imaging.

A 3D volume acquisition would better capture tumour heterogeneity and vascular complexity, as it captures vessels traversing the imaging plane. While capturing parallel slices is an alternative, maintaining consistency across time points (e.g., slice spacing) poses challenges. Advanced setups like motorised sweeps could address this [127]. The number of imaging planes is constrained by the decreasing microbubble concentration over time following contrast bolus injection. In this study, four imaging planes were acquired before microbubble concentration became insufficient. Maintaining consistent contrast concentration throughout imaging is a critical consideration for improving quantitative parameter reliability across planes.

Toward the study's conclusion, a 3D row-column array was introduced for comparison with 2D imaging. However, its limited field of view remains a drawback, as it may not encompass the entire tumour. 3D imaging would enhance the accuracy of quantitative parameters and enable the investigation of parameters not explored in this study, such as tortuosity. Tortuosity is challenging to quantify in 2D, as the vessels traverse in and out of the plane, complicating their segmentation for tortuosity measurement.

Contrast-enhanced ultrasound with SonoVue is clinically licensed for diagnosing liver metastases, coronary artery disease and vesicoureteral reflux, and is a cost-effective, safe, bedside imaging modality. SRUS inherits these advantages and holds the potential for seamless clinical translation. The breast tumour is an ideal candidate for SRUS imaging due to its increased stiffness, which minimises tissue motion, its shallow depth, and the presence of vascular abnormalities and altered perfusion. Only a few scans in this study were discarded due to image artefacts, which predominantly appeared in healthy breast scans. These artefacts were primarily caused by tissue motion or bright reflections that obscured microbubble visualisation.

Standardisation is crucial for clinical adoption. A standardised protocol and user-friendly software are essential for SRUS to be effectively employed in therapy response monitoring. Although this study utilised a research ultrasound machine, other studies have demonstrated the feasibility of using standard clinical ultrasound devices [148]. To address the lower frame rates of clinical systems, advanced tracking algorithms have been developed [131, 260]. Future advancements in clinical ultrasound technology, such as faster frame-rates and integrated post-processing capabilities, are expected to further enhance the clinical translation of SRUS. The motion correction step was a significant bottleneck, requiring approximately 2.5 hours to process 500 frames. Similarly, localisation could take up to 3 hours, particularly in cases with a high density of microbubbles. Improvements in software, such as the integration of deep learning techniques, could substantially reduce these processing times, improving clinical viability.

A promising direction for SRUS is its integration with radiomics [261]. Radiomics would extract high-dimensional quantitative features from SRUS imaging data, which could be applied for disease identification, prediction, and response monitoring.

While validated here in breast tumours, SRUS repeatability must be established for other tumours, and its potential in clinically monitoring microvasculature changes to other anti-cancer therapies, which has been investigated pre-clinically [262–265]. This study only explored intra-operator variability; investigating inter-operator variability and conducting multi-centre studies will further establish the repeatability and reproducibility of SRUS.

This first-in-patient repeatability study demonstrates that super-resolution ultrasound (SRUS) provides robust biomarkers for quantifying tumour microvasculature structure and blood flow

dynamics. These repeatable SRUS-derived quantitative parameters are potentially sensitive to early vascular changes. SRUS provides an abundance of information on vascular structure and critical functional metrics, such as blood velocity and direction, with superior resolution. This highlights its clinical significance and advantages over other imaging modalities. The results of this study are encouraging, showcasing SRUS's potential as an affordable, non-invasive monitoring tool. Although there appeared to be potential differences in baseline values and trends of SRUS parameters between responders and non-responders, the small dataset (only 5 responders and 3 non-responders) limited a comprehensive evaluation of SRUS's prognostic potential.

6.2 Diffusion-Weighted MRI

Diffusion-Weighted (DW) MRI has established itself as an indispensable imaging tool for diagnosing cancer and monitoring tumour response to therapy. Its non-invasive nature and ability to assess tumour microstructure underscores its clinical utility. Quantitative parameters, especially the apparent diffusion coefficient (ADC) derived, provide valuable insights into breast tumour properties.

6.2.1 Repeatability and Sensitivity

From the mono-exponential model, ADC-metrics, including the 25th percentile, median, and 75th percentile, demonstrated excellent repeatability. High Intraclass Correlation Coefficients (ICCs: 0.94−0.96) and low within-subject Coefficients of Variation (wCV: 4.8−5.5%) indicate high reliability. Similarly, in other clinical breast cancer studies, ADC and its statistics have exhibited excellent repeatability, with wCV mostly under 10% across studies and ICCs greater than 0.9 [168–171]

Significant increases in the ADC-metrics were observed in the majority of participants at 2-weeks post-RT (73.5−79.4%) and peaking at 6-months post-RT (84.2−89.5%), demonstrating the high sensitivity of ADC-metrics to early and sustained post-treatment changes.

From the stretched exponential model, DDC-metrics exhibited similarly high ICCs (0.90−0.94) but slightly greater wCV values (8.2−10.1%) in comparison to ADC. This was in agreement

with wCV assessed in benign breast lesions (9.5%) [174]. Fewer participants showed significant increases in the DDC-metrics at early time points (2-weeks post-RT: 47.1−70.6%; 6-months post-RT: 73.7−81.6%) compared to ADC, indicating lower sensitivity to significant change and greater sensitivity to noise or imaging conditions. For both ADC and DDC, the interquartile range was less reliable and less sensitive to change.

The heterogeneity index (α) showed poor ICCs (−0.12−0.20) despite low wCV values (8.1−10.3%), which was also in agreement with wCV assessed in benign breast lesions (11.8%) [174]. This combination implies consistent within-subject measurements but minimal variability between subjects, which limits its ability to capture meaningful heterogeneity among participants. Although large RCs (0.17−0.25) indicate that only substantial changes in α are reliable; these high values may stem from inconsistent signal decay patterns within some participants. The majority of participants had no significant change (81.0−100% across metrics and time-points), suggesting low sensitivity to treatment-induced variations. α might be sensitive to choice of b-values, which might influence its repeatability. The b-values in this study were chosen based on prior literature and experience within the group.

Further complicating the interpretation of α is its clinical significance and ambiguity [266]. α may capture multiple underlying processes, such as perfusion and kurtosis, which can change independently or in opposition. These overlapping diffusion characteristics may obscure each other without reference to specific microstructural properties.

The findings suggest that the mono-exponential model is more robust and sensitive to treatment-induced changes than the stretched exponential model, with greater potential for utility in small-scale studies or routine clinical practice. To strengthen these preliminary results and statistical power, larger cohorts are crucial.

6.2.2 Predictive and Longitudinal Trends

For the overall post-radiotherapy trend, ADC-metrics increased significantly from baseline to 2-weeks, 6-, 12- and 24-months post-RT. The treatment effect is likely due to reduced tumour cellularity after cell death. Responders demonstrated significant increases in ADC values at all post-RT time points, with trends mirroring the overall cohort. Notably, the increase was most

pronounced at 6 months. ADC values remained elevated at 24 months, reflecting a long-term positive treatment response. Significant differences in ADC metrics were observed between baseline and all time points for all participants and responders ($p < 0.001$ to $p < 0.05$).

Across all participants and responders, ADC values decrease from 6-months to 12-months post-RT. In responders, late reductions in ADC may result from radiation-induced fibrosis or scarring [267], which typically exhibit low ADC values due to densely packed collagen fibres and inflammatory infiltrates. However, these values are generally higher than those associated with residual disease or recurrence [268, 269], though some studies have reported challenges in establishing a definitive cut-off [270].

Non-responders (progressive disease participants at 12-months) exhibited a less pronounced increase in ADC values at early time points, with significant changes observed only at 6- and 12-months post-RT. By 12- and 24-months, ADC values approached and returned to baseline levels, indicating transient treatment effects followed by tumour recurrence or progression.

The sustained increase in ADC values among responders supports the utility of ADC as a biomarker for treatment response. The transient changes in non-responders suggest that post-treatment ADC helps identify patients who require additional or alternative therapeutic strategies. This analysis underscores the importance of longitudinal ADC monitoring to evaluate tumour dynamics and optimise patient outcomes.

Although responders exhibited lower pre-treatment values of ADC-metrics (median: 1.01 ± 0.26) compared to non-responders (median: 1.12 ± 0.23), these differences were not statistically significant ($p = 0.17$), indicating that baseline ADC values alone may not reliably predict response.

The correlation between higher pre-treatment ADC values and non-responders is biologically plausible, as elevated ADC is often associated with necrotic and hypoxic regions. These poorly perfused areas are linked to more radioresistant and aggressive tumours, which tend to exhibit poorer responses to radiation therapy [267].

Numerous studies have investigated whether pre-treatment ADC values can predict the pathological complete response (pCR) of breast cancer to treatment, with mixed results [185]. For neoadjuvant chemotherapy, a meta-analysis revealed that the pooled pre-treatment mean

ADC value of responders (0.98: 95% CI = [0.94, 1.03]) was lower than that of non-responders (1.05: 95% CI = [1.00, 1.10]) [185]. However, significant overlap between the two groups suggests that ADC alone is insufficient for predicting pCR. However, for a study investigating breast cancer after neoadjuvant radiation, pathological responders exhibited higher median ADC values (0.87 [0.82-1.07]) compared to non-responders (0.77 [0.61-1.15]) [187].

Similarly, systematic reviews on other cancers, such as oesophageal and head and neck cancer, have reported inconsistent results when evaluating ADC as a predictive marker following chemo- and/or radiotherapy [271, 272]. In colorectal cancer, pooled data showed lower pre-treatment ADC values in responders compared to non-responders, but the differences were not statistically significant [273].

Responders generally exhibited lower pre-RT ADC values and larger changes 2-weeks post-RT. Non-responders, apart from one outlier, tended to have higher pre-RT ADC values and smaller changes 2-weeks post-RT. ADC values in responders increased significantly 2-weeks post-RT, while non-responders did not show a significant change. Although the difference in early ADC changes between responders and non-responders was not statistically significant (p = 0.152), the trend suggests early changes may be predictive of overall response. Furthermore, the 75th percentile of ADC changes at 2-weeks post-RT demonstrated moderate predictive power, with an AUC of 0.83 and a p-value of 0.053. This suggests that larger changes in the upper quartile may provide better differentiation between responders and non-responders.

For a study investigating breast cancer after neoadjuvant radiation therapy [187], pathological responders demonstrated a greater increase in ADC (33%) at 1-week post-treatment compared to non-responders (23%). In colorectal cancer, pooled data revealed significantly higher post-treatment ADC values and greater post-treatment ADC changes in responders compared to non-responders after neoadjuvant chemoradiation - post-treatment timings ranged from 4 to 12 weeks [273]. Similarly, in head and neck cancer, participants with locoregional failure exhibited smaller increases in ADC, observed either one to three weeks after the start of chemoradiation or three weeks after its completion [271].

These findings highlight the potential of ADC metrics as biomarkers for stratifying patients based on their likelihood of long-term response to radiotherapy, emphasising the importance

of early post-RT measurements to assess radiotherapy sensitivity. Further studies with larger sample sizes are required to validate these observations and refine their predictive utility.

The ADC-metrics showed significant overlap across response categories, making it challenging to distinguish between them based on these values alone. However, changes in ADC metrics from baseline provided some separation between response groups, particularly between complete response (CR) and progressive disease (PD), indicating that greater increases in ADC values correlate with better treatment outcomes. Nevertheless, substantial overlap between partial response (PR) and other categories, including stable disease (SD), complicates the establishment of reliable cut-off values for determining response categories. Radiological response assessment was predominantly influenced by DCE-MRI rather than DW-MRI.

While these trends are promising, ADC alone may be insufficient for accurately predicting treatment response in cases of locally advanced breast cancer. Further investigation into combination with other imaging metrics and covariates could enhance predictive modelling.

6.2.3 Breast Cancer Subtype Analysis

Median ADC values were higher at baseline in more aggressive subtypes HER2+ and Triple Negative subtypes compared to hormone receptor-positive subtypes Luminal A and Luminal B. Despite these trends, the differences in ADC metrics were not statistically significant (p = 0.3199, 0.2852, and 0.4856, respectively). Significant overlap in ADC metrics was observed among the subtypes, particularly for Luminal A, which exhibited a wide spread of values. This overlap complicates subtype differentiation based on ADC metrics alone. The small number of participants in certain subtypes (e.g., HER2+ [$n = 4$] and TN [$n = 8$]) limits the ability to draw definitive conclusions about the relationship between ADC metrics and molecular subtypes.

The assumption that ADC-based metrics reliably characterise tumour receptor status and subtypes has been challenged. Large systematic studies [189, 274] found no significant differences in ADC values across breast cancer molecular subtypes, questioning the utility of ADC to discriminate between molecular subtypes. However, ADC-based radiomic features, which go beyond simple ADC measurements and histogram analysis by incorporating textural and spatial information from ADC maps, show potential for tumour phenotyping and could provide

more comprehensive tumour characterisation than traditional biopsy, with enhanced repeatability and reproducibility [275]. Techniques such as radiomics allow for the extraction of complex patterns from ADC maps, offering a more nuanced understanding of tumour heterogeneity and potentially superior predictions of treatment response non-invasively. Further investigation into combination with other imaging metrics and covariates could improve subtype characterisation.

6.2.4 Technical Considerations and Limitations

Several technical and biological factors complicate the clinical application of DW-MRI. Metrics derived from breast imaging are susceptible to errors caused by patient movement, respiratory motion, and cardiac pulsation. These sources of motion can introduce alignment issues, potentially impacting parameter calculations and leading to unreliable estimates [276]. In our 3 T data-set, we observed misalignments across b-values for some participant scans, including bulk shifts with increasing b-values. These distortions are likely attributable to eddy current-induced geometric artefacts common in echo planar imaging sequences [277]. For this study, diffusion images were manually aligned for quantitative parameter estimation. Future studies should incorporate motion-correction techniques to mitigate these errors for more accurate and robust parameter calculations [276].

The repeatability and reproducibility of ADC measurements in clinical practice are strongly influenced by the imaging protocols used. Standardising acquisition parameters such as b-value selection is essential, as variations in b-value ranges and numbers can alter ADC readings, compromise repeatability, and hinder its clinical applicability as an imaging biomarker. Guidelines from the European Society of Breast Radiology (EUSOBI) [278] and Quantitative Imaging Biomarker Alliance (QIBA) [279] emphasise the importance of consensus on acquisition settings. They recommend using at least two b-values, including 0 and 800 s/mm^2, with additional b-values further enhancing measurement robustness. Our study was conducted in compliance with these guidelines.

However, studies suggest that using as low as two b-values maintain repeatability, though a high b-value remains essential for accurately probing tissue diffusion [280]. This study only compared 2 with 4 b-values, whereas our study used 14 b-values. Determining the optimal

set of b-values for accurate estimation of ADC could be explored in future. By reducing b-values, efforts can be focused on improving resolution and signal-to-noise ratio, for instance, by performing multiple averages instead of the single average used in this study. Many b-values were used to explore the potential of advanced DW modelling techniques, such as the stretched exponential model and to probe perfusion effects at low b-values.

Assessing repeatability and reproducibility across different sites remains a significant challenge. Even with centralised quality control, site-specific acquisition variations exist. In this multi-site study, variations were observed in scanner models, field strength, and imaging parameters, including repetition time (TR), echo time (TE) and pixel spacing. However, our findings indicate that the multi-centre repeatability of ADC measurements was consistent with single-site results. There is a lack of research on how varying imaging parameters impact ADC calculations for breast tumours, with most studies using phantoms [281–283]. While some studies have shown reproducible ADC measurements across MRI scanners from different vendors, others have not [282, 283]. Additionally, differences have been noted across sequences [282]. Therefore, further investigation into the impact of parameters such as TR, TE, and pixel spacing on ADC stability in breast tumours is essential, as this will influence the reliability of ADC values. EUSOBI and QIBA advocate for standardised acquisition and analysis methods to ensure diffusion measurements remain reliable imaging biomarkers.

Technological improvements, such as higher magnetic field strengths and optimised acquisition and reconstruction algorithms, have enhanced image resolution and signal-to-noise ratios, minimising distortions, artefacts and acquisition times [284].

6.2.5 Other DW-MRI Techniques

ADC alone may not capture the full complexity of breast tumour microstructure, as diffusion in tissue is often non-Gaussian. Diffusion Kurtosis Imaging (DKI) and bi-exponential diffusion models address this by considering non-Gaussian diffusion. These are particularly useful for characterising intracellular microstructure and highly vascularised tumours as perfusion is non-Gaussian. DKI and other multi-exponential approaches often require higher b-values (above 1500 s/mm^2) to effectively characterise non-Gaussian diffusion and tissue microstructure, lim-

iting their applicability due to greater susceptibility to noise. Furthermore, DKI parameters do not show superior diagnostic performance to ADC to discriminate breast tumours [285]. Models incorporating pseudo-diffusion parameters (bi-exponential model with D$*$ and f) have shown limited diagnostic robustness, low signal-to-noise ratios and poor measurement reproducibility [178], although D was shown to improve diagnostic performance compared to ADC [178]. These parameters rely on low b-values; however, it is difficult to get good-quality data as signal measurements are noisier due to pulsatile motion in larger vessels. No advanced models of diffusion have bypassed ADC in terms of diagnostic performance [286].

Other advanced techniques include VERDICT MRI (vascular, extracellular, and restricted diffusion for cytometry in tumours), which offers the ability to extract detailed information such as cell size, vascular volume fraction, intracellular and extracellular volume fractions, and pseudo-diffusion/perfusion [287]. This approach has shown promise in outperforming traditional ADC and bi-exponential modelling techniques while providing improved correlation with histological findings. Additionally, diffusion tensor imaging (DTI) provides insights into structural orientation and the degree of anisotropy by analysing diffusion directionality, which requires acquiring images along multiple gradient directions [288]. The relevance of DTI in breast cancer management is subject to discussion [289].

Here, we conducted histogram-based analyses; however, future research could explore distinct sub-regions of ADC within tumours and further assess heterogeneity using techniques such as fractal analysis and radiomics [290]. These approaches may enhance predictive accuracy and improve response monitoring capabilities,

6.3 Dynamic Contrast-Enhanced MRI

Dynamic contrast-enhanced (DCE) MRI can provide insight into tissue perfusion, with potential to monitor treatment response in breast cancer. DCE-MRI evaluates tissue perfusion and blood vessel permeability by dynamically imaging the kinetics of an intravenous contrast agent as it traverses and leaks into surrounding tissues. This technique provides critical insights into the microvasculature, which is also not observable with conventional MRI techniques. Tumours

typically exhibit hyperpermeable blood vessels and increased perfusion. Pharmacokinetic models, such as the Tofts model, can be applied to extract quantitative parameters, including the transfer constant (K_{trans}), the plasma volume fraction (v_p), and the extracellular-extravascular volume fraction (v_e). Additionally, non-parametric metrics can be derived to characterize the shape of the time-concentration curves, which have a wash-in and wash-out component.

Within the existing literature, test-retest repeatability studies for Tofts model parameters are limited [279, 291]. To the best of our knowledge, no such studies have been conducted specifically in the context of clinical breast cancer, a gap we aimed to address. Furthermore, while DCE-MRI has been utilised in various applications, its use in evaluating long-term responses to radiotherapy, incorporating both parametric and non-parametric parameters, remains unexplored. This study focuses on identifying the most useful parameters in this setting to further enhance the clinical potential of quantitative DCE-MRI.

6.3.1 Repeatability and Sensitivity

Test-retest repeatability of DCE-MRI was assessed in a small (N=7) multi-centre cohort using double baseline scans. Fifteen quantitative parameters were assessed, including three from the Tofts model (K_{trans}, v_p and v_e), and twelve classifying the shape of the concentration curve. Out of the twelve DCE non-parametric parameters investigated, three were chosen for further evaluation. These included the initial wash-in rate for the first 60 seconds ($iWIR$), the final wash-out rate from 180 to 470 seconds ($fWOR$), and the final wash-out area under the curve from 180 to 470 seconds (AUC_{fWO}). Other semi-quantitative parameters that are often used, including time-to-peak (TTP), peak enhancement (PE), area under the wash-in curve (AUC_{iWI}), total area under the curve (AUC_T), and final enhancement (fE), were either highly correlated with the chosen parameters or showed less sensitivity to change. For each quantitative parameter, the median, 25th percentile, 75th percentile, and interquartile range (IQR) were evaluated.

For the Tofts model, K_{trans}-metrics demonstrated good to excellent repeatability, with high Intraclass Correlation Coefficients (ICCs: $0.88-0.99$) and low within-subject Coefficients of Variation (wCV: $5.4-15.9\%$) indicating high reliability. Significant changes in the K_{trans}-metrics were observed in the majority of participants, excluding IQR (41.9%), at 2-weeks

post-RT (58.1−74.2%), split between significant increases and decreases. By 6-months post-RT, the majority of participants had significant decreases across metrics (71.1−84.2%). This demonstrates the high sensitivity of K_{trans} metrics to early and sustained post-treatment changes.

For v_e-metrics, the median demonstrated poor repeatability, with a negative ICC value (−0.31), high wCV value (44.7%) and large repeatability coefficient (RC) (0.61) in comparison to the range of possible values (from 0 to 1). Although its other metrics performed better (ICCs: 0.70−0.92; wCVs: 8.9−25.0%; RCs: 0.16−0.19), unreliable median measurements signify that voxel-wise analysis is not robust, and v_e should therefore be interpreted with caution. Median v_e was not sensitive to post-treatment changes, with the majority of participants having no change across 2-weeks, 6-, 12-, and 24-months (88.9−100%). The 75th percentile showed the greatest sensitivity for change, with 50% of participants having a significant increase at 6-months post-RT. v_e is modelled based on the height of the curve; however, when there is minimal contrast leakage, its reliability in accurately reflecting the true value diminishes. One participant in the repeatability study had minimal contrast leakage at baseline, resulting in unreliable v_e measurements, which largely biased the repeatability metrics. Consequently, v_e becomes a noisier parameter post-treatment when contrast leakage is reduced.

Although v_p-metrics demonstrated moderate to good ICC values (0.72−0.89), wCVs were high (30.8−57.5%). The majority of participants did not show significant changes across metrics and post-treatment time-points (66.7−96.8%), excluding IQR, where 66.7% of participants had a significant decrease by 24-months post-RT. Of the Tofts parameters, v_p is the most dependent on the arterial input function (AIF), as it reflects the degree of similarity to the AIF. The inconsistency in within-subject measurements may stem from several factors, including the use of a population-averaged AIF, a low temporal resolution that inadequately captures peak contrast concentration or biological factors such as temporal heterogeneity in perfusion. These limitations reduce its utility in detecting clinically meaningful changes. Moreover, similar to v_e, when contrast leakage is minimal, the reliability of v_p in accurately reflecting its true value is further diminished.

$iWIR$-metrics demonstrated good to excellent repeatability, with high ICCs (0.82–0.96) and moderately low wCVs (8.9–24.2%) indicating good reliability. Significant decreases in the

$iWIR$-metrics were observed in the majority of participants by 6-months post-RT (52.6−81.6%), with early decreases seen at 2-weeks post-RT for some participants (16.1−35.5%), demonstrating the sensitivity of $iWIR$ metrics to sustained post-treatment changes.

$fWOR$-metrics showed poor to good repeatability, with a range of ICC values (0.27−0.87) and high wCVs (23.9-167.6%). However, $fWOR$-metrics showed significant post-treatment increases in many participants by 6-months post-RT (42.1−63.2%), excluding IQR, with early decreases seen at 2-weeks post-RT for some participants (32.3−38.7%), demonstrating the sensitivity of $fWOR$ metrics to post-treatment changes. Due to the low wash-out gradient at baseline, $fWOR$ tends to be a noisy parameter. However, its substantial post-treatment changes demonstrate high sensitivity.

AUC_{fWO}-metrics demonstrated excellent repeatability, excluding IQR (ICC: 0.63; wCV: 26.4%) with high ICC values (0.96-0.97) and low wCVs (6.8−8.7%). AUC_{fWO}-metrics were sensitive to post-treatment changes, excluding IQR, with a large number of participants having an early increase in AUC_{fWO} (45.2−51.6%) followed by a decrease at 6-months post-RT (63.2−68.4%).

In a murine model of breast cancer [292], using a DCE sequence with a temporal resolution comparable to ours (12.8 seconds), but on a 7 Tesla MRI scanner for a longer 22-minute scan, K_{trans} exhibited a higher wCV (13.5%) compared to our study (6.9%). However, v_e and v_p showed lower wCVs (6.2% and 8.4% in comparison to 44.7% and 41.1%, respectively). Values at parameter boundaries were excluded, which may have improved repeatability, and an established population-based AIF was employed for analysis [293].

In a clinical setting, double baseline DCE scans were performed across various tumour types, excluding breast cancer, using variable field strengths (1.5T and 3T scanners), temporal resolutions (3 to 11.9 seconds), and scan durations (4 to 7.5 minutes) [294–298]. Across these studies, K_{trans} exhibited wCVs ranging from 7.5 to 24%, with an average wCV of 16.5%, compared to 6.9% in our study. For v_e, wCVs ranged from 8.5 to 16.0%, averaging 11.9%, in contrast to 44.7% in our results. v_p demonstrated wCVs between 30 and 62.5%, with an average of 45.7, compared to 41.1% in our study. The wash-in gradient derived from the time-intensity curve had a wCV of 25%, compared to 16.1% in our analysis [294].

Excluding the one participant who biased the v_e results reduces the wCV to 11.5%, aligning with other studies. However, this participant highlights the unreliability of v_e at later time-points with minimal contrast uptake.

To our knowledge, this is the first study to evaluate DCE-MRI repeatability for clinical breast cancer. The repeatability statistics are comparable to those observed in other cancers, validating our findings. Additionally, repeatability was evaluated for a wide range of semi-quantitative parameters, a large analysis not reported in other studies. To strengthen these preliminary results and statistical power, a larger cohort is crucial.

6.3.2 Predictive and Longitudinal Trends

DCE-MRI is a valuable tool for assessing functional changes in breast cancer after treatment. Both semi-quantitative and pharmacokinetic parameters can be useful in monitoring response over visual assessment. Following successful treatment, decreases in the rate and amount of enhancement are typically observed, whereas minimal changes are indicative of poor outcomes [187, 225].

For the overall post-treatment trend, K_{trans}-metrics decreased at 2-weeks and 6-months post-RT, approaching the healthy range of values. This decrease likely reflects reduced tumour permeability due to treatment effects. K_{trans} values remained low at 12- and 24-months post-RT, reflecting a long-term positive treatment response. Responders demonstrated a trend consistent with the overall cohort.

Non-responders showed an initial decline in K_{trans}-metrics, but values began to increase at 12-months post-RT, away from the healthy range of values. This pattern suggests transient treatment effects followed by tumour progression or recurrence.

The sustained decrease in K_{trans} among responders supports its utility as a biomarker for long-term treatment response. The late-stage increase in non-responders highlights its potential in identifying patients who may require additional or alternative therapies. These findings emphasise the value of longitudinal K_{trans} monitoring for assessing tumour dynamics and optimising patient outcomes.

For all participants, v_e-metrics showed no clear post-treatment trends, apart from a possible

cohort increase immediately post-radiotherapy, and individual changes were not significant. While v_p-metrics also showed minimal individual variations across time-points, responders demonstrated a cohort-wide decrease over time, towards the healthy range and indicating a reduction in tumour blood volume following radiotherapy. In contrast, non-responders showed an increase in v_p-metrics by 24-months post-RT, away from the healthy range.

For the $iWIR$-metrics, responders had values within the healthy range by 6-months post-RT, with values remaining low at 12- and 24-months post-RT, reflecting a long-term positive treatment response. Non-responders exhibited a similar trend at early time points. However, values began to increase again at 12- and 24-months post-RT, away from the healthy range of values. This suggests transient treatment effects, followed by tumour recurrence or progression.

$fWOR$-metrics for responders increased post-treatment, peaking at 6-months and then decreasing into the healthy range at 12- and 24-months post-RT. The non-responders do not have a trend to distinguish them from the responders at 12-months post-RT.

AUC_{fWO}-metrics increase at 2-weeks for responders and non-responders, then decrease at 6-months towards the healthy range. At 12- and 24-months, responders remain near the healthy range, whereas non-responders increase away from the healthy range.

At 2-weeks post-RT, K_{trans} values showed an equal split between increases and decreases. Similar findings have been reported in breast cancer studies, which observed an initial rise in the rate and amount of enhancement shortly after radiotherapy [187, 200, 226]. This is suggested to be attributable to treatment-induced injury, characterised by increased blood flow and microvascular permeability, acute inflammatory effects, and an expanded extracellular space caused by endothelial and tumour cell death. For the semi-quantitative parameters, $iWIR$ decreased at 2-weeks post-RT, while $fWOR$ and AUC_{fWO} increased. This combination further suggests vascular disruption, reflected by reduced similarity to the arterial input function (AIF) and an expanded extracellular space for contrast distribution.

Similarly, one study reported a significant increase in the area under the contrast concentration curve (AUC) and v_e 1-week after radiotherapy [200]. Another observed tumours enhancing more rapidly and extensively, with greater wash-out type kinetics [187]. A significant increase in enhancement and mean K_{trans} was observed at one week post-RT, followed by a mixed

response at 2-3 weeks, which aligns with our observations [226]; an increase in mean v_e was also noted.

In lung cancer, a similar trend was seen at 2-weeks post-radiotherapy [298]. A cohort increase was seen in initial enhancement ($iAUC_{60}$), K_{trans}, and v_e. Similar to our study, this study identified a cohort change in v_e without any significant individual change beyond the repeatability coefficient, whereas K_{trans} and $iAUC_{60}$ experienced both.

Amongst the reports, some suggest that this transient enhancement reflects improved tumour regression and local control due to reduced hypoxia [200], but this pattern was observed in both responders and non-responders in our study. Other studies suggest delayed imaging (>2.5 weeks post-radiotherapy) to minimise these confounding factors [226] and capture a more reliable early assessment of tumour response.

By 6-months post-treatment, the enhancement decreased, and the rate slowed significantly in radiologic complete responders compared to non-complete responders [187]. This suggests that faster reductions in enhancement correlate with better outcomes. In our study, at 6-months there was a similar response between groups. Only at 12-months post-RT did responders and non-responders split, which was when progressive disease was assessed by radiologists.

Similarly, for patients receiving carbon-ion radiotherapy, continuous decreases in wash-in AUC from pre-treatment to 1 and 3 months post-treatment was reported [225]. Lower AUC values at these time points were significantly associated with complete response at 12 months, whereas tumour volumes at those intervals showed no such correlation.

Quantitative DCE-MRI parameters provide valuable surrogate markers for assessing radiotherapy efficacy. Radiotherapy induces endothelial cell damage within tumours [299], leading to vascular injury often observable within days post-treatment. This damage is reflected in DCE-MRI parameters such as K_{trans}, $iWIR$, and $fWOR$. Notably, a significant decrease in $iWIR$ and an increase in $fWOR$ were observed as early as two weeks after radiotherapy, suggesting reduced tumour blood flow and circulatory dysfunction. Such changes align with previous studies highlighting radiotherapy-induced vascular damage. The DCE-MRI parameters highlight regions of progressive disease, identifying patients who may require additional or alternative therapies.

In our study, there was no statistical difference between the pre-treatment values of the Tofts and semi-quantitative parameters analysed for the responder and non-responder groups. This lack of statistical significance implies that baseline values alone do not serve as reliable predictive markers for response.

A review of head and neck cancer treated with chemoradiation highlighted varying early responses among studies, with a statistically significant trend towards larger initial K_{trans}, or blood vessel permeability, in responding patients. Increased permeability might improve cell oxygenation, which reduces radioresistance [300]. However, one study presented contradictory findings, where lower K_{trans} predicted better local control [301], which is in agreement with our study, where responders had lower K_{trans} values, although this was non-significant.

In head and neck cancer treated with radiotherapy, only the 95th percentile of the area under the curve for the initial 60 seconds (AUC_{60}) was found to have prognostic value for overall survival, with low AUC_{60} predicting worse overall survival [302]. This signifies that poorly perfused tumours were associated with worse disease control. Poor perfusion correlates with hypoxia, a condition linked to radioresistance and tumour aggressiveness [303]. Looking at the highest and lowest values (5th and 95th) pre-treatment and post-treatment may give better insight into the areas causing poor outcomes, as progressive disease appears as small nodal responses.

Early changes in permeability and perfusion can also indicate treatment response. One study treating head and neck cancer with chemoradiation observed that patients with an early increase in AUC_{60} had long-term poor responses, suggesting enhanced permeability [304]. However, this was contradictory to our study, where non-responders had more of a tendency to decrease immediately after radiotherapy in contrast with responders.

In cervical cancer studies, conflicting results regarding signal enhancement have also been reported. Some studies associated worse outcomes with high signal enhancement pre-treatment [305], while others linked worse outcomes to low signal enhancement [306–308]. These discrepancies underline the complexity of interpreting the prognostic value of pre-treatment perfusion and permeability metrics.

Across the parametric and non-parametric quantitative parameters investigated, K_{trans} was

the most sensitive biomarker to change post-treatment, however $iWIR$ showed the most potential to separate responders and non-responders at baseline or early changes 2-weeks post-RT.

6.3.3 Technical Considerations and Limitations

For non-parametric analyses, time-signal intensity curves are often used. In this study, the signal was converted to contrast agent concentration, a critical step for ensuring accurate longitudinal analyses both within and across participants. This is particularly important in multi-centre trials, where variations in imaging systems and parameters can occur. This approach facilitates standardised comparisons and improves consistency across participants and study sites.

In this study, T1 mapping was performed using a dual-flip-angle model. While this method is widely used, it may introduce estimation errors, potentially leading to significant inaccuracies in the derived quantitative parameters. Adopting multiple flip angles for T1 calculation could improve reliability and enhance robustness, thereby enabling more accurate quantitative analyses [309]. Future work could investigate the repeatability and stability of T1 calculation.

Additionally, no $B0$ maps were used in this study. Incorporating B1 maps to determine the true flip angle for T1 mapping could improve accuracy of parameter estimation. Techniques such as the Actual Flip Angle Imaging (AFI) method or the slice selective pre-conditioning RF pulse (SS-Pre) method, as described in [226], could be utilised for B1 quantification.

Motion correction was not performed during DCE analysis. Addressing patient movement using rigid or non-rigid registration methods to align tumour positions across phases could enhance the accuracy of pixel-wise analysis. One potential approach is leveraging the corresponding DCE fat images to transform the in-phase images and incorporating a multi-modality correction algorithm to ensure alignment of low and high flip-angle acquisitions for T1 mapping. This would improve the reliability of derived quantitative parameters.

The Tofts model remains a standard in research for evaluating response to cancer treatment, but its reliance on precise arterial input function (AIF) measurements limits its clinical application. Despite the ultra-fast temporal resolution of our sequence, the rapid initial contrast wash-in remains challenging to capture. With a temporal resolution of approximately 12 seconds, only a limited number of time-points are sampled around the peak, potentially underestimating the

true peak due to insufficient sampling. This limitation impacts the accuracy of individual AIFs.

To help mitigate this limitation and to enhance the robustness and reliability of the parametric modelling, this study employed a population-average AIF derived from the aorta of a sub-group of participants. This approach also addressed instances where individual AIFs could not be reliably obtained. Population-based rather than individual AIFs have been shown to improve the repeatability of Tofts model parameters, particularly K_{trans} and v_e [310, 311]. While v_p is the most reliant on AIF accuracy, the use of individual AIFs did not significantly improve its repeatability statistics [295]. This finding reinforces the practicality of population-average AIFs in clinical and research settings where individual AIF measurement is not feasible.

The population-average AIF used in this study was derived from pooled data across three institutions, each utilising 1.5 T MRI scanners. Participant DCE scans with the same temporal resolution were selected to ensure accurate averaging. This AIF was applied across multi-centre DCE-MRI sequences, which varied in imaging systems and protocols. While the modelled AIF is theoretically independent of imaging parameters, future research could explore the impact of higher-field-strength magnets (e.g., 3 T) and alternative imaging protocols (e.g., different temporal resolutions) on AIF estimation and the accuracy of pharmacokinetic parameters.

The bolus arrival time (t_0) was fixed in the Tofts model to limit the number of adjustable parameters. However, this may impact parameter accuracy. Incorporating imaging techniques, such as single slice half-Fourier acquisition single-shot turbo spin echo (HASTE) positioned at the aortic arch during early contrast injection [226], could provide a more accurate estimation of the bolus arrival time.

While the use of a population-average AIF is a well-established and practical technique for estimating Tofts parameters, it does not account for individual variability in AIFs. Such variability may occur across participants or within the same participant at different post-treatment time-points. Furthermore, the aortic-derived AIF might not accurately represent the mammary arteries feeding the tumour. Factors such as cardiac function, vascular physiology, and treatment effects could influence the AIF and introduce inaccuracies in parameter estimation.

Further approaches may include leveraging machine learning models to predict individualised AIFs based on participant-specific data, potentially enhancing parameter accuracy without

requiring direct AIF measurement. Additionally, comparisons with other population-average AIFs, such as the AIF from Weinmann et al. [312], which has performed poorly [313], could provide insights into how our AIF performs relative to established alternatives.

In this study, tumour regions of interest (ROIs) were manually delineated at each time point. Automatic segmentation techniques, such as Otsu's method or k-means clustering, could potentially improve reproducibility. Deep learning-based methods have also been explored to segment breast tumours in MRI volumes, for example, using UNet, Res-UNet or SegNet architectures [314–316]. This could not be explored here due to the insufficient amount of data in this study.

However, manual adaptation was chosen to ensure the accurate inclusion of viable tumour tissue while excluding non-tumour areas like fatty or glandular tissue. Although manual delineation is prone to variability, it avoids the inaccuracies and potential exclusion of scans caused by registration-based approaches. Additionally, the large tumour sizes in this study minimised measurement errors, as the greater number of pixels allowed for more reliable volume assessments. However, as tumours shrink, fewer pixels and increased noise can complicate accurate evaluation.

DCE-MRI parameters discussed in this study are applicable for monitoring other tumour types post-radiotherapy. Despite its advantages, DCE-MRI's clinical adoption may be hindered by the unavailability of high-specification MRI scanners required for advanced acceleration techniques. Continued efforts to standardise protocols and improve accessibility will be critical for broader clinical use.

This prospective, multi-centre study leveraged DCE-MRI data from both 1.5 T and 3 T scanners, providing robust data for assessing treatment responses. Quantitative analysis was feasible for all lesions, irrespective of size. The DCE-MRI parameters could separate responders and non-responders at 12-months post-RT. However, reliance on DCE-MRI for radiological response assessment introduces potential biases for the discriminatory ability of its quantitative parameters. Furthermore, the absence of the incorporation of pathological examination in the response assessment may overlook residual microscopic tumour tissue, even when tumour enhancement disappears.

Chapter 7

Conclusion

Quantitative imaging techniques, such as super-resolution ultrasound (SRUS), diffusion-weighted (DW), and dynamic contrast-enhanced (DCE) MRI, are instrumental in monitoring and assessing treatment responses in breast cancer. This study investigated multiple quantitative parameters from these imaging modalities, identifying those that are repeatable, and sensitive to change. These parameters quantify the pathological state of tumours, for a comprehensive analysis of tumour characteristics and changes post-treatment.

We found that parameters such as the Apparent Diffusion Coefficient (ADC) from mono-exponential modelling of DW-MRI, K_{trans} from Tofts modelling of DCE-MRI, semi-quantitative DCE-MRI parameters $iWIR$, $fWOR$, and AUC_{fWO}, and SRUS-derived metrics (e.g., vessel density, vessel diameter, and blood velocity) are particularly robust.

ADC is sensitive to tumour microstructural changes and cellularity post-radiotherapy, while K_{trans} assesses tumour microvascular permeability. Semi-quantitative parameters $iWIR$, $fWOR$, and AUC_{fWO} classify curve dynamics related to microvasculature properties.

While ADC showed greatest sensitivity to early increases post-radiotherapy, DCE-MRI parameters like K_{trans}, $iWIR$, and AUC_{fWO} were crucial for long-term monitoring, detecting small nodules of relapse that were not apparent with ADC alone.

SRUS-derived parameters quantified tumour microvasculature structure and function. In particular vessel density, vessel diameter and blood velocity were repeatable and potentially sensitive to early biological changes post-treatment, with long-term changes beyond the repeat-

ability coefficient. The results of this preliminary study are encouraging, showcasing SRUS's potential as an affordable non-invasive monitoring tool in identifying response and resistance. A larger cohort size and further correlation with long-term radiological outcomes is needed validate these results.

While the study demonstrated the potential of SRUS, several limitations remain. Highly vascular tumours exhibited lower repeatability due to their significant heterogeneity. Relapse was challenging to detect, as cancer often re-emerged as small nodules that could be missed on 2D planes. Additionally, distinguishing poorly perfused tumours from healthy tissue vasculature proved difficult. The development of whole-breast 3D imaging for full reconstruction of the tumour microvasculature could address these challenges, enhancing repeatability, enabling the detection of relapse, and identifying subtle changes more effectively. Until then, SRUS is unlikely to replace imaging modalities such as DCE-MRI, which offers whole-breast coverage and widespread clinical integration. However, longitudinal cancer monitoring using MRI is often impractical due to limited resources and high costs, making SRUS imaging particularly attractive. Therefore, SRUS remains a promising but still experimental technique that requires further technological advancement and clinical validation.

Variability in treatment regimens introduced challenges in assessing prognostic potential of quantitative parameters and treatment response. The analysis was conducted blinded to KORTUC treatment, which has the potential to enhance tumour sensitivity to radiation through oxygenation. As a result, poorly perfused and typically radioresistant tumours, which are generally associated with worse prognoses, may respond more favourably to treatment. Furthermore, the participant cohort included a mix of molecular subtypes, contributing to a heterogeneous dataset. These factors may have contributed to the lack of statistically significant findings when assessing prognostic potential of quantitative parameters for predicting long-term outcomes, alongside the small subset of participants classified as responders and non-responders at the 12-month post-treatment time-point. Even among responders, there was variability in outcomes, ranging from complete to partial responses.

This dataset will continue to expand over the course of the trial, which will allow us to reassess statistical significance. A retrospective power calculation could also be conducted

as part of future work to estimate the effect size required to achieve significance given the observed sample size and variability, and to evaluate whether such an effect size would be clinically realistic.

This is the first study to utilise SRUS, DW-MRI, and DCE-MRI to monitor long term response (> 6-months) of breast cancer post-radiotherapy. Furthermore, repeatability of SRUS has been established, providing robust biomarkers quantifying tumour microvasculature structure and blood flow dynamics.

The integration of the imaging biomarkers explored in this study with longitudinal follow-up offers promising avenues for personalised treatment strategies, improving outcomes for cancer patients. Standardised protocols are essential for clinical utility, enhancing repeatability and reliability. The potential of these quantitative parameters, particularly SRUS-derived biomarkers, should be established in other oncological contexts, to broaden its applicability.

Bibliography

[1] Sung H, Ferlay J, Siegel RL, Laversanne M, Soerjomataram I, Jemal A, and Bray F. Global Cancer Statistics 2020: GLOBOCAN Estimates of Incidence and Mortality Worldwide for 36 Cancers in 185 Countries. *CA Cancer J Clin* 2021; **71**(3):209-249.

[2] Ginsburg O, Bray F, Coleman MP, Vanderpuye V, Eniu A, Kotha SR, et al. The global burden of women's cancers: a grand challenge in global health. *Lancet* 2017; **389**(10071):847-860.

[3] Benitez Fuentes JD, Morgan E, de Luna Aguilar A, Mafra A, Shah R, Giusti F, et al. Global Stage Distribution of Breast Cancer at Diagnosis: A Systematic Review and Meta-Analysis. *JAMA Oncol* 2024; **10**(1):71-78.

[4] Coles CE, Earl H, Anderson BO, Barrios CH, Bienz M, Bliss JM, et al. The LANCET Breast Cancer Commission. *Lancet* 2024; **403**(10439):1895-1950.

[5] Aebi S, Karlsson P, and Wapnir IL. Locally advanced breast cancer. *Breast* 2022; **62**:S58-S62.

[6] Yee C, Alayed Y, Drost L, Karam I, Vesprini D, McCann C, et al. Radiotherapy for patients with unresected locally advanced breast cancer. *Ann Palliat Med* 2018; **7**(4):373-384.

[7] Kong X, Song J, Gao P, Gao R, Zhang L, Fang Y, et al. Revolutionizing the battle against locally advanced breast cancer: A comprehensive insight into neoadjuvant radiotherapy. *Med Res Rev* 2024; **44**(2):606-631.

[8] Hanahan D, and Weinberg RA. The Hallmarks of Cancer. *Cell* 2000; **100**(1):57-70.

[9] Hanahan D, and Weinberg RA. Hallmarks of Cancer: The Next Generation. *Cell* 2011; **144**(5):646-674.

[10] Pugh CW, and Ratcliffe PJ. Regulation of angiogenesis by hypoxia: role of the HIF system. *Nat Med* 2003; **9**:677–684.

[11] Ruoslahti E. Specialization of tumour vasculature. *Nat Rev Cancer* 2002; **2**:83-90.

[12] Carmeliet P, and Jain RK. Molecular mechanisms and clinical applications of angiogenesis. *Nature* 2011; **473**(7347):298-307.

[13] Lugano R, Ramachandran M, and Dimberg A. Tumor angiogenesis: causes, consequences, challenges and opportunities. *Cell Mol Life Sci* 2020; **77**:1745-1770.

[14] Nagy JA, Chang S-H, Dvorak AM, and Dvorak HF. Why are tumour blood vessels abnormal and why is it important to know? *Br J Cancer* 2009; **100**(6):865-869.

[15] Fukumura D, and Jain RK. Tumor microvasculature and microenvironment: Targets for anti-angiogenesis and normalization. *Microvasc Res* 2007; **74**:72-84.

[16] Siemann DW. The Unique Characteristics of Tumor Vasculature and Preclinical Evidence for its Selective Disruption by Tumor-Vascular Disrupting Agents. *Cancer Treat Rev* 2011; **37**(1):63-74.

[17] Ehling J, Theek B, Gremse F, Baetke S, Möckel D, Maynard J, et al. Micro-CT Imaging of Tumor Angiogenesis: Quantitative Measures Describing Micromorphology and Vascularization. *Am J Pathol* 2014; **184**(2):431-441.

[18] Goel S, Duda DG, Munn LL, Boucher Y, Fukumura D, and Jain RK. Normalization of the vasculature for treatment of cancer and other diseases. *Physiol Rev* 2011; **91**(3):1071-1121.

[19] Horsman MR, and Overgaard J. The impact of hypoxia and its modification of the outcome of radiotherapy. *J Radiat Res* 2016; **57**:90-98.

[20] Thomlinson RH, and Gray LH. The histological structure of some human lung cancers and the possible implications for radiotherapy. *Brit J Cancer* 1955; **9**:539–549.

[21] Hammond EM, Asselin MC, Forster D, O'Connor JP, Senra JM, and Williams KJ. The meaning, measurement and modification of hypoxia in the laboratory and the clinic. *Clin Oncol* 2014; **26**(5):277-288.

[22] Hall E, and Giaccia A. *Radiobiology for the Radiologist*. 7th edn. Philadelphia: Lippincott Williams & Wilkins; 2012.

[23] Begg K, and Tavassoli M. Inside the hypoxic tumour: reprogramming of the DDR and radioresistance. *Cell Death Discov* 2020; **6**(77).

[24] Joiner M, and van der Kogel A. *Basic Clinical Radiobiology*. 4th edn. London: Hodder Education; 2009.

[25] Wilson WR, and Hay MP. Targeting hypoxia in cancer therapy. *Nat Rev Cancer* 2011; **11**(6):393-410.

[26] Brown JM. Inhibiting Vasculogenesis After Radiation: A New Paradigm to Improve Local Control by Radiotherapy. *Semin Radiat Oncol* 2013; **23**(4):281-287.

[27] Brown JM. Radiation Damage to Tumor Vasculature Initiates a Program That Promotes Tumor Recurrences. *Int J Radiation Oncol Biol Phys* 2020; **108**(3):734-744.

[28] Begg AC, Stewart FA, and Vens C. Strategies to improve radiotherapy with targeted drugs. *Nat Rev Cancer* 2011; **11**:239-253.

[29] Wardman P. Chemical Radiosensitizers for Use in Radiotherapy. *Clin Oncol* 2007; **19**(6):397-417.

[30] Overgaard J. Hypoxic Radiosensitization: Adored and Ignored. *J Clin Oncol* 2007; **25**(26):4066-4074.

[31] Gong L, Zhang Y, Liu C, Zhang M, and Han S. Application of Radiosensitizers in Cancer Radiotherapy. *Int J Nanomedicine* 2021; **16**:1083-1102.

[32] Ogawa Y, Takahashi T, Kobayashi T, Kariya S, Nishioka A, Ohnishi T, et al. Apoptotic-resistance of the human osteosarcoma cell line HS-Os-1 to irradiation is converted to

apoptotic-susceptibility by hydrogen peroxide: a potent role of hydrogen peroxide as a new radiosensitizer. *Int J Mol Med* 2003; **12**(6):845-50.

[33] Kariya S, Sawada K, Kobayashi T, Karashima T, Shuin T, Nishioka A, and Ogawa Y. Combination treatment of hydrogen peroxide and X-rays induces apoptosis in human prostate cancer PC-3 cells. *Int J Radiat Oncol Biol Phys* 2009; **75**(2):449-54.

[34] Fang Y, Moore BJ, Bai Q, Cook KM, Herrick EJ, and Nicholl MB. Hydrogen Peroxide Enhances Radiation-induced Apoptosis and Inhibition of Melanoma Cell Proliferation. *Anticancer Res* 2013; **33**(5):1799-1807.

[35] Ogawa Y. Paradigm Shift in Radiation Biology/Radiation Oncology—Exploitation of the "H2O2 Effect" for Radiotherapy Using Low-LET (Linear Energy Transfer) Radiation such as X-rays and High-Energy Electrons. *Cancers* 2016; **8**(3):28.

[36] Ogawa Y, Kobayashi T, Nishioka A, Kariya S, Hamasato S, Seguchi H, and Yoshida S. Radiation-induced reactive oxygen species (ROS) formation prior to oxidative DNA damage in human peripheral T cells. *Int J Mol Med.* 2003; **11**(2):149–152.

[37] Ogawa Y, Kobayashi T, Nishioka A, Kariya S, Ohnishi T, Hamasato S, et al. Reactive oxygen species-producing site in radiation-induced apoptosis of human peripheral T cells: Involvement of lysosomal membrane destabilization. *Int J Mol Med* 2004; **13**(1):69–73.

[38] Ogawa Y, Ue H, Tsuzuki K, Tadokoro M, Miyatake K, Sasaki T, et al. New radiosensitization treatment (KORTUC I) using hydrogen peroxide solution-soaked gauze bolus for unresectable and superficially exposed neoplasms. *Oncol Rep* 2008; **19**(6):1389-1394.

[39] Ogawa Y, Kubota K, Ue H, Kataoka Y, Tadokoro M, Miyatake K, et al. Phase I study of a new radiosensitizer containing hydrogen peroxide and sodium hyaluronate for topical tumor injection: A new enzyme-targeting radiosensitization treatment, Kochi Oxydol-Radiation Therapy for Unresectable Carcinomas, Type II (KORTUC II). *Int J Oncol* 2008; **34**(3):609-618.

[40] Nimalasena S, Gothard L, Anbalagan S, Allen S, Sinnett V, Mohammed K, et al. Intratumoral Hydrogen Peroxide With Radiation Therapy in Locally Advanced Breast Cancer:

Results From a Phase 1 Clinical Trial. *Int J Radiation Oncol Biol Phys* 2020; **108**(4):1019-1029.

[41] Tokuhiro S, Ogawa Y, Tsuzuki K, Akima R, Ue H, Kariya S, and Nishioka A. Development of a novel enzyme-targeting radiosensitizer (KORTUC) containing hydrogen peroxide for intratumoral injection for patients with low linear energy transfer-radioresistant neoplasms. *Oncol Lett* 2010; **1**(6):1025-1028.

[42] Ogawa Y, Kubota K, Ue H, Tadokoro M, Matsui R, Yamanishi T, et al. Safety and effectiveness of a new enzyme-targeting radiosensitization treatment (KORTUC II) for intratumoral injection for low-LET radioresistant tumors. *Int J Oncol* 2011; **39**(3):553-560.

[43] Tsuzuki A, Ogawa Y, Kubota K, Tokuhiro S, Akima R, Yaogawa S, et al. Evaluation of Changes in Tumor Shadows and Microcalcifications on Mammography Following KORTUC II, a New Radiosensitization Treatment without any Surgical Procedure for Elderly Patients with Stage I and II Breast Cancer. *Cancers* 2011; **3**(3):3496-3505.

[44] Ogawa Y, Kubota K, Aoyama N, Yamanishi T, Kariya S, Hamada N, et al. Non-Surgical Breast-Conserving Treatment (KORTUC-BCT) Using a New Radiosensitization Method (KORTUC II) for Patients with Stage I or II Breast Cancer. *Cancers* 2015; **7**(4):2277-2289.

[45] Eisenhauer EA, Therasse P, Bogaerts J, Schwartz LH, Sargent D, Ford R, et al. New response evaluation criteria in solid tumours: revised RECIST guideline (version 1.1). *Eur J Cancer* 2009; **45**(2):228–247.

[46] Gerwing M, Herrmann K, Helfen A, Schliemann C, Berdel WE, Eisenblätter M, and Wildgruber M. The beginning of the end for conventional RECIST — novel therapies require novel imaging approaches. *Nat Rev Clin Oncol* 2019; **16**(7):442-458.

[47] Ko CC, Yeh LR, Kuo YT, and Chen JH. Imaging biomarkers for evaluating tumor response: RECIST and beyond. *Biomark Res* 2021; **9**(1):52.

[48] Padhani AR, Yarnold J, Regan J and Husband JE. Dynamic MRI of Breast Hardness Following Radiation Treatment. *J Magn Reson Imaging* 2003; **17**(4):427-434.

[49] Lee SJ, Mahoney MC and Khan S. MRI Features of Stromal Fibrosis of the Breast With Histopathologic Correlation. *Am J Roentgenol* 2011; **197**(3):755-762.

[50] EL-Adalany MA and Hamed EE. Role of dynamic contrast enhanced MRI in evaluation of post-operative breast lesions. *EJRNM* 2016; **47**(2):631-640.

[51] Sarsenov D, Aktepe F, and Özmen V. Radiation Fibrosis Syndrome Imitating Breast Cancer Reccurence; A Case Report. *J Breast Health* 2017; **13**(1):40–42.

[52] Fournier L, de Geus-Oei LF, Regge D, Oprea-Lager DE, D'Anastasi M, Bidaut L, et al. Twenty Years On: RECIST as a Biomarker of Response in Solid Tumours an EORTC Imaging Group - ESOI Joint Paper. *Front Oncol* 2022; **11**:800547.

[53] Hayes SA, Pietanza MC, O'Driscoll D, Zheng J, Moskowitz CS, Kris MG, et al. Comparison of CT Volumetric Measurement With RECIST Response in Patients With Lung Cancer. *Eur J Radiol* 2016; **85**(3):524–533.

[54] Fenerty KE, Folio LR, Patronas NJ, Marté JL, Gulley JL, and Heery CR. Predicting Clinical Outcomes in Chordoma Patients Receiving Immunotherapy: A Comparison Between Volumetric Segmentation and RECIST. *BMC Cancer* 2016; **16**(1):672.

[55] Bollineni VR, Kramer GM, Jansma EP, Liu Y, and Oyen WJ. A systematic review on [^{18}F]FLT-PET uptake as a measure of treatment response in cancer patients. *Eur J Cancer* 2016; **55**:81–97.

[56] Horsman MR, Mortensen LS, Petersen JB, Busk M, and Overgaard J. Imaging hypoxia to improve radiotherapy outcome. *Nat Rev Clin Oncol* 2012; **9**(12):674-687.

[57] Neves AA, and Brindle KM. Imaging cell death. *J Nucl Med* 2014; **55**(1):1-4.

[58] Wester H-J. Nuclear Imaging Probes: From Bench to Bedside. *Clin Cancer Res* 2007; **13**(12):3470–3481.

[59] Evangelista L, Guarneri V, Conte PF. 18f-Fluoroestradiol Positron Emission Tomography in Breast Cancer Patients: Systematic Review of the Literature & Meta-Analysis. *Curr Radiopharm* 2016; **9**(3):244–57.

[60] O'Connor J, Robinson S, and Waterton J. Imaging tumour hypoxia with oxygen-enhanced MRI and BOLD MRI. *Br J Radiol* 2018; **92**(1095):20180642.

[61] Walsh JC, Lebedev A, Aten E, Madsen K, Marciano L, and Kolb HC. The Clinical Importance of Assessing Tumor Hypoxia: Relationship of Tumor Hypoxia to Prognosis and Therapeutic Opportunities. *Antioxid Redox Signal* 2014; **21**(10):1516-1554.

[62] Cosse J, and Michiels C. Tumour hypoxia affects the responsiveness of cancer cells to chemotherapy and promotes cancer progression. *Anticancer Agents Med Chem* 2008; **8**(7):790-797.

[63] Rockwell S, Dobrucki IT, Kim EY, Marrison ST, and Vu VT. Hypoxia and radiation therapy: past history, ongoing research, and future promise. *Curr Mol Med* 2009; **9**(4):442-458.

[64] Barsoum IB, Koti M, Siemens DR, and Graham CH. Mechanisms of hypoxia-mediated immune escape in cancer. *Cancer Res* 2014; **74**(24):7185:7190.

[65] Madu CO, Wang S, Madu CO, and Lu Y. Angiogenesis in Breast Cancer Progression, Diagnosis, and Treatment. *J Cancer* 2020; **11**(15):4474-4494.

[66] Padhani AR, Harvey CJ, and Cosgrove DO. Angiogenesis imaging in the management of prostate cancer. *Nat Clin Pract Urol* 2005; **2**:596-607.

[67] Toi M, Inada K, Suzuki H, and Tominaga T. Tumor angiogenesis in breast cancer: Its importance as a prognostic indicator and the association with vascular endothelial growth factor expression. *Breast Cancer Res Treat* 1995; **36**:193-204.

[68] Jia WR, Tang L, Wang DB, Chai WM, Fei XC, He JR, et al. Three-dimensional Contrast-enhanced Ultrasound in Response Assessment for Breast Cancer: A Comparison with Dynamic Contrast-enhanced Magnetic Resonance Imaging and Pathology. *Sci Rep* 2016; **6**:33832.

[69] Tolaney SM, Boucher Y, Duda DG, Martin JD, Seano G, Ancukiewicz M, et al. Role of vascular density and normalization in response to neoadjuvant bevacizumab and chemotherapy in breast cancer patients. *PNAS* 2015; **112**(46):14325-14330.

[70] Li CY, Shan S, Huang Q, Braun RD, Lanzen J, Hu K, et al. Initial Stages of Tumor Cell-Induced Angiogenesis: Evaluation Via Skin Window Chambers in Rodent Models. *J Natl Cancer Inst* 2000; **92**(2):143-147.

[71] Mirnezami R, Nicholson J and Darzi A. Preparing for Precision Medicine. *N Engl J Med* 2012; **366**:489-491.

[72] Bullitt E, Lin NU, Ewend MG, Zeng D, Winer EP, Carey LA, and Smith JK. Tumor Therapeutic Response and Vessel Tortuosity: Preliminary Report in Metastatic Breast Cancer. *Med Image Comput Comput Assist Interv* 2006; **9**:561-568

[73] Choi H, Charnsangavej C, Faria SC, Macapinlac HA, Burgess MA, Patel SR, et al. Correlation of Computed Tomography and Positron Emission Tomography in Patients With Metastatic Gastrointestinal Stromal Tumor Treated at a Single Institution With Imatinib Mesylate: Proposal of New Computed Tomography Response Criteria. *Clin Oncol* 2007; **25**(13):1753-1759.

[74] Messiou C, Orton M, Ang JE, Collins DJ, Morgan VA, Mears D, et al. Advanced solid tumors treated with cediranib: comparison of dynamic contrast-enhanced MR imaging and CT as markers of vascular activity. *Radiology* 2012; **265**(2):426-436.

[75] Stieb S, Kiser K, van Dijk L, Livingstone NR, Elhalawani H, Elgohari B, et al. Imaging for Response Assessment in Radiation Oncology: Current and Emerging Techniques. *Hematol Oncol Clin North Am* 2020; 34(1): 293–306.

[76] Konerding MA, Miodonski AJ, and Lametschwandtner A. Microvascular corrosion casting in the study of tumor vascularity: a review. *Scanning Microsc* 1995; **9**(4):1233-1243.

[77] Lin E, and Alessio A. What are the basic concepts of temporal, contrast, and spatial resolution in cardiac CT? *J Cardiovasc Comput Tomogr* 2009; **3**(6):403-408.

[78] Wang L, Cull G, and Cioffi GA. Depth of penetration of scanning laser Doppler flowmetry in the primate optic nerve. *Arch Ophthalmol* 2001; **119**(12):1810-1814.

[79] Vakoc BJ, Fukumura D, Jain RK, and Bouma BE. Cancer imaging by optical coherence tomography: preclinical progress and clinical potential. *Nat Rev Cancer* 2012; **12**:363-368.

[80] Leahy MJ. *Microcirculation imaging*. New York: Wiley; 2012.

[81] Hasebroock KM and Serkova NJ. Toxicity of MRI and CT contrast agents. *Expert Opin Drug Metab Toxicol* 2009; **5**(4):403-416.

[82] Demené C, Tiran E, Sieu LA, Bergel A, Gennisson JL, Pernot M, et al. 4D microvascular imaging based on ultrafast Doppler tomography. *NeuroImage* 2016; **127**:472-483.

[83] Cosgrove D and Lassau N. Imaging of perfusion using ultrasound. *Eur J Nucl Med Mol Imaging* 2010; **37**:65-85.

[84] Dietrich CF, Averkiou M, Nielsen MB, Barr RG, Burns PN, Calliada F, et al. How to perform Contrast-Enhanced Ultrasound (CEUS). *Ultrasound Int Open* 2018; **4**(1):2-15.

[85] Simpson DH, Chin CT, and Burns PN. Pulse inversion Doppler: a new method for detecting nonlinear echoes from microbubble contrast agents. *IEEE Trans Ultrason Ferroelectr Freq Control* 1999; **46**(2):372-382.

[86] Forsberg F, Shi WT, and Goldberg BB. Subharmonic imaging of contrast agents. *Ultrasonics* 2000; **38**(1-8):93-98.

[87] Bouakaz A, Frigstad S, Ten Cate FJ, and de Jong N. Super harmonic imaging: a new imaging technique for improved contrast detection. *Ultrasound Med Biol* 2002; **28**(1):59-68.

[88] Eckersley RJ, Chin CT, and Burns PN. Optimising phase and amplitude modulation schemes for imaging microbubble contrast agents at low acoustic power. *Ultrasound Med Biol* 2005; **31**(2):213-219.

[89] Pasovic M, Danilouchkine M, Faez T, van Neer PLMJ, Cachard C, van der Steen AFW, et al. Second harmonic inversion for ultrasound contrast harmonic imaging. *Phys Med Biol* 2011; **56**(11):3163-3180.

[90] Lin F, Cachard C, Mori R, Varray F, Guidi F, and Basset O. Ultrasound contrast imaging: influence of scatterer motion in multi-pulse techniques. *IEEE Trans Ultrason Ferroelectr Freq Control* 2013; **60**(10):2065-2078.

[91] Gessner RC, Aylward SR, and Dayton PA. Mapping microvasculature with acoustic angiography yields quantifiable differences between healthy and tumor-bearing tissue volumes in a rodent model. *Radiology* 2012; **264**(3):733-740.

[92] Gessner RC, Frederick CB, Foster FS, and Dayton PA. Acoustic angiography: a new imaging modality for assessing microvasculature architecture. *Int J Biomed Imaging* 2013; **2013**(6):936593.

[93] Shelton SE, Lee YZ, Lee M, Cherin E, Foster FS, Aylward SR, and Dayton PA. Quantification of Microvascular Tortuosity during Tumor Evolution Using Acoustic Angiography. *Ultrasound Med Biol* 2015; **41**(7):1896-1904.

[94] Rao SR, Shelton SE, and Dayton PA. The "Fingerprint" of Cancer Extends Beyond Solid Tumor Boundaries: Assessment With a Novel Ultrasound Imaging Approach. *IEEE Trans Biomed Eng* 2016; **63**(5):1082-1086.

[95] Shelton SE, Lindsey BD, Tsuruta JK, Foster FS, and Dayton PA. Molecular acoustic angiography: a new technique for high resolution superharmonic ultrasound molecular imaging. *Ultrasound Med Biol* 2016; **42**(3):769-781.

[96] Lindsey BD, Shelton SE, Foster FS, and Dayton PA. Assessment of Molecular Acoustic Angiography for Combined Microvascular and Molecular Imaging in Preclinical Tumor Models. *Mol Imaging Biol* 2017; **19**(2):194-202.

[97] Forsberg F, Kuruvilla B, Pascua MB, Chaudhari MH, Merton DA, Palazzo JP, and Goldberg BB. Comparing contrast-enhanced color flow imaging and pathological measures of breast lesion vascularity. *Ultrasound Med Biol* 2008; **34**(9):1365-1372.

[98] Palmowski M, Lederle W, Gaetjens J, Socher M, Hauff P, Bzyl J, et al. Comparison of conventional time-intensity curves vs. maximum intensity over time for post-processing of dynamic contrast-enhanced ultrasound. *Eur J Radiol* 2010; **75**(1):149-153.

[99] Pysz MA, Foygel K, Panje CM, Needles A, Tian L, and Willmann JK. Assessment and monitoring tumor vascularity with contrast-enhanced ultrasound maximum intensity persistence imaging. *Invest Radiol* 2011; **46**(3):187-195.

[100] Siepmann M, Schmitz G, Bzyl J, Palmowski M, and Kiessling F. Imaging tumor vascularity by tracing single microbubbles. *2011 IEEE Int Ultrason Symp* 2011.

[101] Lassau N, Bonastre J, Kind M, Vilgrain V, Lacroix J, Cuinet M, et al. Validation of dynamic contrast-enhanced ultrasound in predicting outcomes of antiangiogenic therapy for solid tumors: the French multicenter support for innovative and expensive techniques study. *Invest Radiol* 2014; **49**(12):794-800.

[102] Theek B, Opacic T, Möckel D, Schmitz G, Lammers T, and Kiessling F. Automated Generation of Reliable Blood Velocity Parameter Maps from Contrast-Enhanced Ultrasound Data. *Contrast Media Mol Imaging* 2017; **2017**:2098324.

[103] Wei K, Jayaweera AR, Firoozan S, Linka A, Skyba DM, and Kaul S. Quantification of Myocardial Blood Flow With Ultrasound-Induced Destruction of Microbubbles Administered as a Constant Venous Infusion. *Circulation* 1998; **97**:473-483.

[104] Tang M-X, Mulvana H, Gauthier T, Lim AKP, Cosgrove DO, Eckersley RJ, and Stride E. Quantitative contrast-enhanced ultrasound imaging: a review of sources of variability. *Interface Focus* 2011; **1**(4):520-539.

[105] Couture O, Besson B, Montaldo G, Fink M, and Tanter M. Microbubble ultrasound super-localization imaging (MUSLI). *2011 IEEE Int Ultrason Symp* 2011.

[106] Couture O, Hingot V, Heiles B, Muleki-Seya P, and Tanter M. Ultrasound Localization Microscopy and Super-Resolution: A State of the Art. *IEEE Trans Ultrason Ferroelectr Freq Control* 2018; **65**(8):1304-1320.

[107] Christensen-Jeffries K, Couture O, Dayton PA, Eldar YC, Hynynen K, Kiessling F, et al. Super-resolution Ultrasound Imaging. *Ultrasound Med Biol* 2020; **46**(4):865-891.

[108] Betzig E, Patterson GH, Sougrat R, Lindwasser OW, Olenych S, Bonifacino JS, et al. Imaging intracellular fluorescent proteins at nanometer resolution. *Science* 2006; **313**(5793):1642-1645.

[109] Rust MJ, Bates M, and Zhuang X. Sub-diffraction-limit imaging by stochastic optical reconstruction microscopy (STORM). *Nat Methods* 2006; **3**(1):793-796.

[110] Huang B, Bates M, and Zhuang X. Super-Resolution Fluorescence Microscopy. *Annu Rev Biochem* 2009; **78**:993-1016.

[111] Desailly Y, Pierre J, Couture O, and Tanter M. Resolution limits of ultrafast ultrasound localization microscopy. *Phys Med Biol* 2015; **60**(22):8723-8740.

[112] Christensen-Jeffries K, Browning RJ, Tang MX, Dunsby C, and Eckersley RJ. In vivo acoustic super-resolution and super-resolved velocity mapping using microbubbles. *IEEE Trans Med Imaging* 2015; **34**(2):433-440.

[113] van Sloun RJG, Solomon O, Bruce M, Khaing ZZ, Eldar YC, and Mischi M. Deep Learning for Super-Resolution Vascular Ultrasound Imaging. *IEEE ICASSP 2019* 2019.

[114] Song P, Manduca A, Trzasko JD, Daigle RE, and Chen S. On the effects of spatial sampling quantization in super-resolution ultrasound microvessel imaging. *IEEE T Ultrason Ferr* 2018; **65**(12):2264-2276.

[115] Christensen-Jeffries K, Harput S, Brown J, Wells PNT, Aljabar P, and Dunsby C. Microbubble Axial Localization Errors in Ultrasound Super-Resolution Imaging. *IEEE T Ultrason Ferr* 2017; **64**(11):1644-1654.

[116] Song P, Trzasko JD, Manduca A, Huang R, Kadirvel R, Kallmes DF, and Chen S. Improved super-resolution ultrasound microvessel imaging with spatiotemporal nonlocal means filtering and bipartite graph-based microbubble tracking. *IEEE T Ultrason Ferr* 2017; **65**(2):149-167.

[117] Couture O, Bannouf S, Montaldo G, Aubry JF, Fink M, and Tanter M. Ultrafast imaging of ultrasound contrast agents. *Ultrasound Med Biol* 2009; *35*(11):1908-1916.

[118] Couture O, Fink M, and Tanter M. Ultrasound contrast plane wave imaging. *IEEE Trans Ultrason Ferroelectr Freq Control* 2012; **59**(12):2676-2683.

[119] Huang C, Zhang W, Gong P, Lok U-W, Tang S, Yin T, et al. Super-Resolution Ultrasound Localization Microscopy Based on a High Frame-rate Clinical Ultrasound Scanner: An In-human Feasibility Study. *Phys Med Biol* 2021; **66**(8).

[120] Yan J, Broughton-Venner J, Huang P, and Tang MX. Super-Resolution Ultrasound Through Sparsity-Based Deconvolution and Multi-Feature Tracking. *IEEE Trans Med Imag* 2022; **41**(8):1938–1947.

[121] O'Reilly MA, and Hynynen K. A super-resolution ultrasound method for brain vascular mapping. *Med Phys* 2013; **40**(11):110701.

[122] Viessmann OM, Eckersley RJ, Christensen-Jeffries K, Tang MX, and Dunsby C. Acoustic super-resolution with ultrasound and microbubbles. *Phys Med Biol* 2013; 58(18): 6447–6458.

[123] Desailly Y, Couture O, Fink M, and Tanter M. Sono-activated ultrasound localization microscopy. *Appl Phys Lett* 2013; 103(17):174107.

[124] Errico C, Pierre J, Pezet S, Desailly Y, Lenkei Z, Couture O, and Tanter M. Ultrafast ultrasound localization microscopy for deep super-resolution vascular imaging. *Nature* 2015; **527**(7579):499-502.

[125] Ackermann D, and Schmitz G. Detection and Tracking of Multiple Microbubbles in Ultrasound B-Mode Images. *IEEE Trans Ultrason Ferroelectr Freq Control* 2016; **63**(1):72-82.

[126] Dencks S, Ackermann D, and Schmitz G. Evaluation of bubble tracking algorithms for super-resolution imaging of microvessels. *2016 IEEE Int Ultrason Symp* 2016.

[127] Lin F, Tsuruta JK, Rojas JD, and Dayton PA. Optimizing Sensitivity of Ultrasound Contrast-Enhanced Super-Resolution Imaging by Tailoring Size Distribution of Microbubble Contrast Agent. *Ultrasound Med Biol* 2017; **43**(10):2488-2493.

[128] Foiret J, Zhang H, Ilovitsh T, Mahakian L, Tam S, and Ferrara KW. Ultrasound localization microscopy to image and assess microvasculature in a rat kidney. *Sci Rep* 2017; **7**(13662).

[129] Harput S, Christensen-Jeffries K, Brown J, Li Y, Williams KJ, Davies AH, et al. Two-Stage Motion Correction for Super-Resolution Ultrasound Imaging in Human Lower Limb. *IEEE Trans Ultrason Ferroelectr Freq Control* 2018; **65**(5):803-814.

[130] Song P, Trzasko JD, Manduca A, Huang R, Kadirvel R, Kallmes DF, and Chen S. Improved Super-Resolution Ultrasound Microvessel Imaging with Spatiotemporal Nonlocal Means Filtering and Bipartite Graph-Based Microbubble Tracking. *IEEE Trans Ultrason Ferroelectr Freq Control* 2018; **65**(2):149-167.

[131] Opacic T, Dencks S, Theek B, Piepenbrock M, Ackermann D, Rix A, et al. Motion model ultrasound localization microscopy for preclinical and clinical multiparametric tumor characterization. *Nat Commun* 2018; **9**(1):1527.

[132] Bar-Zion A, Solomon O, Tremblay-Darveau C, Adam D, and Eldar YC. SUSHI: Sparsity-based Ultrasound Super-Resolution Hemodynamic Imaging. *IEEE Trans Ultrason Ferroelectr Freq Control* 2018; **65**(12):2365-2380.

[133] Yu J, Lavery L, and Kim K. Super-resolution ultrasound imaging method for microvasculature in vivo with a high temporal accuracy. *Sci Rep* 2018; **8**(13918).

[134] Zhang G, Harput S, Lin S, Christensen-Jeffries K, Leow CH, Brown J, et al. Acoustic wave sparsely activated localization microscopy (AWSALM): Super-resolution ultrasound imaging using acoustic activation and deactivation of nanodroplets. *Appl Phys Lett* 2018; **113**.

[135] Lok U-W, Huang C, Tang S, Gong P, Lucien F, and Kim Y. Three-dimensional Super-Resolution Ultrasound Microvessel Imaging with Bipartite Graph-based Microbubble

Tracking using a Verasonics 256-channel Ultrasound System. *2019 IEEE Int Ultrason Symp* 2019.

[136] Zhang G, Harput S, Hu H, Christensen-Jeffries K, Zhu J, Brown J, et al. Fast Acoustic Wave Sparsely Activated Localization Microscopy: Ultrasound Super-Resolution Using Plane-Wave Activation of Nanodroplets. *IEEE Trans Ultrason Ferroelectr Freq Control* 2019; **66**(6):1039-1046.

[137] Kanoulas E, Butler M, Rowley C, Voulgaridou V, Diamantis K, Duncan WC, et al. Super-Resolution Contrast-Enhanced Ultrasound Methodology for the Identification of In Vivo Vascular Dynamics in 2D. *Invest Radiol* 2019; **54**(8):500-516.

[138] Zhang J, Li N, Dong F, Liang S, Wang D, An J, et al. Ultrasound Microvascular Imaging Based on Super-Resolution Radial Fluctuations. *J Ultrasound Med* 2020; **39**(8):1507-1516.

[139] Liu X, Zhou T, Lu M, Yang Y, He Q, and Luo J. Deep Learning for Ultrasound Localization Microscopy. *IEEE Trans Med Imaging* 2020; **39**(10):3064-3078.

[140] Huang C, Lowerison MR, Trzasko JD, Manduca A, Bresler Y, Tang S, et al. Short Acquisition Time Super-Resolution Ultrasound Microvessel Imaging via Microbubble Separation. *Sci Rep* 2020; **10**(6007).

[141] van Sloun RJG, Cohen R, and Eldar YC. Deep Learning in Ultrasound Imaging. *Proc IEEE* 2020; **108**(1):11-29.

[142] Kierski TM, Espindola D, Newsome IG, Cherin E, Yin J, Foster FS, et al. Superharmonic Ultrasound for Motion-Independent Localization Microscopy: Applications to Microvascular Imaging From Low to High Flow Rates. *IEEE Trans Ultrason Ferroelectr Freq Control* 2020; **67**(5):957-967.

[143] Tang S, Song P, Trzasko JD, Lowerison M, Huang C, Gong P, et al. Kalman Filter-Based Microbubble Tracking for Robust Super-Resolution Ultrasound Microvessel Imaging. *IEEE Trans Ultrason Ferroelectr Freq Control* 2020; **67**(9):1738-1751.

[144] van Sloun RJG, Solomon O, Bruce M, Khaing ZZ, Wijkstra H, Eldar YC, and Mischi M. Super-Resolution Ultrasound Localization Microscopy Through Deep Learning. *IEEE Trans Med Imaging* 2021; **40**(3):829-839.

[145] Lin F, Shelton SE, Espíndola D, Rojas JD, Pinton G, and Dayton PA. 3-D Ultrasound Localization Microscopy for Identifying Microvascular Morphology Features of Tumor Angiogenesis at a Resolution Beyond the Diffraction Limit of Conventional Ultrasound. *Theranostics* 2017; **7**(1):196-204.

[146] Zhu J, Rowland EM, Harput S, Riemer K, Leow CH, Clark B, et al. 3D Super-Resolution US Imaging of Rabbit Lymph Node Vasculature in Vivo by Using Microbubbles. *Radiology* 2019; **291**(3):642-650.

[147] Lowerison MR, Huang C, Lucien F, Chen S, and Song P. Ultrasound localization microscopy of renal tumor xenografts in chicken embryo is correlated to hypoxia. *Sci Rep* 2020; **10**(2478).

[148] Dencks S, Piepenbrock M, Opacic T, Krauspe B, Stickeler E, Kiessling F, and Schmitz G. Clinical Pilot Application of Super-Resolution US Imaging in Breast Cancer. *IEEE Trans Ultrason Ferroelectr Freq Control* 2019; **66**(3):517-526.

[149] Zhu J, Zhang C, Christensen-Jeffries K, Zhang G, Harput S, Dunsby C, et al. Super-Resolution Ultrasound Localization Microscopy of Microvascular Structure and Flow for Distinguishing Metastatic Lymph Nodes – An Initial Human Study. *Ultraschall Med* 2022; **43**(6):592–8.

[150] Bullitt E, Gerig G, Pizer SM, Lin W, and Aylward SR. Measuring tortuosity of the intracerebral vasculature from MRA images. *IEEE Trans Med Imaging* 2003; **22**(9):1163-1171.

[151] Aylward SR, and Bullitt E. Initialization, noise, singularities, and scale in height ridge traversal for tubular object centerline extraction. *IEEE Trans Med Imaging* 2002; **21**(2):61-75.

[152] Zhang G, Lei YM, Li N, Yu J, Jiang XY, Yu MH, et al. Ultrasound super-resolution imaging for differential diagnosis of breast masses. *Front Oncol* 2022; **12**:1049991.

[153] Messina C, Bignone R, Bruno A, Bruno A, Bruno F, Calandri M, et al. Diffusion-Weighted Imaging in Oncology: An Update. *Cancers* 2020; **12**(6):1493.

[154] Fokkinga E, Hernandez-Tamames JA, Ianus A, Nilsson M, Tax CMW, Perez-Lopez R, and Grussu F. Advanced Diffusion-Weighted MRI for Cancer Microstructure Assessment in Body Imaging, and Its Relationship With Histology. *J Magn Reson Imaging* 2024; **60**(4):1278-1304.

[155] Koh DM, and Collins DJ. Diffusion-weighted MRI in the body: applications and challenges in oncology. *AJR Am J Roentgenol* 2007; **188**(6):1622-1635.

[156] Koh DM, Collins DJ, and Orton MR. Intravoxel incoherent motion in body diffusion-weighted MRI: reality and challenges. *AJR Am J Roentgenol* 2011; **196**(6):1351-1361.

[157] Thomassin-Naggara I, De Bazelaire C, Chopier J, Bazot M, Marsault C, and Trop I. Diffusion-weighted MR imaging of the breast: Advantages and pitfalls. *Eur J Radiol* 2013; **82**(3):435-443.

[158] Surov A, Meyer HJ, and Wienke A. Correlation between apparent diffusion coefficient (ADC) and cellularity is different in several tumors: a meta-analysis. *Oncotarget* 2017; **8**(35):59492–59499.

[159] van Rijswijk CSP, Kunz P, Hogendoorn PCW, Taminiau AHMT, Doornbos J, and Bloem JL. Diffusion-weighted MRI in the characterization of soft-tissue tumors. *J Magn Reson Imaging* 2002; **15**(3):302–307.

[160] Le Bihan D, Breton E, Lallemand D, Aubin ML, Vignaud J, and Laval-Jeantet M. Separation of diffusion and perfusion in intravoxel incoherent motion MR imaging. *Radiology* 1988; **168**(2):497–505.

[161] Thoeny HC, De Keyzer F, Vandecaveye V, Chen F, Sun X, Bosmans H, et al. Effect of vascular targeting agent in rat tumor model: dynamic contrast-enhanced versus diffusion-weighted MR imaging. *Radiology* 2005; **237**(2):492–499.

[162] Sun X, Wang H, Chen F, De Keyzer F, Yu J, Jiang Y, et al. Diffusion-weighted MRI of hepatic tumor in rats: comparison between in vivo and postmortem imaging acquisitions. *J Magn Reson Imaging* 2009; **29**(3):621-628.

[163] Le Bihan D, Turner R, Moonen CT, and Pekar J. Imaging of diffusion and microcirculation with gradient sensitization: design, strategy, and significance. *J Magn Reson Imaging* 1991; **1**(1):7–28.

[164] Pekar J, Moonen CT, and van Zijl PC. On the precision of diffusion/perfusion imaging by gradient sensitization. *Magn Reson Med* 1992; **23**(1):122–129.

[165] Koh DM, Blackledge M, Collins DJ, Padhani AR, Wallace T, Wilton B, et al. Reproducibility and changes in the apparent diffusion coefficients of solid tumours treated with combretastatin A4 phosphate and bevacizumab in a two- centre phase I clinical trial. *Eur Radiol* 2009; **19**(11):2728–2738.

[166] Le Bihan D. What can we see with IVIM MRI? *NeuroImage* 2019; **187**:56-67.

[167] Bennett KM, Schmainda KM, Bennett (Tong) R, Rowe DB, Lu H, and Hyde JS. Characterization of Continuously Distributed Cortical Water Diffusion Rates With a Stretched-Exponential Model. *Magn Reson Med* 2003; **50**(4):727-734.

[168] Spick C, Bickel H, Pinker K, Bernathova M, Kapetas P, Woitek R, et al. Diffusion-weighted MRI of breast lesions: a prospective clinical investigation of the quantitative imaging biomarker characteristics of reproducibility, repeatability, and diagnostic accuracy. *NMR Biomed* 2016; **29**(10):1445-1453.

[169] Newitt DC, Zhang Z, Gibbs JE, Partridge SC, Chenevert TL, Rosen MA, et al. Test–Retest Repeatability and Reproducibility of ADC Measures by Breast DWI: Results from the ACRIN 6698 Trial. *J Magn Reson Imaging* 2018; **49**(6):1617-1628.

[170] Newitt DC, Amouzandeh G, Partridge SC, Marques HS, Herman BA, Ross BD, et al. Repeatability and Reproducibility of ADC Histogram Metrics from the ACRIN 6698 Breast Cancer Therapy Response Trial. *Tomography* 2020; **6**(2):177-185.

[171] Giannotti E, Waugh S, Priba L, Davis Z, Crowe E, and Vinnicombe S. Assessment and quantification of sources of variability in breast apparent diffusion coefficient (ADC) measurements at diffusion weighted imaging. *Eur J Radiol* 2015; **84**(9):1729-1736.

[172] Petralia G, Bonello L, Summers P, Preda L, Malasevschi A, Raimondi S, et al. Intraobserver and interobserver variability in the calculation of apparent diffusion coefficient (ADC) from diffusion-weighted magnetic resonance imaging (DW-MRI) of breast tumours. *Radiol Med* 2011; **116**(3):466-476.

[173] Jang M, Kim SM, Yun BL, Ahn HS, Kim SY, Kang E, and Kim SW. Reproducibility of Apparent Diffusion Coefficient Measurements in Malignant Breast Masses. *J Korean Med Sci* 2015; **30**(11):1689-1697.

[174] Jerome NP, Vidić I, Egnell L, Sjøbakk TE, Østlie A, Fjøsne HE, et al. Understanding diffusion-weighted MRI analysis: Repeatability and performance of diffusion models in a benign breast lesion cohort. *NMR Biomed* 2021; **34**(7):e4508.

[175] Guo Y, Cai YQ, Cai ZL, Gao YG, An NY, Ma L, et al. Differentiation of clinically benign and malignant breast lesions using diffusion-weighted imaging. *J Magn Reson Imaging* 2002; **16**(2):172-178.

[176] Sinha S, Lucas-Quesada FA, Sinha U, DeBruhl N, and Bassett LW. In Vivo Diffusion-Weighted MRI of the Breast: Potential for Lesion Characterization. *J Magn Reson Imaging* 2002; **15**(6):693-704.

[177] Surov A, Meyer HJ, and Wienke A. Can apparent diffusion coefficient (ADC) distinguish breast cancer from benign breast findings? A meta-analysis based on 13 847 lesions. *BMC Cancer* 2019; **19**(1):955.

[178] Liang J, Zeng S, Li Z, Kong Y, Meng T, Zhou C, et al. Intravoxel Incoherent Motion Diffusion-Weighted Imaging for Quantitative Differentiation of Breast Tumors: A Meta-Analysis. *Front Oncol* 2020; **10**:585486.

[179] Shinmoto H, Oshio K, Tanimoto A, Higuchi N, Okuda S, Kuribayashi S, and Mulkern RV. Biexponential apparent diffusion coefficients in prostate cancer. *Magn Reson Imaging* 2009; **27**(3):355–359.

[180] Lemke A, Laun FB, Klauss M, Re TJ, Simon D, Delorme S, et al. Differentiation of pancreas carcinoma from healthy pancreatic tissue using multiple b-values: comparison of apparent diffusion coefficient and intravoxel incoherent motion derived parameters. *Invest Radiol* 2009; **44**(12):769–775

[181] Koh DM, Scurr E, Collins DJ, Pirgon A, Kanber B, Karanjia N, et al. Colorectal hepatic metastases: quantitative measurements using single-shot echo-planar diffusion-weighted MR imaging. *Eur Radiol* 2006; **16**(9):1898-1905.

[182] Wekking DW, Porcu M, De Silva P, Saba L, Scartozzi M, and Solinas C. Breast MRI: Clinical Indications, Recommendations, and Future Applications in Breast Cancer Diagnosis. *Curr Oncol Rep* 2023; **25**(4):257-267.

[183] Durando M, Gennaro L, Cho GY, Giri DD, Gnanasigamani MM, Patil S, et al. Quantitative apparent diffusion coefficient measurement obtained by 3.0Tesla MRI as a potential noninvasive marker of tumor aggressiveness in breast cancer. *Eur J Radiol* 2016; **85**(9):1651–1658.

[184] Surov A, Meyer HJ, and Wienke A. Associations between apparent diffusion coefficient (ADC) and KI 67 in different tumors: a meta-analysis. Part 1: ADC_{mean}. *Oncotarget* 2017; **8**(43):75434–75444.

[185] Surov A, Wienke A, and Meyer HJ. Pretreatment apparent diffusion coefficient does not predict therapy response to neoadjuvant chemotherapy in breast cancer. *Breast* 2020; **53**:59-67.

[186] Park SH, Moon WK, Cho N, Song IC, Chang JM, Park IA, et al. Diffusion-weighted MR imaging: pretreatment prediction of response to neoadjuvant chemotherapy in patients with breast cancer. *Radiology* 2010; **257**(1):56-63.

[187] Vasmel JE, Groot Koerkamp ML, Mandija S, Veldhuis WB, Moman MR, Froeling M, et al. Dynamic Contrast-enhanced and Diffusion-weighted Magnetic Resonance Imaging for Response Evaluation After Single-Dose Ablative Neoadjuvant Partial Breast Irradiation. *Adv Radiat Oncol* 2022; **7**(2):100854.

[188] Surov A, Clauser P, Chang YW, Li L, Martincich L, Partridge SC, et al. Can diffusion-weighted imaging predict tumor grade and expression of Ki-67 in breast cancer? A multicenter analysis. *Breast Cancer Res* 2018; **20**(1):58.

[189] Surov A, Chang YW, Li L, Martincich L, Partridge SC, Kim JY, and Wienke A. Apparent diffusion coefficient cannot predict molecular subtype and lymph node metastases in invasive breast cancer: a multicenter analysis. *BMC Canc* 2019; **19**(1):1043.

[190] Mardor Y, Pfeffer R, Spiegelmann R, Roth Y, Maier SE, Nissim O, et al. Early detection of response to radiation therapy in patients with brain malignancies using conventional and high b-value diffusion-weighted magnetic resonance imaging. *J Clin Oncol* 2003; **21**(6):1094-1100.

[191] Theilmann RJ, Borders R, Trouard TP, Xia G, Outwater E, Ranger-Moore J, et al. Changes in water mobility measured by diffusion MRI predict response of metastatic breast cancer to chemotherapy. *Neoplasia* 2004; **6**(6):831–837.

[192] Moffat BA, Chenevert TL, Lawrence TS, Meyer CR, Johnson TD, Dong Q, et al. Functional diffusion map: a noninvasive MRI biomarker for early stratification of clinical brain tumor response. *Proc Natl Acad Sci U S A* 2005; **102**(15):5524–5529.

[193] Malayeri AA, El Khouli RH, Zaheer A, Jacobs MA, Corona-Villalobos CP, Kamel IR, and Macura KJ. Principles and applications of diffusion-weighted imaging in cancer detection, staging, and treatment follow-up. *Radiographics* 2011; **31**(6):1773-1791.

[194] Naganawa S, Sato C, Kumada H, Ishigaki T, Miura S, and Takizawa O. Apparent diffusion coefficient in cervical cancer of the uterus: comparison with the normal uterine cervix. *Eur Radiol* 2005; **15**(1):71-78.

[195] Koh DM, Scurr E, Collins D, Kanber B, Norman A, Leach MO, and Husband JE. Predicting response of colorectal hepatic metastasis: value of pretreatment apparent diffusion coefficients. *AJR Am J Roentgenol* 2007; **188**(4):1001-1008.

[196] Lang P, Wendland MF, Saeed M, Gindele A, Rosenau W, Mathur A, et al. Osteogenic sarcoma: Noninvasive in vivo assessment of tumor necrosis with diffusion-weighted MR imaging. *Radiology* 1998; **206**(1):227-235.

[197] Moffat BA, Hall DE, Stojanovska J, McConville PJ, Moody JB, Chenevert TL, et al. Diffusion imaging for evaluation of tumor therapies in pre-clinical animal models. *MAGMA* 2004; **17**:249-259.

[198] Wong KH, Panek R, Dunlop A, Mcquaid D, Riddell A, Welsh LC, et al. Changes in multimodality functional imaging parameters early during chemoradiation predict treatment response in patients with locally advanced head and neck cancer. *Eur J Nucl Med Mol Imaging* 2018; **45**:759-767.

[199] Fliedner FP, Engel TB, El-Ali HH, Hansen AE, and Kjaer A. Diffusion weighted magnetic resonance imaging (DW-MRI) as a non-invasive, tissue cellularity marker to monitor cancer treatment response. *BMC Cancer* 2020; **20**(1):134.

[200] Wang C, Horton JK, Yin FF, and Chang Z. Assessment of Treatment Response With Diffusion-Weighted MRI and Dynamic Contrast-Enhanced MRI in Patients With Early-Stage Breast Cancer Treated With Single-Dose Preoperative Radiotherapy: Initial Results. *Technol Cancer Res Treat* 2016; **15**(5):651-660.

[201] Hottat N, Jani J, Badr D, Ridder MD, Nazac A, Houte KV, et al. Diffusion-Weighted MRI in the Evaluation of Early Stage Breast Cancer Treated with a Short Preoperative Radiotherapy: Preliminary Results. *J Belg Soc Radiol* 2023; **107**(1):8.

[202] Luo N, Ji Y, Huang X, Liu Y, Liu L, Jin G, et al. Changes in apparent diffusion coefficient as surrogate marker for changes in Ki-67 index due to neoadjuvant chemotherapy in patients with invasive breast cancer. *Acad Radiol* 2019; **26**(10):1352–1357.

[203] Qadir A, Singh N, Moe AAK, Cahoon G, Lye J, Chao M, et al. Potential of MRI in Assessing Treatment Response After Neoadjuvant Radiation Therapy Treatment in Breast Cancer Patients: A Scoping Review. *Clin Breast Cancer* 2024.

[204] Folkman J. (1995). Clinical applications of research on angiogenesis. *N Engl J Med* 1995; **333**(26):1757–1763.

[205] Kataoka M, Honda M, Sagawa H, Ohashi A, Sakaguchi R, Hashimoto H, et al. Ultrafast Dynamic Contrast-Enhanced MRI of the Breast: From Theory to Practice. *J Magn Reson Imaging* 2024; **60**:401-416.

[206] Tsao J and Kozerke S. MRI Temporal Acceleration Techniques. *J Magn Reson Imaging* 2012; **36**:543-560.

[207] Khalifa F, Soliman A, El-Baz A, Abou El-Ghar M, El-Diasty T, Gimel'farb G, et al. Models and methods for analyzing DCE-MRI: A review. *Med Phys* 2014; **41**(12):124301.

[208] Cheng HLM, and Wright GA. Rapid high-resolution T1 mapping by variable flip angles: Accurate and precise measurements in the presence of radiofrequency field inhomogeneity. *Magn Reson Med* 2006; **55**(3):566-574.

[209] Medved M, Karczmar G, Yang C, Dignam J, Gajewski TF, Kindler H, et al. Semiquantitative Analysis of Dynamic Contrast Enhanced MRI in Cancer Patients: Variability and Changes in Tumor Tissue Over Time. *J Magn Reson Imaging* 2004; **20**(1):122-128.

[210] Larsson HB, Stubgaard M, Frederiksen JL, Jensen M, Henriksen O, and Paulson OB. Quantitation of Blood-Brain Barrier Defect by Magnetic Resonance Imaging and Gadolinium-DTPA in Patients with Multiple Sclerosis and Brain Tumors. *Magn Reson Med* 1990; **16**(1):117-131.

[211] Parker GJM, Roberts C, Macdonald A, Buonaccorsi GA, Cheung S, Buckley DL, et al. Experimentally-derived functional form for a population-averaged high-temporal-resolution arterial input function for dynamic contrast-enhanced MRI. *Magn Reson Med* 2006; **56**(5):993-1000.

[212] Fritz-Hansen T, Rostrup E, Larsson HB, Sondergaard L, Ring P, and Henriksen O. Measurement of the arterial concentration of Gd-DTPA using MRI: A step toward quantitative perfusion imaging. *Magn Reson Med* 1996; **36**(2):225-231.

[213] Fluckiger JU, Schabel MC, and DiBella EVR. Model-based blind estimation of kinetic parameters in dynamic contrast enhanced (DCE)-MRI. *Magn Reson Med* 2009; **62**(6):1477-1486.

[214] Kovar DA, Lewis M, and Karczmar GS. A new method for imaging perfusion and contrast extraction fraction: Input functions derived from reference tissues. *J Magn Reson Imaging* 1998; **8**(5):1126-1134.

[215] Yang C, Karczmar GS, Medved M and Stadler WM. Multiple reference tissue method for contrast agent arterial input function estimation. *Magn Reson Med* 2007; **58**(6):1266-1275.

[216] Tofts PS. Modeling tracer kinetics in dynamic Gd-DTPA MR imaging. *J Magn Reson Imaging* 1997; **7**(1):91-101.

[217] Tofts PS, Brix G, Buckley DL, Evelhoch JL, Henderson E, Knopp MV, et al. Estimating kinetic parameters from dynamic contrast enhanced T(1)-weighted MRI of a diffusable tracer: standardized quantities and symbols. *J Magn Reson Imaging* 1999; **10**:223-232.

[218] Fan WX, Chen XF, Cheng FY, Cheng YB, Xu T, Zhu WB, et al. Retrospective analysis of the utility of multiparametric MRI for differentiating between benign and malignant breast lesions in women in China. *Medicine* 2018; **97**:4

[219] Jansen SA, Fan X, Karczmar GS, Abe H, Schmidt RA, and Newstead GM. Differentiation between Benign and Malignant BreastLesions Detected by Bilateral Dynamic Contrast-Enhanced MRI: A Sensitivity and Specificity Study. *Magn Reson Med* 2008; **59**:747-754.

[220] Cao Y, Wang X, Shi J, Zeng X, Du L, Li Q, et al. Multiple parameters from ultrafast dynamic contrast-enhanced magnetic resonance imaging to discriminate between benign and malignant breast lesions: Comparison with apparent diffusion coefficient. *Diagn Interv Imaging* 2023; **104**(6):275-283.

[221] Schabel MC, Morrell GR, Oh KY, Walczak CA, Barlow RB, and Neumayer LA. Pharmacokinetic Mapping for Lesion Classification in Dynamic Breast MRI. *J Magn Reson Imaging* 2010; **31**(6):1371-1378.

[222] Cheng Z, Wu Z, Shi G, Yi Z, Xie M, Zeng W, et al. Discrimination between benign and malignant breast lesions using volumetric quantitative dynamic contrast-enhanced MR imaging. *Eur Radiol* 2018; **28**:982-991.

[223] Woolf DK, Padhani AR, Taylor NJ, Gogbashian A, Li SP, Beresford MJ, et al. Assessing response in breast cancer with dynamic contrast enhanced magnetic resonance imaging: Are signal intensity–time curves adequate? *Breast Cancer Res Treat* 2014; **147**:335-343.

[224] Abramson RG, Li X, Hoyt TL, Su PF, Arlinghaus LR, Wilson KJ, et al. Early assessment of breast cancer response to neoadjuvant chemotherapy by semi-quantitative analysis of high-temporal resolution DCE-MRI: Preliminary results. *Magn Reson Imaging* 2013; **31**(9).

[225] Ohmatsu K, Omatsu T, Okonogi N, Ikoma Y, Murata K, Kishimoto R, et al. Changes in Intratumor Blood Flow After Carbon-Ion Radiation Therapy for Early-Stage Breast Cancer. *Int J Part Ther* 2024; **12**:100018.

[226] Mouawad M, Biernaski H, Brackstone M, Lock M, Yaremko B, Shmuilovich O, et al. DCE-MRI assessment of response to neoadjuvant SABR in early stage breast cancer: Comparisons of single versus three fraction schemes and two different imaging time delays post-SABR. *Clin Transl Radiat Oncol* 2019; **21**:25-31.

[227] O'Connor JPB, Aboagye EO, Adams JE, Aerts HJWL, Barrington SF, Beer AJ, et al. Imaging biomarker roadmap for cancer studies. *Nat Rev Clin Oncol* 2017; **14**(3):169–186.

[228] Hylton NM, Gatsonis CA, Rosen MA, Lehman CD, Newitt DC, Partridge SC, et al. Neoadjuvant Chemotherapy for Breast Cancer: Functional Tumor Volume by MR Imaging Predicts Recurrence-free Survival-Results from the ACRIN 6657/CALGB 150007 I-SPY 1 TRIAL. *Radiology* 2016; **279**(1):44-55.

[229] Partridge SC, Zhang Z, Newitt DC, Gibbs JE, Chenevert TL, Rosen MA, et al. Diffusion-weighted MRI Findings Predict Pathologic Response in Neoadjuvant Treatment of Breast Cancer: The ACRIN 6698 Multicenter Trial. *Radiology* 2018; **289**(3):618-627.

[230] Li W, Partridge SC, Newitt DC, Steingrimsson J, Marques HS, Bolan PJ, et al. Breast Multiparametric MRI for Prediction of Neoadjuvant Chemotherapy Response in Breast Cancer: The BMMR2 Challenge. *Radiol Imaging Cancer* 2024; **6**(1):e230033.

[231] Virostko J, Hainline A, Kang H, Arlinghaus LR, Abramson RG, Barnes SL, et al. Dynamic contrast-enhanced magnetic resonance imaging and diffusion-weighted magnetic resonance imaging for predicting the response of locally advanced breast cancer to neoadjuvant therapy: a meta-analysis. *J Med Imaging (Bellingham)* 2018; **5**(1):011011.

[232] Jun W, Cong W, Xianxin X, and Daqing J. Meta-Analysis of Quantitative Dynamic Contrast-Enhanced MRI for the Assessment of Neoadjuvant Chemotherapy in Breast Cancer. *Am Surg* 2019; textbf85(6):645-653.

[233] Li Z, Li J, Lu X, Qu M, Tian J, and Lei J. The diagnostic performance of diffusion-weighted imaging and dynamic contrast-enhanced magnetic resonance imaging in evaluating the pathological response of breast cancer to neoadjuvant chemotherapy: A meta-analysis. *Eur J Radiol* 2021; **143**:109931.

[234] Dakhil HA, Arian A, Ahmadinejad N, Bustan RA, Sahib MA, and Anjomrooz M. The value of dynamic contrast-enhanced magnetic resonance imaging (DCE-MRI) in the prediction of neoadjuvant chemotherapy response in breast cancer: A Meta-Analysis. *Int J Radiat Res* 2024; **22**(3):749-755.

[235] Rueckert D, Sonoda LI, Hayes C, Hill DL, Leach MO, and Hawkes DJ. Nonrigid registration using free-form deformations: Application to breast MR images. *IEEE Trans Med Imag* 2009; **18**(8):712–21.

[236] Shackleford JA, Kandasamy N, and Sharp GC. On developing B-spline registration algorithms for multi-core processors. *Phys Med Biol* 2010; **55**(21):6239-6351.

[237] Otsu N. A Threshold Selection Method from Gray-Level Histograms. *IEEE Trans Syst Man Cybern* 1979; **9**(1):62-66.

[238] Yan J, Huang B, Tonko J, Toulemonde M, Hansen-Shearer J, Tan Q, et al. Transthoracic Super-Resolution Ultrasound Localization Microscopy of Myocardial Vasculature in Patients. *ArXiv* 2023.

[239] Forster JC, Harriss-Phillips WM, Douglass MJ and Bezak E. A review of the development of tumor vasculature and its effects on the tumor microenvironment. *Hypoxia* 2017; **5**:21-32.

[240] Blackledge MD, Collins DJ, Koh DM, and Leach MO. Rapid development of image analysis research tools: Bridging the gap between researcher and clinician with pyOsiriX. *Comput Biol Med* 2016; **69**:203-212.

[241] Virtanen P, Gommers R, Oliphant TE, Haberland M, Reddy T, Cournapeau D, et al. SciPy 1.0: fundamental algorithms for scientific computing in Python. *Nat Methods* 2020; **17**(3):261-272.

[242] Shen Y, Goerner FL, Snyder C, Morelli JN, Hao D, Hu D, et al. T1 relaxivities of gadolinium-based magnetic resonance contrast agents in human whole blood at 1.5, 3, and 7 T. *Invest Radiol* 2015; **50**(5):330-338.

[243] Harris CR, Millman KJ, van der Walt SJ, Gommers R, Virtanen P, Cournapeau D, et al. Array programming with NumPy. *Nature* 2020; **585**(7825):357-362.

[244] Tofts PS. T1-weighted DCE Imaging Concepts: Modelling, Acquisition and Analysis. *MAGNETOM Flash* 2010.

[245] Orton MR, d'Arcy JA, Walker-Samuel S, Hawkes DJ, Atkinson D, Collins DJ, and Leach MO. Computationally efficient vascular input function models for quantitative kinetic modelling using DCE-MRI. *Phys Med Biol* 2008; **53**:1225-1239.

[246] Chao S-L, Metens T, and Lemort M. TumourMetrics: a comprehensive clinical solution for the standardization of DCE-MRI analysis in research and routine use. *QIMS* 2017; **7**(5).

[247] Koo TK, and Li MY. A Guideline of Selecting and Reporting Intraclass Correlation Coefficients for Reliability Research. *J Chiropr Med* 2016; **15**(2):155-163.

[248] Feingold S, Gessner R, Guracar IM, and Dayton PA. Quantitative volumetric perfusion mapping of the microvasculature using contrast ultrasound. *Invest Radiol* 2010; **45**(10):669-674.

[249] Kaffas AE, Sigrist RMS, Fisher G, Bachawal S, Liau J, Wang H, et al. Quantitative Three-Dimensional Dynamic Contrast-Enhanced Ultrasound Imaging: First-In-Human Pilot Study in Patients with Liver Metastases. *Theranostics* 2017; **7**(15):3745–58.

[250] Kasoji SK, Rivera JN, Gessner RC, Chang SX, and Dayton PA. Early Assessment of Tumor Response to Radiation Therapy using High-Resolution Quantitative Microvascular Ultrasound Imaging. *Theranostics* 2018; **8**(1):156–68.

[251] Wu D, Xu N, Xie Y, Shen Y, Fu Y, Liu L, et al. Noninvasive optoacoustic imaging of breast tumor microvasculature in response to radiotherapy. *Front Physiol* 2022; **13**:1044308.

[252] Demidov V, Maeda A, Sugita M, Madge V, Sadanand S, Flueraru C, and Vitkin IA. Preclinical longitudinal imaging of tumor microvascular radiobiological response with functional optical coherence tomography. *Sci Rep* 2018; **8**(1).

[253] Choi DH, Oh D, Na K, Kim H, Choi D, Jung YH, et al. Radiation induces acute and subacute vascular regression in a three-dimensional microvasculature model. *Front Oncol* 2023; **13**:1252014.

[254] Byun MR, Lee SW, Paulson B, Lee S, Lee W, Lee KK, et al. Micro-endoscopic In Vivo Monitoring in the Blood and Lymphatic Vessels of the Oral Cavity after Radiation Therapy. *Int J Med Sci* 2019; **16**(11):1525-1533.

[255] Mohanty K, Papadopoulou V, Newsome IG, Shelton S, Dayton PA, and Muller M. Ultrasound multiple scattering with microbubbles can differentiate between tumor and healthy tissue in vivo. *Phys Med Biol* 2019; **64**(11):115022.

[256] Andonegui-Elguera MA, Alfaro-Mora Y, Cáceres-Gutiérrez R, Caro-Sánchez CHS, Herrera LA and Díaz-Chávez J. An Overview of Vasculogenic Mimicry in Breast Cancer. *Front Oncol* 2020; **10**:220.

[257] Lerendegui M, Riemer K, Wang B, Dunsby C, and Tang MX. BUbble Flow Field: a Simulation Framework for Evaluating Ultrasound Localization Microscopy Algorithms. *ArXiv* 2022.

[258] Belgharbi H, Poree J, Damseh R, Perrot V, Milecki L, Delafontaine-Martel P, et al. An anatomically and hemodynamically realistic simulation framework for 3D ultrasound localization microscopy. *J Ultrason Ferroelectr Freq Control* 2023; **3**:1–13.

[259] Hoferer I, Jourdain L, Girot C, Benatsou B, Leguerney I, Cournede PH, et al. New calibration setup for quantitative DCE-US imaging protocol: Toward standardization. *Med Phys* 2023; **50**(9):5541-5552.

[260] Huang B, Yan J, Morris M, Sinnett V, Somaiah N, and Tang MX. Acceleration-Based Kalman Tracking for Super-Resolution Ultrasound Imaging In Vivo. *IEEE Trans Ultrason Ferroelectr Freq Control* 2023; **70**(12):1739-1748.

[261] Xia S, Zheng Y, Hua Q, Wen J, Luo X, Yan J, et al. Super-resolution ultrasound and microvasculomics: a consensus statement. *Eur Radiol* 2024; **34**(11):7503-7513.

[262] Hoyt K. Super-Resolution Ultrasound Imaging for Monitoring the Therapeutic Efficacy of a Vascular Disrupting Agent in an Animal Model of Breast Cancer. *J Ultrasound Med* 2024; **43**(6):1099-1107.

[263] Yin J, Dong F, An J, Guo T, Cheng H, Zhang J, and Zhang J. Pattern recognition of microcirculation with super-resolution ultrasound imaging provides markers for early tumor response to anti-angiogenic therapy. *Theranostics* 2024; **14**(3):1312-1324.

[264] Brown KG, Li J, Margolis R, Trinh B, Eisenbrey JR, and Hoyt K. Assessment of Transarterial Chemoembolization Using Super-resolution Ultrasound Imaging and a Rat Model of Hepatocellular Carcinoma. *Ultrasound Med Biol* 2023; **49**(5): 1318-1326.

[265] Lowerison MR, Zhang W, Chen X, Fan TM, and Song P. Characterization of Anti-Angiogenic Chemo-Sensitization via Longitudinal Ultrasound Localization Microscopy in Colorectal Carcinoma Tumor Xenografts. *IEEE Trans Biomed Eng* 2022; **69**(4):1449-1460.

[266] Suo S, Yin Y, Geng X, Zhang D, Hua J, Cheng F, et al. Difusion-weighted MRI for predicting pathologic response to neoadjuvant chemotherapy in breast cancer: evaluation with mono-, bi-, and stretched-exponential models. *J Transl Med* 2021; **19**(1):236.

[267] Afaq A, Andreou A, and Koh DM. Diffusion-weighted magnetic resonance imaging for tumour response assessment: why, when and how? *Cancer Imaging* 2010; **10**(1):S179-S188.

[268] Xu J-F, Wu X-W, Wang W-Q, Kong L-L, Wu L-M, and Wang F. Value of diffusion-weighted magnetic resonance imaging on the follow-up of nasopharyngeal carcinoma after radiotherapy. *J Xray Sci Technol* 2014; **22**(5):605-612.

[269] Kirshenboim Z, Lantsman CD, Appel S, Klug M, Onn A, Truong MT, and Marom EM. Magnetic resonance imaging for prospective assessment of local recurrence of non-small cell lung cancer after stereotactic body radiation therapy. *Lung Cancer* 2023; **182**:107265.

[270] Fusco R, Granata V, Sansone M, Grimm R, Delrio P, Rega D, et al. Intravoxel Incoherent Motion Model of Diffusion Weighted Imaging and Diffusion Kurtosis Imaging in Differentiating of Local Colorectal Cancer Recurrence from Scar/Fibrosis Tissue by Multivariate Logistic Regression Analysis. *Appl Sci* 2020; **10**(23):8609.

[271] Chung SR, Choi YJ, Suh CH, Lee JH, and Baek JH. Diffusion-weighted Magnetic Resonance Imaging for Predicting Response to Chemoradiation Therapy for Head and Neck Squamous Cell Carcinoma: A Systematic Review. *Korean J Radiol* 2019; **20**(4):649-661.

[272] Vollenbrock SE, Voncken FEM, Bartels LW, Beets-Tan RGH, and Bartels-Rutten A. Diffusion-weighted MRI with ADC mapping for response prediction and assessment of oesophageal cancer: A systematic review. *Radiother Oncol* 2020; **142**:17-26.

[273] Amodeo A, Rosman AS, Desiato V, Hindman NM, Newman E, Berman R, et al. MRI-Based Apparent Diffusion Coefficient for Predicting Pathologic Response of Rectal Cancer After Neoadjuvant Therapy: Systematic Review and Meta-Analysis. *AJR AM J Roentgenol* 2018; *211*(5):W205-W216.

[274] Meyer H-J, Wienke A, and Surov A. Diffusion-Weighted Imaging of Different Breast Cancer Molecular Subtypes: A Systematic Review and Meta-Analysis. *Breast Care* 2022; **17**(1):47-54.

[275] Teng X, Zhang J, Zhang X, Fan X, Zhou T, Huang Y-H, et al. Noninvasive imaging signatures of HER2 and HR using ADC in invasive breast cancer: repeatability, reproducibility, and association with pathological complete response to neoadjuvant chemotherapy. *Breast Cancer Res* 2023; **25**(1):77.

[276] Arlinghaus LR, Welch EB, Chakravarthy AB, Xu L, Farley JS, Abramson VG, et al. Motion correction in diffusion-weighted MRI of the breast at 3T. *J Magn Reson Imaging* 2011; **33**(5):1063-1070.

[277] Jezzard P, Barnett AS, and Pierpaoli C. Characterization of and correction for eddy current artifacts in echo planar diffusion imaging. *Magn Reson Med* 1998; **39**(5):801-812.

[278] Baltzer P, Mann RM, Iima M, Sigmund EE, Clauser P, Gilbert FJ, et al. Diffusion-weighted imaging of the breast-a consensus and mission statement from the EUSOBI International Breast Diffusion-Weighted Imaging working group. *Eur Radiol* 2020; **30**(3):1436-1450.

[279] Shukla-Dave A, Obuchowski NA, Chenevert TL, Jambawalikar S, Schwartz LH, Malyarenko D, et al. Quantitative imaging biomarkers alliance (QIBA) recommendations for improved precision of DWI and DCE-MRI derived biomarkers in multicenter oncology trials. *J Magn Reson Imaging* 2019; **49**(7):e101-e121.

[280] Partridge SC, Steingrimsson J, Newitt DC, Gibbs JE, Marques HS, Bolan PJ, et al. Impact of Alternate b-Value Combinations and Metrics on the Predictive Performance and Repeatability of Diffusion-Weighted MRI in Breast Cancer Treatment: Results from the ECOG-ACRIN A6698 Trial. *Tomography* 2022; **8**(2):701-717.

[281] Basukala D, Mikheev A, Sevilimedu V, Gilani N, Moy L, Pinker K, et al. Multisite MRI Intravoxel Incoherent Motion Repeatability and Reproducibility across 3 T Scanners in a Breast Diffusion Phantom: A BReast Intravoxel Incoherent Motion Multisite (BRIMM) Study. *J Magn Reson Imaging* 2024; **59**(6):2226-2237.

[282] Fang LK, Keenan KE, Carl M, Ojeda-Fournier H, Rodriguez-Soto AE, and Rakow-Penner RA. Apparent Diffusion Coefficient Reproducibility Across 3 T Scanners in a Breast Diffusion Phantom. *J Magn Reson Imaging* 2023; **57**(3):812-823.

[283] Giannelli M, Sghedoni R, Iacconi C, Iori M, Traino AC, Guerrisi M, et al. MR scanner systems should be adequately characterized in diffusion-MRI of the breast. *PLoS One* 2014; **9**(1):e86280.

[284] Chilla GS, Tan CT, Xu C, and Poh CL. Diffusion weighted magnetic resonance imaging and its recent trend—a survey. *Quant Imaging Med Surg* 2015; **5**(3):407-422.

[285] Li Z, Li X, Peng C, Dai W, Huang H, Li X, et al. The Diagnostic Performance of Diffusion Kurtosis Imaging in the Characterization of Breast Tumors: A Meta-Analysis. *Front Oncol* 2020; **10**:575272.

[286] He M, Ruan H, Ma M, and Zhang Z. Application of Diffusion Weighted Imaging Techniques for Differentiating Benign and Malignant Breast Lesions. *Front Oncol* 2021; **11**:694634.

[287] Panagiotaki E, Walker-Samuel S, Siow B, Johnson SP, Rajkumar V, Pedley RB, et al. Noninvasive quantification of solid tumor microstructure using VERDICT MRI. *Cancer Res* 2014; **74**(7):1902-1912.

[288] O'Donnell LJ, and Westin C-F. An introduction to diffusion tensor image analysis. *Neurosurg Clin N Am* 2012; **22**(2):185.

[289] Honda M, Sigmund EE, Le Bihan D, Pinker K, Clauser P, Karampinos D, et al. Advanced breast diffusion-weighted imaging: what are the next steps? A proposal from the EUSOBI International Breast Diffusion-weighted Imaging working group. *Eur Radiol* 2024.

[290] Mendez AM, Fang LK, Meriwether CH, Batasin SJ, Loubrie S, Rodriguez-Soto AE, and Rakow-Penner RA. Diffusion Breast MRI: Current Standard and Emerging Techniques. *Front Oncol* 2022; **12**:844790.

[291] Sorace AG, Wu C, Barnes SL, Jarrett AM, Avery S, Patt D, et al. Repeatability, reproducibility, and accuracy of quantitative mri of the breast in the community radiology setting. *J Magn Reson Imaging* 2018.

[292] Barnes SL, Whisenant JG, Loveless ME, Ayers GD, and Yankeelov TE. Assessing the Reproducibility of Dynamic Contrast Enhanced Magnetic Resonance Imaging in a Murine Model of Breast Cancer. *Magn Reson Med* 2013; **69**:1721-1734.

[293] Loveless M, Halliday J, Liess C, Xu L, Dortch R, Whisenant J, et al. A quantitative comparison of the influence of individual versus population-derived vascular input functions on a dynamic contrast enhanced-MRI in small animals. *Magn Reson Med* 2012; **67**:226–236.

[294] Galbraith SM, Lodge MA, Taylor NJ, Rustin GJS, Bentzen S, Stirling JJ, and Padhani AR. Reproducibility of dynamic contrast-enhanced MRI in human muscle and tumours: comparison of quantitative and semi-quantitative analysis. *NMR Biomed* 2002; **15**:132-142.

[295] Rata M, Collins DJ, Darcy J, Messiou C, Tunariu N, Desouza N, et al. Assessment of repeatability and treatment response in early phase clinical trials using DCE-MRI:

comparison of parametric analysis using MR- and CT-derived arterial input functions. *Eur Radiol* 2016; **26**:1991-1998.

[296] Roberts C, Issa B, Stone A, Jackson A, Waterton JC, and Parker GJM. Comparative Study into the Robustness of Compartmental Modeling and Model-Free Analysis in DCE-MRI Studies. *J Magn Reson Imaging* 2006; **23**(4):554-563.

[297] Wang H, Su Z, Ye H, Xu X, Sun Z, Li L, et al. Reproducibility of Dynamic Contrast-Enhanced MRI in Renal Cell Carcinoma. *Medicine* 2015; **94**(37).

[298] Sridharan N, Salem A, Little RA, Tariq M, Cheung S, Dubec MJ, et al. Measuring repeatability of dynamic contrast-enhanced MRI biomarkers improves evaluation of biological response to radiotherapy in lung cancer. *Eur Radiol* 2024.

[299] Jarosz-Biej M, Smolarczyk R, Cichoń T, and Ku lach N. Tumor Microenvironment as A "Game Changer" in Cancer Radiotherapy. *Int J Mol Sci* 2019; **20**(13):3212.

[300] Bos P, van der Hulst HJ, van den Brekel MWM, Schats W, Jasperse B, Beets-Tan RGH, and Castelijns JA. Prognostic functional MR imaging parameters in head and neck squamous cell carcinoma: A systematic review. *Eur J Radiol* 2021; **144**:109952.

[301] Martens RM, Koopman T, Lavini C, Ali M, Peeters CFW, Noij DP, et al. Multiparametric functional MRI and 18F-FDG-PET for survival prediction in patients with head and neck squamous cell carcinoma treated with (chemo)radiation. *Eur Radiol* 2021; **31**(2):616-628.

[302] Smits HJG, Vink SJ, de Ridder M, Philippens MEP, and Dankbaar JW. Prognostic value of pretreatment radiological MRI variables and dynamic contrast-enhanced MRI on radiotherapy treatment outcome in laryngeal and hypopharyngeal tumors. *Clin Transl Tadiat Oncol* 2024; **49**:100857.

[303] Muz B, de la Puente P, Azab F, and Azab AK. The role of hypoxia in cancer progression, angiogenesis, metastasis, and resistance to therapy. *Hypoxia* 2015; **3**:83-92.

[304] Mui AWL, Lee AWM, Ng W-T, Lee VHF, Vardhanabhuti V, Man S-Y, et al. Optimal time for early therapeutic response prediction in nasopharyngeal carcinoma with functional magnetic resonance imaging. *Phys Imaging Radiat Oncol* 2023; **27**:100458.

[305] Donaldson SB, Buckley DL, O'Connor JP, Davidson SE, Carrington BM, Jones AP, and West CML. Enhancing fraction measured using dynamic contrast-enhanced MRI predicts disease-free survival in patients with carcinoma of the cervix. *Br J Cancer* 2010; **102**(1):23-26.

[306] Zahra MA, Tan LT, Priest AN, Graves MJ, Arends M, Crawford RAF, et al. Semiquantitative and quantitative dynamic contrast-enhanced magnetic resonance imaging measurements predict radiation response in cervix cancer. *Int J Radiat Oncol Biol Phys* 2009; **74**(3):766-773.

[307] Mayr NA, Huang Z, Wang JZ, Lo SS, Fan JM, Grecula JC, et al. Characterizing tumor heterogeneity with functional imaging and quantifying high-risk tumor volume for early prediction of treatment outcome: cervical cancer as a model. *Int J Radiat Oncol Biol Phys* 2012; **83**(3):972-979.

[308] Lund KV, Simonsen TG, Hompland T, Kristensen GB, and Rofstad EK. Short-term pretreatment DCE-MRI in prediction of outcome in locally advanced cervical cancer. *Radiother Oncol* 2015; **115**(3):379-385.

[309] Yuan J, Chow SKK, Yeung DKW, Ahuja AT, and King AD. Quantitative evaluation of dual-flip-angle T1 mapping on DCE-MRI kinetic parameter estimation in head and neck. *Quant Imaging Med Surg* 2012; **2**(4):245-253.

[310] Azahaf M, Haberley M, Betrouni N, Ernst O, Behal H, Duhamel A, et al. Impact of arterial input function selection on the accuracy of dynamic contrast-enhanced MRI quantitative analysis for the diagnosis of clinically significant prostate cancer. *JMRI* 2016; **43**:737-749.

[311] Peled S, Vangel M, Kikinis R, Tempany CM, Fennessy FM, and Fedorov A. Selection of Fitting Model and Arterial Input Function for Repeatability in Dynamic Contrast-Enhanced Prostate MRI. *Acad Radiol* 2019; **26**:e241-e251.

[312] Weinmann HJ, Brasch RC, Press WR, and Wesbey GE. Characteristics of gadolinium-DTPA complex: a potential NMR contrast agent. *AJR Am J Roentgenol* 1984; **142**(3):619-624.

[313] Othman AE, Falkner F, Kessler D-E, Martirosian P, Weiss J, Kruck S, et al. Comparison of different population-averaged arterial-input-functions in dynamic contrast-enhanced MRI of the prostate: effects on pharmacokinetic parameters and their diagnostic performance. *Magn Reson Imaging* 2016; **34**(4):496-501.

[314] Carvalho ED, Silva RRV, Mathew MJ, Araujo FHD, and Filho AODC. Tumor Segmentation in Breast DCE- MRI Slice Using Deep Learning Methods. *2021 IEEE ISCC* 2021.

[315] Anand I, Negi H, Kumar D, Mittal M, Kim T, and Roy S. Residual U-Network for Breast Tumor Segmentation from Magnetic Resonance Images. *Comput Mater Con* 2021; **67**(3):3107-3127.

[316] Yue W, Zhang H, Zhou J, Li G, Tang Z, Sun Z, et al. Deep learning-based automatic segmentation for size and volumetric measurement of breast cancer on magnetic resonance imaging. *Front Oncol* 2022; **12**:984626.

Appendix A

Results Chapter 2: Diffusion-Weighted MRI

A.1 Repeatability

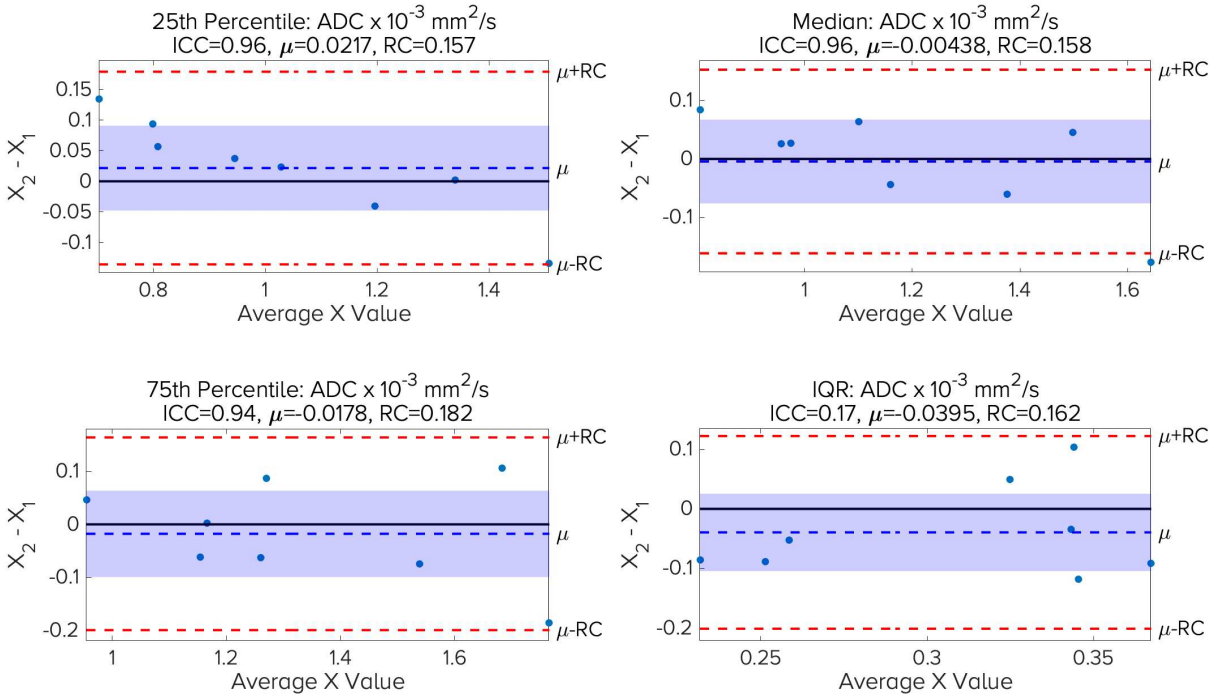


Figure A.1: Bland-Altman plots for 8 repeatability diffusion-weighted MRI, with the Apparent Diffusion Coefficient (ADC) extracted from each pixel across the entire tumour. The median, 25th percentile, 75th percentile and interquartile range (IQR) of ADC was assessed for repeatability. The y-axis is the difference between the quantitative parameter X from the 2 repeat measurements (after the first baseline scan X1 and second baseline scan X2). The x-axis shows the average value of the 2 repeat measurements of the quantitative parameter. The mean of the differences (μ) is indicated by the blue dashed line, with its 95% confidence interval represented as the shaded blue area. The dotted line represents 0 difference between the test-retest measurement. The mean of the differences ± the repeatability coefficient ($\mu\pm$ RC) is shown as the red dashed line. The 95% confidence interval of the repeatability coefficient is not displayed due to overlap with the shaded blue area. The Intraclass Correlation Coefficient (ICC) is also provided.

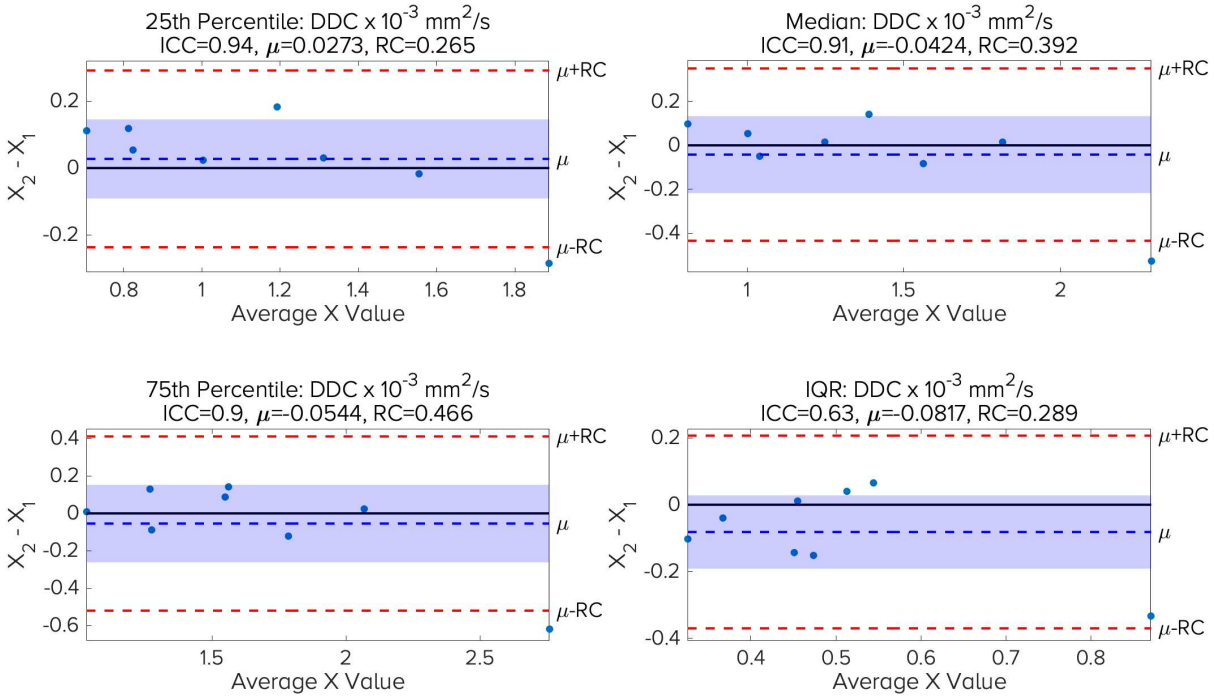


Figure A.2: Bland-Altman plots for 8 repeatability diffusion-weighted MRI, with the Distributed Diffusion Coefficient (DDC) extracted from each pixel across the entire tumour. The median, 25th percentile, 75th percentile and interquartile range (IQR) of DDC was assessed for repeatability. The y-axis is the difference between the quantitative parameter X from the 2 repeat measurements (after the first baseline scan X1 and second baseline scan X2). The x-axis shows the average value of the 2 repeat measurements of the quantitative parameter. The mean of the differences (μ) is indicated by the blue dashed line, with its 95% confidence interval represented as the shaded blue area. The dotted line represents 0 difference between the test-retest measurement. The mean of the differences ± the repeatability coefficient ($\mu\pm$ RC) is shown as the red dashed line. The 95% confidence interval of the repeatability coefficient is not displayed due to overlap with the shaded blue area. The Intraclass Correlation Coefficient (ICC) is also provided.

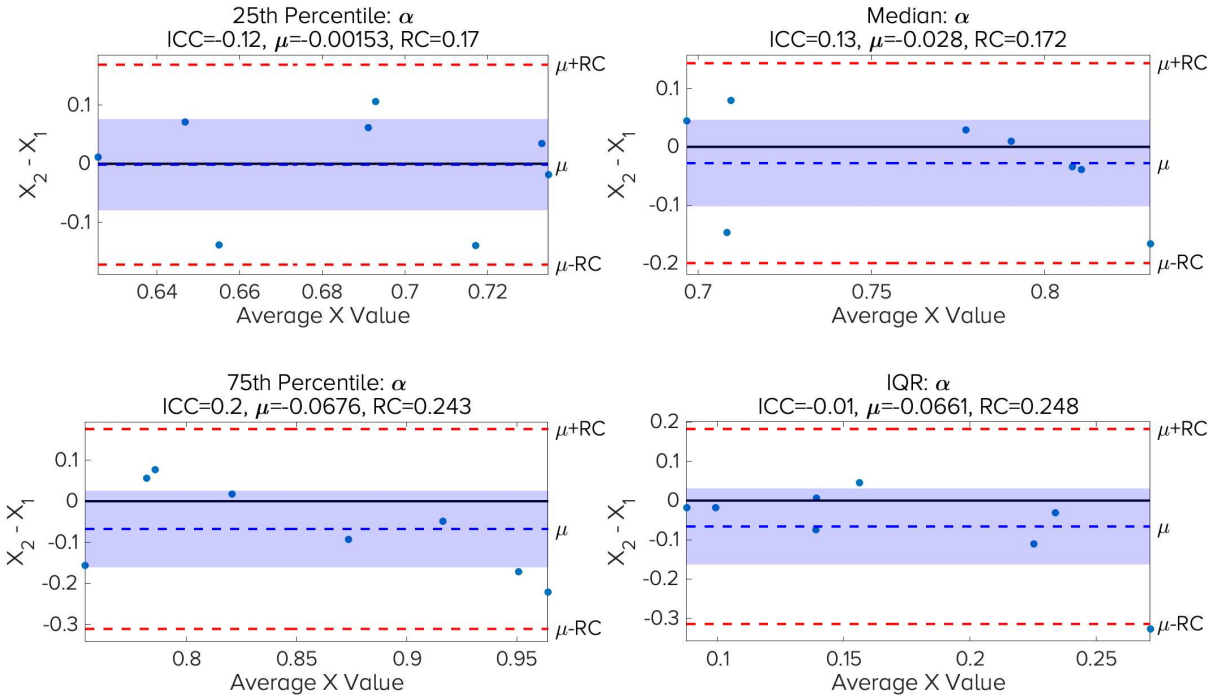


Figure A.3: Bland-Altman plots for 8 repeatability diffusion-weighted MRI, with the Heterogeneity Index (α) extracted from each pixel across the entire tumour. The median, 25th percentile, 75th percentile and interquartile range (IQR) of α was assessed for repeatability. The y-axis is the difference between the quantitative parameter X from the 2 repeat measurements (after the first baseline scan X1 and second baseline scan X2). The x-axis shows the average value of the 2 repeat measurements of the quantitative parameter. The mean of the differences (μ) is indicated by the blue dashed line, with its 95% confidence interval represented as the shaded blue area. The dotted line represents 0 difference between the test-retest measurement. The mean of the differences ± the repeatability coefficient ($\mu\pm$ RC) is shown as the red dashed line. The 95% confidence interval of the repeatability coefficient is not displayed due to overlap with the shaded blue area. The Intraclass Correlation Coefficient (ICC) is also provided.

A.2 Response Assessment

A.2.1 Sensitivity to Post-Treatment Changes

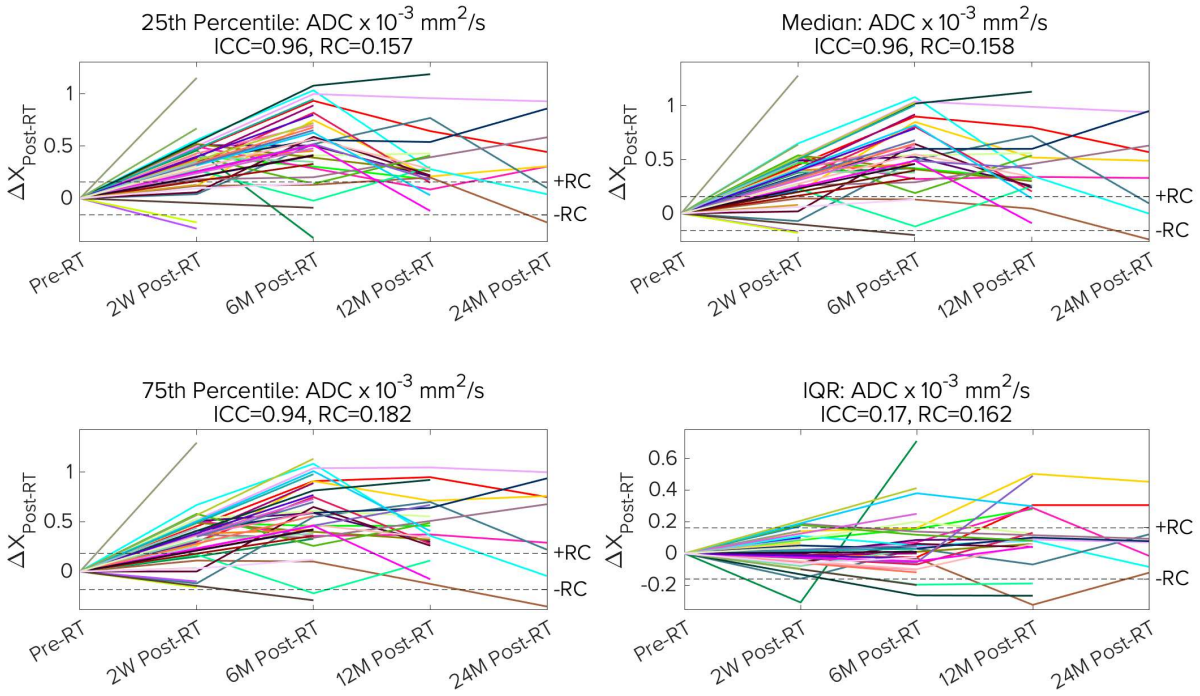


Figure A.4: The change in the *ADC* statistics (25th percentile, median, 75th percentile and interquartile range (IQR)) derived from the diffusion-weighted MRI data of the entire breast tumour, at 2-week (N=34), 6-month (N=38), 12-month (N=21) and 24-month (N=9) post-radiotherapy (RT) from 51 participants. The dashed black lines represent the repeatability coefficient, as indicator of significant change, i.e., if the difference post-treatment is larger than the repeatability coefficient, then the change is significant.

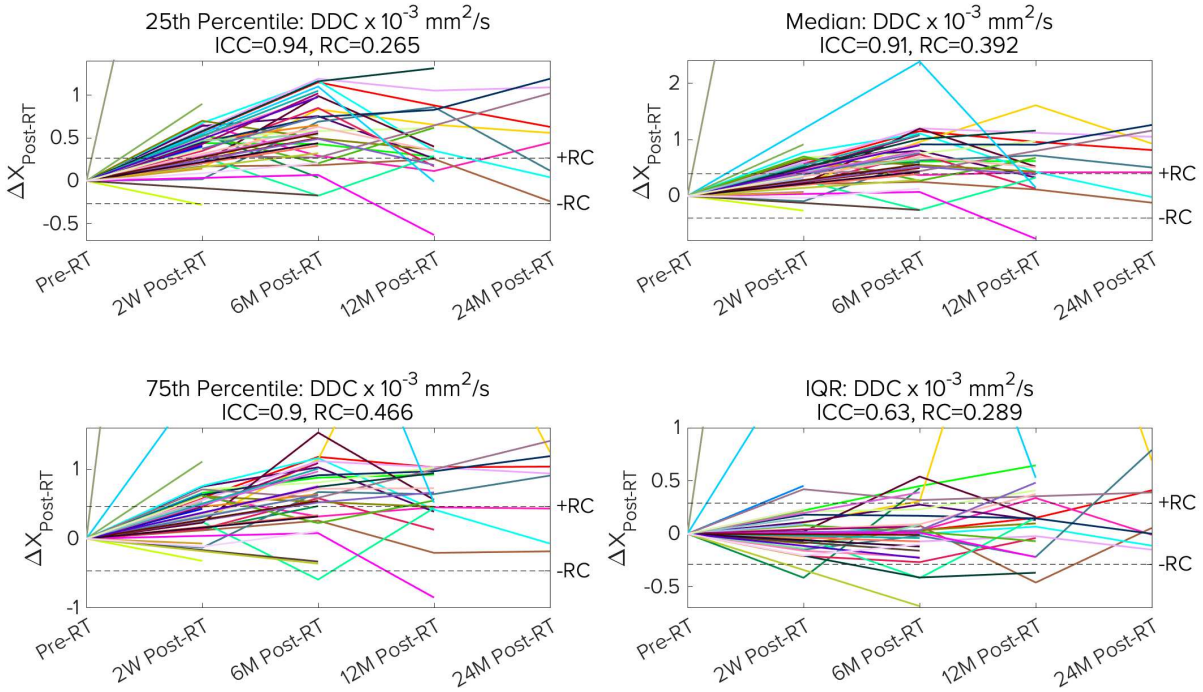


Figure A.5: The change in the DDC statistics (25th percentile, median, 75th percentile and interquartile range (IQR)) derived from the diffusion-weighted MRI data of the entire breast tumour, at 2-week (N=34), 6-month (N=38), 12-month (N=21) and 24-month (N=9) post-radiotherapy (RT) from 51 participants. The dashed black lines represent the repeatability coefficient, as indicator of significant change, i.e., if the difference post-treatment is larger than the repeatability coefficient, then the change is significant. Due to the some participants having much larger, unphysical changes post-treatment changes, the plots show the zoomed in version.

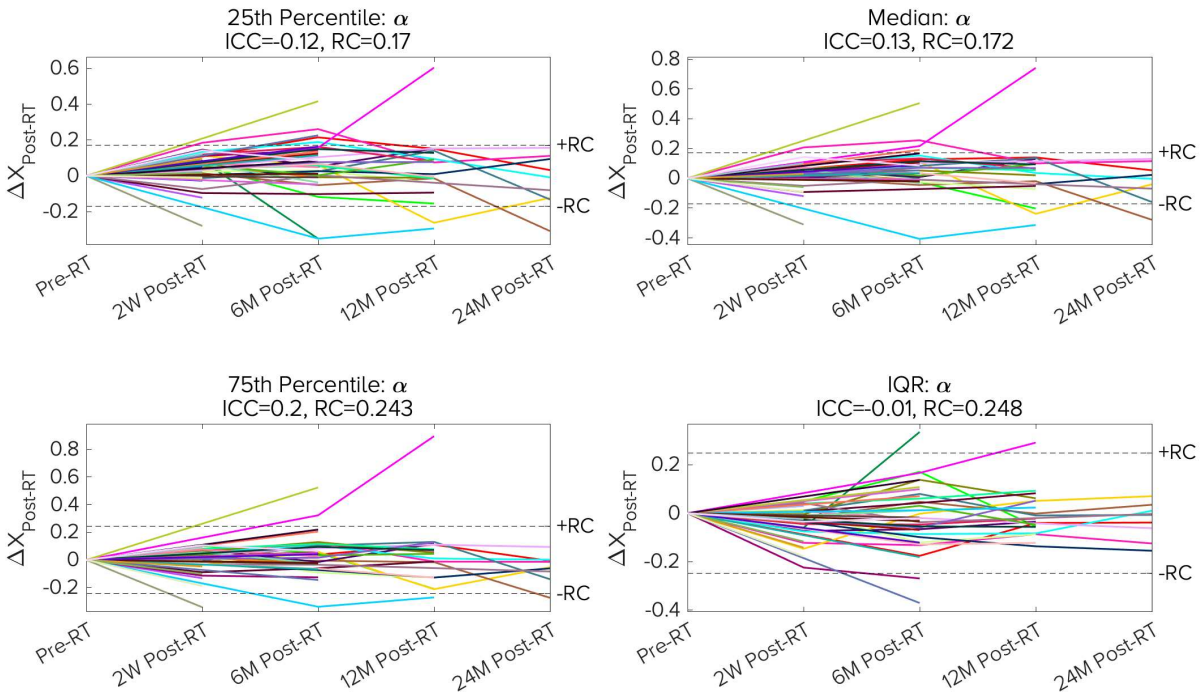


Figure A.6: The change in the α statistics (25th percentile, median, 75th percentile and interquartile range (IQR)) derived from the diffusion-weighted MRI data of the entire breast tumour, at 2-week (N=34), 6-month (N=38), 12-month (N=21) and 24-month (N=9) post-radiotherapy (RT) from 51 participants. The dashed black lines represent the repeatability coefficient, as indicator of significant change, i.e., if the difference post-treatment is larger than the repeatability coefficient, then the change is significant.

A.2.2 Whole Tumour Response Assessment

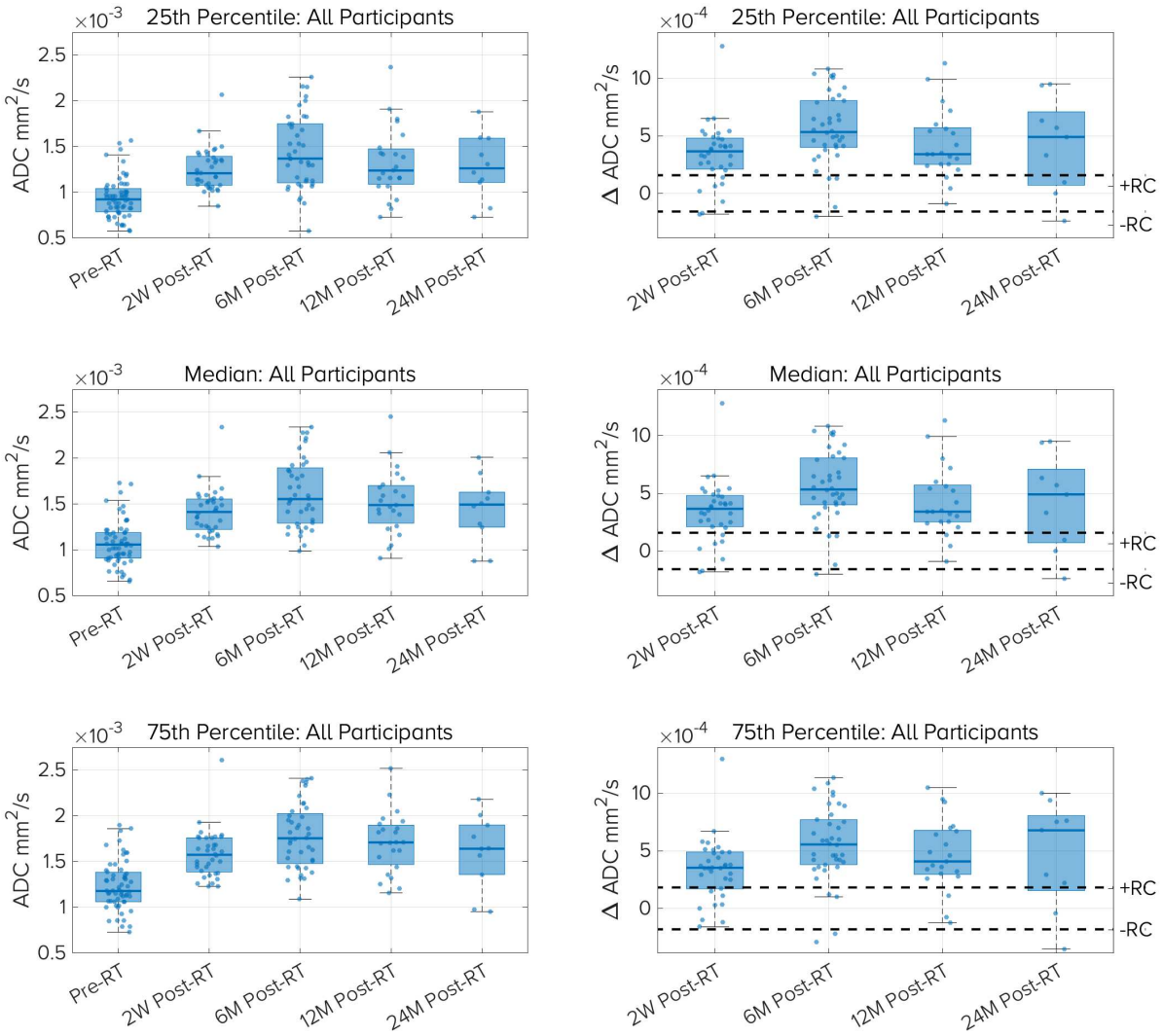


Figure A.7: (Left) The *ADC* statistics (25th percentile, median, and 75th percentile) derived from the diffusion-weighted MRI data of the entire breast tumour, pre-RT (N=59) and at 2-week (N=36), 6-month (N=40), 12-month (N=23) and 24-month (N=10) post-radiotherapy (RT) for all participants. (Right) The change in the *ADC* statistics from baseline (pre-RT) at 2-week (N=36), 6-month (N=40), 12-month (N=23) and 24-month (N=10) post-radiotherapy (RT) for all participants. The dots are individual participants.

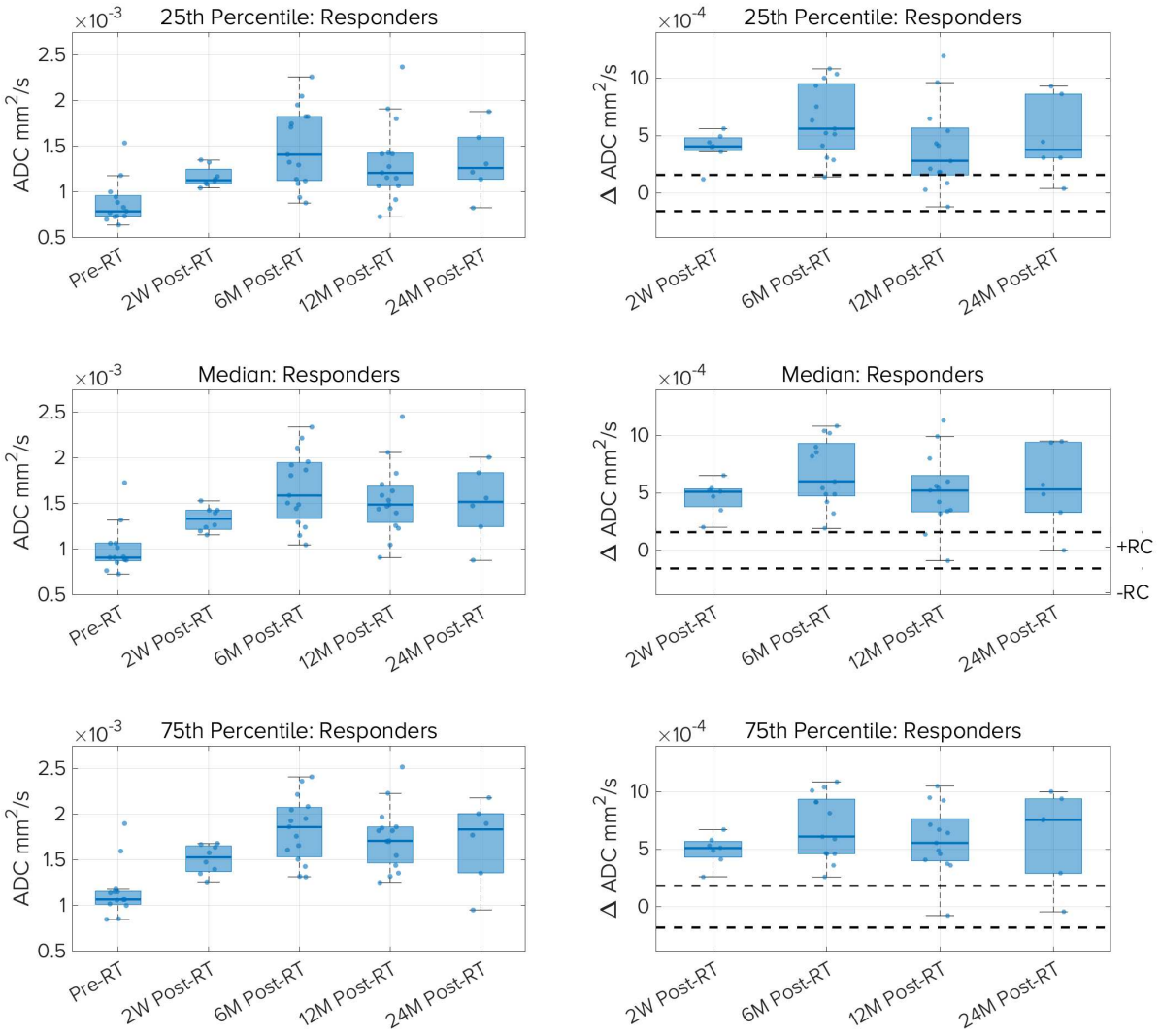


Figure A.8: (Left) The *ADC* statistics (25th percentile, median, and 75th percentile) derived from the diffusion-weighted MRI data of the entire breast tumour, pre-RT (N=59) and at 2-week (N=36), 6-month (N=40), 12-month (N=23) and 24-month (N=10) post-radiotherapy (RT) for the responders. (Right) The change in the *ADC* statistics from baseline (pre-RT) at 2-week (N=36), 6-month (N=40), 12-month (N=23) and 24-month (N=10) post-radiotherapy (RT) for the responders. The dots are individual participants.

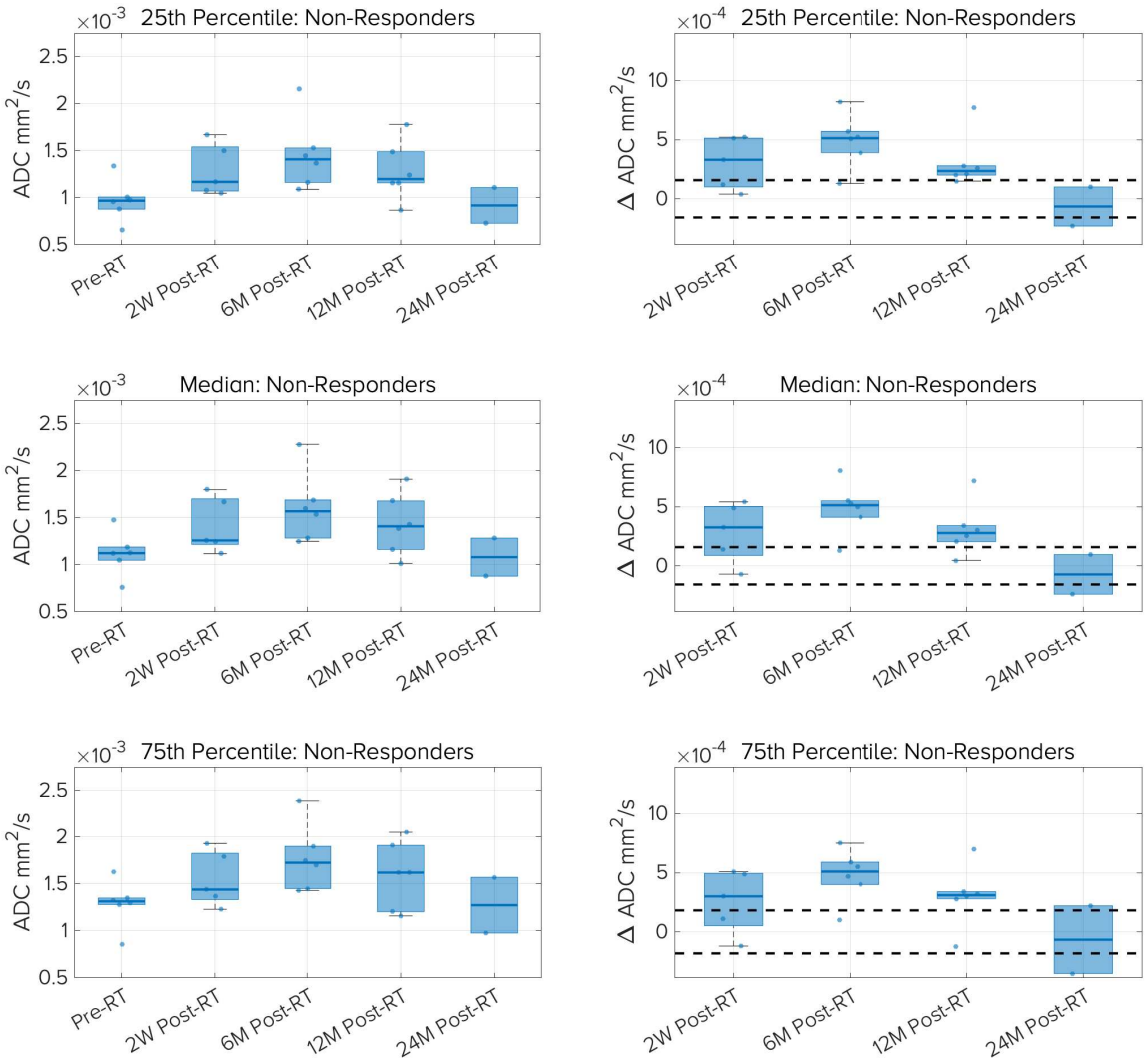


Figure A.9: (Left) The *ADC* statistics (25th percentile, median, and 75th percentile) derived from the diffusion-weighted MRI data of the entire breast tumour, pre-RT (N=59) and at 2-week (N=36), 6-month (N=40), 12-month (N=23) and 24-month (N=10) post-radiotherapy (RT) for the non-responders. (Right) The change in the *ADC* statistics from baseline (pre-RT) at 2-week (N=36), 6-month (N=40), 12-month (N=23) and 24-month (N=10) post-radiotherapy (RT) for the non-responders. The dots are individual participants.

A.2.3 Estimating Response

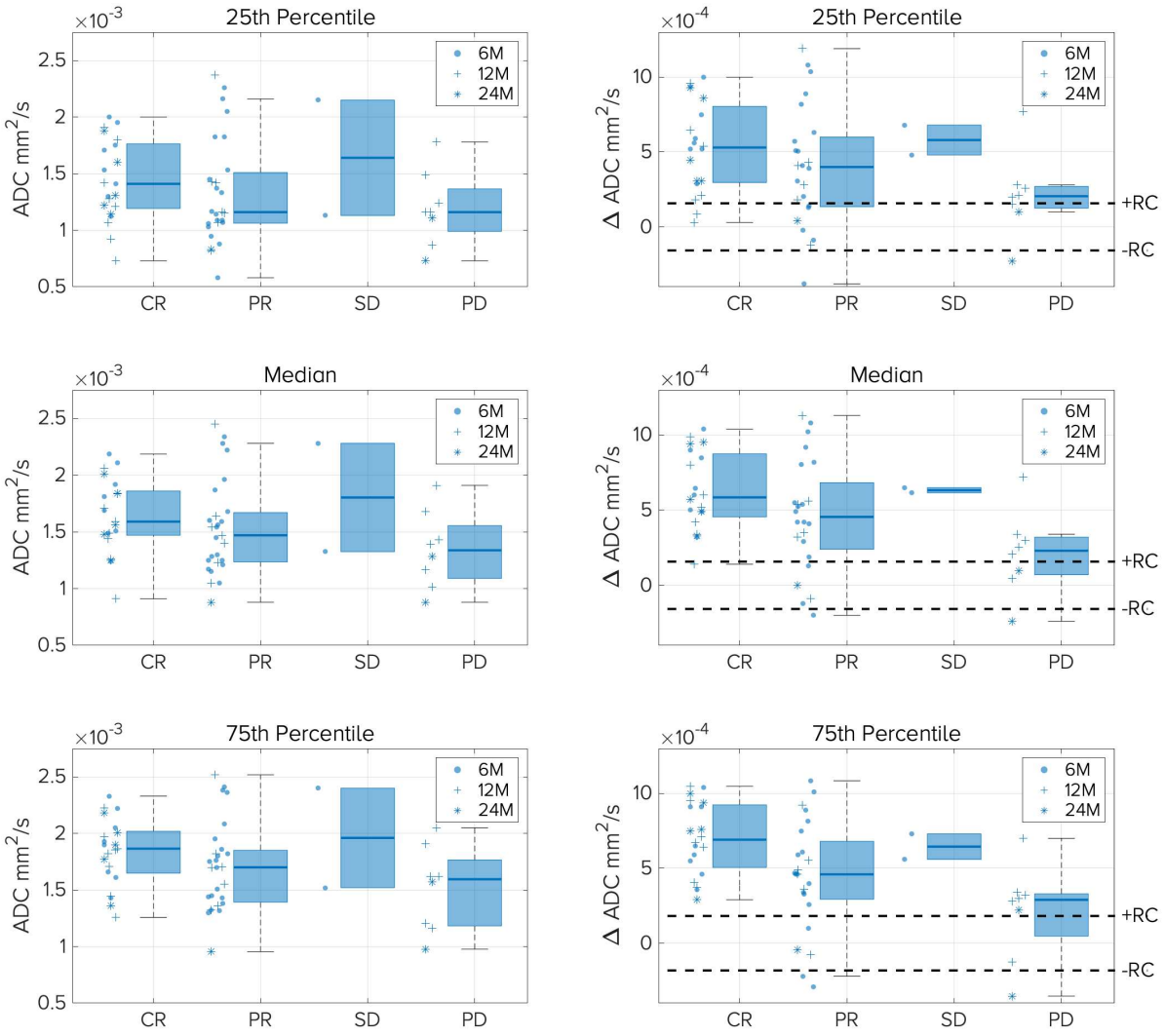


Figure A.10: Boxplots of the *ADC* metrics (25th percentile, median, and 75th percentile) and their radiological response assessment at 6-months (blue dot), 12-months (blue plus) and 24-months (blue asterisk). The radiological response assessment groups are complete response (CR), partial response (PR), stable disease (SD) and progressive disease (PD). On the left is the absolute values, and on the right is the change from baseline; the dashed lines are the repeatability coefficients, and changes beyond this are significant changes.

A.3 Sub-Types

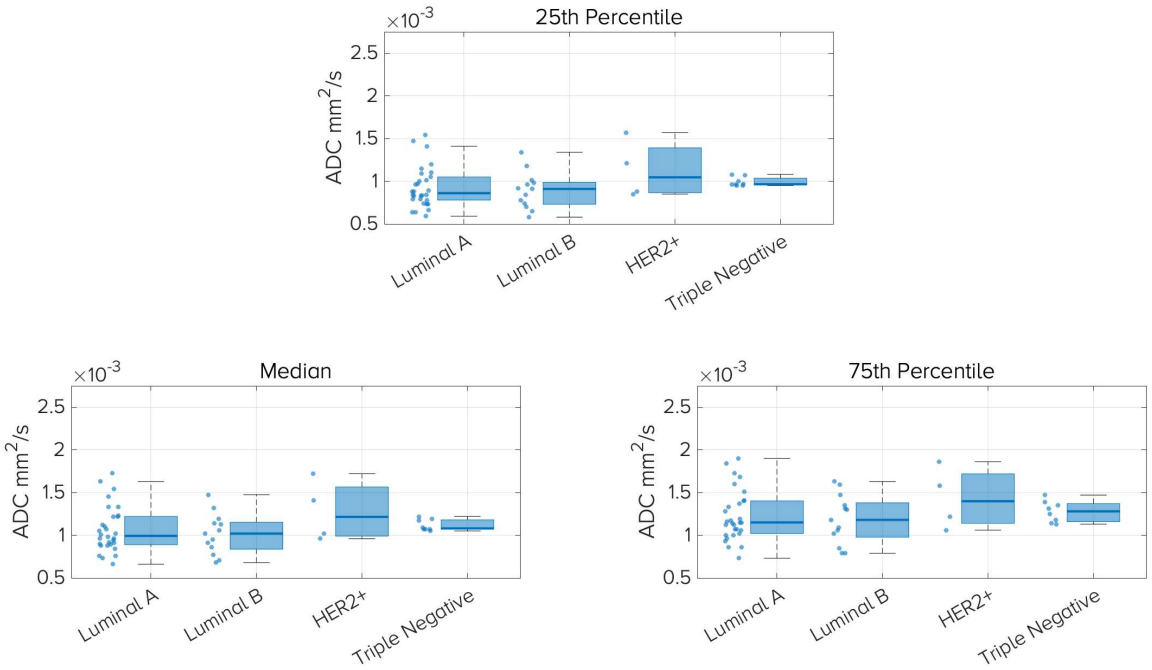


Figure A.11: Boxplots of the *ADC* metrics (25th percentile, median, 75th percentile and IQR) and their subtypes. The subtype groups are Luminal A, Luminal B, HER2+ and Triple Negative.

Appendix B

Results Chapter 3: Dynamic Contrast-Enhanced MRI

B.1 Repeatability

B.1.1 Tofts Model Parameters

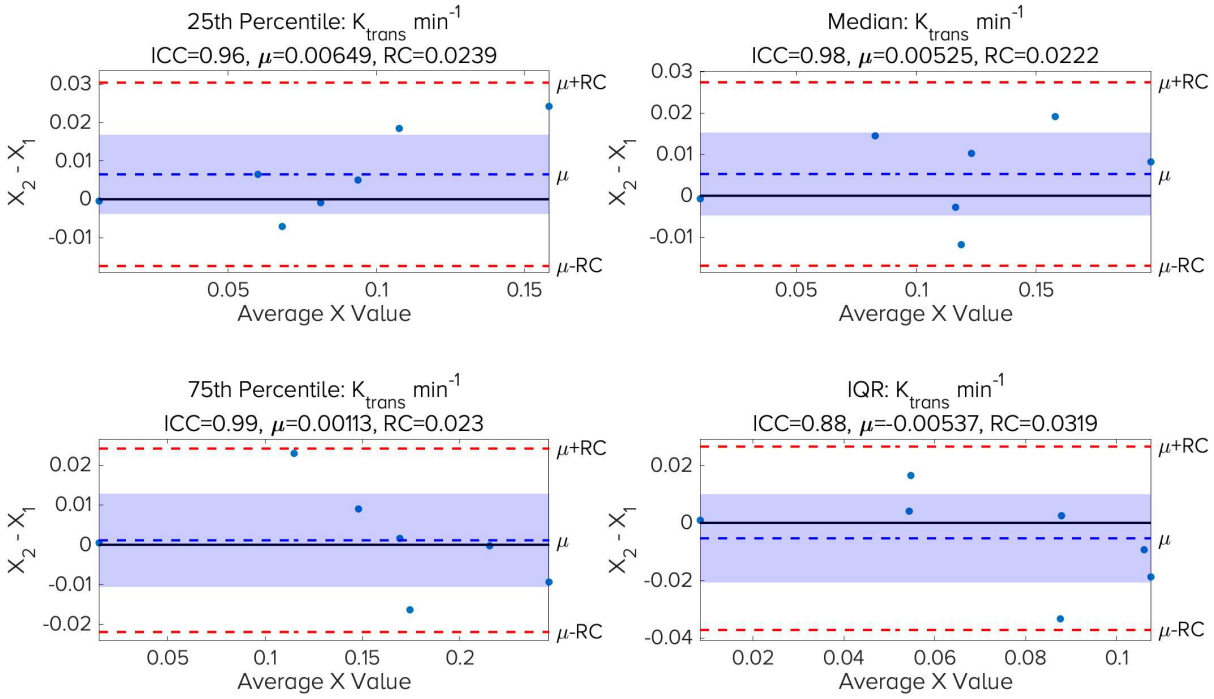


Figure B.1: Bland-Altman plots for 7 repeatability dynamic contrast-enhanced MRI participants, with the K_{trans} values extracted from each pixel across the entire tumour. The median, 25th percentile, 75th percentile, and interquartile range (IQR) of K_{trans} were assessed for repeatability. The y-axis represents the difference between the quantitative parameter X from the 2 repeat measurements (after the first baseline scan X_1 and second baseline scan X_2). The x-axis shows the average value of the 2 repeat measurements of the quantitative parameter. The mean of the differences (μ) is indicated by the blue dashed line, with its 95% confidence interval represented as the shaded blue area. The dotted line represents 0 difference between the test-retest measurement. The mean of the differences ± the repeatability coefficient ($\mu\pm$ RC) is shown as the red dashed line. The 95% confidence interval of the repeatability coefficient is not displayed due to overlap with the shaded blue area. The Intraclass Correlation Coefficient (ICC) is also provided.

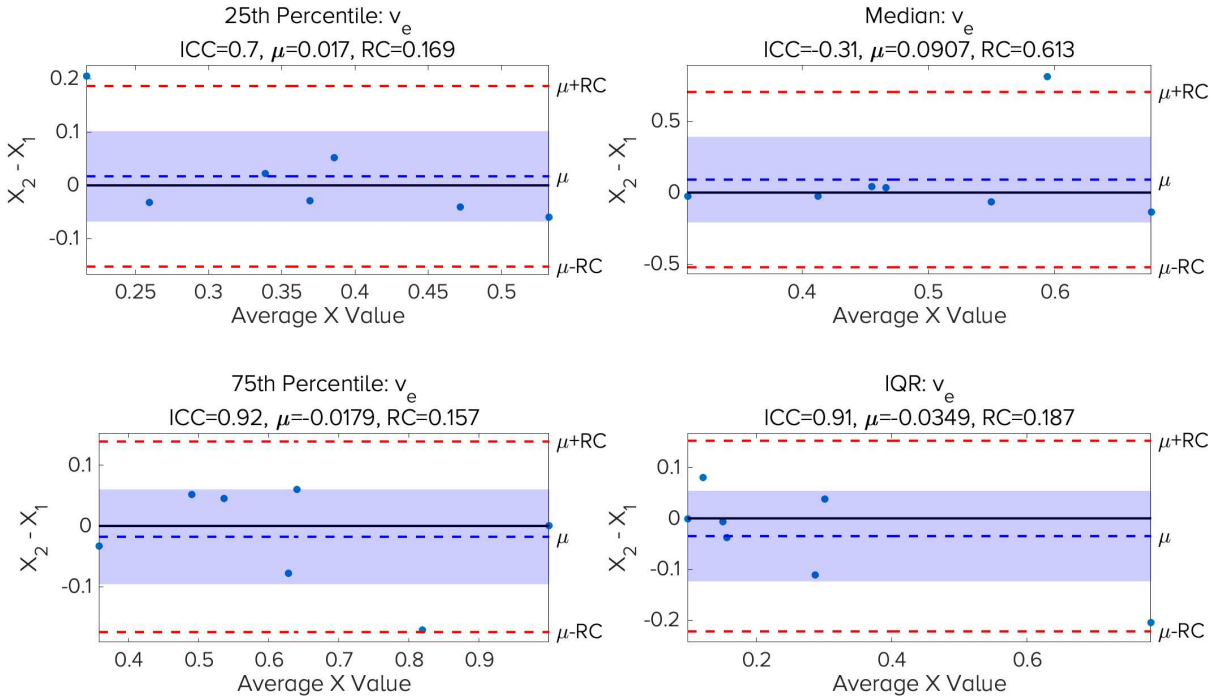


Figure B.2: Bland-Altman plots for 7 repeatability dynamic contrast-enhanced MRI participants, with the v_e values extracted from each pixel across the entire tumour. The median, 25th percentile, 75th percentile, and interquartile range (IQR) of v_e were assessed for repeatability. The y-axis represents the difference between the quantitative parameter X from the 2 repeat measurements (after the first baseline scan X_1 and second baseline scan X_2). The x-axis shows the average value of the 2 repeat measurements of the quantitative parameter. The mean of the differences (μ) is indicated by the blue dashed line, with its 95% confidence interval represented as the shaded blue area. The dotted line represents 0 difference between the test-retest measurement. The mean of the differences ± the repeatability coefficient ($\mu\pm$ RC) is shown as the red dashed line. The 95% confidence interval of the repeatability coefficient is not displayed due to overlap with the shaded blue area. The Intraclass Correlation Coefficient (ICC) is also provided.

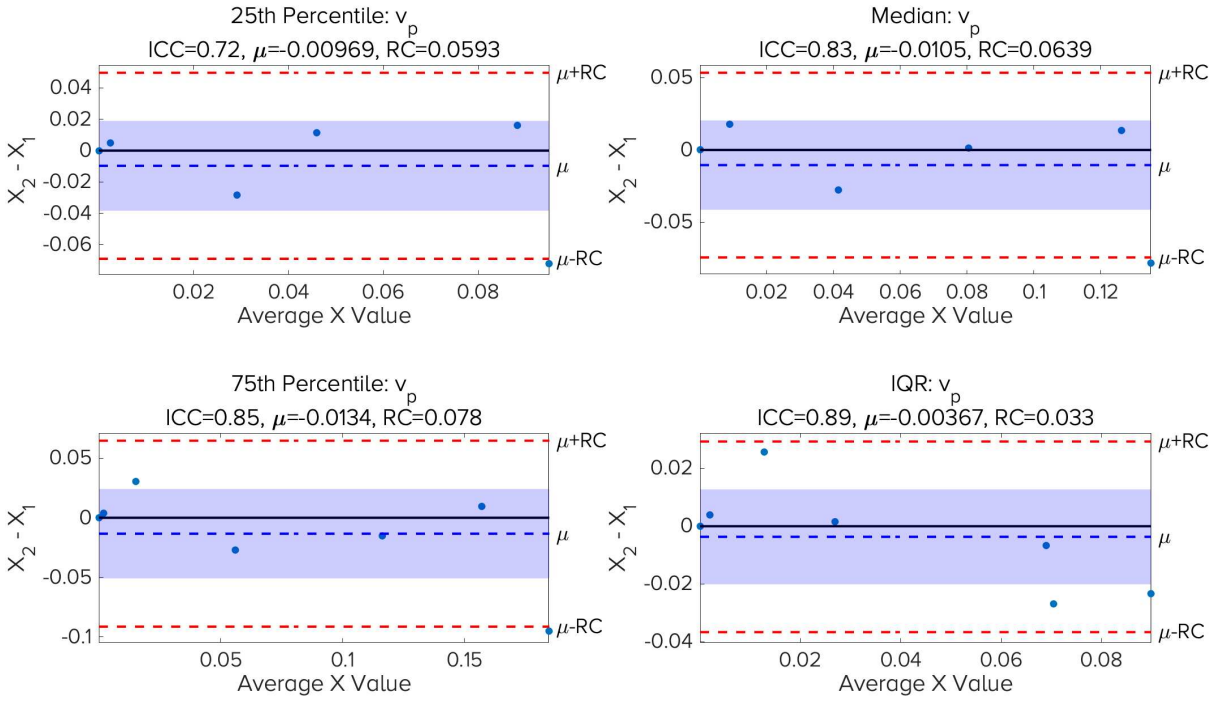


Figure B.3: Bland-Altman plots for 7 repeatability dynamic contrast-enhanced MRI participants, with the v_p values extracted from each pixel across the entire tumour. The median, 25th percentile, 75th percentile, and interquartile range (IQR) of v_p were assessed for repeatability. The y-axis represents the difference between the quantitative parameter X from the 2 repeat measurements (after the first baseline scan X_1 and second baseline scan X_2). The x-axis shows the average value of the 2 repeat measurements of the quantitative parameter. The mean of the differences (μ) is indicated by the blue dashed line, with its 95% confidence interval represented as the shaded blue area. The dotted line represents 0 difference between the test-retest measurement. The mean of the differences ± the repeatability coefficient ($\mu\pm$ RC) is shown as the red dashed line. The 95% confidence interval of the repeatability coefficient is not displayed due to overlap with the shaded blue area. The Intraclass Correlation Coefficient (ICC) is also provided.

B.1.2 Piecewise Linear Model Parameters

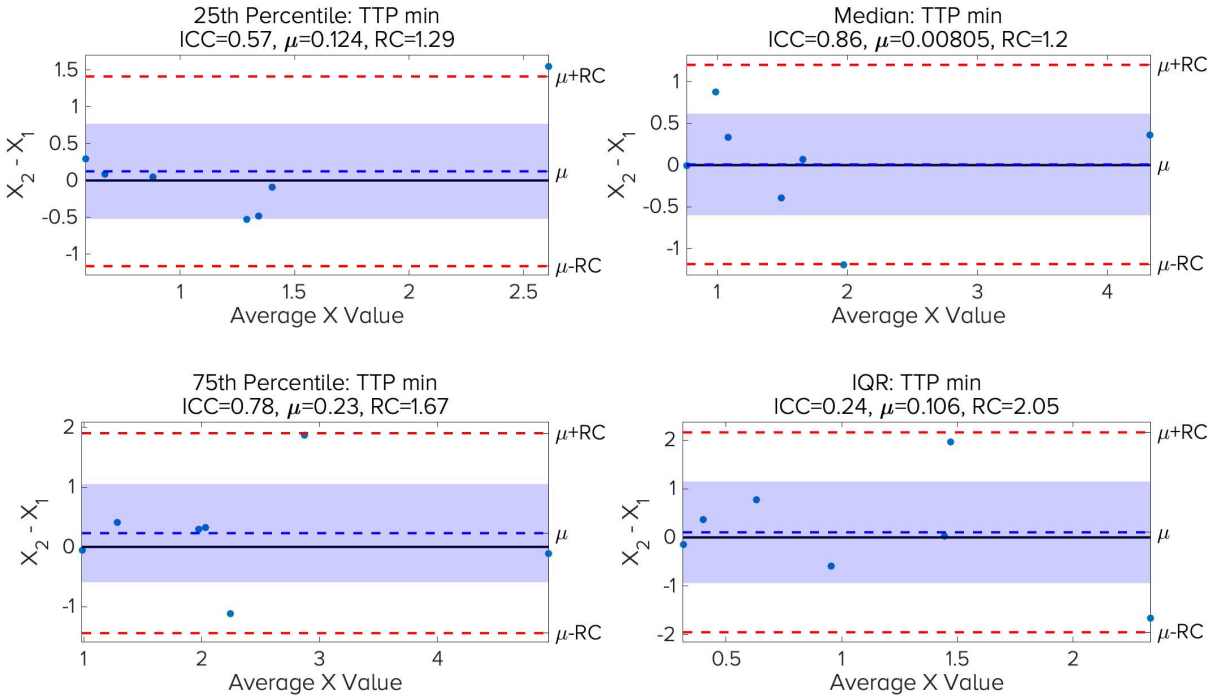


Figure B.4: Bland-Altman plots for 7 repeatability dynamic contrast-enhanced MRI participants, with the Time to Peak TTP values extracted from each pixel across the entire tumour. The median, 25th percentile, 75th percentile, and interquartile range (IQR) of TTP were assessed for repeatability. The y-axis represents the difference between the quantitative parameter X from the 2 repeat measurements (after the first baseline scan X_1 and second baseline scan X_2). The x-axis shows the average value of the 2 repeat measurements of the quantitative parameter. The mean of the differences (μ) is indicated by the blue dashed line, with its 95% confidence interval represented as the shaded blue area. The dotted line represents 0 difference between the test-retest measurement. The mean of the differences ± the repeatability coefficient ($\mu\pm$ RC) is shown as the red dashed line. The 95% confidence interval of the repeatability coefficient is not displayed due to overlap with the shaded blue area. The Intraclass Correlation Coefficient (ICC) is also provided.

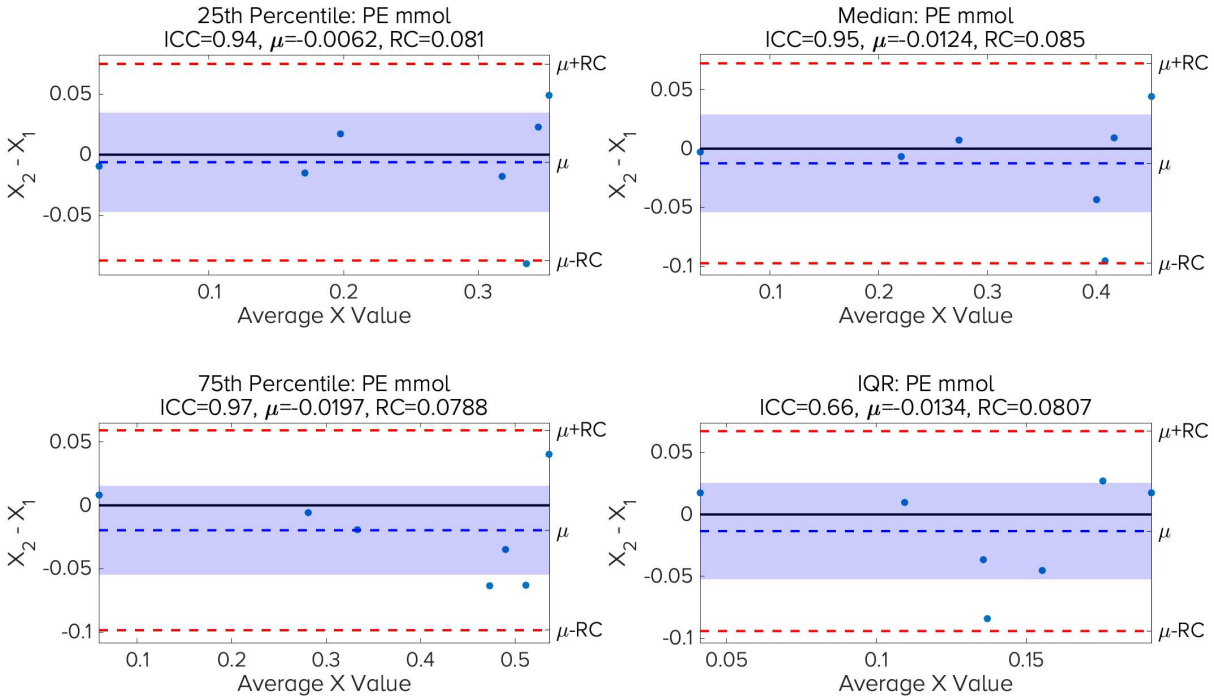


Figure B.5: Bland-Altman plots for 7 repeatability dynamic contrast-enhanced MRI participants, with the Peak Enhancement PE values extracted from each pixel across the entire tumour. The median, 25th percentile, 75th percentile, and interquartile range (IQR) of PE were assessed for repeatability. The y-axis represents the difference between the quantitative parameter X from the 2 repeat measurements (after the first baseline scan X_1 and second baseline scan X_2). The x-axis shows the average value of the 2 repeat measurements of the quantitative parameter. The mean of the differences (μ) is indicated by the blue dashed line, with its 95% confidence interval represented as the shaded blue area. The dotted line represents 0 difference between the test-retest measurement. The mean of the differences ± the repeatability coefficient ($\mu\pm$ RC) is shown as the red dashed line. The 95% confidence interval of the repeatability coefficient is not displayed due to overlap with the shaded blue area. The Intraclass Correlation Coefficient (ICC) is also provided.

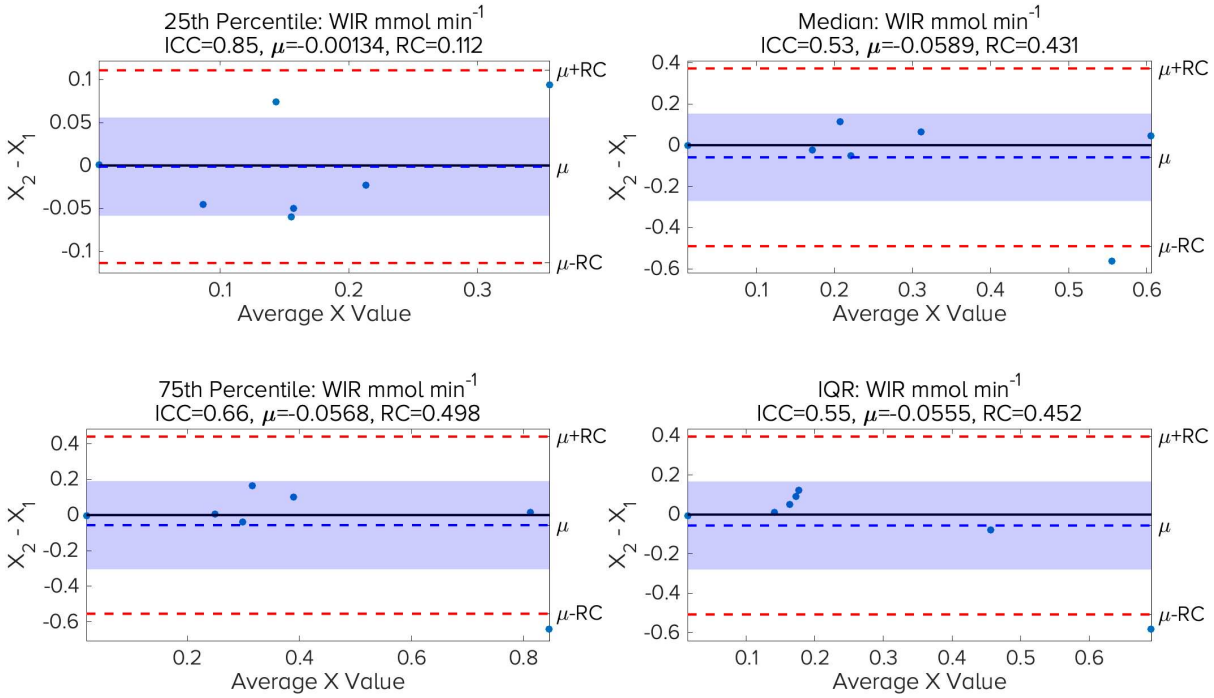


Figure B.6: Bland-Altman plots for 7 repeatability dynamic contrast-enhanced MRI participants, with the Wash-In Rate WIR values extracted from each pixel across the entire tumour. The median, 25th percentile, 75th percentile, and interquartile range (IQR) of WIR were assessed for repeatability. The y-axis represents the difference between the quantitative parameter X from the 2 repeat measurements (after the first baseline scan X_1 and second baseline scan X_2). The x-axis shows the average value of the 2 repeat measurements of the quantitative parameter. The mean of the differences (μ) is indicated by the blue dashed line, with its 95% confidence interval represented as the shaded blue area. The dotted line represents 0 difference between the test-retest measurement. The mean of the differences ± the repeatability coefficient ($\mu\pm$ RC) is shown as the red dashed line. The 95% confidence interval of the repeatability coefficient is not displayed due to overlap with the shaded blue area. The Intraclass Correlation Coefficient (ICC) is also provided.

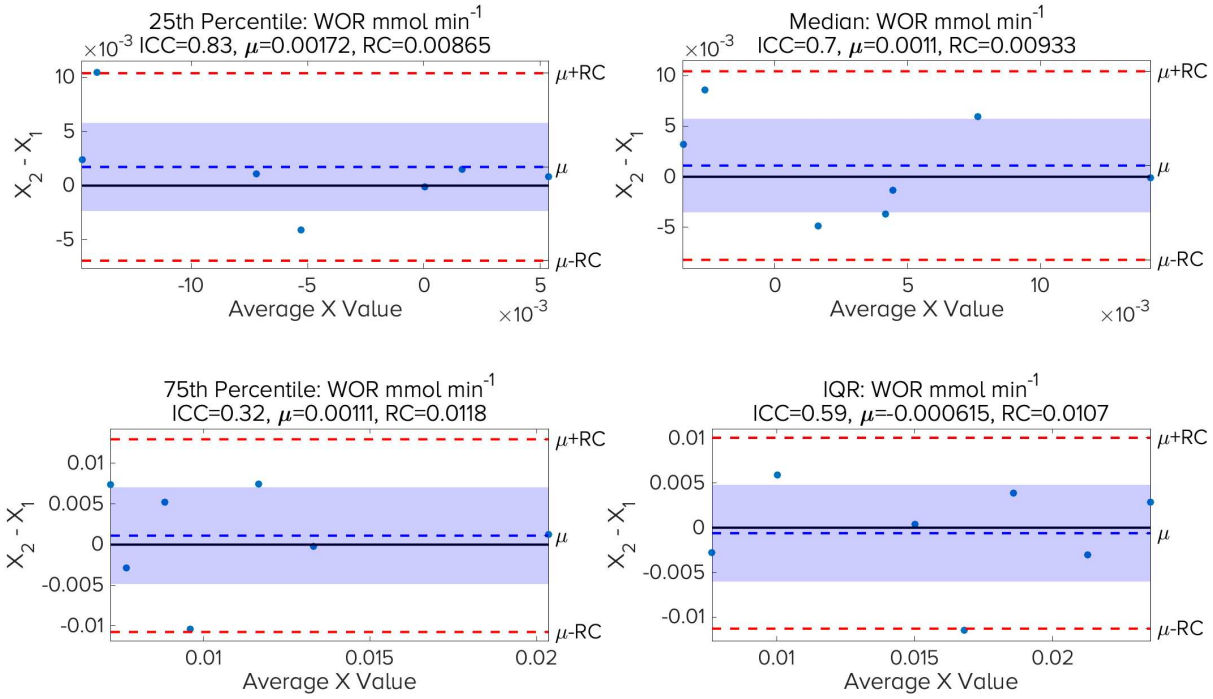


Figure B.7: Bland-Altman plots for 7 repeatability dynamic contrast-enhanced MRI participants, with the Wash-Out Rate WOR values extracted from each pixel across the entire tumour. The median, 25th percentile, 75th percentile, and interquartile range (IQR) of WOR were assessed for repeatability. The y-axis represents the difference between the quantitative parameter X from the 2 repeat measurements (after the first baseline scan X_1 and second baseline scan X_2). The x-axis shows the average value of the 2 repeat measurements of the quantitative parameter. The mean of the differences (μ) is indicated by the blue dashed line, with its 95% confidence interval represented as the shaded blue area. The dotted line represents 0 difference between the test-retest measurement. The mean of the differences ± the repeatability coefficient ($\mu\pm$ RC) is shown as the red dashed line. The 95% confidence interval of the repeatability coefficient is not displayed due to overlap with the shaded blue area. The Intraclass Correlation Coefficient (ICC) is also provided.

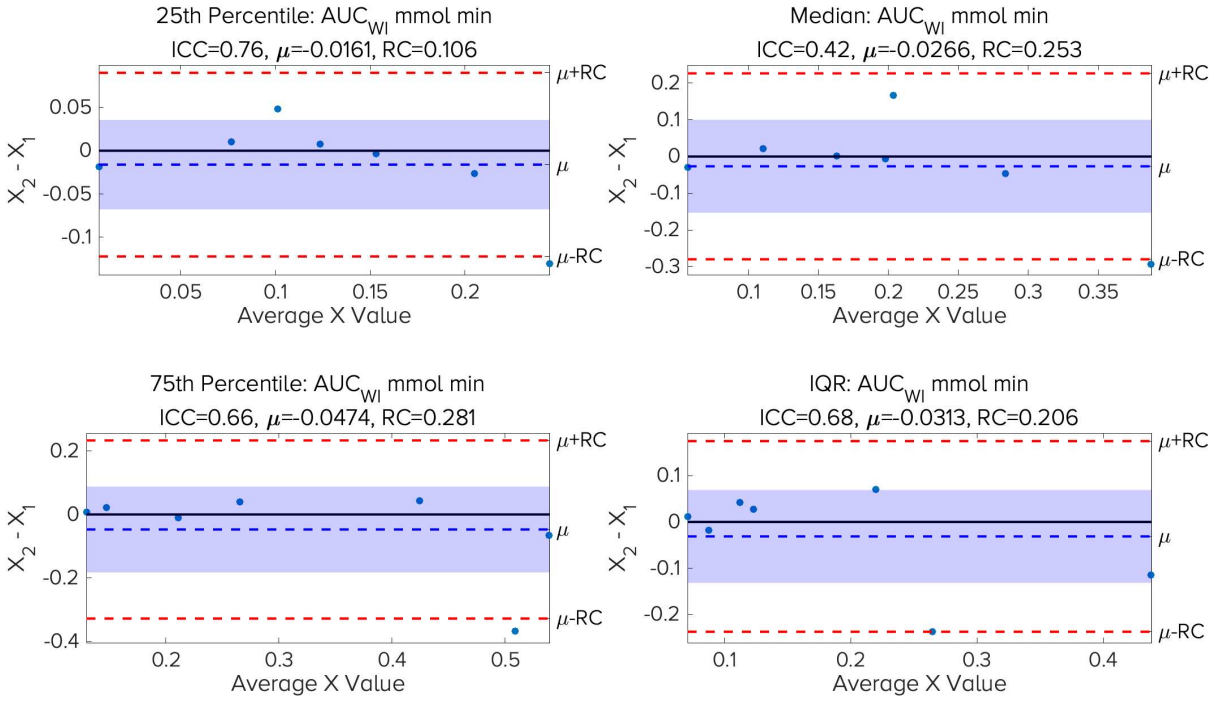


Figure B.8: Bland-Altman plots for 7 repeatability dynamic contrast-enhanced MRI participants, with the Wash-In Area Under the Curve AUC_{WI} values extracted from each pixel across the entire tumour. The median, 25th percentile, 75th percentile, and interquartile range (IQR) of AUC_{WI} were assessed for repeatability. The y-axis represents the difference between the quantitative parameter X from the 2 repeat measurements (after the first baseline scan X_1 and second baseline scan X_2). The x-axis shows the average value of the 2 repeat measurements of the quantitative parameter. The mean of the differences (μ) is indicated by the blue dashed line, with its 95% confidence interval represented as the shaded blue area. The dotted line represents 0 difference between the test-retest measurement. The mean of the differences ± the repeatability coefficient (μ± RC) is shown as the red dashed line. The 95% confidence interval of the repeatability coefficient is not displayed due to overlap with the shaded blue area. The Intraclass Correlation Coefficient (ICC) is also provided.

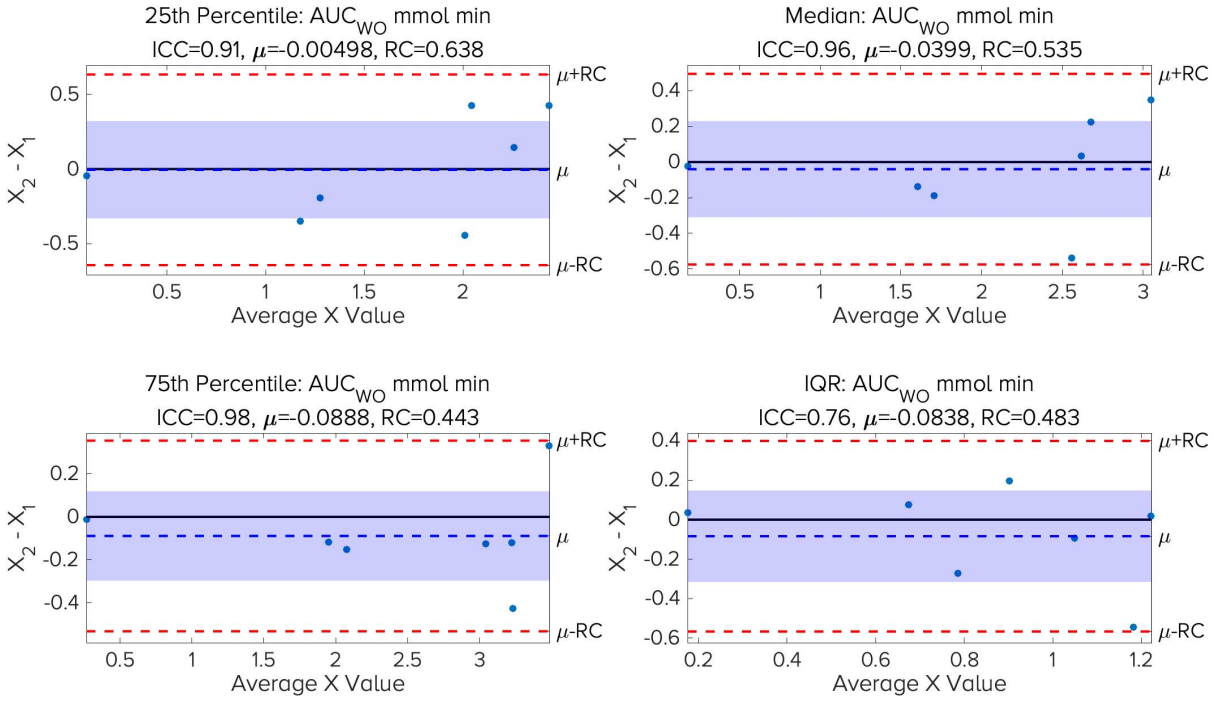


Figure B.9: Bland-Altman plots for 7 repeatability dynamic contrast-enhanced MRI participants, with the Wash-Out Area Under the Curve AUC_{WO} values extracted from each pixel across the entire tumour. The median, 25th percentile, 75th percentile, and interquartile range (IQR) of AUC_{WO} were assessed for repeatability. The y-axis represents the difference between the quantitative parameter X from the 2 repeat measurements (after the first baseline scan X_1 and second baseline scan X_2). The x-axis shows the average value of the 2 repeat measurements of the quantitative parameter. The mean of the differences (μ) is indicated by the blue dashed line, with its 95% confidence interval represented as the shaded blue area. The dotted line represents 0 difference between the test-retest measurement. The mean of the differences ± the repeatability coefficient (μ± RC) is shown as the red dashed line. The 95% confidence interval of the repeatability coefficient is not displayed due to overlap with the shaded blue area. The Intraclass Correlation Coefficient (ICC) is also provided.

B.1.3 Semi-Quantitative Parameters

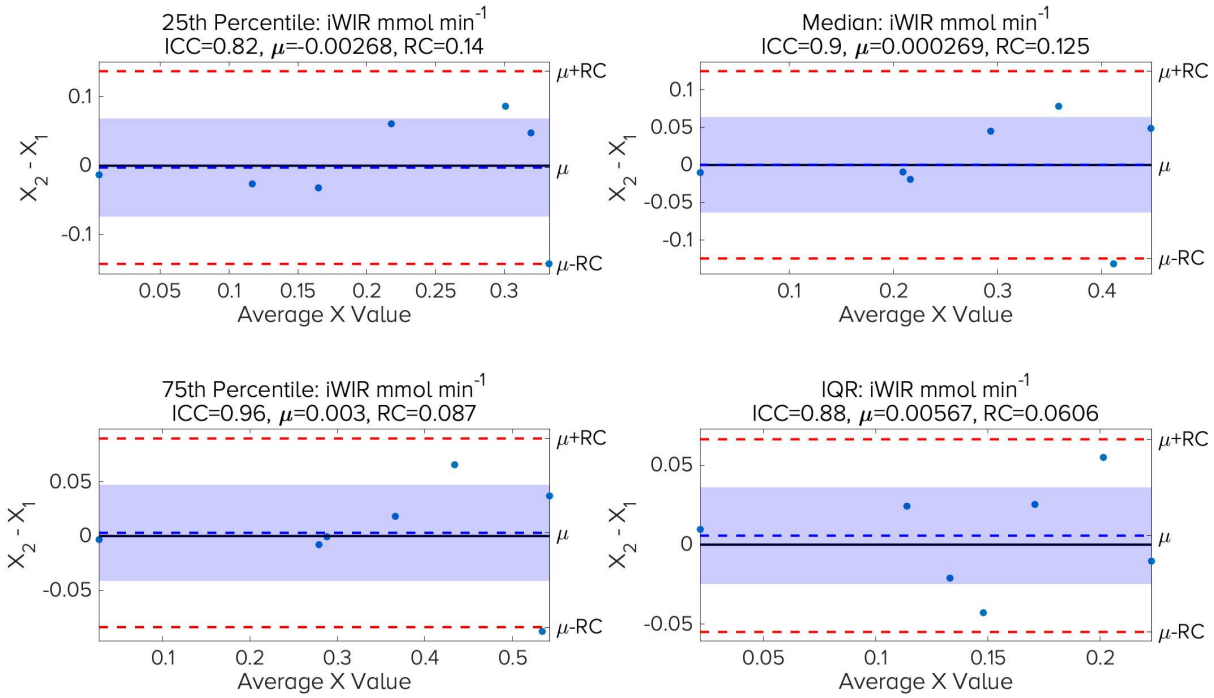


Figure B.10: Bland-Altman plots for 7 repeatability dynamic contrast-enhanced MRI participants, with the initial Wash-In Rate, for the first 60 seconds, ($iWIR$) values extracted from each pixel across the entire tumour. The median, 25th percentile, 75th percentile, and interquartile range (IQR) of $iWIR$ were assessed for repeatability. The y-axis represents the difference between the quantitative parameter X from the 2 repeat measurements (after the first baseline scan X_1 and second baseline scan X_2). The x-axis shows the average value of the 2 repeat measurements of the quantitative parameter. The mean of the differences (μ) is indicated by the blue dashed line, with its 95% confidence interval represented as the shaded blue area. The dotted line represents 0 difference between the test-retest measurement. The mean of the differences $\pm$ the repeatability coefficient ($\mu\pm$ RC) is shown as the red dashed line. The 95% confidence interval of the repeatability coefficient is not displayed due to overlap with the shaded blue area. The Intraclass Correlation Coefficient (ICC) is also provided.

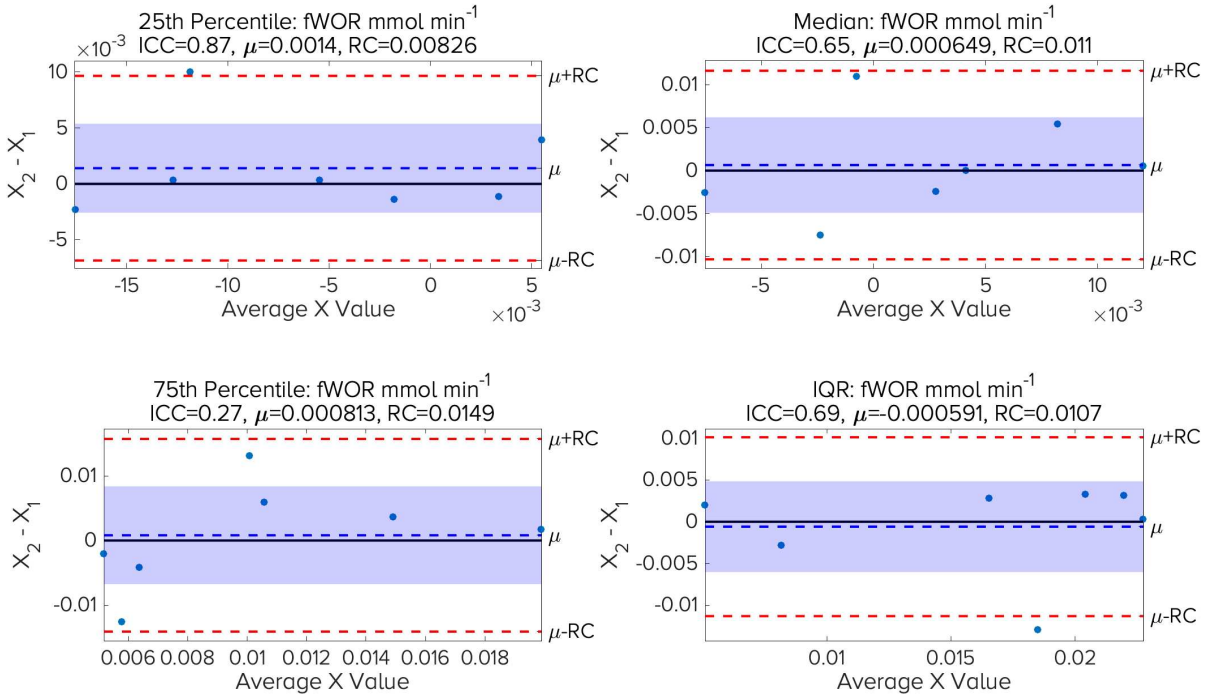


Figure B.11: Bland-Altman plots for 7 repeatability dynamic contrast-enhanced MRI participants, with the final Wash-Out Rate, from 180 to 470 seconds, ($fWOR$) values extracted from each pixel across the entire tumour. The median, 25th percentile, 75th percentile, and interquartile range (IQR) of $fWOR$ were assessed for repeatability. The y-axis represents the difference between the quantitative parameter X from the 2 repeat measurements (after the first baseline scan X_1 and second baseline scan X_2). The x-axis shows the average value of the 2 repeat measurements of the quantitative parameter. The mean of the differences (μ) is indicated by the blue dashed line, with its 95% confidence interval represented as the shaded blue area. The dotted line represents 0 difference between the test-retest measurement. The mean of the differences ± the repeatability coefficient ($\mu\pm$ RC) is shown as the red dashed line. The 95% confidence interval of the repeatability coefficient is not displayed due to overlap with the shaded blue area. The Intraclass Correlation Coefficient (ICC) is also provided.

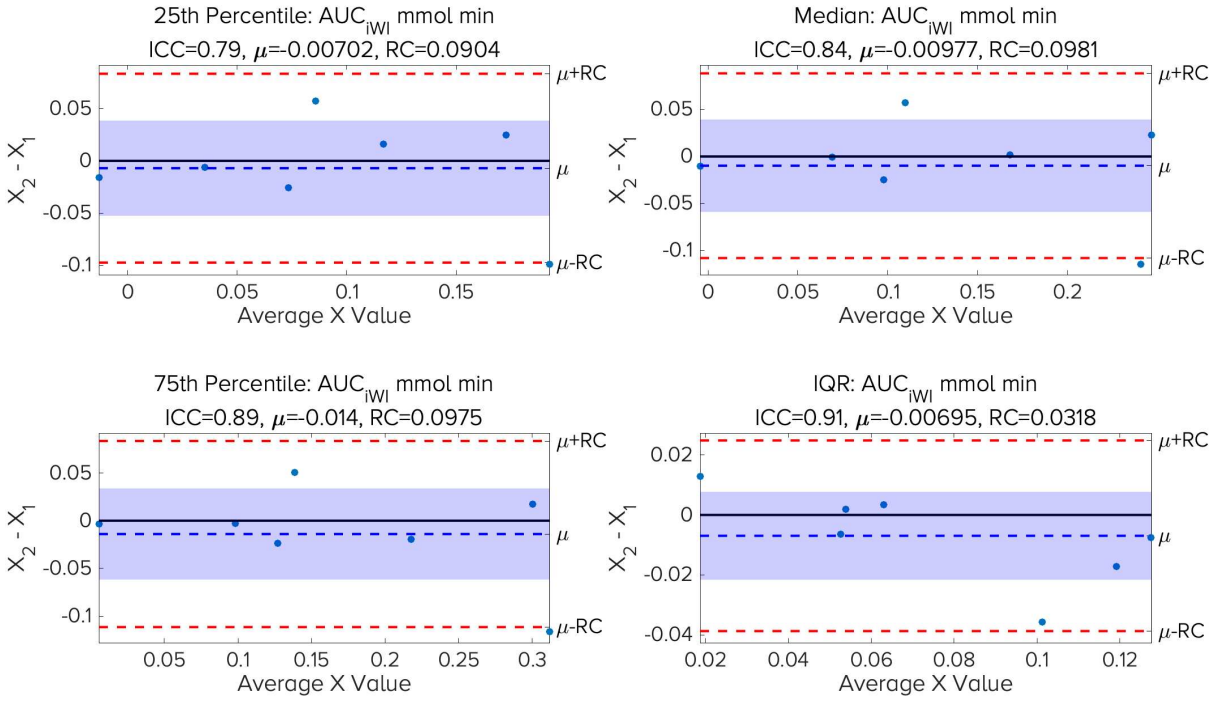


Figure B.12: Bland-Altman plots for 7 repeatability dynamic contrast-enhanced MRI participants, with the initial Wash-In Area Under the Curve, for the first 60 seconds, (AUC_{iWI}) values extracted from each pixel across the entire tumour. The median, 25th percentile, 75th percentile, and interquartile range (IQR) of AUC_{iWI} were assessed for repeatability. The y-axis represents the difference between the quantitative parameter X from the 2 repeat measurements (after the first baseline scan X_1 and second baseline scan X_2). The x-axis shows the average value of the 2 repeat measurements of the quantitative parameter. The mean of the differences (μ) is indicated by the blue dashed line, with its 95% confidence interval represented as the shaded blue area. The dotted line represents 0 difference between the test-retest measurement. The mean of the differences ± the repeatability coefficient ($\mu\pm$ RC) is shown as the red dashed line. The 95% confidence interval of the repeatability coefficient is not displayed due to overlap with the shaded blue area. The Intraclass Correlation Coefficient (ICC) is also provided.

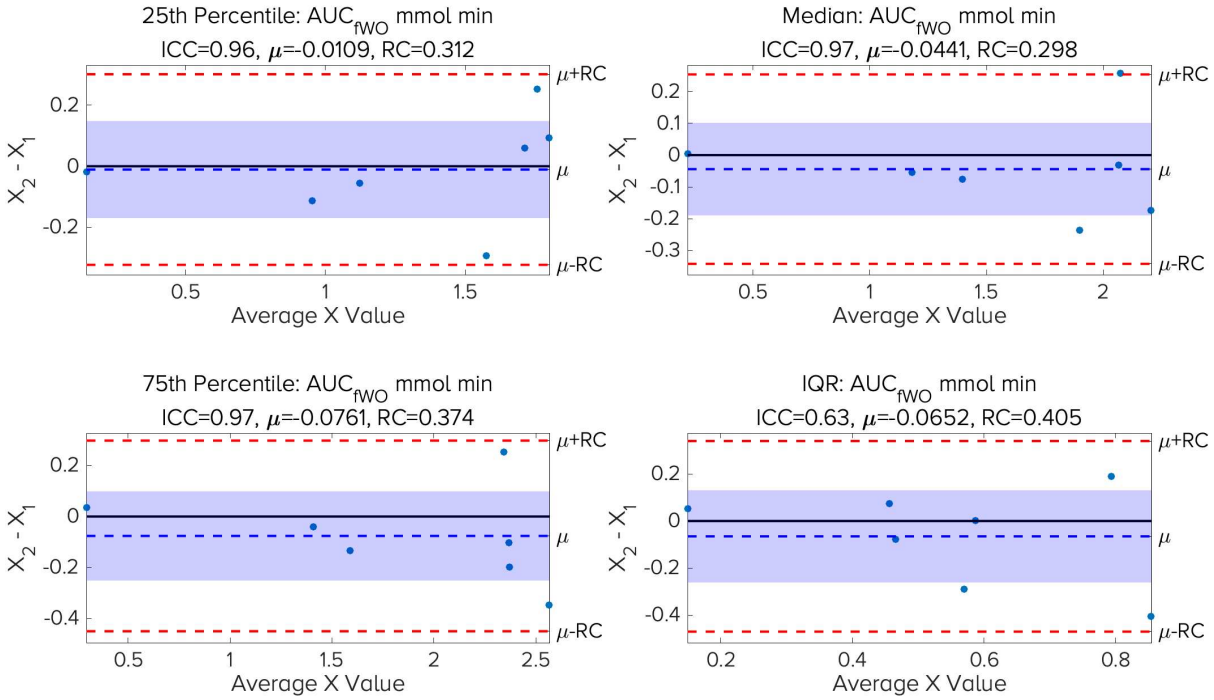


Figure B.13: Bland-Altman plots for 7 repeatability dynamic contrast-enhanced MRI participants, with the final Wash-Out Area Under the Curve, from 180 to 470 seconds, (AUC_{fWO}) values extracted from each pixel across the entire tumour. The median, 25th percentile, 75th percentile, and interquartile range (IQR) of AUC_{fWO} were assessed for repeatability. The y-axis represents the difference between the quantitative parameter X from the 2 repeat measurements (after the first baseline scan X_1 and second baseline scan X_2). The x-axis shows the average value of the 2 repeat measurements of the quantitative parameter. The mean of the differences (μ) is indicated by the blue dashed line, with its 95% confidence interval represented as the shaded blue area. The dotted line represents 0 difference between the test-retest measurement. The mean of the differences ± the repeatability coefficient ($\mu\pm$ RC) is shown as the red dashed line. The 95% confidence interval of the repeatability coefficient is not displayed due to overlap with the shaded blue area. The Intraclass Correlation Coefficient (ICC) is also provided.

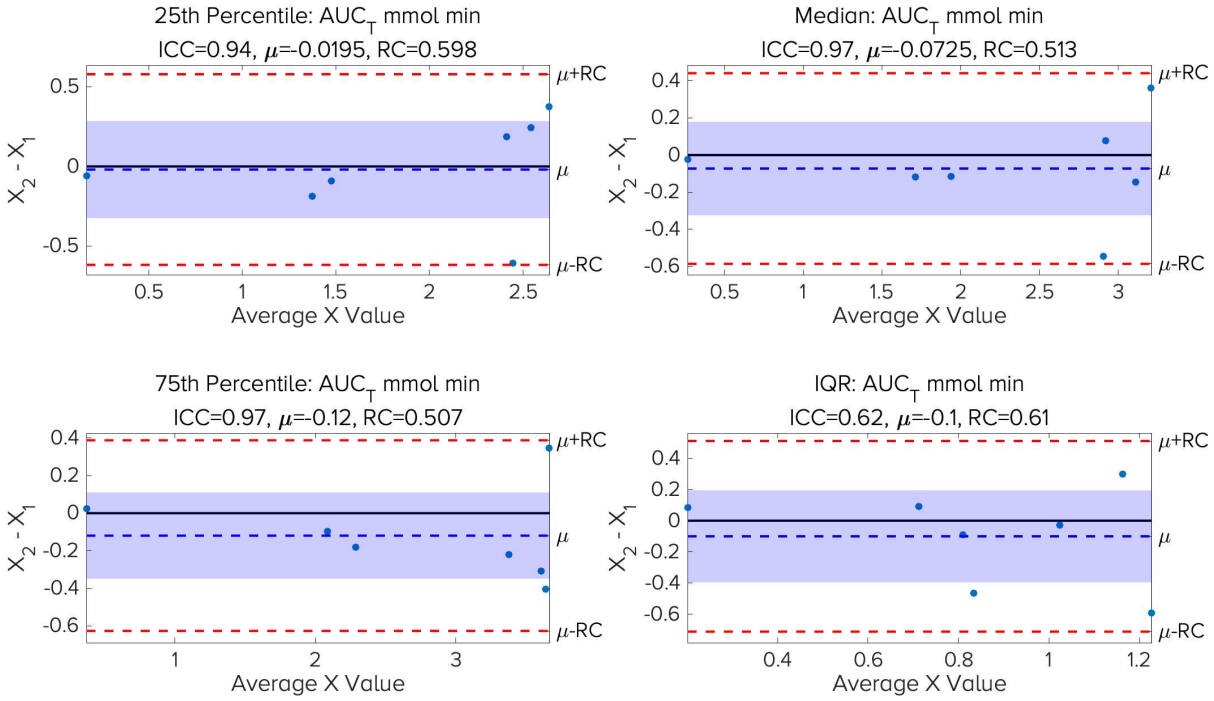


Figure B.14: Bland-Altman plots for 7 repeatability dynamic contrast-enhanced MRI participants, with the Total Area Under the Curve (AUC_T) values extracted from each pixel across the entire tumour. The median, 25th percentile, 75th percentile, and interquartile range (IQR) of AUC_T were assessed for repeatability. The y-axis represents the difference between the quantitative parameter X from the 2 repeat measurements (after the first baseline scan X_1 and second baseline scan X_2). The x-axis shows the average value of the 2 repeat measurements of the quantitative parameter. The mean of the differences (μ) is indicated by the blue dashed line, with its 95% confidence interval represented as the shaded blue area. The dotted line represents 0 difference between the test-retest measurement. The mean of the differences ± the repeatability coefficient (μ± RC) is shown as the red dashed line. The 95% confidence interval of the repeatability coefficient is not displayed due to overlap with the shaded blue area. The Intraclass Correlation Coefficient (ICC) is also provided.

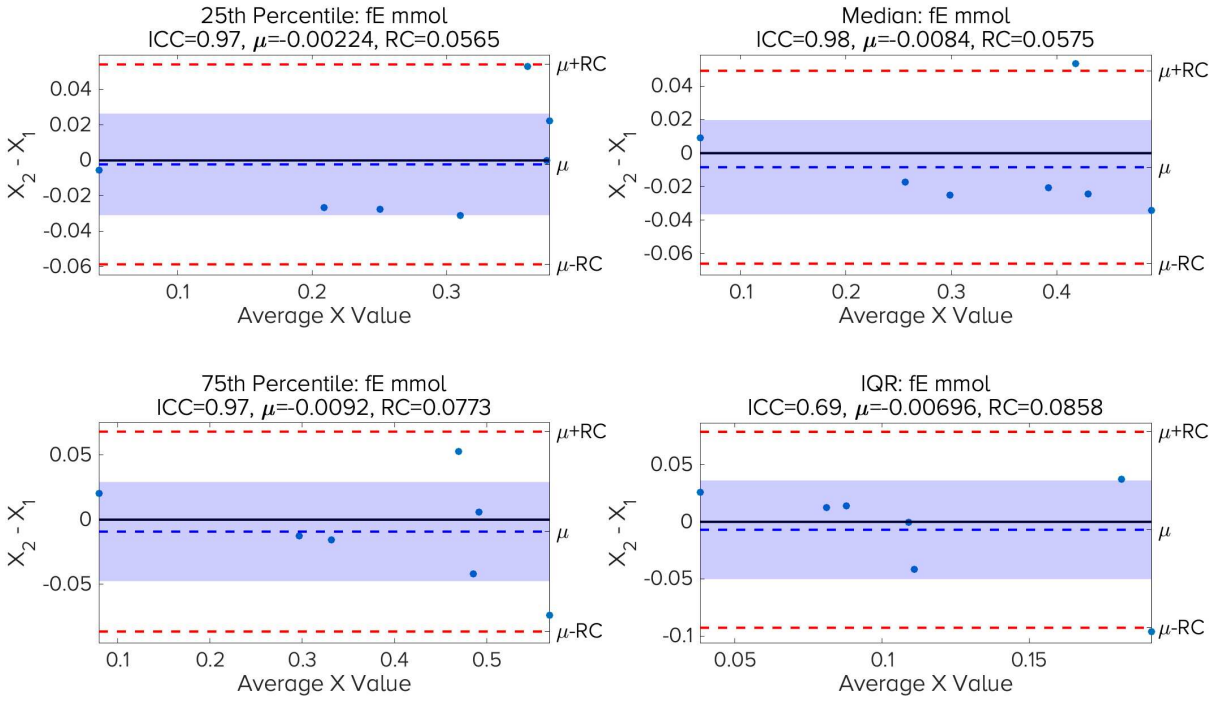


Figure B.15: Bland-Altman plots for 7 repeatability dynamic contrast-enhanced MRI participants, with the Final Enhancement (fE) values extracted from each pixel across the entire tumour. The median, 25th percentile, 75th percentile, and interquartile range (IQR) of fE were assessed for repeatability. The y-axis represents the difference between the quantitative parameter X from the 2 repeat measurements (after the first baseline scan X_1 and second baseline scan X_2). The x-axis shows the average value of the 2 repeat measurements of the quantitative parameter. The mean of the differences (μ) is indicated by the blue dashed line, with its 95% confidence interval represented as the shaded blue area. The dotted line represents 0 difference between the test-retest measurement. The mean of the differences ± the repeatability coefficient ($\mu\pm$ RC) is shown as the red dashed line. The 95% confidence interval of the repeatability coefficient is not displayed due to overlap with the shaded blue area. The Intraclass Correlation Coefficient (ICC) is also provided.

B.2 Response Assessment

B.2.1 Sensitivity to Post-Treatment Changes

Tofts Model Parameters

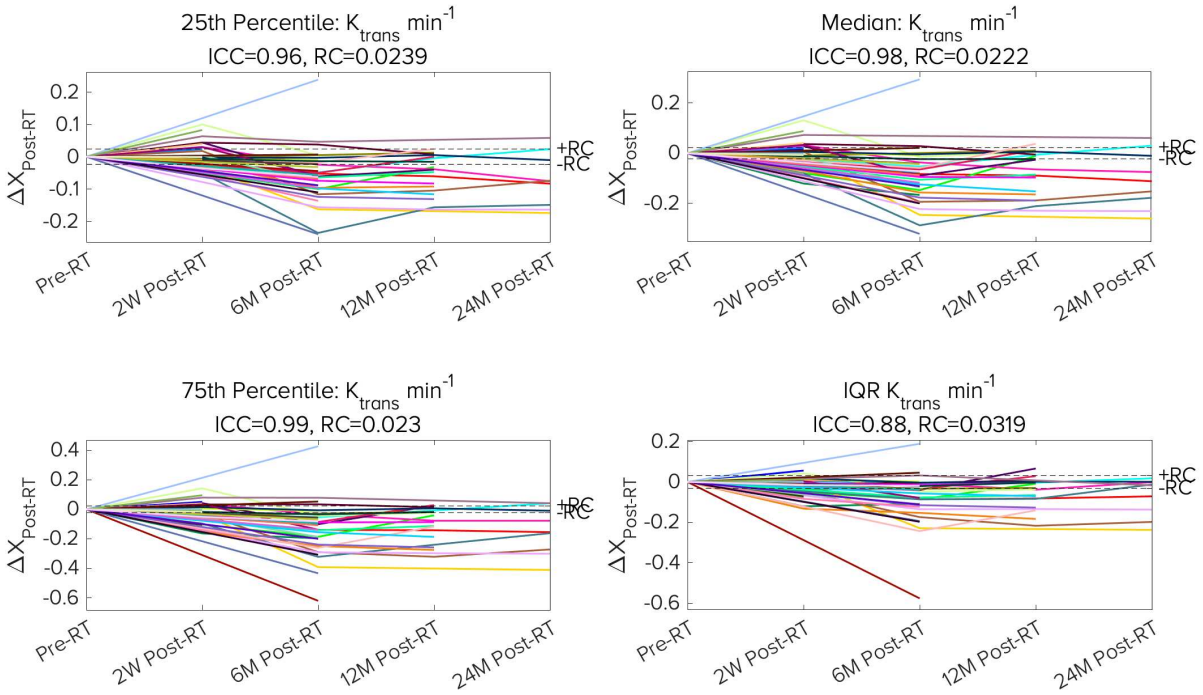


Figure B.16: The change in the K_{trans} statistics (25th percentile, median, 75th percentile and interquartile range (IQR)) derived from the dynamic contrast-enhanced MRI data of the entire breast tumour, at 2-week (N=34), 6-month (N=38), 12-month (N=21) and 24-month (N=9) post-radiotherapy (RT) from 51 participants. The dashed black lines represent the repeatability coefficient, as indicator of significant change, i.e., if the difference post-treatment is larger than the repeatability coefficient, then the change is significant.

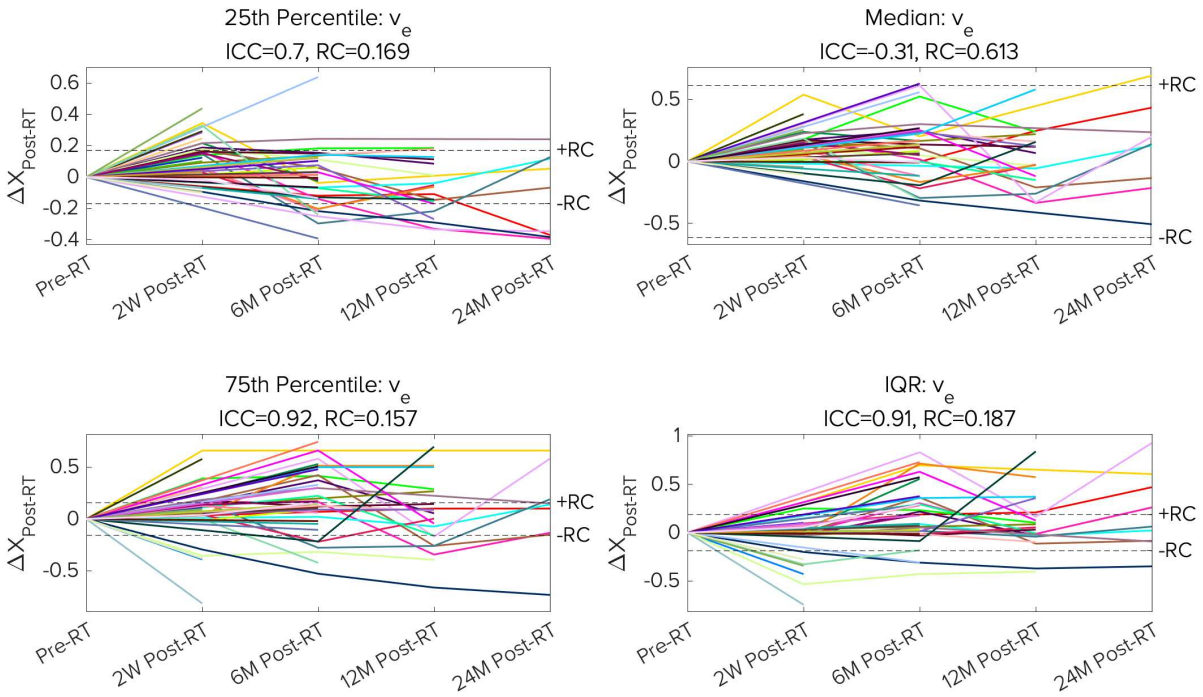


Figure B.17: The change in the v_e statistics (25th percentile, median, 75th percentile and interquartile range (IQR)) derived from the dynamic contrast-enhanced MRI data of the entire breast tumour, at 2-week (N=34), 6-month (N=38), 12-month (N=21) and 24-month (N=9) post-radiotherapy (RT) from 51 participants. The dashed black lines represent the repeatability coefficient, as indicator of significant change, i.e., if the difference post-treatment is larger than the repeatability coefficient, then the change is significant.

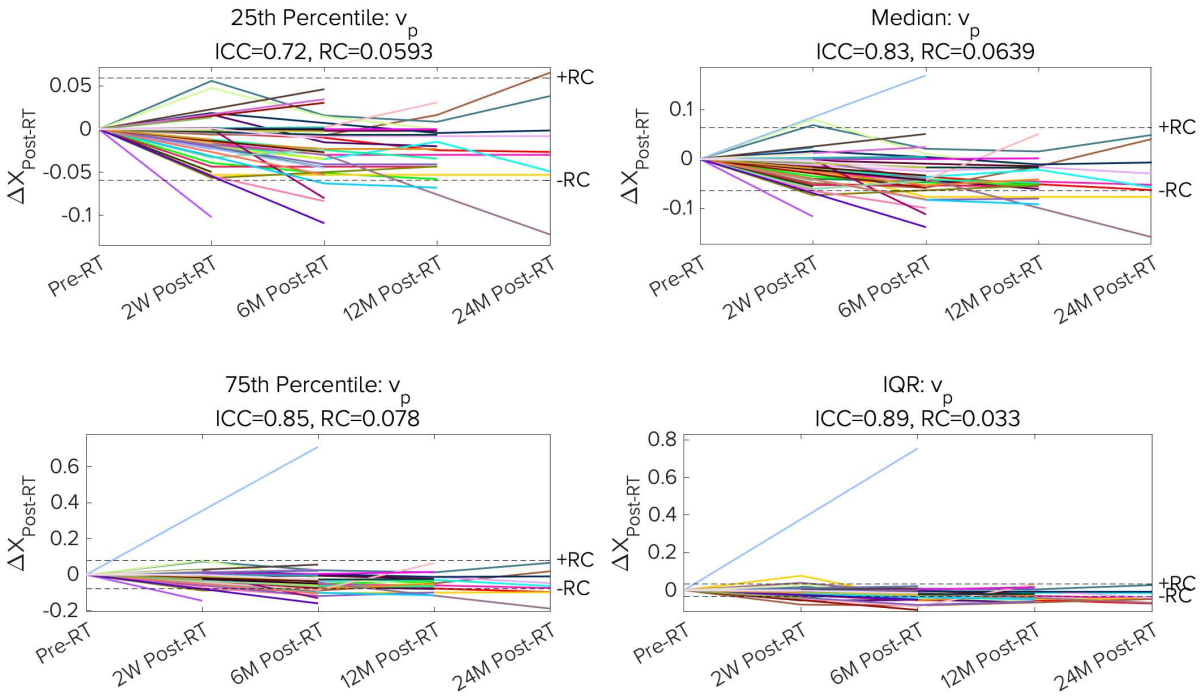


Figure B.18: The change in the v_p statistics (25th percentile, median, 75th percentile and interquartile range (IQR)) derived from the dynamic contrast-enhanced MRI data of the entire breast tumour, at 2-week (N=34), 6-month (N=38), 12-month (N=21) and 24-month (N=9) post-radiotherapy (RT) from 51 participants. The dashed black lines represent the repeatability coefficient, as indicator of significant change, i.e., if the difference post-treatment is larger than the repeatability coefficient, then the change is significant.

Piecewise Linear Model and Semi-Quantitative Parameters

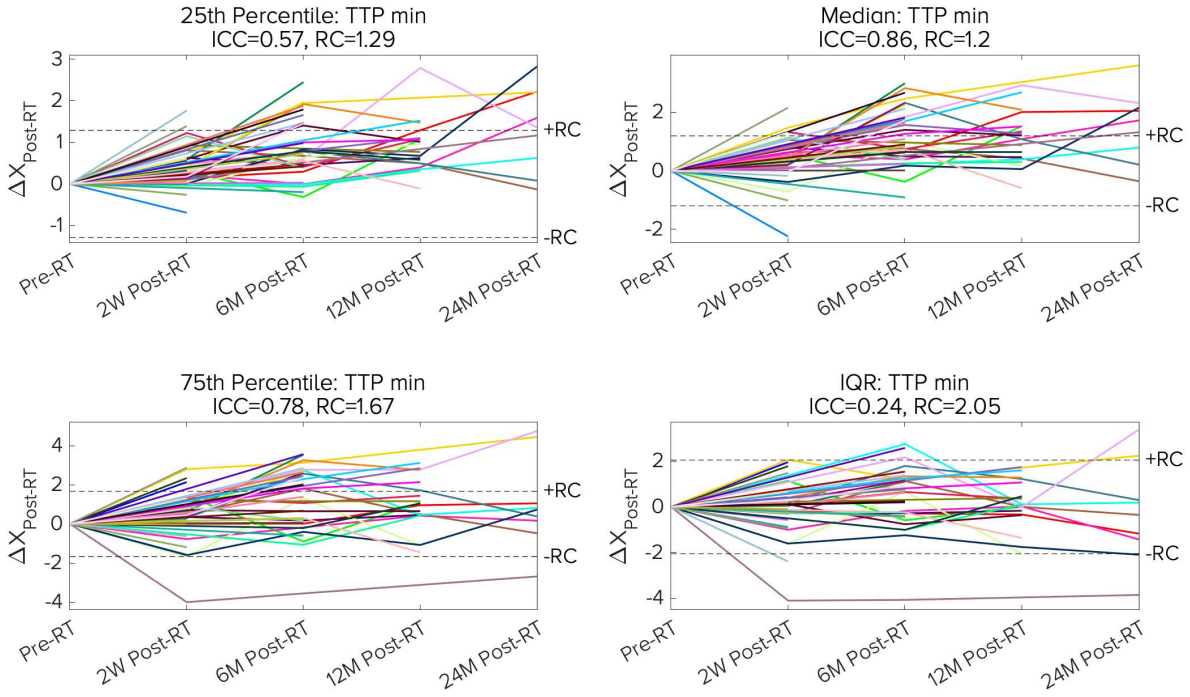


Figure B.19: The change in the *TTP* statistics (25th percentile, median, 75th percentile and interquartile range (IQR)) derived from the dynamic contrast-enhanced MRI data of the entire breast tumour, at 2-week (N=34), 6-month (N=38), 12-month (N=21) and 24-month (N=9) post-radiotherapy (RT) from 51 participants. The dashed black lines represent the repeatability coefficient, as indicator of significant change, i.e., if the difference post-treatment is larger than the repeatability coefficient, then the change is significant.

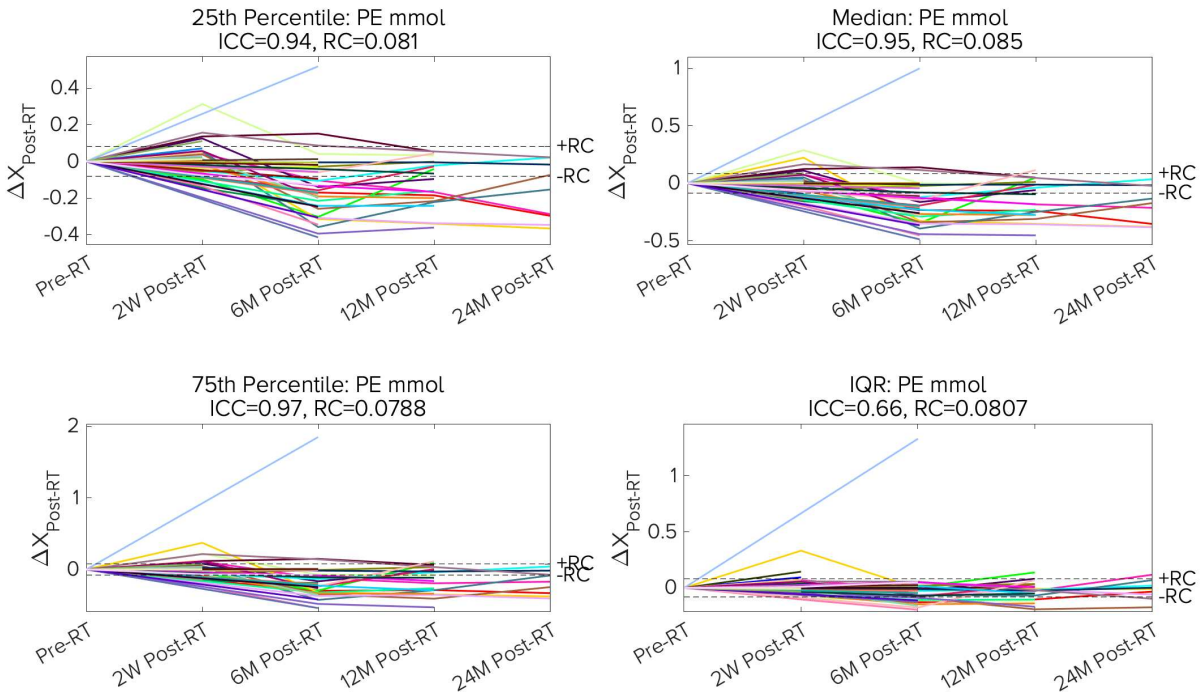


Figure B.20: The change in the *PE* statistics (25th percentile, median, 75th percentile and interquartile range (IQR)) derived from the dynamic contrast-enhanced MRI data of the entire breast tumour, at 2-week (N=34), 6-month (N=38), 12-month (N=21) and 24-month (N=9) post-radiotherapy (RT) from 51 participants. The dashed black lines represent the repeatability coefficient, as indicator of significant change, i.e., if the difference post-treatment is larger than the repeatability coefficient, then the change is significant.

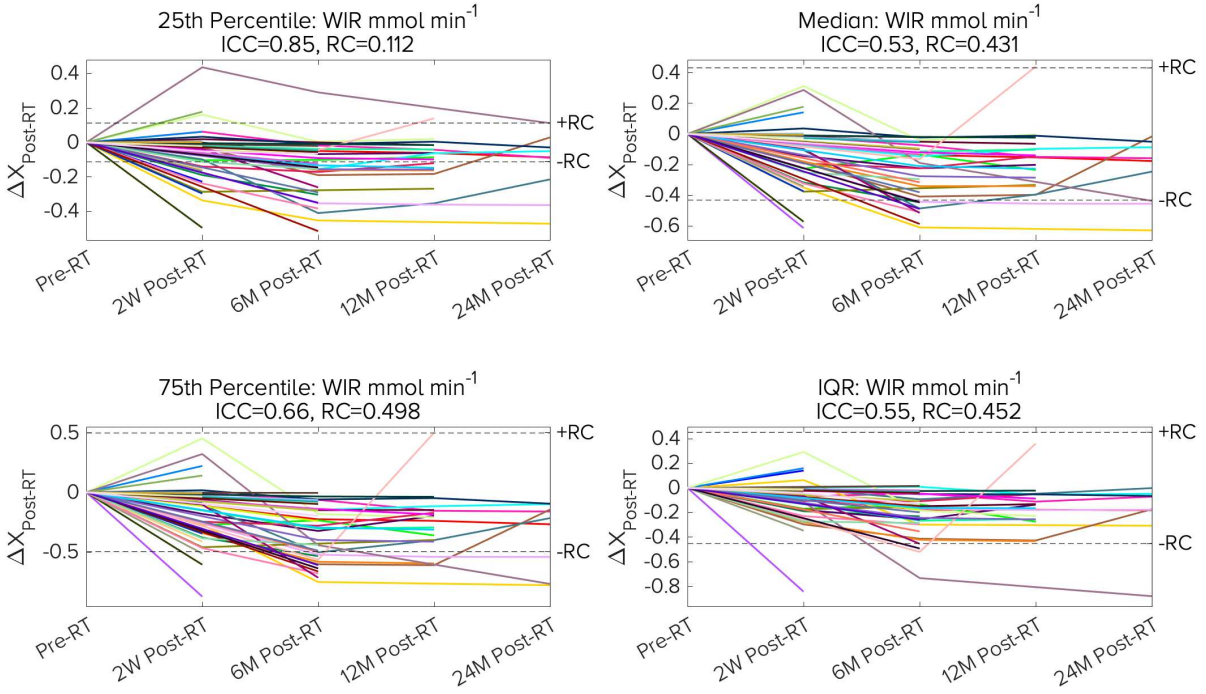


Figure B.21: The change in the *WIR* statistics (25th percentile, median, 75th percentile and interquartile range (IQR)) derived from the dynamic contrast-enhanced MRI data of the entire breast tumour, at 2-week (N=34), 6-month (N=38), 12-month (N=21) and 24-month (N=9) post-radiotherapy (RT) from 51 participants. The dashed black lines represent the repeatability coefficient, as indicator of significant change, i.e., if the difference post-treatment is larger than the repeatability coefficient, then the change is significant.

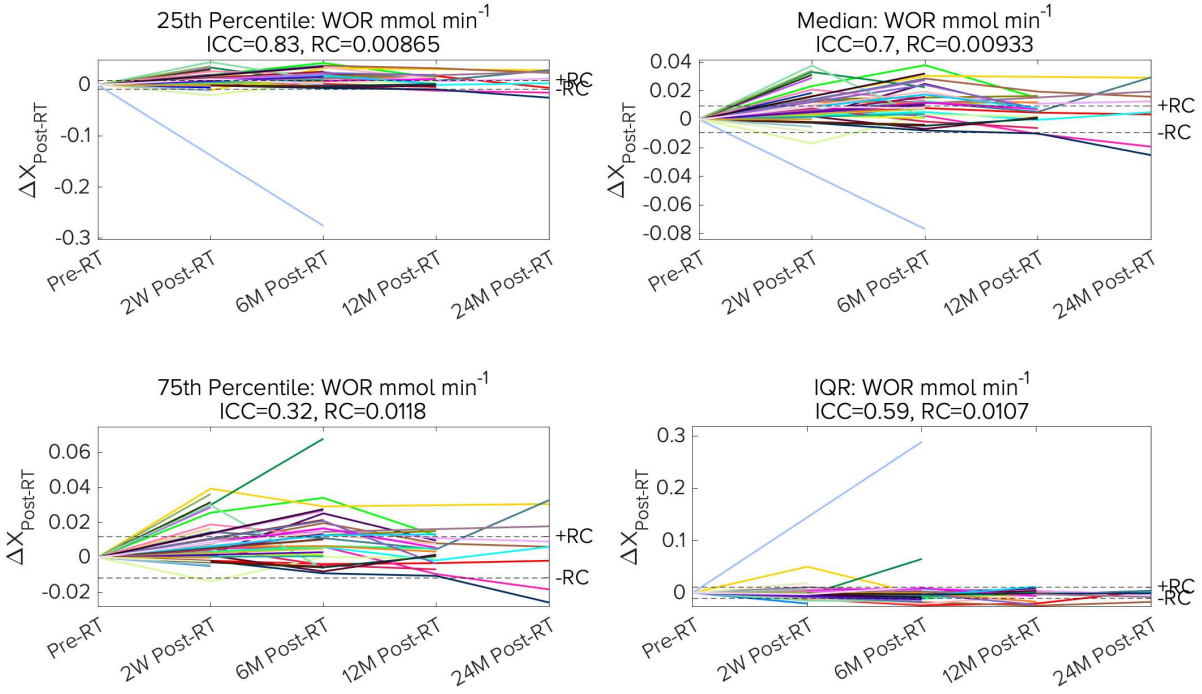


Figure B.22: The change in the *WOR* statistics (25th percentile, median, 75th percentile and interquartile range (IQR)) derived from the dynamic contrast-enhanced MRI data of the entire breast tumour, at 2-week (N=34), 6-month (N=38), 12-month (N=21) and 24-month (N=9) post-radiotherapy (RT) from 51 participants. The dashed black lines represent the repeatability coefficient, as indicator of significant change, i.e., if the difference post-treatment is larger than the repeatability coefficient, then the change is significant.

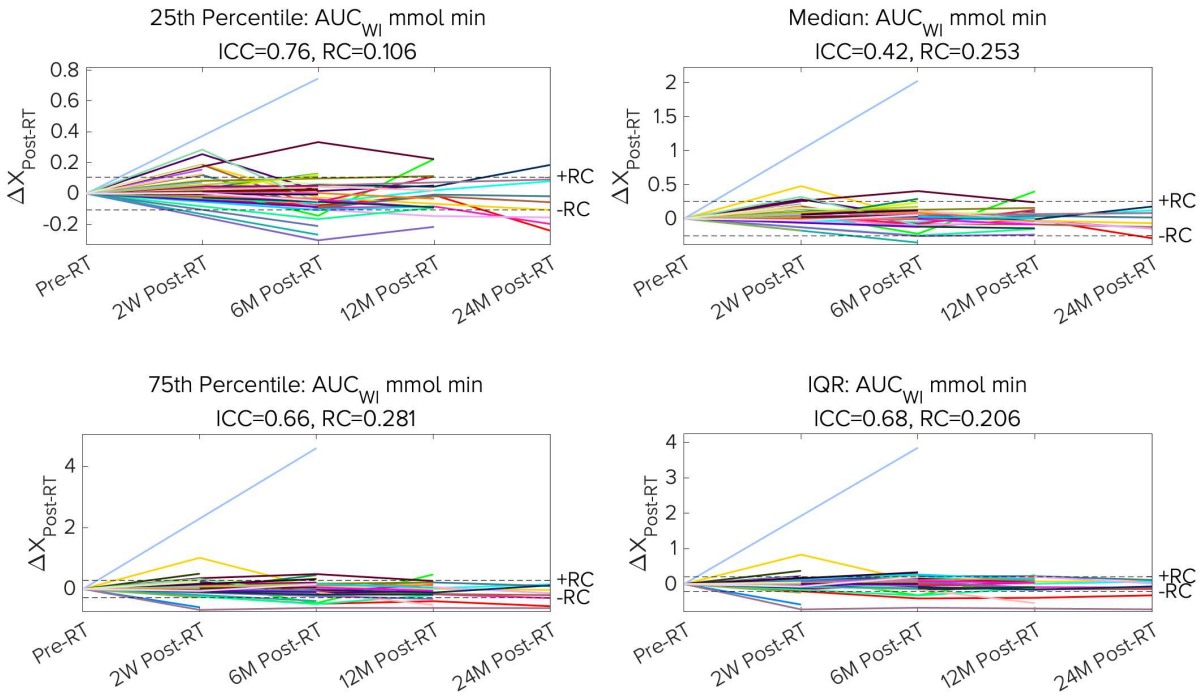


Figure B.23: The change in the AUC_{WI} statistics (25th percentile, median, 75th percentile and interquartile range (IQR)) derived from the dynamic contrast-enhanced MRI data of the entire breast tumour, at 2-week (N=34), 6-month (N=38), 12-month (N=21) and 24-month (N=9) post-radiotherapy (RT) from 51 participants. The dashed black lines represent the repeatability coefficient, as indicator of significant change, i.e., if the difference post-treatment is larger than the repeatability coefficient, then the change is significant.

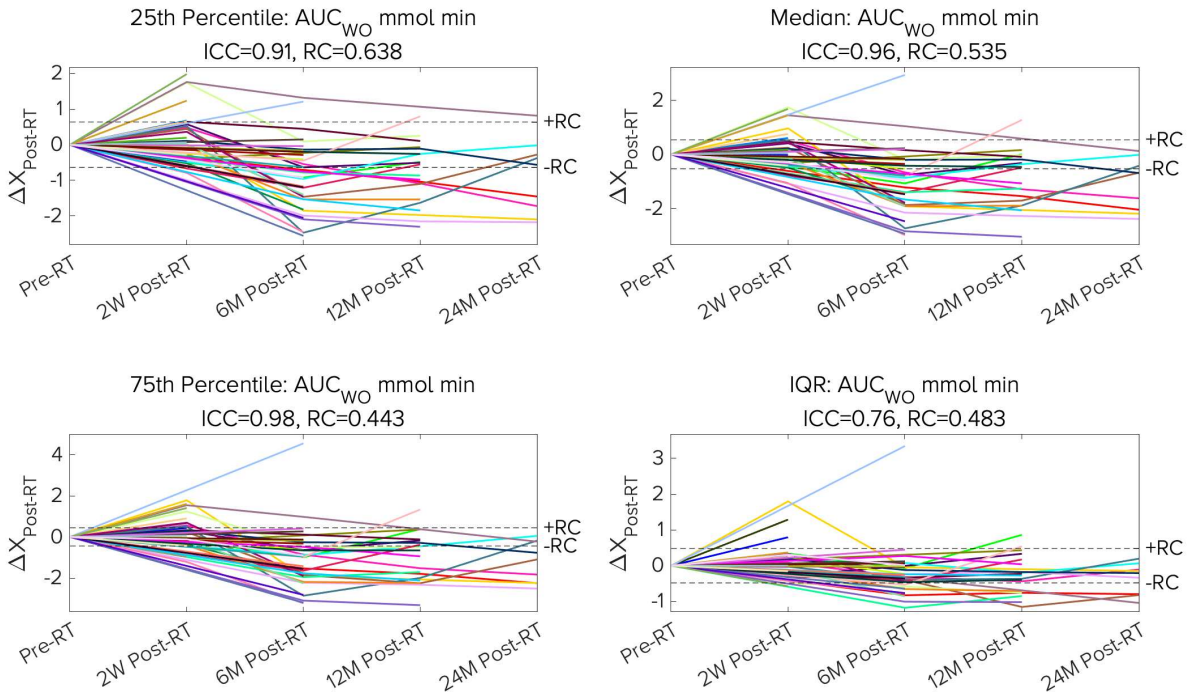


Figure B.24: The change in the AUC_{WO} statistics (25th percentile, median, 75th percentile and interquartile range (IQR)) derived from the dynamic contrast-enhanced MRI data of the entire breast tumour, at 2-week (N=34), 6-month (N=38), 12-month (N=21) and 24-month (N=9) post-radiotherapy (RT) from 51 participants. The dashed black lines represent the repeatability coefficient, as indicator of significant change, i.e., if the difference post-treatment is larger than the repeatability coefficient, then the change is significant.

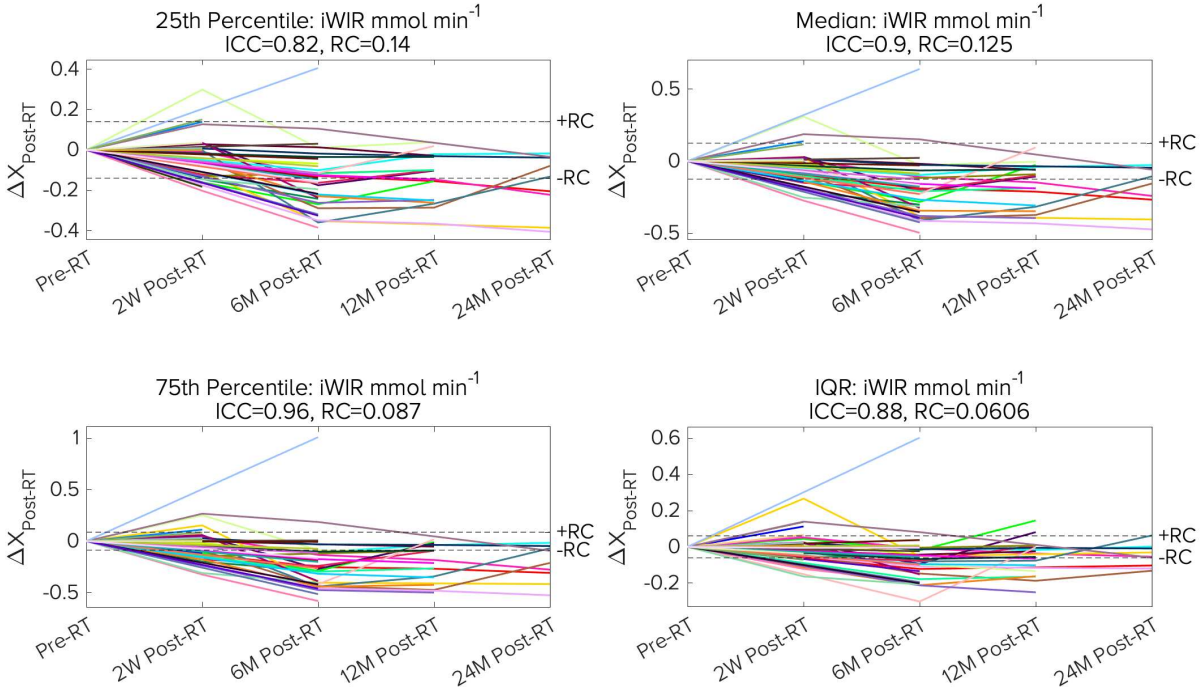


Figure B.25: The change in the *iWIR* statistics (25th percentile, median, 75th percentile and interquartile range (IQR)) derived from the dynamic contrast-enhanced MRI data of the entire breast tumour, at 2-week (N=34), 6-month (N=38), 12-month (N=21) and 24-month (N=9) post-radiotherapy (RT) from 51 participants. The dashed black lines represent the repeatability coefficient, as indicator of significant change, i.e., if the difference post-treatment is larger than the repeatability coefficient, then the change is significant.

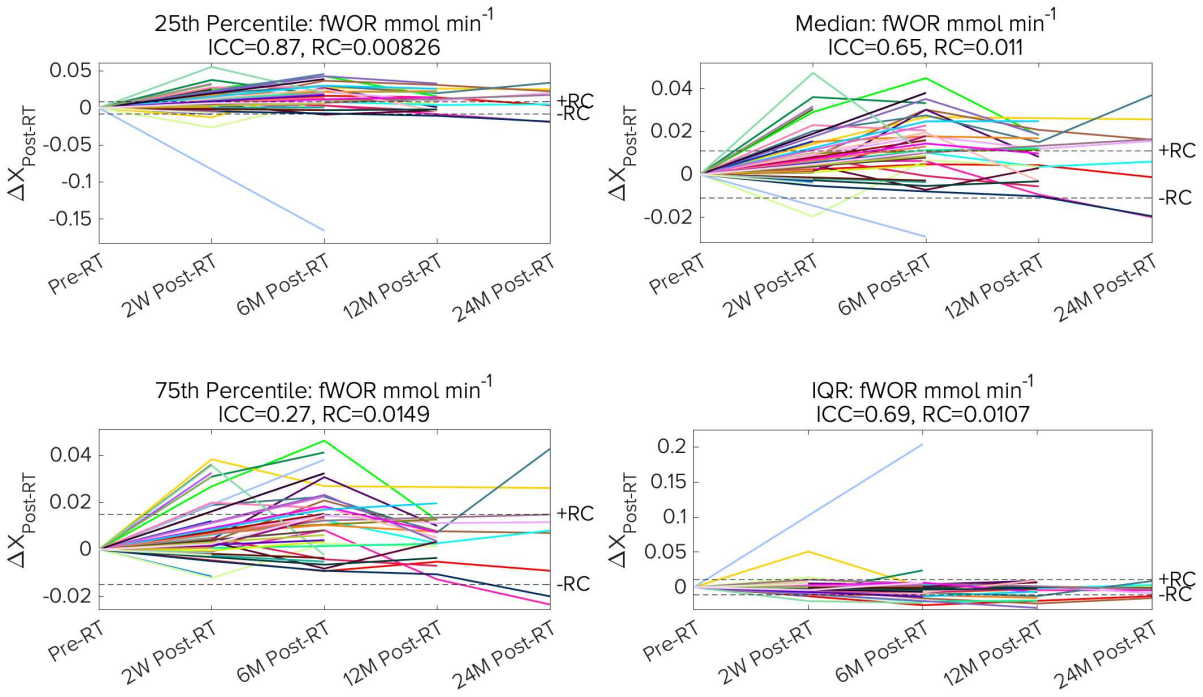


Figure B.26: The change in the $fWOR$ statistics (25th percentile, median, 75th percentile and interquartile range (IQR)) derived from the dynamic contrast-enhanced MRI data of the entire breast tumour, at 2-week (N=34), 6-month (N=38), 12-month (N=21) and 24-month (N=9) post-radiotherapy (RT) from 51 participants. The dashed black lines represent the repeatability coefficient, as indicator of significant change, i.e., if the difference post-treatment is larger than the repeatability coefficient, then the change is significant.

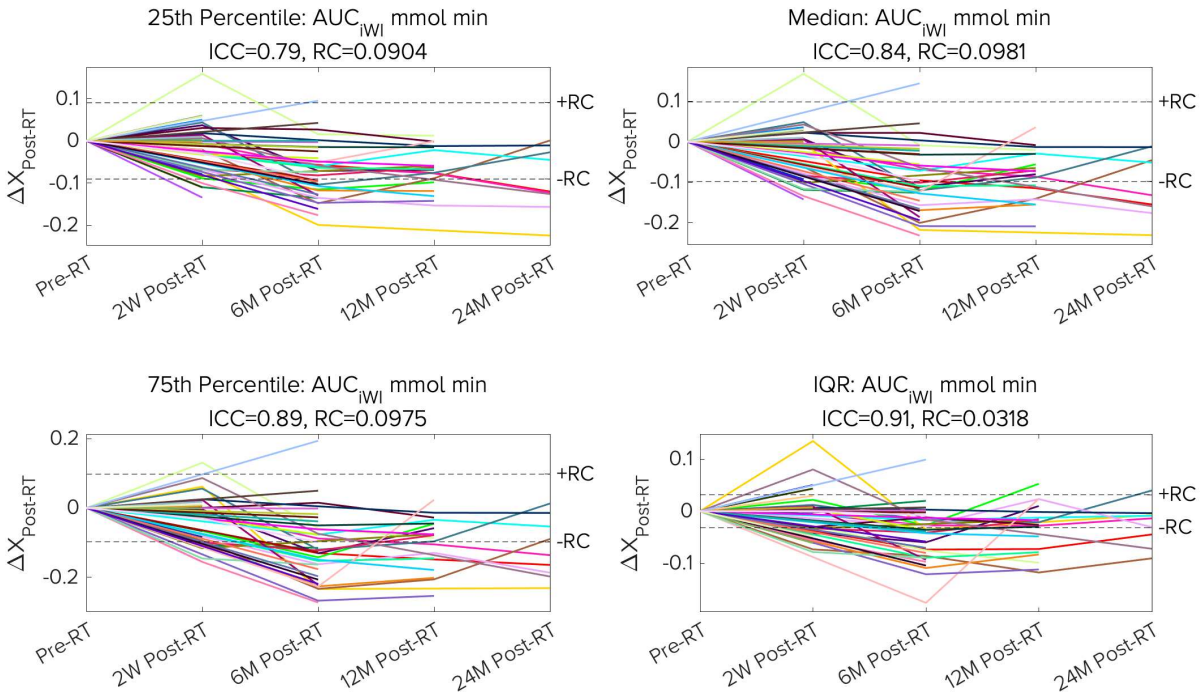


Figure B.27: The change in the AUC_{iWI} statistics (25th percentile, median, 75th percentile and interquartile range (IQR)) derived from the dynamic contrast-enhanced MRI data of the entire breast tumour, at 2-week (N=34), 6-month (N=38), 12-month (N=21) and 24-month (N=9) post-radiotherapy (RT) from 51 participants. The dashed black lines represent the repeatability coefficient, as indicator of significant change, i.e., if the difference post-treatment is larger than the repeatability coefficient, then the change is significant.

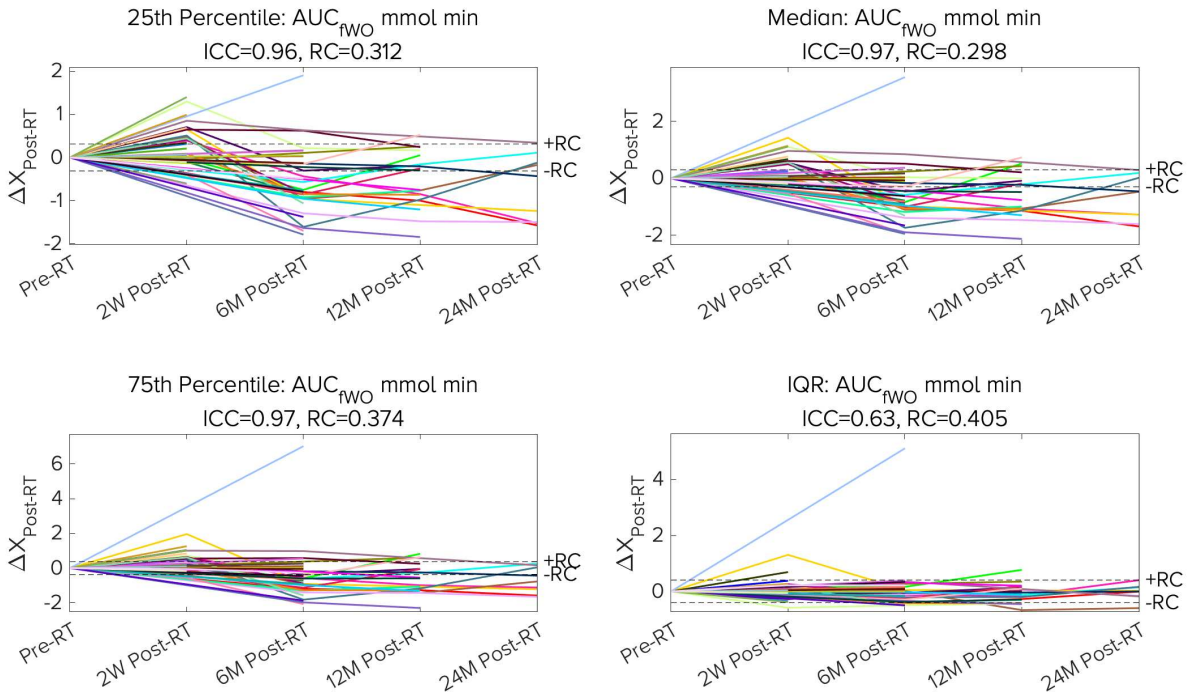


Figure B.28: The change in the AUC_{fWO} statistics (25th percentile, median, 75th percentile and interquartile range (IQR)) derived from the dynamic contrast-enhanced MRI data of the entire breast tumour, at 2-week (N=34), 6-month (N=38), 12-month (N=21) and 24-month (N=9) post-radiotherapy (RT) from 51 participants. The dashed black lines represent the repeatability coefficient, as indicator of significant change, i.e., if the difference post-treatment is larger than the repeatability coefficient, then the change is significant.

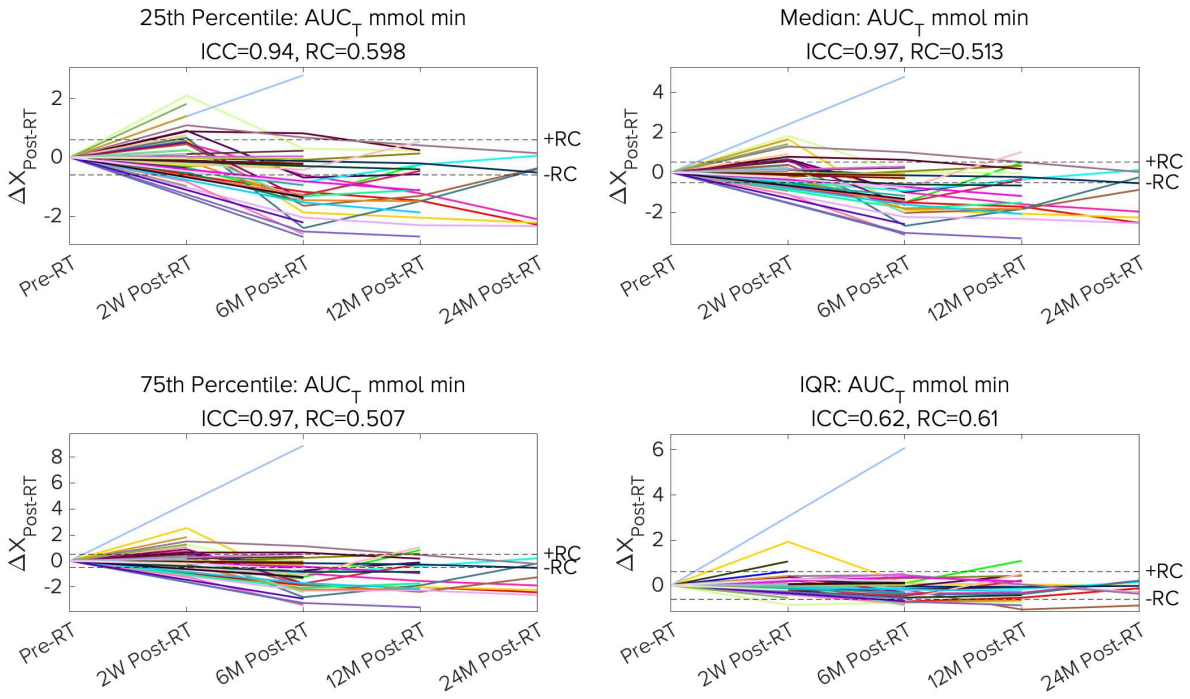


Figure B.29: The change in the AUC_T statistics (25th percentile, median, 75th percentile and interquartile range (IQR)) derived from the dynamic contrast-enhanced MRI data of the entire breast tumour, at 2-week (N=34), 6-month (N=38), 12-month (N=21) and 24-month (N=9) post-radiotherapy (RT) from 51 participants. The dashed black lines represent the repeatability coefficient, as indicator of significant change, i.e., if the difference post-treatment is larger than the repeatability coefficient, then the change is significant.

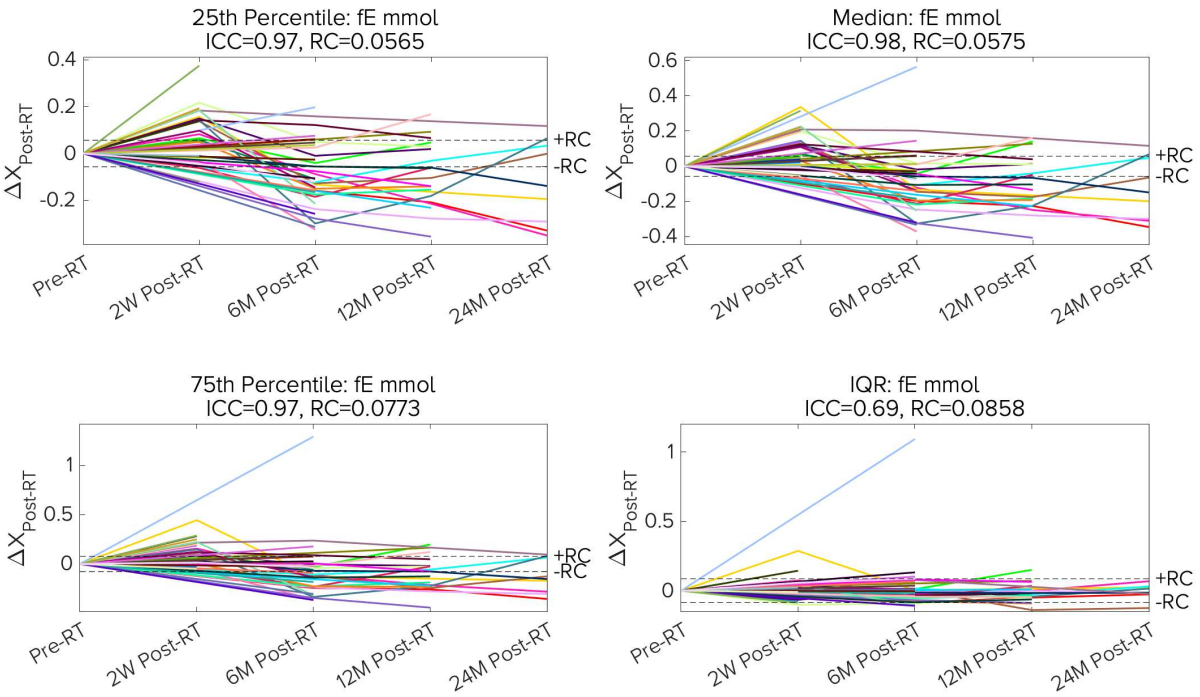


Figure B.30: The change in the fE statistics (25th percentile, median, 75th percentile and interquartile range (IQR)) derived from the dynamic contrast-enhanced MRI data of the entire breast tumour, at 2-week (N=34), 6-month (N=38), 12-month (N=21) and 24-month (N=9) post-radiotherapy (RT) from 51 participants. The dashed black lines represent the repeatability coefficient, as indicator of significant change, i.e., if the difference post-treatment is larger than the repeatability coefficient, then the change is significant.

B.2.2 Whole Tumour Response Assessment

Tofts Model Parameters

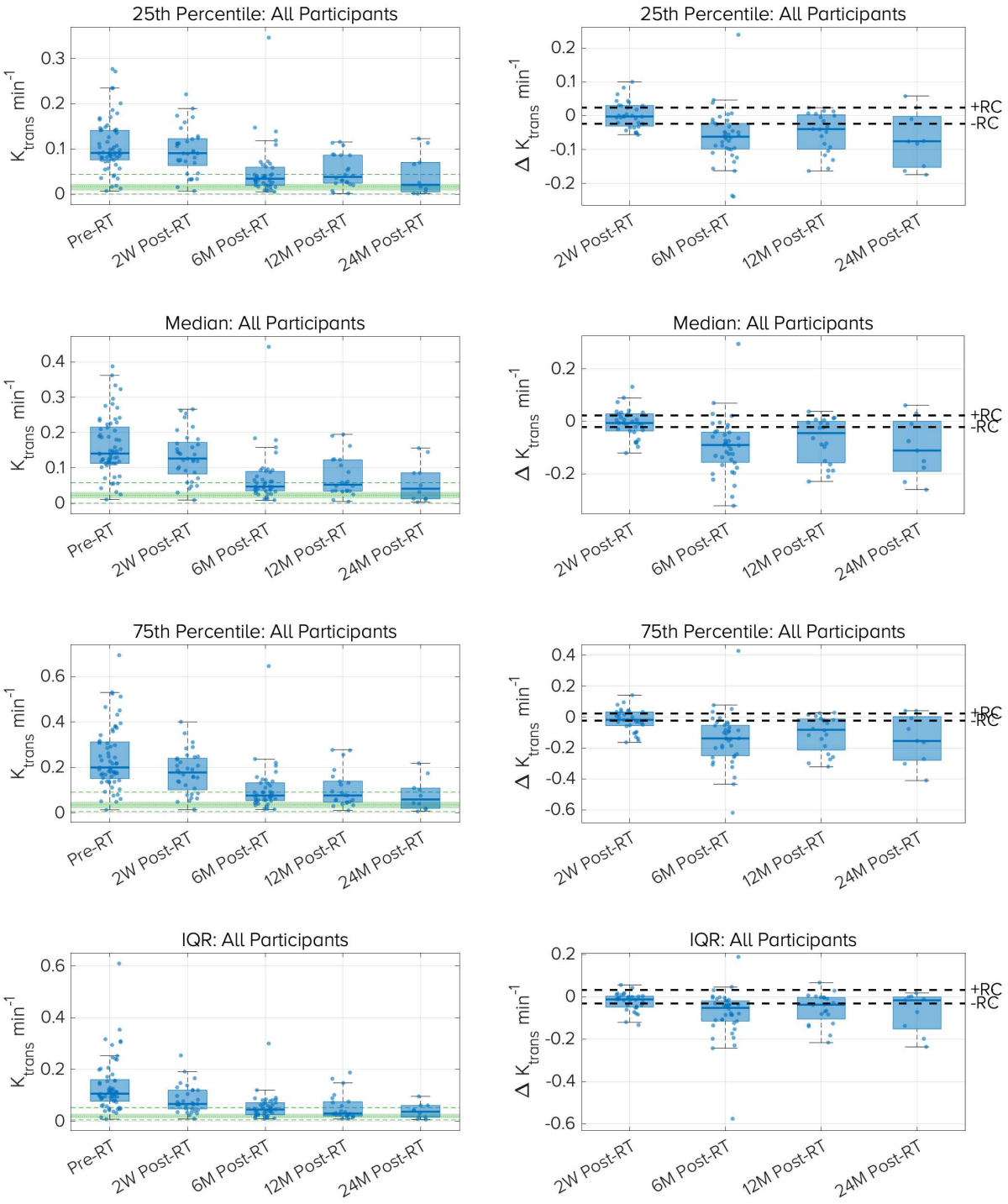


Figure B.31: (Left) The K_{trans} statistics (25th percentile, median, 75th percentile, and IQR) derived from the dynamic contrast-enhanced MRI data of the entire breast tumour, pre-RT (N=59) and at 2-week (N=32), 6-month (N=40), 12-month (N=22) and 24-month (N=10) post-radiotherapy (RT) for all participants. (Right) The change in the K_{trans} statistics from baseline (pre-RT) at 2-week (N=34), 6-month (N=38), 12-month (N=21) and 24-month (N=9) post-radiotherapy (RT). The dots are individual participants. The green shaded area is the 25th and 75th percentile range of the healthy breast, and the dashed green lines are the whiskers.

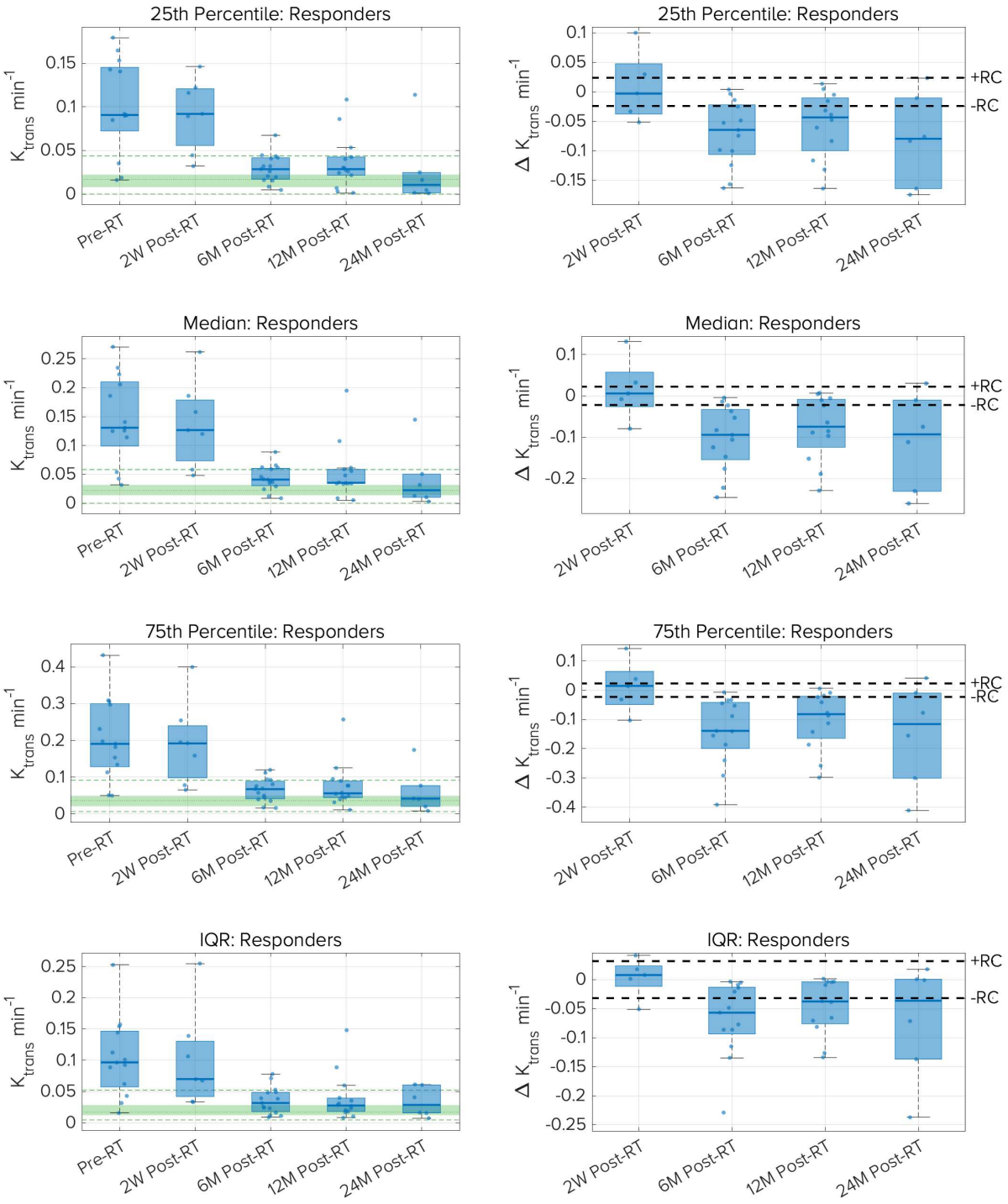


Figure B.32: (Left) The K_{trans} statistics (25th percentile, median, 75th percentile, and IQR) derived from the dynamic contrast-enhanced MRI data of the entire breast tumour, pre-RT (N=13) and at 2-week (N=7), 6-month (N=15), 12-month (N=14) and 24-month (N=6) post-radiotherapy (RT) for the responders. (Right) The change in the K_{trans} statistics from baseline (pre-RT) at 2-week (N=5), 6-month (N=13), 12-month (N=12) and 24-month (N=6) post-radiotherapy (RT). The dots are individual participants. The green shaded area is the 25th and 75th percentile range of the healthy breast, and the dashed green lines are the whiskers.

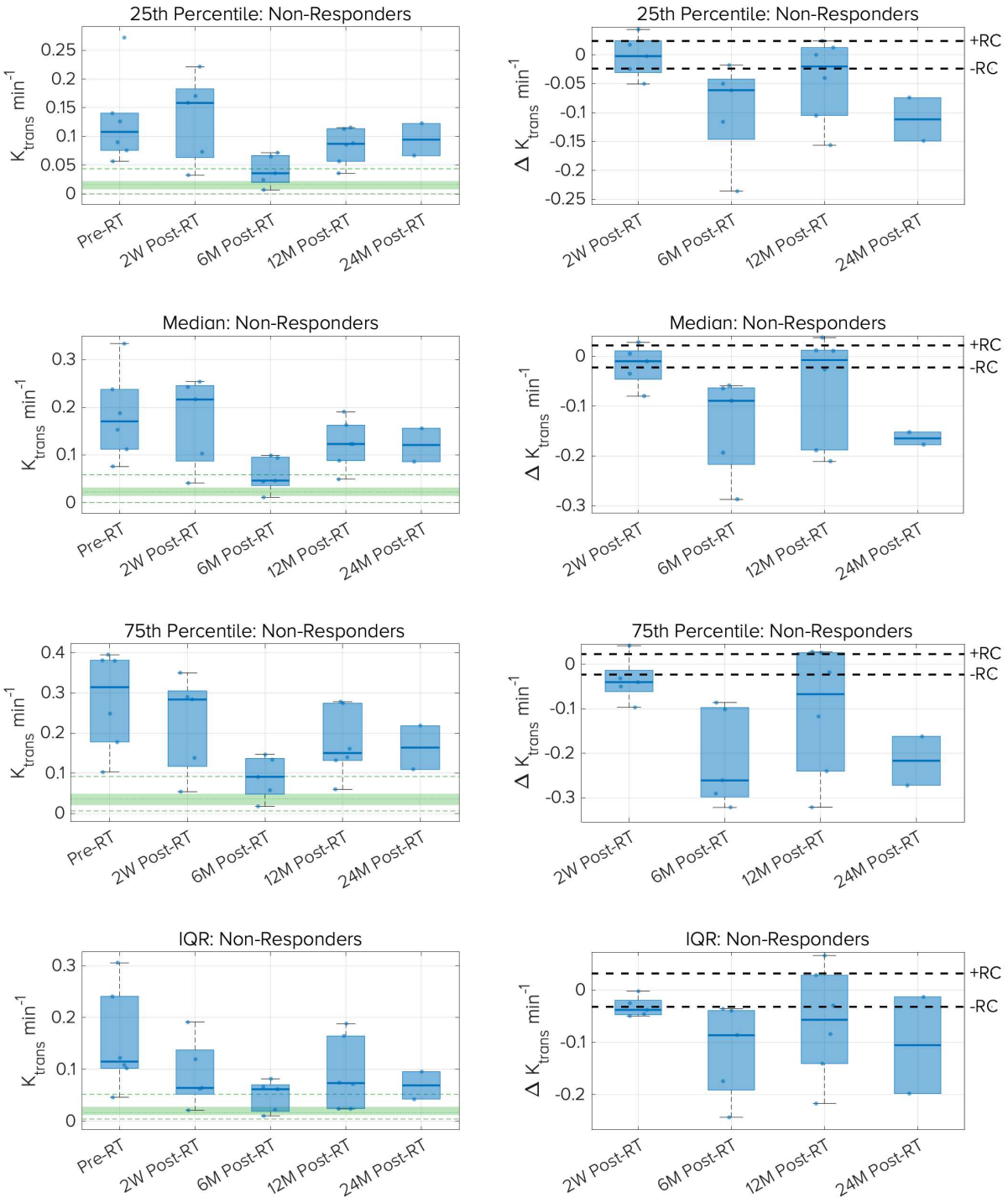


Figure B.33: (Left) The K_{trans} statistics (25th percentile, median, 75th percentile, and IQR) derived from the dynamic contrast-enhanced MRI data of the entire breast tumour, pre-RT (N=6) and at 2-week (N=5), 6-month (N=5), 12-month (N=6) and 24-month (N=2) post-radiotherapy (RT) for the non-responders. (Right) The change in the K_{trans} statistics from baseline (pre-RT) at 2-week (N=5), 6-month (N=5), 12-month (N=6) and 24-month (N=2) post-radiotherapy (RT). The dots are individual participants. The green shaded area is the 25th and 75th percentile range of the healthy breast, and the dashed green lines are the whiskers.

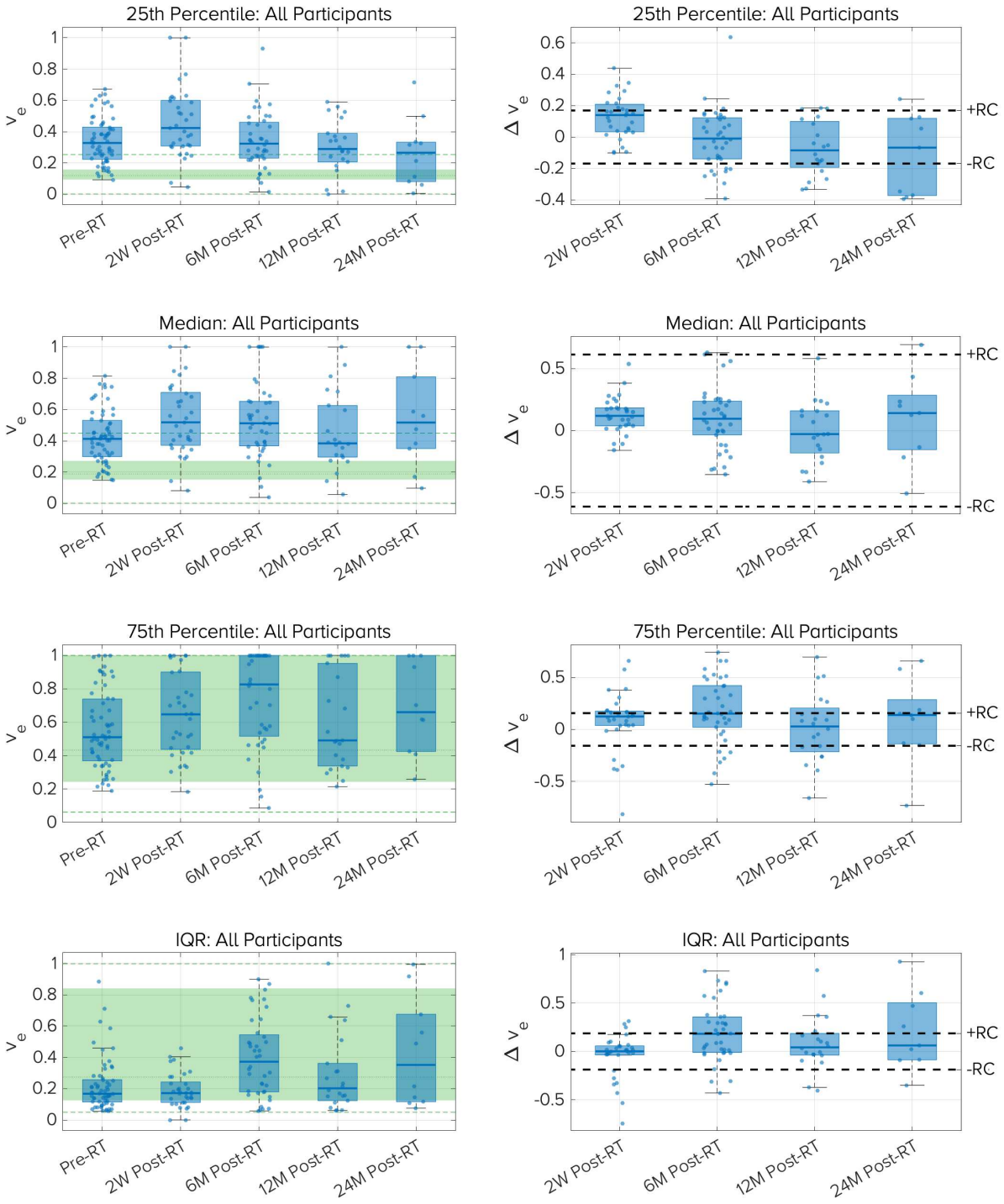


Figure B.34: (Left) The v_e statistics (25th percentile, median, 75th percentile, and IQR) derived from the dynamic contrast-enhanced MRI data of the entire breast tumour, pre-RT (N=59) and at 2-week (N=32), 6-month (N=40), 12-month (N=22) and 24-month (N=10) post-radiotherapy (RT) for all participants. (Right) The change in the v_e statistics from baseline (pre-RT) at 2-week (N=34), 6-month (N=38), 12-month (N=21) and 24-month (N=9) post-radiotherapy (RT). The dots are individual participants. The green shaded area is the 25th and 75th percentile range of the healthy breast, and the dashed green lines are the whiskers.

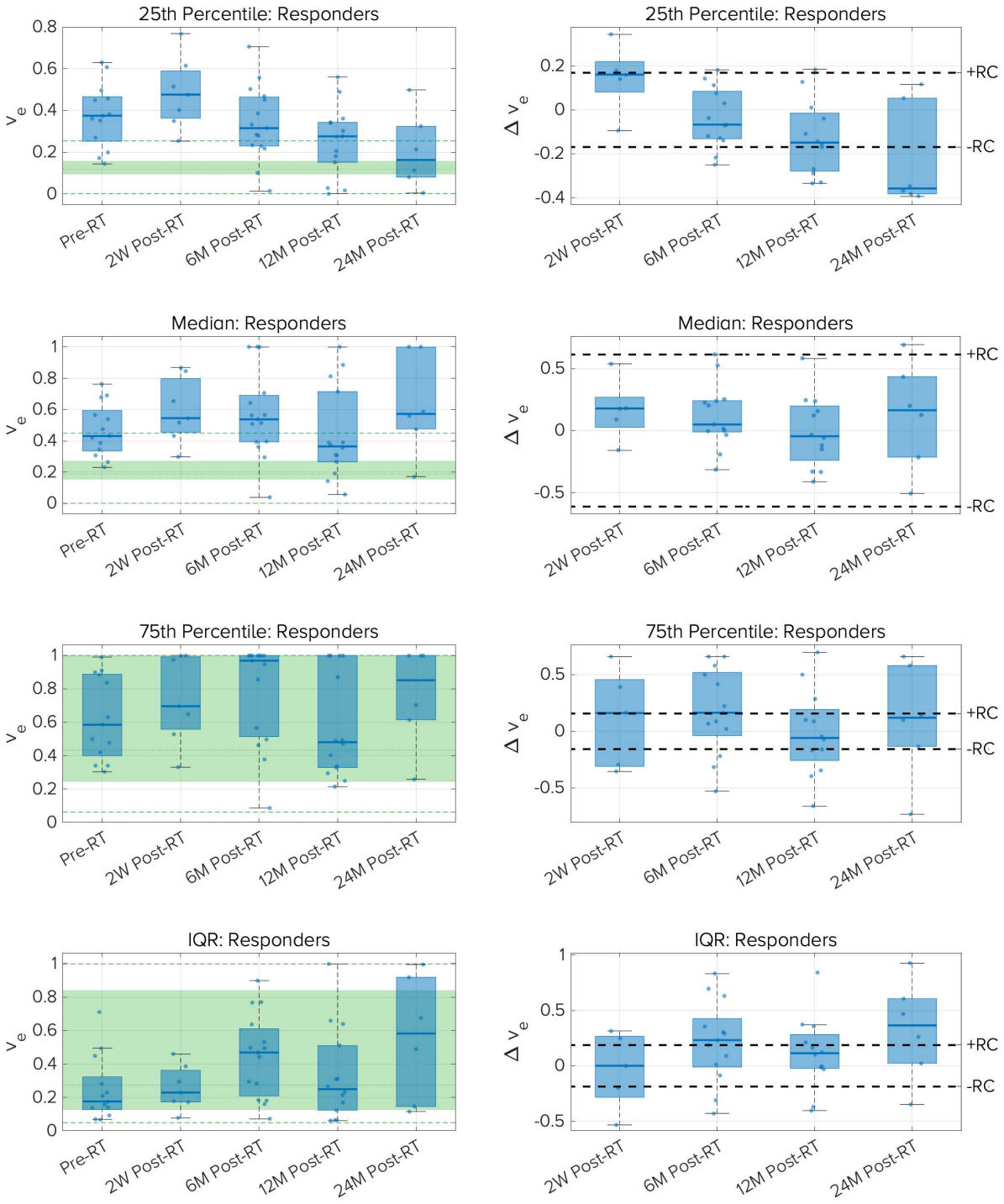


Figure B.35: (Left) The v_e statistics (25th percentile, median, 75th percentile, and IQR) derived from the dynamic contrast-enhanced MRI data of the entire breast tumour, pre-RT (N=13) and at 2-week (N=7), 6-month (N=15), 12-month (N=14) and 24-month (N=6) post-radiotherapy (RT) for the responders. (Right) The change in the v_e statistics from baseline (pre-RT) at 2-week (N=5), 6-month (N=13), 12-month (N=12) and 24-month (N=6) post-radiotherapy (RT). The dots are individual participants. The green shaded area is the 25th and 75th percentile range of the healthy breast, and the dashed green lines are the whiskers.

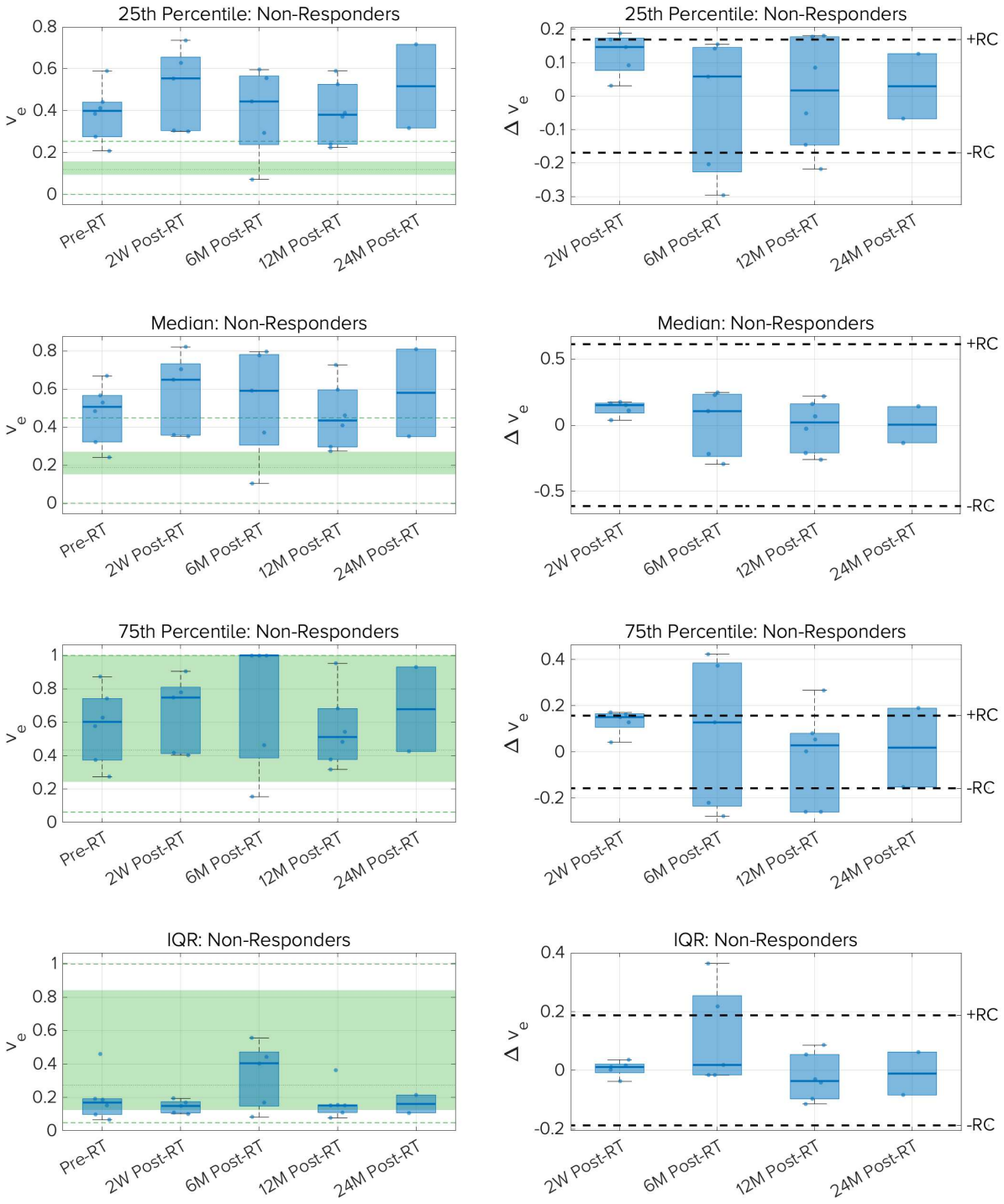


Figure B.36: (Left) The v_e statistics (25th percentile, median, 75th percentile, and IQR) derived from the dynamic contrast-enhanced MRI data of the entire breast tumour, pre-RT (N=6) and at 2-week (N=5), 6-month (N=5), 12-month (N=6) and 24-month (N=2) post-radiotherapy (RT) for the non-responders. (Right) The change in the v_e statistics from baseline (pre-RT) at 2-week (N=5), 6-month (N=5), 12-month (N=6) and 24-month (N=2) post-radiotherapy (RT). The dots are individual participants. The green shaded area is the 25th and 75th percentile range of the healthy breast, and the dashed green lines are the whiskers.

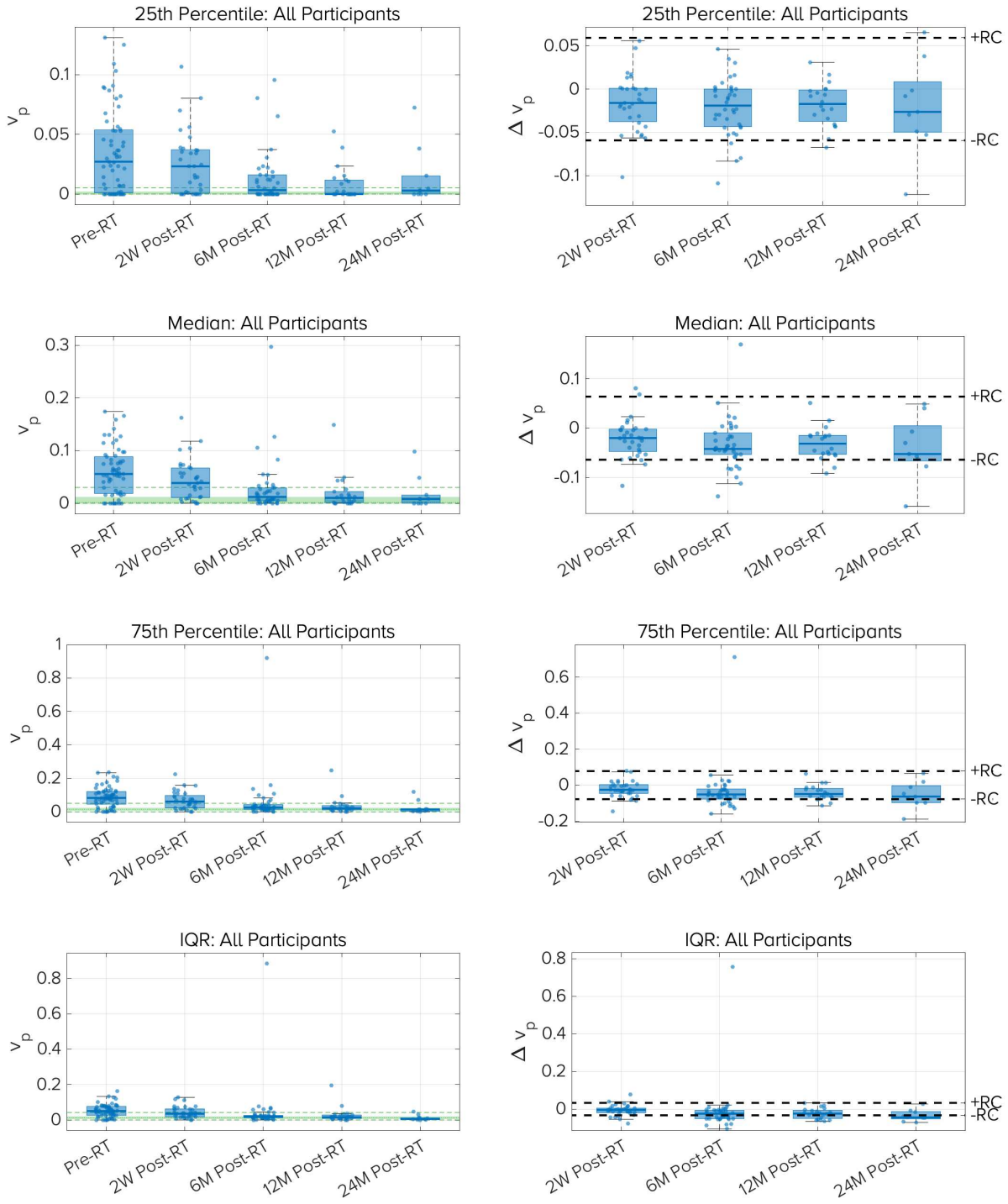


Figure B.37: (Left) The v_p statistics (25th percentile, median, 75th percentile, and IQR) derived from the dynamic contrast-enhanced MRI data of the entire breast tumour, pre-RT (N=59) and at 2-week (N=32), 6-month (N=40), 12-month (N=22) and 24-month (N=10) post-radiotherapy (RT) for all participants. (Right) The change in the v_p statistics from baseline (pre-RT) at 2-week (N=34), 6-month (N=38), 12-month (N=21) and 24-month (N=9) post-radiotherapy (RT).. The dots are individual participants. The green shaded area is the 25th and 75th percentile range of the healthy breast, and the dashed green lines are the whiskers.

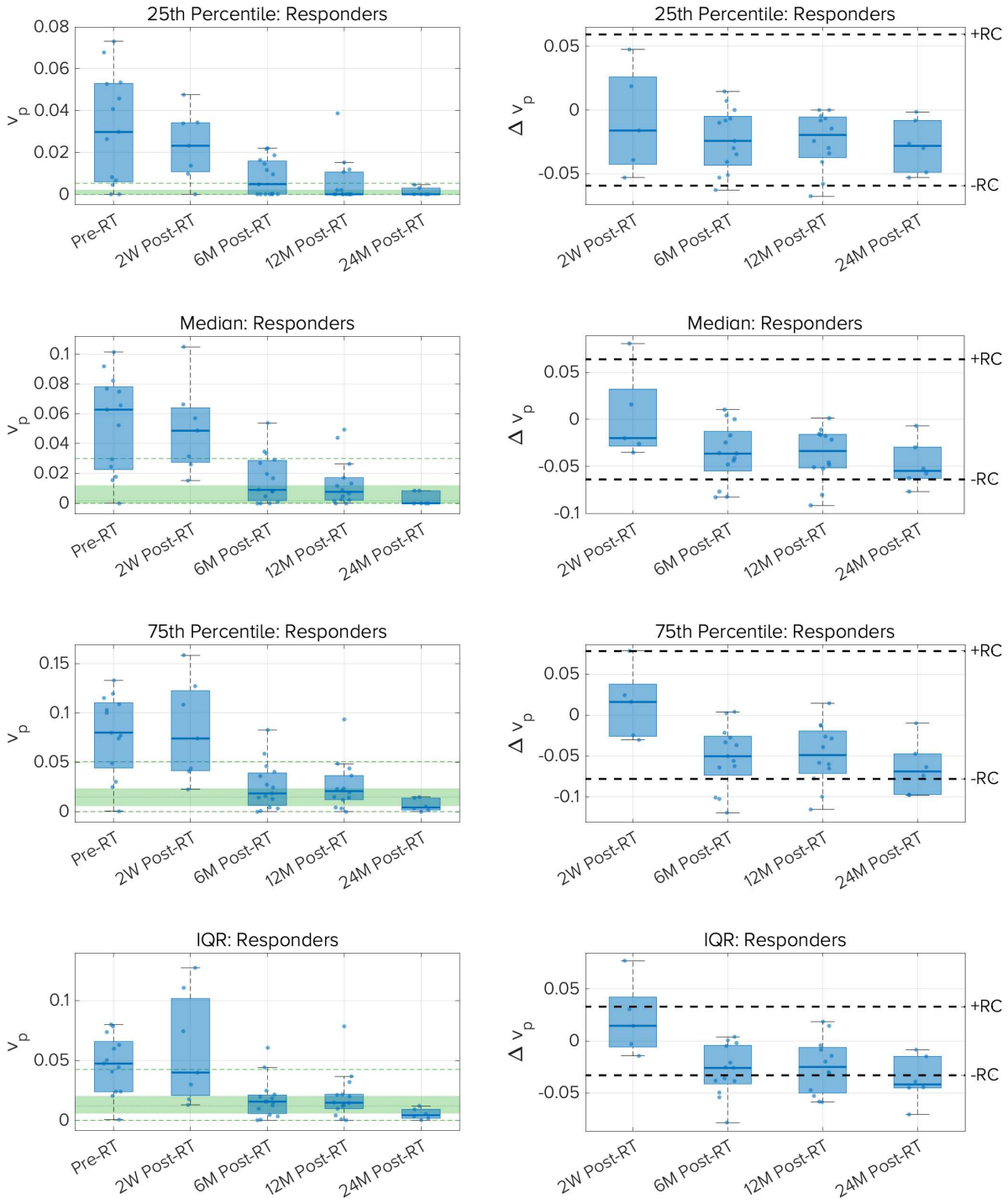


Figure B.38: (Left) The v_p statistics (25th percentile, median, 75th percentile, and IQR) derived from the dynamic contrast-enhanced MRI data of the entire breast tumour, pre-RT (N=13) and at 2-week (N=7), 6-month (N=15), 12-month (N=14) and 24-month (N=6) post-radiotherapy (RT) for the responders. (Right) The change in the v_p statistics from baseline (pre-RT) at 2-week (N=5), 6-month (N=13), 12-month (N=12) and 24-month (N=6) post-radiotherapy (RT). The dots are individual participants. The green shaded area is the 25th and 75th percentile range of the healthy breast, and the dashed green lines are the whiskers.

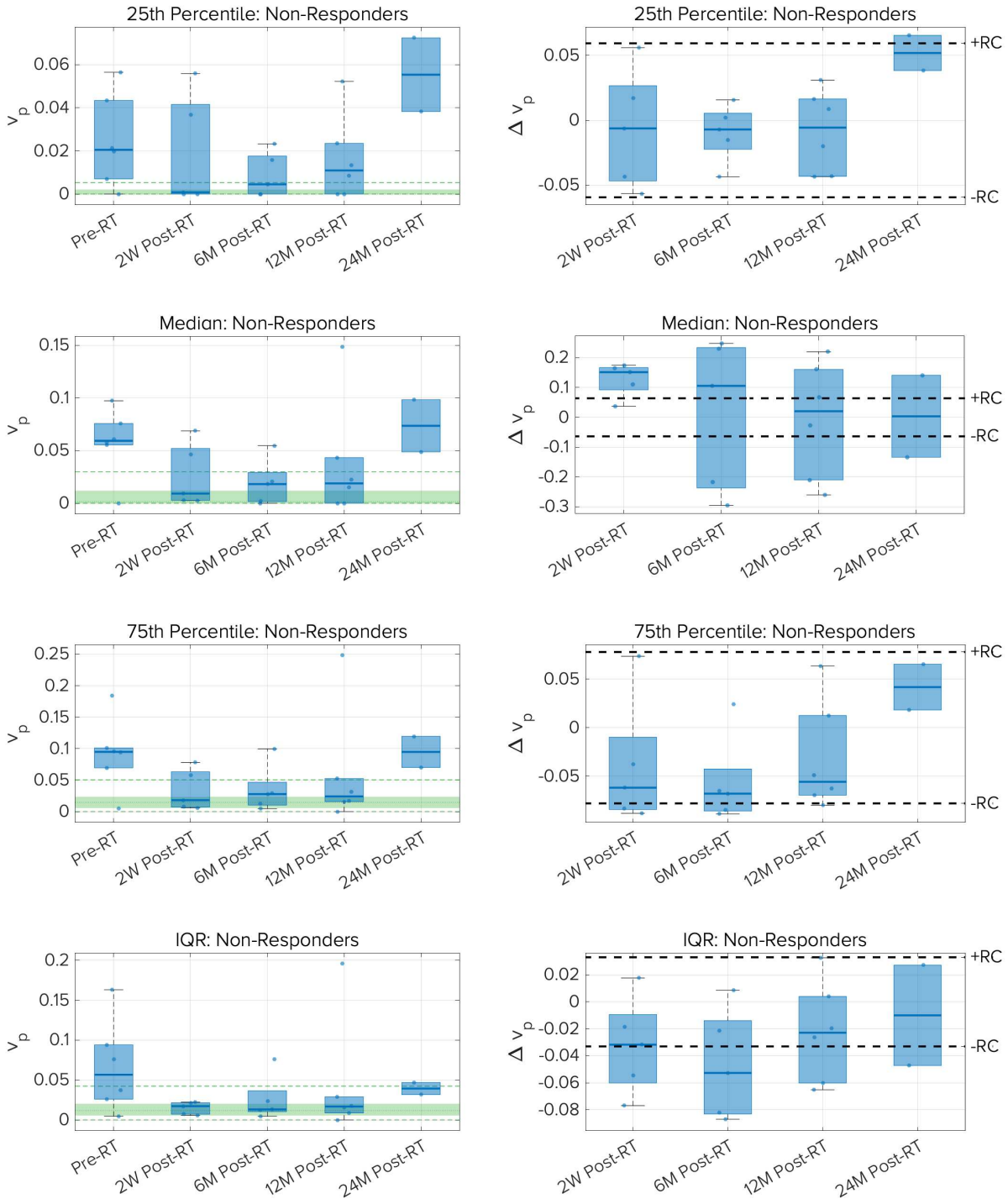


Figure B.39: (Left) The v_p statistics (25th percentile, median, 75th percentile, and IQR) derived from the dynamic contrast-enhanced MRI data of the entire breast tumour, pre-RT (N=6) and at 2-week (N=5), 6-month (N=5), 12-month (N=6) and 24-month (N=2) post-radiotherapy (RT) for the non-responders. (Right) The change in the v_p statistics from baseline (pre-RT) at 2-week (N=5), 6-month (N=5), 12-month (N=6) and 24-month (N=2) post-radiotherapy (RT). The dots are individual participants. The green shaded area is the 25th and 75th percentile range of the healthy breast, and the dashed green lines are the whiskers.

Semi-Quantitative Parameters

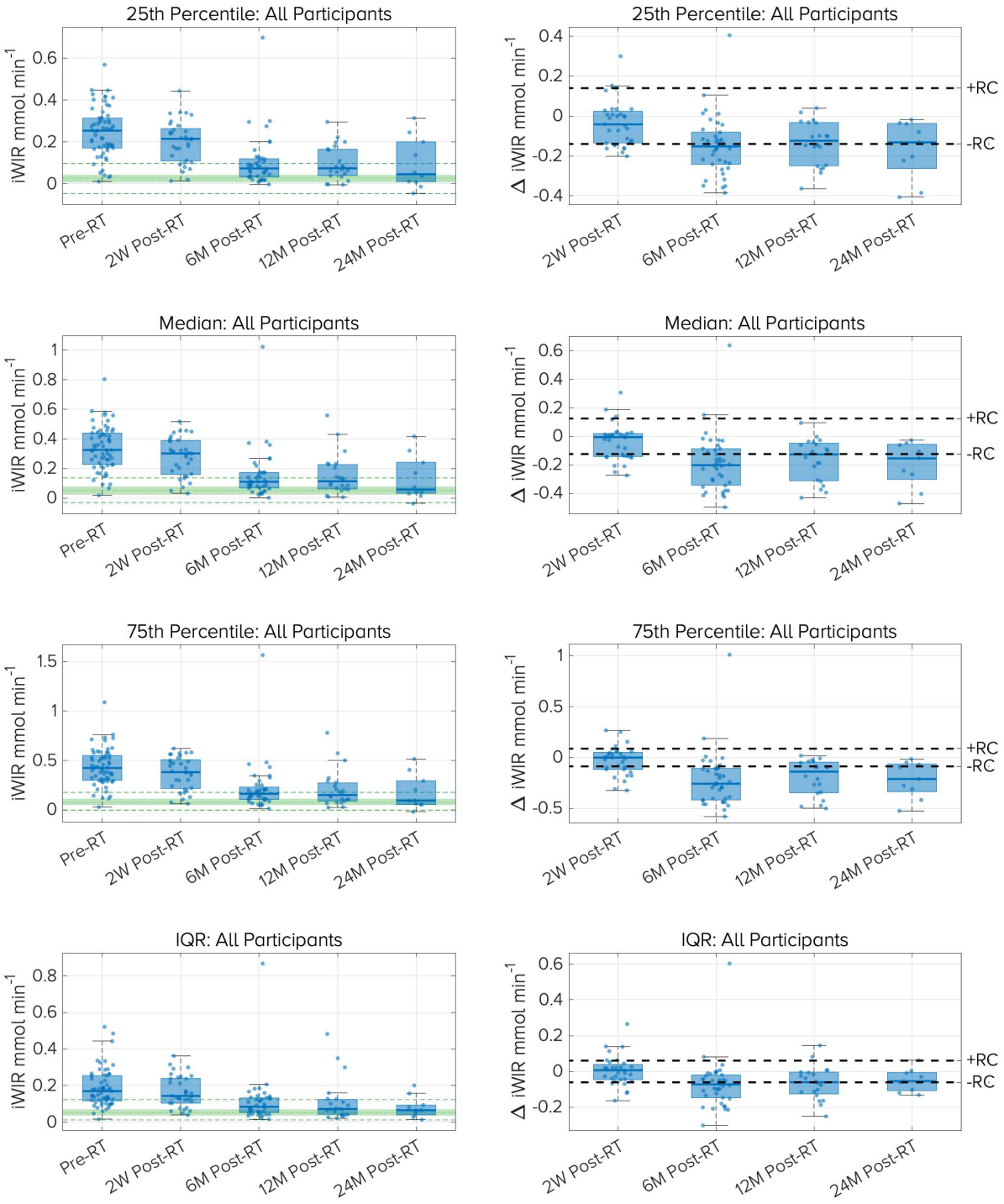


Figure B.40: (Left) The *iWIR* statistics (25th percentile, median, 75th percentile, and IQR) derived from the dynamic contrast-enhanced MRI data of the entire breast tumour, pre-RT (N=59) and at 2-week (N=32), 6-month (N=40), 12-month (N=22) and 24-month (N=10) post-radiotherapy (RT) for all participants. (Right) The change in the *iWIR* statistics from baseline (pre-RT) at 2-week (N=34), 6-month (N=38), 12-month (N=21) and 24-month (N=9) post-radiotherapy (RT). The dots are individual participants. The green shaded area is the 25th and 75th percentile range of the healthy breast, and the dashed green lines are the whiskers.

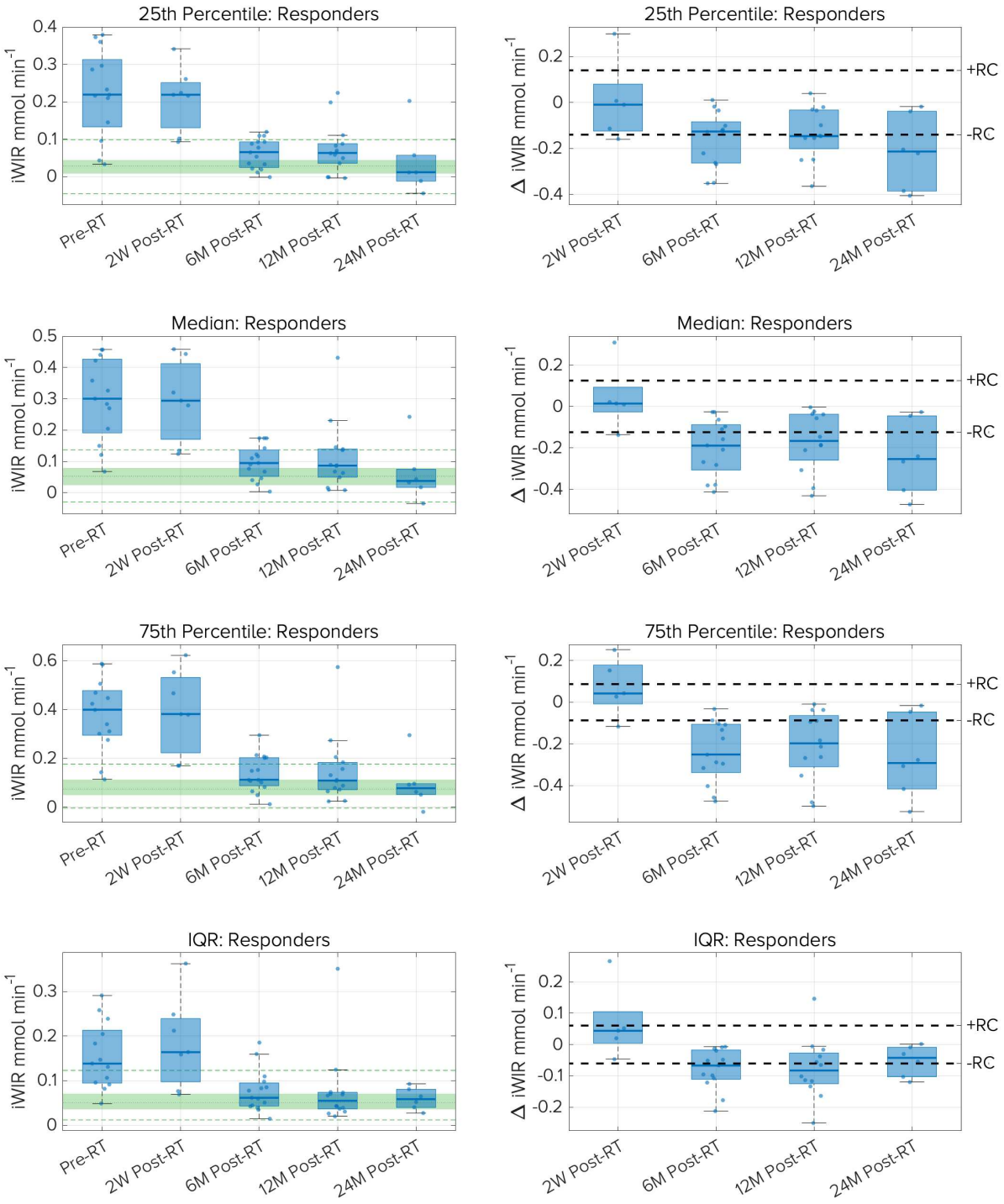


Figure B.41: (Left) The *iWIR* statistics (25th percentile, median, 75th percentile, and IQR) derived from the dynamic contrast-enhanced MRI data of the entire breast tumour, pre-RT (N=13) and at 2-week (N=7), 6-month (N=15), 12-month (N=14) and 24-month (N=6) post-radiotherapy (RT) for the responders. (Right) The change in the *iWIR* statistics from baseline (pre-RT) at 2-week (N=5), 6-month (N=13), 12-month (N=12) and 24-month (N=6) post-radiotherapy (RT). The dots are individual participants. The green shaded area is the 25th and 75th percentile range of the healthy breast, and the dashed green lines are the whiskers.

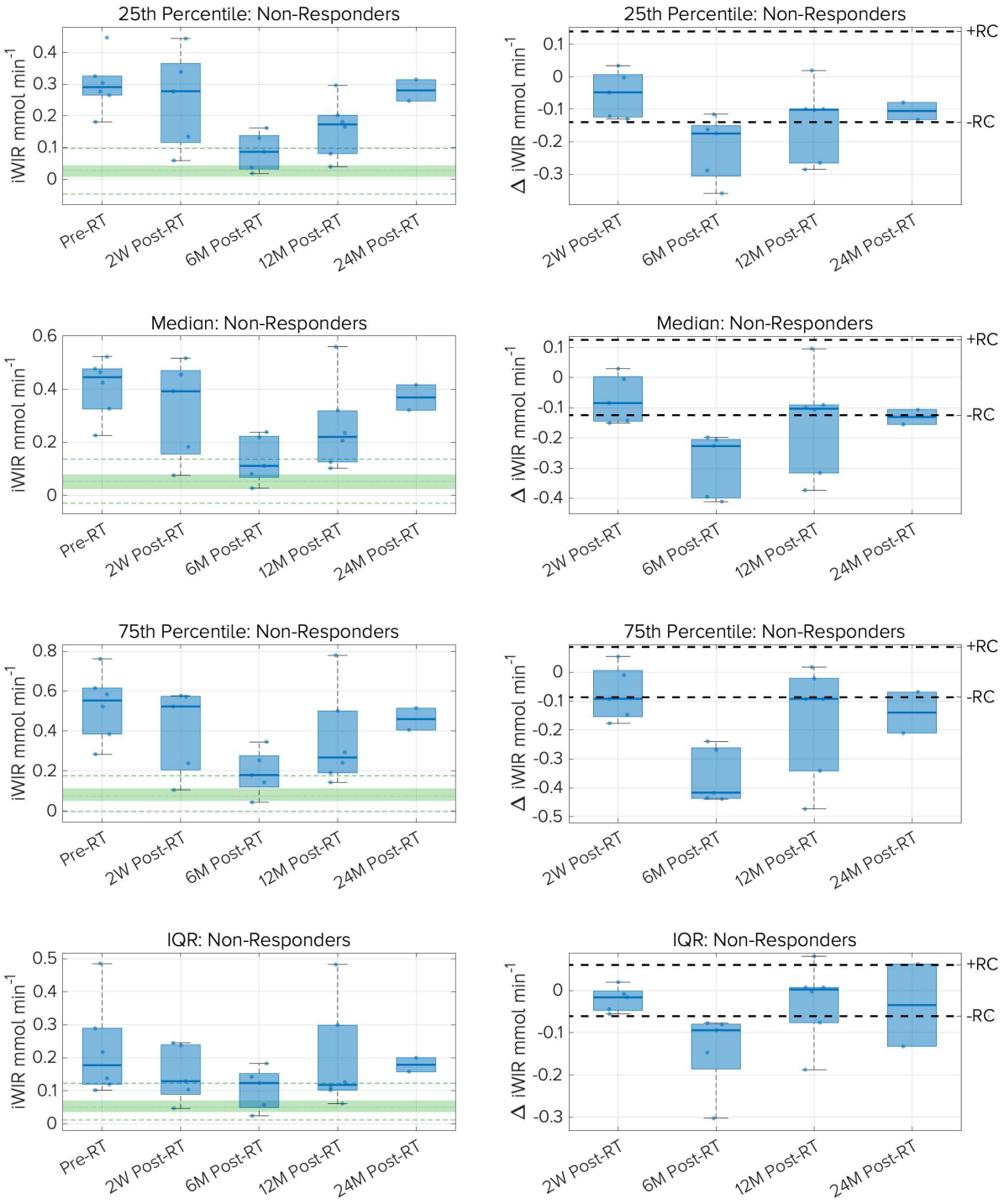


Figure B.42: (Left) The *iWIR* statistics (25th percentile, median, 75th percentile, and IQR) derived from the dynamic contrast-enhanced MRI data of the entire breast tumour, pre-RT (N=6) and at 2-week (N=5), 6-month (N=5), 12-month (N=6) and 24-month (N=2) post-radiotherapy (RT) for the non-responders. (Right) The change in the *iWIR* statistics from baseline (pre-RT) at 2-week (N=5), 6-month (N=5), 12-month (N=6) and 24-month (N=2) post-radiotherapy (RT). The dots are individual participants. The green shaded area is the 25th and 75th percentile range of the healthy breast, and the dashed green lines are the whiskers.

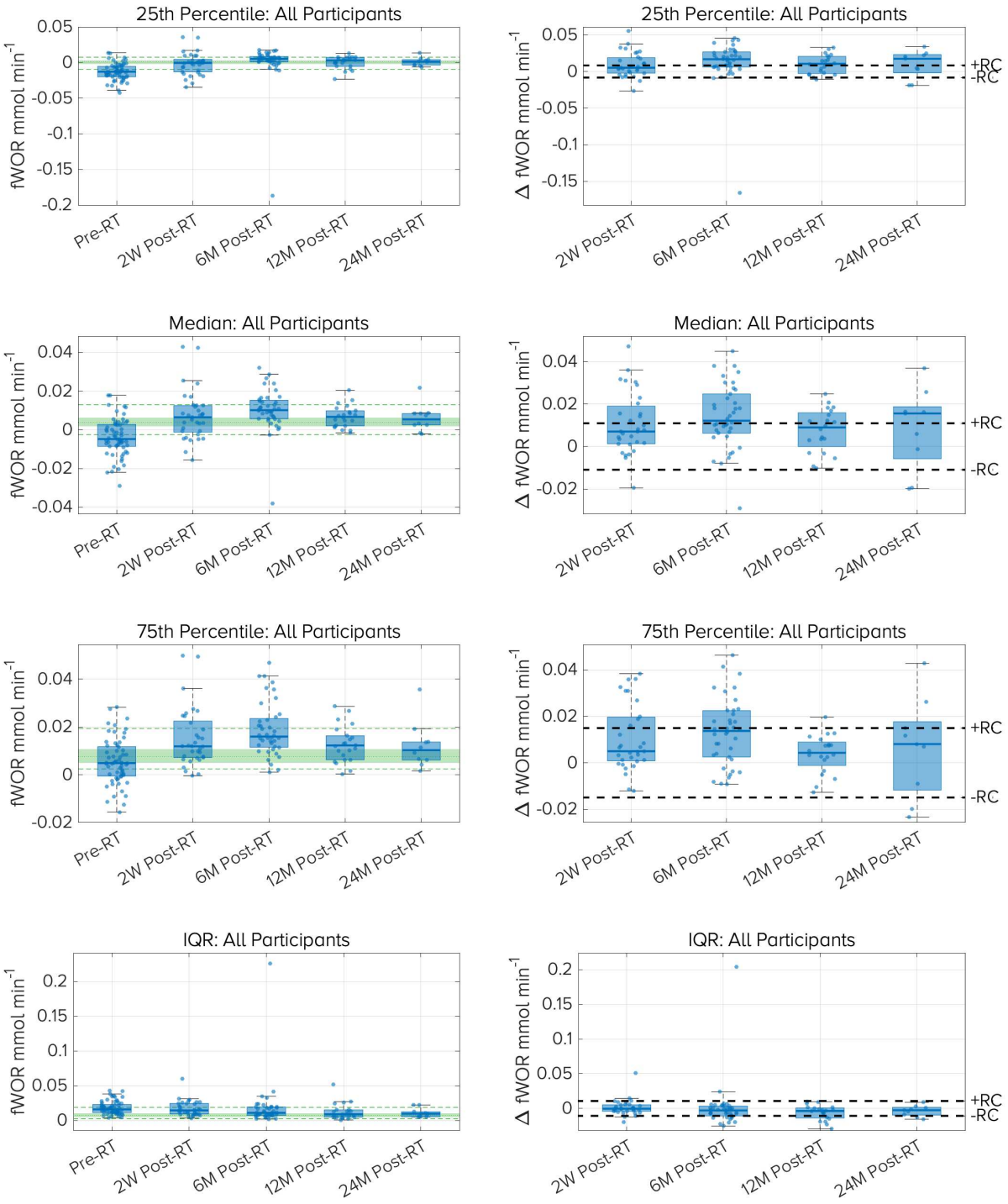


Figure B.43: (Left) The $fWOR$ statistics (25th percentile, median, 75th percentile, and IQR) derived from the dynamic contrast-enhanced MRI data of the entire breast tumour, pre-RT (N=59) and at 2-week (N=32), 6-month (N=40), 12-month (N=22) and 24-month (N=10) post-radiotherapy (RT) for all participants. (Right) The change in the $fWOR$ statistics from baseline (pre-RT) at 2-week (N=34), 6-month (N=38), 12-month (N=21) and 24-month (N=9) post-radiotherapy (RT). The dots are individual participants. The green shaded area is the 25th and 75th percentile range of the healthy breast, and the dashed green lines are the whiskers.

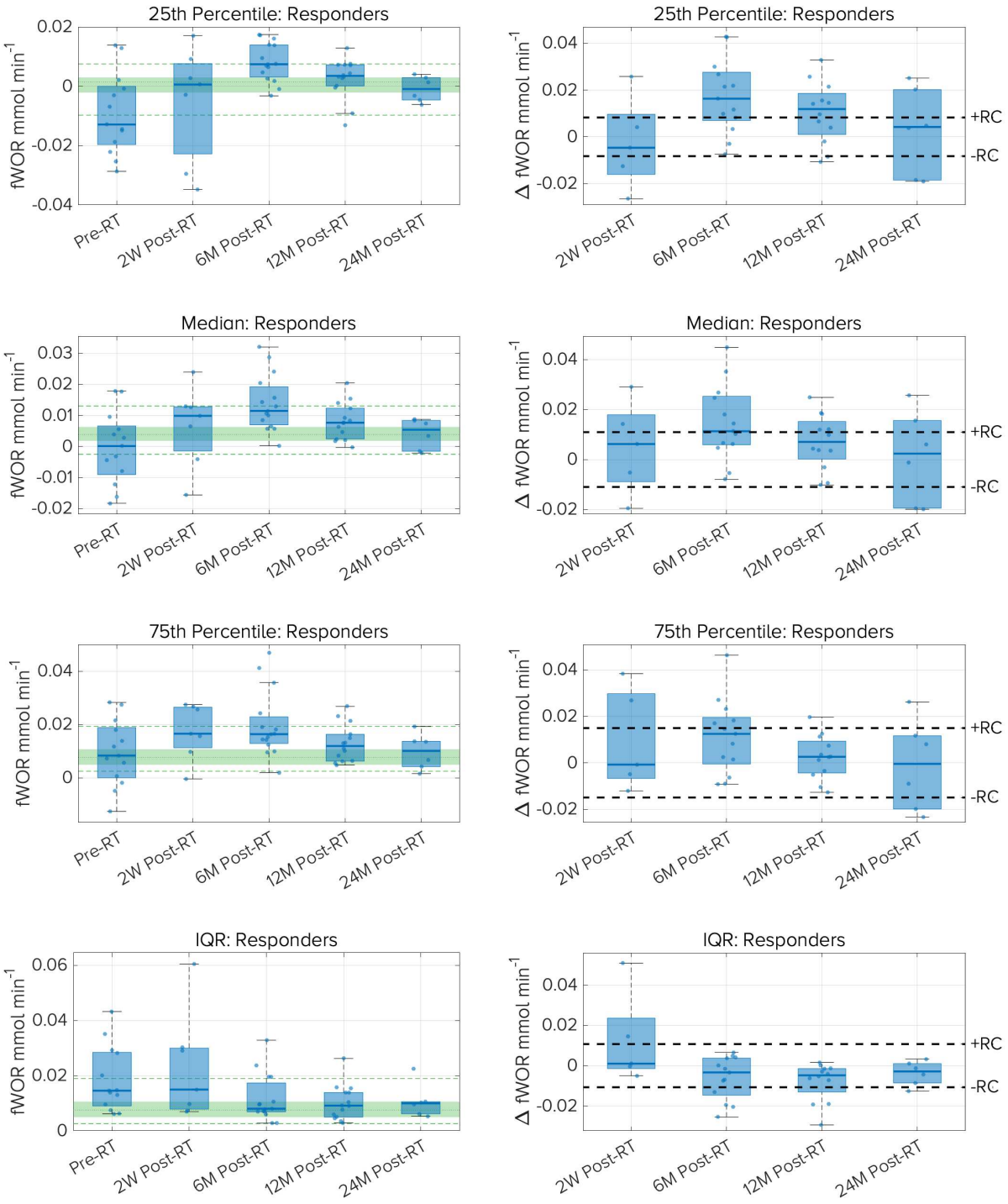


Figure B.44: (Left) The $fWOR$ statistics (25th percentile, median, 75th percentile, and IQR) derived from the dynamic contrast-enhanced MRI data of the entire breast tumour, pre-RT (N=13) and at 2-week (N=7), 6-month (N=15), 12-month (N=14) and 24-month (N=6) post-radiotherapy (RT) for the responders. (Right) The change in the $fWOR$ statistics from baseline (pre-RT) at 2-week (N=5), 6-month (N=13), 12-month (N=12) and 24-month (N=6) post-radiotherapy (RT). The dots are individual participants. The green shaded area is the 25th and 75th percentile range of the healthy breast, and the dashed green lines are the whiskers.

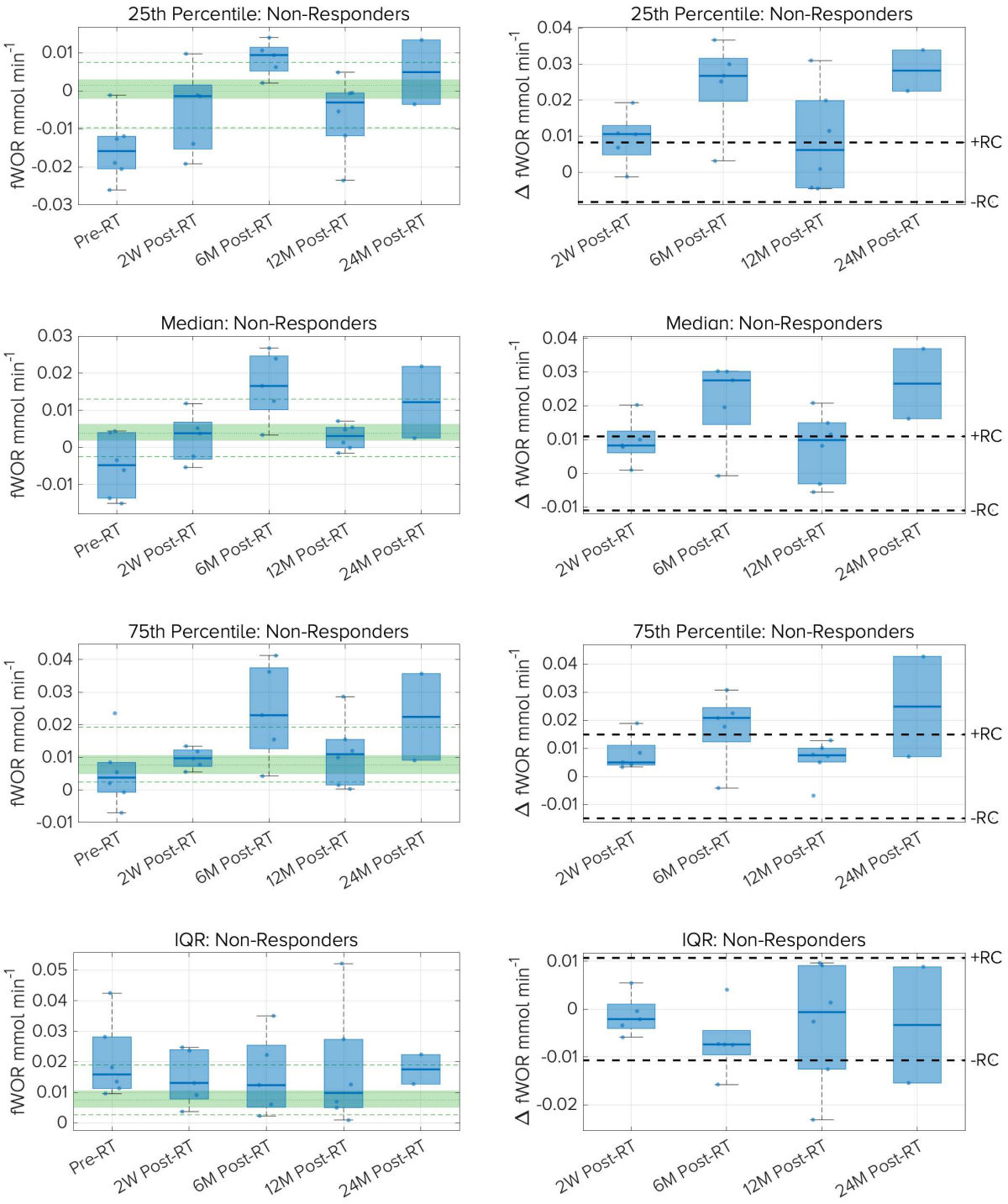


Figure B.45: (Left) The $fWOR$ statistics (25th percentile, median, 75th percentile, and IQR) derived from the dynamic contrast-enhanced MRI data of the entire breast tumour, pre-RT (N=6) and at 2-week (N=5), 6-month (N=5), 12-month (N=6) and 24-month (N=2) post-radiotherapy (RT) for the non-responders. (Right) The change in the f_{WOR} statistics from baseline (pre-RT) at 2-week (N=5), 6-month (N=5), 12-month (N=6) and 24-month (N=2) post-radiotherapy (RT). The dots are individual participants. The green shaded area is the 25th and 75th percentile range of the healthy breast, and the dashed green lines are the whiskers.

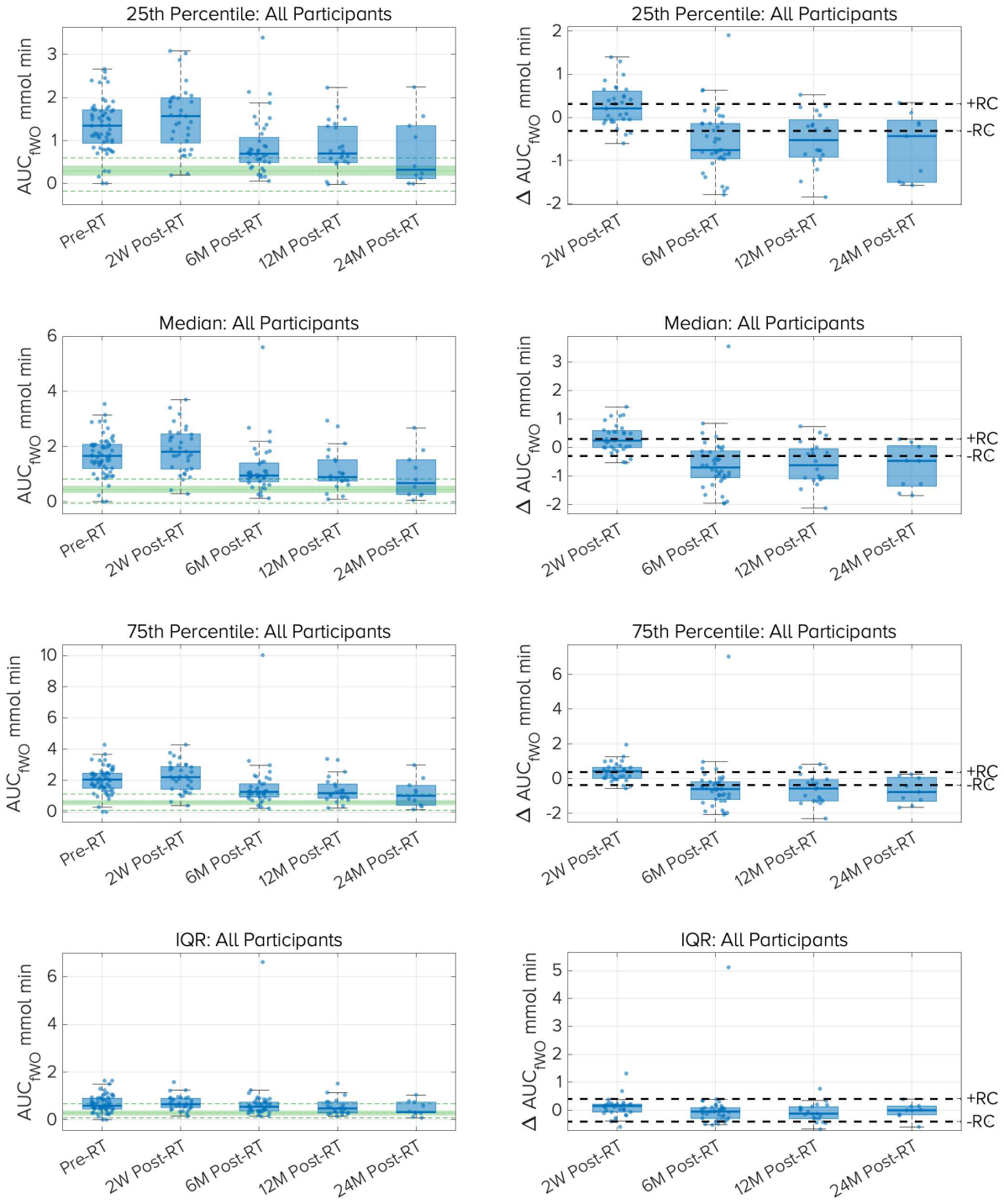


Figure B.46: (Left) The AUC_{fWO} statistics (25th percentile, median, 75th percentile, and IQR) derived from the dynamic contrast-enhanced MRI data of the entire breast tumour, pre-RT (N=59) and at 2-week (N=32), 6-month (N=40), 12-month (N=22) and 24-month (N=10) post-radiotherapy (RT) for all participants. (Right) The change in the AUC_{fWO} statistics from baseline (pre-RT) at 2-week (N=34), 6-month (N=38), 12-month (N=21) and 24-month (N=9) post-radiotherapy (RT). The dots are individual participants. The green shaded area is the 25th and 75th percentile range of the healthy breast, and the dashed green lines are the whiskers.

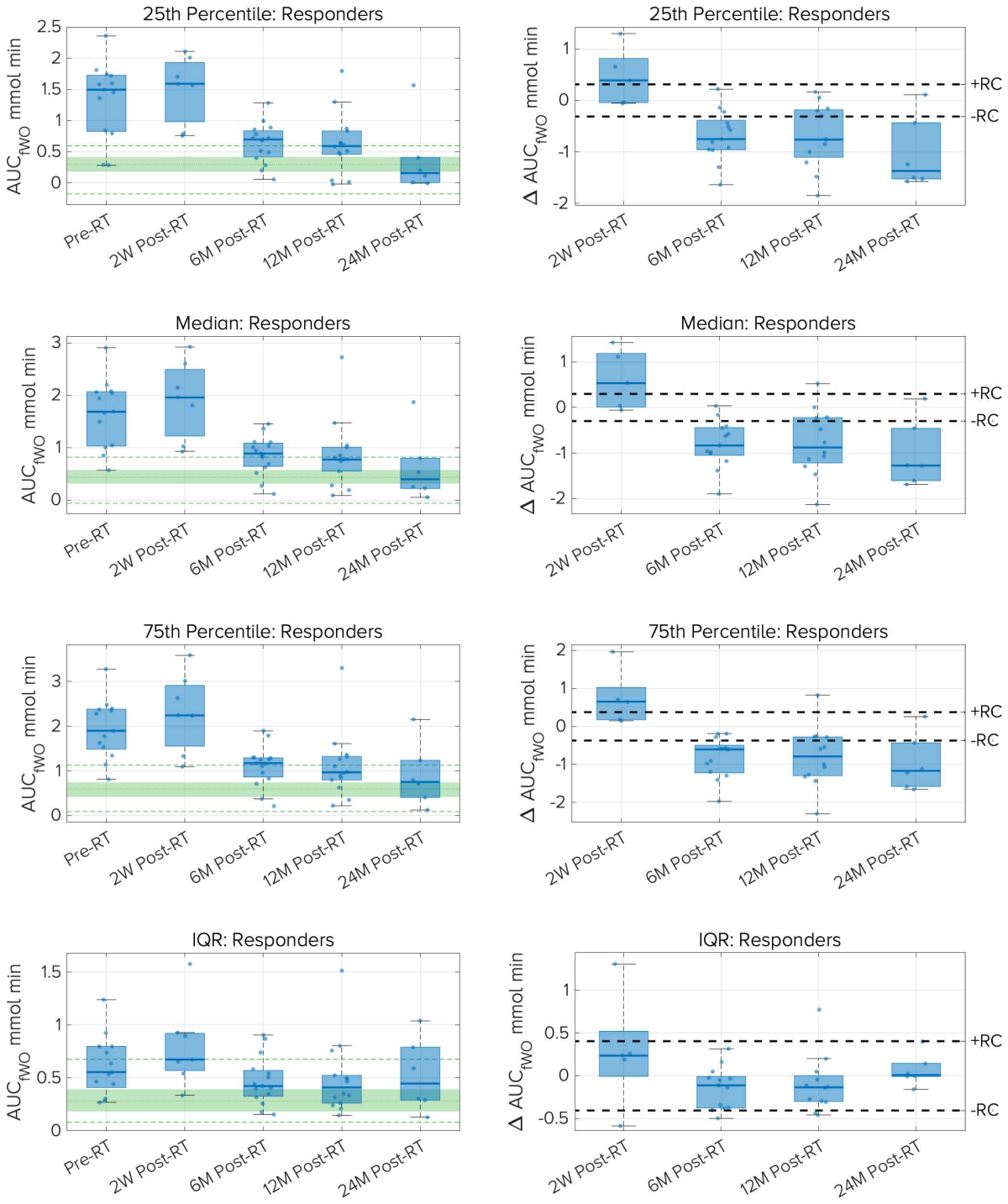


Figure B.47: (Left) The AUC_{fWO} statistics (25th percentile, median, 75th percentile, and IQR) derived from the dynamic contrast-enhanced MRI data of the entire breast tumour, pre-RT (N=13) and at 2-week (N=7), 6-month (N=15), 12-month (N=14) and 24-month (N=6) post-radiotherapy (RT) for the responders. (Right) The change in the AUC_{fWO} statistics from baseline (pre-RT) at 2-week (N=5), 6-month (N=13), 12-month (N=12) and 24-month (N=6) post-radiotherapy (RT). The dots are individual participants. The green shaded area is the 25th and 75th percentile range of the healthy breast, and the dashed green lines are the whiskers.

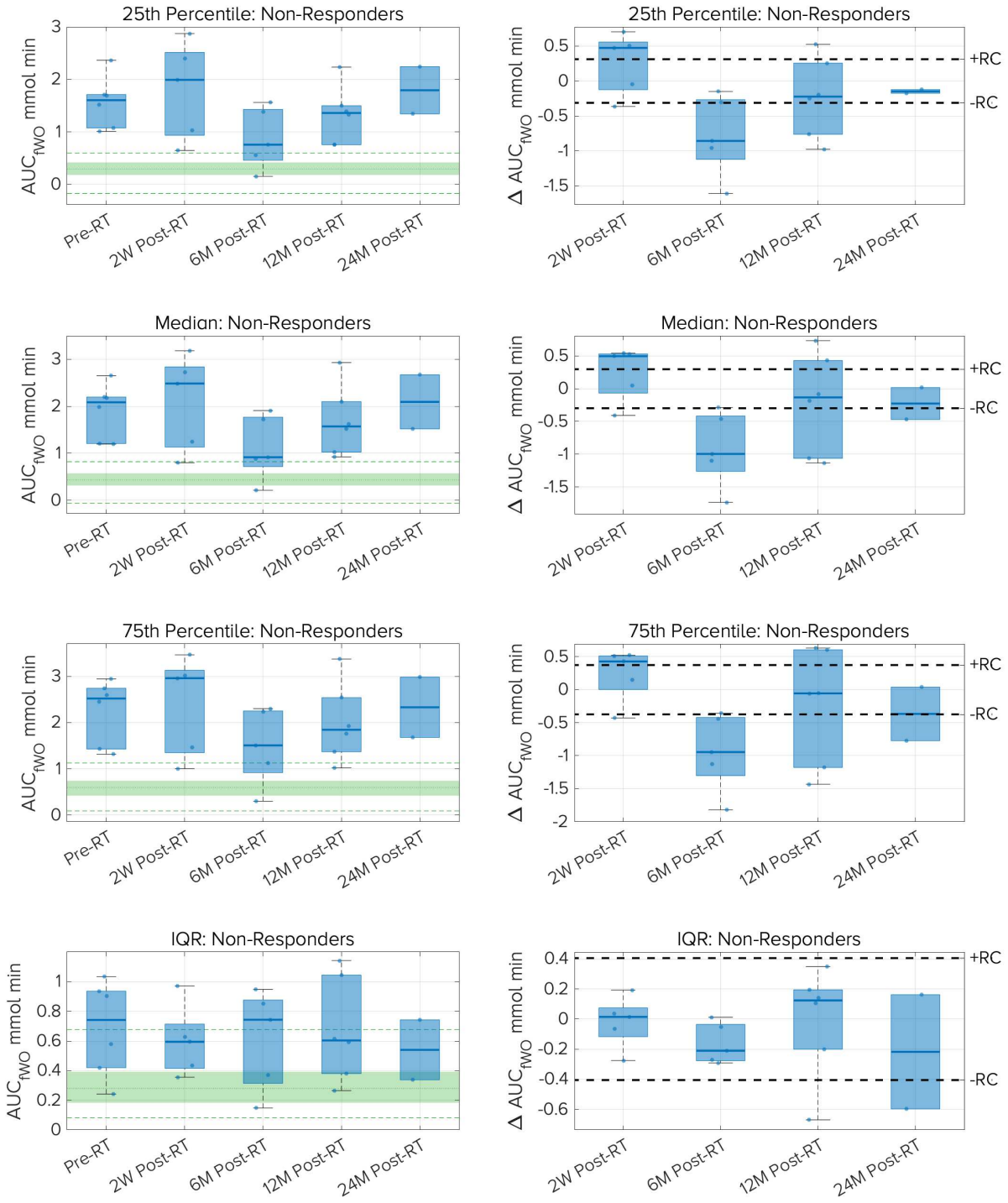


Figure B.48: (Left) The AUC_{fWO} statistics (25th percentile, median, 75th percentile, and IQR) derived from the dynamic contrast-enhanced MRI data of the entire breast tumour, pre-RT (N=6) and at 2-week (N=5), 6-month (N=5), 12-month (N=6) and 24-month (N=2) post-radiotherapy (RT) for the non-responders. (Right) The change in the AUC_{fWO} statistics from baseline (pre-RT) at 2-week (N=5), 6-month (N=5), 12-month (N=6) and 24-month (N=2) post-radiotherapy (RT). The dots are individual participants. The green shaded area is the 25th and 75th percentile range of the healthy breast, and the dashed green lines are the whiskers.

B.2.3 Estimating Response

Tofts Model Parameters

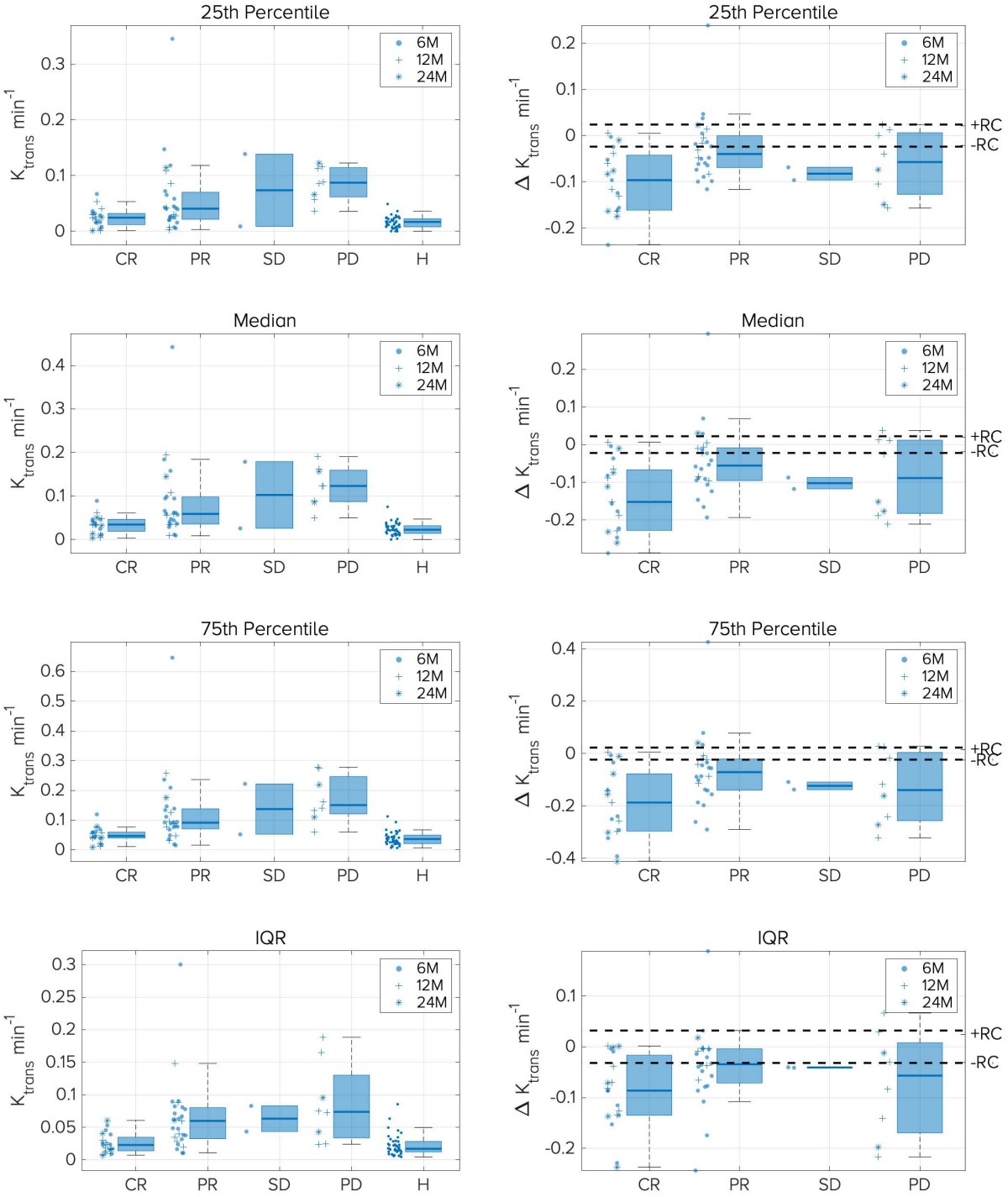


Figure B.49: Boxplots of the K_{trans} metrics (25th percentile, median, 75th percentile and IQR) and their radiological response assessment at 6-months (blue dot), 12-months (blue plus) and 24-months (blue asterisk). The radiological response assessment groups are complete response (CR), partial response (PR), stable disease (SD) and progressive disease (PD). On the left is the absolute values, and on the right is the change from baseline; the dashed lines are the repeatability coefficients, and changes beyond this are significent changes.

Semi-Quantitative Parameters

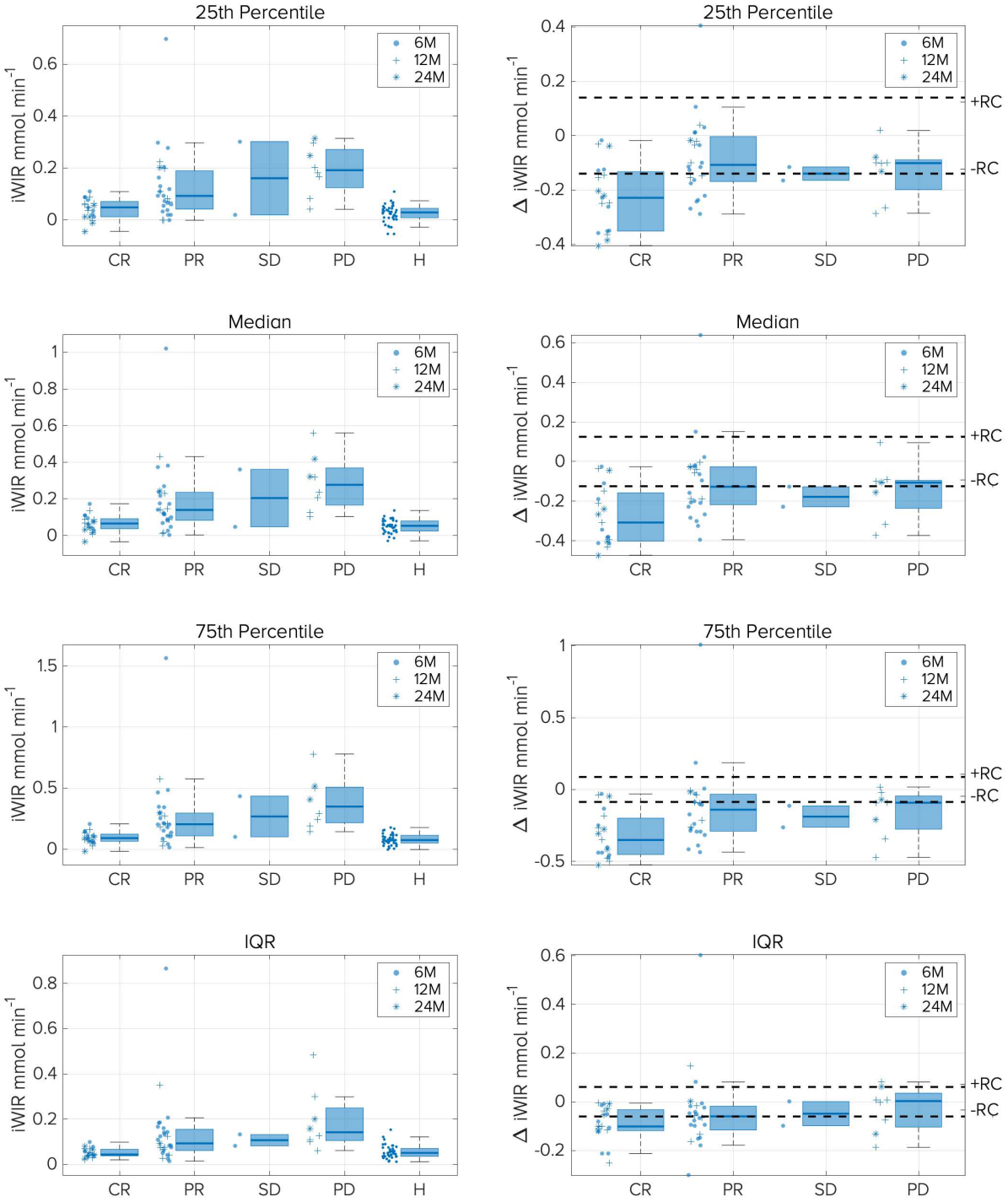


Figure B.50: Boxplots of the *iWIR* metrics (25th percentile, median, 75th percentile and IQR) and their radiological response assessment at 6-months (blue dot), 12-months (blue plus) and 24-months (blue asterisk). The radiological response assessment groups are complete response (CR), partial response (PR), stable disease (SD) and progressive disease (PD). On the left is the absolute values, and on the right is the change from baseline; the dashed lines are the repeatability coefficients, and changes beyond this are significant changes.

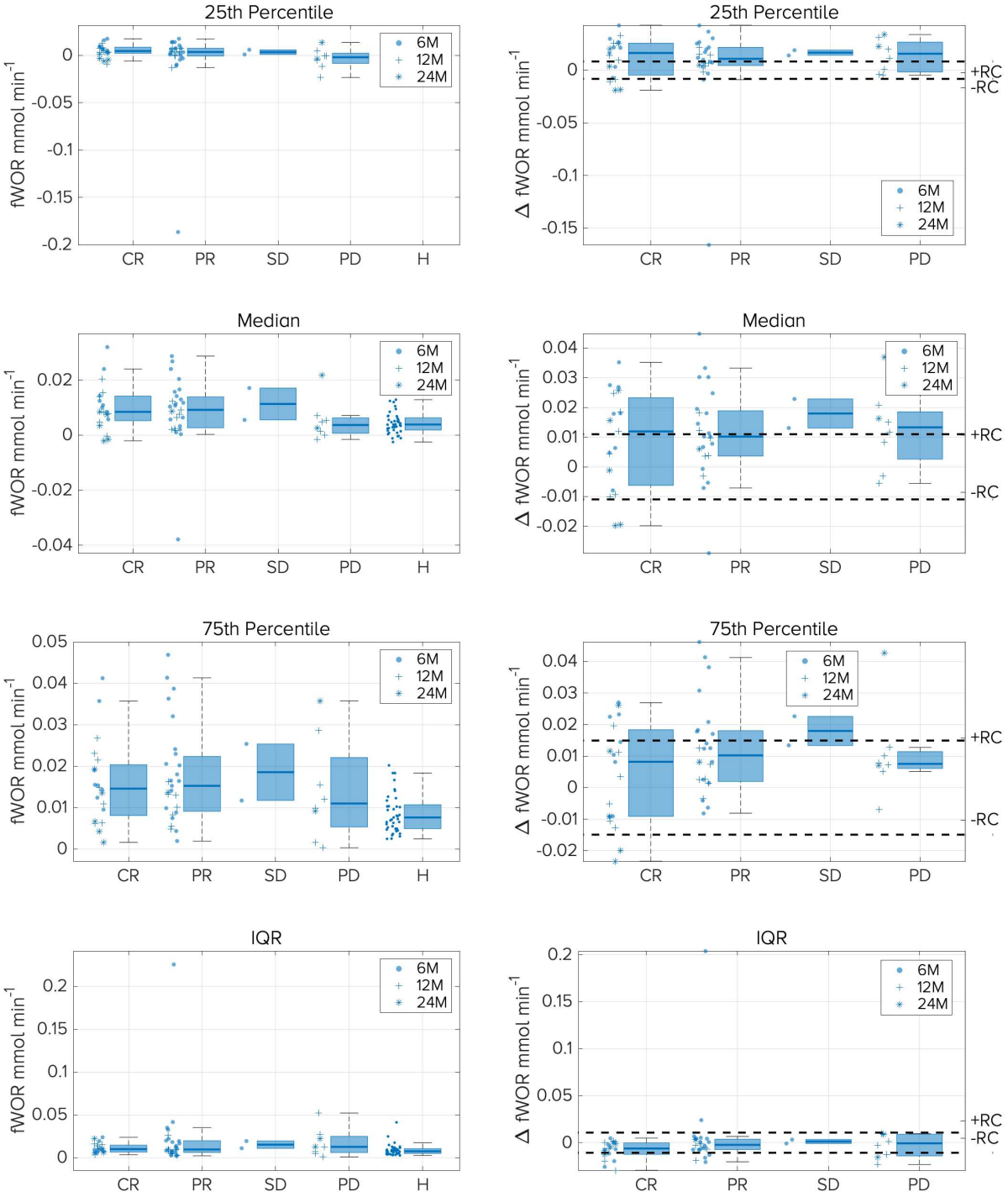


Figure B.51: Boxplots of the $fWOR$ metrics (25th percentile, median, 75th percentile and IQR) and their radiological response assessment at 6-months (blue dot), 12-months (blue plus) and 24-months (blue asterisk). The radiological response assessment groups are complete response (CR), partial response (PR), stable disease (SD) and progressive disease (PD). On the left is the absolute values, and on the right is the change from baseline; the dashed lines are the repeatability coefficients, and changes beyond this are significent changes.

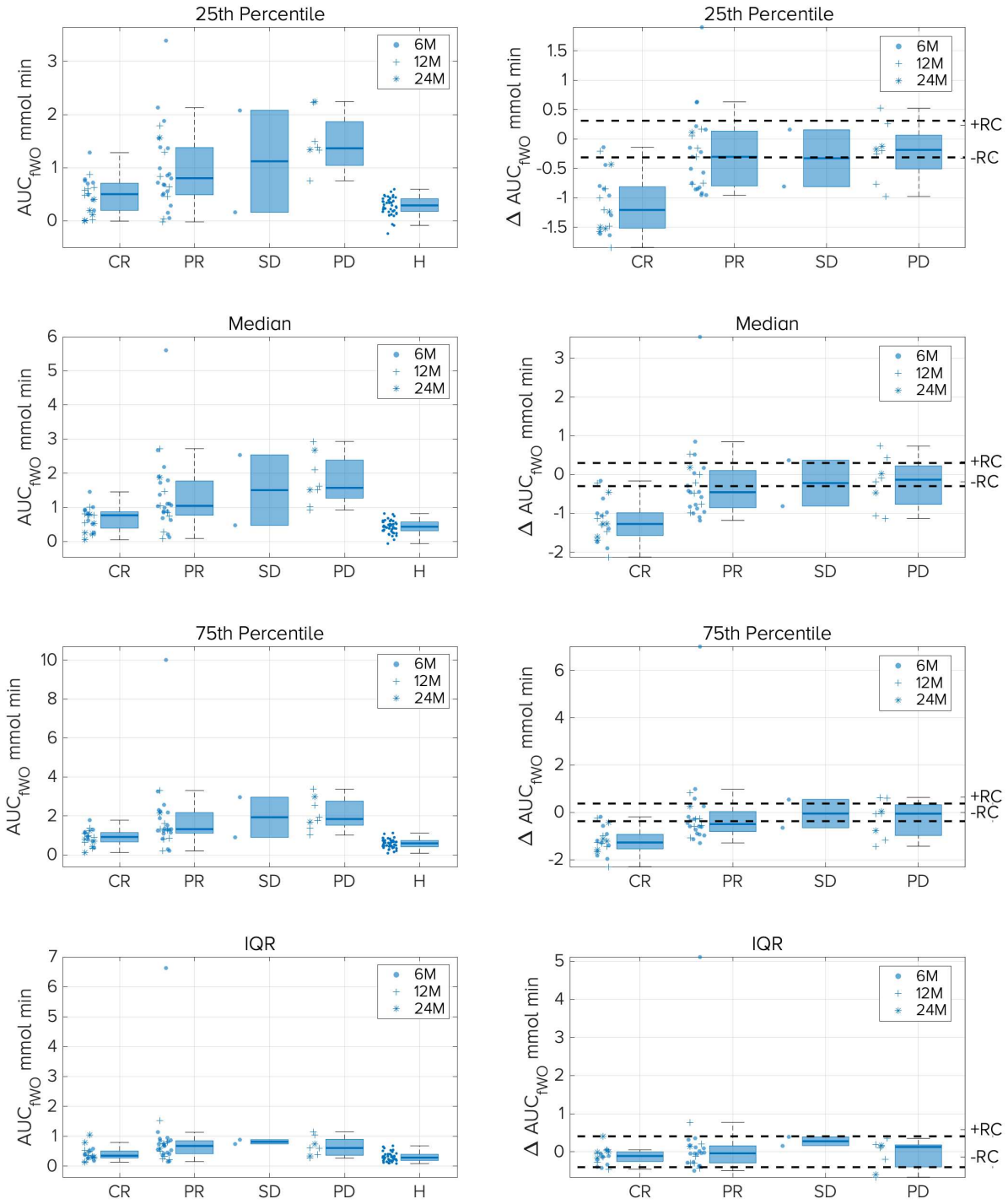


Figure B.52: Boxplots of the AUC_{fWO} metrics (25th percentile, median, 75th percentile and IQR) and their radiological response assessment at 6-months (blue dot), 12-months (blue plus) and 24-months (blue asterisk). The radiological response assessment groups are complete response (CR), partial response (PR), stable disease (SD) and progressive disease (PD). On the left is the absolute values, and on the right is the change from baseline; the dashed lines are the repeatability coefficients, and changes beyond this are significent changes.

B.3 Sub-Types

B.3.1 Tofts Model Parameters

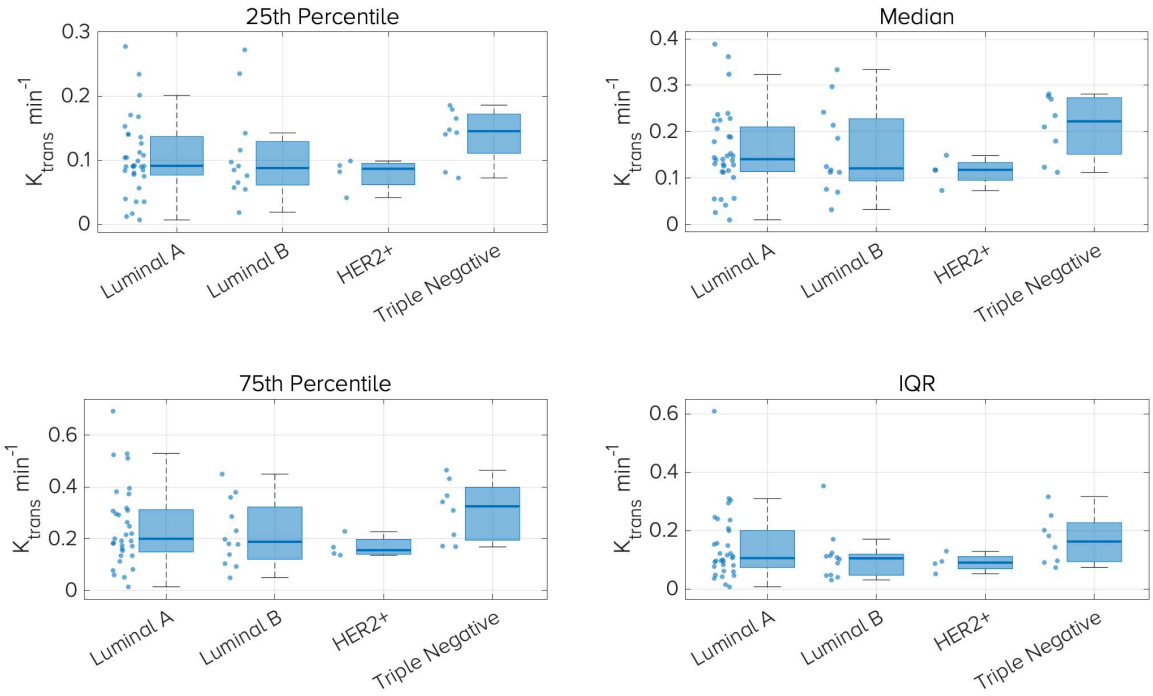


Figure B.53: Boxplots of the K_{trans} metrics (25th percentile, median, 75th percentile and IQR) and their subtypes. The subtype groups are Luminal A, Luminal B, HER2+ and Triple Negative.

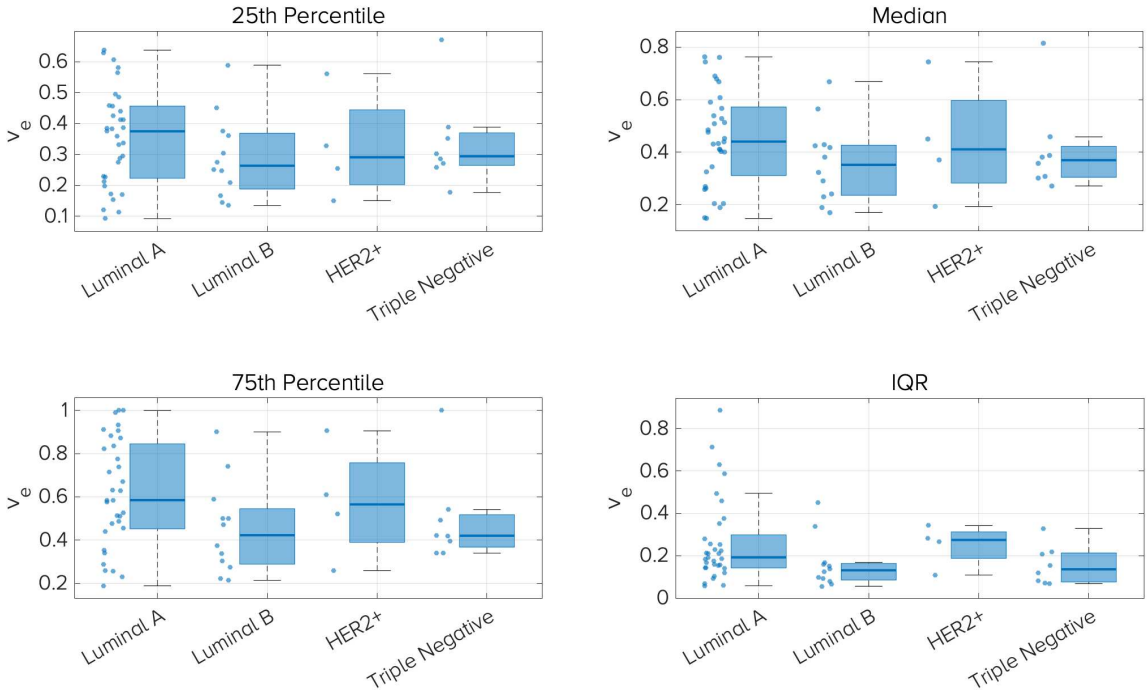


Figure B.54: Boxplots of the v_e metrics (25th percentile, median, 75th percentile and IQR) and their subtypes. The subtype groups are Luminal A, Luminal B, HER2+ and Triple Negative.

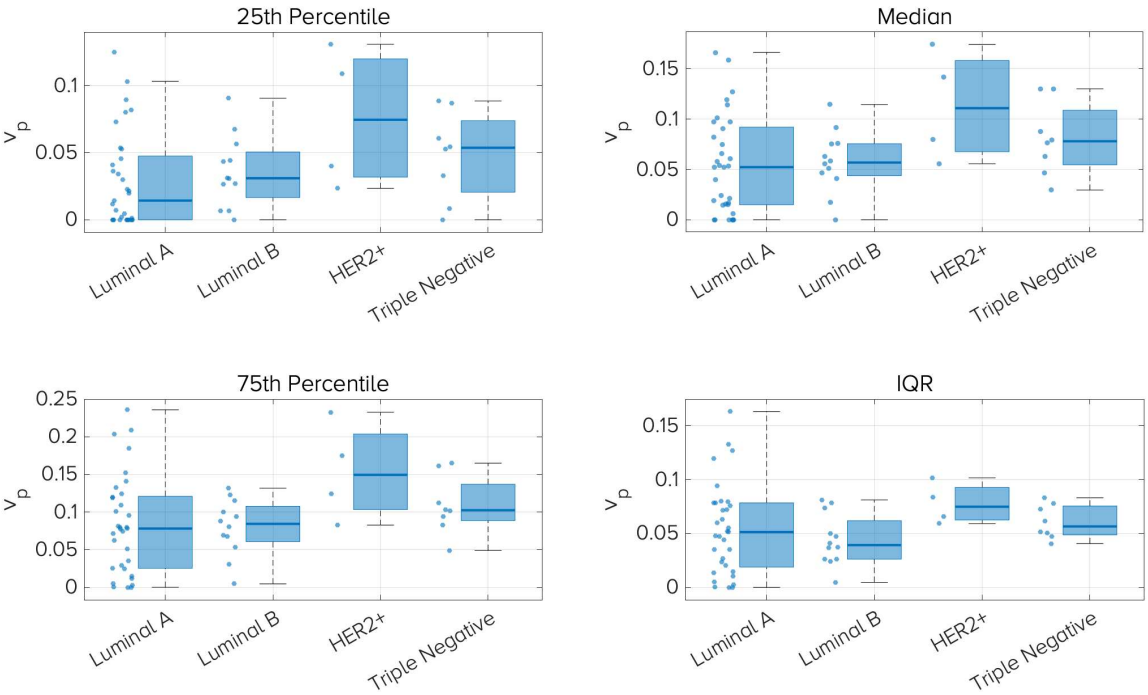


Figure B.55: Boxplots of the v_p metrics (25th percentile, median, 75th percentile and IQR) and their subtypes. The subtype groups are Luminal A, Luminal B, HER2+ and Triple Negative.

B.3.2 Semi-Quantitative Parameters

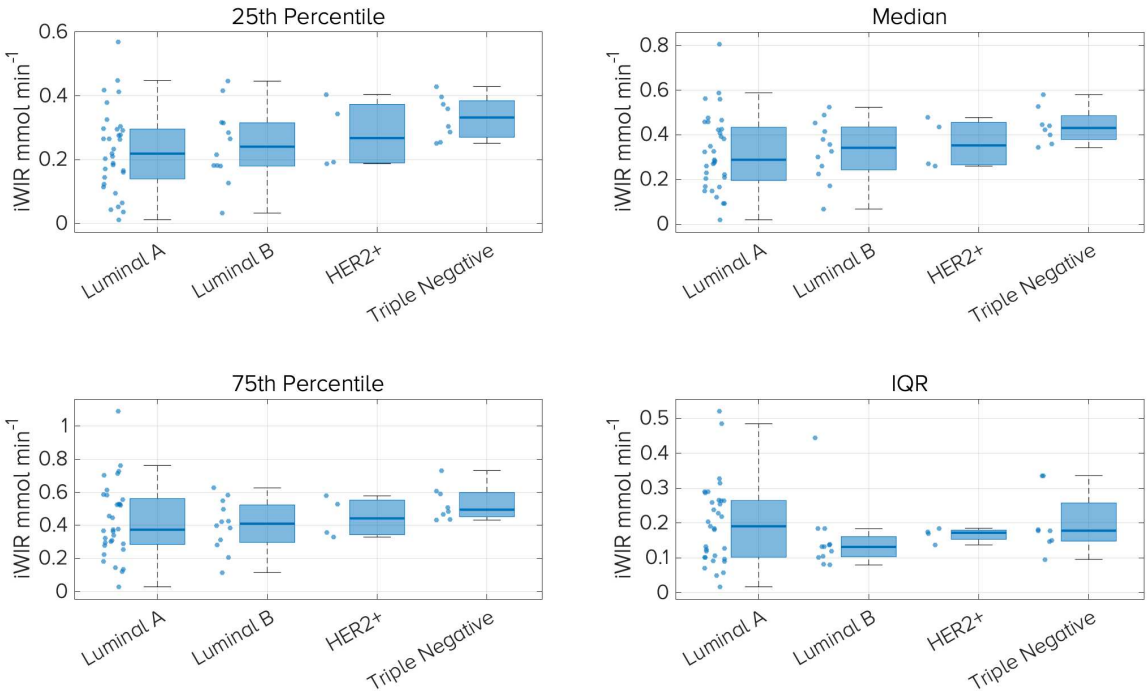


Figure B.56: Boxplots of the *iWIR* metrics (25th percentile, median, 75th percentile and IQR) and their subtypes. The subtype groups are Luminal A, Luminal B, HER2+ and Triple Negative.

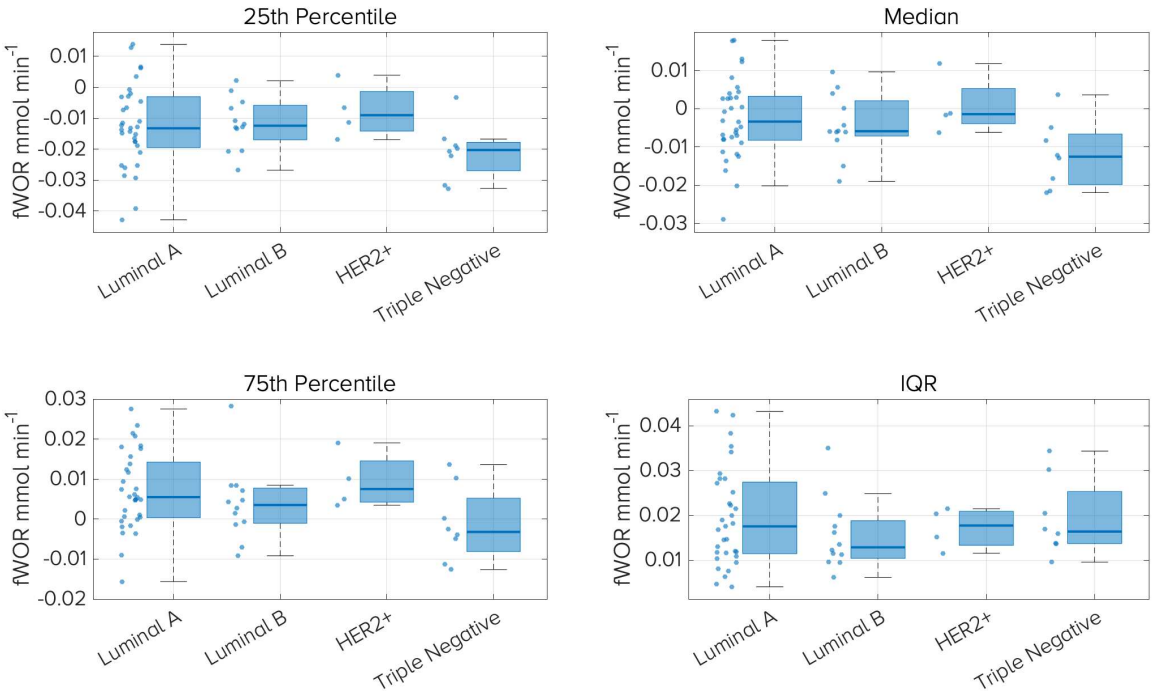


Figure B.57: Boxplots of the $fWOR$ metrics (25th percentile, median, 75th percentile and IQR) and their subtypes. The subtype groups are Luminal A, Luminal B, HER2+ and Triple Negative.

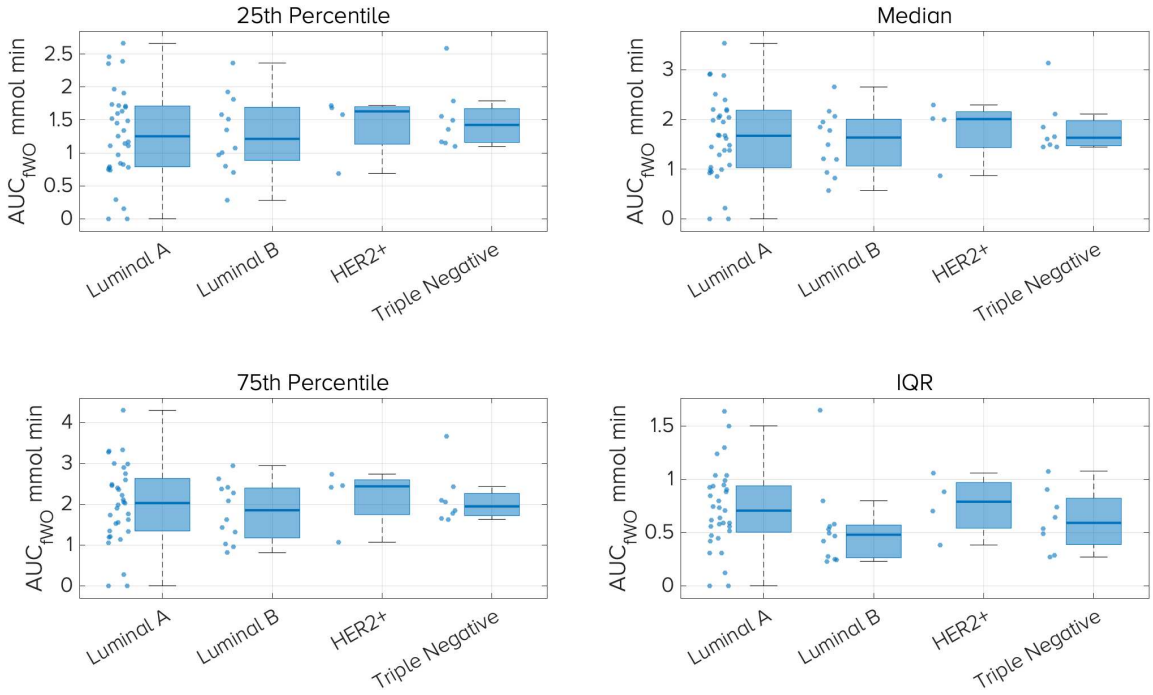


Figure B.58: Boxplots of the AUC_{fWO} metrics (25th percentile, median, 75th percentile and IQR) and their subtypes. The subtype groups are Luminal A, Luminal B, HER2+ and Triple Negative.